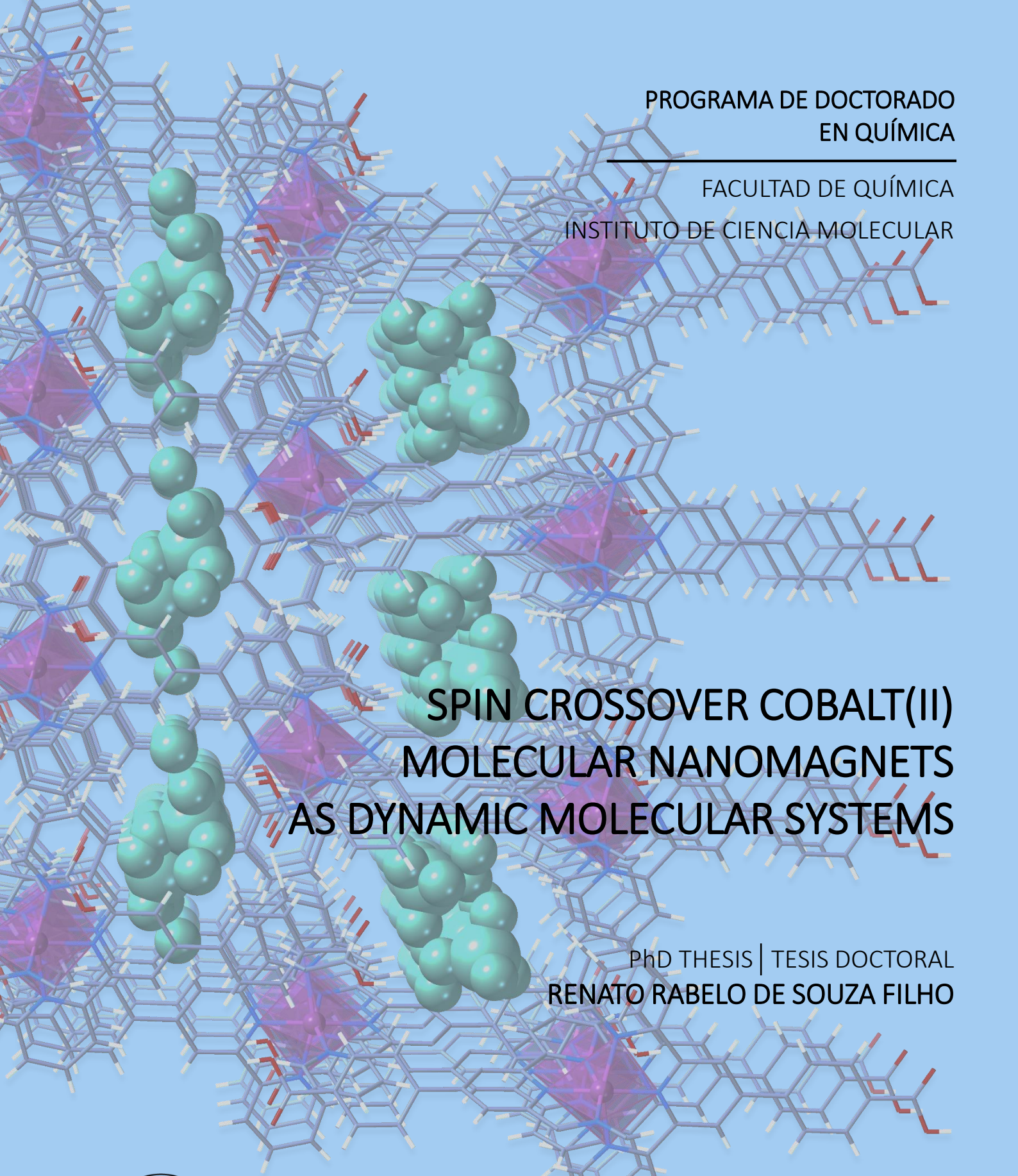

PROGRAMA DE DOCTORADO
EN QUÍMICA

FACULTAD DE QUÍMICA

INSTITUTO DE CIENCIA MOLECULAR

SPIN CROSSOVER COBALT(II) MOLECULAR NANOMAGNETS AS DYNAMIC MOLECULAR SYSTEMS

PhD THESIS | TESIS DOCTORAL

RENATO RABELO DE SOUZA FILHO

VNIVERSITAT DE VALÈNCIA

SUPERVISORS:
PROF. DR. FRANCISCO LLORET PASTOR
DR. JOAN CANO BOQUERA

June 2022

VNIVERSITAT DE VALÈNCIA

INSTITUTO DE CIENCIA MOLECULAR
UNIVERSITAT DE VALÈNCIA

Programa de Doctorado en Química (RD 99/2011) - Facultad de Química

Spin Crossover Cobalt(II) Molecular Nanomagnets as Dynamic Molecular Systems

From Molecular Magnetism towards Molecular Spintronics and Quantum Computing Technologies

Tesis Doctoral

Renato Rabelo de Souza Filho

June 2022

Dirigida por los Drs.:

Francisco Lloret Pastor y Joan Cano Boquera

Dr. Francisco Lloret Pastor, Catedrático del Departamento de Química Inorgánica de la Universidad de Valencia, y

Dr. Juan Bernardo Cano Boquera, Profesor Titular del Departamento de Química Inorgánica de la Universidad de Valencia,

CERTIFICAN:

Que el trabajo que presenta **Renato Rabelo de Souza Filho** en esta memoria titulada "**Spin Crossover Cobalt(II) Molecular Nanomagnets as Dynamic Molecular Systems**", en el marco del Programa de Doctorado en Química, para optar al título de Doctor en Química ha sido realizado bajo nuestra dirección en el Instituto de Ciencia Molecular de la Universidad de Valencia.

Para que así conste, firmamos el presente certificado.

Fdo.: Francisco Lloret Pastor

Fdo.: Juan Bernardo Cano Boquera

Valencia, 03 de junio de 2022.

Yo no sé lo que es el destino.

Caminando fui lo que fui.

(Silvio Rodríguez)

TABLE OF CONTENTS

ACKNOWLEDGEMENTS

ABSTRACT

SINOPSIS

CHAPTER I – INTRODUCTION AND BACKGROUND 1

CHAPTER II – ELECTROCHEMICALLY-ACTIVE SPIN CROSSOVER MOLECULAR NANOMAGNETS (I) 15

II.1 – Background and Highlights 17

II.2 – Ligands Design and Synthetic Strategy 17

II.3 – Description of the Structures 18

II.4 – Electrochemical Properties 21

II.5 – Magnetic Properties and EPR Spectra 22

II.6 – Concluding Remarks 29

II.7 – Experimental Section 29

References

Supporting Information

CHAPTER III – ELECTROCHEMICALLY-ACTIVE SPIN CROSSOVER MOLECULAR NANOMAGNETS (II) 47

III.1 – Background and Highlights 49

III.2 – Ligands Design and Synthetic Strategy 49

III.3 – Description of the Structures 50

III.4 – Spectrochemical Properties 52

III.5 – Electrochemical Properties 55

III.6 – Magnetic Properties and EPR Spectra 56

III.7 – Proof-of-Concept of a Spin Electro-switch 59

III.8 – Concluding Remarks 61

III.9 – Experimental Section 61

References

Supporting Information

CHAPTER IV – LUMINESCENT SPIN CROSSOVER MOLECULAR NANOMAGNETS 87

IV.1 – Background and Highlights 89

IV.2 – Ligands Design and Synthetic Strategy 90

IV.3 – Thermal Stability 90
IV.4 – Description of the Structures 91
IV.5 – Sorption Properties 94
IV.6 – Magnetic Properties and EPR Spectra 95
IV.7 – Photophysical Properties 98
IV.6 – Proof-of-Concept of a Luminescent Spin Solvato-switch 99
IV.7 – Concluding Remarks 100
IV.8 – Experimental Section 101
References
Supporting Information

CHAPTER V – PHOTOCHEMICALLY-ACTIVE SPIN CROSSOVER MOLECULAR NANOMAGNETS 121
V.1 – Background and Highlights 123
V.2 – Ligands Design and Synthetic Strategy 123
V.3 – Description of the Structures 124
V.4 – Magnetic Properties and EPR Spectra 126
V.5 – Spectrophotochemical Solution Studies 128
V.6 – Concluding Remarks 129
V.7 – Experimental Section 129
References
Supporting Information

CHAPTER VI – CHEMICALLY-ACTIVE SPIN CROSSOVER MOLECULAR NANOMAGNETS 143
IV.1 – Background and Highlights 145
IV.2 – Ligands Design and Synthetic Strategy 145
IV.3 – Description of the Structures 146
IV.4 – Magnetic Properties and EPR Spectra 149
IV.5 – Proof-of-Concept of a Spin Chemo-switch 151
IV.7 – Concluding Remarks 154
IV.8 – Experimental Section 154
References
Supporting Information

CHAPTER VII – CONCLUSIONS AND OUTLOOK 177

RESUMEN 191

ACKNOWLEDGEMENTS

Existe un deslumbre en lo efímero. Quizás por esto trate con tanto romanticismo lo que tiene un fin inminente. ¿Hay alguien capaz de no ver la belleza en las flores? Tras cuatro años, solo tengo que agradecer y espero poder alcanzar con mis palabras de gratitud a los responsables por este periodo fundamental en mi vida.

Las páginas numeradas de 1 a 189 de esta tesis se encuentran rellenadas de experimentos, resultados y discusiones científicas que certifican la evolución de mi consciencia profesional durante cuatro años. En contrapartida, dispongo de estas pocas páginas para dedicarme a resaltar los responsables de mi crecimiento profesional y personal. La discrepancia no hace juicio a la importancia que ambas contribuciones tienen y a la gratitud que siento, pero haré lo posible para que, en pocas palabras, se quede todo registrado.

Primeramente, me gustaría agradecer a mi amiga, colaboradora y ex tutora Danielle, pues fue como todo comenzó. Cuando fui apenas un estudiante de inicio de grado que simplemente buscaba hacer trabajos en tu laboratorio para pasar mi tiempo libre en la universidad a cambio de una beca, supiste despertar en mí el interés por la investigación. Tu amistad y dedicación me inspiraron y las puertas que me has abierto me permitieron soñar a lo grande.

Rafa, no hay palabras que puedan expresar lo agradecido que seré contigo eternamente. Esta tesis doctoral no habría sido posible sin ti y, por ello, no hay otra persona a quien podría habérsela dedicado. Contagiado por tu enorme positividad, conseguí alcanzar el equilibrio necesario para seguir mejorando el trabajo. Siempre disponible y paciente, supiste aguantar mis días de mal humor cuando el mundo parecía tragarme. Te pido disculpas por ello. Sé que protesto mucho y debo concordar con que me merezco la fama de discutidor que me has asignado, pero la verdad disfruté de todas nuestras discusiones de ámbito científico. Fueron esenciales para mi formación y siento que el simple hecho de estar en tu presencia me ha hecho crecer. Gracias por compartir conmigo tus conocimientos y sabiduría, los cuales llevaré para siempre.

Paco y Miguel, gracias por haberme recibido con los brazos abiertos en el grupo de Química de Coordinación y ofrecido todas las oportunidades para formarme en la investigación científica. Gracias por preocuparos no solamente con mi futuro, sino también con mi presente en el día-a-día del laboratorio. Me siento afortunado por haber conocido a dos gigantes. Vuestra humildad y profunda pasión por la química se destacan en medio de un mundo académico actual donde se cultiva vanidad. Espero haber aprendido la lección y que no se me olvide: Solo es gigante aquél que sabe ser pequeño.

Cuando se trata de dejarse la piel para poner delante una prioridad ajena, Joan es invencible. Y con esta tesis doctoral no fue diferente. Gracias por haberme dedicado parte de tu recurso más escaso, el tiempo. Gracias también por la confianza depositada en mí. Espero algún día estar a la altura de un colaborador como tú y, quien sabe, retribuirte por todo lo que me fue enseñado. Tu trabajo arduo y constante te hace ocupar el puesto más alto entre los investigadores en los cuales quiero espejarme.

Nico, por un lado te tengo que dar las gracias por la importancia que tuviste en cuanto al carácter técnico de la tesis debido a darme prioridad a la hora de realizar medidas siempre que era posible y necesario, echándome una mano con ajustes, e incluso en tareas que no entran en tus actividades laborales. Por otro lado, gracias por las conversaciones amenas y las risas durante estos años que hemos compartido despacho y mesa al comer. Eres todo corazón. Que sepas que la propuesta sigue valiendo: ¡Me puedes adoptar cuando quieras!

A todos aquellos que cruzaron mi camino y decidieron quedarse, gracias por el abrazo constante. Estar a una distancia transatlántica de nuestro lugar de origen puede volverse complicado, pero vuestra presencia y cariño han matizado estos momentos e hicieron mis días más felices. Lumi, siempre haciendo juicio al nombre que te fue dado, por muchas veces me has escuchado y me guiaste a la dirección correcta para entenderme y entender quien quiero ser. A ti, a Filipe y a Mari Carmen, gracias por el cuidado y preocupación, por las palabras de consejo y calma, y por siempre extenderme la mano incluso antes del pedido de ayuda. Cristina y Fani, fui enamorado a la primera vista. Hay tanta luz en vosotras, que se me llena el corazón cuando estoy en vuestra presencia. Os llevo conmigo. Adrián, eres un tío formidable, de lo más auténtico que he visto y juntos hemos reído y sufrido mucho en el laboratorio (¡mola que flipas!). Ni fuerza, ni resistencia, ni mucho menos cuerpazo… El beneficio más grande que el gimnasio me podrá traer fue nuestra amistad, Marta P. y Carlos P. ¿¿¿Quién diría que se puede hacer buenos amigos allí??? A todas estas personas, independiente de lo que pase en los próximos años, yo sé que en el momento en que tengamos que despedirnos no será con un adiós.

Marta O., sin dudas es necesario dedicarte algunas palabras de gratitud. Al final, fuiste parte importante de mi larga estancia en Valencia. Sigo creyendo que nuestra amistad "hizo" todo el sentido en su momento y el apoyo mutuo que nos dimos fue indispensable para superar ciertas fases. A lo largo de estos cuatro años fueron muchas las horas compartidas, las cuales generaron muy buenos recuerdos. No los voy a olvidar. Hoy, dos personajes más conscientes, espero que sepamos emplear toda nuestra experiencia a favor de nuevas y más fuertes relaciones con quien nos rodea.

Una tesis no se hace solo. El trabajo presentado tiene la contribución fundamental de muchas personas a las cuales me gustaría agradecer por la ayuda y colaboración. Toda la base de los estudios presentados no habría sido posible sin la resolución de las estructuras cristalinas de los compuestos sintetizados. Por ello, debo agradecer especialmente a Jorge Pasán, miembro del Laboratorio de Rayos-X y Materiales Moleculares de la Universidad de la Laguna, por el interés en difractar los cristales y el detalle al refinar las estructuras, elevando la calidad del trabajo. A Enrique García España y Mario Inclán del grupo de Química Supramolecular por haberme autorizado el uso del fluorímetro, por el auxilio con los estudios en disolución y su posterior tratamiento. A Chema y Gloria, gracias por las innúmeras medidas físicas realizadas a lo largo de estos años, pero principalmente por toda la disponibilidad, buena voluntad, buen humor y empeño que siempre ponéis al hacerlas. También agradezco a Salah Stiriba y Pedro Amorós por el interés demostrado hacia mi trabajo, contribuyendo con tópicos de discusión que lo enriquecieron.

Mirando hacia tras, ha sido un camino bonito y yo no podría estar más contento con los resultados o más agradecido por la oportunidad y experiencia. Una etapa efímera de la cual, con nostalgia, me despido. Acerca de la pregunta que hice al inicio, aún me intriga la respuesta… Solía pensar que tontos eran los que no veían la belleza en las flores. Pero quizás tontos seamos nosotros. Aun sabiendo que los pétalos de las flores van a caer no dejamos de encantarnos con ellas.

ABSTRACT

Paramagnetic mononuclear 3d-metal complexes with tailor-made "non-innocent" ligands have recently emerged as archetypical examples of dynamic molecular systems (DMSs). The enormous impact of DMSs on several domains of molecular nanoscience and nanotechnology stands from their ability to perform specific and selective functions under the control of an external stimulus that appropriately tunes their structural and electronic (optical, redox, and magnetic) properties. In this PhD Thesis, we describe, along with seven chapters, the chemistry and physics of a unique class of molecular nanomagnets based on mononuclear octahedral spin crossover cobalt(II) complexes with potential chemo-, electro-, or photoactive pyridinediimine (PDI) and terpyridine (TERPY)-type ligands. Because of their unusual combination of chemical (Brønsted or Lewis acidity, and redox) and physical (optical or luminescent, and magnetic) properties resulting from the metal and the ligand counterpart, they can be used in designing multifunctional and multiresponsive advanced magnetic materials for molecular spintronics and quantum computing technologies. One of the major achievements in this PhD Thesis was being able to modulate their spin crossover (SCO) and single-molecule magnet (SMM) properties by the ligand design through a variety of internal factors, either electronic (metal oxidation and spin states) or steric ones (ligand substituents and conformation), and eventually to switch them under the presence of an external stimulus, either chemical (pH and chemical analytes) or physical ones (light, electric and magnetic fields). Hence, mononuclear octahedral cobalt(II)-PDI and TERPY complexes behaving as spin crossover molecular nanomagnets afford an excellent chemical set of DMS models for fundamental studies on magnetic field-induced and chemo-, redox-, or photo-triggered, slow magnetic relaxation phenomena. In particular, they seem to be promising candidates for molecular spintronics and quantum computing devices like spin switches and capacitors or spin transistors and qubits. Besides, as briefly outlined in the last chapter, the spin crossover molecular nanomagnets presented in this PhD Thesis are particularly well-suited for their processing and addressing on different supports and measuring their single-molecule electron transport and quantum coherence properties, which are two major topics in molecular spintronics and quantum computing.

SINOPSIS

Los complejos mononucleares de iones metálicos paramagnéticos de la primera serie de transición con ligandos "no-inocentes" hechos a medida han surgido recientemente como prototípicos de sistemas moleculares dinámicos (DMSs, del inglés “dynamic molecular systems”). El enorme impacto de los DMSs en varios dominios de la nanociencia y nanotecnología molecular se debe a su capacidad para ejecutar funciones específicas y selectivas bajo el control de un estímulo externo que modula adecuadamente sus propiedades estructurales y electrónicas (ópticas, redox y magnéticas). En esta Tesis Doctoral, a lo largo de siete capítulos describimos la química y las propiedades físicas de una clase única de nano-imanes moleculares basados en complejos mononucleares octaédricos de cobalto(II) de transición de espín con ligandos del tipo piridindiimina (PDI) y terpiridina (TERPY) potencialmente quimio-, electro- o fotoactivos. Debido a su inusual combinación de propiedades químicas (acidez de Brønsted o Lewis y rédox) y físicas (ópticas o luminiscentes y magnéticas) resultantes del metal y del ligando, pueden ser usados en el diseño de materiales magnéticos avanzados multifuncionales y de respuesta múltiple para tecnologías de espintrónica molecular y computación cuántica. Uno de los principales logros de esta Tesis Doctoral fue poder modular sus propiedades de transición de espín (SCO, del inglés “spin crossover”) y de molécula imán (SMM, del inglés “single-molecule magnet”) mediante el diseño de ligando a través de una variedad de factores internos, ya sean electrónicos (oxidación y estados de espín de metales) o estéricos (sustituyentes y conformación de ligandos), y eventualmente canjearlos bajo la presencia de un estímulo externo, ya sea químico (pH y analitos químicos) o físico (luz, campos eléctricos y magnéticos). Por lo tanto, los complejos mononucleares octaédricos de cobalto(II)-PDI y -TERPY que se comportan como nano-imanes moleculares de transición de espín proporcionan un excelente conjunto químico de modelos de DMS para estudios fundamentales sobre los fenómenos de la relajación lenta de la magnetización inducida por el campo magnético y quimio-, rédox- o foto-desencadenada. En particular, parecen ser candidatos prometedores para la espintrónica molecular y los dispositivos de computación cuántica como interruptores y capacitores o transistores de espín y qubits. Además, tal como se señala brevemente en el último capítulo, los nano-imanes moleculares de transición de espín presentados en esta Tesis Doctoral son particularmente adecuados para su procesamiento en diferentes soportes, incluidas las uniones moleculares metálicas y las redes metalorgánicas porosas (MOF, del inglés “metal-organic framework”), y para medir su transporte de electrones molecular y sus propiedades de coherencia cuántica, que son dos temas principales de la espintrónica molecular y la computación cuántica.

A Rafa

CHAPTER I

INTRODUCTION AND BACKGROUND

Dynamic Molecular Systems on the Road to Molecular Spintronics and Quantum Computing Nanotechnologies

Faster, smaller, cheaper – this has been the trend in computing for the past several decades. Electronics and Computing have experienced a booming revolution since 1947 with the invention of the primary examples of working transistors based on germanium and silicon materials and their subsequent developments as integrated systems. These technologies guided us to what nowadays is lived and known as the Digital Revolution. Unfortunately, one of the established bases of the Digital Revolution, the Intel co-founder Gordon Moore's prediction that the density of transistors in integrated systems would be double every two years, the Moore's Law,[1] is facing its imminent halt. Back in 1959, the physicist and Nobel-prize winner Richard Feynman and his iconic phrase "There's plenty of room in the bottom" granted thoughtful insights to the scientists and warmed up the nanotechnology and nanoscience fields.[2] According to Feynman's visionary speculations, nanotechnology could offer a proper toolkit to take the miniaturisation to atom scale, accomplishing the desired modulation of the systems and selected functionalities.

Spintronics is not only considered a promising way for miniaturisation of electronic circuits but also a more efficient technology that might replace the Complementary Metal-Oxide-Semiconductor (CMOS) current one by leading to highly integrated systems. This novelty resides in the use of spin (and thus, its associated magnetic moment) instead of only the electrical charge for device functionality. The electron spin is being already applied in computing to read data in hard disk drives based on the giant magnetoresistance (GMR) effect, discovered by the Nobel Prize-awardees Albert Fert and Peter Grunberg.[3,4] Nevertheless, beyond that, once the electron spin is a two-level system, it is an inherent candidate for the realising of a quantum bit (qubit) in **Quantum Information Processing** (QIP).[5]

A variety of qubit-based algorithms have been developed since the 1990s. A priori, these algorithms can handle very complex calculations that are not available to current classical computers. In 2018, IBM unveiled the first quantum computer designed for commercial use, the IBM Q System One, which operates with 20 qubits. Recently, Google claimed the achievement of the Quantum Supremacy by its 54-qubit Sycamore Processor, which was capable of performing in two hundred seconds a calculation that would have taken ten thousand years to the most powerful non-quantum computer.[6] As the race towards quantum supremacy gets more competitive and Electronics approaches the limits of silicon, the development and implementation of Spintronics components start to play a crucial role in ensuring improvements in information processing performance and higher-density storage at lower costs – faster, smaller, cheaper.[7,8]

So far, only conventional materials like inorganic metals and semiconductors have been used to construct spintronic devices. However, it is not nonsense to think that a spin-based quantum computing machine could come true in the near future.[9–11] That being so, a new field has emerged to combine the ideas and concepts of Spintronics with the unique properties offered by the molecular systems to exhibit quantum behaviour at the nanoscale, the so-called **Molecular Spintronics** (MS).[12–27] Its advantages are remarkable: (i) it constitutes the most straightforward ideal platform for the studying and understanding of the fundamental concepts that govern Spintronics; (ii) it allows creating devices ruled by the laws of quantum mechanics; (iii) it sets up the ultimate level of miniaturisation for molecular spintronic devices; (iv) it enables the use of a comprehensive set of chemical tools to optimise tailor-made quantum properties towards diverse device architectures and applications, but more importantly, (v) it opens the road to retrying information from a dynamic device, integrated into a computer or a sensor, and displaying it understandably (information "read-out" process).

The gigantic impact of **Dynamic Molecular Systems** (DMS) in several molecular nanoscience and nanotechnology domains emanates from their ability to perform specific and selective functions under the control of an external stimulus that properly and reversibly tunes their structural (steric and chemical), electronic (optical and redox) and magnetic properties in a reversible manner. In this respect, a wide spectrum of valuable works has been emerged in the last decade reporting attempts to mimic the classical electronic components or biological functions (biomimetic systems) in the light of the nanoscale and quantum effects.[28–39]

"Molecular machines" are a powerful illustration of DMS. The most representative examples of molecular machines are [2]catenanes and [2]rotaxanes, where molecular motion can be directed in a controlled and reversible ways (Figure I.1).[40–48] An archetypical [2]catenane consists of two interlocked rings, in which one ring rotates inside the other using the distinct preferred coordination geometry of the Cu^{I}/Cu^{II} redox pair as a driving force. So, through an electrochemically triggered process, it is possible to achieve a sliding motion that causes a profound rearrangement of the molecule (Figure I.1b).[43–45] In the case of [2]rotaxanes, the molecular motion works like a shuttle, where one ring is trapped in a linear molecule with the bulky stopper groups on its extremes. For instance, a positively charged π-electron-acceptor ring can be forced to shuttle back and forth between two different π-electron donor stations (benzidine and biphenol units) originating two translational isomers (Figure I.1c). At equilibrium, both stations are occupied by the ring, being the benzidine preferred instead of the biphenol in an 84:16 ratio. However, the position of the ring can be switched over to the biphenol station using external stimuli, either by protonation of the basic nitrogen atoms of the benzidine (chemical) or by its electrochemical oxidation (redox). The occupancy ratio of the benzidine and biphenol stations change to 2:98 under these conditions (Figure I.1c).[41]

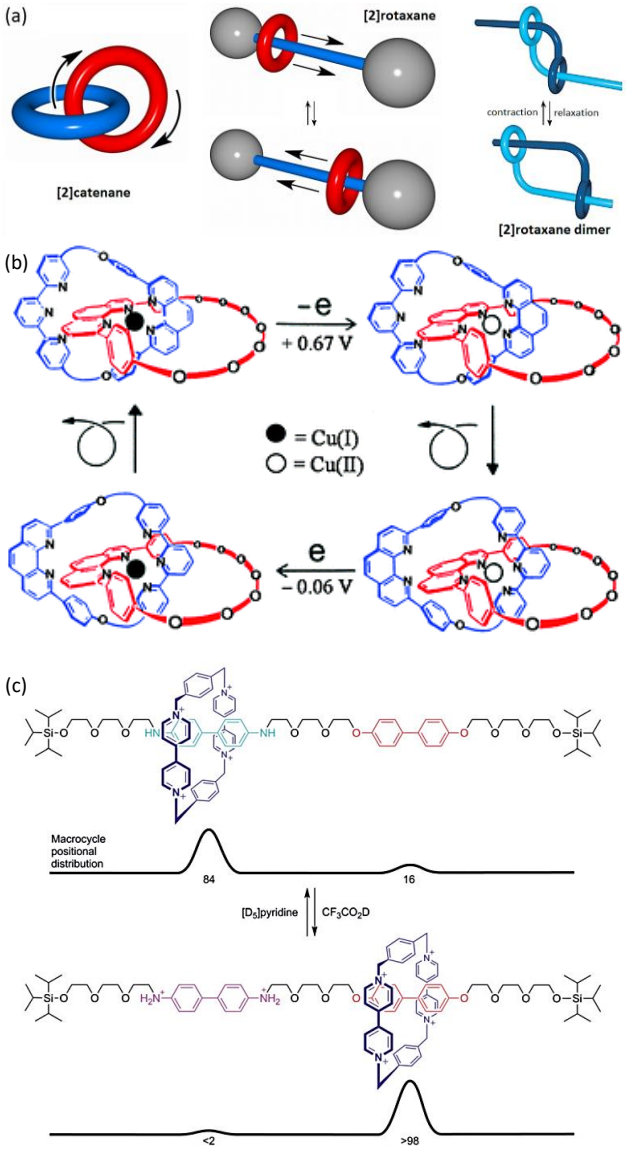

Figure I.1 (a) [2]catenane (left), [2]rotaxane (middle) and [2]rotaxane dimer (right) illustrative representations. (b) Electrochemically triggered molecular rotatory motion in a copper-[2]catenane complex showing the interconversion between the four- and five-coordinated isomers of Cu(I) (empty circle) and Cu(II) (filled circle), respectively. (c) First switchable molecular shuttle undergoing a translational motion by protonation/deprotonation or electrochemical oxidation/reduction of the benzidine fragment. Adapted with permission from ref [45].

Indeed, the potentiality of DMS is almost limitless. Some systems were conceived to mimic biological functions performed by some proteins or even cells. It is the case of the [2]rotaxane dimer (Figure I.1a, right), known as "molecular muscle" by its ability to realise a contraction/relaxation motion mimicking a muscle cell.[46–48]

However, that is not the limit! The concepts of DMS can be translated into the quantum level, where there is the chance to take advantage of some inherent dynamic quantum property and control it by the physicochemical properties that were rationally designed for this purpose. The precise and selective access and control of the spin carrier, together with the fine tuning of its quantum properties in a given dynamic system, constitute a current major challenge in MS.

One of the most appealing pathways to accomplish that goal is combining a diversity of properties into a metal-containing material (or molecule, thinking at the ultimate scale) that respond (the output) differently to each stimulus (the input), bringing up synergic interactions. Such a multiresponsive material is named multifunctional, in which the remarkable characteristic is **bistability** (or multistability). And, in this PhD Thesis, the term "bistability" should be interpreted in a broader sense, representing two different concepts not inimical to each other. The first and more abstract one is applied to a genuine bistable dynamic system, resulting from the quantum superposition, which establishes that the system is in equilibrium with all possible states simultaneously (until it is measured). Nevertheless, the bistability should also be understood in its palpable logic, describing a system with two distinct accessible states that can be transformed reversibly under certain external stimuli.

SCO and SMM as classical DMS in Molecular Magnetism

Spin Crossover (SCO)[48–59] compounds and **Single-Molecule Magnets** (SMM)[60–68] represent the most attractive multifunctional and multiresponsive bistable DMS among the molecule-based magnetic materials.

A first-row transition metal ion with [Ar]$3d^4$–d^7 electronic configurations –such as Mn(III), Fe(III), Fe(II), or Co(II)– in an octahedral environment can exhibit two possible electronic ground states, low spin (LS) and high spin (HS), resulting from the 3d orbitals splitting by the ligand field into e_g and t_{2g} subsets separated by an energy gap, the ligand field strength (Δ). In the narrow region where Δ and the interelectronic repulsion energy (P) are similar, the reversible interconversion between both spin states occurs assisted by the action of an external stimulus (most commonly temperature, pressure, and light irradiation). This situation describes the SCO phenomenon. The electronic depopulation of the t_{2g} and consequent population of the e_g orbitals is accompanied by a spin flip. Given the antibonding character of the e_g subset, its population increases the metal-ligand bond length. The mean metal-ligand bond length increment (ΔR) is around 0.2 and 0.1 Å for Fe(II) and Co(II), respectively.[69,70] These subtle structural variations upon the LS/HS conversion cause changes in the intermolecular interactions. In turn, they eventually are enough to result in cooperative effects in the solid state. As a consequence of the greater ΔR, these supramolecular changes are more significant in Fe(II) than in Co(II) compounds. That being so, there are rare examples of mononuclear cobalt-based compounds displaying abrupt SCO phenomenon (Figure I.2). They include a fascinating case of triply thermal-, piezo- and electro-switchable behaviour in the $[Co^{II}(dpzca)_2]$ complex [dpzca = bis(2-pyrazinylcarbonyl)amidate] that shows an abrupt and complete SCO with a hysteresis loop of 11 K (Figure I.2).[71]

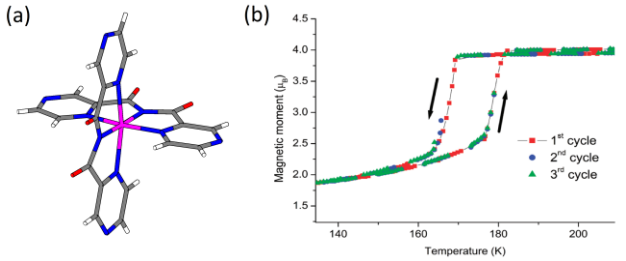

Figure I.2 Perspective view of the triply thermal-, piezo- and electro-switchable [Co^{II}(dpzca)$_2$] complex (a) showing abrupt, reversible and hysteretic SCO behaviour expressed by the temperature dependence of the effective magnetic moment in three cycles (b). Adapted with permission from ref [71].

The potential energy diagram for the HS and LS configurations of a mononuclear cobalt(II) complex may be represented as a function of the average metal-ligand bond length (R) following the expression $E = 1/2[fR^2]$ (Figure I.3). This plot makes it easy to see that the LS state is stabilised compared to the HS state. So, at low temperatures, the population of the LS state is predominant. Upon heating, and consequently, with the increase of the vibrational energy, excited vibrational levels start to be populated until the point X in the diagram, where the geometry of LS and HS metal centres are the same. At this point, the LS/HS interconversion occurs. In other words, spin state transition takes place when the enthalpy gap between the two states (ΔE) is compensated by the increase of entropy associated with the HS state population at high temperatures, that is, free energy becomes negative because of the entropic contributions.

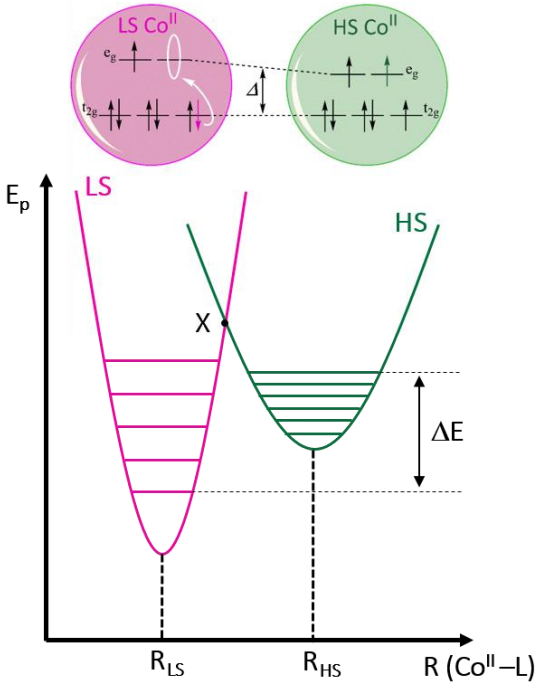

Figure I.3 Configurational coordination diagram of the potential energy for the LS/HS transformation in an octahedral Co(II) complex. Adapted with permission from ref [69].

The thermally induced SCO process may be monitored through variable-temperature direct current (dc) magnetic susceptibility (χ) measurements under a static magnetic field (H_{dc}). So, the influence of diverse intramolecular (Δ) and intermolecular (counterion and crystallisation solvent) effects on the completeness and abruptness (cooperativity) of the LS/HS interconversion can be systematically studied, which constitutes classic textbook examples in Molecular Magnetism.[72]

On the other hand, SMM behaviour in mononuclear complexes is a more recently discovered phenomenon attributed, in principle, to the high magnetic anisotropy of the metal centre resulting from the zero-field splitting (zfs) of the spin ground state (S) of the molecule, being bistability a physical consequence of the thermal equilibrium restoration between the states of $m_s = +S$ and $m_s = -S$ (Figure I.4). In the absence of an external magnetic field (H), the two degenerated m_s states from a Kramers doublet remains equally populated (Figure I.4, top). When H is applied, the magnetic moment (or the spin momentum, in the context of this PhD Thesis) comes to align with the H orientation, causing a perturbation of the system (Figure I.4, middle). The magnetic relaxation of the aligned spins occurs to restore the equilibrium either by thermally induced spin relaxation or by temperature-independent quantum tunnelling of the magnetisation (QTM) (Figure I.4, bottom). This process requires a certain time, called magnetic relaxation time (τ). That being so, the system temporally remains magnetically blocked below a certain temperature, the so-called magnetisation blocking temperature (T_B).

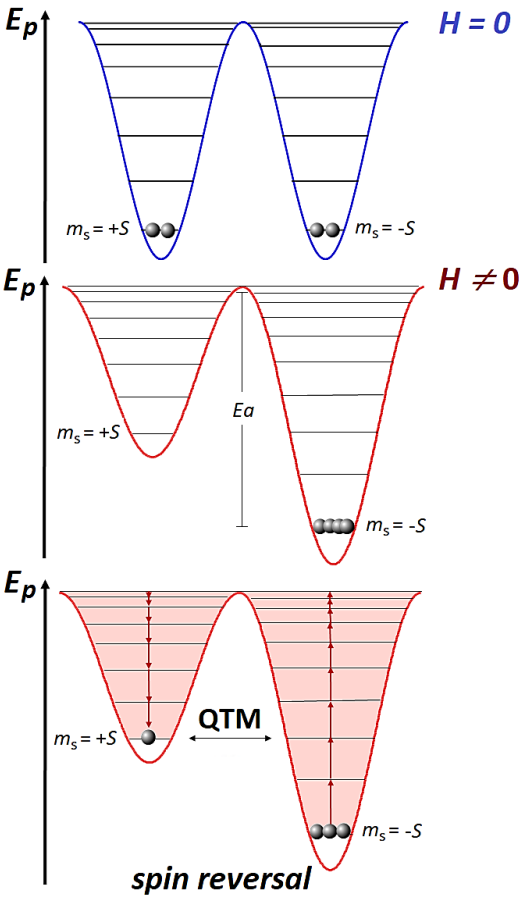

Figure I.4 Double well potential energy diagram for a SMM. The situation is depicted for the external magnetic field's absence (top) and presence (middle and bottom). The red and black arrows represent the thermal-induced spin relaxation and temperature-independent quantum tunnelling of the magnetisation (QTM) processes.

An axial symmetry (axial anisotropy) cause the occurrence of high axial magnetic anisotropy, meaning that the magnetisation will occur preferentially in one direction. The higher the axial or rhombic anisotripy (transcribed by the magnitude of *D* and *E* magnetic parameters of the zfs), the higher the energy cost to flip the spin from the preferred alignment. In spin dynamics studies, this cost is known as the activation barrier (E_a) for magnetic relaxation (Figure I.4), equal to DS^2 or $DS^2 - 1/4$ for non-Kramer and Kramer systems. This feature explains why the SMM behaviour strongly correlates with the system's magnetic anisotropy.

The spin dynamics of the SMM may be investigated through variable-frequency alternating current (*ac*) magnetic susceptibility measurements, in which an oscillating magnetic field (H_{ac}) is applied. If the time for spin reversal is sufficiently slow, i.e. the frequency of variation of H_{ac} is faster, the thermal equilibrium of spin population cannot be completely restored. This way, the slow relaxation of the magnetisation is stressed by a frequency-dependent loss of the in-phase magnetic susceptibility (χ') signal compared with the *dc* magnetic susceptibility (χ) and the appearance of a non-zero frequency-dependent out-of-phase magnetic susceptibility (χ'') signal.

The big breakthrough of SMMs came in 2003 with the reported series of anionic double-decker bis(phthalocyaninato)lanthanide(III) complexes, $[Ln^{III}(Pc)_2]^-$, where Ln varies from Tb to Yb with $[Ar]4f^7$–f^{13} electronic configurations. Among them, the terbium(III) and dysprosium(III) derivatives showed slow magnetic relaxation at zero-field with activation barriers of 230 and 27.8 cm^{-1}.[73–75] The terbium derivative held the highest E_a value reported until then due to the well-separated doublet ground state ($m_J = \pm 6$) from the excited states as a result of the large magnetic anisotropy of the Tb^{III} ion originated from both spin and orbital contributions ($J = 6$ with $S = 3$ and $L = 5$). The discovery of a simple mononuclear compound behaving like such a magnet on its own thrilled the MS community opening many chemical possibilities to maximise the T_B and apply them for storage information in QIP (provided that the QTM process is not operative).

However, only in 2012 the full potentiality of mononuclear first-row transition metal complexes as magnetic field-induced SMM was depicted by Vallejo *et al.* in a neutral, high-spin, and highly distorted octahedral *cis*-bis(thiocyanato)cobalt(II)-dimethylphenanthroline complex, $[Co^{II}(dmphen)_2(NCS)_2]$, with large positive axial and rhombic magnetic anisotropy of the Co^{II} ion ($D = +98$ cm^{-1} and $E = +8.4$ cm^{-1}).[76] The observed E_a value (17.0 cm^{-1}), much smaller than the expected theoretical axial anisotropy barrier ($2|D| = 196$ cm^{-1}), suggests the transverse anisotropy barrier ($2E = 16.8$ cm^{-1}) is, in principle, responsible for the SMM behaviour. However, the observation of this behaviour in easy-axis magnetisation compounds with low or null rhombic zfs moved to think Raman or direct relaxation mechanisms or lowest vibrational modes are responsible for it. Although the magnitude of magnetic anisotropy in 3d ions is usually much smaller than in 4f ions, their rich coordination chemistry could offer the key to finding an alternative route on the road for new cheaper SMM materials.

Mononuclear SCO and SMM compounds constitute the smallest possible magnetic units in the Coordination Chemistry field, which hold potential applications in quantum computing and high-density information storage due to their dynamic molecular and quantum behaviour. All the intrinsic characteristics of SCO and SMM systems cited above combined with their nanometer scale, easy handling and multiple addressing possibilities make them an excellent chemical set of synthetic and theoretical models for fundamental studies regarding the comprehension of the phenomena that rule MS and QIP.[61–64] Indeed, both classes of molecules appear as potential candidates to build active device components of molecular spintronic circuits and quantum computers (see representative examples in Boxes A and B).

SCO and SMM: Two worlds as one

An enormous quantity of SCO systems based on mononuclear iron(II), iron(III), and cobalt(II) complexes are well known and have served as an essential platform to the understanding of the SCO phenomenon.[52,53,77–83] At the same time, mononuclear cobalt(II) SMMs have been of significant interest due to the inherent high magnetic anisotropy of the HS Co^{II} ion and its vast coordination chemistry.[84–93] Nonetheless, the coexistence of both bistabilities in the same system, reported to date, is still very limited. The SMM behaviour in first-row transition metal complexes only materialises at very low temperatures, and the thermally induced HS/LS transition occurs at higher temperatures to yield a diamagnetic or magnetically isotropic LS state ($S = 0$ or 1/2 for LS Fe^{II} and Co^{II} ions) at low temperatures. Therefore, unfortunately, the coexistence of SCO and SMM in the same material, as well as the synergy between them, renders one of the biggest paradoxes in MM. That being so, conceiving a system that contemplates both behaviours is not a simple task and requires searching for an intermediate situation where both phenomena are favoured at a certain level simultaneously.

With iron(II), there are only three examples of SCO/SMM systems achieved on the trapped metastable, magnetically anisotropic HS excited state of iron(II) complexes ($S^* = 2$) through light irradiation [by a light-induced excited spin-state trapping (LIESST) process].[94–96] Similarly, examples of cobalt(II)-based SCO/SMM systems exhibiting both phenomena are also scarce.

Examples of SCO/SMM systems include a series of double salts whereby the SCO and SMM behaviours have been separately identified for the cationic octahedral and the anionic tetrahedral cobalt(II) complexes, respectively two components of the ion pair.[97,98] More interestingly, two series of mononuclear square-pyramidal cobalt(II) SCO complexes exhibit a field-induced SMM behaviour in the LS state,[99,100] being one of them recently tested as a prototype of a **molecular qubit**.[101] They also include two dynamic **molecular switches** featuring reversible water molecule-driven on-off switching of SCO and SMM behaviours in the octahedral cobalt(II)-terpyridine

complex and its 4-bromophenyl-substituted derivative, independently reported by Shao and Kobayashi (Scheme I.1).[102,103]

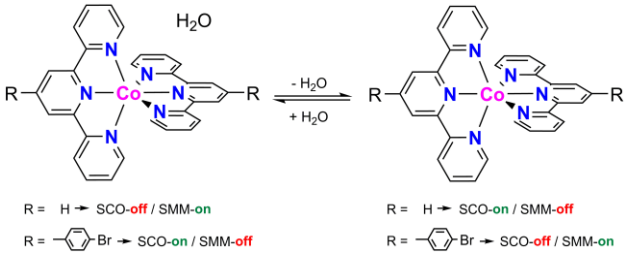

Scheme I.1 Illustrative dehydration-rehydration process and the consequent influence in the SCO and SMM behaviours of the Co(II)-TERPY and its 4-bromophenyl derivative.

In both cases, the solvatoswitching of SCO and SMM behaviours occurs from a hydrated to an anhydrous phase, where the LS state of the Co^{II} does not present slow magnetic relaxation effects (off). The transformations were executed and followed by single crystal-to-single crystal (SC-SC) post-synthetic methods.

Although, to our knowledge, only a few works report the coexistence of SCO and SMM phenomena in cobalt(II)-based systems, they are very valuable in providing insights into how sensitive to small changes in the metal environment (electronic, steric, and chemical characteristics of the ligand) and the crystal packing (intermolecular hydrogen bonding, π-stacking, and Van der Waals interactions) can be the spin transition and the magnetic relaxation dynamics. These results suggest that minor modifications on the ligand field or the weak supramolecular interactions could lead to switchable dynamic SCO/SMM systems in the solid state.

In Coordination Chemistry and Molecular Magnetism (MM), first-row transition metal ions have always played an essential role in the synthetic aspects due to their diverse Lewis acidity and properties, constituting a rich playground to react with a ligand of interest resulting in a desired magnetic behaviour. In this doctoral dissertation, the strategy applied to build up multifunctional and multiresponsive DMS was to select well-known SCO platforms primarily studied back in the last century in the field of MM as a starting point or base unity (Figure I.6).

Cobalt(II) complexes with tridentate N_3 ligands like *2,2':6',2''*-terpyridine (TERPY) and related pyridine-2,6-diimine (PDI) derivatives constitute a common class of SCO systems exhibiting gradual LS/HS transitions. In this respect, Figgins reported the first examples of mononuclear octahedral cobalt(II) complexes with PDI ligands exhibiting the SCO phenomenon in 1960.[104] It is worth bringing out that the study of their magnetic properties has largely contributed to the birth and further development of the SCO phenomenon, which still now constitutes a crucial topic in MM that extends to potential applications in MS (see Box A). The LS Co^{II} ion is a genuine two-level magnetic quantum system represented by the m_S = +1/2 and –1/2 states. Thus, the yet elusive mononuclear LS Co(II) SMMs appear as appropriate candidates to molecular spin-based qubits for the physical implementation of QIP. In this respect, it is not surprising that the more promising examples of transition metal-based qubits are mononuclear vanadium(IV) complexes with a doublet ground spin state (S = 1/2).[26]

For these reasons, both platforms (TERPY and PDI, Figure I.6) seem suitable to merge the two main metal-based bistabilities targeted by this PhD Thesis (SCO and SMM). This strategy will allow us to go one step further, focusing the novelty on the rational design of the ligand counterpart functionalising it with one or more switchable units expressed by their inherent physical and/or chemical properties (redox, luminescence, proton affinity, etc.). In this **ligand design chemical approach**, the control and modulation of the physicochemical properties over the Co(II)-PDI and Co(II)-TERPY platforms can be achieved through synthetic tools to give multifunctional and multiresponsive DMS as its whole concept. We refer to this novel class of SCO/SMM compounds as **Spin Crossover Molecular Nanomagnets**.

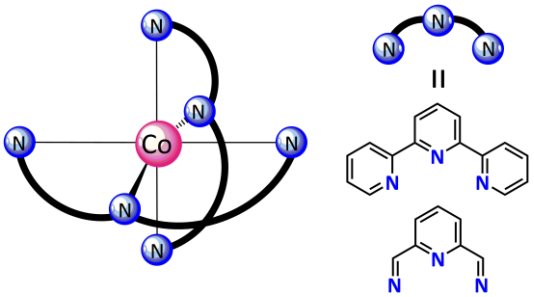

Figure I.6 Selected TERPY and PDI platforms to create a new chemical library of SCO/SMM materials in this work.

Due to the interdisciplinary character of this doctoral thesis is impossible to place it in a unique domain. Instead, it should be in the intercrossing area of several disciplines like coordination chemistry, spectro-, photo-, electro- and magnetochemistry. The synthetic procedures and the study of the magneto-structural correlations in spin crossover molecular nanomagnets are of considerable interest in the consolidated field of MM. The addition of non-innocent electro-, optic-, photo- or chemoactive components in the ligands allowed us to permeate the emerging field of Molecular Spintronics and Quantum Computing, presenting herein a plethora of cobalt(II)-based DMS as potential candidates of spin quantum devices.

BOX A

Box A | *Spin Crossover complexes as Dynamic Molecular Systems for Quantum Spintronic Devices*

Using a single molecule as a spin carrier sets up the ultimate miniaturisation of a Molecular Spintronic device. In particular, due to their multiple stimuli-response conveniences, SCO molecules have been studied in the form of conducting units with the size of a few nanometers, so-called molecular junctions or quantum dots. The simplest possible device requires a source and drain electrode, setting the electron flux. Transistors are a slightly more complex device, comprising an additional electrode called "gate", which control the electron flow along the molecule by applying a potential through the device. Some exciting results have been achieved by placing SCO molecules on these devices.

In the experiment of Park *et al.*, two gold electrodes were connected by thiol-functionalised terpyridine-cobalt(II) complexes of formula $[Co\{TERPY\{CH_2\}_nSH\}_2]^{2+}$, with n = 0 and 5.[105] These molecules belong to the well-known family of octahedral SCO cobalt(II) complexes. They showed that it is possible to control the electron transport properties by varying the number of methylene groups on the ligand. A Kondo peak evinces the strong coupling regime when the LS Co(II) complex with the short linker (n = 0) is connected to the two gold electrodes. In contrast, if a long carbon chain is used as a linker (n = 5), the device presents a weak coupling in which the standard Coulomb blockage rules the behaviour. Later, the same $[Co\{TERPY(CH_2)_nSH\}_2]^{2+}$ was connected to two mobile gold electrodes (Figure A.1).[106] The mechanical control on the junction enables the spin control by modifying the molecular symmetry, leading to the splitting of the Kondo peak as a function of the stretching. However, the authors conclude that this Kondo resonance is originated from a S = 1 ground state resulting from the metal reduction to HS Co(I) complex as the current is passing through the molecule instead of molecular changes associated with HS/LS transition of the original Co(II) complex.

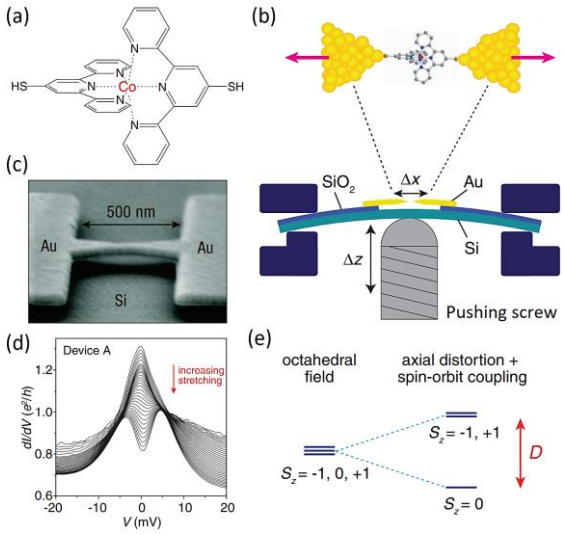

Figure A.1 (a) Scheme of the structure of the LS complex $[Co(TERPYSH)_2]^{2+}$. (b) Schematic representation of the single-molecule junction device. (c) Scanning electron image of the break junction before molecule deposition. (d) Bias voltage (V) dependence of the differential conductance (dI/dV) at 1.6 K for different values of the electrode spacing (Δx), showing the splitting of the Kondo peak upon increasing the molecular stretching. (e) Simplified energy level diagram for the splitting of the triplet ground state of the Co^{I} ion after applying an axial distortion. Adapted with permission from ref [106].

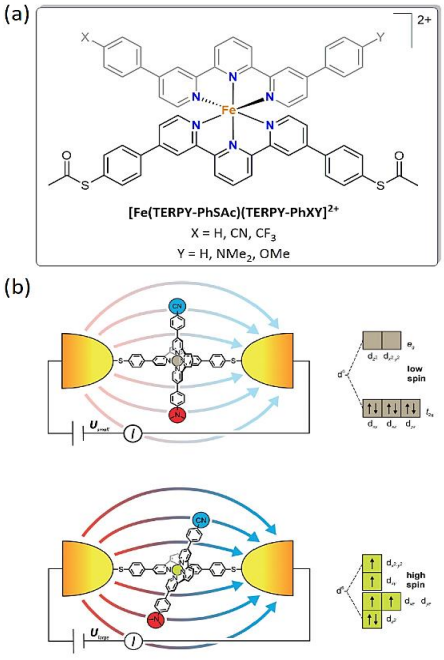

Figure A.2 (a) General chemical structure of the series of polar heteroleptic iron(II) complexes of formula $[Fe(TERPY\text{-}PhSAc)(TERPY\text{-}PhXY)]^{2+}$. (b) Illustration of the single-molecule junction constructed from the Fe(II) complex connecting two gold electrodes at a small applied voltage (top) and the distorted HS Fe(II) complex due to the alignment of the ligand Me_2-TERPY-PhCN to the applied electric field. Adapted with permission from ref [107].

Another innovative approach to control the electron transport properties over single-molecule spintronic devices was reported by Harzmann.[107] The novelty relies on the sensitivity of the spin state towards the spatial arrangement of the ligands and the global distortion of the complex of general formula $[Fe(TERPY\text{-}PhSAc)(TERPY\text{-}PhXY)]^{2+}$ (Figure A.2). One of the TERPY ligands was tailored with sulphur-containing groups responsible for anchoring the complex onto the surface of the gold electrodes, while the other TERPY containing two opposite polar groups remains free to rotate. The almost perfect octahedron is strong enough to pair up the electrons giving a diamagnetic LS ground state for the Fe(II) complex (S = 0) (Figure A.2b, top). However, the reduction of symmetry due to the mechanical distortion of the coordination environment results in a decrease of the ligand field strength and accessible e_g orbitals. This situation leads to a paramagnetic HS ground state for the Fe(II) complex (S = 2) (Figure A.2b, bottom). Upon application of an electric field, the polarisation of the free TERPY ligand causes a shift from the ideal octahedron to a lower symmetry coordination sphere that changes the conductance over the junction as a bias-dependent spin switching mechanism of control. Contrastingly, when the SCO iron(II) complex $[Fe(S\text{-}BPP)_2](ClO_4)_2$, [S-BPP = (s)-(4-{[2,6-(dipyrazol-1-yl)pyrid-4-yl]ethynyl}phenyl)ethanethioate], was introduced in gold nanoparticles arrays, the resistance exhibits a minimum around 200 K supporting the hypothesis that the molecular resistance of the HS state is greater than the one of the LS state.[108]

When it comes to hybrid materials for devices, graphene is the most attractive constituent because of its extreme surface sensitivity to the dielectric properties of the environment.[109] In this respect, the electrical read-out of light-induced spin transition was investigated by building a thin film of the SCO iron(II) complex $Fe[HB(3,5\text{-}Me_2Pz)_3]_2$ [$HB(3,5\text{-}Me_2Pz)_3$ = hydrotris(3-5-dimethylpyrazole)borate] on a graphene sensing layer. The switch from diamagnetic LS to paramagnetic HS resulted in increased conductance of the graphene channel under both light irradiation and temperature stimulus.[110]

BOX B

Box B | *Single-Molecule Magnets as Dynamic Molecular Systems for Quantum Spintronic Devices*

Organic molecules have been widely used in designing promising electronic devices. Several of them resulted in important applications like semiconductors, light-emitting diodes (LEDs), photovoltaic cells, spin valves and field-effect transistors.[111] Since discovering the GMR in purely inorganic materials, the electron transport combined with magnetic properties associated with the spin that these electrons carry has pushed Molecular Electronics into a newly emerging area where the possibilities are vast, the Molecular Spintronics. Some examples of spintronic uses of SMMs as quantum spin transistors and spin valves are detailed hereunder.

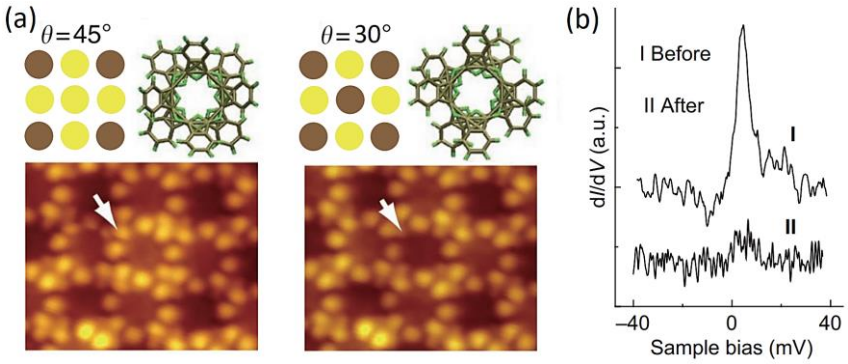

Figure B.1 (a) STM images of the conversion of the mononuclear terbium(III) complex [Tb(Pc)$_2$] from θ = 45° (left) to θ = 30° (right) by applying a current pulse. An arrow maks the target molecule, and magnified images are shown in the bottom panel. Changes in the contrast and the top view of the centre molecule are schematically illustrated. (b) Comparison of the Kondo peaks before and after the application of the pulse. Adapted with permission from ref [112].

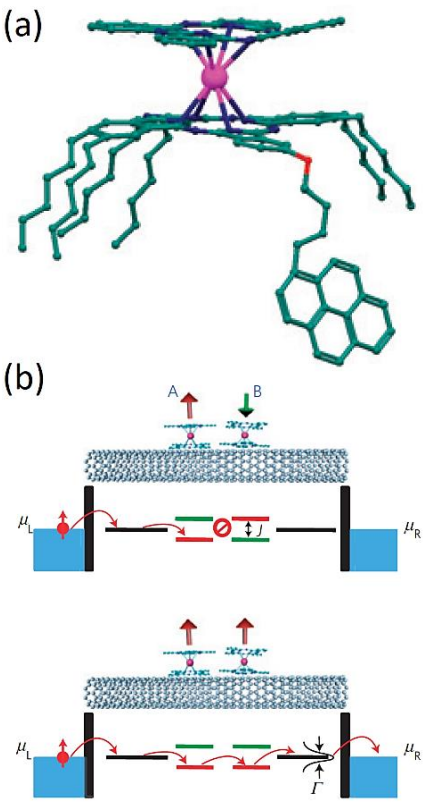

Figure B.2 (a) Chemical structure of the mononuclear terbium(III) complex [Tb(pc)(Hx$_6$BuOpyrpc)]. (b) Illustration of the magnetoresistance switching mechanism for a SWCNT with two anchored 4f SMMs. The thick orange and green arrows are the localized spins of the 4f SMMs, while the thin narrow red arrows represent the spin-polarized conduction electrons across the SWCNT. Adapted with permission from ref [113].

One outstanding example of a spintronic transistor is found on the oxidised double-decker [Tb(Pc)$_2$] SMM molecule absorbed on a gold surface (Figure B.1).[112] This device exhibits a resonance Kondo peak in the electrical conductance at zero-bias voltage (V = 0). The Kondo effect responsible for the transistor-like behaviour originates from the unpaired spin on a π-orbital of the oxidised Pc ligand since the large magnetic anisotropy arising from the Tb^{III} ion precludes degenerate states, needed to produce a Kondo signal. Moreover, the application of controlled pulses of current significantly alters the conformation of the SMM, rotating the upper Pc ligand of [Tb(Pc)$_2$] from the ideal azimuthal angle (θ) of 45° to 30° (Figure B.1a). This change in the conformation reversibly switches the spin on and off, hence the Kondo state (Figure B.1b).

Spin valves constitute another possibility for the memory device's implementation. Such devices take advantage of the GMR and constitute the core of nowadays hard disks. However, instead of metal layers used initially in spin valves, an innovative design was proposed as a supramolecular array of SMMs laterally coupled to a single-wall carbon nanotube (SWCNT). The choice for the SMM was the mononuclear terbium(III) derivative [Tb(Pc)(Hx$_6$BuOpyrPc)] accounting with one modified pyrene group and six hexyl groups into one of the two Pc rings as anchoring groups (Figure B.2a).[113] The resulting device consists of a source and a drain connected by a SWCNT, onto which the SMM randomly binds via supramolecular interactions. The proposal was that the giant magnetic anisotropy might influence the electron transport through the SWCNT. Indeed, when a magnetic field is applied in the plane of the device and then reversed, the magnetoresistance ratios increment up to 300% at very low temperatures (below 1 K). The explanation comes from a simplified model with only two SMM molecules in the channel (A and B). An effective energy barrier is generated when the spin momenta of the polarised molecules A and B are antiparallel, hindering de charge flow (Figure B.2b top). When B switches, thanks to the control of the magnetic field, high conductance occurs across the SWCNT (Figure B.2b, bottom).

The results reported in this doctoral dissertation were gathered in five chapters based on the ligand design approach used to target specific functionalities that hints at a future physical implementation as components of highly integrated spintronic circuits and quantum computers.

In the second and third chapters, we present two related series of Co^{II} SCO/SMM complexes with non-innocent electroactive *N*-phenyl substituted PDI ligands bearing different electron-withdrawing or -donor substituents as new electroactive materials that include a case of **molecular electro-switch** in the form of the *p*-methoxyphenyl-substituted Co^{II}-PDI complex.

In the fourth chapter, we take advantage of the easy handling of Co^{II}-PDI complexes and the knowledge obtained from the two first chapters to design optically active (luminescent) SCO/SMM complexes with *N*-oligoacene-substituted PDI ligands that can act as spin quantum luminescent sensors. In addition, as a "mention of honour" to the seminal works in the spin crossover molecular magnetism field, the influence of the solvent on the thermal-induced spin transition and field-induced slow magnetic relaxation is investigated in the naphthalene-substituted Co^{II}-PDI complex exemplar, which reveals as a new example of **molecular solvato-switch**.

By acknowledging the historical importance of the counterion influence on the MM, the fifth chapter presents a rare pair of counterion tuning of SCO and SMM behaviours, consisting of isomorphic perchlorate and hexafluorophosphate salts of Co^{II} SCO/SMM complexes with a non-innocent photoactive styryl-substituted TERPY ligand initially proposed as a new exemplar of **molecular photo-switch**.

At last, the full potential of the multifunctional Co(II) SCO/SMM complexes as candidates to active components and devices of spintronic circuits is depicted in the sixth chapter. Therein we report a unique example of multiresponsive electro, photo- and chemoactive Co(II) SCO/SMM complex accomplished by the rational design of a benzoic acid/benzoate-substituted TERPY ligand. Indeed, on the road to spin-based quantum computing, discovering multiple electro-, photo- and chemoswitchable DMS represents a crucial step towards Quantum Supremacy.

References

1 Moore, G. E. Electronics Magazine, **1965**, 4.

2 Feynman, R. P. There's Plenty of Room in the Bottom: An Invitation to Enter a New Field of Phisycs, *Eng. Sci.* **1960**, *23*, 22–36.

3 Baibich, M. N.; Broto, J. M.; Fert, A.; Nguyen Van Dau, F.; Petroff, F.; Etienne, P.; Creuzet, G.; Friederich, A.; Chazelas, J. Giant Magnetoresistance of (001)Fe/(001)Cr Magnetic Superlattices. *Phys. Rev. Lett.* **1988**, *61*, 2472–2475.

4 Binash, G.; Grünberg, P.; Saurenbach, F.; Zinn, W. Enhanced Magnetoresistance in Layered Magnetic Structures with Antiferromagnetic Interlayer Exchange. *Phys. Rev. B* **1989**, *39*, 4828–4830.

5 Awschalom, D. D.; Bassett, L. C.; Dzurak, A. S.; Hu, E. L.; Petta, J. R. Quantum Spintronics: Engineering and Manipulating Atom-Like Spins in Semiconductors. *Science* **2013**, *339*, 1174–1179.

6 Arute, F.; Arya, K.; Babbush, R; et al. Quantum Supremacy Using a Programmable Superconducting Processor. *Nature* **2019**, *574*, 505–510.

7 Coronado, E. Molecular Magnetism: from Chemical Design to Spin Control in Molecules, Materials and Devices. *Nat. Rev. Mater.* **2020**, *5*, 87–104.

8 Fert, A. Nobel Lecture: Origin, Development, and Future of Spintronics. *Rev. Mod. Phys.* **2008**, *8*, 1517–1530.

9 Shor, P. W. Algorithms for Quantum Computation: Discrete Logarithms and Factoring. *Proc. 35nd Annual Symposium on Foundations of Computer Science* (Shafi Goldwasser, ed.), IEEE Computer Society Press **1994**, 124–134.

10 Grover, L. K. Quantum Computers Can Search Arbitrarily Large Databases by a Single Query. *Phys. Rev. Lett.* **1997**, *79*, 4709–4712.

11 Kloeffel, C.; Loss, D. Prospects for Spin-Based Quantum Computing in Quantum Dots. *Annual Review of Condensed Matter Physics* **2013**, *4*, 51–81.

12 Sanvito, S. Molecular Spintronics. *Chem. Soc. Rev.* **2011**, 40, 3336–3355.

13 Sanvito, S. Injecting and Controlling Spins in Organic Materials. *J. Mater. Chem.* **2007**, *17*, 4455–4459.

14 Affronte, M.; Troiani, F.; Ghirri, A.; Candini, A.; Evangelisti, M.; Corradini, V.; Carretta, S.; Santini, P.; Amoretti, G.; Tuna, F.; Timco, G.; Winpenny, R. E. P. Single Molecule Magnets for Quantum Computation. *J. Phys. D: Appl. Phys.* **2007**, *40*, 2999–3004.

15 Bogani, L.; Wernsdorfer, W. Molecular Spintronics Using Single-Molecule Magnets. *Nature Mater.* **2008**, *7*, 179–186.

16 Winpenny, R. E. P. Quantum Information Processing Using Molecular Nanomagnets as Qubits. *Angew. Chem. Int. Ed.* **2008**, *47*, 7992–7994.

17 Lehmann, J.; Gaita-Ariño, A.; Coronado, E.; Loss, D. Quatum Computing with Molecular Spin Systems. *J. Mater. Chem*. **2009**, *19*, 1672–1677.

18 Stamp, P. C. E.; Gaita-Ariño, A. Spin-Based Quantum Computers Made by Chemistry: Hows and Whys. *J. Mater. Chem*. **2009**, *19*, 1718–1730.

19 Affronte, M. Molecular Nanomagnets for Information Technologies. *J. Mater Chem*. **2009**, *19*, 1731–1737.

20 Ardavan, A.; Blundell, S. J. Storing Quantum Information in Chemically Engineered Nanoscale Magnets. *J. Mater. Chem*. **2009**, *19*, 1754–1760.

21 Dei, A.; Gatteschi, D. Molecular (Nano)Magnets as Test Grounds of Quantum Mechanics. *Angew. Chem. Int. Ed.* **2011**, *50*, 11852–11858.

22 Timco, G. A.; Faust, T. B.; Tuna, F.; Winpenny, R. E. P. Linking Heterometallic Rings for Quantum Information Processing and Amusement. *Chem. Soc. Rev.* **2011**, *40*, 3067–3075.

23 Troiani, F.; Affronte, M. Molecular Spins for Quantum Information Technologies. *Chem. Soc. Rev.* **2011**, *40*, 3119–3129.

24 Aromí, G.; Aguilà, D.; Gamez, P.; Luis, F.; Roubeau, O. Design of Magnetic Coordination Complexes for Quantum Computing. *Chem. Soc. Rev*. **2012**, *41*, 537–546.

25 Ghirri, A.; Troiani, F.; Affronte, M. Quantum Computation with Molecular Nanomagnets: Achievements, Challenges, and New Trends. *Struct. Bond*. **2015**, *164*, 383–430.

26 Sessoli, R. Toward the Quantum Computer: Magnetic Molecules Back in the Race. *ACS Cent. Sci.* **2015**, *1*, 473–474.

27 Gaita-Ariño, A.; Luis, F.; Hill, S.; Coronado, E. Molecular Spins for Quantum Computation. *Nature Chem.* **2019**, *11*, 301–309.

28 Adréasson, J.; Pischel, U. Light-Stimulated Molecular and Supramolecular Systems for Information Processing and Beyond. *Coord. Chem. Rev.* **2021**, *429*, 213695–213710.

29 Sato, O. Dynamic Molecular Crystals with Switchable Physical Properties. *Nature Chem.* **2016**, *8*, 644–656.

30 Lubbe, A. S.; Leeuwen, T. Wezenberg, S. J.; Feringa, B. L. Designing Dynamic Functional Molecular Systems, *Tetrahedron* **2017**, *73*, 4837–4848.

31 Muraoka, T.; Kinbara, K. Development of Photoresponsive Supramolecular Machines Inspired by Biological Molecular Systems. *Journal of Photochemistry and Photobiology C* **2012**, *13*, 136–147.

32 Balzani, V.; Bergamini, G.; Ceroni, P. From the Photochemistry of Coordination Compounds to Light-Powered Nanoscale Devices and Machines. *Coord. Chem. Rev.* **2008**, *252*, 2456–2469.

33 Ferrando-Soria, J.; Vallejo, J.; Castellano, M.; Martínez-Lillo, J.; Pardo, E.; Cano, J.; Castro, I.; Lloret, F.; Ruiz-García, R.; Julve, M. Molecular Magnetism, quo vadis? A Historical Perspective from a Coordination Chemist Viewpoint. *Coord. Chem. Rev.* **2017**, *339*, 17–103.

34 Vukotic, V. N.; Harris, K. J.; Zhu, K. L.; Schurko, R. W.; Loeb, S. J. Metal-Organic Frameworks with Dynamic Interlocked Components. *Nature Chem.* **2012**, *4*, 456–460.

35 Kumar, K. S.; Ruben, M. Sublimable Spin-Crossover Complexes: From Spin-State Switching to Molecular Devices. *Angew. Chem. Int. Ed.* **2021**, *60*,7502–7521.

36 Martynov, A. G.; Polovkova, M. A.; Berezhnoy, G. S.; Sinelshchikova, A. A.; Khrustalev, V. N.; Birin, K. P.; Kirakosyan, G. A.; Gorbunova, Y. G.; Tsivadze, A. Y. Heteroleptic Crown-Substituted Tris(phthalocyaninates) as Dynamic Supramolecular Scaffolds with Switchable Rotational States and Tunable Magnetic Properties. *Inorg. Chem.* **2021**, *60*, 9110–9121.

37 Mauro, M. Phosphorescent Multinuclear Complexes for Optoelectronics: Tuning of the Excited-State Dynamics. *Chem. Comm.* **2021**, *57*, 5857–5870.

38 Karmakar, M.; Pal, A.; Mondal, B.; Adarsh, N. N.; Thakur, A. Light-Triggered Metal Coordination Dynamics in Photoswitchable Dithienylethene-Ferrocene System. *Inorg. Chem.* **2021**, *60*, 6086–6098.

39 Gotico, P.; Coitrel, B.; Guillot, R.; Sircoglou, M.; Quaranta, A.; Halime, Z.; Leibl, W.; Aukauloo, A. Second-Sphere Biomimetic Multipoint Hydrogen-Bonding Patterns to Boost CO_2 Reduction of Iron Porphyrins. *Angew. Chem. Int. Ed.* **2019**, *58*, 4504 –4509.

40 Ballardini, R.; Balzani, V.; Gandol, M. T.; Prodi, L.; Venturi, M.; Philp, D.; Ricketts, H. G.; Stoddart, J. F. A Photochemically Driven Molecular Machine. *Angew. Chem. Int. Ed.* **1993**, *32*, 1301–1303.

41 Bissel, R. A.; Cordova, E.; Kaifer, A.E.; Stoddart, J.F. A Chemically and Electrochemically Switchable Molecular Shuttle. *Nature* **1994**, *369*, 133–137.

42 Schill, G. (1971) Catenanes, Rotaxanes and Knots. New York/London: Academic Press.

43 Livoreil, A.; Sauvage, J.-P.; Armaroli, N.; Balzani, V.; Flamigni, L.; Ventura, B. Electrochemically and Photochemically Driven Ring Motions in a Dissymmetrical Copper [2]Catenate. *J. Am. Chem. Soc.* **1997**, *119*, 12114–12124.

44 Livoreil, A.; Dietrich-Buchecker, C. O.; Sauvage, J.-P. Electrochemically Triggerred Swinging of a [2]catenate. *J. Am. Chem. Soc.* **1994**, *116*, 9399–9400.

45 Baumann, F.; Livoreil, A.; Kaim, W.; Sauvage, J.-P. Changover in a Multimodal Copper(II) Catenane as Monitored by EPR Spectroscopy. *Chem. Comm.* **1997**, 35–36.

46 Jiménez-Molero, M.C.; Dietrich-Buchecker, C.; Sauvage, J.-P. Towards Synthetic Molecular Muscles: Contraction and Stretching of a Linear Rotaxane Dimer. *Angew. Chem. Int. Ed.* **2000**, *39*, 3284–3287.

47 Jiménez-Molero, M.C., Dietrich-Buchecker, C., Sauvage, J.-P. Chemically Induced Contraction and Stretching of a Linear Rotaxane Dimer. *Chem. Eur. J.* **2002**, *8*, 1456–1466.

48 Collin, J. P.; Dietrich-Buchecker, C.; Gavina, P.; Jimenez-Molero, M. C.; Sauvage, J. P. Shuttles and Muscles: Linear Molecular Machines Based on Trasition Metals. *Acc. Chem. Res.* **2001**, *34*, 477–487.

49 Goodwin, H.A. Spin Transitions in Six-Coordinate Iron(II) Complexes. *Coord. Chem. Rev*. **1976**, *18*, 293–325.

50 Gütlich, P. Spin Crossover in Iron(II) Complexes. *Struct. Bonding (Berlin)* **1981**, *44*, 83–195.

51 König, E.; Ritter, G.; Kulshreshtha, S. K. The Nature of Spin-State Transitions in Solid Complexes of Iron(II) and the Interpretation of Some Associated Phenomena. *Chem. Rev.* **1985**, *85*, 219–234.

52 Boillot, M. L.; Sour, A.; Delhaes, P.; Mingotaud, C.; Soyer, H. A Photomagnetic Effect for Controlling Spin States of Iron(II) Complexes in Molecular Materials. *Coord. Chem. Rev*. **1999**, *192*, 47–59.

53 Gütlich, P., Godwin, H. A. (2004) *Spin Crossover in Transition Metal Compounds*. Vol. 233–235. Berlin: Springer.

54 Real, J. A.; Gaspar, A. B.; Muñoz, M. C. Thermal, Pressure and Light Switchable Spin-Crossover Materials. *Dalton Trans*. **2005**, 2062–2079.

55 Bousseksou, A.; Molnár, G.; Salmon, L.; Nicolazzi, W. Molecular Spin Crossover Phenomenon: Recent Achievements and Prospects. *Chem. Soc. Rev*. **2011**, *40*, 3313–3335.
56 Ruiz, E. Charge Transport Properties of Spin Crossover Systems. *Phys. Chem. Chem. Phys*. **2014**, *16*, 14–22.
57 Bertoni, R.; Cammarata, M.; Lorenc, M.; Matar, S. F.; Matar, J.-F.; Létard, J. F.; Lemke, E. Collet, H. T. Ultrafast Light-Induced Spin-State Trapping Photophysics Investigated in $Fe(phen)_2(NCS)_2$ Spin-Crossover Crystal. *Acc. Chem. Res*. **2015**, *48*, 774–781.
58 Harding, D. J.; Harding, P.; Phonsri, W. Spin Crossover in Iron(II) Complexes. *Coord. Chem. Rev*. **2016**, *313*, 38–61.
59 Khusniyarov, M. M. How to Switch Spin-Crossover Metal Complexes at Constant Room Temperature. *Chem. Eur. J.* **2016**, *22*, 15178–15191.
60 Cirera, J.; Ruiz, E.; Alvarez, S.; Neese, F.; Kortus, J. How to Build Molecules with Large Magnetic Anisotropy. *Chem. Eur. J*. **2009**, *15*, 4078–4087.
61 Neese, F.; Pantazis, D. A. What is not Required to Make a Single Molecule Magnet. *Faraday Discuss*. **2011**, *148*, 229–238.
62 Atanasov, M.; Aravena, D.; Suturina, E.; Bill, E.; Maganas, D.; Neese, F. First Principles Approach to the Electronic Structure, Magnetic Anisotropy and Spin Relaxation in Mononuclear 3d-Transition Metal Single Molecule Magnets. *Coord. Chem. Rev*. **2015**, *289–290*, 177–214.
63 Gomez-Coca, S.; Aravena, D.; Morales, R.; Ruiz, E. Large Magnetic Anisotropy in Mononuclear Metal Complexes. *Coord. Chem. Rev*. **2015**, *289–290*, 379–392.
64 Chibotaru, L. F. Theoretical Understanding of Anisotropy in Molecular Nanomagnets. *Struct. Bond*. **2015**, *164*, 185–229.
65 Craig, G. A.; Murrie, M. 3d Single-Ion Magnets. *Chem. Soc. Rev*. **2015**, *44*, 2135–2147.
66 Frost, J. M.; Harriman, K. L. M.; Murugesu, M. The Rise of 3-d Single-Ion Magnets in Molecular Magnetism: Towards Materials from Molecules? *Chem. Sci*. **2016**, *7*, 2470–2491.
67 Bar, A. K.; Pichon, C.; Sutter, J.-P. Magnetic Anisotropy in Two- to Eight-Coordinated Transition-Metal Complexes: Recent Developments in Molecular Magnetism. *Coord. Chem. Rev*. **2016**, *308*, 346–380.
68 Meng, Y.-S.; Jiang, S.-D.; Wang, B.-W.; Gao, S. Understanding the Magnetic Anisotropy toward Single-Ion Magnets. *Acc. Chem. Res*. **2016**, *49*, 2381–2389.
69 Muñoz, M.C; Real, J.A. Thermo-, Piezo-, Photo- and Chemo-Switchable Spin Crossover Iron(II)-Metallocyanate Based Coordination Polymers. *Coord. Chem. Rev.* **2011**, *255*, 2068–2093.
70 Goodwin, H. A. Spin Crossover in Cobalt(II) Systems. *Top Curr. Chem.* **2004**, *234*, 23–47.
71 Cowan, M. G.; Olguín, J.; Narayanaswamy, S. Tallon, J. L.; Brooker, S. Reversible Switching of a Cobalt Complex by Thermal, Pressure, and Electrochemical Stimuli: Abrupt, Complete, Hysteretic Spin Crossover. *J. Am. Chem. Soc.* **2012**, *134*, 2892–2894.
72 Kahn, O. Molecular Magnetism. VCH Publishers, New York, 1993.
73 Ishikawa, N.; Sugita, M.; Ishikawa, T., Koshihara, S.Y.; Kaizu, Y. Lanthanide Double-Decker Complexes Functioning as Magnets at the Single-Molecular Level. *J. Am. Chem. Soc.* **2003**, *125*, 8694–8695.
74 Ishikawa, N.; Sugita, M.; Okubo, T.; Tanaka, N.; Iino, T.; Kaizu, Y. Determination of Ligand-Field Parameters and f-Electronic Structures of Double-Decker Bis(phthalocyaninato)lanthanide Complexes. *Inorg. Chem.* **2003**, *42*, 2440–2446.
75 Ishikawa, N.; Sugita, M.; Ishikawa, T.; Koshihara, S.-Y.; Kaizu, Y. Mononuclear Lanthanide Complexes with a Long Magnetisation Relaxation Time at High Temperatures: A New Category of Magnets at the Single-Molecular Level. *J. Phys. Chem. B* **2004**, *108*, 11265–11271.
76 Vallejo, J.; Castro, I.; Ruiz-García, R.; Cano, J.; Julve, M.; Lloret, F.; De Munno, G.; Wernsdorfer, W.; Pardo, E. Field-Induced Slow Magnetic Relaxation in a Six-Coordinate Mononuclear Cobalt(II) Complex with a Positive Anisotropy. *J. Am. Chem. Soc*. **2012**, *134*, 15704–15707.
77 Gaspar, A. B; Ksenofontov, V.; Seredyuk, M.; Gutlich, P. Multifunctionality in Spin Crossover Materials, *Coord. Chem Rev.* **2005**, 249, 2661–2676.
78 Bousseksou, A.; Molnár, G.; Demont, P.; Menegotto, J. Observation of a Thermal Hysteresis Loop in the Dielectric Constant of Spin Crossover Complexes: Towards Molecular Memory Devices. *J. Mater. Chem.* **2003**, *13*, 2069–2071.
79 Kumar, K. S.; Ruben M. Emerging Trends in Spin Crossover (SCO) Based Functional Materials and Devices. *Coord. Chem. Rev.* **2017**, *346*, 176–205.
80 Gutlich, P.; Hauser, A. Thermal and Light-Induced Spin Crossover in Iron(II) Complexes. *Coord. Chem. Rev.* **1990**, *97*, 1–22.
81 Krivokapic, I.; Zerara, M.; Daku, M. L.; Vargas, A.; Enachescu, C.; Ambrus, C.; Tregenna-Piggott, P.; Amstutz, N.; Krausz, E.; Hauser, A. Spin Crossover in Cobalt(II) Imine Complexes. *Coord. Chem. Rev.* **2007**, *251*, 364–378.
82 Hayami, S.; Komatsu, Y.; Shimizu, T.; Kamihata, H.; Lee, Y. H. Spin-Crossover in Cobalt(II) Compounds Containing Terpyridine and its Derivatives. *Coord. Chem. Rev.* **2011**, *255*, 1981–1990.
83 Galet, A; Gaspar, A. B.; Muñoz, M. C.; Real, J. A. Influence of the Counterion and the Solvent Molecules in the Spin Crossover System $[Co(4\text{-terpyridone})_2]X_p{\cdot}nH_2O$, *Inorg. Chem.* **2006**, *45*, 4413–4422.
84 Murrie, M. Cobalt(II) Single-Molecule Magnets. *Chem. Soc. Rev.* **2010**, *39*, 1986–1995.
85 Ding, Y.-S.; Deng, Y.-F.; Zheng, Y.-Z. The Rise of Single-Ion Magnets as Spin Qubits. *Magnetochemistry* **2016**, *2*, 40–59.
86 Zadrozny, J.M; Long, J. R. Slow Magnetic Relaxation at Zero Field in the Tetrahedral Complex $[Co(SPh)_4]_2^-$. *J. Am. Chem. Soc.* **2011**, *133*, 20732–20734.
87 Lloret, F.; Julve, M.; Cano, J.; Ruiz-García, R.; Pardo, E. Magnetic Properties of Six-Coordinated High-Spin Cobalt(II) Complexes: Theoretical Background and its Application. *Inorg. Chim. Acta* **2008**, *361*, 3432–3445.
88 Vallejo, J.; Castro, I.; Ruiz-García, R.; Cano, J.; Julve, M.; Lloret, F.; De Munno, G.; Wernsdorfer, W.; Pardo, E. Field-Induced Slow Magnetic Relaxation in a Six-Coordinate Mononuclear Cobalt(II) Complex with a Positive Anisotropy. *J. Am. Chem. Soc*. **2012**, *134*, 15704–15707.
89 R. Herchel, L. Váhovská, I. Potocnák, Z. Trávnícek, Slow Magnetic Relaxation in Octahedral Cobalt(II) Field-Induced Single-Ion Magnet with Positive Axial and Large Rhombic Anisotropy. *Inorg. Chem.* **2014**, *53*, 5896–5898.
90 Roy, S.; Oyarzabal. I.; Vallejo, J.; Cano, J.; Colacio, E.; Bauza, A.; Frontera, A.; Kirillov, A. M.; Drew, M. G. B.; Das, S. Two Polymorphic Forms of a Six-Coordinate Mononuclear Cobalt(II) Complex with Easy-Plane Anisotropy: Structural Features, Theoretical Calculations, and Field-Induced Slow Relaxation of the Magnetisation. *Inorg. Chem.* **2016**, *55*, 8502–8513.
91 Ding, Z.-Y.; Meng, Y.-S.; Xiao, Y.; Zhang, Y.-Q.; Zhu, Y.-Y.; Gao, S. Probing the Influence of Molecular Symmetry on the Magnetic Anisotropy of Octahedral Cobalt(II) Complexes. *Inorg. Chem. Front.* **2017**, *4*, 1909–1916.
92 Wu, Y.; Tian, D.; Ferrando-Soria, J.; Cano, J.; Yin, L.; Ouyang, Z.; Wang, Z.; Luo, S.; Liu, X.; Pardo, E. Modulation of the Magnetic Anisotropy of Octahedral Cobalt(II) Single-Ion Magnets by Fine-Tuning the Axial Coordination Microenvironment. *Inorg. Chem. Front.* **2019**, *6*, 848–856.
93 Cen, P.; Yuan, W.; Tan, M.; Chen, B.; Song, W.; Wang, Z.; Liu, X. Field-Induced Slow Magnetic Relaxation in an Octahedral High-Spin Co(II) Complex. *Inorg. Chem. Commun.* **2019**, *99*, 195–198.
94 Urtizberea, A.; Roubeau, O. Switchable Slow Relaxation of Magnetization in the Native Low Temperature Phase of a Cooperative Spin Crossover Compound. *Chem. Sci.* **2017**, *8*, 2290– 2295.
95 Feng, X.; Mathonière, C.; Jeon, I.-R.; Rouzières, M.; Ozarowski, A.; Aubrey, M. L.; Gonzalez, M. I.; Clérac, R.; Long, J. R. Tristability in a Light-Actuated Single-Molecule Magnet. *J. Am. Chem. Soc.* **2013**, *135*, 15880–15884.
96 Mathonière, C.; Lin, H.-J.; Siretanu, D.; Clérac, R.; Smith, J. M. Photoinduced Single-Molecule Magnet Properties in a Four-Coordinate Iron(II) Spin Crossover Complex. *J. Am. Chem. Soc.* **2013**, *135*, 19083–19086.
97 Palion-Gazda, J.; Machura, B.; Kruszynski, R.; Grancha, T.; Moliner, N.; Lloret, F.; Julve, M. Spin Crossover in Double Salts Containing Six- and Four-Coordinate Cobalt(II) Ions. *Inorg. Chem.* **2017**, *56*, 6281–6296.
98 Shao, D.; Deng, L.-D.; Shi, L.; Wu, D.-Q.; Wei, X.-Q.; Yang, S.-R.; Wang, X.-Y. Slow Magnetic Relaxation and Spin Crossover Behaviour in a Bicomponent Ion-Pair Cobalt(II) Complex. *Eur. J. Inorg. Chem.* **2017**, 3862–3867.
99 Cui, H.-H.; Wang, J.; Chen, X.-T.; Xue, Z.-L. Slow Magnetic Relaxation in Five-Coordinate Spin-Crossover Cobalt(II) Complexes, *Chem. Commun.* **2017**, *53*, 9304–9307.
100 Chen, L.; Song, J.; Zhao, W.; Yi, G.; Zhou, Z.; Yuan, A.; Song, Y.; Wang, Z.; Ouyang, Z.-W. A Mononuclear Five-Coordinate Co(II) Single Molecule Magnet with a Spin Crossover between the S = 1/2 and 3/2 States. *Dalton Trans.* **2018**, *47*, 16596–16602.
101 Xu, M.-X.; Liu, Z.; Dong, B.-W.; Cui, H.-H. Wang, Y.-X.; Su, J.; Wang, Z.; Song, Y.; Chen, X.-T.; Jiang, S.-D.; Gao, S. Single-Crystal Study of a Low Spin Co(II) Molecular Qubit: Observation of Anisotropic Rabi Cycles. *Inorg. Chem.* **2019**, *58*, 2330–2335.
102 Shao, D.; Shi, L.; Yin, J.; Wang, B.-L.; Wang, Z.-X.; Zhang, Y.-Q.; Wang, X.-Y. Reversible On-Off Switching of Both Spin Crossover and Single-Molecule Magnet Behaviours *via* a Crystal-to-Crystal Transformation. *Chem. Sci.* **2018**, *9*, 7986–7991.
103 Kobayashi, F.; Komatsumaru, Y.; Akiyoshi, R; Nakamura, M.; Zhang, Y.; Lindoy, L. F.; Hayami, S. Water Molecule-Induced Reversible Magnetic Switching in a Bis-Terpyridine Cobalt(II) Complex Exhibiting Coexistence of Spin Crossover and Orbital Transition Behaviors. *Inorg. Chem.* **2020**, *59*, 16843–16852.
104 Figgins, P. E.; Busch, D. H. Complexes of Iron(II), Cobalt(II) and Nickel(II) with Biacetyl-bis-methylimine, 2-Pyridinal-methylimine and 2,6-Pyridindial-bis-methylimine. *J. Am. Chem. Soc.* **1960**, *82*, 820–824.
105 Park, J.; Pasupathy, A. N.; Goldsmith, J. I.; Chang, C; Yaish, Y.; Petta, J. R.; Rinkoski, M.; Sethna, J. P.; Abruña, H. D.; McEuen, P. L.; Ralph, D. C. Coulomb Blockade and the Kondo Effect in Single-Atom Transistors. *Nature Materials* **2002**, *417*, 722–725.
106 Parks, J. J.; Champagne, A. R.; Costi, T. A.; Shum, W. W.; Pasupathy, A. N.; Neuscamman, E.; Flores-Torres, S.; Cornaglia, P. S.; Aligia, A. A.; Balseiro, C. A.; Chan, G. K.-L.; Abruña, H. D.; Ralph, D. C. Mechanical Control of Spin States in Spin-1 Molecules and the Underscreened Kondo Effect. *Science* **2010**, *328*, 1370–1373.

107 Harzmann, G. D.; Frisenda, R.; van der Zant, H. S. J.; Mayor, M. Single-Molecules Spin Switch Based on Voltage-Triggered Distortion of the Coordination Sphere. *Angew. Chem. Int. Ed.* **2015**, *54*, 13425–13430.
108 Devid, E. J; Martinho, P. N.; Kamalakar, M. V., Salitros, I.; Prendergast, Ú.; Dayen, J.-F.; Meded, V.; Lemma, T.; González-Pietro, R.; Evers, F.; Keyes, T. E.; Ruben, M.; Doudin, B.; van der Molen, S. J. Spin Transition in Arrays of Gold Nanoparticles and Spin Crossover Molecules. *ACS Nano* **2015**, *9*, 4486–4507.
109 Katsnelson, M. I. Graphene: Carbon in Two Dimensions. *Mater. Today* **2007**, *10*, 20–27.
110 Konstantinov, N; Tauzin, A.; Noumbé, U. N.; Dragoe, D.; Kundys, B.; Majjad, H.; Brosseau, A.; Lenertz, M.; Singh, A.; Berciaud, S.; Boillot, M.-L.; Doudin, B.; Mallah, T.; Dayen, J. F. Electrical Read-Out of Light-Induced Spin Transition in Thin Film Spin Crossover/Graphene Heterostructures. *J. Mater. Chem. C* **2021**, *9*, 2712–2720.
111 Lee, C.W.; Kim, O.Y.; Lee, J.Y. Organic Materials for Organic Electronic Devices. *J. Ind. Eng. Chem.* **2014**, *20*, 1198–1208.
112 Komeda, T.; Isshiki, H.; Liu, J.; Zhang, Y.-F.; Lorente, N.; Katoh, K.; Breedlove, B. K.; Yamashita, M. Observation and Electric Current Control of a Local Spin in a Single-Molecule Magnet. *Nat. Commum.* **2011**, *2*, 217–223.
113 Urdampilleta, M.; Klyatskaya, S.; Cleuziou, J-P.; Ruben, M.; Wernsdorfer, W. Supramolecular Spin Valves. *Nature Materials* **2011**, *10*, 502–506.

CHAPTER II

ELECTROCHEMICALLY-ACTIVE SPIN CROSSOVER MOLECULAR NANOMAGNETS (I)

Electrochemically-active Spin Crossover Molecular Nanomagnets (I)

II.1 – Background and Highlights

Mononuclear transition metal complexes constitute the smallest molecular magnetic systems for quantum data storage and processing applications in the emerging field of molecular spintronics and quantum computing.[1] Spin crossover (SCO) compounds[2–13] and mononuclear single-molecule magnets (SMMs),[14–24] in their excellent paradigms of addressable and stimuli-responsive, are bistable magnetic molecules with potential applications in molecular spintronic devices and quantum computers.[25–48] From a historical viewpoint, in the molecular magnetism field, great attention was devoted to mononuclear cobalt(II) complexes as illustrative examples of SCO compounds[49–52] and SMMs.[53,54] Now, many cobalt(II)-based SCO compounds and SMMs are known, where both high- (HS, S_{Co} = 3/2) and low-spin (LS, S_{Co} = 1/2) states are available for a $3d^7$ cobalt(II) ion depending on the metal coordination environment. To date, a few examples are known where both properties coexist in the same system, leading to a new class of multiresponsive and multifunctional SCO/SMM materials as potential candidates for multistable molecular quantum bits (qubits) for quantum information processing (QIP).[55–57]

Known cobalt(II)-based SCO/SMM systems include a series of double salts whereby the SCO and SMM behaviour have been separately identified on the two components of the ion pair.[58,59] In such cases, the SCO feature occurs in cationic six-coordinate octahedral complexes, and the SMM response arises from anionic four-coordinate tetrahedral ones. More interestingly, a series of mononuclear five-coordinate cobalt(II) SCO complexes with a square-pyramidal coordination geometry exhibits a field-induced SMM behaviour in the LS state,[60,61] one of them was recently tested as a molecular qubit prototype.[62] In truth, the LS cobalt(II) ion is a genuine two-level magnetic quantum system represented by the m_S = +1/2 and –1/2 states, able to play the role of a qubit for quantum computing applications. By comparison, the HS cobalt(II) ion possesses an effective doublet ground spin state (S_{eff} = 1/2) coming from the well-isolated ground Kramers doublet resulting from a large first-order spin-orbit coupling (SOC). This feature makes this effective spin state an alternative candidate for a "single" qubit. Likewise, related mononuclear octahedral cobalt(II) complexes exhibit a solvato-switching of the SCO and SMM behaviour.[56,57]

Cobalt(II) complexes with bidentate 2,2'-bipyridine (bipy) or tridentate 2,2':6',2''-terpyridine (TERPY) ligands and related imine derivatives constitute a major class of SCO systems.[63,64] In this respect, Figgins and Busch reported in 1960 the first examples of the SCO phenomenon in mononuclear octahedral cobalt(II) complexes with *N*-methyl substituted, pyridine-2-imine (PI) and pyridine-2,6-diimine type (PDI) ligands.[65,66] In this chapter, we report the synthesis, structural, electrochemical and spectroscopic characterisation, as well as the static (dc) and dynamic (ac) magnetic properties for a related series of mononuclear octahedral cobalt(II) compounds of formula $[Co(n\text{-XPhPDI})_2](ClO_4)_2 \cdot x$Solv [**1**: X = I (*n* = 4), Solv = MeCN (x = 1); **2**: X = Br (*n* = 4), Solv = MeCN (x = 1); **3**: X = Cl (*n* = 4), Solv = $MeCO_2Et$ (x = 1); and **4**: X = Br (*n* = 3), x = 0] (Scheme II.1). This novel family of redox-active cobalt(II) complexes displays both thermally-induced LS-HS transition and field-induced slow magnetic relaxation (SMR) in the LS and HS states. The distinct SCO and SMM behaviours depend on the electron-withdrawing character of the halogen substituent, the *para* or *meta* substitution, or occasionally the presence of additional crystallisation solvent molecules (acetonitrile or ethyl acetate). Hence, the influence on the SCO and SMM behaviours of geometric and electronic, both intra- and intermolecular, effects induced by ligand and solvent was systematically analysed in this series. This study allows us to obtain appropriate magneto-structural correlations that could be useful in designing new SCO/SMM materials as prototypes of molecular spintronic devices for quantum information processing (QIP).

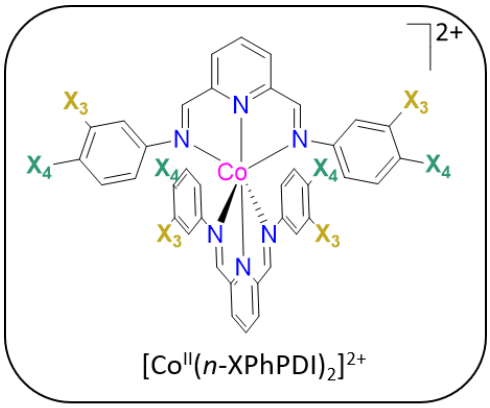

	n-XPhPDI	X_4	X_3
1	4-IPhPDI	I	H
2	4-BrPhPDI	Br	H
3	4-ClPhPDI	Cl	H
4	3-BrPhPDI	H	Br

Scheme II.1 General chemical formula of the $[Co^{II}(n\text{-XPhPDI})]^{2+}$ complex cation in **1–4**.

II.2 – Ligand Design and Synthetic Strategy

The combination of SCO and SMM behaviours linked to metal centre with the multi-electron transfer (MET) properties of the ligand counterpart in one single molecule can be achieved by using redox non-innocent bis-chelating PDI-type ligands. Moreover, the relatively easy synthetic chemistry of the *N*-phenyl substituted PDI ligands would allow the fine-tuning of the SCO, SMM and MET properties by preparing of a vast chemical library of electro-active bis-chelating cobalt(II)-PDI complexes.

In this chapter, we could modulate the SCO and SMM behaviours via electronic and steric effects by varying the substitution pattern and nature of the substituent since both electronic structure and crystal packing interactions play decisive roles in the spin transition and slow magnetic relaxation

phenomena. However, we also realised that using PDI ligands bearing electron-withdrawing groups on the phenyl substituents could be a reasonable way to favour the ligand-based electronic reductions, improving the MET properties by increasing the π-acceptor character of the ligands. Otherwise, the great stabilisation provided by these modified PDI ligands to the oxidisable metal centre in the N_6 coordination environment may open up the pathway to a new class of electro-switchable spin quantum switches and capacitors, as we will see in the following second chapter of this doctoral dissertation.

The *n*-XPhPDI ligands (with *n*-X = 4-I, 4-Br, 3-Br, 4-Cl) were synthesised from the straightforward condensation of pyridine-2,6-diformaldehyde and the corresponding *para*- or *meta*-monosubstituted aniline (1:2 molar stoichiometry) in acid media, as reported earlier for the parent unsubstituted PhPDI ligand.[2] All these 4-XPhPDI ligands were isolated as crystalline powders in good yields, and they were characterised by elemental analyses (C, H, N), Fourier-transform infrared (FT-IR) and proton nuclear magnetic resonance (^{1}H NMR) spectroscopies. In contrast, the 3-BrPhPDI ligand could not be isolated, and it was used as an oil crude product (see II.7 - Experimental Section).

The reaction between cobalt(II) perchlorate hexahydrate and the corresponding 4-XPhPDI ligand (X = I, Br and Cl) substituted PDI ligands in the 1:2 molar ratio in methanol led to crystalline powders of **1**–**3**. Compound **4** was synthesised by an *in situ* reaction of pyridine-2,6-diformaldehyde and 3-bromoaniline with cobalt(II) perchlorate hexahydrate. X-ray suitable single crystals of **1**–**4** were grown in a test tube by layering ethyl acetate on saturated acetonitrile solutions of the crystalline powder (see II.7 - Experimental Section).

II.3 – Description of the Structures

Compounds **1** and **2** crystallise in the *P2$_1$/c* space group of the monoclinic system; **3** and **4** do so in the *P–1* and *P2$_1$/n* space groups of triclinic and monoclinic systems (Table II.1). All structures consist of mononuclear cobalt(II) complex cations, $[Co^{II}(n\text{-XPhPDI})_2]^{2+}$ [*n* = 4 (**1**–**3**) and 3 (**4**); X = I (**1**), Br (**2** and **4**) and Cl (**3**)], perchlorate anions, and acetonitrile (**1** and **2**) or ethyl acetate (**3**) crystallisation solvent molecules except **4**. However, while **3** embodies a single crystallographically independent cationic complex, two coexist in **1** and **2** and even three in **4** (Figures II.1 and II.2).

Molecular structures. All cobalt atoms in the four compounds exhibit the same rhombically distorted, axial compressed octahedral CoN_6 environment (Figures II.1 and II.S3), as reported earlier for the parent complex of formula $[Co^{II}(PhPDI)_2](ClO_4)_2{\cdot}CH_3OH$.[66] In the coordination sphere, imine-nitrogen atoms (N_{im} and N'_{im}) from each *n*-XPhPDI ligand define the equatorial plane while pyridyl-nitrogen atoms (N_{py} and N'_{py}) occupy the axial positions. Co–N bond lengths are grouped into two shorter Co–N_{py} and Co–N'_{py} [average R_1 = 1.905 (**1**), 1.888 (**2**), 2.028 (**3**), and 1.922 and 2.024 Å (**4**)], two intermediate Co–N_{im} [average R_2 = 2.070 (**1**), 2.065 (**2**), 2.185 (**3**), and 2.050 and 2.205 Å (**4**)], and two longer Co–N'_{im} bonds [average R_3 = 2.168 Å (**1**) and 2.159 (**2**), 2.228 (**3**), and 2.200 and 2.214 Å (**4**)] (see Table II.2). The average values of the axial bond lengths (R_{ax}) are rather shorter than the equatorial ones [average values: $R_{eq} = (R_2 + R_3)/2$ = 2.117 (**1**), 2.112 (**2**), 2.207 (**3**), and 2.125 and 2.210 Å (**4**)]. Due to some asymmetry observed in these compounds, these bond distances are difficult to assign to a specific spin state when viewed individually. Nevertheless, the mean values [$R = (2R_{eq} + R_{ax})/3$ = 2.047 (**1**), 2.037 (**2**), and 2.147 Å (**3**)] are typical for LS Co^{II} complexes in **1** and **2**, but HS in **3**. However, both LS and HS Co^{II} complexes coexist in **4** in a 2:1 ratio [R = 2.057 (Co1/Co2) and 2.148 Å (Co3)]. The stronger electron-withdrawing character of the *p*-chloro substituent (**3**) compared to the *p*-iodo- and *p*-bromo ones (**1** and **2**) should provide a weaker ligand field, explained by the HS $t_{2g}^5e_g^2$ electronic configuration in **3**. Since the d orbitals mainly participate in antibonding molecular orbitals and the e_g ones have their electron density better directed to the bond regions than the t_{2g} ones, the greater occupation of the former in the HS state (**3**) is responsible for its Co-N bond lengthening. However, the

Table II.1 Summary of Crystallographic Data for **1**–**4**

	1	**2**	**3**	**4**
Formula	$C_{40}H_{29}N_7O_8Cl_2I_4Co$	$C_{40}H_{29}N_7O_8Cl_2Br_4Co$	$C_{42}H_{34}N_6O_{10}Cl_6Co$	$C_{38}H_{26}N_6O_8Cl_2Br_4Co$
M (g mol^{-1})	1373.13	1185.13	1054.38	1144.12
Crystal system	Monoclinic	Monoclinic	Triclinic	Monoclinic
Space group	*P2$_1$/c*	*P2$_1$/c*	*P–1*	*P2$_1$/n*
a (Å)	12.5152(3)	12.3179(1)	10.1717(8)	8.1978(1)
b (Å)	39.5528(8)	38.8295(3)	10.3299(6)	41.0395(6)
c (Å)	18.4447(4)	18.2714(2)	21.7926(15)	36.5103(4)
α (°)	90	90	95.702(2)	90
b (°)	92.044(1)	92.694(1)	98.578(3)	93.874(1)
γ (°)	90	90	91.896(2)	90
V (Å^3)	9124.5(3)	8729.51(14)	2250.3(3)	12255.2(3)
Z	8	8	2	12
r_{calc} (g cm^{-3})	1.999	1.804	1.556	1.860
μ (mm^{-1})	3.258	4.238	0.802	4.523
T (K)	150	150	150	150
Reflect. collcd.	130575	109444	151552	56042
Reflect. obs. [$I > 2\sigma(I)$]	23025 (20062)	28683 (17682)	12609 (9558)	23462 (17684)
Data Restraints/ Parameters	142/1152	0/1119	21/628	62/1680
R_1[a] [$I > 2\sigma(I)$]	0.0325 (0.0400)	0.0568 (0.1106)	0.0458 (0.0708)	0.0625 (0.0899)
wR_2[b] [$I > 2\sigma(I)$]	0.0636 (0.0664)	0.0981 (0.1132)	0.1062 (0.1226)	0.1269 (0.1391)
S[c]	1.158	1.013	1.056	1.080

[a] $R_1 = \sum(||F_o| - |F_c||)/\sum|F_o|$. [b] $wR_2 = [\sum w(F_o^2 - F_c^2)^2/\sum w(F_o^2)^2]^{1/2}$. [c] $S = [\sum w(|F_o| - |F_c|)^2/(N_o - N_p)]^{1/2}$.

Table II.2 Selected Structural Data for **1**–**4**[a]

	1	**2**	**3**	**4**
R_1(Co–N_{py})[b] (Å)	1.907(2)/1.902(2)	1.892(3)/1.884(3)	2.0255(19)	1.904(5)/1.940(5)/2.024(5)
R_2(Co–N_{im})[c] (Å)	2.113(3)/2.026(2)	2.035(3)/2.094(3)	2.185(2)	2.018(5)/2.081(5)/2.205(5)
R_3(Co–N'$_{im}$)[c] (Å)	2.126(3)/2.209(2)	2.192(3)/2.126(3)	2.228(2)	2.245(5)/2.194(5)/2.214(5)
R_{eq}[d] (Å)	2.117(3)/2.117(2)	2.114(3)/2.110(3)	2.207(2)	2.132(5)/2.138(5)/2.210(5)
R[e] (Å)	2.047(3)/2.046(2)	2.039(3)/2.035(3)	2.146(2)	2.055(5)/2.071(5)/2.148(5)
Δ_R[f]	0.103(3)/0.105(2)	0.108(3)/0.111(3)	0.084(2)	0.110(5)/0.095(5)/0.087(5)
δ_R[g]	0.004(3)/0.086(2)	0.074(3)/0.015(3)	0.019(2)	0.106(5)/0.053(5)/0.004(5)
N_{py}–Co–N_{py}[h] (°)	175.70(11)/179.34(11)	179.6(1)/175.5(1)	164.85(8)	174.5(2)/173.1(2)/174.1(2)
N_{im}–Co–N'$_{im}$[i] (°)	101.11(10)/99.91(9)	100.3(1)/100.2(1)	94.22(8)	100.8(2)/101.0(2)/103.7(2)
N'$_{im}$–Co–N_{im}[i] (°)	83.71(10)/84.56(9)	84.2(1)/84.1(1)	93.03(8)	84.0(2)/84.6(2)/83.8(2)
δ[j] (Å)	±0.431(2)/±0.422(2)	±0.416(2)/±0.407(2)	±0.555(2)	±0.437(5)/±0.469(5)/ ±0.557(5)
Φ[k] (°)	75.42(3)/78.70(3)	78.06(3)/77.20(4)	87.65(3)	75.3(3)/75.9(3)/73.5(3)
h[l] (Å)	4.248(5)/4.623(5)	4.471(5)/4.035(5)	3.845(3)	3.800(8)/4.026(8)/4.305(8)
θ[m] (°)	44.61(2)/47.56(2)	47.38(3)/33.55(3)	26.47(3)	20.3(7)/21.7(7)/35.5(8)
φ[n] (°)	48.35(6)/53.45(6)	46.0(5)/42.8(5)	44.08(4)	35.4(8)/29.8(8)/34.3(9)

[a]Structural data for each crystallographically independent cobalt atom are separated by a slash. [b]Average axial cobalt to pyridyl-nitrogen bond distance from the two ligands. [c]Average equatorial cobalt to imine-nitrogen bond lengths from each ligand. [d]Average equatorial cobalt-nitrogen bond distance defined as $R_{eq} = (R_2 + R_3)/2$. [e]Average cobalt-nitrogen bond distance defined as $R = (R_1 + R_2 + R_3)/3$. [f]Axial distortion parameter defined as $\Delta_R = (R_{eq} - R_1)/R$. [g]Rhombic distortion parameter defined as $\delta_R = (R_2 - R_3)/R_{eq}$. [h]Average axial cobalt to pyridyl-nitrogen bond angle from the two ligands. [i]Average equatorial cobalt to imine-nitrogen bond angle from the two ligands. [j]Mean deviation of the imine nitrogen donor atoms from the equatorial plane at the cobalt atom. [k]Dihedral angle between the mean planes of the pyridyldiimine ligand fragments. [l]Intramolecular distance between the centroids of the pyridyl and phenyl rings of the two ligands. [m]Average torsion angle for the phenylimine ligand fragments. [n]Average dihedral angle between the mean planes of the pyridyl and phenyl rings of the two ligands.

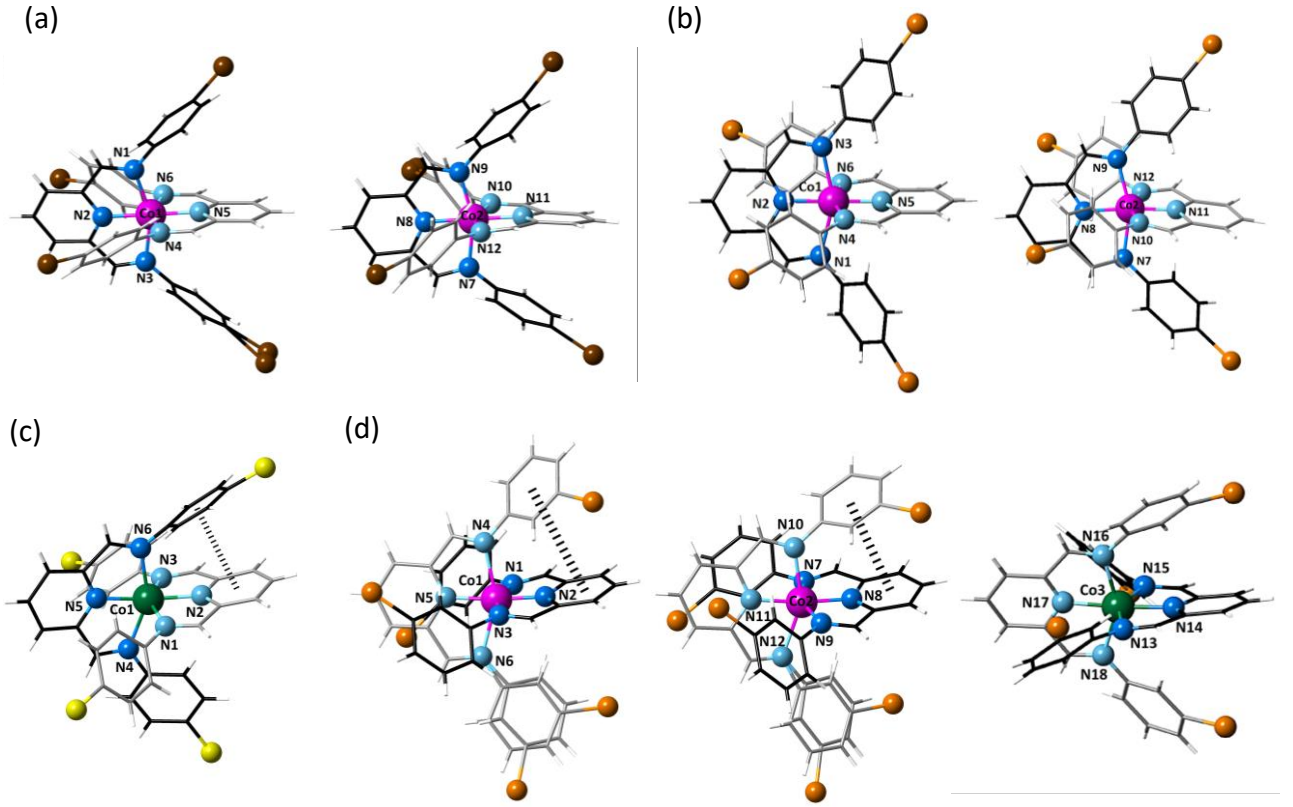

Figure II.1 Perspective views of the crystallographically independent mononuclear cobalt(II) units of **1**–**4** (a–d) with the atom numbering scheme of the coordination sphere at the cobalt atom. The ligand backbones are drawn in grey and black colours for clarity whereas the pink and green cobalt atoms correspond to the LS and HS configuration, respectively.

electronic effects induced in **4** by the weaker inductive character of the bromine substituent are partially compensated by its meta placement in the phenyl ring. Nevertheless, it is well known that the network, including the crystal packing, plays a relevant role in stabilising a particular electronic configuration of a SCO system, which is probably the case here where there are Br···Br strong intermolecular contacts. This circumstance is probably why both the HS and LS configurations occur together in **4**.

Although the distortion in all metal ions is similar, the correspondence (closeness) is more remarkable when LS and HS sites are independently compared, the latter being slightly less distorted, as reflected by axial [average values: $\Delta R = (R_{eq} - R_{ax})/R$ = 0.104 (**1**), 0.110 (**2**), 0.083 (**3**), and 0.099 and 0.088 (**4**)] and rhombic distortion parameters [average values: $\delta_R = (R_3 - R_2)/R_{eq}$ = 0.046 (**1**), 0.045 (**2**), 0.019 (**3**), and 0.071 and 0.004 (**4**)] (see Table II.2). Interbond angles also reflect their rhombic distortion. Whereas the axial cobalt(II)-pyridyl nitrogen bond angles [average N_{py}–Co–N_{py} = 177.5 (**1**), 177.6 (**2**), 164.9 (**3**), and 173.9° (**4**)] are close to the ideal value of 180°, the two distinct equatorial cobalt(II)-imine nitrogen bond angles [average N'$_{im}$–

Co–N_{im} = 100.5/84.1 (**1**), 100.3/94.1 (**2**), 94.2/93.0 (**3**), and 101.8/84.1° (**4**); Table II.2] deviate 90°, mainly in the LS sites. Moreover, the tridentate coordination mode of the *n*-XPhPDI ligands, forming two fused five-membered chelate rings with the Co^{II} ions, imposes a severe nonplanar ruffling distortion upon the equatorial plane. The large displacements from the mean equatorial plane of the imine nitrogen atoms reflect their significant deviations from the planarity [average δ = 0.43 (**1**), 0.42 (**2**), 0.56 (**3**), and 0.45 and 0.56 Å (**4**); Table II.2].

Although the $[Co^{II}(n\text{-XPhPDI})_2]^{2+}$ units in all compounds have two almost perpendicularly oriented tridentate PDI motifs (Figures II.1 and II.S3), as reflected by the values of the dihedral angle between the mean planes of the pyridyldiimine fragments [average Φ = 77.6 (**1**), 77.6 (**2**), 87.7 (**3**), and 75.6 and 73.5° (**4**); Table II.2], their molecular symmetries are different, being C_{2v} in **1** and **2**, and C_1 in **3** and **4**. Most likely due to the steric hindrance between the nearby methylene hydrogen and *o*-hydrogen atoms of the phenyl ring, the whole *n*-XPhPDI ligands are not planar, as

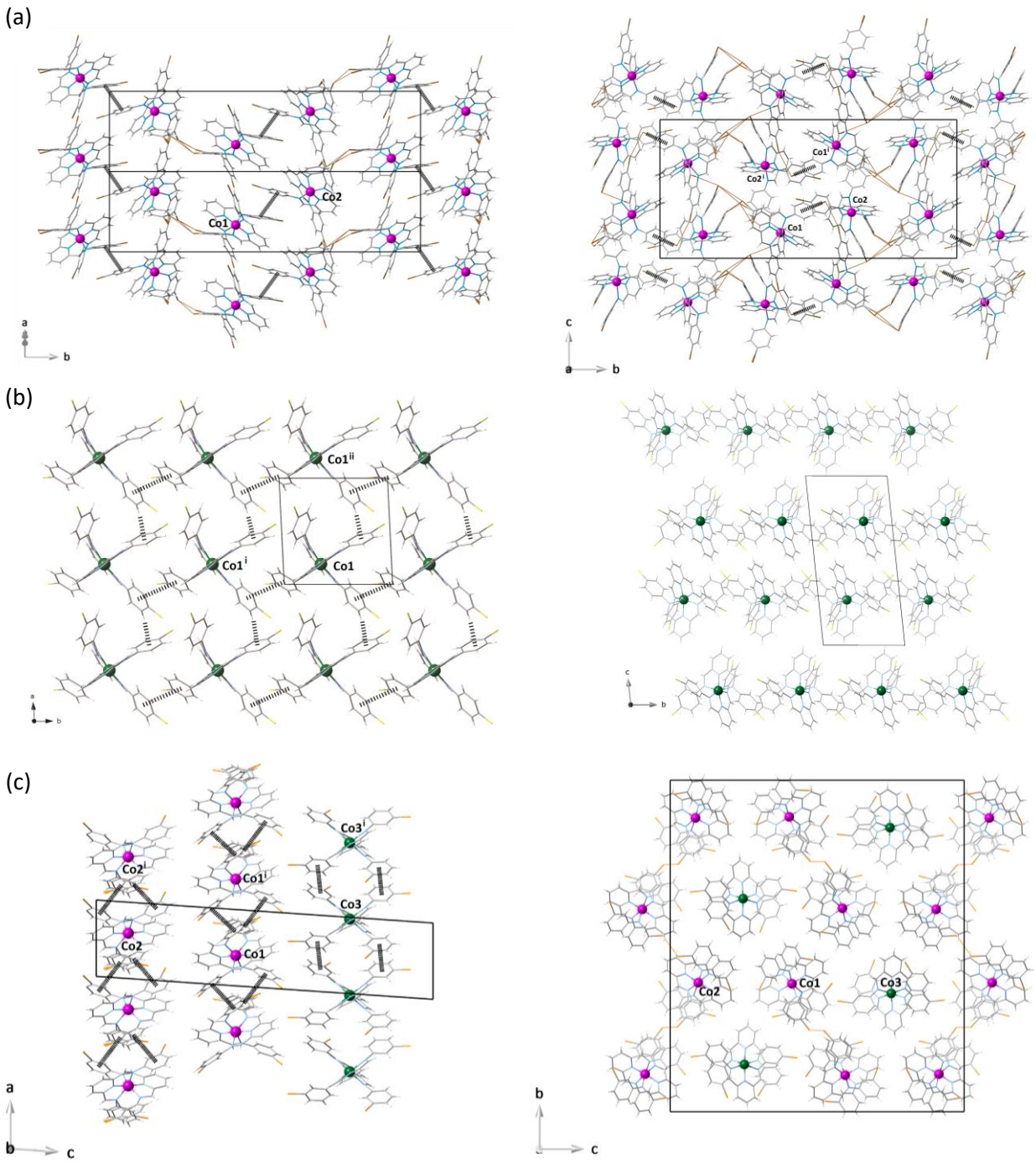

Figure II.2 Projection views of the crystal packing of **1**, **3** and **4** showing the supramolecular three-dimensional network in **1** (a), two-dimensional array of π-π stacked hexagonal grids in **3** (b) and three-dimensional array of π-connected chains in **4** (c) through π-π stacking (dashed lines) and X···X contacts (brown and orange solid lines) among the mononuclear units [symmetry operation: (i) = –*x*+1, –*y*+1, –*z*+1 (**1**); (i) = *x*, *y* – 1, *z* (**3**); (i) = 1 + *x*, *y*, *z* (**4**); (ii) = 1 + *x*, *y*, *z* (**3**)].

the torsion angle for the halo-substituted phenylimine fragments shows [average φ = 50.9 (**1**), 44.4 (**2**), 44.1 (**3**), and 32.6 and 34.3° (**4**); Table II.2]. However, they exhibit a helical conformation in **1**–**4**, whereby the inner rim of each terminal phenyl ring is oriented upwards and downwards relative to the central pyridyldiimine fragment. Hence, the mononuclear octahedral cobalt(II) units are chiral, and both enantiomers are present in the crystal lattice in **1**–**4**. The significant deviations from the ideal C_{2v} molecular symmetry in **3** and **4** are most likely due to the occurrence of a weak intramolecular face-to-face π-π stacking interaction between the central pyridyl and terminal phenyl rings from the ligand (Figure II.1), as evidenced by the intramolecular distance between the centroids of both rings (*h*) and the dihedral angle (θ) between their mean planes [average values: *h* = 3.85 (**3**), and 3.90 and 4.31 Å (**4**); θ = 26.5 (**3**), and 21.0 and 35.5° (**4**); Table II.2].

Crystal Structures. Moderate and weak intermolecular face-to-face π-π stacking interactions occur in the crystal lattices of **1**–**4** between halophenyl rings (only three of the four ones in **3**) from neighbouring crystallographically independent $[Co^{II}(n\text{-XPhPDI})_2]^{2+}$ units, as shown in Figures II.2. These interactions are similar in the four compounds, as the intermolecular distances between the centroids of the two facing phenyl rings and the dihedral angle between their mean planes show [*h* = 4.25–4.62 (**1**), 4.47–4.04 (**2**), 4.10 (**3**) and 3.94–4.49 Å (**4**); average θ = 44.6–47.6 (**1**), 47.4–33.6 (**2**), 19.6 (**3**), and 17.4–20.9° (**4**)]. The presence of these contacts, together with "edge-to-face" π-π interactions in **3** [*h* = 5.004(3) Å with θ = 86.73(9)°], lead to supramolecular dimers, hexagonal grid, and double-connected chains of complex cations in **1** and **2**, **3**, and **4**.

The springing up of intermolecular halogen-halogen interactions between neighbouring $[Co^{II}(n\text{-XPhPDI})_2]^{2+}$ units also contribute to stabilising the crystal packing of **1**, **2**, and **4** (Figures II.2 and II.S4), but they are not present in **3** or with HS cobalt(II) units of **4**. The shorter interhalogen distances [I···I = 3.858–3.964 Å (**1**), Br···Br = 3.624–3.680 Å (**2**), and Br···Br = 3.072–3.492 Å (**4**)] are slightly shorter than the sum of the van der Waals radii (I···I < 4.0 Å and Br···Br < 3.7 Å). In **1** and **2**, the intradimer Co1···Co2 distance through the face-to-face π-π stacking [*r* = 10.375(2) Å (**1**) and 10.383(3) Å (**2**)] is comparable to the shortest interdimer Co1···Co2^{i} separation across the interhalogen X···X contacts [r' = 10.487(2) Å (**1**) and 10.232(3) Å (**2**)]. While, in **4**, the intrachain Co1···Co1^{i}, Co2···Co2^{i}, and Co3···Co3^{i} distances through equivalent contacts are identical for symmetry reasons and equal to the value of the *a* parameter [*r* = 8.198(1) Å] but much shorter than those of the interchain Co1···Co2^{ii} and Co2···Co2^{iii} separations across the Br···Br contacts [*r*' = 14.108(1) and 14.712(1) Å]. Both intermolecular interactions in **1** and **2** lead to a supramolecular three-dimensional array with tiny hexagonal pores along the crystallographic *a* axis (Figure II.S4 and S5) filled by perchlorate anions and acetonitrile molecules. In contrast, this situation in **4** promotes π-linked supramolecular chains of cationic mononuclear cobalt(II) complexes rather well-isolated from each by perchlorate anions placed into the interchain space (Figure II.S7d). Mononuclear cobalt(II) complex cations and perchlorate anions in **3** are arranged to build a segregated layer array (Figure II.S6), where ethyl acetate molecules occupy the interlayer space establishing weak intermolecular Van der Waals contacts with complex cations. The intralayer Co1···Co1^{i} and Co1···Co1^{ii} distances through the single face-to-face and edge-to-face π-stacked triad interacting motif [*r* = 10.330(3) and 10.172(3) Å] are shorter than the shortest interlayer Co1···Co1^{iii} distance [*r*' = 11.184(4) Å; symmetry code: (iii) = –*x*+1, –*y*+1, –*z*+1].

II.4 – Electrochemical Properties

Electrochemical properties of the cobalt(II)-PDI complexes were investigated by cyclic voltammetry (CV) to analyse the influence of the nature of the electron-withdrawing phenyl substituents, as well as their *meta* and *para* substitution pattern, on the metal- and ligand-centred, multiredox behaviour. A summary of the electrochemical data for **1**–**4** is listed in Table II.3.

Cyclic voltammograms in acetonitrile at room temperature show a qualitatively similar redox behaviour of **1**–**4** (Figure II.3 and S8). They exhibit one reversible (or almost reversible) oxidation (E_1) and two reversible reduction waves (E_2 and E_3; Table II.3). Also, an utterly irreversible reduction wave appears at very high negative formal potentials for all four complexes (E_4; Table II.3). The values of the anodic to cathodic peak separation for two first reduction and oxidation waves ($\Delta E_{p,1-3}$; Table II.3), except for **4**, are comparable to that of the Fc^+/Fc redox couple under the same conditions (ΔE_p = 80 mV), stating them as reversible in the voltammetric-time scale. When decreasing the scan rate range in the range of 20–250 mVs^{-1}, a later satellite oxidation peak becomes visible only for **4** (insets of Figure II.S8), revealing the coupling of a slow chemical decomposition to the principal one.

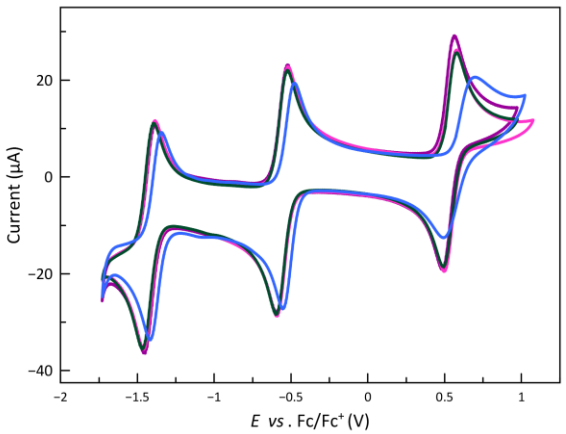

Figure II.3 Cyclic voltammograms of **1** (purple), **2** (pink), **3** (green), and **4** (blue) in acetonitrile (0.1 M nBu$_4$NPF$_6$) at 25 °C and 200 mV s^{-1}.

The reversible oxidation wave for **1**–**4** corresponds to the one-electron metal oxidation to afford the resulting cobalt(III) complex. The first pair of reduction waves conforms to the stepwise one-electron reduction of the ligands to give the single and double imide-type π-radical anion cobalt(II) species.[67,68]

Ligands could still undergo further stepwise one-electron reductions leading to non-radical dianion cobalt(II) species; therefore, the appearance of a pair of reduction waves at higher potentials could be expected. The correlation between the formal redox potential of reversible processes and the electron-withdrawing nature of the ligand substituents expressed by the Hammett constants [σ_H = 0.18 (*p*-I), 0.23 (*p*-Br or *p*-Cl), and 0.39 (*m*-Br)] is almost linear.[69] As shown by the formal redox potentials and according to the σ_H, the more extensive σ-type inductive withdrawing effect of the halogen atom in the *m*-bromine derivative removes more electron density from the Co^{II} ion than the other substituted ligands, making both the oxidation of the metal centre harder and the reduction of the coordinated ligand easier.

Table II.3. Selected Electrochemical Data for **1–4**[a]

	Ligand	E_1[b] (V)	E_2[b] (V)	E_3[b] (V)	E_4[b] (V)
1	4-IPhPDI	0.53 (78)	-0.56 (73)	-1.42 (76)	-1.88 (i)
2	4-BrPhPDI	0.54 (80)	-0.56 (71)	-1.42 (78)	-1.88 (i)
3	4-ClPhPDI	0.54 (85)	-0.56 (78)	-1.42 (78)	-1.88 (i)
4	3-BrPhPDI	0.59 (202)	-0.52 (76)	-1.38 (73)	-1.85 (i)

[a]In acetonitrile (25 °C, 0.1 M nBu$_4$NPF$_6$) with a scan rate of 200 mV s^{-1}. [b]All formal potential (E/V) values were taken as the half-wave potentials *vs*. Fc^+/Fc, except for the irreversible (i) reduction waves for which the catodic peak potentials are given instead. The values of the peak-to-peak separation ($\Delta E_{p,i}$/mV) between the anodic and cathodic peak potentials are given in parentheses.

II.5 – Magnetic Properties and EPR Spectra

Static magnetic behaviour. The dc magnetic properties of **1–4** in the form of the $\chi_M T$ *vs* T and M *vs* H/T plots (χ_M and M being the molar dc magnetic susceptibility and magnetisation per mononuclear unit, T the absolute temperature, and H the applied magnetic field) are shown in Figures II.4 and II.S9).

The $\chi_M T$ versus T plots for **1–4** reveal a behaviour dependence on the electron-withdrawing character of the substituents and their *meta* or *para* location (Figure II.4a). At 300 K, $\chi_M T$ for **3** is equal to 2.68 cm^{3}mol^{-1}K, a value expected for a HS cobalt(II) ion with an unquenched orbital momentum contribution (2.70 cm^{3}mol^{-1}K with g_{Co} = 2.4). However, the $\chi_M T$ values at room temperature for **1**, **2**, and **4** (2.15, 1.33, and 1.98 cm^{3}mol^{-1}K, respectively) are much smaller. For **3**, the smoothly but gradual decrease in $\chi_M T$ on cooling to 1.85 cm^{3}mol^{-1}K at 2.0 K reveals the occurrence of a significant zero-field splitting (zfs) coming from the first-order spin-orbit coupling (SOC) typical of an octahedral HS cobalt(II) complex ($^4T_{1g}$ term with S_{Co} = 3/2 and L_{Co} = 1). Upon cooling, a complete spin transition (with no hysteresis) occurs for **1** and **2**, as revealed by the gradual decrease of $\chi_M T$ to reach a sort of plateau [*ca*. 50 (**1**) and 150 K (**2**)]. The $\chi_M T$ value of 0.45 cm^{3}mol^{-1}K at 2.0 K for **1** and **2** is expected for an LS cobalt(II) ion [$\chi_M T = (N\beta^2 g_{Co}^2/3k_B)S_{Co}(S_{Co}+1)$ = 0.45 cm^{3}mol^{-1}K with S_{Co} = 1/2 and g_{Co} = 2.2]. In contrast, compound **4** exhibits a gradual and incomplete spin transition, as reported earlier for the parent unsubstituted complex.[66] The $\chi_M T$ value of 0.92 cm^{3}mol^{-1}K at 2.0 K for **4** agrees with that estimated for one HS and two LS cobalt(II) ions, in agreement with its single-crystal X-ray structure.

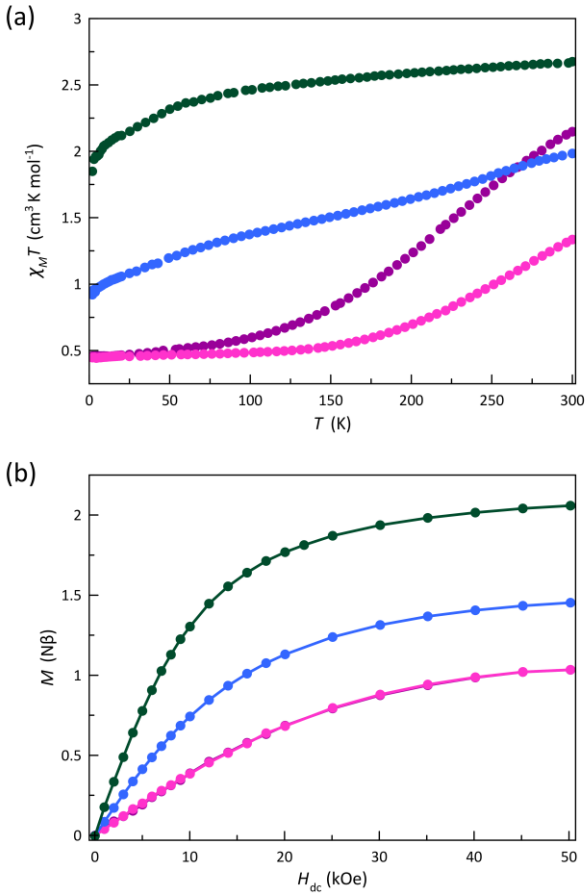

Figure II.4 (a) Temperature dependence of $\chi_M T$ and (b) field dependence of M at 2.0 K for **1** (●), **2** (●), **3** (●), and **4** (●).The solid lines are only eye guides.

The M versus H plots at 2.0 K for **1–4** further conform to the aforementioned interpretation (Figure II.4b). So, the value of M at 50 kOe for **1** and **2** is 1.00 $N\beta$, being then close to the calculated one for the saturation magnetisation of a doublet spin state of an LS cobalt(II) ion ($Ms = g_{Co}S_{Co}N\beta$ = 1.10 $N\beta$ with S_{Co} = 1/2 and g_{Co} = 2.2). Besides, for an LS octahedral cobalt(II) complex with S_{Co} = 1/2 on which a magnetic anisotropy does not cause any splitting, the isothermal magnetisation curves should superimpose if they are magnetically isolated, as practically occurs for **1** and **2** in the temperature range from 2.0 to 10.0 K (Figures SII.9a,b). In contrast, M at 50 kOe for **3** is 2.06 $N\beta$, a value which agrees with the calculated one for the saturation magnetisation for an effective doublet spin state of an HS cobalt(II) ion ($Ms = g_{Co}S_{Co}N\beta$ = 2.10 $N\beta$ with $S_{Co} = S_{eff}$ = 1/2 and g_{Co} = 4.2). In this case, the ground ±3/2 and excited ±1/2 Kramers doublets for $D < 0$, or *vice versa* for $D > 0$, are well-separated due to the sizeable *zfs* effects operating on the quartet ground state, recording only the magnetisation for the ground Kramers' doublet. On the other hand, the value of M equal to 1.45 $N\beta$ for **4** at 50 KOe is close to that estimated for the saturation magnetisation corresponding to one HS and two LS cobalt(II) ions [Ms = (2.10 + 2 × 1.10)/3 = 1.43 $N\beta$]. In contrast, isothermal magnetisation curves of **3** and **4** do not superimpose below 10.0 K (Figures II.S9c and d), supporting the occurrence of substantial zfs effects resulting from the significant SOC acting on their HS

cobalt(II) ions. Unfortunately, all the attempts to fit the $\chi_M T$ *vs* T and M *vs* H/T data of **3** taking into account either a first-order spin-orbit coupling or a dominant zfs were unsuccessful, a consequence of the presence of a residual LS phase, evidenced in the EPR study (see below).

EPR spectra. Q-Band EPR spectra of crushed crystals of **1**–**4** at 4.0 K are in Figure II.5. All spectra show a strong predominant signal around g = 2.0 (12000 G), typical for LS cobalt(II) complexes, split in two by the high distortion (axial and rhombic) imposed by PDI-type ligands. However, two low-field signals, whose patterns are characteristic of HS cobalt(II) octahedral complexes, are also recorded for **2**–**4**.[51] The presence of additional signatures, either HS (**2**) or LS (**3**), indicates a small residual fraction of the HS and LS phases, not inferred from the less sensitive magnetometry techniques. Nevertheless, the coexistence of these signatures in **4** agrees with the incomplete spin transition observed by magnetometry.

EPR spectra of **1**–**4** were simulated jointly for the LS and HS fractions. LS contributions were satisfactorily simulated considering a highly axial ($g_x = g_y \neq g_z$) for **3** and a rhombic octahedron ($g_x \neq g_y \neq g_z$) for the rest. Table II.4 summarises the g values used in theses simulations.

Table II.4 Best parameters for simulation of the LS contribution in the Q-band EPR spectra of **1**–**4** from the experimental data in solid state at 4.0 K

	g_x	g_y	g_z	g^a
1	2.025	2.126	2.310	2.157
2	2.023	2.126	2.238	2.141
3	2.060	2.075	2.234	2.128
4	2.023	2.126	2.238	2.139

[a]Overall g value estimated by the equation $g^2 = (g_1^2 + g_2^2 + g_3^2)/3$.

Based on the crystal structure and supported by magnetometry, **4** is the only compound in which HS and LS configurations patently coexist. Its low-field EPR signals (g_{eff} = [2.39, 3.47, 6.42]), marked with an asterisk in Figure II.5d, can only correspond to the ground Kramers doublet of the HS fraction. These values are typical of a non-uniaxial zfs ($D > 0$), the most common situation in octahedral cobalt(II) complexes, and agree with those found by *ab initio* CASSCF/NEVPT2 calculations (g_x = 3.25, g_y = 7.21 and g_z = 2.06). A subsequent analysis considering a zfs on the quartet ground state (g_x = 2.47, g_y = 2.77, g_z = 2.13, $D > 0$, and E/D = 0.11) and *ab initio* calculations (D = +92.6 cm^{-1} and E/D = 0.207) confirm the easy-plane zfs and a moderate rhombicity. This same EPR footprint is repeated in the unexpected residual HS fraction in **2**, with g_{eff} = [2.34, 3.55, 6.56].

However, among the four compounds, the only one exhibiting an HS configuration down to 2.0 K is **3**, which shows a split signal at very low fields, also occurring in the X-band

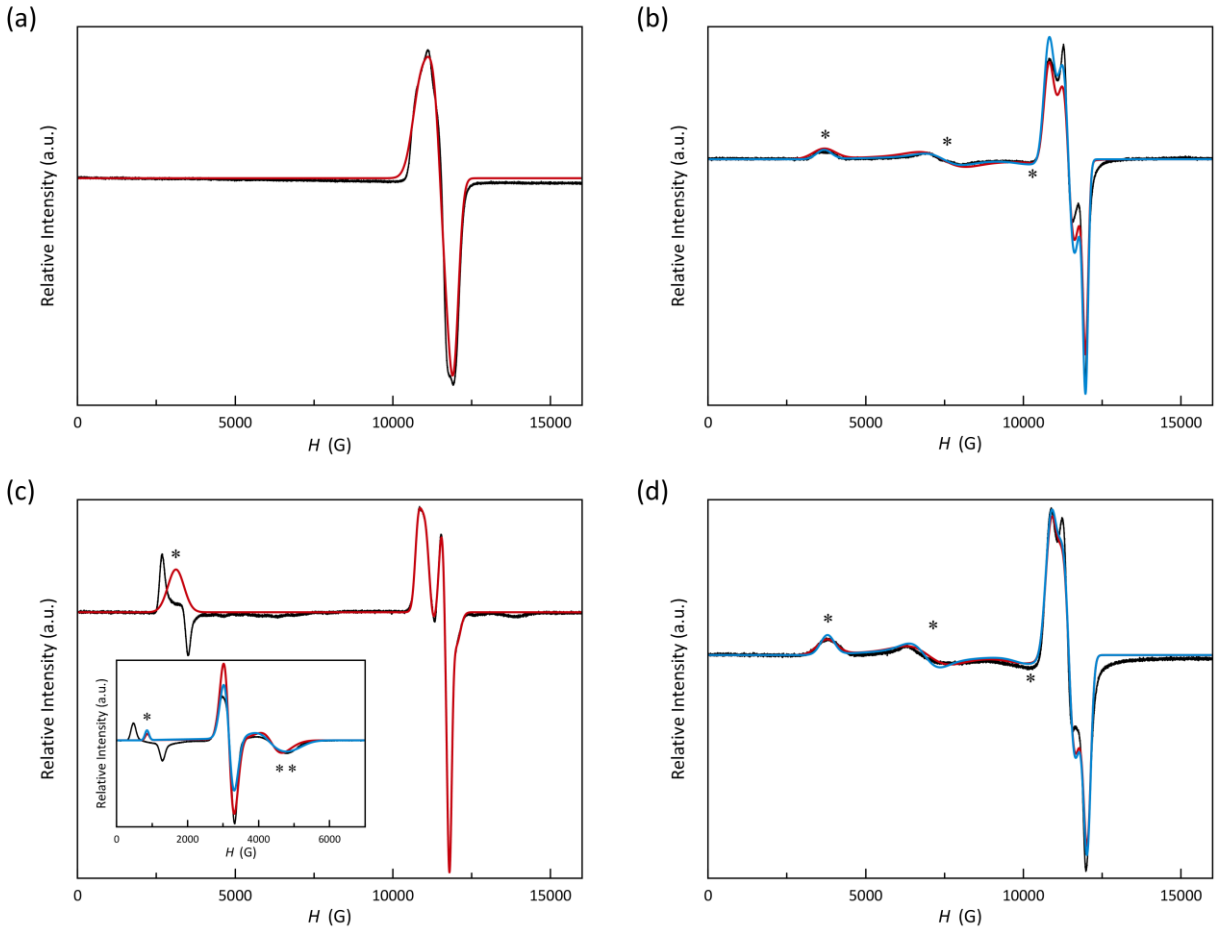

Figure II.5 Experimental Q-band EPR spectra of **1**–**4** (a–d) in the solid state at 4.0 K (black solid lines). X-band spectrum of **3** appears as inset. Red and blue solid lines are the simulated curves for S_{eff} = 1/2 and anisotropic S = 3/2 approaches (see text). The asterisks indicate the signals from the HS fraction.

spectrum. The g_i values for the two components of this signal are strongly dependent on the microwave frequency band but not their centre of gravity, which is indicative of an effect of the field-modulation amplitude, being this midpoint that provides the real *g* value. This signal at g_z = 7.8 is conclusive evidence of a uniaxial zfs (D < 0). In such a situation, the two remaining g_{eff} components must take very low values, enough so that they cannot be observed by Q-band EPR spectroscopy, but it does in X-band. Thus, the X-band spectrum shows an asymmetric signal at fields higher than those for the residual LS fraction, a consequence of the proximity between the signals at g_x = 1.43 and g_y = 1.54. According with that, the analysis of the X-band spectrum considering a zfs on a quartet spin state provided the following results: g_x = 2.25, g_y = 2.05, g_z = 2.78, D < 0, and E/D = 0.25, which are in agreement with the previous discussion and those found from *ab initio* calculations (g_{eff} = [1.19, 1.39, 8.56] or $g_{3/2}$ = [1.95, 2.15, 3.04], D = –92.1 cm^{-1}, and E/D = 0.196).

In conclusion, EPR spectroscopy allows determining the spin state and also the presence of the minor molecules undergoing a spin transition or the opposite. Supported by theoretical calculations, this spectroscopic technique has shown that this family of compounds, with unusual molecular geometries, can show both uniaxial and non-uniaxial anisotropies on the HS configurations. These electronic changes in a highly distorted geometry must occur by subtle geometric modifications imposed by the packing in the crystal network arising from the observation or not of a spin transition phenomenon.

Dynamic magnetic behaviour. Ac magnetic properties of **1**–**4** were studied in the absence and under applied dc magnetic fields of 1.0 and 2.5 kOe. The in-phase (χ_M') and out-of-phase (χ_M'') ac molar magnetic susceptibility show frequency dependence under a dc magnetic field (Figures II.S10–S13). However, they show neither frequency dependence of χ_M' nor a χ_M'' signal (data not shown) in the absence of a dc magnetic field, more likely because of a fast quantum tunnelling of magnetisation (QTM). Although QTM can avoid a slow relaxation of magnetisation, it becomes less efficient when applying a dc magnetic field, as in **1**–**4**. This particular field-dependent behaviour, typical of mononuclear SMMs and known as field-induced SMMs, must exhibit an energy barrier governing the spin reversal and arising from a uniaxial zfs (D < 0). However, this argument does not apply for LS or non-uniaxial HS electronic configurations in cobalt(II) complexes since both procure ground ±1/2 Kramers doublets that make a fast spin-reversal possible eluding other excited ones. Such a process is known as intra-Kramer (IK) relaxation.

This series of compounds reveals that the HS and LS configurations behave differently, being the blocking temperature higher for the former and intermediate for **4** (Figure II.S13), which contains both in a 1:2 ratio below 150 K (see above). Similarly, while the blocking temperature is strongly dependent on the magnetic field for the LS configuration, it is entirely invariant for the HS one. These characteristics suggest that the mechanisms of magnetic relaxation or how they operate will be different in the two spin configurations, and they are probably strongly linked to electronic aspects such as mixing of M_s functions by the rhombic parameter of zfs, nature of the occupied 3d orbitals, spin delocalisation on the ligands, or low-energy molecular vibrational modes. Additionally, new signals displayed as incipient or a shoulder appear in the χ_M'' *vs T* curves, mainly in **3** and under the highest dc magnetic field, allowing to discern higher (HT) and lower (LT) temperature magnetic relaxation processes.

The best way to calculate the magnetic relaxation time (τ) is the jointly analysis of the χ_M' and χ_M'' *vs v* data (Figures II.6 and II.7) through the generalised Debye model (Eqn. 1 and 2), which also takes into account the static and infinite frequency magnetic susceptibility (χ_S and χ_T), and the exponential factor that describes the spectral breadth (α), as additional fitting parameters.

$$\chi' = \chi_s + (\chi_t - \chi_s)\frac{1+(\omega\tau)^{1-\alpha}\sin(\alpha\pi/2)}{1+2(\omega\tau)^{1-\alpha}\sin(\alpha\pi/2)+(\omega\tau)^{2-2\alpha}} \quad (1)$$

$$\chi'' = (\chi_t - \chi_s)\frac{(\omega\tau)^{1-\alpha}\cos(\alpha\pi/2)}{1+2(\omega\tau)^{1-\alpha}\sin(\alpha\pi/2)+(\omega\tau)^{2-2\alpha}} \quad (2)$$

This analysis in **3** required the inclusion of a second relaxation acting below 3.5 K previously confirmed from the χ_M'' *vs T* plots (Figure II.S12). In this new model, each relaxation process is additive, independent and runs with its own set of parameters (χ_{Si}, χ_{Ti}, τ_i, and α_i, as described by Eqn. 3 and 4). Among these parameters, τ is most accurately evaluated, and is also the one of interest in the subsequent analysis of competing relaxation mechanisms. Since the contribution of this LT second process becomes irrelevant above 3.5 K, it was omitted in the analysis. This concurrent process could not be furhter analysed due to the narrow temperature range in which this process has some relevance and the lack of accuracy of the extracted values of τ. Although, it is worthy to emphasize that the introduction of the LT second process significantly improves the quality of the results obtained from the predominant HT one.

$$\chi' = \chi_1' + \chi_2' \quad (3)$$

$$\chi'' = \chi_1'' + \chi_2'' \quad (4)$$

The χ_M'' *vs* χ_M' plots at H_{dc} = 1.0/2.5 kOe for **1**–**4** give almost perfect semicircles in the temperature ranges 2.0–10.0 K (Figures II.S14 and S15). These Argand plots can be well simulated by using the values of χ_S, χ_T, τ and α obtained through the fitting of the χ_M' and χ_M'' *vs v* plots by the generalised Debye model.[70] The values of α are generally small for **1**–**4**, supporting a single magnetic relaxation process (α = 0 for an ideal Debye model), while the corresponding $\chi_T - \chi_S$ values are typical of field-induced SMMs.

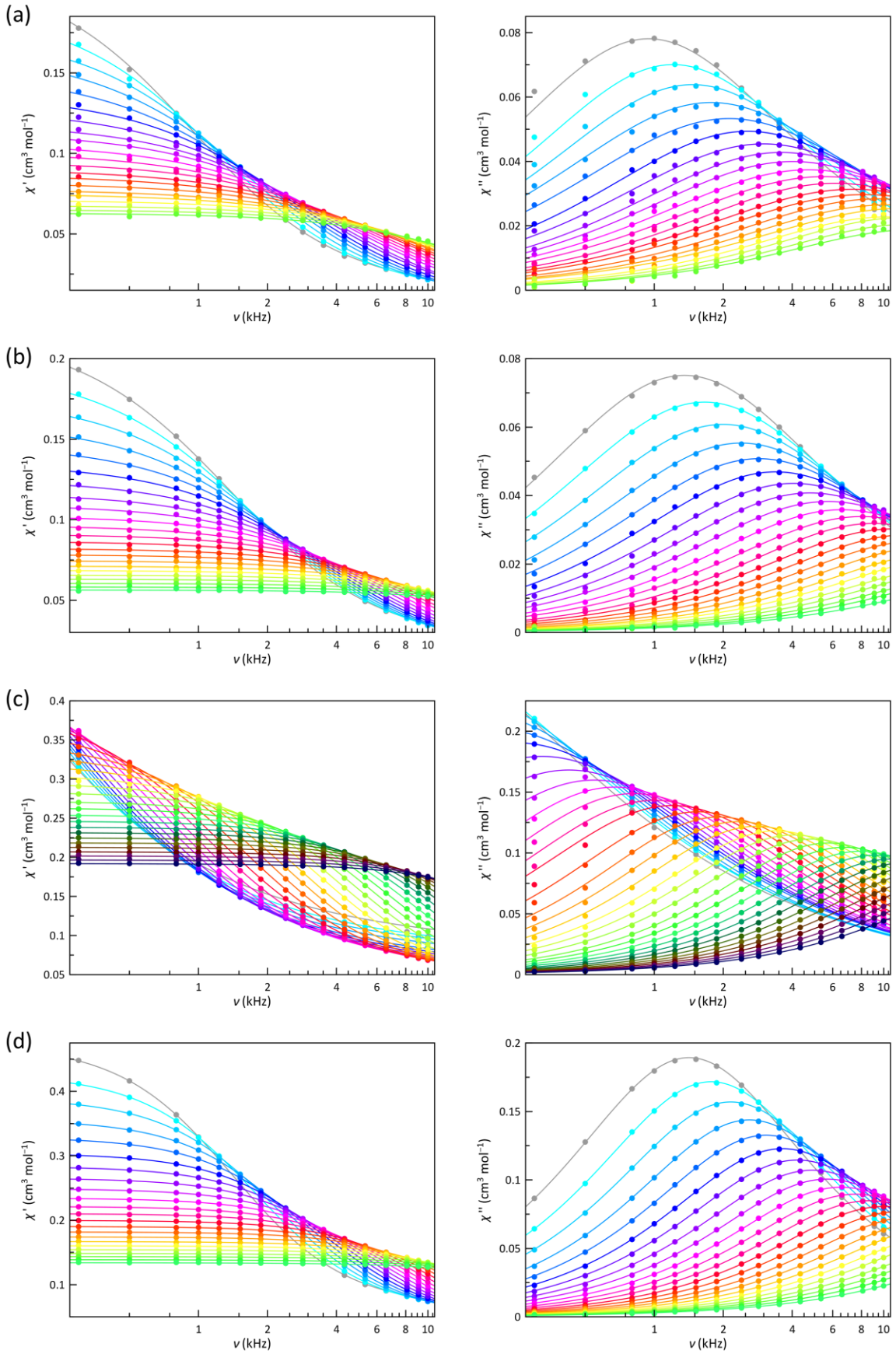

Figure II.6 Frequency dependence of χ_M' (left) and χ_M'' (right) for **1** (a), **2** (b), **3** (c), and **4** (d) at a ±5.0 G oscillating field in the temperature range of 2.0–10 K under an applied static magnetic field of 1.0 kOe. The solid lines are the best fit curves simulated by using the generalised Debye model (see text).

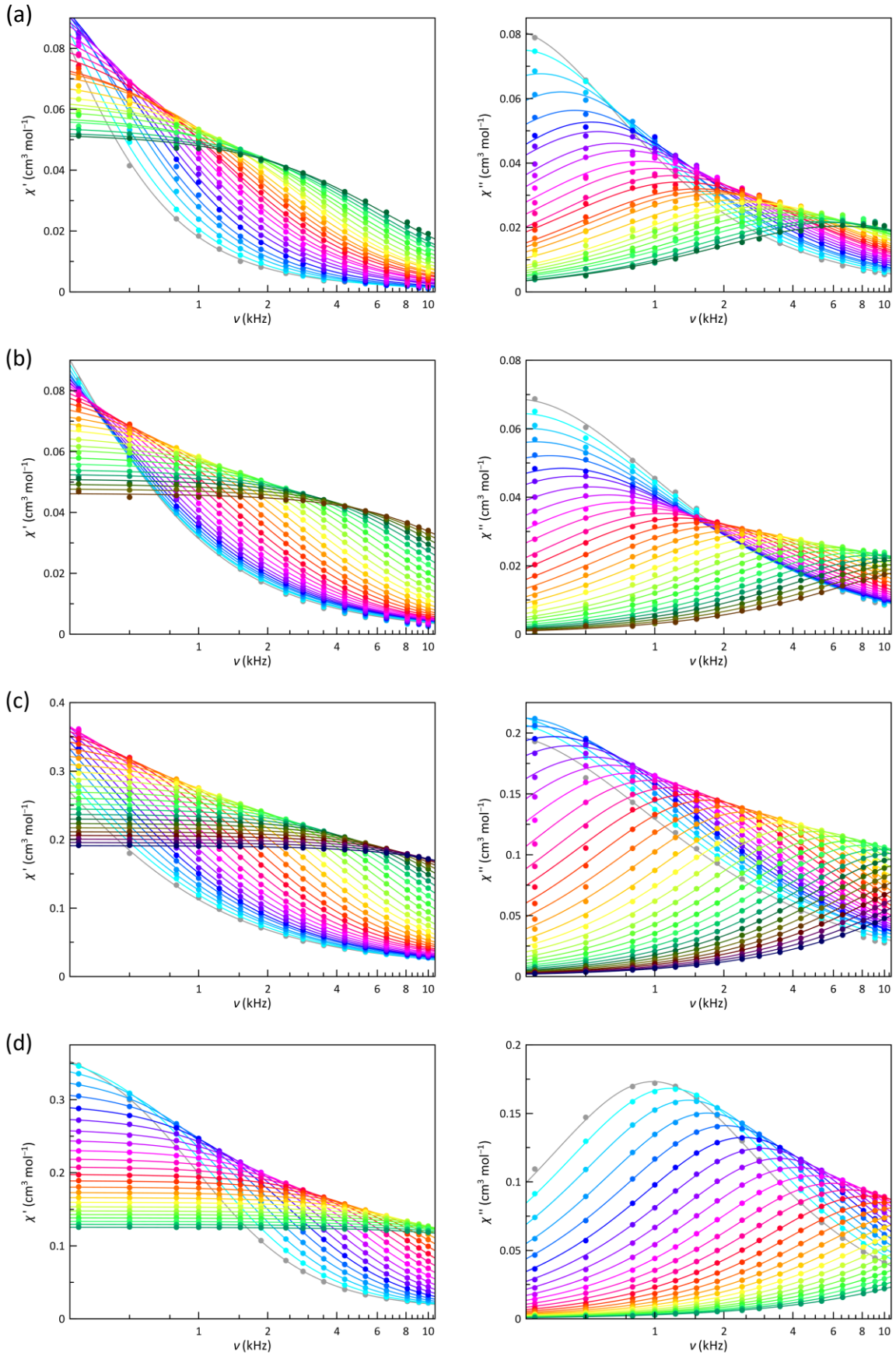

Figure II.7 Frequency dependence of χ_M' (left) and χ_M'' (right) for **1** (a), **2** (b), **3** (c), and **4** (d) at a ±5.0 G oscillating field in the temperature range of 2.0–10 K under an applied static magnetic field of 2.5 kOe. The solid lines are the best fit curves simulated by using the generalised Debye model (see text).

According to the nature of the relaxation mechanisms involved, two types of graphic representations are recommended. For thermally activated two-phonon Orbach-type relaxations [$\tau_{ORB}^{-1} = \tau_0^{-1} \exp(-U_{eff}/T]$ an Arrhenius plot is preferable since they show a linear dependence where the slope directly estimates the energy barrier (U_{eff}) controlling the spin reversal. However, for one-phonon direct or two-phonons Raman-like mechanisms ($\tau_{RAM}^{-1} = CT^n$), a $\ln\tau$ vs $\ln T$ plot showing linear dependencies of slope n is more appropriate. When n takes values close to 2 or 8, optical or acoustic phonon-assisted Raman mechanisms dispense the fastest spin reversal. Instead, a direct mechanism plays the main role for n values close to unity. Nevertheless, both representations are helpful for temperature-independent relaxations, such as QTM or IK.

That being so, $\ln\tau$ *vs* $\ln T$ (Figure SII.16) and $\ln\tau$ *vs* $1/T$ Arrhenius plots (Figure II.8) were drawn for **1**–**4** at H_{dc} = 1.0 and 2.5 kOe. There is a deviation from a linear dependence in all cases, suggesting several relaxations coexist and compete. In the Arrhenius plots (Figure II.8), it is not easy to distinguish straight lines, indicating that one of the mechanisms utterly prevails, which is not surprising for LS **1** and **2**, since a S = 1/2 spin state cannot present an energy barrier for the spin reversal. However, the energy barrier so evaluated has sometimes been related to the energy required to reach low-lying vibrational modes that make the spin reversal easier and faster. A similar case would be that for a non-uniaxial HS cobalt(II) complex ($D > 0$), as in the HS site of **4**, where the ground Kramers doublet allows fast relaxation, at least in the absence of a magnetic field. However, **3**, exhibiting a uniaxial zfs ($D < 0$), should be a different case where an energy barrier exists. Therefore, these representations were analysed for the four compounds. In general, a relatively high energy barrier acts at high temperatures and a significantly lower one at low temperatures. The values of this second energy barrier are too low to be related to vibrational modes and are probably a consequence of the magnetic effect on a fast IK relaxation or even competing direct or Raman mechanisms. Similarly, the energy barriers found for **3** are quite lower than that provided by the zfs. So, the fastest relaxation mechanisms must be of a different nature, and probably, once again, Raman or direct type.

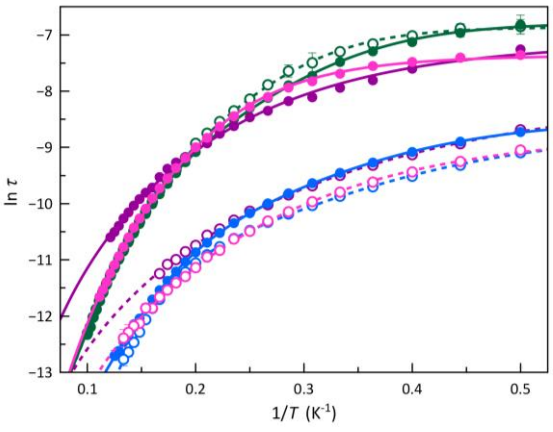

Figure II.8 Arrhenius plot for the calculated magnetic relaxation times (τ) of **1** (purple), **2** (pink), **3** (green), and **4** (blue) under applied *dc* magnetic fields of 1.0 (○) and 2.5 kOe (●). Dashed and solid lines are the best-fit curves (see text). Vertical error bars denote the standard deviation.

As with the Arrhenius plots, the $\ln\tau$ vs $\ln T$ plots for **1**–**4** do not usually show regions with linear dependencies. However, for **2** under a 2.5 kOe magnetic field, these features are observed at high and low temperatures. The derived n values show that Raman mechanisms assisted by optical and acoustic phonons govern the relaxation of the magnetisation at low and high temperatures, respectively. Although linear dependencies are not clearly observed in other magnetic fields or compounds, there is no reason to think that this does not occur in all of them, particularly in those that also exhibit a LS configuration. In this sense, these cases are usually described with n values intermediate between those corresponding to optical and acoustic phonons. However, good simulations are also found with values closer to what might be expected. Therefore, obtaining accurate values for n requires an extensive data range, which is not always possible, and a meticulous analysis of the experimental data to obtain the relaxation times. Besides, it is also essential to avoid, without physical evidence, using an oversized set of relaxation mechanisms, which will lead to additional overparameterisation problems. Considering these conclusions, we have tried to proceed to a similar analysis in all cases. Furthermore, a dominant temperature-independent relaxation becomes apparent under specific magnetic fields. For a LS electronic configuration, this new process can only be assigned to an IK relaxation, a direct and enabled interchange between the two M_s components of ground doublet ($|+1/2> \Leftrightarrow |-1/2>$). The difficulties in achieving accurate relaxation times and its subsequent analysis can make it challenging to establish general conclusions, but a qualitative scrutiny of the $\ln\tau$ vs $\ln T$ and Arrhenius plots is often more informative. Let us see below.

It is worth noting that the temperature-independent relaxation in **3**, due to the presence of an energy barrier arising from a negative D, is instead governed by a QTM mechanism. Thus, the relaxation times corresponding to this process prevailing at lower temperatures are greater for the QTM mechanism (**3**) than the IK one (**1**, **2**, and **4**), consistent with its lower probability and wavefunctions mixing between the components of the ground Kramers doublet (Tables II.5 and II.S1). As the rhombicity of the zfs tensor (E/D) increases, so does this probability, and the QTM process becomes faster. Similarly, the relaxation rate for IK and QTM processes, as expected, decreases as the magnetic field increases and, therefore, the splitting of the Kramers doublet.

However, in **4**, the two spin configurations coexist, the majority being the LS form (2/3). Thus, the relaxation time for the temperature-independent process is expected to be closer to those observed for **1** and **2**. A slower IK is still expected for the HS portion even though it exhibits a $|\pm1/2>$ ground Kramers doublet, as does the LS form. However, this Kramers doublet arises from an S = 3/2 and not an S = 1/2 state, or what is the same from an HS and not an LS form, so it does not surprise this conclusion, also confirmed by the way it depends on H_{dc}, which is more like **3**. However, what is the cause behind it?

Table II.5 Selected parameters from the least-squares fit of the ac magnetic data of **1**–**4**[a]

	H_{dc} (kOe)	τ_{IK}[b] (x 10^{-3} s)	C_1[c] ($s^{-1}K^{-n}$)	n_1[c]	C_2[c] ($s^{-1}K^{-n}$)	n_2[c]
1	1.0	-	1480 ± 50	1.98 ± 0.03	1.13 ± 0.09	5.6 ± 0.4
	2.5	1.1 ± 0.4	23 ± 2	2.4 ± 1.0	3.73 ± 0.03	4.69 ± 0.07
2	1.0	0.32 ± 0.23	900 ± 600	2.5 ± 0.4	1.3 ± 0.3	5.7 ± 0.8
	2.5	1.10 ± 0.07	58 ± 9	1.92 ± 0.10	1.15 ± 0.03	5.26 ± 0.09
3	1.0	1.39 ± 0.06	25 ± 5	2.5 ± 0.6	1.43 ± 0.19	5.16 ± 0.06
	2.5	2.4 ± 0.4	96 ± 22	2.20 ± 0.15	1.000 ± 0.016	5.30 ± 0.05
4	1.0	-	2340 ± 80	1.91 ± 0.03	0.10 ± 0.03	7.33 ± 0.13
	2.5	0.59 ± 0.09	1050 ± 60	1.95 ± 0.15	8.1 ± 1.3	5.04 ± 0.07

[a]The fits correspond to double or triple relaxation models. [b]Coefficient factor for the temperature-independent *IK* process ($\tau^{-1} = IK$). [c]Coefficient and polynomial factor for the Raman process ($\tau^{-1} = CT^n$).

An isolated electron, i.e. a single |±1/2> Kramers doublet, in the absence of an external magnetic field or even being moderate, must show a swift spin reversal with an oscillating field. This same doublet arising from an unpaired electron in a metal complex cannot be described as that of an isolated electron since its spin density is delocalised in the ligands. Moreover, the local spin densities caused by a spin delocalisation mechanism polarise spin densities into neighbouring atoms and even into some internal orbitals of the own metal ion. In such a situation, reversing the spin density laying on the paramagnetic centre entails opposing spin densities in inner layers and also on neighbouring atoms becomes a more difficult task that requires a reversal at once of the overall density on the complex, leading to a significant slowdown in the spin reversal. On the other hand, the spin delocalisation in the HS configuration in cobalt(II) complexes is larger than the LS form since the former shows a larger occupation of the e_g orbitals, as confirmed by DFT calculations (Figure II.9 and Table II.S2). Hence, the relaxation of the magnetisation in a HS configuration is expected to be slower, as is the case.

How the magnetic field affects the particular dynamic magnetic behaviour of HS and LS forms is not obvious and requires a more detailed study, as will be shown in later chapters. However, it can be argued that the most significant influence at lower temperatures observed in the LS form may be due solely to the fact that such effect has already "saturated" under smaller magnetic fields since the Zeeman splitting is larger on a S = 3/2 than a S = 1/2 state. In contrast, the dynamic behaviour tends to become invariant with H_{dc} for both HS and LS forms in the high-temperature region since a Raman mechanism governs the spin reversal relaxation,[57,60,61] which involves virtual states associated with a spin-phonon coupling or low-energy vibrations for the complex or the network and therefore do not are affected by H_{dc}.

Recently, one square pyramidal LS cobalt(II) complex has been positively tested as a qubit prototype by observing anisotropic Rabi cycles with long enough quantum phase memory times (Tm ≈ 1 μs at 5.0 K).[62] In fact, the LS (S_{Co} = 1/2) cobalt(II) ion is a genuine two-level magnetic quantum system, represented by the pair of m_S = +1/2 and –1/2 states, which can play the role of a qubit for quantum computing applications. Interestingly, the magnetic relaxation time for a doublet spin ground state is identical to the spin-lattice time ($T_1 = \tau$), which acts in turn as a limiting factor for the phase memory time ($Tm \leq T_1$). So, T_1 values varying from around 0.05 up to 2.5 μs for H_{dc} = 1.0 and 2.5 kOe, respectively, are available for **1** and **2** at 2.0 K.

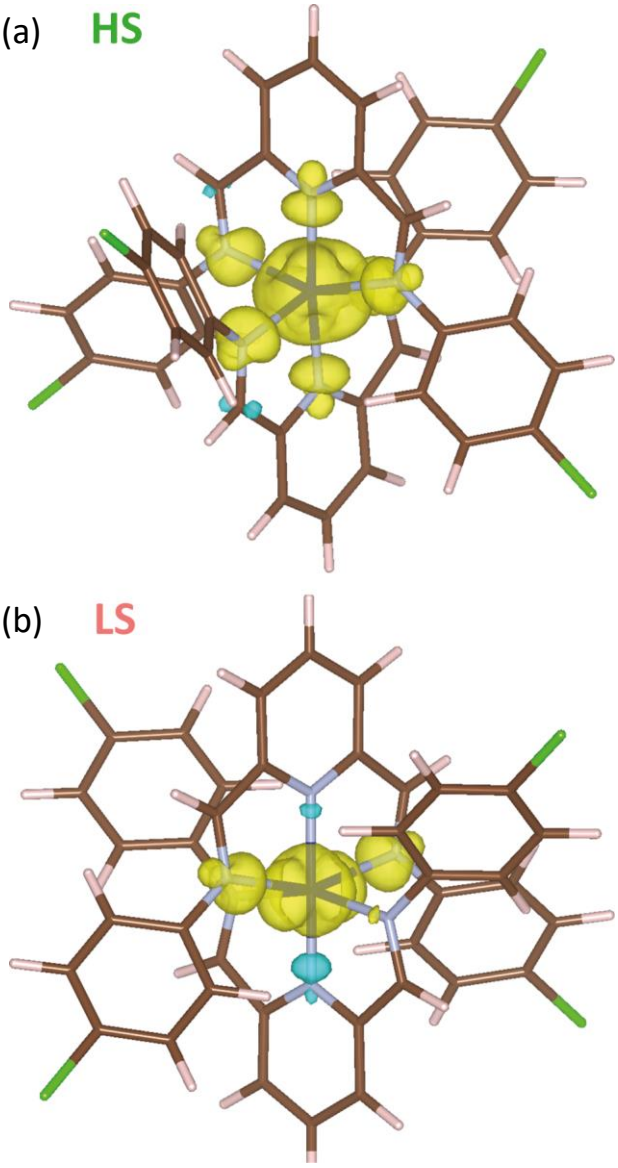

Figure II.9 Spin density maps for the optimised geometries on HS (a) and LS (b) configurations of the cobalt(II) complex in **3**. Isosurfaces are shown setting cut-off at 0.0002 e $bohr^{-3}$. Colour code: dark blue, cobalt; light blue, nitrogen; brown, carbon; green, Chlorine; pink, hydrogen. Positive and negative spin densities are displayed in yellow and blue colours.

II.6 – Concluding Remarks

A novel series of mononuclear spin crossover cobalt(II) molecular nanomagnets has been prepared through ligand design from a series of multichannel redox-active *N*,*N*'-diphenyl-substituted pyridine-2,6-diimine (*n*-XPhPDI) tridentate ligands bearing electron-withdrawing iodo, bromo, or chloro substituents at the para or meta positions of the terminal *N*-substituted phenyl rings. They possess both metal-centred oxidation and ligand-centred reduction activity because of the dual σ-donor and π-acceptor character of the non-innocent *n*-XPhPDI ligands. It is found an overall correlation of the redox behaviour with the electron-withdrawing nature of the ligand substituents, that are eventually responsible for the different thermodynamic and kinetic stability of the corresponding cobalt(III) and the single or double imide-type π-radical anion cobalt(II) species depending on the *para* or *meta* substitution pattern of the terminal phenyl groups.

This series of compounds exhibit from complete and gradual, thermally-induced spin transition to its absence including partial transitions. No direct correlation of the SCO phenomenology with the electron acceptor nature of the ligand substituents is observed along this series. Otherwise, the role played by the crystal lattice through its organization through covalent bonds or intermolecular interactions in the SCO phenomenon must be highlighted. Then, the effects of the intermolecular halogen···halogen contacts seem responsible for the distinct SCO behaviour. Thus, weak X···X interactions are only present between the LS cobalt(II) units.

These cobalt(II)-*n*-XPhPDI complexes show dual spin relaxation dynamics under a magnetic dc field with slower- (SR) and faster-relaxing (FR) character depending on the magnitude of the applied dc magnetic field or their LS and HS nature. This multiple field-induced SMM behaviour is dominated by IK or QTM plus Raman processes at low- and high-temperature regions. The observed Raman mechanisms are assisted by both optical and acoustic phonons, involving virtual states that can be ascribed to low-energy vibrational modes. The presence of two-phonon Raman processes at higher temperatures was confirmed by its weak or null dependence on the dc magnetic field; however, at least for the LS configuration, the strong magnetic field influence suggests that IK, QTM or even direct mechanisms govern the spin reversal at lower temperatures. Our results and theoretical studies support that the larger spin delocalisation in the HS configuration slows down the magnetic relaxation.

Finally, we would like to point out that the design and implementation of multiple SMM properties in this unique family of octahedral SCO cobalt(II) compounds appear thus as a convenient route in order to obtain a new class of multiresponsive and multifunctional SCO/SMM materials as multistable molecular spin qubit candidates in QIP. Hence, our results suggest the possibility of manipulating the SMM properties of the LS cobalt(II) ions under the control of an external magnetic field, opening thus the way for their applications as molecular magnetic devices in a future spin-based quantum computing machine. The switching of the spin relaxation dynamics between the low magnetic field FR and the high magnetic field SR forms could, in principle, be exploited to develop a new class of magnetic field-effect, molecular spin transistors (MFE-MSTs). Different quantum coherence properties can be presumed for the FR and SR LS cobalt(II) complexes upon varying the dc magnetic field. In contrast to conventional electronic transistors of classic computers controlled by an electric voltage, the functioning of MFE-MSTs in quantum computers would be governed by a magnetic field. Current efforts are devoted to investigating the magnetic field effect on the quantum coherence properties of this new class of spin crossover cobalt(II) molecular nanomagnets.

II.7 – Experimental Section

Materials. All chemicals were of reagent grade quality, purchased from commercial sources, and used as received.

Physical Techniques. Elemental analyses (C, H, N) were performed at the Servicio Central de Soporte a la Investigación (SCSIE) at the Universitat de València (Spain). FTIR spectra were recorded on a Nicolet-5700 spectrophotometer as KBr pellets. Electronic absorption spectra of the ligands and complexes **1**–**4** ($c_L = c_M = 5 \times 10^{-3}$ mM) were carried out in acetonitrile solutions at room temperature with a Jasco UV/Vis/NIR V-670 spectrophotometer. ^{1}H NMR spectra were recorded at room temperature on a Bruker AC 300 (300 MHz) spectrometer. Deuterated chloroform was used as solvent and internal standard (δ = 7.26 ppm). Q-band EPR spectra of powdered samples of **1**–**4** were recorded at 4.0 K under non-saturating conditions with a Bruker ER 200 D spectrometer equipped with a helium-flow cryostat. PXRD data were obtained on a powder X-ray diffractometer (model Ultima IV, Rigaku, Japan) using Cu K_α radiation (λ = 1.5418 Å) at a voltage of 40 kV and a current of 30 mA with θ-2θ geometry. Data were collected using a 2θ step of 0.02° and a counting time of 0.25° 2θ min^{-1} in the angular range from 5 to 40° (2θ). The experimental and calculated (from the CIF files) PXRD patterns of **1**–**4** (Figure II.S1) showed a remarkable coincidence of the position of all peaks, confirming the purity of the bulk materials for each sample.

Electrochemical Measurements. Cyclic voltammetry (CV) studies were performed using an AUTOLAB 204 scanning potentiostat operating at a scan rate of 20–250 mVs^{-1}. Cyclic voltammograms were carried out at room temperature using 0.1 M nBu$_4$NPF$_6$ as supporting electrolyte and 1.0 mM of **1**–**4** in acetonitrile. The working electrode was a glassy carbon disk (0.32 cm^2) polished with 1.0 μm diamond powder, sonicated, washed with absolute ethanol and acetone, and finally air-dried. The reference electrode was AgCl/Ag separated from the test solution by a salt bridge containing the solvent/supporting electrolyte and platinum as the auxiliary electrode. All experiments were performed in standard electrochemical cells under argon. The investigated potential range was in the range of –2.0 to +2.0 V *vs* AgCl/Ag. Ferrocene was added as internal

standard at the end of the measurements. The formal potentials were measured at a scan rate of 200 mVs^{-1} and referred to the ferrocenium/ferrocene (Fc^+/Fc) couple. The values of the measured formal potential and the anodic to cathodic peaks separation of ferrocene under the same conditions were $E(Fc^+/Fc)$ = +0.40 V *vs* AgCl/Ag and $\Delta E_p(Fc^+/Fc)$ = 80 mV (CH_3CN, 0.1 M nBu_4NPF_6, 25 °C).

Magnetic Measurements. Variable-temperature (2.0–300 K) direct current (dc) magnetic susceptibility measurements under applied fields of 0.25 (T < 20 K) and 5.0 kOe (T > 20 K) and variable-field (0–50 kOe) magnetisation measurements at 2.0 K were carried out on crushed crystals of **1**–**4** with a Quantum Design SQUID magnetometer. Alternating current (ac) magnetic susceptibility measurements of **1**–**4** in the temperature range 0–12.0 K under ±5.0 Oe oscillating field at frequencies in the range of 0.1–10.0 kHz were performed under different applied static dc fields (0–2.5 kOe) with a Quantum Design Physical Property Measurement System (PPMS). The magnetic susceptibility data were corrected for the diamagnetism of the constituent atoms and the sample holder (a plastic bag).

Crystal Structure Data Collection and Refinement. X-ray data on single crystals of **1**–**4** were collected with Mo-K_α radiation (λ = 0.71073 Å) at 150 K on a Bruker APEX-II CCD (**1** and **3**) and an Agilent Supernova diffractometers (**2** and **4**), the last one equipped with an EosS2 detector. Collection, scalation, and integration of data were carried out with Bruker SAINT[71] (**1** and **3**) and CrysAlisPro[72] (**2** and **4**) software. The crystal structures were solved by intrinsic phasing methods integrated into the SHELXTL software[73] with the Olex2 platform.[74] The obtained models were refined with the 2018/3 version of SHELXL against F^2 on all data by full-matrix least-squares. Non-hydrogen atoms were anisotropically refined. Hydrogen atoms were set on geometrical positions and refined with a riding model. Two positions were found for the I2 and I7 iodine and perchlorate (Cl4) oxygen atoms of **1**. Whereas site occupancy factors (s.o.f., 0.454 and 0.546 for I2 and I2A, and 0.817 and 0.183 for I7 and I7A) of iodine atoms were refined, constraints were applied to the bond lengths and anisotropic factors of the perchlorate oxygen atoms. Since the perchlorate Cl6 in **3** is disordered in two positions, their s.o.f. were refined considering soft restraints on the distances between oxygen atoms. Two bromophenyl groups in **4** occupy two positions connected by a rotation (ca. 180°) around the N_{im}–C_{Ph} bond; therefore, they were modelled in these positions, and their s.o.f. refined (0.484 and 0.516 for Br8 and Br8B, and 0.831 and 0.169 for Br4 and Br4B). Some constraints were also applied to the anisotropic displacements of the carbon atoms. Three perchlorate groups in **4** are also disordered in two positions; their s.o.f. were refined, and some restraints on Cl–O bond lengths and anisotropic displacements of the chlorine and oxygen atoms were applied to make easier the convergence of the refinement. The graphical manipulations and calculations were performed with the CRYSTALMAKER and MERCURY programs.[75,76] Tables II.1 and II.2 summarise crystallographic data, refinement conditions, and relevant structural parameters for **1**–**4**. Crystallographic data (excluding structure factors) of **1**–**4** have been deposited with the Cambridge Crystallographic Data Centre.

DFT study: Geometries and spin densities. Because in an SCO system the crystal structure is strongly temperature-dependent, there may be some problems in recognizing a molecular geometry as purely one of the two competing configurations, HS and LS, from the experimental data at a given temperature. For this reason, the geometry of the mononuclear complex $[Co(n\text{-}XPhXPDI)_2]^{2+}$ of one of the compounds, specifically **3**, has been chosen, and its geometry has been optimized in the two electronic configurations. This study was also carried out by DFT type calculations through the Gaussian 09 package by using the hybrid B3LYP functional,[77,78] the quadratic convergence approach and an Ahlrichs' triple-z and double-z (TZVP) basis sets for cobalt and the rest of atoms.[79,80] A polarisable continuum model (PCM) was used with the parameters corresponding to the acetonitrile in order to avoid the usual electronic overdelocalisation in DFT calculations.[81] Optimized geometries were then confirmed as global minima by frequency calculations.

Ab initio calculations on the zfs tensors. The parameters that determine the axial (D) and rhombic (E) components of the local zero-field splitting (zfs), the g-tensor for the S = 3/2 state ($g_{3/2}$) and the ground Kramers doublet (g_{eff}) of **3** and the HS form of **4** were estimated from theoretical calculations based on a second-order *N*-electron valence state perturbation theory (CASSCF/NEVPT2) through an effective Hamiltonian for the spin-orbit coupling (SOC),[82–84] which often provides accurate values of the nearby excited states energies and for the *zfs* tensor of mononuclear first-row transition metal complexes. Experimental geometries were used in this study. Calculations were carried out on the experimental geometries with version 4.0.1 of the ORCA programme[85] using the def2-TZVP basis set proposed by Ahlrichs[86] and the auxiliary TZV/C Coulomb fitting basis sets.[87–89] The contributions to *zfs* from 10 quartet and 20 doublet excited states generated from an active space with seven electrons in five *d* orbitals were included using an effective Hamiltonian. RIJCOSX method was used combining resolution of the identity (RI) and "chain of spheres" COSX approximations for the Coulomb and exchange terms, respectively.[90–92]

Preparation of the ligands.

4-XPhPDI (X = I, Br, and Cl). Pyridine-2,6-diformaldehyde (0.135 g, 1.0 mmol) and 4-iodoaniline (0.438 g, 2.0 mmol), 4-bromoaniline (0.344 g, 2.0 mmol) or 4-cloroaniline (0.255 g, 2.0 mmol) were dissolved in 5.0 mL of ethanol containing 100 µL of acetic acid. The reaction mixture was refluxed for 30 min and cooled in an ice bath. The white (X = I and Cl) and brown (X = Br) crystalline solids were collected by filtration, washed with a small amount of ethanol, and dried in the open air. Yield: 94, 90 and 93% for X = I, Br and Cl, respectively. Anal. Calc. for $C_{19}H_{13}N_3I_2$ (4-IPhPDI): C, 42.49; H, 2.44; N, 7.82. Found: C, 42.88; H, 2.54; N, 7.61%. IR (KBr, cm^{-1}): 1622(m) [ν(C=N) from 4-IPhPDI ligand]. ^1H

NMR ($CDCl_3$; 300 MHz, ppm): δ = 8.64 (s, 2H, H_{im}), 8.28 (d, 2H, *m*-H_{py}, J = 7.8 Hz), 7.95 (t, 1H, *p*-H_{py}, J = 7.8 Hz), 7.75 (d, 4H, *m*-H_{Ph}, J = 8.6 Hz), 7.06 (d, 4H, *o*-H_{Ph}, J = 8.6 Hz). Anal. Calc. for $C_{19}H_{13}N_3Br_2$ (4-BrPhPDI): C, 51.50; H, 2.96; N, 9.48. Found: C, 51.25; H, 3.12; N, 9.66%. IR (KBr, cm^{-1}): 1625(m) [ν(C=N) from 4-BrPhPDI ligand]. ^1H NMR ($CDCl_3$; 300 MHz, ppm): δ = 8.64 (s, 2H, H_{im}), 8.28 (d, 2H, *m*-H_{py}, J = 7.8 Hz), 7.95 (t, 1H, *p*-H_{py}, J = 7.8 Hz), 7.55 (d, 4H, *m*-H_{Ph}, J = 8.6 Hz), 7.19 (d, 4H, *o*-H_{Ph}, J = 8.6 Hz). Anal. Calc. for $C_{19}H_{13}N_3Cl_2$ (4-ClPhPDI): C, 64.42; H, 3.70; N, 11.86. Found: C, 63.25; H, 3.65; N, 11.99%. IR (KBr, cm^{-1}): 1626(m) [ν(C=N) from 4-ClPhPDI ligand]. ^1H NMR ($CDCl_3$; 300 MHz, ppm): δ = 8.65 (s, 2H, H_{im}), 8.28 (d, 2H, *m*-H_{py}, J = 7.8 Hz), 7.95 (t, 1H, *p*-H_{py}, J = 7.8 Hz), 7.40 (d, 4H, *m*-H_{Ph}, J = 8.6 Hz), 7.26 (d, 4H, *o*-H_{Ph}, J = 8.6 Hz).

3-BrPhPDI. Pyridine-2,6-diformaldehyde (0.135 g, 1.0 mmol) and 3-bromoaniline (218 µL, 2 mmol) were poured into 5.0 mL of ethanol containing 100 µL of acetic acid. The reaction mixture was refluxed for 30 min, and the resulting solution evaporated under reduced pressure to afford an oil of the crude product lately dried under vacuum. Yield 98%. ^1H NMR ($CDCl_3$; 300 MHz, ppm): δ = 8.65 (s, 2H, H_{im}), 8.28 (d, 2H, *m*-H_{py}, J = 7.8 Hz), 7.95 (t, 1H, *p*-H_{py}, J = 7.8 Hz), 7.40 (d, 4H, *m*-H_{Ph}, J = 8.6 Hz), 7.26 (d, 4H, *o*-H_{Ph}, J = 8.6 Hz).

Preparation of the complexes.

*$[Co(4\text{-}IPhPDI)_2](ClO_4)_2{\cdot}MeCN$ (**1**), $[Co(4\text{-}BrPhPDI)_2](ClO_4)_2{\cdot}MeCN$ (**2**) and $[Co(4\text{-}ClPhPDI)_2](ClO_4)_2{\cdot}EtOAc$ (**3**).* A methanolic solution (5.0 mL) of cobalt(II) perchlorate hexahydrate (0.037 g, 0.1 mmol) was added dropwise to a suspension of 4-IPhPDI (0.107 g, 0.2 mmol), 4-BrPhPDI (0.088 g, 0.2 mmol) or 4-ClPhPDI (0.071 g, 0.2 mmol) in methanol (10.0 mL). The reaction mixtures were heated at 50 °C for 30 minutes. The resulting red precipitate was collected by filtration and washed with a small amount of methanol in all three cases. X-ray quality crystals of **1**–**3** were grown by slow diffusion of ethyl acetate through saturated acetonitrile/chloroform (1:1 v/v) solutions in glass tubes. Yield: 66 (**1**), 73 (**2**) and 62% (**3**). Anal. Calc. for $C_{40}H_{29}N_7O_8Cl_2I_4Co$ (**1**): C, 34.99; H, 2.13; N, 7.14. Found: C, 35.21; H, 2.08; N, 7.42%. IR (KBr, cm^{-1}): 2244(w) [ν(C≡N) from acetonitrile], 1580(m) [ν(C=N) from 4-IPhPDI], 1086(vs) [ν(Cl–O) from perchlorate]. UV-Vis (MeCN): ν_{max} (cm^{-1})/ε ($M^{-1}cm^{-1}$) = 50762/114883, 43479/71901 and 28654/34774. Anal. Calc. for $C_{40}H_{29}N_7O_8Cl_2Br_4Co$ (**2**): C, 40.54; H, 2.47; N, 8.27. Found: C, 40.66; H, 2.45; N, 8.45%. IR (KBr, cm^{-1}): 2244(w) [ν(C≡N) from acetonitrile], 1580(m) [ν(C=N) from 4-BrPhPDI], 1086(vs) [ν(Cl–O) from perchlorate]. ν_{max} (cm^{-1})/ε ($M^{-1}cm^{-1}$) = 51282/105132, 43860/51854) and 29326/26960). Anal. Calc. for $C_{42}H_{34}N_6O_{10}Cl_6Co$ (**3**): C, 47.84; H, 3.25; N, 7.97. Found: C, 47.66; H, 3.35; N, 7.92%. IR (KBr, cm^{-1}): 1730 (m) [ν(C=O) from ethyl acetate], 1580(m) [ν(C=N) from 4-ClPhPDI], 1086(vs) [ν(Cl–O) from perchlorate]. ν_{max} (cm^{-1})/ε ($M^{-1}cm^{-1}$) = 51282/10351, 44053/55620) and 29586/28428.

*$[Co(3\text{-}BrPhPDI)_2](ClO_4)_2$ (**4**).* Pyridine-2,6-diformaldehyde (0.027 g, 0.2 mmol) and 3-bromoaniline (44 µL, 0.4 mmol) were poured into 5.0 mL of ethanol containing 100 µL of acetic acid. Over the reaction mixture refluxed for 30 min was added dropwise a methanolic solution (5.0 mL) of cobalt(II) perchlorate hexahydrate (0.037 g, 0.1 mmol), and then heated at 50 °C for 30 minutes. The resulting red precipitate was filtered and washed with a small amount of methanol. X-ray quality crystals of **4** were grown by slow diffusion of ethyl acetate through a saturated acetonitrile/chloroform (1:1 v/v) solution in a glass tube. Yield 83%. Anal. Calc. for $C_{38}H_{26}N_6O_8Cl_2Br_4Co$ (**4**): C, 39.89; H, 2.29; N, 7.35. Found: C, 40.02; H, 2.36; N, 7.65%. IR (KBr, cm^{-1}): 1572(m) [ν(C=N) from 3-BrPhPDI], 1088(vs) [ν(Cl–O) from perchlorate]. ν_{max} (cm^{-1})/ε ($M^{-1}cm^{-1}$) = 50505/68630), 45872/61543), and 30395/19985).

References

1 Ferrando-Soria, J.; Vallejo, J.; Castellano, M.; Martínez-Lillo, J.; Pardo, E.; Cano, J.; Castro, I.; Lloret, F.; Ruiz-García, R.; Julve, M. Molecular Magnetism, *Quo Vadis?* A Historical Perspective from a Coordination Chemist Viewpoint. *Coord. Chem. Rev.* **2017**, *339*, 17–103.

2 Goodwin, H.A. Spin Transitions in Six-Coordinate Iron(II) Complexes. *Coord. Chem. Rev*. **1976**, *18*, 293–325.

3 Gütlich, P. Spin Crossover in Iron(II) Complexes. *Struct. Bonding (Berlin)* **1981**, *44*, 83–195.

4 König, E.; Ritter, G.; Kulshreshtha, S. K. The Nature of Spin-State Transitions in Solid Complexes of Iron(II) and The Interpretation of Some Associated Phenomena. *Chem. Rev.* **1985**, *85*, 219–234.

5 Boillot, M. L.; Sour, A.; Delhaes, P.; Mingotaud, C.; Soyer, H. A Photomagnetic Effect for Controlling Spin States of Iron(II) Complexes in Molecular Materials. *Coord. Chem. Rev*. 190–**1999**, *192*, 47–59.

6 *Spin Crossover in Transition Metal Compounds* (Eds.: Gütlich, P., Godwin, H. A.); Springer, Berlin: Germany, 2004, vol. 233–235.

7 Real, J. A.; Gaspar, A. B.; Muñoz, M. C. Thermal, Pressure and Light Switchable Spin-Crossover Materials. *Dalton Trans*. **2005**, 2062–2079.

8 Bousseksou, A.; Molnár, G.; Salmon, L.; Nicolazzi, W. Molecular Spin Crossover Phenomenon: Recent Achievements and Prospects. *Chem. Soc. Rev*. **2011**, *40*, 3313–3335.

9 Quintero, C. M.; Félix, G.; Suleimanov, I.; Costa, J. S.; Molnár, G.; Salmon, L.; Nicolazzi, W.; Bousseksou, A. Hybrid Spin-Crossover Nanostructures. *Beilstein J. Nanotechnol*. **2014**, *5*, 2230–2239.

10 Ruiz, E. Charge Transport Properties of Spin Crossover Systems. *Phys. Chem. Chem. Phys*. **2014**, *16*, 14–22.

11 Bertoni, R.; Cammarata, M.; Lorenc, M.; Matar, S. F.; Matar, J.-F.; Létard, J. F.; Lemke, E. Collet, H. T. Ultrafast Light-Induced Spin-State Trapping Photophysics Investigated in $Fe(phen)_2(NCS)_2$ Spin-Crossover Crystal. *Acc. Chem. Res*. **2015**, *48*, 774–781.

12 Harding, D. J.; Harding, P.; Phonsri, W. Spin Crossover in Iron(II) Complexes. *Coord. Chem. Rev*. **2016**, *313*, 38–61.

13 Khusniyarov, M. M. How to Switch Spin-Crossover Metal Complexes at Constant Room Temperature. *Chem. Eur. J.* **2016**, *22*, 15178–15191.

14 Cirera, J.; Ruiz, E.; Alvarez, S.; Neese, F.; Kortus, J. How to Build Molecules with Large Magnetic Anisotropy. *Chem. Eur. J*. **2009**, *15*, 4078–4087.

15 Neese, F.; Pantazis, D. A. What is not Required to Make a Single Molecule Magnet. *Faraday Discuss*. **2011**, *148*, 229–238.

16 Atanasov, M.; Aravena, D.; Suturina, E.; Bill, E.; Maganas, D.; Neese, F. First Principles Approach to the Electronic Structure, Magnetic Anisotropy and Spin Relaxation in Mononuclear 3d-Transition Metal Single Molecule Magnets. *Coord. Chem. Rev*. **2015**, *289–290*, 177–214.

17 Gomez-Coca, S.; Aravena, D.; Morales, R.; Ruiz, E. Large Magnetic Anisotropy in Mononuclear Metal Complexes. *Coord. Chem. Rev*. **2015**, *289–290*, 379–392.

18 Chibotaru, L. F. Theoretical Understanding of Anisotropy in Molecular Nanomagnets. *Struct. Bond*. **2015**, *164*, 185–229.

19 Craig, G. A.; Murrie, M. 3d Single-Ion Magnets. *Chem. Soc. Rev*. **2015**, *44*, 2135–2147.

20 Frost, J. M.; Harriman, K. L. M.; Murugesu, M. The Rise of 3-d Single-Ion Magnets in Molecular Magnetism: Towards Materials from Molecules? *Chem. Sci*. **2016**, *7*, 2470–2491.

21 Bar, A. K.; Pichon, C.; Sutter, J.-P. Magnetic Anisotropy in Two- to Eight-Coordinated Transition-Metal Complexes: Recent Developments in Molecular Magnetism. *Coord. Chem. Rev*. **2016**, *308*, 346–380.

22 Meng, Y.-S.; Jiang, S.-D.; Wang, B.-W.; Gao, S. Understanding the Magnetic Anisotropy toward Single-Ion Magnets. *Acc. Chem. Res*. **2016**, *49*, 2381–2389.

23 Frost, J. M.; Harriman, K. L. M.; Murugesu, M. The Rise of 3-d Single-Ion Magnets in Molecular Magnetism: Towards Materials from Molecules? *Chem. Sci.* **2016**, *7*, 2470–2491.

24 Moreno-Pineda E.; Godfrin, C.; Balestro, F.; Wernsdorfer, W.; Ruben, M. Molecular Spin Qubits for Quantum Algorithms. *Chem. Soc. Rev*. **2018**, *47*, 501–513.

25 Parks, J. J.; Champagne, A. R.; Costi, T. A.; Shum, W. W.; Pasupathy, A. N.; Neuscamman, E.; Flores-Torres, S.; Cornaglia, P. S.; Aligia, A. A.; Balseiro, C. A.; Chan, G.-K.-L.; Abruña, H. D.; Ralph, D. C. Mechanical Control of Spin States in Spin-1 Molecules and the Underscreened Kondo Effect. *Science* **2010**, *328*, 1370–1373.

26 Sessoli, R. Toward the Quantum Computer: Magnetic Molecules Back in the Race. *ACS Cent. Sci.* **2015**, *1*, 473–474.

27 Doistau, B.; Benda, L.; Hasenknopf, B.; Marvaud, V.; Vives, G. Switching Magnetic Properties by a Mechanical Motion. *Magnetochemistry* **2018**, *4*, 5.

28 Ding, Y.-S.; Deng, Y.-F.; Zheng, Y.-Z. The Rise of Single-Ion Magnets as Spin Qubits. *Magnetochemistry* **2016**, *2*, 40.

29 Warner, M.; Din, S.; Tupitsyn, I. S.; Morley, G. W.; Stoneham, A. M.; Gardener, J. A.; Wu, Z.; Fisher, A. J.; Heutz, S.; Kay, C. W. M.; Aeppli, G. Potential for Spin-Based Information Processing in a Thin-Film Molecular Semiconductor. *Nature* **2013**, *503*, 504–508.

30 Atzori, M.; Tesi, L.; Morra, E.; Chiesa, M.; Sorace, L.; Sessoli, R. Room-Temperature Quantum Coherence and Rabi Oscillations in Vanadyl Phthalocyanine: Toward Multifunctional Molecular Spin Qubits. *J. Am. Chem. Soc.* **2016**, *138*, 2154–2157.

31 Bader, K.; Dengler, D.; Lenz, S.; Endeward, B.; Jiang, S.-D.; Neugebauer, P.; van Slageren, J. Room Temperature Quantum Coherence in a Potential Molecular Qubit. *Nature Commun*. **2014**, *5*, 5304.

32 Harzmann, G. D.; Frisenda, R.; van der Zant, H. S. J.; Mayor, M. Single-Molecule Spin Switch Based on Voltage-Triggered Distortion of the Coordination Sphere. *Angew. Chem. Int. Ed.* **2015**, *54*, 13425–13430.

33 Aragonès, A. C.; Aravena, D.; Cerdá, J. I.; Acís-Castillo, Z.; Li, H.; Real, J. A.; Sanz, F.; Hihath, J.; Ruiz, E.; Díez-Pérez, I. Large Conductance Switching in a Single-Molecule Device through Room Temperature Spin-Dependent Transport. *Nano Lett.* **2016**, *16*, 218–226.

34 Devid, E. J.; Martinho, P. N.; Kamalakar, M. V.; Salitros, I.; Prendergast, U.; Dayen, J.-F.; Meded, V.; Lemma, T.; González-Prieto, R.; Evers, F.; Keyes, T. E.; Ruben, M.; Doudin, B.; van der Molen, S. J. Spin Transition in Arrays of Gold Nanoparticles and Spin Crossover Molecules. *ACSNano* **2015**, *9*, 4496–4507.

35 Bousseksou, A.; Molnár, G.; Demont, P.; Menegotto, J. Observation of a Thermal Hysteresis Loop in the Dielectric Constant of Spin Crossover Complexes: Towards Molecular Memory Devices. *J. Mater. Chem.* **2003**, *13*, 2069–2071.

36 Hasegawa, Y.; Takahashi, K.; Kume, S.; Nishihara, H. Complete Solid State Photoisomerization of Bis(Dipyrazolylstyrylpyridine)Iron(II) to Change Magnetic Properties. *Chem. Commun*. **2011**, *47*, 6846–6848.

37 Takahashi, K.; Hasegawa, Y.; Sakamoto, R.; Nishikawa, M.; Kume, S.; Nishibori, E.; Nishihara, H. Solid-State Ligand-Driven Light-Induced Spin Change at Ambient Temperatures in Bis(dipyrazolylstyrylpyridine)iron(II) Complexes. *Inorg. Chem*. **2012**, *51*, 5188–5198.

38 Milek, M.; Heinemann, F. W.; Khusniyarov, M. M. Spin Crossover Meets Diarylethenes: Efficient Photoswitching of Magnetic Properties in Solution at Room Temperature. *Inorg. Chem*. **2013**, *52*, 11585–11592.

39 Cowan, M. G.; Olguín, J.; Narayanaswamy, S.; Tallon, J. L.; Brooker, S. Reversible Switching of a Cobalt Complex by Thermal, Pressure, and Electrochemical Stimuli: Abrupt, Complete, Hysteretic Spin Crossover. *J. Am. Chem. Soc*. **2012**, *134*, 2892–2894.

40 Aravena, D.; Ruiz, E. Coherent Transport through Spin-Crossover Single Molecules. *J. Am. Chem. Soc*. **2012**, *134*, 777–779.

41 Warner, B.; Oberg, J. C.; Gill, T. G.; El Hallak, F.; Hirjibehedin, C. F.; Serri, M.; Heutz, S.; Arrio, M.-A.; Sainctavit, P.; Mannini, M.; Poneti, G.; Sessoli, R.; Rosa, P. Temperature- and Light-Induced Spin Crossover Observed by X-ray Spectroscopy on Isolated Fe(II) Complexes on Gold. *J. Phys. Chem. Lett*. **2013**, *4*, 1546–1552.

42 Meded, V.; Bagrets, A.; Fink, K.; Chandrasekar, R.; Ruben, M.; Evers, F.; Bernand-Mantel, A.; Seldenthuis, J. S.; Beukman, A.; van der Zant, H. S. J. Electrical Control over the Fe(II) Spin Crossover in a Single Molecule: Theory and Experiment. *Phys. Rev. B* **2011**, *83*, 245415.

43 Rösner, B.; Milek, M.; Witt, A.; Gobaut, B.; Torelli, P.; Fink, R. H.; Khusniyarov, M. M. Reversible Photoswitching of a Spin-Crossover Molecular Complex in the Solid State at Room Temperature. *Angew. Chem. Int. Ed*. **2015**, *54*, 12976–12980.

44 Mahfoud, T.; Molnár, G.; Cobo, S.; Salmon, L.; Thibault, C.; Vieu, C.; Demont, P.; Bouseksou, A. Electrical Properties and Non-Volatile Memory Effect of the $[Fe(HB(Pz)_3)_2]$ Spin Crossover Complex Integrated in a Microelectrode Device. *App. Phys. Lett*. **2011**, *99*, 053307.

45 Bairagi, K.; Iasco, O.; Bellec, A.; Kartsev, A.; Li, D.; Lagoute, J.; Chacon, C.; Girard, Y.; Rousset, S.; Miserque, F.; Dappe, Y. J.; Smogunov, A.; Barreteau, C.; Boillot, M.-L.; Mallah, T.; Repain, V. Molecular-Scale Dynamics of Light-Induced Spin Cross-Over in a Two-Dimensional Layer. *Nat. Commun*. **2016**,*7*, 12212.

46 Jenkins, M. D.; Zueco, D.; Roubeau, O.; Aromí, G.; Majer, J.; Luis, F. A Scalable Architecture for Quantum Computation with Molecular Nanomagnets. *Dalton Trans.* **2016**, *45*, 16682–16693.

47 Aragonès, A. C.; Aravena, D.; Valverde-Muñoz, F. J.; Real, J. A.; Sanz, F.; Hihath, J.; Díez-Pérez, I.; Ruiz, E. Metal-Controlled Magnetoresistance at Room Temperature in Single-Molecule Devices. *J. Am. Chem. Soc.* **2017**, *139*, 5768–5778.

48 Jasper-Toennies, T.; Gruber, M.; Karan, S.; Jacob, H.; Tuczek, F.; Berndt, R. Robust and Selective Switching of an Fe^{III} Spin-Crossover Compound on Cu_2N/Cu(100) with Memristance Behavior. *Nano Lett*. **2017**, *17*, 6613–6619.

49 Beckmann, U.; Brooker, S. Cobalt(II) Complexes of Pyridazine or Triazole Containing Ligands: Spin-State Control. *Coord. Chem. Rev*. **2003**, *245*, 17–29.

50 Goodwin, H. A. Spin Crossover in Cobalt(II) Systems. *Top Curr. Chem.* **2004**, *234*, 23–47.

51 Krivokapic, I.; Zerara, M.; Daku, M. L.; Vargas, A.; Enachescu, C.; Ambrus, C.; Tregenna-Piggott, P.; Amstutz, N.; Krausz, E.; Hauser, A. Spin Crossover in Cobalt(II) Imine Complexes. *Coord. Chem. Rev.* **2007**, *251*, 364–378.

52 Hayami, S.; Komatsu, Y.; Shimizu, T.; Kamihata, H.; Lee, Y. H. Spin-Crossover in Cobalt(II) Compounds Containing Terpyridine and its Derivatives. *Coord. Chem. Rev.* **2011**, *255*, 1981–1990.

53 Lloret, F.; Julve, M.; Cano, J.; Ruiz-García, R.; Pardo, E. Magnetic Properties of Six-Coordinated High-Spin Cobalt(II) Complexes: Theoretical Background and its Application. *Inorg. Chim. Acta* **2008**, *361*, 3432–3445.

54 Murrie, M. Cobalt(II) Single-Molecule Magnets. *Chem. Soc. Rev.* **2010**, *39*, 1986–1995.

55 Urtizberea, A.; Roubeau, O. Switchable Slow Relaxation of Magnetization in the Native Low Temperature Phase of a Cooperative Spin-Crossover Compound. *Chem. Sci*. **2017**, *8*, 2290–2295.

56 Shao, D.; Shi, L.; Yin, J.; Wang, B.-L.; Wang, Z.-X.; Zhang, Y.-Q.; Wang, X.-Y. Reversible On-Off Switching of Both Spin Crossover and Single-Molecule Magnet Behaviours *via* a Crystal-to-Crystal Transformation. *Chem. Sci.* **2018**, *9*, 7986–7991.

57 Rabelo, R.; Toma, L.; Moliner, N.; Julve, M.; Lloret, F.; Pasán, J.; Ruiz-Pérez, C.; Ruiz-García, R.; Cano, J. Electroswitching of the Single-Molecule Magnet Behaviour in an Octahedral Spin Crossover Cobalt(II) Complex with a Redox-Active Pyridinediimine Ligand. *Chem. Commun.* **2020**, *56,* 12242–12245.

58 Palion-Gazda, J.; Machura, B.; Kruszynski, R.; Grancha, T.; Moliner, N.; Lloret, F.; Julve, M. Spin Crossover in Double Salts Containing Six- and Four-Coordinate Cobalt(II) Ions. *Inorg. Chem.* **2017**, *56*, 6281–6296.

59 Shao, D.; Deng, L.-D.; Shi, L.; Wu, D.-Q.; Wei, X.-Q.; Yang, S.-R.; Wang, X.-Y. Slow Magnetic Relaxation and Spin Crossover Behaviour in a Bicomponent Ion-Pair Cobalt(II) Complex. *Eur. J. Inorg. Chem.* **2017**, 3862–3867.

60 Cui, H.-H.; Wang, J.; Chen, X.-T.; Xue, Z.-L. Slow Magnetic Relaxation in Five-Coordinate Spin-Crossover Cobalt(II) Complexes, *Chem. Commun.* **2017**, *53*, 9304–9307.

61 Chen, L.; Song, J.; Zhao, W.; Yi, G.; Zhou, Z.; Yuan, A.; Song, Y.; Wang, Z.; Ouyang, Z.-W. A Mononuclear Five-Coordinate Co(II) Single Molecule Magnet with a Spin Crossover between the *S* = 1/2 and 3/2 States. *Dalton Trans.* **2018**, *47*, 16596–16602.

62 Xu, M.-X.; Liu, Z.; Dong, B.-W.; Cui, H.-H. Wang, Y.-X.; Su, J.; Wang, Z.; Song, Y.; Chen, X.-T.; Jiang, S.-D.; Gao, S. Single-Crystal Study of a Low Spin Co(II) Molecular Qubit: Observation of Anisotropic Rabi Cycles. *Inorg. Chem.* **2019**, *58*, 2330–2335.

63 Baibich, M. N.; Broto, J. M.; Fert, A.; Nguyen Van Dau, F.; Petroff, F.; Etienne, P.; Creuzet, G.; Friederich, A.; Chazelas, J. Giant Magnetoresistance of (001)Fe/(001)Cr Magnetic Superlattices. *Phys. Rev. Lett*. **1988**, *61*, 2472.

64 Binash, G.; Grünberg, P.; Saurenbach, F.; Zinn, W. Enhanced Magnetoresistance in Layered Magnetic Structures with Antiferromagnetic Interlayer Exchange. *Phys. Rev. B* **1989**, *39*, 4828.

65 Figgins, P. E.; Busch, D. H. Complexes of Iron(II), Cobalt(II) and Nickel(II) with Biacetyl-bis-methylimine, 2-Pyridinal-methylimine and 2,6-Pyridinal-bis-methylimine. *J. Am. Chem. Soc.* **1960**, *82*, 820–824.

66 Juhász, G.; Hayami, S.; Inoue, K.; Maeda, Y. $[Co^{II}(phimpy)_2](ClO_4)_2$ and $[Co^{II}(ipimpy)_2](ClO_4)_2$: New Cobalt(II) Spin Crossover Compounds, and the Role of the Ligand Flexibility in Spin Transition Behavior. *Chem. Lett.* **2003**, *32*, 882–883.

67 De Bruin, B.; Bill, E.; Bothe, E.; Weyhermüller, T.; Wieghardt, K. Molecular and Electronic Structures of Bis(pyridine-2,6-diimine)metal Complexes $[ML_2](PF_6)_n$ (n = 0, 1, 2, 3; M = Mn, Fe, Co, Ni, Cu, Zn). *Inorg. Chem.* **2000**, *39*, 2936.

68 Römelt, C.; Weyhermüller, T.; Wieghardt, K. Structural Characteristics of Redox-active Pyridine-1,6-diimine Complexes: Electronic Structures and Ligand Oxidation Levels. *Coord. Chem. Rev.* **2019**, *380*, 287–317.

69 Hansch, C.; Leo, A.; Taft, W. A Survey of Hammett Substituent Constants and Resonance and Field Parameters. *Chem. Rev.* **1991**, *91*, 165–195.

70 Cole, K. S.; Cole, R. H. Dispersion and absorption in dielectrics. I. Alternating Current Characteristics. *J. Chem. Phys.* **1941**, *9*, 341–351.

71 Bruker. *SAINT*. Bruker AXS Inc., Madison, Wisconsin, USA, **2012**.

72 Agilent. *CrysAlis PRO*. Agilent Technologies Ltd, Yarnton, Oxfordshire, England, **2014**.

73 Sheldrick, G. M. SHELXT - Integrated Space-Group and Crystal-Structure Determination. *Acta Cryst.* **2015**, *A71*, 3–8.

74 Dolomanov, O.V., Bourhis, L.J., Gildea, R.J, Howard, J.A.K. & Puschmann, H. *J.* OLEX2: A Complete Structure Solution, Refinement and Analysis Program. *Appl. Cryst*. **2009**, *42*, 339-341.

75 *CrystalMaker*, CrystalMaker Software, Bicester, England, **2015**.

76 *Mercury*, The Cambridge Crystallographic Data Centre, Cambridge, UK.

77 Frisch, M. J.; Trucks, G. W.; Schlegel, H. B.; Scuseria, G. E.; Robb, M. A.; Cheeseman, J. R.; Scalmani, G.; Barone, V.; Mennucci, B.; Petersson, G. A.; Nakatsuji, H.; Caricato, M.; Li, X.; Hratchian, H. P.; Izmaylov, A. F.; Bloino, J.; Zheng, G.; Sonnenberg, J. L.; Hada, M.; Ehara, M.; Toyota, K.; Fukuda, R.; Hasegawa, J.; Ishida, M.; Nakajima, T.; Honda, Y.; Kitao, O.; Nakai, H.; Vreven, T.; Montgomery Jr., J. A.; Peralta, J. E.; Ogliaro, F.; Bearpark, M.; Heyd, J. J.; Brothers, E.; Kudin, K. N.; Staroverov, V. N.; Kobayashi, R.; Normand, J.; Raghavachari, K.; Rendell, A.; Burant, J. C.; Iyengar, S. S.; Tomasi, J.; Cossi, M.; Rega, N.; Millam, J. M.; Klene, M.; Knox, J. E.; Cross, J. B.; Bakken, V.; Adamo, C.; Jaramillo, J.; Gomperts, R.; Stratmann, R. E.; Yazyev, O.; Austin, A. J.; Cammi, R.; Pomelli, C.; Ochterski, J. W.; Martin, R. L.; Morokuma, K.; Zakrzewski, V. G.; Voth, G. A.; Salvador, P.; Dannenberg, J. J.; Dapprich, S.; Daniels, A. D.; Farkas, Ö.; Foresman, J. B.; Ortiz, J. V.; Cioslowski, J.; Fox, D. J. Gaussian 09, Revision D.01, Gaussian, Inc., Wallingford CT, 2009.

78 Becke, A. D. Density-Functional Thermochemistry. III. The Role of Exact Exchange. *J. Chem. Phys.* **1993**, 98, 5648–5652.

79 Schäfer, A.; Horn, H.; Ahlrichs, R. Fully Optimized Contracted Gaussian Basis Sets for Atoms Li to Kr. *J. Chem. Phys.* **1992**, *97*, 2571–2577.

80 Schäfer, A.; Huber, C.; Ahlrichs, R. Fully Optimized Contracted Gaussian Basis Sets of Triple Zeta Valence Quality for Atoms Li to Kr. *J. Chem. Phys.* **1994**, *100*, 5829–5835.

81 Tomasi, J.; Mennucci, B.; Cammi, R. Quantum Mechanical Continuum Solvation Models. *Chem. Rev.* **2005**, *105*, 2999–3093.

82 Angeli, C.; Cimiraglia, R.; Malrieu, J. P. n-Electron Valence State Perturbation Theory: a Fast Implementation of the Strongly Contracted Variant. *Chem. Phys. Lett.* **2001**, *350*, 297–305.

83 Angeli, C.; Cimiraglia, R.; Malrieu, J.-P. n-Electron Valence State Perturbation Theory: A Spinless Formulation and an Efficient Implementation of the Strongly Contracted and of the Partially Contracted Variants. *J. Chem. Phys.* **2002**, *117*, 9138–9153.

84 Angeli, C.; Cimiraglia, R.; Evangelisti, S.; Leininger, T.; Malrieu, J.-P. Introduction of n-Electron Valence States for Multireference Perturbation Theory. *J. Chem. Phys.* **2001**, *114*, 10252–10264.

85 Neese, F. The ORCA Program System. *Wires Comput. Mol. Sci.* **2012**, *2*, 73–78.

86 Weigend, F.; Ahlrichs, R. Balanced Basis Sets of Split Valence, Triple Zeta Valence and Quadruple Zeta Valence Quality for H to Rn: Design and Assessment of Accuracy. *Phys. Chem. Chem. Phys.* **2005**, *7*, 3297–3305.

87 Weigend, F. Accurate Coulomb-Fitting Basis Sets for H to Rn. *Phys. Chem. Chem. Phys.* **2006**, *8*, 1057–1065.

88 Eichkorn, K.; Treutler, O.; Ohm, H.; Haser, M.; Ahlrichs, R. Auxiliary Basis Sets to approximate Coulomb Potentials. *Chem. Phys. Lett.* **1995**, *242*, 652–660.

89 Eichkorn, K.; Weigend, F.; Treutler, O.; Ohm, H.; Ahlrichs, R. *Theor. Chem. Acc.* **1997**, *97*, 119–124.

90 Neese, F.; Wennmohs, F.; Hansen, A.; Becker, U. Efficient, Approximate and Parallel Hartree–Fock and Hybrid DFT Calculations. A 'Chain-of-Spheres' Algorithm for the Hartree–Fock Exchange. *Chem. Phys.* **2009**, *356*, 98–109.

91 Izsák, R.; Neese, F. An Overlap Fitted Chain of Spheres Exchange Method. *J. Chem. Phys.* **2011**, *135*, 144105.

92 Izsák, R.; Hansen, A.; Neese, F. The Resolution of Identity and Chain of Spheres Approximations for the LPNO-CCSD Singles Fock Term. *Mol. Phys.* **2012**, *110*, 2413–2417.

Supporting Information

TABLE OF CONTENTS

General characterisation (Figure II.S1 and II.S2)

X-ray crystallographic data collection and structure refinement (Figures II.S3 – II.S7)

Electrochemical measurements (Figure II.S8)

Static and dynamic magnetic measurements (Figures II.S9 – II.S16 and Table II.S1)

Theoretical calculations (Scheme II.S1 and Table II.S2)

General characterisation

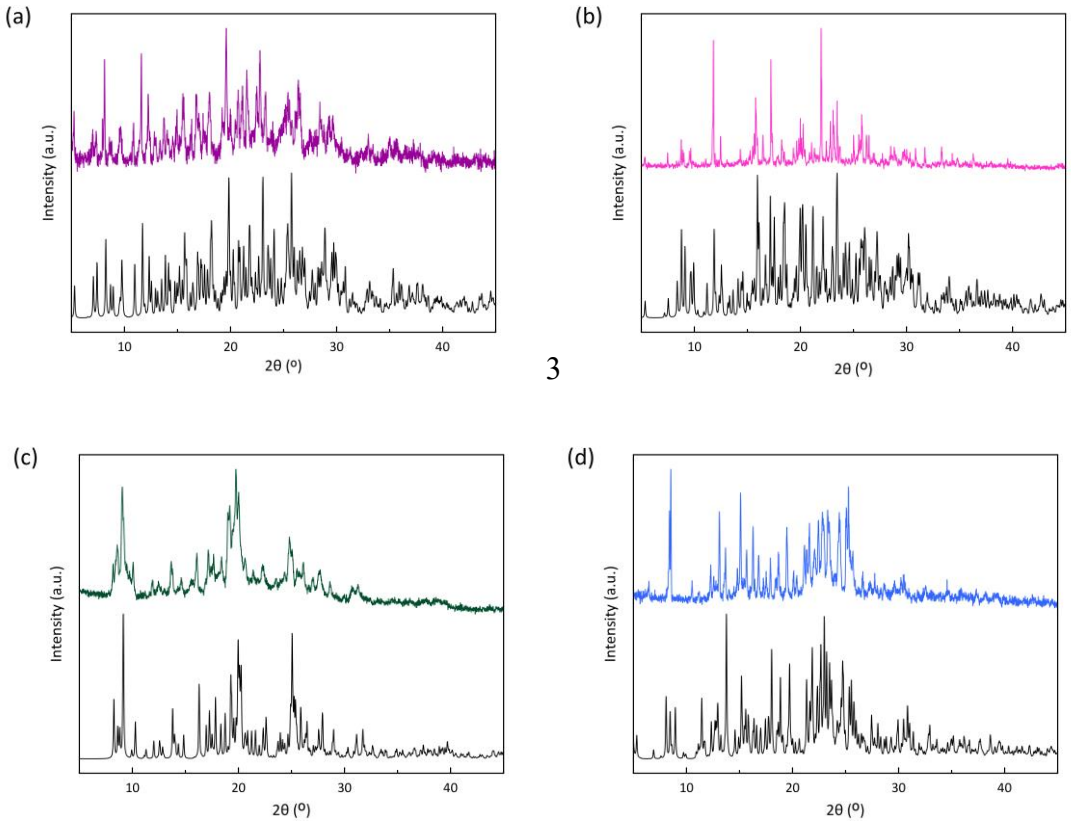

Figure II.S1 Powder X-ray diffractograms of **1** (a), **2** (b), **3** (c), and **4** (d). The solid black lines correspond to the calculated X-ray diffractograms.

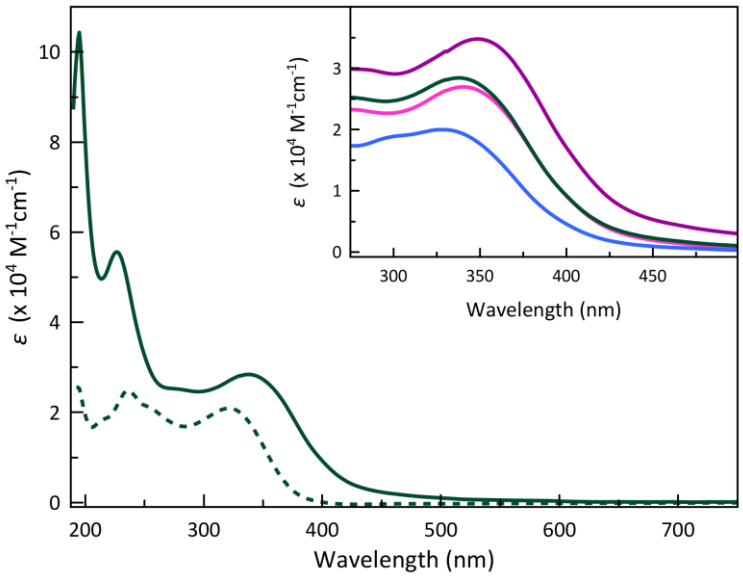

Figure II.S2 Electronic absorption spectra of the 4-ClPDI ligand (dashed line) compared to the corresponding cobalt(II) complex in acetonitrile solution at room temperature (solid line). The inset shows the lower energy UV-Vis band for **1** (purple), **2** (pink), **3** (green) and **4** (blue).

X-ray crystallographic data collection and structure refinement

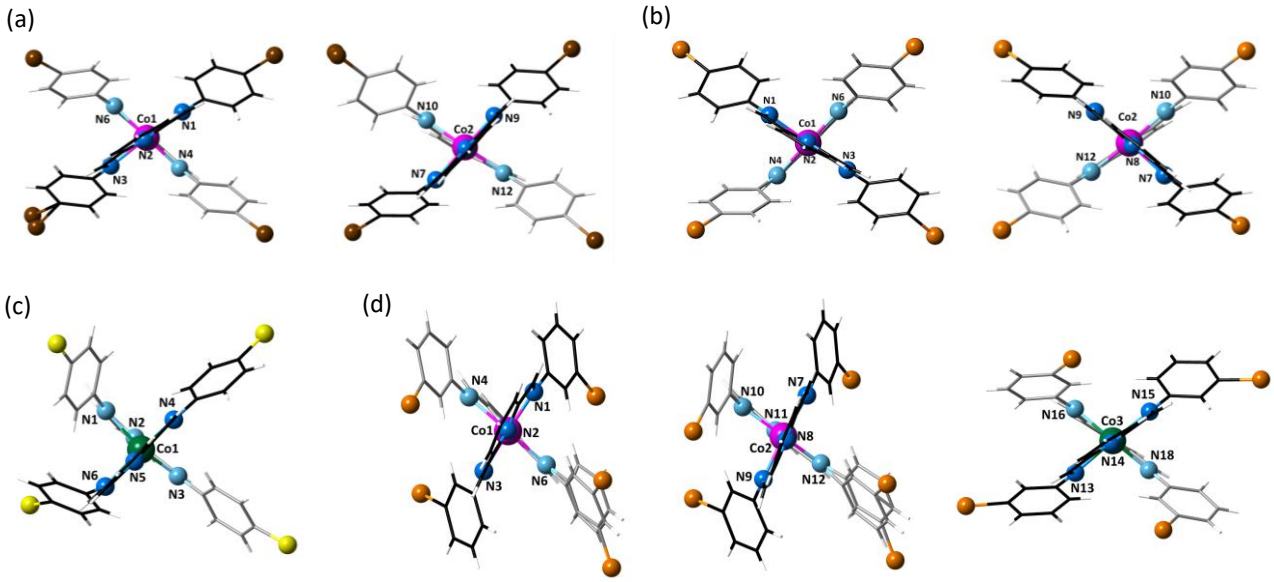

Figure II.S3 Perspective side views of the crystallographically independent mononuclear cobalt(II) units of **1**–**4** (a–d) with the atom numbering scheme of the coordination sphere at the cobalt atom. The ligand backbones are drawn in grey and black colours for clarity whereas the pink and green cobalt atoms correspond to the LS and HS configuration, respectively.

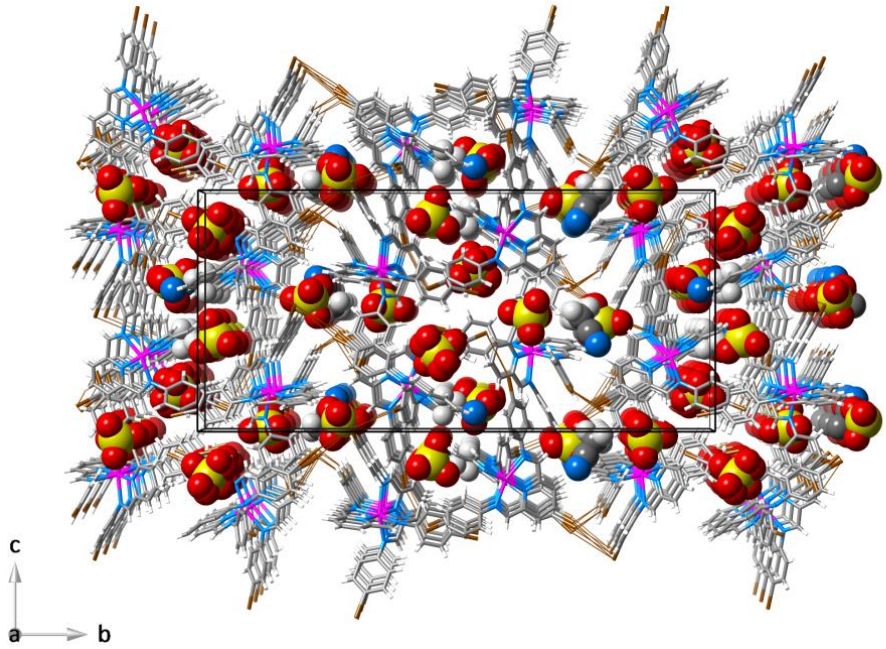

Figure II.S4 Perspective view of the crystal packing of **1** along the crystallographic *a* axis. The perchlorate anions and the acetonitrile molecules of crystallisation are shown in a space filling representation.

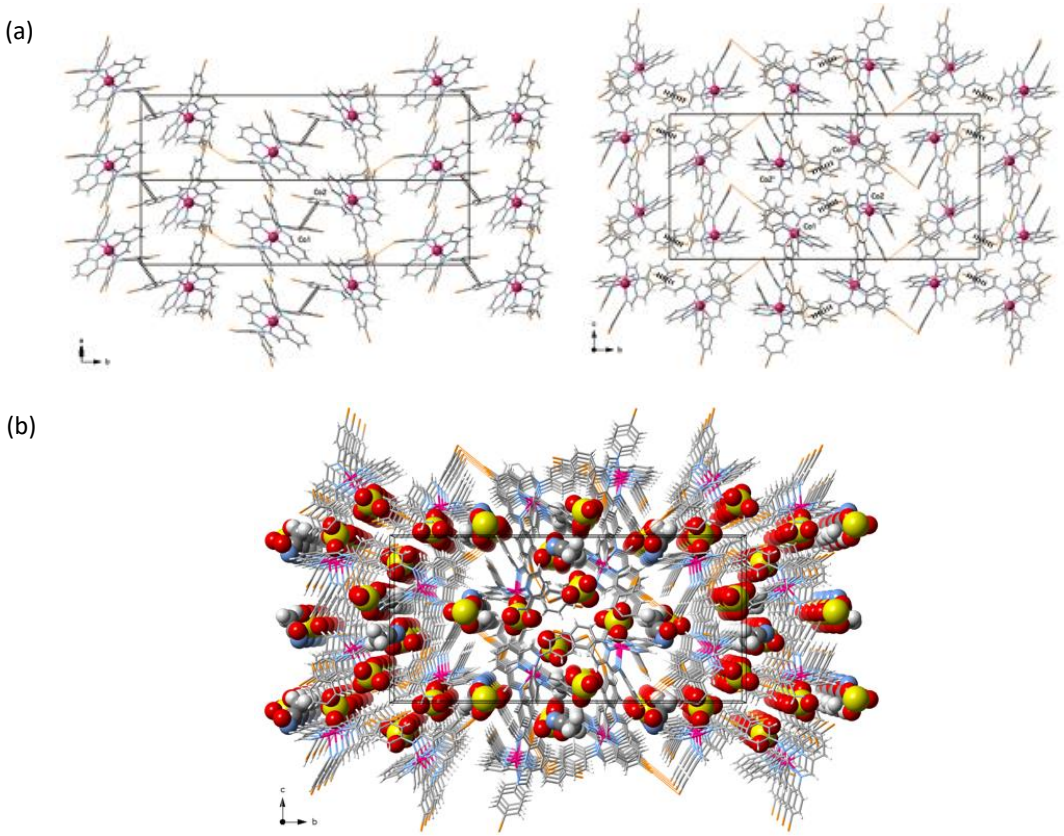

Figure II.S5 (a) Projection views of the crystal packing of **2** along the [–101] (left) and [-100] (right) directions showing the supramolecular three-dimensional network through π-π stacking (dashed lines) and Br···Br contacts (brown solid lines) among the mononuclear units [symmetry operation: (i) = -*x*+1, -*y*+1, -*z*+1]. (b) Perspective view of the crystal packing of **2** along the crystallographic *a* axis. The perchlorate anions and the acetonitrile molecules of crystallisation are shown in a space filling representation.

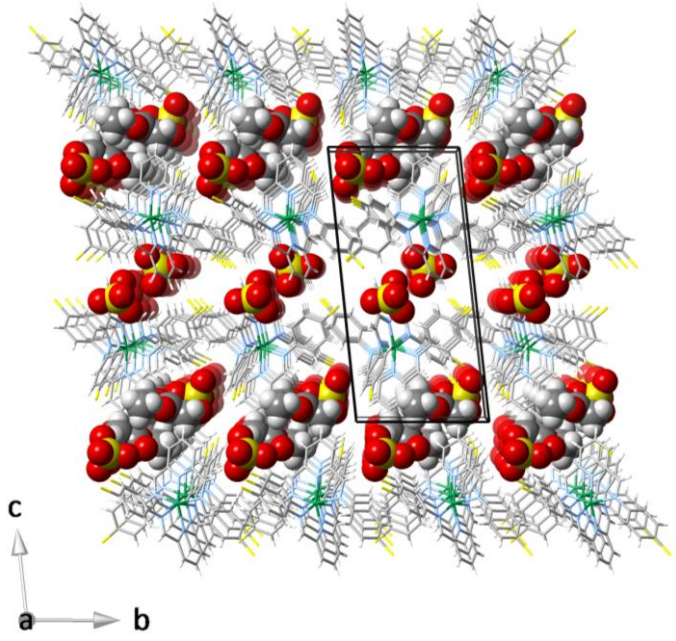

Figure II.S6 Perspective view of the crystal packing of **3** along the crystallographic *a* axis. The perchlorate anions and the ethyl acetate molecules of crystallisation are shown in a space filling representation.

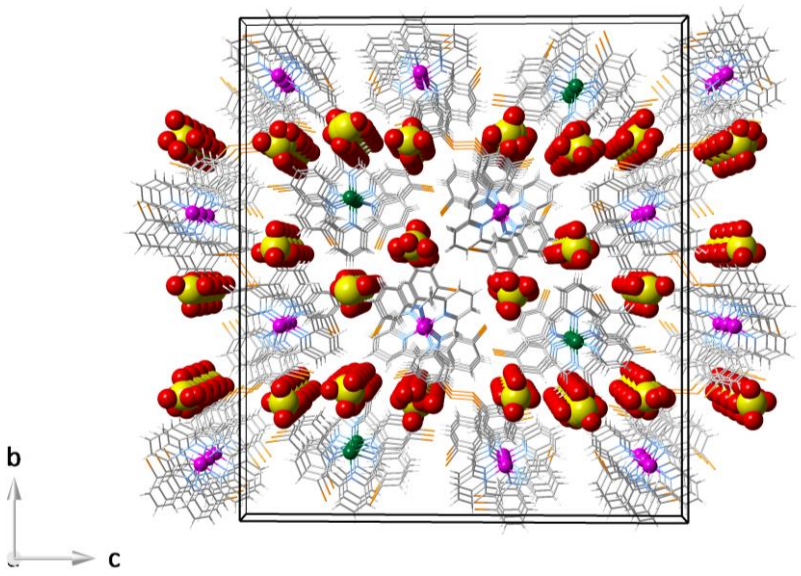

Figure II.S7 Perspective view of the crystal packing of **4** along the crystallographic *a* axis. The perchlorate anions are shown in a space filling representation. The pink and green cobalt atoms correspond to the LS and HS configuration, respectively.

Electrochemical measurements

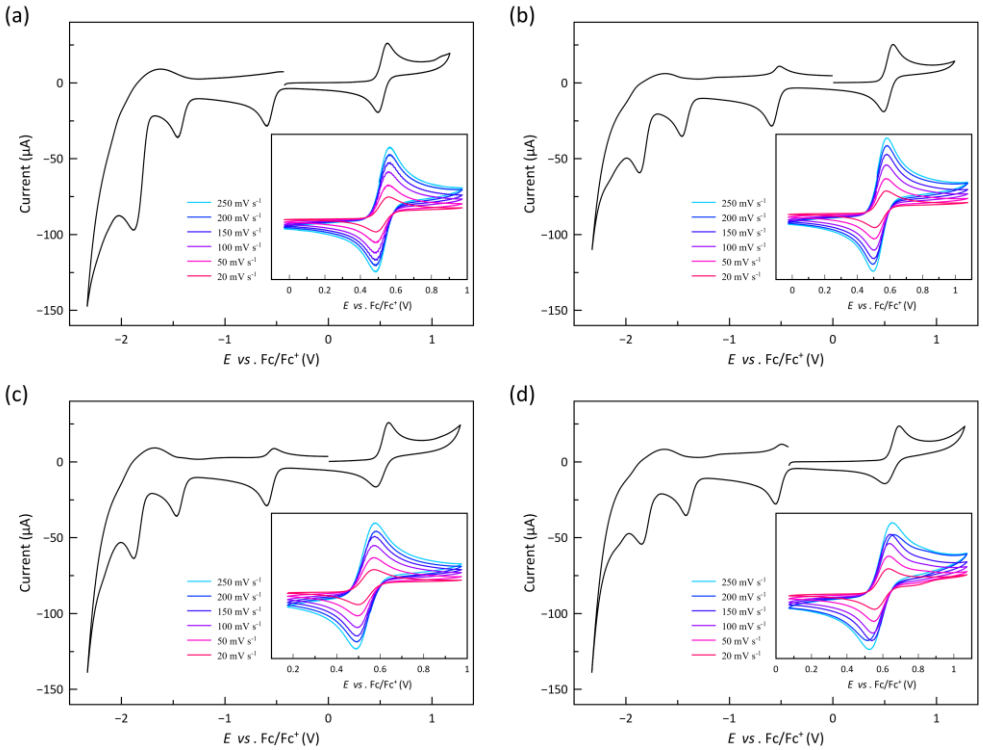

Figure II.S8 Cyclic voltammograms of **1**–**4** (a–d) in acetonitrile (0.1 M nBu$_4$NPF$_6$) at 25 °C and 200 mV s^{-1}. The insets show the cyclic voltammograms of the oxidation wave in the scan rate range of 20–250 mV s^{-1}.

Static and dynamic magnetic measurements

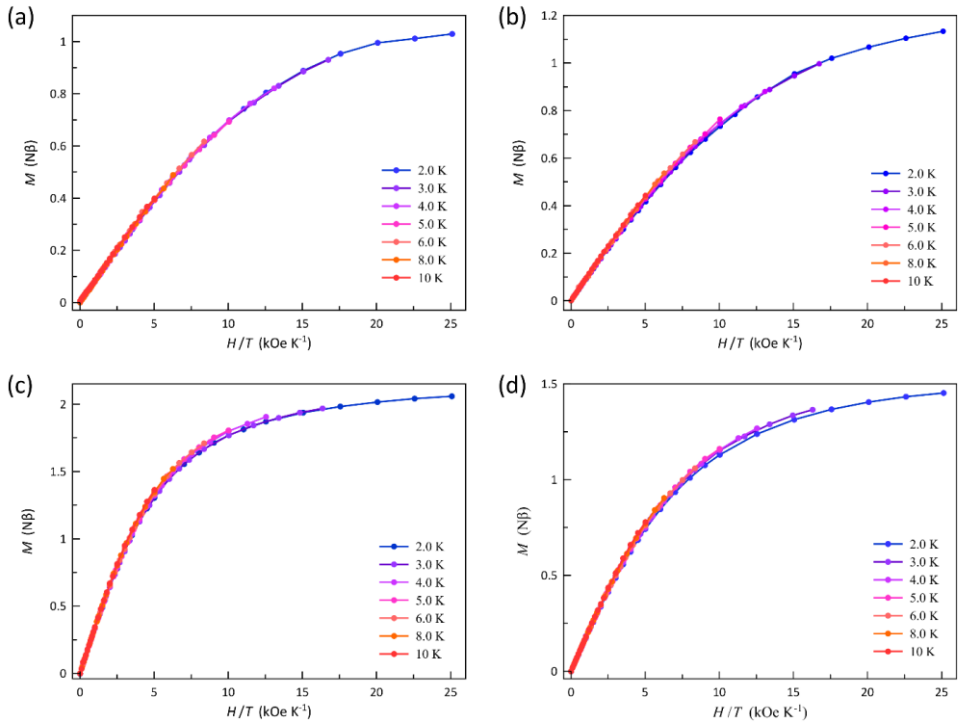

Figure II.S9 *M vs H*/*T* plots for **1**–**4** (a–d) in the temperature range of 2.0–10 K. The solid lines are only eye-guides.

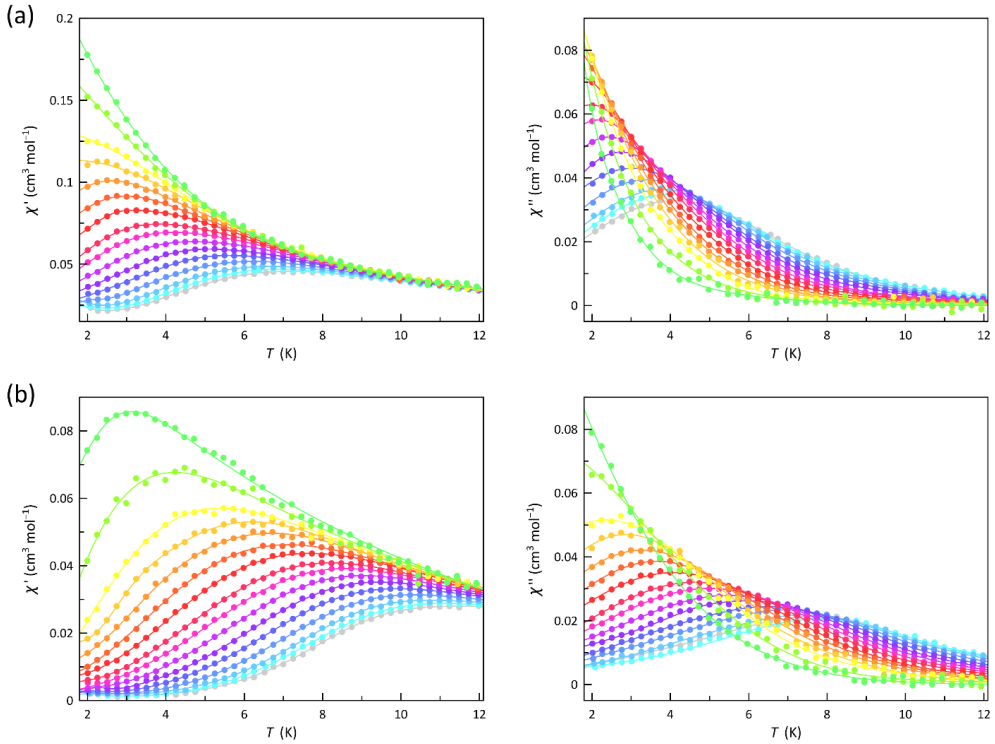

Figure II.S10 Temperature dependence of χ_M' (left) and χ_M'' (right) for **1** at a ±5.0 G oscillating field in the frequency range of 0.3–10.0 kHz (green to grey) under applied static magnetic fields of 1.0 (a) and 2.5 kOe (b). The solid lines are only eye-guides.

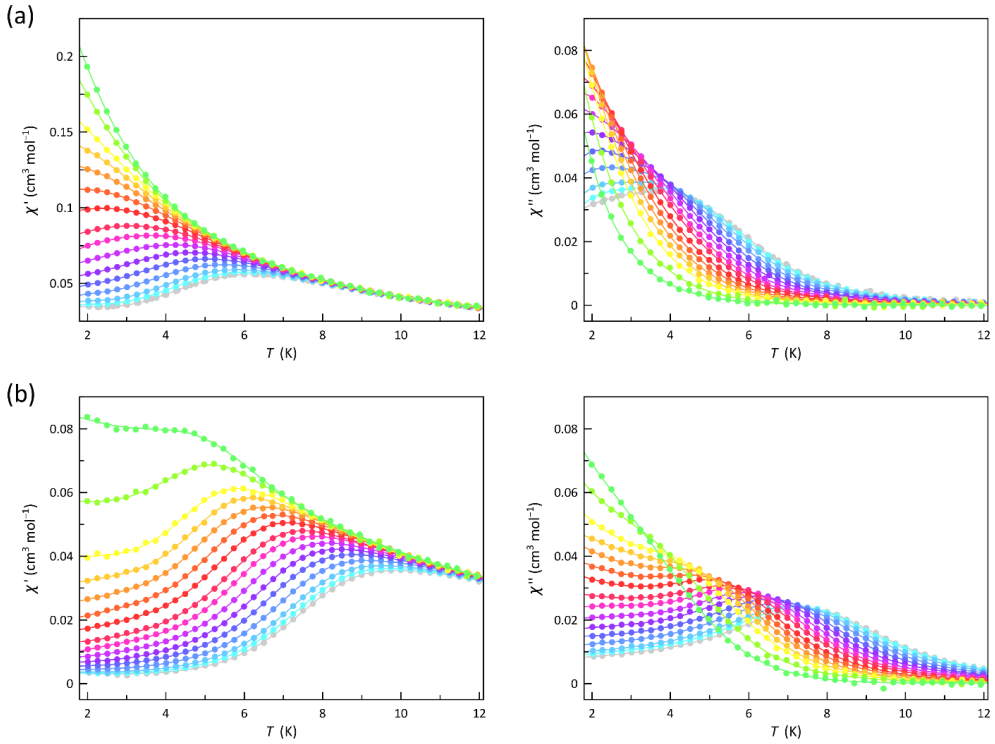

Figure II.S11 Temperature dependence of χ_M' (left) and χ_M'' (right) for **2** at a ±5.0 G oscillating field in the frequency range of 0.3–10.0 kHz (green to grey) under applied static magnetic fields of 1.0 (a) and 2.5 kOe (b). The solid lines are only eye-guides.

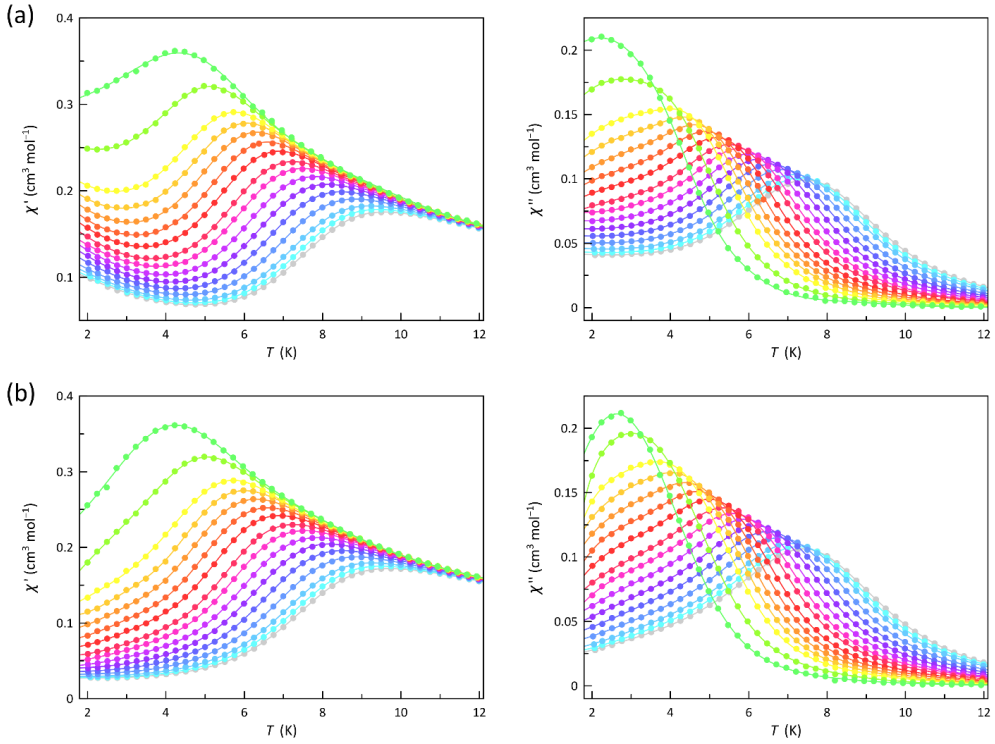

Figure II.S12 Temperature dependence of χ_M' (left) and χ_M'' (right) for **3** at a ±5.0 G oscillating field in the frequency range of 0.3–10.0 kHz (green to grey) under applied static magnetic fields of 1.0 (a) and 2.5 kOe (b). The solid lines are only eye-guides.

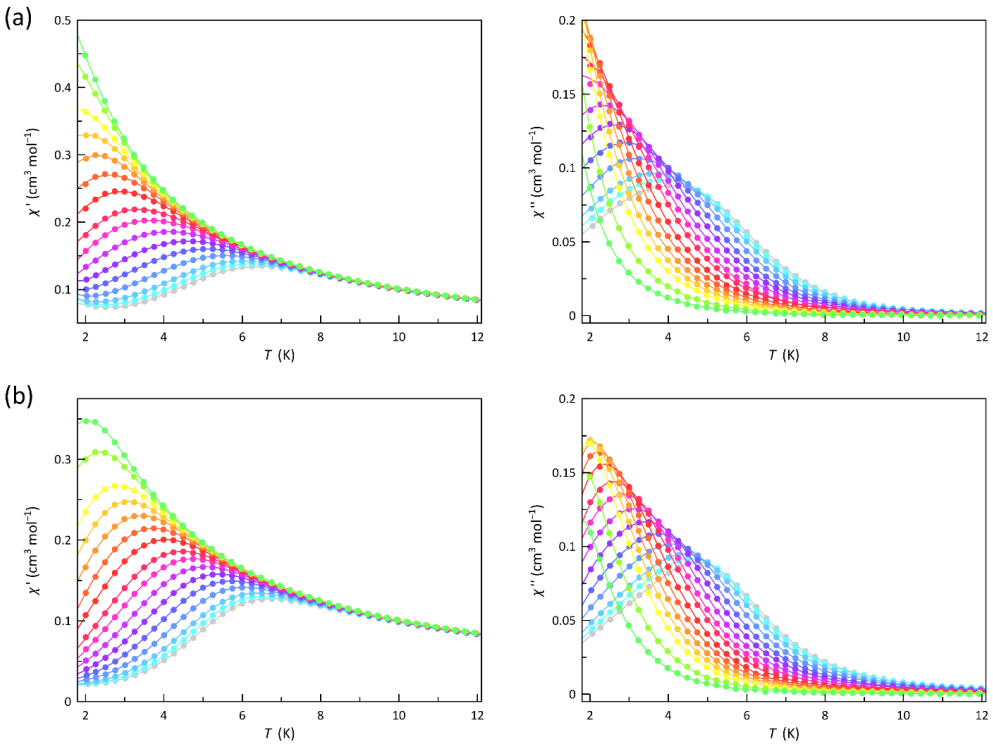

Figure II.S13 Temperature dependence of χ_M' (left) and χ_M'' (right) for **4** at a ±5.0 G oscillating field in the frequency range of 0.3–10.0 kHz (green to grey) under applied static magnetic fields of 1.0 (a) and 2.5 kOe (b). The solid lines are only eye-guides.

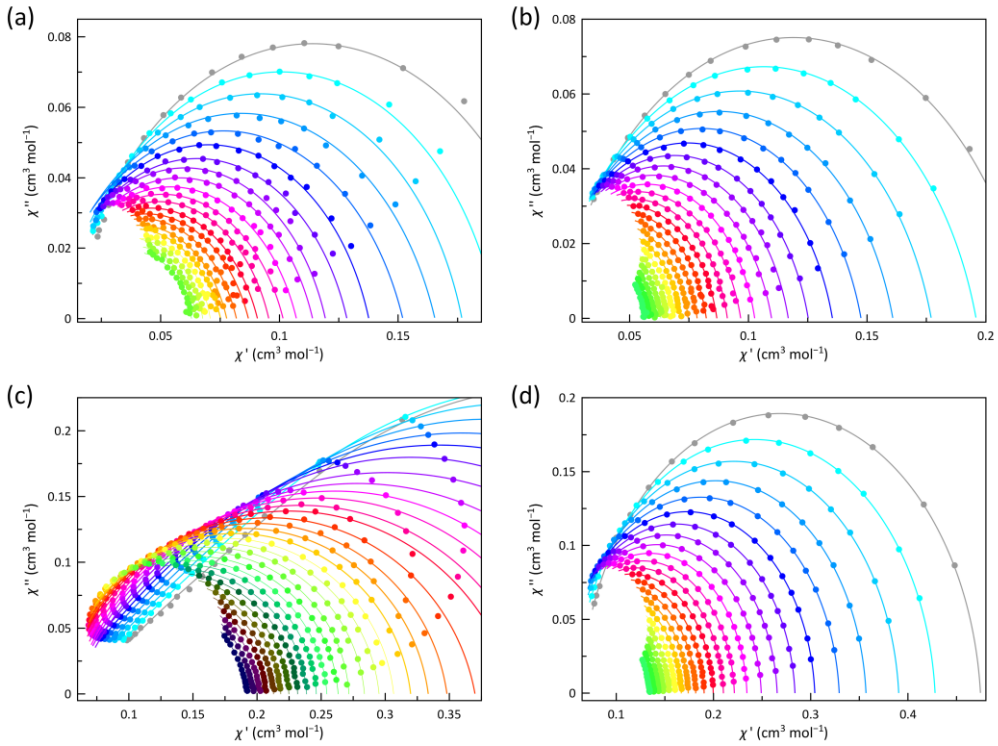

Figure II.S14 Argand plots for the calculated magnetic relaxation times (τ) of **1**–**4** (a–d) under an applied *dc* magnetic field of 1.0 kOe. The solid lines are the simulated curves by using the best-fit parameters obtained through the fitting of the χ_M' and χ_M'' *vs* ν plots by the generalised Debye model.

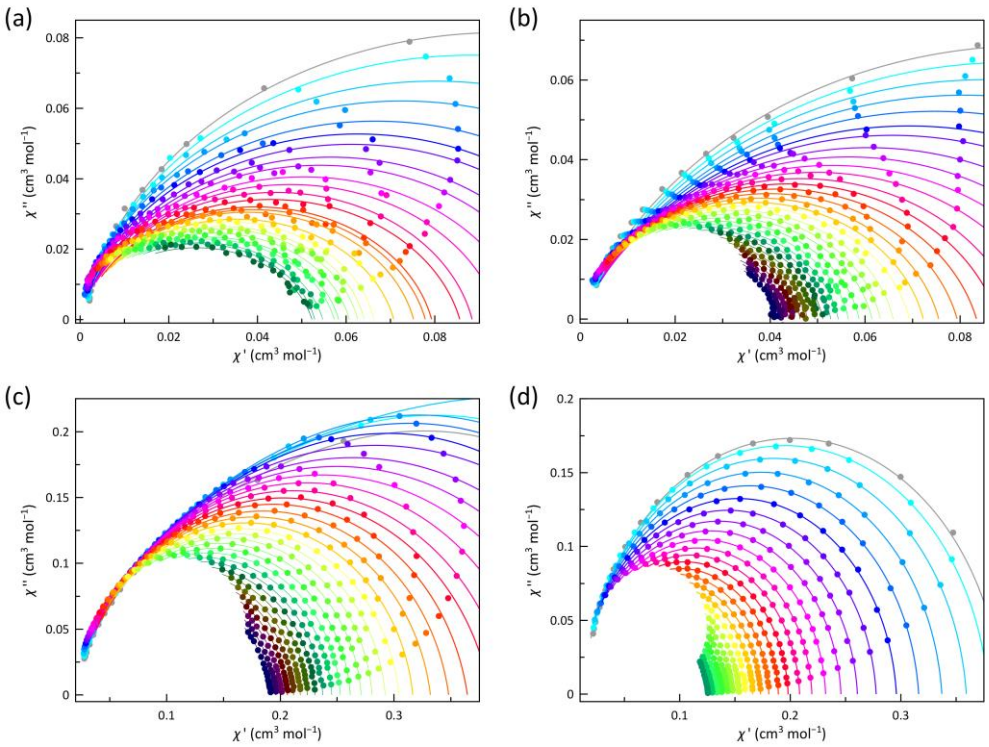

Figure II.S15 Argand plots for the calculated magnetic relaxation times (τ) of **1**–**4** (a–d) under an applied *dc* magnetic field of 2.5 kOe. The solid lines are the simulated curves by using the best-fit parameters obtained through the fitting of the χ_M' and χ_M'' *vs* ν plots by the generalised Debye model.

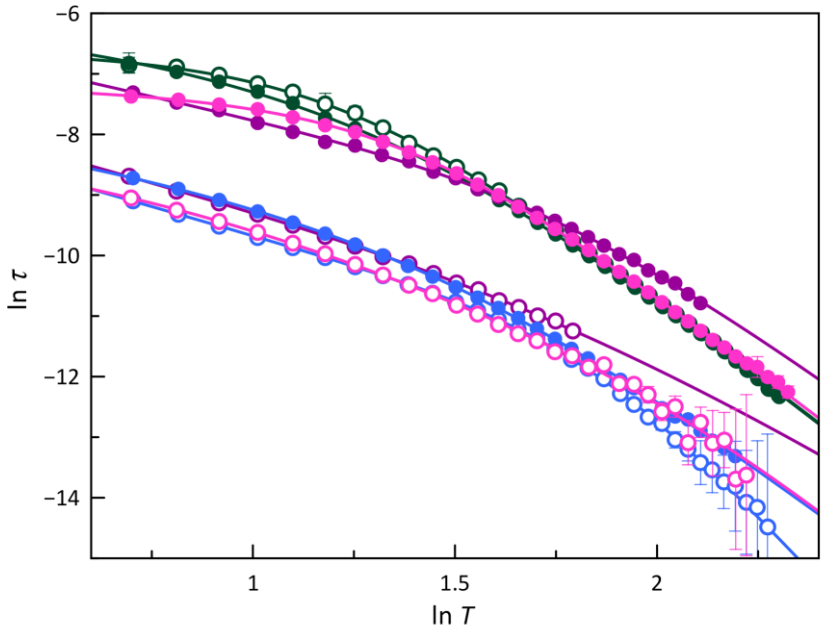

Figure II.S16 The ln τ *vs* ln *T* plots for the calculated magnetic relaxation times (τ) of **1** (purple), **2** (pink), **3** (green), and **4** (blue) under applied *dc* magnetic fields of 1.0 (○) and 2.5 kOe (●). Dashed and solid lines are the best-fit curves (see text). Vertical error bars denote the standard deviation.

Table II.S1 Selected parameters from the least-squares fit of the ac magnetic data of **1**–**4**[a]

	H_{dc} (kOe)	τ_{IK}[b] (x 10^{-3} s)	C_1[c] ($s^{-1}K^{-n}$)	n_1[c]	C_2[c] ($s^{-1}K^{-n}$)	n_2[c]
1	1.0	-	1480 ± 50	1.98 ± 0.03	1.13 ± 0.09	5.6 ± 0.4
	2.5	1.1 ± 0.4	23 ± 2	2.4 ± 1.0	3.73 ± 0.03	4.69 ± 0.07
2	1.0	0.32 ± 0.23	900 ± 600	2.5 ± 0.4	1.3 ± 0.3	5.7 ± 0.8
	2.5	1.10 ± 0.07	58 ± 9	1.92 ± 0.10	1.15 ± 0.03	5.26 ± 0.09
3	1.0	1.39 ± 0.06	25 ± 5	2.5 ± 0.6	1.43 ± 0.19	5.16 ± 0.06
	2.5	2.4 ± 0.4	96 ± 22	2.20 ± 0.15	1.000 ± 0.016	5.30 ± 0.05
4	1.0	-	2340 ± 80	1.91 ± 0.03	0.10 ± 0.03	7.33 ± 0.13
	2.5	0.59 ± 0.09	1050 ± 60	1.95 ± 0.15	8.1 ± 1.3	5.04 ± 0.07

[a]The fits correspond to double or triple relaxation models. [b]Coefficient factor for the temperature-independent *IK* process ($\tau^{-1} = IK$). [c]Coefficient and polynomial factor for the Raman process ($\tau^{-1} = CT^n$).

Theoretical calculations

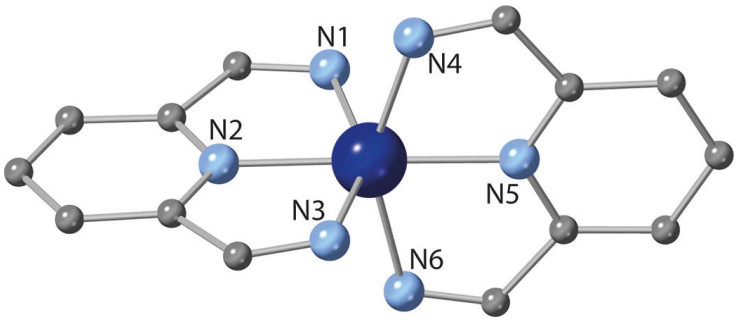

Scheme II.S1 A mononuclear cobalt(II)-PDI unit with the atom numbering scheme for the coordination sphere at the cobalt atom.

Table II.S2 Calculated atomic spin densities (ρ, in electrons) on the cobalt the nitrogen atoms conforming the coordination sphere and spin densities on the cobalt orbital of valence and inner shells for the HS and LS configurations. The used atomic notation is described in Scheme II.S1

Atoms and Orbitals	ρ (HS)	ρ (LS)
Co	+2.73185 (91.1%)[a]	+0.97065 (97.1%)[a]
N1	+0.03688	+0.04502
N2	+0.04144	–0.00829
N3	+0.05310	+0.04502
N4	+0.05279	+0.00588
N5	+0.04263	–0.01266
N6	+0.03553	+0.00588
Co(1s)	+0.00000	+0.00000
Co(2s)	+0.00009	+0.00004
Co(2p)	–0.00058	–0.00021
Co(3s)	+0.00244	+0.00084
Co(3p)	–0.00426	+0.00161
Co(4s)	+0.01454	+0.00643
Co(3d)	+2.71109	+0.96195

[a] In parentheses, percentage of the total spin density.

CHAPTER III

ELECTROCHEMICALLY-ACTIVE SPIN CROSSOVER MOLECULAR NANOMAGNETS (II)

Electrochemically-active Spin Crossover Molecular Nanomagnets (II)

III.1 – Background and Highlights

Multi-electron transfer (MET) processes, responsible for many biological and chemical functions, are fundamental in designing new electroactive materials for Molecular Electronics and Spintronics uses.[1–3] The coordination chemistry of redox-active ligands also plays a critical role in catalytic redox transformations,[4] as well as artificial photosynthetic systems (solar cells) for light-driven MET processes which improves solar energy harvest.[5–9] Dithiolenes, diimines, diamines, and catecholates are non-innocent redox-active ligands with a distinctive ability to form radical ligand species when coordinated to transition metal ions.[10–14]

Our studies on electroactive spin crossover molecular nanomagnets (SCO/SMMs) rely on the ability of pyridinediimine (PDI) ligands[15–17] to impart an additional reducible capacity to the oxidisable metal centre in their mononuclear cobalt(II) complexes. Hence, reducing the redox-active PDI ligands involves two sequential and reversible one-electron transfer steps to give an imine-type $PDI^{\bullet-}$ π-radical anion and a diimine-type PDI^{2-} dianion, as illustrated in Scheme III.1.[17] As we demonstrated in Chapter II, the inclusion of electron-withdrawing groups in the benzene ring imino substituent favours electron-acceptor properties of PDI ligands, leading thus to a unique class of spin capacitors based on this family of electroactive SCO/SMMs.

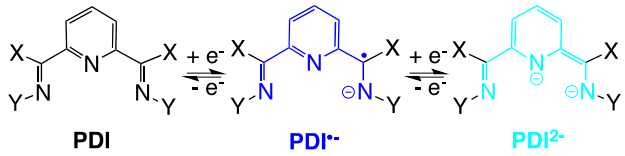

Scheme III.1 Redox isomers for the PDI ligands.

In the present chapter, we propose to go one step further by focusing on metal oxidation instead of ligand reductions. For this, we have alternatively incorporated electron-donating groups to the PDI ligand, trying to facilitate metal oxidation. Herein, we report the synthesis, structural, redox, and spectroscopic characterisation, static and dynamic magnetic studies for a series of cobalt(II) compounds of general formula $[CoL_2](ClO_4)_2{\cdot}Solv$ [L = 2,6-bis(N-4-methylphenylformimidoyl)pyridine (4-MePhPDI) **1** (Solv = H_2O), 2,6-bis(N-4-methoxyphenylformimidoyl)pyridine (4-MeOPhPDI) **2**, 2,6-bis(N-4-thiomethylphenylformimidoyl)pyridine (4-MeSPhPDI) **3**, 2,6-bis(N-4-dimethylaminophenylformimidoyl)pyridine (4-Me_2NPhPDI) **4**, and 2,6-bis(N-2,4-dimethylphenylformimidoyl)pyridine (2,4-Me_2PhPDI) **5**] (Scheme III.2), as well as the synthesis and structural characterisation of the oxidised cobalt(III) compound of formula $[Co(4\text{-MeOPhPDI})_2](Br_3)_{2.35}(Br_5)_{0.65}{\cdot}0.25H_2O$ (**2'**).

This novel family of mononuclear octahedral cobalt(II) complexes with redox-active tridentate PDI ligands featuring electron donor group-substituted benzene rings also exhibits thermally-induced spin transition and field-induced slow magnetic relaxation. Hence, the influence of both intra- and intermolecular ligand features and solvent effects in the SCO and SMM behaviours is systematically analysed in this series.

Finally, we provide a proof-of-concept demonstration of a spin electro-switch based on this unique class of electroactive spin-crossover molecular nanomagnets. So, for instance, we also report the reversible electro-switching of the SMM behaviour upon metal oxidation in the octahedral SCO cobalt(II)-4-MeOPhPDI complex bearing two electron-donating 4-methoxyphenyl substituents.

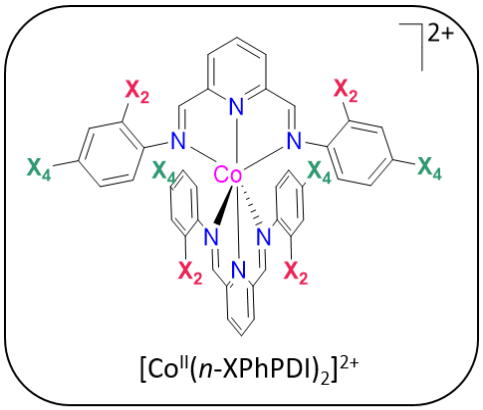

	n-XPhPDI	X_4	X_2
1	4-MePhPDI	Me	H
2	4-OMePhPDI	OMe	H
3	4-SMePhPDI	SMe	H
4	4-NMe_2PhPDI	NMe_2	H
5	2,4-Me_2PhPDI	Me	Me

Scheme III.2 General chemical formula of the cationic mononuclear octahedral cobalt(II) complexes with PDI ligands accounting with electron-donor substituents.

III.2 - Ligand Design and Synthetic Strategy

We follow the same strategy as in the previous chapter. By changing the substituent and its position on the phenyl group, we aim to modulate MET, SCO and SMM properties. The electron donor nature of the substituents provides easy access and additional stabilisation to the monooxidised form of the complexes, making them exciting candidates for the realisation of a spin electro-switch.

The ligands were synthesised from the straightforward condensation of pyridine-2,6-diformaldehyde and the aromatic substituted amine (1:2 molar ratio) in acid media. Scheme III.2 shows the emplacement of the donor groups Me, OMe, SMe and NMe_2 selected for this study. All ligands were isolated as crystalline powders in good yields, and they were characterised by elemental analyses (C, H, N), Fourier-transform infrared (FT-IR) and proton nuclear magnetic resonance (^{1}H NMR) spectroscopies (see Experimental Section).

Cobalt(II) complexes were synthesised from the reaction of cobalt(II) perchlorate hexahydrate and the previously isolated ligands (1:2 molar ratio). The oxidised cobalt(III)-4MeoPhPDI complex **2'** was obtained by chemical oxidation of a solution of **2** with an excess of bromine in a chloroform/acetonitrile mixture (1:1). All of them were isolated as X-ray quality single crystals in moderate yields by slow evaporation of ethanol (**1**) and methanol (**4** and **5**) solutions or by slow diffusion methods in a methanol/chloroform (**2**) and acetonitrile/ethyl

acetate/chloroform (**2'** and **3**) solvent mixtures. They were characterised by elemental analyses (C, H, N), Fourier-transform infrared (FT-IR), electronic absorption (UV-Vis), and electron paramagnetic resonance (EPR) spectroscopies (see Experimental section). Single-crystal and powder X-ray diffraction determined the chemical identity of **1**–**5** and **2'** (Figure III.S1).

III.3 – Description of the Structures

The cobalt(II)-PDI complexes here presented are not isostructural, reflecting thus the different nature of the electron-donating substituents and their *ortho* or *para* substitution and, occasionally, the presence of crystallisation water molecules. **1** and **3** crystallise in the triclinic *P–1* space group. In contrast, **4** and **5** crystallise in the monoclinic *P2₁/n* and *P2₁/c* space groups, as occurs in the parent unsubstituted compound described in the literature.[18] **2** and **2'** crystallise in the tetragonal *P43* and *I-42m* space groups. A summary of crystallographic and selected structural data for **1**–**5** and **2'** are listed in Tables III.1 and III.2.

These crystal structures consist of either one (**1**, **3**, **4**, and **5**) or four (**2**) crystallographically independent mononuclear cobalt(II) complex cations, $[Co^{II}L_2]^{2+}$, perchlorate anions, and water molecules of crystallisation (**1**) (Figures III.1 and III.S2–S7). The structure of **2'** consists of only one kind of crystallographically independent mononuclear cobalt(III) complex cations, $[Co^{III}(4\text{-MeOPhPDI})_2]^{3+}$, together with tri- and pentabromide anions and crystallisation water molecules (Figure III.S8).

Molecular structures. Whereas cobalt(II) complexes in **1**–**5** exhibit a distorted C_{2v} molecular symmetry (Figures III.1a–e), the unique crystallographically independent one in **2'** shows a C_2 molecular symmetry (Figure III.1f). Nonetheless, in all cases, the PDI ligands are almost but not perfectly perpendicularly oriented (Φ = 72.2–90.0; Table III.2), likely due to single (**1**, **2**, **2'** and **5**) or double (**3**), moderate to weak intramolecular ("face-to-face") π-π stacking interactions between pyridine and phenyl rings of different ligands (Figure III.S2). The intramolecular distance between the centroids of those rings and the dihedral angle between their mean planes [h = 3.6–4.5 (**1**–**5**) and 3.9 Å (**2'**) with θ = 17.8–59.1 (**1**–**5**) and 22.9° (**2'**); Table III.2] are below or close to the limiting values for "face-to-face" π-π stacking interactions (h < 4.4 Å and θ < 30°).

The cobalt's octahedral coordination sphere in **1**–**5** is axially compressed with certain rhombic distortion. The two pairs of imine nitrogen atoms (N_{im} and N'_{im}) from each PDI ligand define the equatorial plane, while the two pyridine nitrogen atoms (N_{py}) occupy the axial positions. Overall, the Co–N bonds of **1**–**5** are grouped into three different classes with two long Co–N_{im} and two intermediate Co–N'_{im} distances [R_1 = 2.085(4)–2.217(2) Å and R_2 = 2.029(2)–2.186(2) Å; Table III.2], and two short Co–N_{py} ones [R_3 = 1.872(5)–2.047(2) Å; Table III.2]. Because the e_g orbital occupancy in the ion is greater in the HS ($t_{2g}^5e_g^2$) than in the LS ($t_{2g}^6e_g^1$) configuration and because they form antibonding molecular orbitals with the ligands, the metal-ligand bond lengths are longer for the former configuration. These axial and equatorial Co–N bond lengths are almost linearly dependent on the electron-withdrawing ability of the X substituent in the ligand, expressed by the Hammet parameter,[19] as shown in Figure III.2. So that by removing or injecting electron density in the coordination regions of the PDI ligand, the antibonding nature of the molecular orbital is weakened or intensified and thus, the metal-ligand bonds are shortened or lengthened.

The rhombic distortion of the coordination sphere in **1**–**5** is manifested in the Δ_R and δ_R parameters that deviate from zero, being more significant for the LS configuration (Table III.2), which was expected because of the relative importance of the Jahn-Teller effect for $^2E_g(t_{2g}^6e_g^1)$ and $^4T_{1g}(t_{2g}^5e_g^2)$ states.

Otherwise, the octahedral cobalt coordination sphere in **2'** is slightly axially compressed. The rather short average metal to nitrogen bond lengths are typical for LS Co^{III} ions with a $^1A_g(t_{2g}^6)$ ground state (R = 1.93 Å; Table III.2). Hence, the average axial distances are shorter than those of the equatorial ones [R_{ax} = 1.841(8) Å and R_{eq} = 1.982(9) Å with ΔR = 0.071(9); Table III.2]. But, the null δ_R value points to a less rhombic distortion.

Table III.1 Summary of Crystallographic Data for **1**–**5** and **2'**

	1	**2**	**2'**	**3**	**4**	**5**
Formula	$C_{42}H_{40}N_6O_9Cl_2Co$	$C_{42}H_{38}N_6O_{12}Cl_2Co$	$C_{42}H_{38}N_6O_{4.25}Br_{9.65}Co$	$C_{42}H_{38}N_6O_8Cl_2CoS_4$	$C_{46}H_{50}N_{10}O_8Cl_2Co$	$C_{46}H_{42}N_6O_8Cl_2Co$
M (g mol^{-1})	902.63	948.61	1546.80	1012.85	1000.79	940.72
Crystal system	Triclinic	Tetragonal	Tetragonal	Triclinic	Monoclinic	Monoclinic
Space group	*P–1*	*P4₃*	*I-42m*	*P–1*	*P2₁/n*	*P2₁/c*
a (Å)	13.3841(9)	19.3426(1)	24.552(5)	9.6346(3)	10.6359(3)	20.2948(6)
b (Å)	13.5571(9)	19.3426(1)	24.552(5)	10.2111(4)	26.3995(9)	12.1110(5)
c (Å)	13.5951(9)	43.5392(5)	17.693(4)	22.5333(8)	17.1889(6)	18.9256(7)
α (°)	64.786(6)	90	90	88.0330(10)	90	90
β (°)	83.381(5)	90	90	85.7490(10)	99.6030(10)	108.743(4)
γ (°)	67.121(6)	90	90	82.9460(10)	90	90
V (Å^3)	2052.5(3)	16289.6(3)	10665(5)	2193.28(13)	4758.71(3)	4405.05(5)
Z	2	16	8	2	4	3
ρ_{calc} (g cm^{-3})	1.461	1.547	1.964	1.534	1.397	1.493
μ (mm^{-1})	5.014	0.627	8.084	0.928	0.536	1.121
T (K)	150	150	120	150	150	150
Reflect. collcd.	8104	88667	43052	16741	11788	19272
Reflect. obs. [$I > 2\sigma(I)$]	6894	30594	3616	13076	7967	7275
Data	8104	36206	3798	16741	11788	19272
Parameters	548	2286	324	572	612	556
Restraints	0	1	8	0	82	0
R_1[a] [$I > 2\sigma(I)$]	0.0476	0.0505	0.0468	0.0472	0.0878	0.0590
wR_2[b] [$I > 2\sigma(I)$]	0.1209	0.1135	0.1273	0.1645	0.2438	0.1253
S[c]	1.031	0.978	1.098	1.362	1.624	1.026

[a] $R_1 = \sum(|F_o| - |F_c|)/\sum|F_o|$. [b] $wR_2 = [\sum w(F_o^2 - F_c^2)^2/\sum w(F_o^2)^2]^{1/2}$. [c] $S = [\sum w(|F_o| - |F_c|)^2/(N_o - N_p)]^{1/2}$.

Table III.2 Selected Structural Data for **1**–**5** and **2'** [a]

	1	**2**	**2'**	**3**	**4**	**5**
R_1(Co–N_{im})[b] (Å)	2.206(2)	2.085(4)/2.180(4)/2.090(4)/2.185(4)	1.979(10)	2.217(2)	2.195(4)	2.215(2)
R_2(Co–N'_{im})[b] (Å)	2.029(2)	2.085(4)/2.114(4)/2.076(4)/2.096(4)	1.979(10)	2.186(2)	2.0325(4)	2.156(2)
R_3(Co–N_{py})[c] (Å)	1.896(3)	1.872(5)/1.905(5)/1.874(5)/1.902(5)	1.842(9)	2.047(2)	1.8850(4)	2.018(2)
R_{eq}[d] (Å)	2.118(2)	2.085(4)/2.147(4)/2.083(4)/2.141(4)	1.979(10)	2.202(2)	2.11385(4)	2.186(2)
δ_R[e]	0.084	0/0.031/0.007/0.042	0	0.014	0.077	0.027
R[f] (Å)	2.043(3)	2.014(5)/2.066(5)/2.013(5)/2.061(5)	1.933(10)	2.150(2)	2.037(4)	2.130(2)
Δ_R[g]	0.108(3)	0.106(5)/0.117(5)/0.103(5)/0.115(5)	0.071(9)	0.072(2)	0.112(4)	0.079(2)
N_{im}–Co–N'_{im}[h] (°)	87.73(9)	84.1(2)/92.0(2)/84.2(2)/92.1(2)	85.6(4)	89.7(4)	83.20(9)	88.82(9)
N'_{im}–Co–N_{im}[h] (°)	96.45(9)	100.1(2)/92.6(2)/100.0(2)/92.4(2)	96.5(6)	98.5(4)	101.08(8)	98.52(8)
N_{py}–Co–N_{py}[i] (°)	176.1(1)	177.4(2)/176.6(2)/178.4(2)/178.5(2)	175.1(6)	164.3(4)	177.1(9)	162.38(9)
δ[j] (Å)	±0.407	±0.395/±0.430/±0.395/±0.421	±0.295	±0.560	±0.410	±0.555
Φ[k](°)	81.74(2)	72.24(2)/89.88(2)/72.72(2)/89.97(2)	80.8(6)	80.42(4)	74.01(4)	79.33(2)
φ[l](°)	41.41(4)	43.7(8)/41.3(8)/44.5(8)/40.5(8)	47.5(6)	46.1(4)	38.1(4)	63.3(4)
d_0(C_{ph}–N_{im})[m] (Å)	1.431(4)	1.425(7)/ 1.424(7)/ 1.420(7)/ 1.422(7)	1.449(5)	1.423(3)	1.408(5)	1.432(3)
d_1(C_{py}–N_{py})[n] (Å)	1.349(4)	1.347(7)/ 1.345(7)/ 1.347(7)/ 1.345(7)	1.342(5)	1.337(3)	1.347(5)	1.338(3)
d_2(C_{py}–C_{im})[o] (Å)	1.465(4)	1.459(8)/ 1.454(8)/ 1.466(8)/ 1.453(8)	1.565(5)	1.467(3)	1.456(5)	1.474(4)
d_3(C_{im}–N_{im})[p] (Å)	1.282(4)	1.288(7)/ 1.289(7)/ 1.287(7)/ 1.291(7)	1.309(5)	1.285(3)	1.290(5)	1.276(3)
Δd[q] (Å)	0.1495(4)	0.1415(7)/ 0.1370(7)/ 0.1490(7)/ 0.1350(7)	0.240(2)	0.156(3)	0.137(5)	0.1670(3)
h[r] (Å)	3.716	3.839/4.273/3.938/4.502	3.905(9)	3.760/3.828	4.202	3.614
θ [s](°)	26.76	26.17/49.58/29.42/59.14	22.9(6)	19.50/26.15	47.76	17.76

[a] Structural data for each crystallographically independent cobalt atom. [b] Average cobalt-nitrogen imine equatorial bond distances from each PDI ligand. [c] Average cobalt-pyridine nitrogen axial bond distances from the two PDI ligands. [d] Average cobalt-nitrogen equatorial bond distances defined as $R_{eq} = (R_1 + R_2)/2$. [e] Rhombic distortion parameter defined as $\delta_R = (R_1 - R_2)/R_{eq}$. [f] Average cobalt-nitrogen bond distances defined as $R = (R_1 + R_2 + R_3)/3$. [g] Axial distortion parameter defined as $\Delta_R = (R_{eq} - R_{ax})/R$. [h] Average cobalt-nitrogen imine equatorial bond angles from the two PDI ligands. [i] Cobalt-nitrogen pyridine axial bond angle from the two PDI ligands. [j] Mean deviations of the imine nitrogen donor atoms from the metal equatorial plane. [k] Dihedral angle between the mean planes of the pyridinediimine fragments from the two PDI ligands. [l] Average torsional angle for the phenylimine ligand fragments from each PDI ligand. [m] Average phenyl carbon-imine nitrogen bond distance from the phenylimine ligand fragment. [n] Average pyridine carbon-pyridine nitrogen bond distance from the pyridinediimine ligand fragment. [o] Average pyridine carbon-imine carbon bond distance from the pyridinediimine ligand fragment. [p] Average imine carbon-nitrogen bond distance from the pyridinediimine ligand fragment. [q] Alternance bond parameter for the pyridinediimine ligand fragment defined as $\Delta_d = d_2 - (d_1 + d_3)/2$. [r] Intramolecular distance between the centroids of the pyridine and phenyl rings from the two PDI ligands. [s]Dihedral angle between the mean planes of the pyridine and phenyl rings from the two PDI ligands.

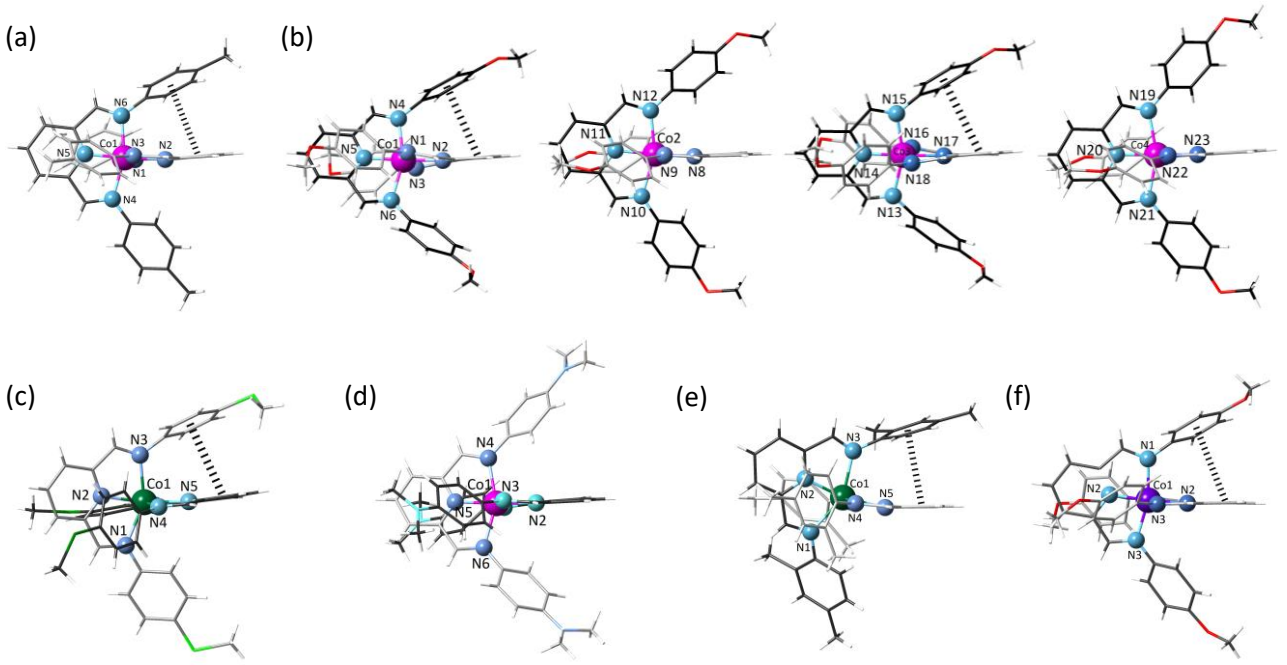

Figure III.1 Perspective views of the crystallographically independent mononuclear cobalt(II) units of **1**–**5** and **2'** (a–e and f) with the atom numbering scheme of the coordination sphere at the cobalt atom. The ligand backbones are drawn in grey and black colours for clarity whereas the pink, green and purple cobalt atoms correspond to the LS Co^{II}, HS Co^{II} and LS Co^{III}, respectively.

The differences in the rhombic distortion between **1**–**5** and **2'** are also reflected in the metal-ligand bond angles. The axial cobalt-nitrogen pyridine bond angles of the LS Co^{II} or even Co^{III} ions [N_{py}–Co–N_{py} = 176.1(1)–178.5(2)° for Co^{II} and [N_{py}–Co–N_{py} = 175.1(6)° for Co^{III}; Table III.2] are closer to the ideal value of 180° than those of the HS Co^{II} ions [N_{py}–Co–N_{py} = 162.38(9)–164.3(8)°; Table III.2]. Yet, as far as the angle in the equatorial plane is concerned, it systematically deviates from the ideal value of 90° in all cases [N_{im}–Co–N'_{im} = 83.20(9)–92.1(2) (**1**–**5**) and 85.6(4)° (**2'**) with N'_{im}–Co–N_{im} = 92.4(2)–101.08(8) (**1**–**5**) and 96.5(6)° (**2'**); Table III.2]. Besides, the two five-membered fused rings resulting from the tridentate coordination mode of the ligand impose a severe non-planar ruffling distortion, particularly on the HS Co^{II}, which is reflected by the larger mean out-of-plane N_{im} displacements (δ = 0.555–0.560 Å, 0.395–0.430 Å, and 0.295 Å for HS Co^{II}, LS Co^{II} and LS Co^{III} ions, respectively; Table III.2).

The PDI ligands in **1**–**5** and **2'** exhibit a helical conformation owing to the free rotation around the single phenyl carbon-imine nitrogen bond. Hence, the octahedral cobalt units of **1**–**5** and **2'** are chiral, being both enantiomers present in the crystal lattice.

The average torsional angles for the phenylimine ligand fragments are similar (φ = 38.1–47.5°; Table III.2) except for **5**, which are significantly greater (φ = 63.3°; Table III.2), more likely, due to the steric hindrance between the *ortho*-methyl substituent on the phenyl rings and the methylene hydrogen atom from the imine groups.

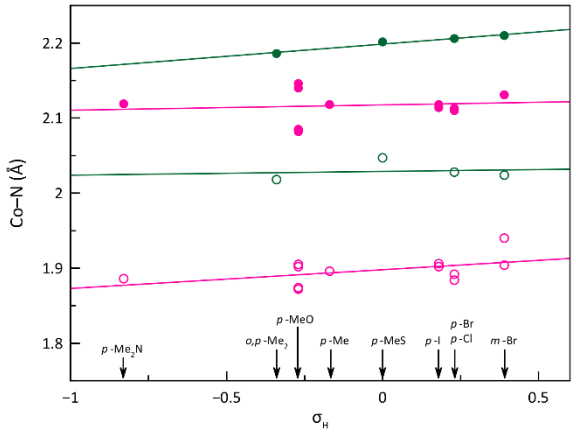

Figure III.2 Variation of the R_{eq} (●) and R_3 (○) values for each crystallographically independent cobalt atom with the Hammett constants (σ_H) of the ligand substituents (data taken from Table III.2). The structural data for the HS (green) and LS (pink) Co^{II} ions are drawn in green and pink colours. The identity of the ligand substituents is included for clarity. The solid lines are the linear fit curves (see text).

Within the central pyridinediimine fragment from each ligand, the average C_{py}–C_{im} [d_2 = 1.453(5)–1.474(4) (**1–5**) and 1.565(5) Å (**2'**); Table III.2] and C_{im}–N_{im} distances [d_3 = 1.276(3)–1.291(7) (**1–5**) and 1.309(5) Å (**2'**); Table III.2] are typical for single carbon-carbon and double carbon-nitrogen bonds, while the average C_{py}–N_{py} distance [d_1 = 1.337(5)–1.349(4) (**1–5**) and 1.342(5) Å (**2'**); Table III.2] is intermediate between a single and a double carbon-nitrogen bond. Yet, the alternation bond parameter, defined as $\Delta_d = d_2 - (d_1 + d_3)/2$, reflects a slightly greater π-electron delocalisation within the pyridinediimine fragment for the LS Co^{II} and Co^{III} ions [Δ_d = 0.135–0.150 (**1**, **2**, and **4**) and 0.120(2) Å (**2'**); Table III.2] than for the HS Co^{II} ions [Δ_d = 0.156–0.167 (**3** and **5**); Table III.2], as observed in Figure III.3. This is likely explained by the greater electron population of t_{2g} shell for the LS ($t_{2g}^6e_g^1$) than the HS Co^{II} ions ($t_{2g}^5e_g^2$), which would eventually lead to enhanced π-backbonding interactions with the empty ligand orbitals.[17]

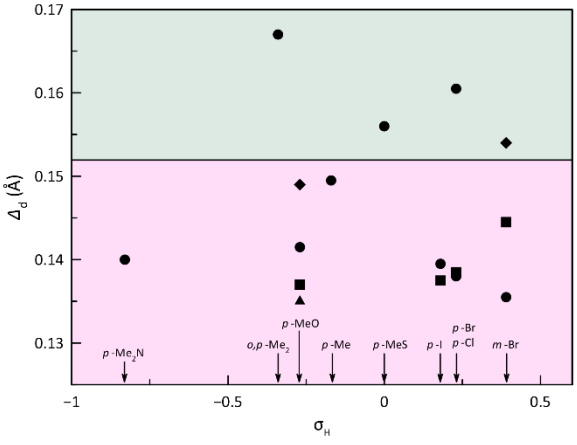

Figure III.3 Variation of the Δd values for each crystallographically independent cobalt atom with the Hammett constants (σ_H) of the ligand substituents (data taken from Table III.2). The identity of the ligand substituents is included.

Crystal structures. In the crystal lattices of **1–5** exist a segregated array of cationic mononuclear cobalt(II) complexes and an anionic perchlorate layer linked by electrostatic forces and Van der Waals contacts (Figure III.S3–S7). Additional water molecules of crystallisation occupy the interlayer space in **1**, establishing moderate to weak intermolecular hydrogen-bonding interactions with the perchlorate anions [O···H–O = 2.982(5)–3.273(4)°] and Van der Waals contacts with the mononuclear cobalt(II) complex cations. In contrast, **2'** exhibits mixed columnar arrays of cationic mononuclear cobalt(III) complexes and highly disordered pentabromide anions further separated by weakly interacting tribromide anions (Figure III.S8).

Mononuclear complexes in **1–5** interact with each other through moderate to weak intermolecular "face-to-face" (**1–5**) or "edge-to-face" (**3**) π-π stacking interactions between their phenyl rings (Figures III.4), leading to different supramolecular π-bonded motifs of variable dimensionality (*n*D, *n* = 0–2) and topology, including either discrete (**5**) or chain arrays (**4**) of dimers (Figures III.4e and III.4d, respectively), as well as square (**2**) or rhomb (**1** and **3**) grids (Figures III.4a–c). Within each cationic layer of **4** and **5**, the intradimer intermetallic distance through the "face-to-face" π-stacking [Co···Co = 10.967 (**4**) and 10.762 (**5**)] are comparable to those of the shortest interdimer ones [Co···Co = 10.401 (**4**) and 11.586 (**5**)] (Figures III.4d and III.4e). Otherwise, the intralayer intermetallic distances through "face-to-face" [Co···Co = 8.664–13.110 (**1**), 9.359–9.759 (**2**), and 10.211 Å (**3**)] and "edge-to-face" π-stacking [Co···Co = 9.635 Å (**3**)] are similar, so that the mononuclear units are rather well-isolated from each other (Figures III.4a–c).

III.4 – Spectrochemical Properties

The spectroscopic properties of the PDI ligands and their cobalt(II) complexes have been investigated by proton nuclear magnetic resonance (^{1}H NMR), Fourier-transform infrared (FT-IR), and electronic absorption (UV-Vis) to analyse the influence of the substituents and their substitution pattern.

^{1}H NMR spectra. The ^{1}H NMR spectra of the PDI ligands show a similar pattern. The central diiminomethylpyridine exhibits the characteristic doublet and triplet signals of the *meta*- and *para*-pyridine hydrogen atoms [δ(*p*-H_{py}) = 8.21–8.32 ppm and δ(*m*-H_{py}) = 7.86–7.95 ppm], together with a singlet signal corresponding to the methylene-imine hydrogen atom [$\delta(H_{im})$ = 8.57–8.74 ppm]. The *para*-substituted phenyl groups from 4-MePDI, 4-MeOPDI, 4-MeSPDI, 4-Me_2NPDI, 4-IPDI, 4-BrPDI, and 4-ClPDI ligands show two doublet signals attributed to the *ortho*- and *meta*- hydrogen atoms [δ(*o*-H_{Ph}) = 7.06–7.40 ppm and δ(*m*-H_{Ph}) = 6.77–7.75 ppm], while a multiplet signal corresponding to the *ortho*-, *meta*-, and *para*-phenyl hydrogen atoms appears for the 2,4-Me_2PDI [δ(*o*,*m*-H_{Ph}) = 7.04 ppm], and 3-BrPDI ligands [δ(*o*,*m*,*p*-H_{Ph}) = 7.30 ppm]. In addition, a singlet signal corresponding to the hydrogen atoms from the para-dimethylamino, *para*-methoxy, and *para*- or *ortho*-methyl substituents is observed for 4-MePDI [δ(*p*-H_{Me}) = 2.39 ppm], 4-MeOPDI [δ(*p*-H_{OMe}) = 3.85 ppm], 4-MeSPDI [δ(*p*-H_{SMe}) = 3.85 ppm], 4-Me_2NPDI [δ(*p*-H_{NMe_2}) = 3.01 ppm] and 2,4-Me_2PDI [δ(*p*-H_{Me}) = 2.35 ppm and δ(*o*-H_{Me}) = 2.40 ppm].

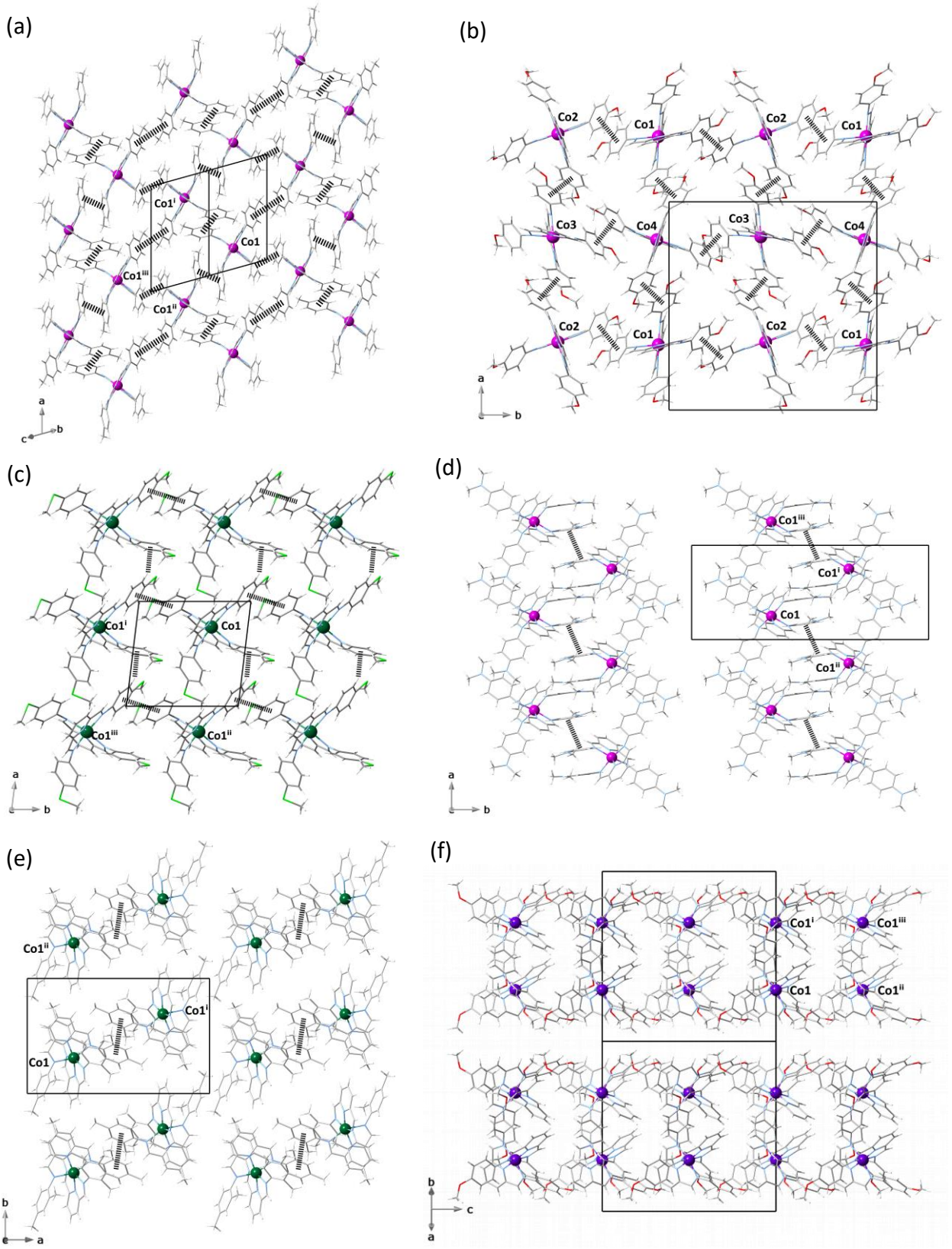

Figure III.4 Projection views of the crystal packing of **1**–**5** (a–e) and **2'** (f) showing a layer of cationic mononuclear cobalt units in the array of π-bonded rhomb grids in **1** and **3** (a and c), square grids in **2** (b), dimers in **4** and **5** (d and e) and double columns in **2'** (f) through π-π stacking (dashed lines) among the mononuclear units [symmetry operation: (i) = 1–*x*, 1–*y*, 1–*z*; (ii) = 1+*x*, *y*, *z*; (iii) = 1–*x*, *y*, *z* (**1** and **3**); (i) = –*x*, –*y*, –*z*; (ii) = 1/2–*x*, 1/2+*y*, 1/2–*z*; (iii) = 1/2+*x*, 1/2–*y*, 1/2+*z* (**2**); (i) = –*x*, –*y*, –*z*; (ii) = 1/2–*x*, 1/2+*y*, 1/2–*z*; (iii) = 1/2+*x*, 1/2–*y*, 1/2+*z* (**4** and **5**); (i) = –*x*, –1–*y*, *z*; (ii) = –1/2-*x*, –1/2+*y*, 1/2–*z*; (iii) = 1/2+*x*, –1/2–*x*, 1/2–*z* (**2'**)].

These chemical shifts display a linear correlation with the substituent σ_H (Figure III.5). Hence, within the pyridinediimine, whereas δ(*p*-H_{py}) remains almost constant, δ(H_{im}) and δ(*m*-H_{py}) slightly decrease and increase with the electron-withdrawing character of the ligand substituents.

In contrast, the δ(*o*-H_{Ph}) and δ(*p*-H_{Ph}) largely decrease with the electron-withdrawing character of the ligand substituents, whereas the δ(*m*-H_{Ph}) increases instead. Overall, these upfield (lower δ) or downfield (higher δ) shifts depending on the substitution pattern reflect the less efficient shielding or deshielding effect of the substituent with the increasing distance from the hydrogen atom.

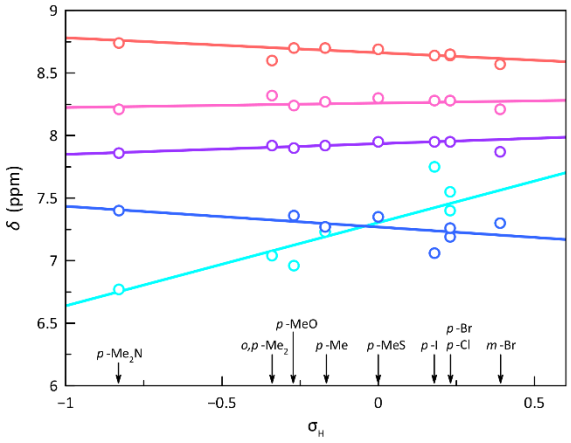

Figure III.5 Variation of the chemical shift (δ) values with the Hammett constants (σ_H) of the ligand substituents for the imine (red), *para*- (pink) or *meta*- (purple) pyridine, and *ortho*/*para*- (blue), *meta*- (cyan) phenyl protons from the PDI ligands. The identity of the ligand substituents is included for clarity. The solid lines are the linear fit curves (see text).

FT-IR spectra. The FT-IR spectra of the ligands and cobalt(II) complexes display a moderate band in the range of 1618–1626 and 1572–1608 cm^{-1}, respectively, assigned to the C=N stretching vibration. This vibrational frequency linearly decreases with the electron-withdrawing nature of the ligand substituent for the complexes (Figure III.6); in contrast, it remains almost constant through the ligand series. This fact may be likely explained by the increase of the aforementioned π-back-bonding metal-ligand interactions with increasing the ligand's electron-withdrawing nature leading to the weakness of the C=N bond.

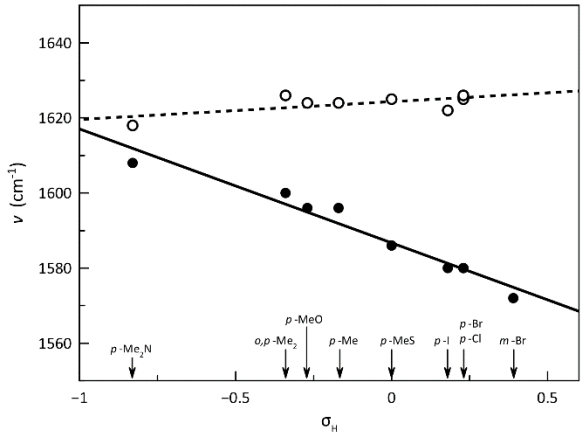

Figure III.6 Variation of the energy values of the ν(C=N) imine stretching vibration for the PDI ligands (○) and the corresponding cobalt(II) complexes (●) with the Hammett constants (σ_H) of the ligand substituents. The identity of the ligand substituents is included for clarity. The dashed and solid lines are the linear fit curves for the ligands and complexes, respectively (see text).

UV-Vis spectra. The electronic absorption spectra in solution of the 4-Me_2NPDI and 4-ClPDI ligands and those of their cobalt(II) complexes as representative examples of these two related series, are compared in Figure III.8 and Figure II.S2 (see Supporting Information of Chapter II). The cobalt(II)-PDI complexes exhibit two very intense sharp absorption bands in the high-energy UV region (λ_1 = 195–199 nm and λ_2 = 218–258 nm), together with a broad, less intense low-energy UV band that extends into the visible region (λ_3 = 335–489 nm) (insets of Figure III.7 and Figure II.S2).

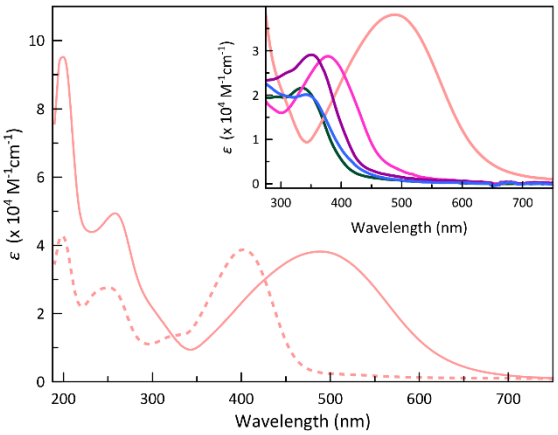

Figure III.7 Electronic absorption spectra of the 4-Me_2NPDI ligand (dashed line) compared to the corresponding cobalt(II) complex in acetonitrile solution at room temperature (solid line). The inset shows the lower energy UV-Vis band for **1** (purple), **2** (pink), **3** (green), **4** (pale pink) and **5** (blue).

The higher (λ_1 = 195–200 nm and λ_2 = 217–260 nm) and the lowest energy (λ_3 = 335–489 nm) UV bands found for the ligands are formally attributed to intraligand π-π* and n-π* transitions, as it was done for the similar *para*-substituted phenyl- and azabenzene derivatives.[20–23] Although the transition energies change along the series of ligands (Figure III.8), the shift is only significant for the lowest energy one (λ_3), which moves to lower energies by increasing the electron-withdrawing character of the substituent, being confirmed by time-dependent DFT (TDDFT) calculations on the optimised geometries of the *p*-Me and *p*-NMe_2 derivatives (Table III.3).

When the cobalt(II) complex is formed, again, this λ_3 transition, particularly in the *p*-NMe_2 derivative (**4**), undergoes a redshift (Figure III.8). The similarity of these spectra with those of their ligands is so apparent that it seems evident that the recorded transitions occur exclusively in the PDI ligands (Figure III.8), the shifts being associated with the participation of the metal ion even through contributions from ligand-to-metal (LMCT) or metal-to-ligand (MLCT) charge transfers. However, in these electronic transitions showing a partial intraligand charge transfer between the phenyl and pyridinediimine groups occurs (Figure III.S9), the conformation adopted by the ligand into the complex may play a crucial role. Thus, a TDDFT calculation restricted on the conformation of the 4-Me_2NPDI ligand found in the optimised geometry of its cobalt complex (**4**) shows the observed energy displacement (Table III.3), so that the contribution from the metal ion is not exclusively electronic. Still, it allows the approach of two PDI ligands intensifying the steric effects already observed in the isolated ligand, modifying the electronic transitions.

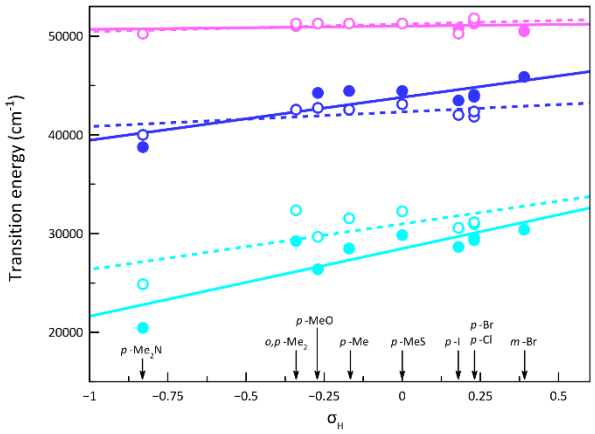

Figure III.8 Variation of the transition energy of the electronic transitions [λ_n with n = 1 (pink), 2 (blue), and 3 (cyan)] for the PDI ligands (open symbols) and the corresponding cobalt(II) complexes (closed symbols) with the Hammett constants (σ_H) of the ligand substituents. The identity of the ligand substituents is included for clarity. The dotted and solid lines are the linear fit curves for the ligands and complexes, respectively (see text).

Table III.3 Calculated wavelengths (in nm) for the main electronic transitions on the optimised geometries of the 4-MePDI and 4-Me_2NPDI ligands and that of the latter in the conformation adopted in the optimised geometry of its cobalt(II) complex

Electr. transition	4-MePDI	4-NMe_2PDI	4-NMe_2PDI in **4**
λ_3, n-π*	385	479	529
$\lambda_{2,2'}$, n-π*	339	419/411	468
λ_1, π-π *	288	287	350
π-π *	245	263	299
π-π *	237	244	276

III.5 – Electrochemical Properties

The electrochemical properties of the cobalt(II)-PDI complexes have been investigated by cyclic voltammetry (CV) in order to analyse the influence of the nature of the electron-donating phenyl substituents, as well as their *ortho* or *para* substitution pattern, on the metal- and ligand-centred, multiredox behaviour. A summary of the electrochemical data for **1**–**5** is listed in Table III.4.

Table III.4 Selected electrochemical data for **1**–**5**[a]

	E_1[b] (V)	E_2[b] (V)	E_3[b] (V)	E_4[b] (V)	E_5[b] (V)	$K_{c,23}$[c] (× 10^{-14})	$K_{c,45}$[c] (× 10^{-3})
1	0.38 (105)	-0.67 (93)	-1.55 (93)	-2.06 (i)	-	8.2	-
2	0.33 (83)	-0.71 (71)	-1.59 (73)	2.0 (i)	2.19 (i)	8.2	0.8
3	0.40 (137)	-0.64 (95)	-1.51 (93)	-1.95 (i)	-	5.6	-
4	0.14 (88)	-0.82 (77)	-1.67 (83)	-2.10 (i)	-	2.6	-
5	0.52 (260)	-0.65 (76)	-1.52 (71)	-2.04 (i)	-	5.6	-

[a]In acetonitrile (25 °C, 0.1 M nBu$_4$NPF$_6$) with a scan rate of 200 mV s^{-1}. [b]All formal potential (E/V) were taken as the half-wave potentials *vs* Fc^+/Fc, except for the irreversible (i) reduction waves for which the cathodic peak potentials are given instead. The peak-to-peak separation (ΔE) between the anodic and cathodic peak potentials are given in parentheses. [c]The comproportionation constant (K_c) were calculated from the E values between the two pairs of one-electron reduction waves ($\Delta E_{23} = E_2 - E_3$ and $\Delta E_{45} = E_4 - E_5$) through the expression $\log K_c = \Delta E/0.059$.

The cyclic voltammograms of **1**–**5** in acetonitrile at room temperature show a pattern of qualitatively similar redox behaviour (Figure III.9 and Figure III.S10). They exhibit one reversible oxidation wave (E_1) and two reversible reduction waves (E_2 and E_3; Table III.4) together with one or two completely irreversible reduction waves at very high negative formal potentials (E_4 and E_5; Table III.4). In addition, one completely irreversible oxidation wave appears at very high positive formal potentials for **4** (data not shown).

The anodic to cathodic peak separations for the three reversible redox waves ($\Delta E_{p,1}$, $\Delta E_{p,2}$ and $\Delta E_{p,3}$; Table III.4) are comparable to that of the Fc^+/Fc redox couple under the same conditions (ΔE_p = 80 mV), except for that metal-based oxidation (E_1) of **5**, which reveals a two stepwise oxidation process. This conclusion is further supported by the scan rate-dependence studies in the range 20–250 mV s^{-1}, in which no variation is observed for the cathodic and anodic peak potentials, being then stated to be reversible in the voltammetric time-scale. (Figure III.S10).

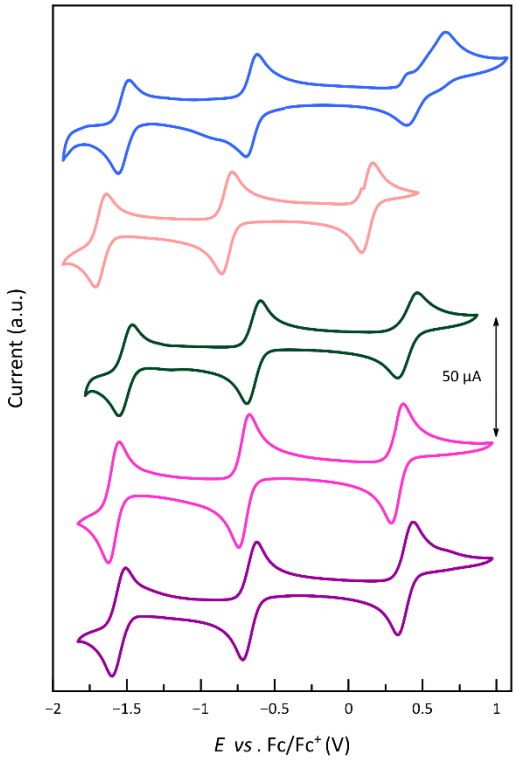

Figure III.9 Cyclic voltammograms of **1**–**5** (from purple in bottom to blue in top) in acetonitrile (0.1 M nBu$_4$NPF$_6$) at 25 °C and 200 mV s^{-1}.

The assignment of the observed redox processes for **1**–**5** is illustrated in Scheme III.3, as earlier reported for the related series of cobalt(II)-PDI complexes with electron acceptor-substituted phenyl.[17] The reversible oxidation wave corresponds to the one-electron metal oxidation to afford the cobalt(III) species (Scheme III.3a). In contrast, the first pair of well-separated reversible reduction waves conform to the ligand's stepwise one-electron reduction (Scheme III.1) to give the single and double imide-type π-radical anion cobalt(II) species (Scheme III.3b). That being so, the second pair of irreversible reduction waves is likely attributed to the further stepwise one-electron

reduction of the ligands (Scheme III.1) to give the single and double imide-type (non-radical) dianion cobalt(II) species (Scheme III.3c).

The σ-donor capacity of the electron-donating ligand substituents at the phenyl groups, on the one hand, and the π-acceptor ability of the central pyridinediimine ligand fragment, on the other hand, are the leading causes of the dual metal- and ligand-centred multiredox behaviour of this unique series of mononuclear cobalt(II)-PDI complexes. Moreover, they are eventually responsible for the observed thermodynamic and kinetic stability of the corresponding cobalt(III) and the single or double imide-type π-radical anion cobalt(II) species. Hence, the significant separation between the first pair of reversible reduction waves along this series (ΔE_{23}; Table III.4) indicates high thermodynamic stability of the mixed-valent, one-electron reduced cobalt(II) π-radical species resulting from a substantial electronic delocalisation, as evidenced by the estimated values of the comproportionation constant [$K_{c,23}$; Table III.4].

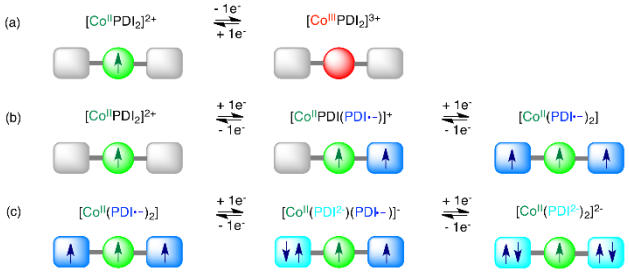

Scheme III.3 Proposed redox model for the multi-electron transfer series in mononuclear octahedral cobalt(II)-PDI complexes as prototypes of molecular spin capacitors (see Scheme III.1 for ligand redox isomer abbreviations).

There are linear correlations between the formal redox potential values for each of the three reversible redox potentials of these series of cobalt(II)-PDI complexes and the electron-withdrawing nature of the ligand substituents expressed by the σ_H (Figure III.10). E_{1-3} moderately decrease with reducing σ_H, making easier thus the metal oxidation and disfavouring the ligand reduction. Various reasons can cause the deviation of **5** from this correlation. Among them, the strong distortion undergone by the PDI ligand due to steric hindrances between formimidoyl hydrogen atoms and the *o*-methyl groups leading to a loss of aromaticity is the most probable cause. It should note that **5** systematically deviates from all correlations established in this chapter between a physical property and the Hammet parameter. This situation is more noticeable in the correlation for the ^{1}H NMR chemical shift, carried out only on the ligands, supporting the hypothesis that the ligand distortion is the cause. It must be emphasised that the Hammet parameter is applied without considering other factors such as geometric changes, leading in **5** to a non-real estimation of the electron-withdrawing from the substituents. Thus, this electronic feature can be in **5** less than in **1**, despite the former containing an additional donor group, both chemical groups being not very efficient in the geometry shown.

Calculations of NMR chemical shifts on the ligands confirm these conclusions (Table III.S1). Thus, ligands 4-MePDI and 4-Me$_2$NPDI follow the observed correlations with the substituent's Hammet parameter, but 2,4-Me$_2$PDI deviates, showing a δ (imine) less than expected one for the 4-MePDI ligand. When a hydrogen atom replaces the *ortho*-methyl group in 2,4-Me$_2$PDI, which is equivalent to building the 4-MePDI ligand conserving the most stable geometry of 2,4-Me$_2$PDI, no effect is observed on δ (imine) and less on the pyridine hydrogen atoms. This last result is apparent evidence that the distortions originated from steric hindrances dim electronic factors in the 2,4-Me$_2$PDI ligand.

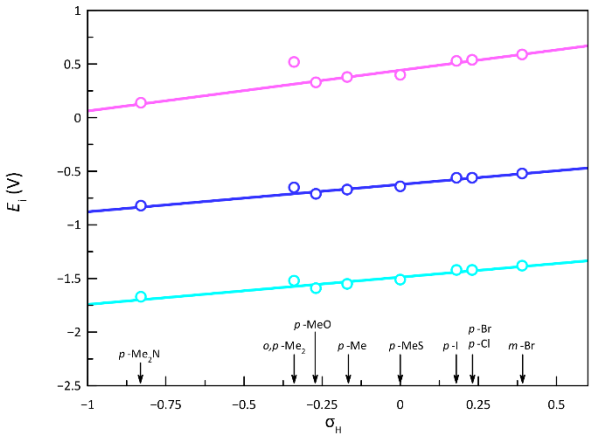

Figure III.10 Variation of the formal redox potential values [E_i, i = 1 (pink), 2 (blue) and 3 (cyan)] for the cobalt(II)-PDI complexes with the Hammett constants (σ_H) of the ligand substituents. The identity of the ligand substituents is included for clarity. The solid lines are the linear fit curves (see text).

III.6 – Magnetic and EPR Properties

Static magnetic behaviour. The dc magnetic properties of **1**–**5** in the form of the $\chi_M T$ *vs* T plots (χ_M being the molar magnetic susceptibility per mononuclear unit and T the absolute temperature) and M *vs* H plots (M being the molar magnetisation per mononuclear unit and H the applied magnetic field) are shown in Figure III.11.

The $\chi_M T$ versus T plots for **1**–**5** (Figure III.11a) reveal the occurrence of distinct SCO behaviours as well as the absence of it, similar to the related series with electron-withdrawing substituents presented in the previous chapter.

The $\chi_M T$ at room temperature of 2.87 and 2.90 cm^3 mol^{-1} K for **3** and **5** are within the range expected for an HS Co^{II} ion with an unquenched orbital momentum contribution [$\chi_M T = (N\beta^2 g^2/3k_B)S(S+1)$ = 2.70 cm^3 mol^{-1} K with S = 3/2 and g = 2.4], while those of **1**, **2**, and **4** are rather lower [2.05 (**1**), 1.42 (**2**), and 0.967 cm^3 mol^{-1} K (**4**)]. Upon cooling, $\chi_M T$ for **3** decreases smoothly down to 1.85 cm^3 mol^{-1} K at 2.0 K, revealing the occurrence of a significant zero-field splitting (zfs) arisen from the spin-orbit coupling (SOC) of the HS Co^{II} ion. In contrast, a partial spin transition occurs for **5**, as revealed by the decrease of $\chi_M T$ around 100 K for **5** ($T_{1/2}$ = 75 K). The $\chi_M T$ value of 1.48 cm^3 mol^{-1} K at 2.0 K agrees with an approximate 2:1 ratio for the HS and LS configurations. Instead, a complete and gradual spin transition is observed for **1**, **2**, and **4**. Upon cooling, $\chi_M T$ decreases smoothly to reach of plateau around 100 (**1** and **2**) and 150 K (**4**). The $\chi_M T$ values of 0.49, 0.45 and 0.40 cm^3 mol^{-1} K for **1**, **2** and **4**, respectively, at 2.0 K are expected for a LS Co^{II} ion [$\chi_M T = (N\beta^2 g^2/3k_B)S(S+1)$= 0.45 cm^{3}mol^{-1}K with S = 1/2 and g = 2.2]. However, the slightly higher value for **1** somehow may indicate the presence of a residual fraction of HS Co^{II} ions.

This scenario is further supported by the M versus H plots at 2.0 K for **1**–**5** (Figure III.11b). Hence, the M value at H = 50 kOe

for **1**, **2** and **4** are close (**1** and **2**) or below (**4**) to the calculated value of the saturation magnetisation for a LS Co^{II} ion ($M_s = gSN\beta$ = 1.10 $N\beta$ with S = 1/2 and g = 2.2). The reduced magnetisation curves for **2** and **4** in the temperature range of 2.0–10.0 K perfectly superimpose (Figures III.S12b and d), as expected for an S = 1/2 state, while a slight deviation is observed for **1**, a fact consistent with the presence of a small fraction of the HS phase. On the other hand, the M value of 2.06 $N\beta$ at 50 kOe for **3** is close to the calculated saturation magnetisation for an effective doublet spin state coming from the ground Kramers doublet that is well-separated from the excited Kramers doublet due to a large zfs ($M_s = gSN\beta$ = 2.10 $N\beta$ with $S = S_{eff}$ = 1/2 and g = 4.2). The maximum M value of 1.87 $N\beta$ for **5** is close to the calculated saturation magnetisation for a 2:1 ratio between the HS and LS forms [Ms = (2 × 2.10 + 1.10)/3 = 1.77 $N\beta$]. Moreover, the reduced magnetisation curves of **3** and **5** below 10.0 K do not superimpose (Figures III.S11c and e), supporting the occurrence of a large zfs on the quartet ground state.

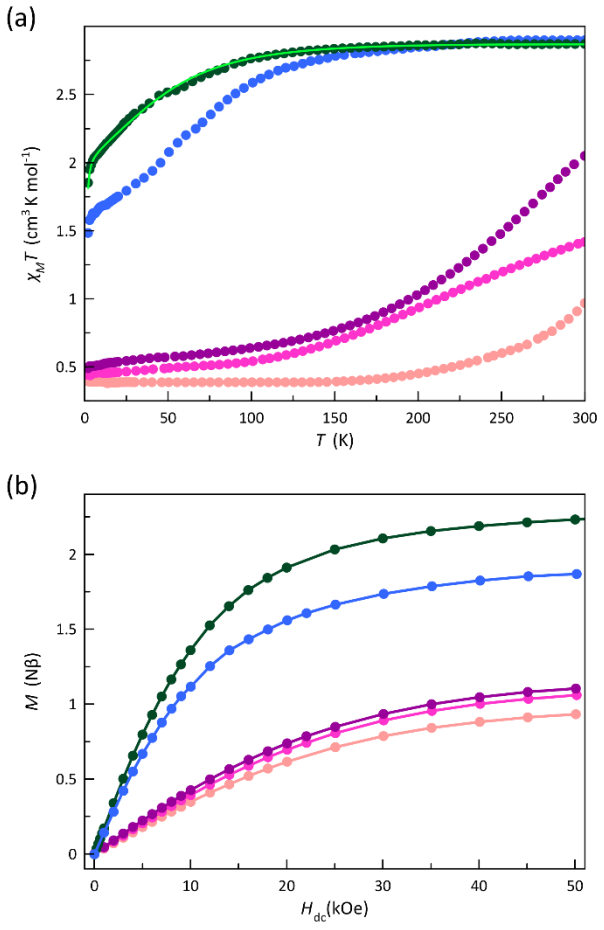

Figure III.11 (a) Temperature dependence of $\chi_M T$ and (b) field dependence of M at 2.0 K for **1** (purple), **2** (pink), **3** (dark green), **4** (pale pink) and **5** (blue). The light green line is the best-fit curve for **3** (see text).

The experimental magnetic data of **3** could be well simulated by the joint analysis of the magnetisation and magnetic susceptibility data performed by employing full-matrix diagonalization, as implemented in the PHI program.[24] The spin Hamiltonian used is defined by Eqn (1)

$$\boldsymbol{H} = D[\boldsymbol{S}_z^2 - S(S+1)/3] + E(\boldsymbol{S}_x^2 + \boldsymbol{S}_y^2) + \beta H(g_x\boldsymbol{S}_x + g_y\boldsymbol{S}_y + g_z\boldsymbol{S}_z) \quad (1)$$

where D and E are the axial and rhombic magnetic anisotropy parameters, respectively. Since the experimental measurements were carried out on finely crushed crystal samples, g_x and g_y Landé components of the g-factor are indistinguishable. Therefore, only perpendicular and parallel components were preserved ($g_x = g_y = g_\perp$ and $g_z = g_{||}$). This approach usually leads to reasonable estimations of the g factor, the sign of D and even the E/D quotient, the latter being the one that carries the most significant uncertainty in its determination. This fitting (Figures III.11a and III.S13) revealed a large uniaxial zfs (D < 0) acting on the quartet ground state of the complex and a high magnetic rhombicity. The best-fit values of these parameters are $g_\perp$ = 2.32, $g_{||}$ = 2.71, D = –59.4 cm^{-1} and E/D = 0.262.

EPR spectra. The Q-band EPR spectra of **1**–**5** at 4.0 K are depicted in Figure III.12 (see Experimental Section). Except for the pure HS compound **3**, all spectra are constituted by a strong signal at the high field region around g = 2.0 (*ca*. 12000 G), typical for LS Co(II) complexes, whose pattern is split as a consequence of the high axiality and rhombicity present in these compounds. Additionally, **3** and **5** exhibit signals in the low-field region around g = 8.0 (*ca*. 3000 G), a signature of the presence of HS Co^{II} complexes in an octahedral environment.[25] The presence of low-field signals agrees with the magnetometry for the incomplete spin transition or its absence.

EPR spectra of **1**–**5** were simulated jointly for the LS and HS fractions. LS contributions were satisfactorily simulated considering a highly axial ($g_x = g_y \neq g_z$) for **2** and **5** and a rhombic octahedron ($g_x \neq g_y \neq g_z$) for the rest. Somehow, there is an inversion of the g values for **5**, in which g_z value is the closest one to the electron g-factor (2.0). This fact suggests that the magnetic orbital is allocated in the d_{z^2} instead of the $d_{x^2-y^2}$orbital, as in the other members of the series. Table II.5 summarises the g values used in these simulations.

Among these five compounds, **3** and **5** exhibit an HS fraction at 4.0 K evidenced by the signature EPR signals appearing at very low fields in both Q- and X- band spectra. In **5**, this signal is split most likely due to an effect of the field-modulation amplitude; thus, the real g value is provided by its midpoint. These signals at g_z = 7.5 (**3**) and 8.0 (**5**) are evidence of a uniaxial zfs (D < 0), which is consistent with the results from the dc magnetic data of **3**. In this case, the two remaining g_{eff} components are expected to adopt very low values, enough so they cannot be observed by Q-band EPR spectroscopy, but they do in X-band. Thus, the X-band spectrum of **3** and **5** shows two signals at high fields with g_x = 1.65 (**3**)/0.85 (**5**) and g_y = 2.30 (**3**)/1.01 (**5**). Moreover, when considering a zfs on a quartet spin state, we could only achieve good simulations for the X-band spectra with very large and moderate rhombicities. The parameters used in these simulations were: g_x = 2.23(**3**)/2.15(**5**), g_y = 2.67(**3**)/2.18(**5**), g_z = 2.90 (**3**)/2.65(**5**), D < 0, and E/D = 0.33(**3**)/0.15(**5**), which are in agreement with those found from *ab initio* calculations for **5** but the g values slightly differs for **3** {g_{eff} = [1.35, 1.81, 8.09] (**3**)/[0.91, 1.06, 8.55] (**5**) or $g_{3/2}$ = [2.01, 2.27, 2.89] (**3**)/[2.01, 2.17, 2.96] (**5**), D = –69.9 (**3**)/–79.8 (**5**) cm^{-1}, and E/D = 0.252 (**3**)/0.152 (**5**)}.

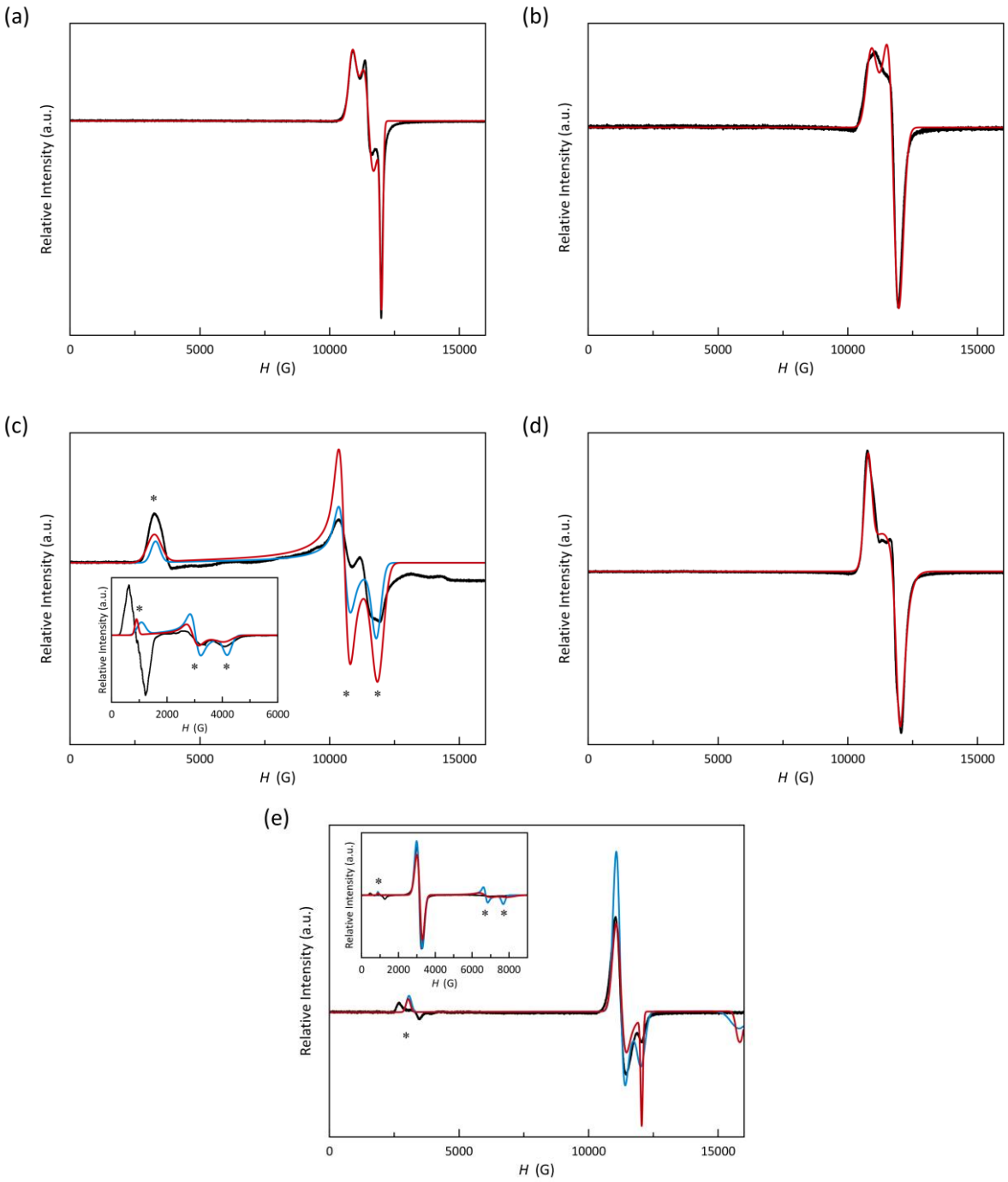

Figure III.12 Experimental Q-band EPR spectra of **1**–**4** (a–d) in the solid state at 4.0 K (black solid lines). X-band spectrum of **3** appears as inset. Red and blue solid lines are the simulated curves for S_{eff} = 1/2 and anisotropic S = 3/2 approaches (see text).

Table III.5 Best parameters for simulation of the LS contribution in the Q-band EPR spectra of **1**–**5** from the experimental data in solid state at 4.0 K

	g_x	g_y	g_z	g^a
1	2.029	2.116	2.237	2.129
2	2.053	2.053	2.233	2.115
3	-	-	-	-
4	2.034	2.066	2.249	2.118
5	2.182	2.182	2.010	2.126

[a]Overall g value estimated by the equation $g^2 = (g_x^2 + g_y^2 + g_z^2)/3$.

Dynamic magnetic behaviour. The ac magnetic properties of **1**–**5** in the presence of an applied dc magnetic field (H_{dc}) of 1.0 and 2.5 kOe are shown in Figures III.S14–S18 in the form of the χ_M' and χ_M'' *vs* T plots (χ_M' and χ_M'' being the in-phase and out-of-phase ac molar magnetic susceptibility, respectively). No frequency dependence of χ_M' and χ_M'' signals are observed for **1**–**5** (data not shown) in the absence of H_{dc}, more likely because of a fast quantum tunnelling of magnetisation (QTM)[26] or an intraKramer (IK) relaxation on the ground Kramers doublet of a LS or a non-uniaxial HS (D > 0) cobalt(II) complex.

Under a small dc magnetic field (H_{dc} = 1.0 or 2.5 kOe), both frequency- and field-dependent χ_M' and χ_M'' signals are observed for **1**–**5**, the last ones being only incipient at 1.0 kOe for **1**, **2** and **4**, but shifting towards higher temperatures at 2.5 kOe, whereas those curves for **3** and **5** remain almost unaltered. These features resemble the conclusions from the previous chapter, in which the LS and HS Co(II) complexes account for a different field dependence of the slow magnetic relaxation behaviour. Besides the low-temperature χ_M'' incipient signals, a distinct shoulder develops for **1** at higher temperatures under both dc magnetic fields, suggesting a double magnetic relaxation process.

The joint analysis of the χ_M' and χ_M'' *vs* ν plots (Figures III.S19 and S20) through the generalised Debye model provided magnetic relaxation times (τ) for **1**–**5**.[27] The occurrence of two relaxation processes in **1** required a second contribution for its analysis. This second low-temperature (LT) process loses importance with increasing temperature until 4.0 K. Above this temperature, the LT contribution was cut off from the analysis.

The Arrhenius plots for **1**–**5** are built from these relaxation times, as displayed in Figure III.14. For the LS form, τ is about three times greater under the highest than the lowest field, as seen in Chapter II. Instead, those HS Co(II) complexes (**3** and **5**) present slower relaxation rates, being barely affected by H_{dc}, as seen in Chapter II.

The lnτ *vs* ln$T$ plots (Figure III.S24) clearly show linear dependencies in some temperature regions. The temperature-independent IK process prevails with variable significance and relaxation rate at low temperatures except for **4** and the other LS **1** and **2** at the lowest H_{dc}. The found n values show that Raman mechanisms assisted by optical phonons govern the relaxation of the magnetisation for LS **2** and **4**, whereas acoustic ones with n *ca.* 6 are responsible for the magnetic relaxation in HS **3**. An intermediate situation is observed for the mixed LS/HS **5** and **1** at the highest H_{dc}, for which n values of 4–5 were found, being between those for optical and acoustic phonons. The second LT relaxation in **1** was simulated by considering a Raman mechanism involving optical phonons (n ≈ 2), although the narrow temperature range in which this process is relevant compromises this result. The found values for the parameters in the employed model to analyse the lnτ vs ln$T$ plots of **1**–**5** are summarised in Table III.6.

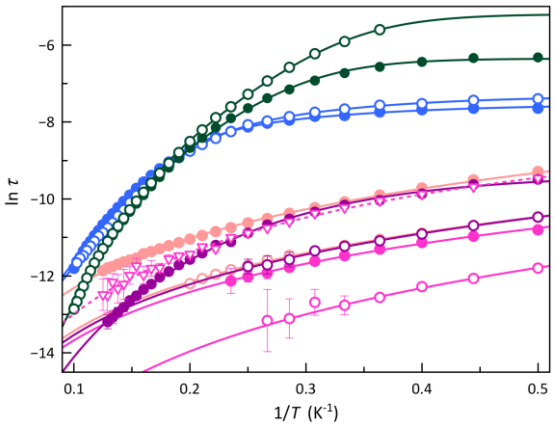

Figure III.13 Arrhenius plots for **1** (purple), **2** (pink), **3** (green), **4** (pale pink) and **5** (blue) under applied *dc* magnetic fields of 1.0 (O), 2.5 (●). The Arrhenius plot of **2** in frozen matrix acetonitrile solution at 2.5 kOe (▽) is also shown for comparison. The solid and dashed lines are the best-fit curves (see text).

Some conclusions about the magnetic relaxation dynamics of the spin crossover cobalt(II)-PDI molecular nanomagnets from the previous chapter are reinforced here: (i) this new class of mononuclear SMMs are governed by two distinct regimes, regarding slower-relaxing (SR) and fast-relaxing (FR) centres depending on the HS and LS nature of Co(II) complexes; (ii) a strong dual field-dependence of the SMM behaviour is observed for LS Co^{II} ions, in which the spin reversal is slowed by increasing the applied magnetic field; (iii) distinct optical and acoustic two-phonon Raman mechanistic pathways are involved in the slow magnetic relaxation of LS and HS Co(II) complexes, which may or may not count with the additional temperature-independent Intra-Kramer (IK) mechanism.

Table III.6 Selected parameters from the least-squares fit of the ac magnetic data of **1**–**5**[a]

	H_{dc} (kOe)	τ_{IK}[b] (x 10^{-3} s)	C[c] ($s^{-1}K^{-n}$)	n[c]
1	1.0	-	9120 ± 500	1.94 ± 0.05
	2.5	0.091 ± 0.004	225 ± 20	3.77 ± 1.0
2	1.0	-	25000 ± 1000	2.37 ± 0.5
	2.5	0.061 ± 0.013	6880 ± 1000	2.23 ± 0.11
	2.5[d]	0.35 ± 0.05	2000 ± 400	2.35 ± 0.11
3	1.0	7.0 ± 0.4	0.30 ± 0.01	6.01 ± 0.02
	2.5	1.90 ± 0.03	0.47 ± 0.02	5.81 ± 0.02
4	1.0	-	10000 ± 200	1.818 ± 0.015
	2.5	-	3000 ± 50	1.875 ± 0.011
5	1.0	0.61 ± 0.02	1.9 ± 0.2	4.88 ± 0.05
	2.5	0.481 ± 0.004	1.33 ± 0.06	4.97 ± 0.02

[a]The fits correspond to double or triple relaxation models. [b]Coefficient factor for the temperature-independent *IK* process ($\tau^{-1} = IK$). [c]Coefficient and polynomial factor for the Raman process ($\tau^{-1} = CT^n$). [d]Measurement performed in acetonitrile solution.

III.7 – Proof-of-Concept of a Spin Electro-switch

This section describes a proof-of-concept demonstration of the electro-switching of both SCO and SMM that occurs in one exemplar of the electroactive series of cobalt(II) molecular nanomagnets presented in this chapter, as illustrated in Scheme III.4.

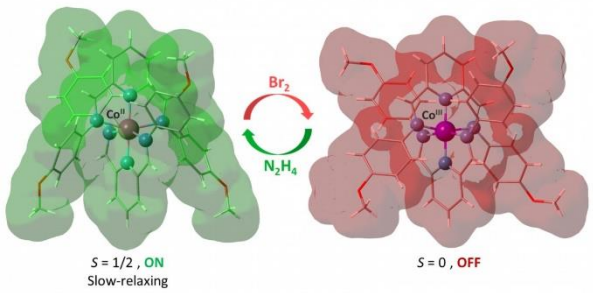

Scheme III.4 Proposed proof-of-concept for a spin switch based on a unique example of electro-switchable spin crossover cobalt(II) molecular nanomagnet which proceeds through the one-electron oxidation of the slow-relaxing paramagnetic low-spin Co^{II} ion (S_{Co} = ½, ON) to the diamagnetic low-spin Co^{III} ion (S_{Co} = 0, OFF).

Compound **4** shows a high thermodynamic stability of the correspondent cobalt(III) complex due to the stronger electron

donor nature of the dimethylamino group. However, it is not an appropriated choice because of the additional accessible ligand-based irreversible oxidations at relatively low potentials that difficult its isolation in pure form by chemical oxidation. That being so, the best choice is **2** for which the corresponding cobalt(III) complex (**2'**) was successfully isolated by oxidation with bromine and structurally characterised.

The reversible interconversion between the paramagnetic cobalt(II) and diamagnetic cobalt(III)-4-MeOPhPDI complexes was monitored by X-band EPR spectra in acetonitrile solution. The X-band EPR spectrum of **2** at 4.0 K in the solid state (Figure III.14) exhibits an axial signal ($g_x = g_y = 2.09$ and $g_z = 2.42$) similar to that in frozen acetonitrile solutions ($g_x = g_y = 2.08$ and $g_z = 2.37$). This situation is typical for a LS Co^{II} ion with a $d_{x^2-y^2}$ magnetic orbital, as expected for an axially compressed coordination geometry, both in the solid state and in solution. Upon the addition of an excess of bromine to an acetonitrile solution of **2**, the axial EPR signal of the paramagnetic LS Co^{II} ion (S = 1/2) disappears to give the corresponding EPR-silent diamagnetic LS Co^{III} (S = 0) oxidised species. Conversely, the axial EPR signal found for **2** is restored by adding a stoichiometric amount of hydrazine to the solution resulting from the oxidation of **2** (inset of Figure III.14).

As the last test for the proof-of-concept, a solution of **2** in acetonitrile at 0 ˚C was subjected to electrochemical oxidation (E_{ox} = +1.0 V) and subsequent reduction (E_{red} = 0 V) (Figure III.S11). Then, ac measurements of the solution were performed before and after a complete redox cycle. Notably, the slow magnetic relaxation is preserved in frozen matrix solution under a static magnetic field of 2.5 kOe, the χ_M' and χ_M'' *vs* T plots before and after the electrolysis cycle being almost identical (Figure III.15). In both cases, χ_M' and χ_M'' maxima progressively shift toward higher temperatures as far as the frequency of the

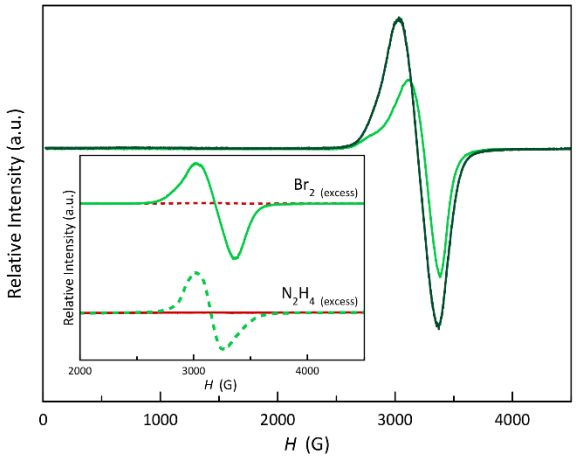

Figure III.14 X-band EPR spectra of **2** at 4.0 K, both in the solid state (pale green line) and in a frozen acetonitrile solution (dark green line). The inset shows the X-band EPR spectra of **2** and **2'** at 4.0 K in frozen acetonitrile solution (green and red solid lines), compared with those for the monooxidised and monoreduced species generated in situ (red and green dotted lines).

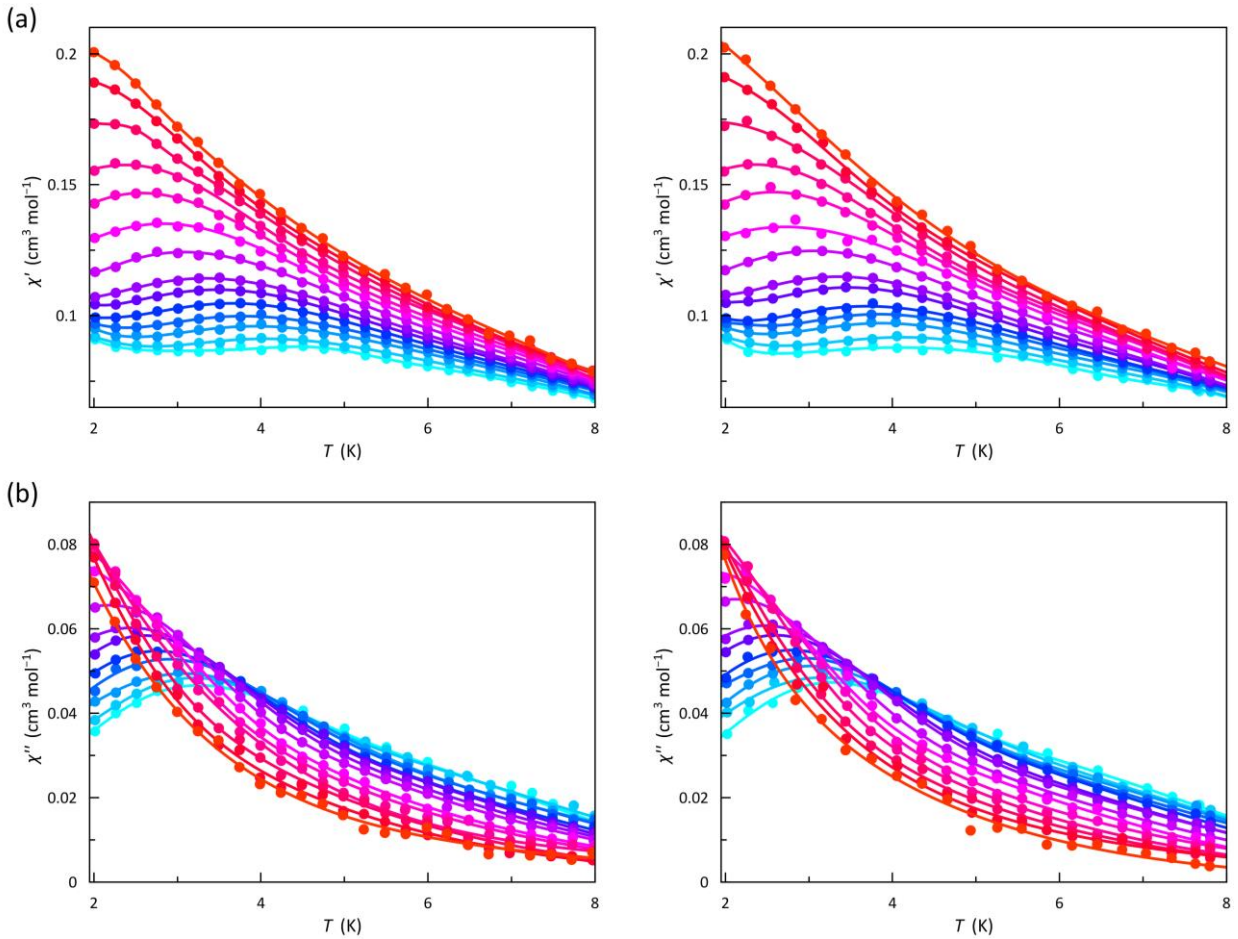

Figure III.15 Temperature dependence of χ_M' (a) and χ_M'' (b) of **2** in acetonitrile solution, either before (left) or after (right) one electrochemical redox cycle, at a ±5.0 G oscillating field in the frequency range of 1.23–10 kHz (from red to light blue), under an applied static magnetic field of 2.5 kOe. The solid lines are only eye-guides.

oscillating *ac* magnetic field increases, occurring at even higher temperatures than those in the solid state, probably because the intermolecular interactions playing their role in the Raman mechanism change. Hence, the calculated τ values for **2** are about two times greater in solution than in the solid state (see Figure III.13). Additionally, an extra temperature-independent Intra-Kramer (τ^{-1} = *IK*) mechanism is needed to reproduce low-temperature magnetic relaxation data in solution (see Table III.6). Hence, the SMM behaviour of **2** is preserved in solution but also enhanced. This reversible response demonstrates that this interconvertible system works as a genuine molecular magnetic switch in solution, even if it proceeds as two different compounds in the solid state.

III.8 – Concluding Remarks

Designing and implementing multi-electron transfer (MET) and single-molecule magnet (SMM) properties in spin-crossover (SCO) compounds constitute a promising way to obtain a new class of multiresponsive and multifunctional SCO/SMM materials as candidates for electro-switchable and charge storage molecular spintronic devices like spin transistors and capacitors for quantum information processing (QIP). In this chapter, we presented a novel series of multichannel redox-active mononuclear cobalt(II)-pyridinediimine (PDI) complexes displaying both thermally-induced LS ↔ HS transition and field-induced slow magnetic relaxation in the LS and HS states and dual metal- and ligand-centred electrochemical activity, all phenomena being modulated by the different electron-donating substituents at the terminal ligand phenyl rings.

As in the previous chapter, this series also comprehend complete or partial gradual thermally-induced spin transitions and even the absence of it. Regardless of the spin state, all systems show field-induced spin relaxation dynamics at low temperature, coexisting faster-relaxing (FR) and slower-relaxing (SR) forms for the LS and HS configurations, respectively. This multiple field-induced SMM behaviour is determined by IK and Raman processes at low- and high-temperature regions for both spin configurations.

This unique series of redox-active cobalt(II)-PDI complexes possesses both metal- and ligand-centred electrochemical activity because of the strong σ-donor capacity of the electron-donating ligand substituents at the phenyl groups and the π-acceptor character of the central pyridinediimine ligand fragment. An overall correlation between the redox behaviour and the electron donor nature of the ligand para-substituent is observed along this series. Otherwise, the distinct redox behaviour of the *ortho*, *para*-dimethyl derivative is likely due to the steric effects of the *ortho*-methyl group, so that the larger deviations from planarity of the ligand cause a significant reduction of the π-type inductive donor effects of the *para*-methyl group.

This combined magnetic and electrochemical investigation, together with the information obtained from the previous chapter, allowed us to get appropriate magneto and redox-structural correlations, which would aid the design and synthesis of multiresponsive and multifunctional SCO/SMM magnetic materials as candidates for multistable charge storage spintronic devices like molecular spin capacitors and switches. This new class of triply thermal-, magneto-, and electro-switchable molecular nanomagnet possesses multiple metal- or ligand-based redox and spin states, which reversibly interconvert under different external stimuli (temperature, magnetic field, and redox potential). The reported magnetic and electronic multistability here illustrates the potential of multiresponsive and multifunctional SCO/SMM molecules in the emerging fields of molecular spintronics and quantum computation.

III.9 – Experimental Section

Materials. All chemicals were of reagent grade quality. They were purchased from commercial sources and used as received.

Physical Techniques. Elemental analyses (C, H, N) were performed at the Servicio Central de Soporte a la Investigación (SCSIE) at the Universitat de València (Spain). FT–IR spectra were recorded on a Nicolet-5700 spectrophotometer as solid KBr pellets. Electronic absorption spectra of the ligands and complexes **1**–**5** were recorded in acetonitrile solutions (5.0×10^{-3} mM) at room temperature with a Jasco UV/Vis/NIR V-670 spectrophotometer. ^{1}H NMR spectra were recorded at room temperature on a Bruker AC 300 (300 MHz) spectrometer. Deuterated chloroform was used as solvent and internal standard (δ = 7.26 ppm). Q-band EPR spectra (ν = 34.03 GHz) of crushed crystal samples of **1**–**5** were recorded at 4.0 K under non-saturating conditions with a Bruker ER 200 D spectrometer equipped with a helium-flow cryostat. Powder X-ray diffraction (XRD) patterns of crushed crystal samples were collected at room temperature on a D8 Avance A25 Bruker diffractometer using graphite-monochromated Cu-Kα radiation (λ = 1.54056 Å).

Electrochemical measurements. Cyclic voltammetry and electrolytic studies were performed using an AUTOLAB 204 scanning potentiostat operating at a scan rate of 20–250 mV s^{-1} and equipped with a BOOSTER10A module to perform high current electrolysis. Cyclic voltammograms were collected at room temperature using 0.1 M nBu$_4$NPF$_6$ as supporting electrolyte and 1.0 mM of **1**–**5** in acetonitrile. The working electrode was a platinum disk (0.32 cm^2), while the reference electrode was AgCl/Ag, and a glassy carbon rod (76 mm) was used as auxiliary electrode. All experiments were performed in standard electrochemical cells under argon. The investigated potential range was in the range of –2.0 to +2.0 V *vs* AgCl/Ag. Ferrocene was added as internal standard at the end of the measurements. The formal potentials were measured at a scan rate of 200 mV s^{-1}, and they were calibrated against the ferrocenium/ferrocene (Fc^+/Fc) couple. The values of the measured formal potential and the anodic to cathodic peaks separation of ferrocene under the same conditions are E(Fc^+/Fc) = +0.40 V *vs* AgCl/Ag and $\Delta E_{p(Fc+/Fc)}$ = 80 mV (CH_3CN, 0.1 M nBu$_4$NPF$_6$, 25 °C). Electrolysis were performed at 0 °C on concentrated 15 mM acetonitrile solutions of **2** at fixed oxidation (E_{ox} = +1.0 V) and reduction potentials (E_{red} = 0 V) using 0.1 M nBu$_4$NPF$_6$ as supporting electrolyte. The monooxidised and monoreduced species were obtained by addition of a 10.0 and 1.0 mM acetonitrile solution (0.1 mL) of bromine and hydrazine, respectively, to a 1.0 mM acetonitrile solution of **2** and **2'** (0.1

mL) at –40 °C. X-band EPR spectra (ν = 9.463 GHz) of frozen-matrix acetonitrile solutions were recorded under non-saturating conditions on a Bruker ER 200 D spectrometer equipped with a helium cryostat.

Magnetic measurements. Variable-temperature (T = 2.0–300 K) direct current (dc) magnetic susceptibility measurements under applied fields of 0.25 (T < 20 K) and 5.0 kOe (T > 20 K) and variable-field (H = 0–50 kOe) magnetisation measurements in the temperature range of 2.0–10 K were carried out on crushed crystals of **1**–**5** with a Quantum Design SQUID magnetometer. The magnetic susceptibility data were corrected for the diamagnetism of the constituent atoms and the sample holder. Variable-temperature (T = 2.0–10 K) alternating current (ac) magnetic susceptibility measurements under ±5.0 Oe oscillating field at frequencies in the range of 0.1–10 kHz were performed under different applied static dc fields (H_{dc} = 0–2.5 kOe) with a Quantum Design Physical Property Measurement System (PPMS). A quartz tube (8 cm height x 5 mm outer diameter with 0.5 mm wall thickness) filled with 5 mm (height) of the concentrated acetonitrile solution of **2** (15 mM) was employed to carry out ac magnetic measurements in solution.

Crystal structure data collection and refinement. X-ray diffraction data of single crystals of **1** and **2** were collected on an Agilent Supernova diffractometer equipped with an EosS2 detector with Mo-Kα radiation (λ = 0.71073 Å) at 150 K, while those of **3**–**5** and **2'** were collected on a Bruker D8 Venture diffractometer with a PHOTON II detector by using monochromatic Mo-Kα radiation (λ = 0.71073 Å) at 120 K. Diffraction data of **1**–**5** and **2'** were collected, scaled, and integrated using the CrysAlisPro software[28] for **1** and **2**, and Bruker SAINT[29] for **3**–**5** and **2'**. The structures were solved by intrinsic phasing methods integrated into the SHELXTL software[30] with the Olex2 platform.[31] The obtained models were refined with version 2018/3 of SHELXL against F^2 on all data by full-matrix least squares. All non-hydrogen atoms were anisotropically refined. The hydrogen atoms were set in geometrical position and refined with a riding model, except those of the water molecules, which were neither found nor set. The crystals of **2'** exhibit poor diffraction power, maybe because of the disorder of the polybromide anions, and it readily decomposes. The crystallographic data presented here correspond to our best attempt to measure **2'** at 120 K, but with the resolution cut at 1.0 Å, that is why completeness is not very good. Also, the crystals of **2'** decompose with time, and some meaningless electron density peaks appear in the Fourier integration, in particular the maximum residual peak of 2.58 e-/Å^3, very close to a phenyl ring.

Compound **2'** were refined as inversion twin, given the non-centrosymmetry of the space groups, introducing the TWIN/BASF instruction with a value of the Flack parameter of 0.07(3). The methyl group of one of the methoxyphenyl-substituted pyridinediimine ligands in **2'** is disordered between two positions, and some restraints were applied to the anisotropic displacements of the C atoms, although the s.o.f. could be refined. One of the Br_3^- and the Br_5^- anions in **2'** were disordered. The occupation factor was refined in preliminary steps, but once converged, s.o.f. was fixed to the values 0.35 and 0.65 for Br_3^- and Br_5^- anions, respectively. The graphical manipulations and calculations were performed with the CRYSTALMAKER[32] and MERCURY[33] programs.

DFT study: Geometries, electronic transitions and NMR chemical shifts. This study was also carried out by DFT type calculations through the Gaussian 09 package by using the hybrid B3LYP functional,[34,35] and the quadratic convergence approach. Ahlrichs' triple-ζ with a p polarization function (TZVP) was used for all atoms in the optimized geometries of ligands and the evaluation of their electronic properties.[36,37] In the optimisation of the geometry of the cobalt(II) complex in **4**, the same basis set was used for cobalt atom but an Ahlrichs' double-ζ basis set with a polarization function (SVP) was employed for the non-metal atoms in order to reduce the cpu time. A polarizable continuum model (PCM) was used with the parameters corresponding to the acetonitrile in order to avoid the usual electronic overdelocalisation in DFT calculations.[38] Dichloromethane parameters were used in the evaluation of the NMR chemical shifts. Optimized geometries were then confirmed as global minima by frequency calculations. Electronic transitions were analysed from calculations based on the time-dependent (TD) formalism applied to the density functional theory (TDDFT).[39–40] NMR shielding tensors were computed with the gauge-independent atomic orbital (GIAO) method.[41–44] Independently, the ^{1}H NMR spectrum of tetramethylsilane (TMS) was calculated to be used as reference.

Ab initio calculations on the zfs tensors. Ab initio calculations on the zfs tensors. The parameters that determine the axial (D) and rhombic (E) components of the local zero-field splitting (zfs), the g-tensor for the S = 3/2 state ($g_{3/2}$) and the ground Kramers doublet (g_{eff}) of **3** and **5** were estimated from theoretical calculations based on a second-order N-electron valence state perturbation theory (CASSCF/NEVPT2) through an effective Hamiltonian for the spin-orbit coupling (SOC),[45–47] which often provides accurate values of the nearby excited states energies and for the *zfs* tensor of mononuclear first-row transition metal complexes. Experimental geometries were used in this study. Calculations were carried out on the experimental geometries with version 4.0.1 of the ORCA programme[48] using the def2-TZVP basis set proposed by Ahlrichs[49] and the auxiliary TZV/C Coulomb fitting basis sets.[50–52] The contributions to *zfs* from 10 quartet and 20 doublet excited states generated from an active space with seven electrons in five *d* orbitals were included using an effective Hamiltonian. RIJCOSX method was used combining resolution of the identity (RI) and "chain of spheres" COSX approximations for the Coulomb and exchange terms, respectively.[53–55]

Preparation of ligands and complexes.

4-MePhPDI. A mixture of pyridine-2,6-diformaldehyde (0.135 g, 1.0 mmol) and aniline (181 µL, 2.0 mmol) in 5.0 mL of ethanol under the presence of 100 µL of acetic acid was allowed to reflux for 30 min. The mixture was cooled in an ice bath leading to a white crystalline powder, which was filtered and washed with a small quantity of ethanol. Yield 84%. Anal. Calc. for $C_{21}H_{19}N_3$ (4-MePhPDI): C, 80.48; H, 6.11; N, 13.41. Found: C, 80.96; H, 5.87; N, 13.75%. IR (KBr, cm^{-1}): 2916(m) [ν(C–H) from methyl substituent of 4-MePhPDI ligand], 1624(m) [ν(C=N) from

4-MePhPDI ligand]. ^{1}H NMR ($CDCl_3$; 300 MHz, ppm): δ = 8.70 (s, 2H, H_{im}), 8.27 (d, 2H, *p*-H_{py}, *J* = 7.8 Hz), 7.92 (t, 1H, *m*-H_{py}, *J* = 7.8 Hz), 7.27 (d, 4H, *o*-H_{Ph}, *J* = 8.9 Hz), 7.23 (d, 4H, *m*-H_{Ph}, *J* = 8.9 Hz), 2.39 (s, 6H, *p*-H_{Me}).

4-MeOPhPDI. A mixture of pyridine-2,6-diformaldehyde (0.135 g, 1.0 mmol) and *p*-anisidine (0.246 g, 2.0 mmol) in 5.0 mL of ethanol under the presence of 100 µL of acetic acid was allowed to reflux for 30 min. The mixture was cooled in an ice bath leading to a brownish crystalline powder, which was filtered and washed with a small quantity of ethanol. Yield 88%. Anal. Calc. for $C_{21}H_{19}N_3O_2$ (4-MeOPhPDI): C, 73.03; H, 5.54; N, 12.17. Found: C, 73.94; H, 5.13; N, 12.29%. IR (KBr, cm^{-1}): 2965(w) [ν(C–H) from methoxy substituent of 4-MeOPhPDI ligand], 1624(m) [ν(C=N) from 4-MeOPhPDI ligand], 1245(s) [ν(C–O) from methoxy substituent of 4-MeOPhPDI ligand]. ^{1}H NMR ($CDCl_3$; 300 MHz, ppm): δ = 8.70 (s, 2H, H_{im}), 8.24 (d, 2H, *p*-H_{py}, *J* = 7.8 Hz), 7.90 (t, 1H, *m*-H_{py}, *J* = 7.8 Hz), 7.36 (d, 4H, *o*-H_{Ph}, *J* = 8.9 Hz), 6.96 (d, 4H, *m*-H_{Ph}, *J* = 8.9 Hz), 3.85 (s, 6H, *p*-H_{OMe}).

4-MeSPhPDI. A mixture of pyridine-2,6-diformaldehyde (0.135 g, 1.0 mmol) and 4-(methylthio)aniline (250 µL, 2.0 mmol) in 5.0 mL of ethanol under the presence of 100 µL of acetic acid was allowed to reflux for 30 min. The mixture was cooled in an ice bath leading to a yellowish crystalline powder, which was filtered and washed with a small quantity of ethanol. Yield 88%. Anal. Calc. for $C_{21}H_{19}N_3S_2$ (4-MeSPhPDI): C, 66.81; H, 5.07; N, 11.13. Found: C, 66.95; H, 5.04; N, 11.42%. IR (KBr, cm^{-1}): 2916(m) [ν(C–H) from thiomethyl substituent of 4-MeSPhPDI ligand], 1621(m) [ν(C=N) from 4-MeSPhPDI ligand]. ^{1}H NMR ($CDCl_3$; 300 MHz, ppm): δ = 8.67 (s, 2H, H_{im}), 8.24 (d, 2H, *p*-H_{py}, *J* = 7.8 Hz), 7.90 (t, 1H, *m*-H_{py}, *J* = 7.8 Hz), 7.23 (d, 4H, *o*-H_{Ph}, *J* = 8.9 Hz), 6.94 (d, 4H, *m*-H_{Ph}, *J* = 8.9 Hz), 2.47 (s, 6H, *p*-H_{SMe}).

4-Me$_2$NPhPDI. A mixture of pyridine-2,6-diformaldehyde (0.135 g, 1.0 mmol) and *N*,*N*-dimethyl-*p*-phenylenediamine (0.272 g, 2.0 mmol) in 5.0 mL of ethanol under the presence of 100 µL of acetic acid was allowed to reflux for 30 min. The mixture was cooled in an ice bath leading to a green powder, which was filtered and washed with a small quantity of ethanol. Yield 77%. Anal. Calc. for $C_{23}H_{25}N_5$ (4-Me$_2$NPhPDI): C, 74.36; H, 6.78; N, 18.85%. Found: C, 73.84; H, 6.95; N, 18.90%. IR (KBr, cm^{-1}): 2882(s) [ν(C–H) from dimethylamine substituent of 4-Me$_2$NPhPDI ligand], 1618(m) [ν(C=N) from 4-Me$_2$NPhPDI ligand]. ^{1}H NMR ($CDCl_3$; 300 MHz, ppm): δ = 8.74 (s, 2H, H_{im}), 8.21 (d, 2H, *p*-H_{py}, *J* = 7.8 Hz), 7.86 (t, 1H, *m*-H_{py}, *J* = 7.8 Hz), 7.40 (d, 4H, *o*-H_{Ph}, *J* = 8.9 Hz), 6.77 (d, 4H, *m*-H_{Ph}, *J* = 8.9 Hz), 3.01 (s, 12H, *p*-H_{NMe2}).

2,4-Me$_2$PhPDI. A mixture of pyridine-2,6-diformaldehyde (0.135 g, 1.0 mmol) and 2,4-dimethylaniline (247 µL, 2.0 mmol) in 5.0 mL of ethanol under the presence of 100 µL of acetic acid was allowed to reflux for 30 min. The mixture was cooled in an ice bath leading to a yellow crystalline powder, which was filtered and washed with a small quantity of ethanol. Yield 85%. Anal. Calc. for $C_{23}H_{23}N_3$ (2,4-Me$_2$PhPDI): C, 80.90; H, 6.79; N, 12.31. Found: C, 80.72; H, 6.62; N 12.65%. IR (KBr, cm^{-1}): 2914(s) [ν(C–H) from methyl substituent of 2,4-Me$_2$PhPDI ligand], 1626(m) [ν(C=N) from 2,4-Me$_2$PhPDI ligand]. ^{1}H NMR ($CDCl_3$; 300 MHz, ppm): δ = 8.60 (s, 2H, H_{im}), 8.32 (d, 2H, *p*-H_{py}, *J* = 7.8 Hz), 7.92 (t, 1H, *m*-H_{py}, *J* = 7.8 Hz), 7.04 (m, 3H, *o*- and *m*-H_{Ph}), 2.40 (s, 3H, *o*-H_{Me}), 2.35 (s, 3H, *p*-H_{Me}).

*[Co(4-MePhPDI)$_2$](ClO$_4$)$_2$·H$_2$O (**1**).* 4-MePDI (0.032 g, 0.10 mmol) was suspended in ethanol (10 mL). To this mixture was slowly added an ethanolic solution (2.0 mL) of cobalt(II) perchlorate hexahydrate (0.018 g, 0.05 mmol). The resulting red solution was evaporated at room temperature and red needles of **1** appeared on the very next day. They were collected and dried over filter paper. Yield 65%. Anal. Calc. for $C_{42}H_{40}N_6O_9Cl_2Co$ (**1**): C, 54.43; H, 3.98; N, 9.77. Found: C, 53.92; H, 4.02; N, 9.65%. IR (KBr, cm^{-1}): 3426(s) [ν(O–H) from crystallization water], 2920(m) [ν(C–H) from methyl substituent of 4-MePhPDI ligand], 1596(m) [ν(C=N) from 4-MePhPDI ligand], 1088(vs) [ν(Cl–O) from perchlorate anion]. UV-Vis (MeCN): ν_{max} = 51282 cm^{-1} (ε = 108743 $M^{-1}cm^{-1}$), 44445 (56561), and 28490 (29118).

*[Co(4-MeOPhPDI)$_2$](ClO$_4$)$_2$ (**2**).* 4-MeOPDI (0.017 g, 0.05 mmol) was dissolved in chloroform (0.5 mL) and putted in the bottom of a glass tube. A 4:1 mixture of methanol/chloroform (8.0 mL) was slowly added to allow for a separation of the solutions. A methanolic solution (0.5 mL) of cobalt(II) perchlorate hexahydrate (0.010 g, 0.025 mmol) was added on the top of the tube. X-ray suitable red plates of **2** were grown through slow diffusion after a few days. Yield 82%. Anal. Calc. for $C_{41}H_{35}N_6O_{12}Cl_2Co$ (**2**): C, 53.18; H, 4.04; N, 8.86. Found: C, 53.98; H, 4.17; N, 8.90%. IR (KBr, cm^{-1}): 2973(m) [ν(C–H) from methoxy substituent of 4-MeOPDI ligand], 1596(s) [ν(C=N) from 4-MeOPDI ligand], 1082(vs) [ν(Cl–O) from perchlorate anion]. UV-Vis (MeCN): ν_{max} = 51282 cm^{-1} (ε = 99048 $M^{-1}cm^{-1}$), 44248 (59889), and 26385 (28780).

*[Co(4-MeOPhPDI)$_2$](Br$_3$)$_{2.35}$(Br$_5$)$_{0.65}$·0.25H$_2$O (**2'**).* An excess of molecular bromine (75 µL, 0.150 mmol) was added to a chloroform/acetonitrile solution (1:1, 1.0 mL) of **2** (0.014 g, 0.015 mmol). X-ray suitable dark brown crystals of **2'** were obtained by slow diffusion of ethyl acetate on the resulting dark brown solution in a glass tube. Yield: 78%. Anal. Calc. for $C_{41}H_{35.5}N_6O_{4.25}Br_{10.3}Co$ (**2**): C, 31.52; H, 2.29; N, 5.38. Found: C, 31.55; H, 2.40; N, 5.70%. IR (KBr, cm^{-1}): 2974(m) [ν(C–H) from the methoxy substituents of 4-MeOPhPDI], 1593(s) [ν(C=N) from the imine groups of 4-MeOPhPDI].

*[Co(4-MeSPhPDI)$_2$](ClO$_4$)$_2$ (**3**).* An ethanol solution (2.0 mL) of cobalt(II) perchlorate hexahydrate (0.035 g, 0.10 mmol) was added dropwise to a suspension of 4-MeSPhPDI (0.075 g, 0.20 mmol) in ethanol (20.0 mL) under stirring. The mixture was further stirred for one hour under gentle warming. The resulting polycrystalline powder was filtered and washed with a small quantity of ethanol. X-ray quality dark red crystals of **3** were obtained by slow diffusion of ethyl acetate on a saturated chloroform/acetonitrile solution (1:1) of the polycrystalline powder in a glass tube. Yield 90%. Anal. Calc. for $C_{41}H_{35}N_6O_{12}Cl_2Co$ (**3**): C, 49.80; H, 3.78; N, 8.30. Found: C, 50.12; H, 3.84; N, 8.45%. IR (KBr, cm^{-1}): 2919(w) [ν(C–H) from the thiomethyl substituents of 4-MeSPhPDI], 1585(s) [ν(C=N) from the imine groups of 4-MeSPhPDI], 1093(vs) [ν(Cl–O) from perchlorate anion].

*[Co(4-Me$_2$NPhPDI)$_2$](ClO$_4$)$_2$ (**4**).* Cobalt(II) perchlorate hexahydrate (0.037 g, 0.1 mmol) was dissolved in methanol (5.0 mL) and added dropwise to a 4-Me$_2$NPDI (0.0635 g, 0.2 mmol) suspension in methanol (20.0 mL). The dark purple solution was allowed to evaporate at room temperature and black block-like crystals of **4** appeared after one week. They were collected and dried over filter paper. Yield 76%. Anal. Calc. for

$C_{46}H_{50}N_{10}O_8Cl_2Co$ (**4**): C, 55.21; H, 5.04; N, 14.00; Found: C, 55.72; H, 4.87; N, 14.05%. IR (KBr, cm^{-1}): 3434(w) [*ν*(O–H) from crystallization water], 2892(w) [*ν*(C–H) from dimethylamine substituent of 4-Me_2NPhPDI ligand], 1608(s) [*ν*(C=N) from 4-Me_2NPDI ligand], 1094(vs) [*ν*(Cl–O) from perchlorate anion]. UV-Vis (MeCN): ν_{max} = 50252 cm^{-1} (ε = 95194 $M^{-1}cm^{-1}$), 38760 (49366), and 20450 (38164).

*[Co(2,4-Me_2PhPDI)$_2$](ClO$_4$)$_2$ (**5**).* Cobalt(II) perchlorate hexahydrate (0.037 g, 0.1 mmol) was dissolved in methanol (5.0 mL) and added dropwise to a 2,4-Me_2PhPDI (0.0684 g, 0.2 mmol) suspension in methanol (10.0 mL). The red solution was allowed to evaporate at room temperature and red needles of **5** appeared at the very next day. They were collected and dried over filter paper. Yield 72%. Anal. Calc. for $C_{45}H_{42}N_6O_8Cl_2Co$ (**5**): C, 58.73; H, 4.93; N, 8.93; Found: C, 58.92; H, 4.74; N, 9.45%. IR (KBr, cm^{-1}): 2921(s) [*ν*(C–H) from methyl substituent of 2,4-Me_2PhPDI ligand], 1600(s) [*ν*(C=N) from 2,4-Me_2PhPDI ligand], 1091(vs) [*ν*(Cl–O) from perchlorate anion]. UV-Vis (MeCN): ν_{max} = 51021 cm^{-1} (ε = 115934 $M^{-1}cm^{-1}$), 42554 (48508), and 29240 (20132).

References

1 Savéant, J.-M.; Constentin, C. *Elements of Molecular and Biomolecular Electrochemistry: An Electrochemical Approach to Electron Transfer Chemistry*, John Wiley & Sons, 2006.

2 Stubbe, J.; Van der Donk, W. A. Protein Radicals in Enzyme Catalysis. *Chem. Rev.* **1998**, *98*, 705–762

3 Mukhopadhyay, S.; Mandal, S. K.; Bhaduri, S.; Armstrong, W. H. Manganese Clusters with Relevance to Photosystem II. *Chem. Rev.* **2004**, *104*, 3981–4026.

4 Praneeth, V. K. K.; Ringenberg, M. R.; Ward, T. R. Redox-Active Ligands in Catalysis. Angew. Chem. Int. Ed. **2012**, *51*, 10228–10234.

5 Schrauzer, G. N.; Mayweg, V. Reaction of Diphenylacetylene with Nickel Sulfides. *J. Am. Chem. Soc.* **1962**, *84*, 3221.

6 Gray, H. B.; Williams, R.; Bernal, I.; Billig, E. The Electronic Structures of Metal Nitrosyls and Carbonyls. *J. Am. Chem. Soc.* **1962**, *84*, 3404–3405.

7 Davison, A.; Edelstein, N.; Holm, R. H.; Maki, A. H. E.s.r. Studies of Four-Coordinate Complexes of Nickel, Palladium and Platinum Related by Electron Transfer Reactions. *J. Am. Chem. Soc.* **1963**, *85*, 2029–2030.

8 Billig, E.; Williams, R.; Bernal, I.; Waters, J. H.; Gray, H. B. The Electronic Structures of Square-Planar Metal Complexes. II. The Complexes of Maleonitriledithiolate with Copper(II), Nickel(II), Palladium(II), and Platinum(II). *Inorg. Chem.* **1964**, *3*, 663–666.

9 Jorgensen, C. K. Differences between the Four Halide Ligands, and Discussion Remarks on Trigonal-Bipyramidal Complexes, on Oxidation States, and on Diagonal Elements of One-Electron Energy. *Coord. Chem. Rev.* **1966**, *1*, 164–178.

10 Ray, K.; Petrenko, T.; Wieghardt, K.; Neese, F. Joint Spectroscopic and Theoretical Investigations of Transition Metal Complexes Involving Non-Innocent Ligands. *Dalton Trans.* **2007**, 1552–1566.

11 Ward, M. D.; McCleverty, J. A. Non-Innocent Behaviour in Mononuclear and Polynuclear Complexes: Consequences for Redox and Electronic Spectroscopic Properties. *J. Chem. Soc., Dalton Trans.* **2002**, 275–288.

12 Eisenberg, R.; Gray, H. B. Noninnocence in Metal Complexes: A Dithiolene Dawn. *Inorg. Chem.* **2011**, *50*, 9741–9751.

13 Kaim, W. Manifestations of Noninnocent Ligand Behavior. *Inorg. Chem.* **2011**, *50*, 9752-9765.

14 Pierpont, C. G. Ligand Redox Activity and Mixed Valency in First-Row Transition-Metal Complexes Containing Tetrachlorocatecholate and Radical Tetrachlorosemiquinonate Ligands. *Inorg. Chem.* **2011**, *50*, 9766–9772.

15 Figgins, P. E.; Busch, D. H. Complexes of Iron(II), Cobalt(II) and Nickel(II) with Biacetyl-bis-methylimine, 2-Pyridinal-methylimine and 2,6-Pyridindial-bis-methylimine. *J. Am. Chem. Soc.*, **1960**, *82*, 820–824.

16 Römelt, C.; Weyhermüller, T.; Wieghardt, K. Structural Characteristics of Redox-Active Pyridine-1,6-Diimine Complexes: Electronic Structures and Ligand Oxidation Levels. *Coord. Chem. Rev.* **2019**, *380*, 287–317.

17 De Bruin, B.; Bill, E.; Bothe, E.; Weyhermüller, T.; Wieghardt, K. Molecular and Electronic Structures of Bis(pyridine-2,6-diimine)metal Complexes $[ML_2](PF_6)n$ (n = 0, 1, 2, 3; M = Mn, Fe, Co, Ni, Cu, Zn). *Inorg. Chem.* **2000**, *39*, 2936–2947.

18 Juhász, G.; Hayami, S.; Inoue, K.; Maeda, Y. $[Co^{II}(PDI)_2](ClO_4)_2$ and $[Co^{II}(ipimpy)_2](ClO_4)_2$: New Cobalt(II) Spin Crossover Compounds, and the Role of the Ligand Flexibility in Spin Transition Behavior. *Chem. Lett.* **2003**, *32*, 882–883.

19 Hansch, C.; Leo, A.; Taft, R. W. A Survey of Hammett Substituent Constants and Resonance and Field Parameters. *Chem. Rev.* **1991**, *91*, 165–195.

20 Sun, S.; Liang, S.; Xu, W.-C.; Xu, G.; Wu, Y. Photoresponsive Polymers with Multi-Azobenzene Groups. *Polym. Chem.* **2019**, *10*, 4389–4401.

21 Bandara, H. M. D.; Burdette, S. C. Photoisomerization in Different Classes of Azobenzene. *Chem. Soc. Rev.* **2012**, *41*, 1809–1825.

22 Williams, J. A. G. Photochemistry and Photophysics of Coordination Compounds: Platinum. In: Photochemistry and Photophysics of Coordination Compounds II. Edited by Balzani, V. and Campagna, S. 2007, Springer, Berlin, 2007.

23 Knoll, H. Photoisomerism of Azobenzenes. In: CRC Handbook of Organic Photochemistry and Photobiology. Edited by Horspool, W. M. and Lenci, F. 2nd edition, Boca Raton, Florida, USA, 2003.

24 Chilton, N. F.; Anderson, R. P.; Turner, L. D.; Soncini, A.; Murray, K. S. PHI: A Powerful New Program for the Analysis of Anisotropic Monomeric and Exchange-Coupled Polynuclear d- and f-Block Complexes. *J. Comput. Chem.* **2013**, *34*, 1164–1175.

25 Krivokapic, I., Zerara, M., Daku, M. L., Vargas, A., Enachescu, C., Ambrus, C., Tregenna-Piggott, P., Amstutz, N., Krausz, E., Hauser, A. Spin-crossover in cobalt(II) imine complexes. *Coord. Chem. Rev.* **2007**, *251*, 364–378.

26 Chen, L.; Song, J.; Zhao, W.; Yi, G.; Zhou, Z.; Yuan, A.; Song, Y.; Wang, Z.; Ouyang, Z.-W. A Mononuclear Five-Coordinate Co(II) Single Molecule Magnet with a Spin Crossover between the S = 1/2 and 3/2 States. *Dalton Trans.* **2018**, *47*, 16596–16602.

27 Cole, K. S.; Cole, R. H. Dispersion and absorption in dielectrics. I. Alternating current characteristics. *J. Chem. Phys.* **1941**, *9*, 341–351.

28 Agilent. *CrysAlis PRO*. Agilent Technologies Ltd, Yarnton, Oxfordshire, England, **2014**.

29 Bruker. *SAINT*. Bruker AXS Inc., Madison, Wisconsin, USA, **2012**.

30 Sheldrick, G. M. SHELXT - Integrated Space-Group and Crystal-Structure Determination. *Acta Cryst.* **2015**, *A71*, 3–8.

31 Dolomanov, O.V., Bourhis, L.J., Gildea, R.J, Howard, J.A.K. & Puschmann, H. *J.* OLEX2: a Complete Structure Solution, Refinement and Analysis Program. *Appl. Cryst*. **2009**, *42*, 339-341.

32 *CrystalMaker*, CrystalMaker Software, Bicester, England, **2015**.

33 *Mercury*, The Cambridge Crystallographic Data Centre, Cambridge, UK.

34 Frisch, M. J.; Trucks, G. W.; Schlegel, H. B.; Scuseria, G. E.; Robb, M. A.; Cheeseman, J. R.; Scalmani, G.; Barone, V.; Mennucci, B.; Petersson, G. A.; Nakatsuji, H.; Caricato, M.; Li, X.; Hratchian, H. P.; Izmaylov, A. F.; Bloino, J.; Zheng, G.; Sonnenberg, J. L.; Hada, M.; Ehara, M.; Toyota, K.; Fukuda, R.; Hasegawa, J.; Ishida, M.; Nakajima, T.; Honda, Y.; Kitao, O.; Nakai, H.; Vreven, T.; Montgomery Jr., J. A.; Peralta, J. E.; Ogliaro, F.; Bearpark, M.; Heyd, J. J.; Brothers, E.; Kudin, K. N.; Staroverov, V. N.; Kobayashi, R.; Normand, J.; Raghavachari, K.; Rendell, A.; Burant, J. C.; Iyengar, S. S.; Tomasi, J.; Cossi, M.; Rega, N.; Millam, J. M.; Klene, M.; Knox, J. E.; Cross, J. B.; Bakken, V.; Adamo, C.; Jaramillo, J.; Gomperts, R.; Stratmann, R. E.; Yazyev, O.; Austin, A. J.; Cammi, R.; Pomelli, C.; Ochterski, J. W.; Martin, R. L.; Morokuma, K.; Zakrzewski, V. G.; Voth, G. A.; Salvador, P.; Dannenberg, J. J.; Dapprich, S.; Daniels, A. D.; Farkas, Ö.; Foresman, J. B.; Ortiz, J. V.; Cioslowski, J.; Fox, D. J. Gaussian 09, Revision D.01, Gaussian, Inc., Wallingford CT, 2009.

35 Becke, A. D. Density-Functional Thermochemistry. III. The Role of Exact Exchange. *J. Chem. Phys.* **1993**, 98, 5648–5652.

36 Schäfer, A.; Horn, H.; Ahlrichs, R. Fully Optimized Contracted Gaussian Basis Sets for Atoms Li to Kr. *J. Chem. Phys.* **1992**, *97*, 2571–2577.

37 Schäfer, A.; Huber, C.; Ahlrichs, R. Fully Optimized Contracted Gaussian Basis Sets of Triple Zeta Valence Quality for Atoms Li to Kr. *J. Chem. Phys.* **1994**, *100*, 5829–5835.

38 Tomasi, J.; Mennucci, B.; Cammi, R. Quantum Mechanical Continuum Solvation Models. *Chem. Rev.* **2005**, *105*, 2999–3093.

39 Casida, M. E.; Huix-Rotllant, M. Progress in Time-Dependent Density-Functional Theory. *Annu. Rev. Phys. Chem.* 2012, **63**, 287.

40 Casida, M. E.; Jamorski, C.; Casida, K. C.; Salahub, D. R. *J. Chem. Phys.* 1998, **108**, 4439.

41 London, F. Quantum Theory of Interatomic Currents in Aromatic Compounds. *J. Phys. Radium* 1937, **8**, 397–409.

42 McWeeny, R. Perturbation Theory for the Fock-Dirac Density Matrix. *Phys. Rev*. 1962, **126**, 1028−1034.

43 Ditchfield, R. Self-Consistent Perturbation Theory of Diamagnetism: I. A Gauge-Invariant LCAO Method for N.M.R. Chemical Shifts. *Mol. Phys*. 1974, **27**, 789−807.

44 Wolinski, K.; Hilton, J. F.; Pulay, P. Efficient Implementation of the Gauge-Independent Atomic Orbital Method for NMR Chemical Shift Calculations. *J. Am. Chem. Soc*. 1990, **112**, 8251−8260.

45 Angeli, C.; Cimiraglia, R.; Malrieu, J. P. n-Electron Valence State Perturbation Theory: a Fast Implementation of the Strongly Contracted Variant. *Chem. Phys. Lett.* **2001**, *350*, 297–305.

46 Angeli, C.; Cimiraglia, R.; Malrieu, J.-P. n-Electron Valence State Perturbation Theory: A Spinless Formulation and an Efficient Implementation of the Strongly Contracted and of the Partially Contracted Variants. *J. Chem. Phys.* **2002**, *117*, 9138–9153.

47 Angeli, C.; Cimiraglia, R.; Evangelisti, S.; Leininger, T.; Malrieu, J.-P. Introduction of n-Electron Valence States for Multireference Perturbation Theory. *J. Chem. Phys.* **2001**, *114*, 10252–10264.

48 Neese, F. The ORCA Program System. *Wires Comput. Mol. Sci.* **2012**, *2*, 73–78.

49 Weigend, F.; Ahlrichs, R. Balanced Basis Sets of Split Valence, Triple Zeta Valence and Quadruple Zeta Valence Quality for H to Rn: Design and Assessment of Accuracy. *Phys. Chem. Chem. Phys.* **2005**, *7*, 3297–3305.

50 Weigend, F. Accurate Coulomb-Fitting Basis Sets for H to Rn. *Phys. Chem. Chem. Phys.* **2006**, *8*, 1057–1065.
51 Eichkorn, K.; Treutler, O.; Ohm, H.; Haser, M.; Ahlrichs, R. Auxiliary Basis Sets to approximate Coulomb Potentials. *Chem. Phys. Lett.* **1995**, *242*, 652–660.
52 Eichkorn, K.; Weigend, F.; Treutler, O.; Ohm, H.; Ahlrichs, R. *Theor. Chem. Acc.* **1997**, *97*, 119–124.
53 Neese, F.; Wennmohs, F.; Hansen, A.; Becker, U. Efficient, Approximate and Parallel Hartree–Fock and Hybrid DFT Calculations. A 'Chain-of-Spheres' Algorithm for the Hartree–Fock Exchange. *Chem. Phys.* **2009**, *356*, 98–109.
54 Izsák, R.; Neese, F. An Overlap Fitted Chain of Spheres Exchange Method. *J. Chem. Phys.* **2011**, *135*, 144105.
55 Izsák, R.; Hansen, A.; Neese, F. The Resolution of Identity and Chain of Spheres Approximations for the LPNO-CCSD Singles Fock Term. *Mol. Phys.* **2012**, *110*, 2413–2417.

Supporting Information

TABLE OF CONTENTS

General characterisation (Figure III.S1)

X-ray crystallographic data collection and structure refinement (Figures III.S2 – III.S7)

Theoretical calculations (Figure III.S8, Scheme III.S1 and Table III.S1)

Electrochemical measurements (Figures III.S9 and IIII.S10)

Static and dynamic magnetic measurements (Figures III.S11 – III.S23)

General characterisation

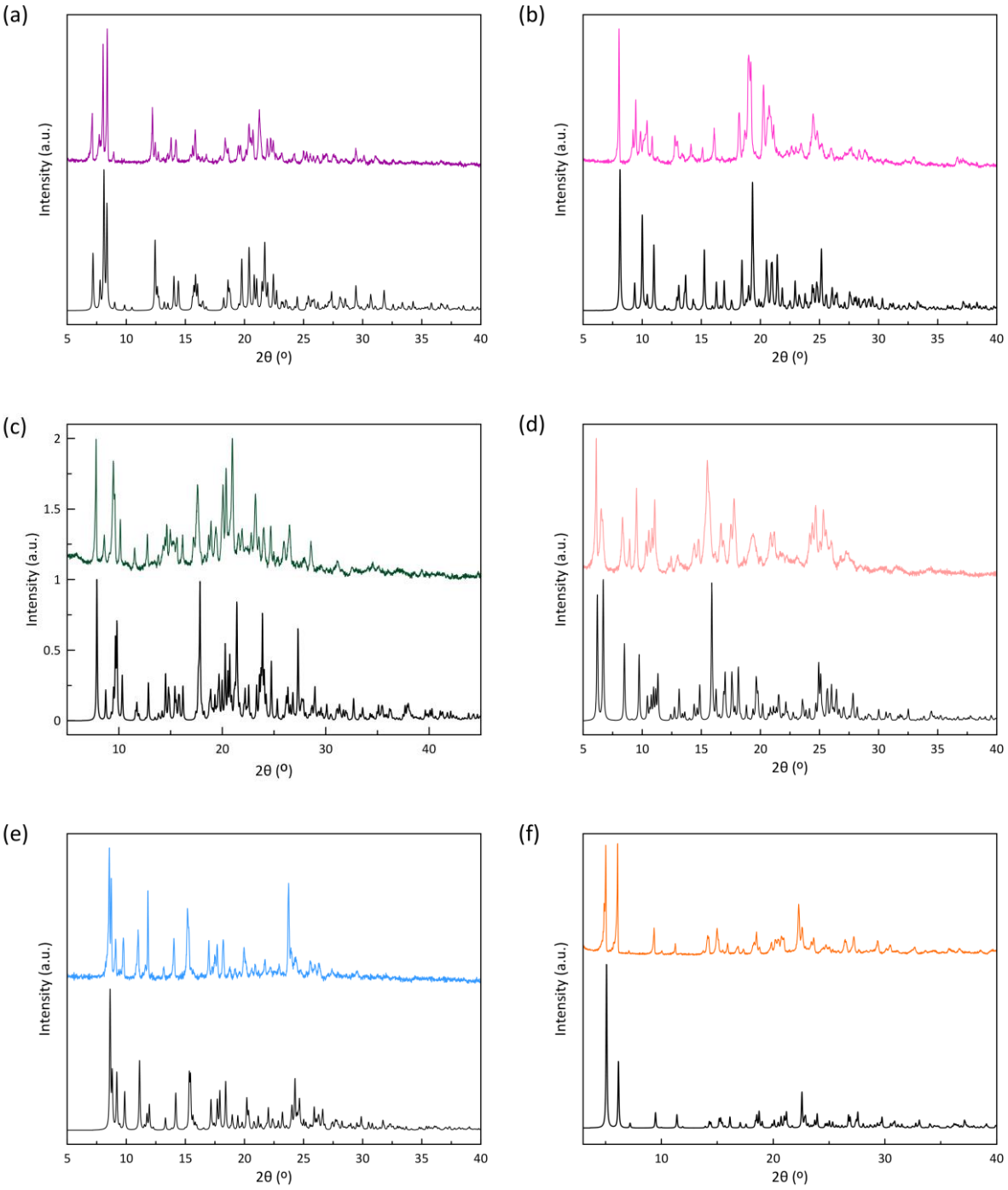

Figure III.S1 Powder X-ray diffractograms of **1** (a), **2** (b), **3** (c), **4** (d), **5** (e) and **2'** (f). The solid black lines correspond to the calculated X-ray diffractograms.

X-ray crystallographic data collection and structure refinement

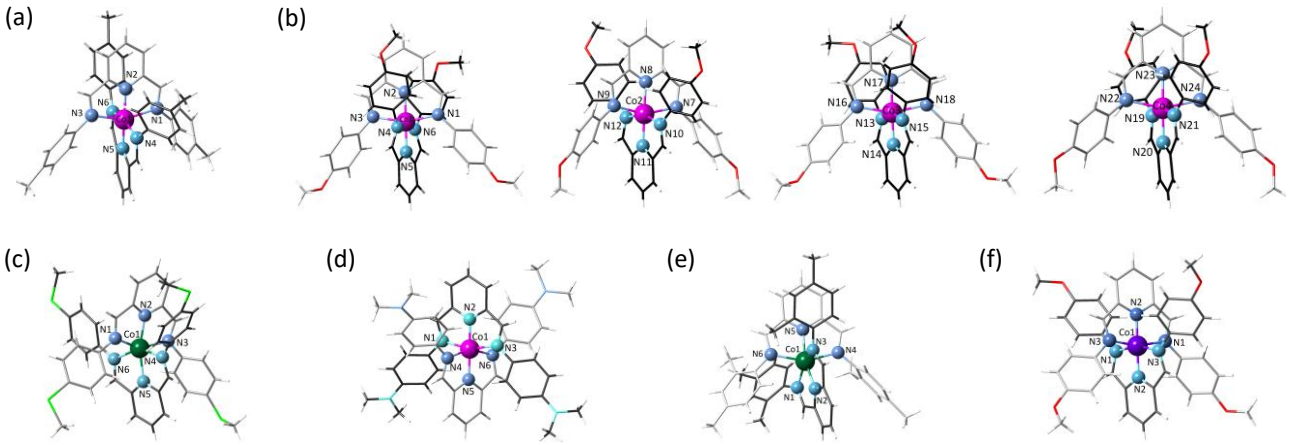

Figure III.S2 Perspective side views of the crystallographically independent mononuclear cobalt(II) units of **1**–**5** (a–e) and **2'** (f) with the atom numbering scheme of the coordination sphere at the cobalt atom. The ligand backbones are drawn in grey and black colours for clarity. The pink and green cobalt atoms correspond to the LS and HS configuration, whereas the Co(III) ion is represented in purple.

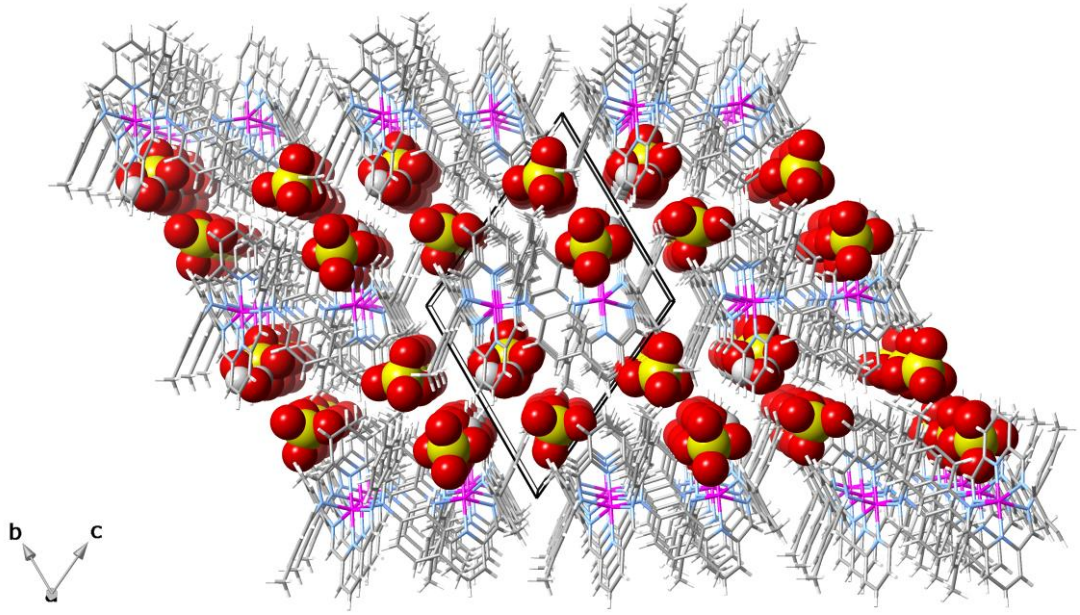

Figure III.S3 Perspective view of the crystal packing of **1** along the crystallographic *a* axis. The perchlorate anions and water molecules of crystallisation are shown in a space filling representation.

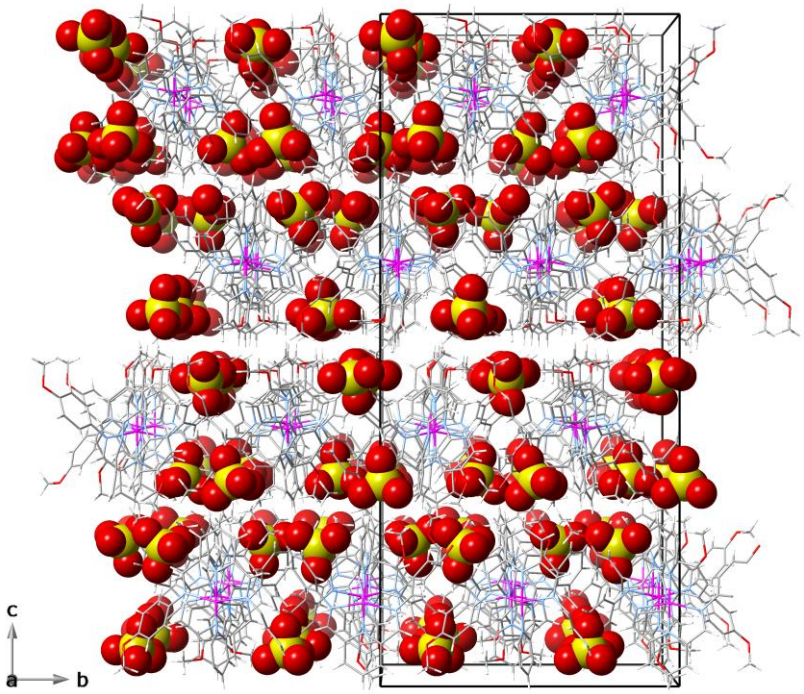

Figure III.S4 Perspective view of the crystal packing of **2** along the crystallographic *a* axis. The perchlorate anions are shown in a space filling representation.

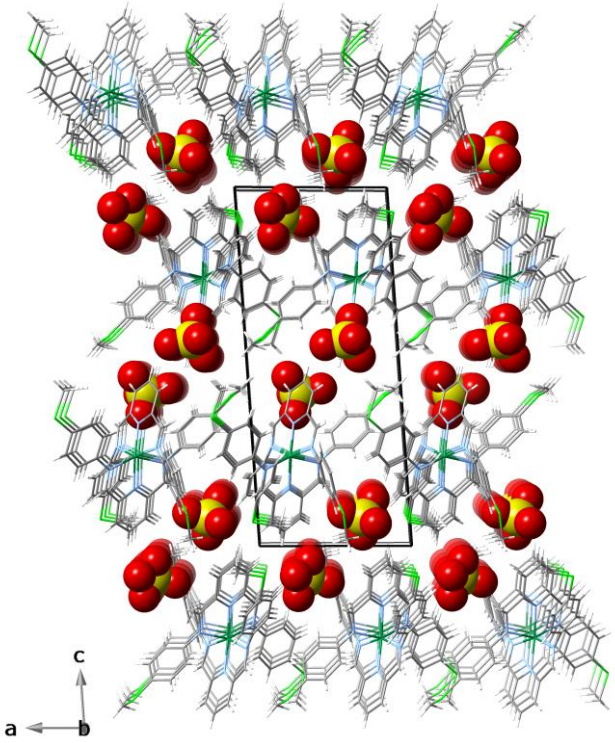

Figure III.S5 Perspective view of the crystal packing of **3** along the crystallographic *b* axis. The perchlorate anions are shown in a space filling representation.

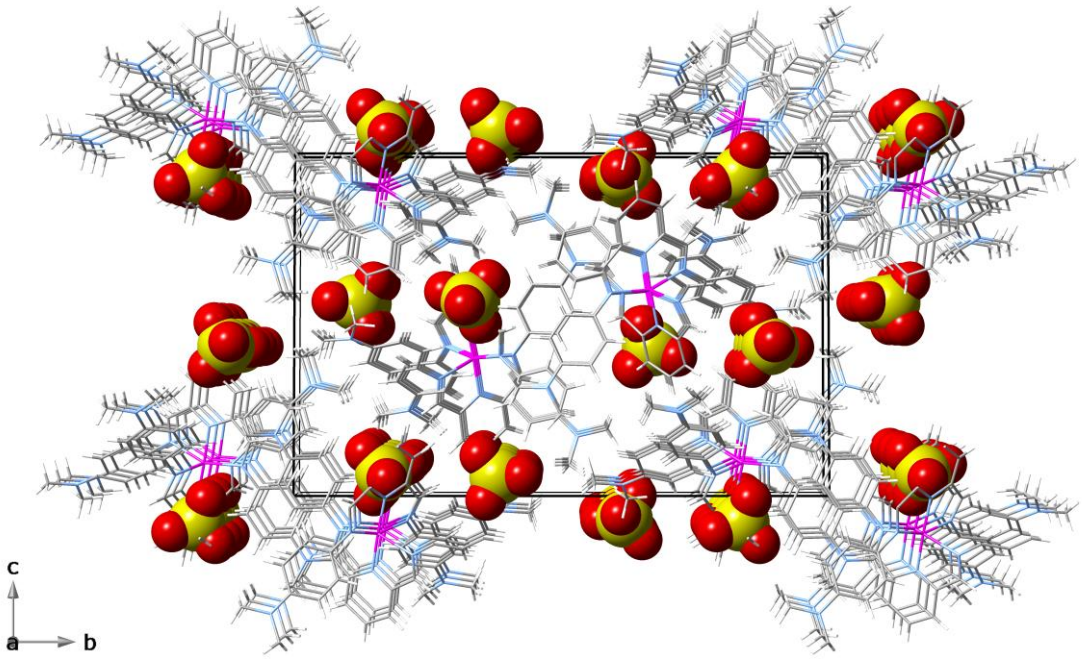

Figure III.S6 Perspective view of the crystal packing of **4** along the crystallographic *a* axis. The perchlorate anions are shown in a space filling representation.

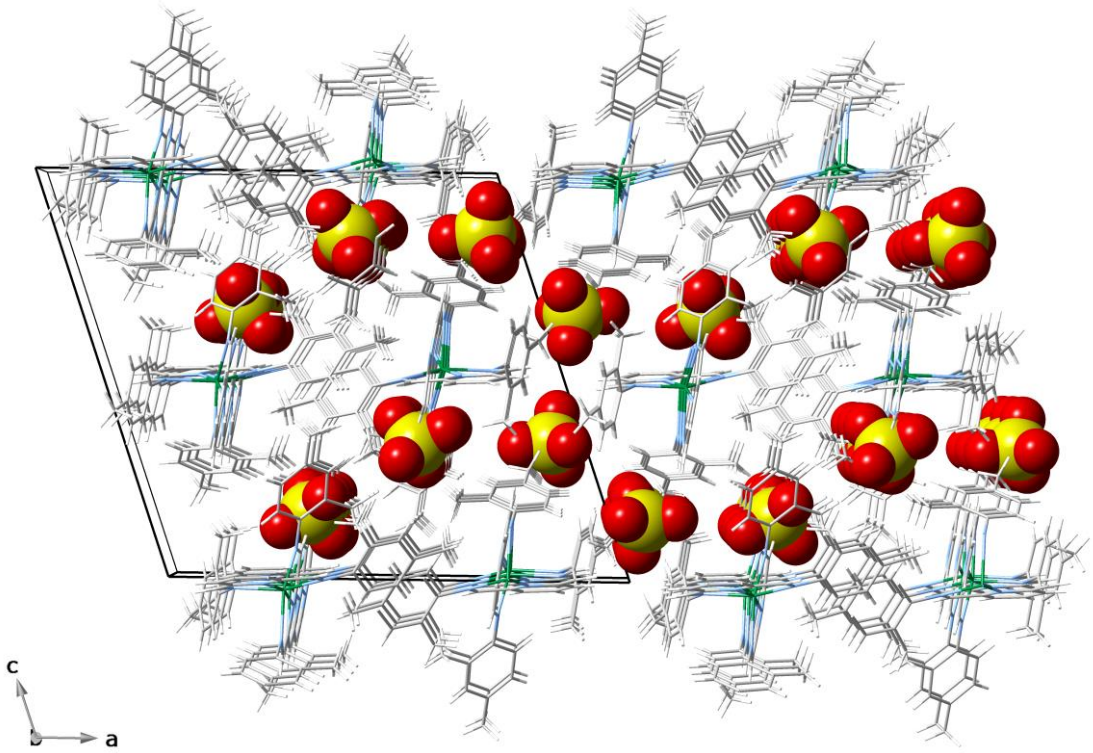

Figure III.S7 Perspective view of the crystal packing of **5** along the crystallographic *b* axis. The perchlorate anions are shown in a space filling representation.

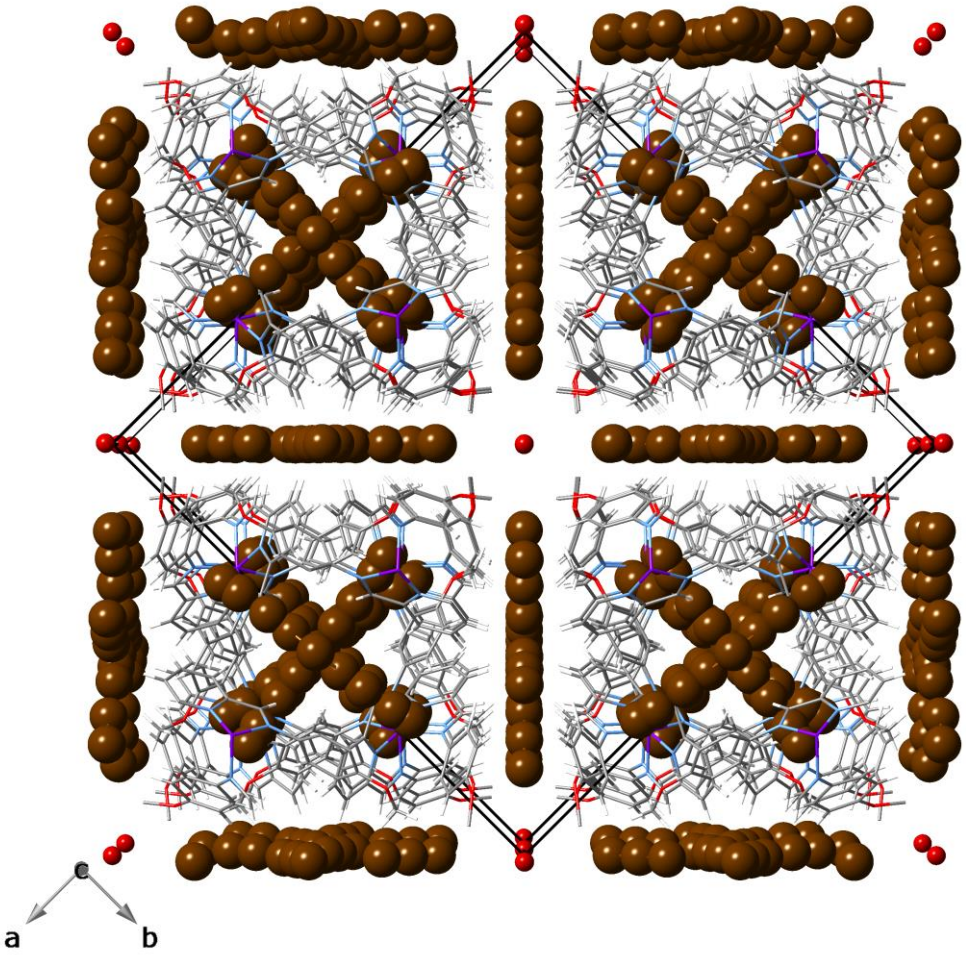

Figure III.S8 Crystal packing view of **2'** along the *c* axis. The tri- and pentabromide anions are shown in a space filling representation.

Theoretical calculations

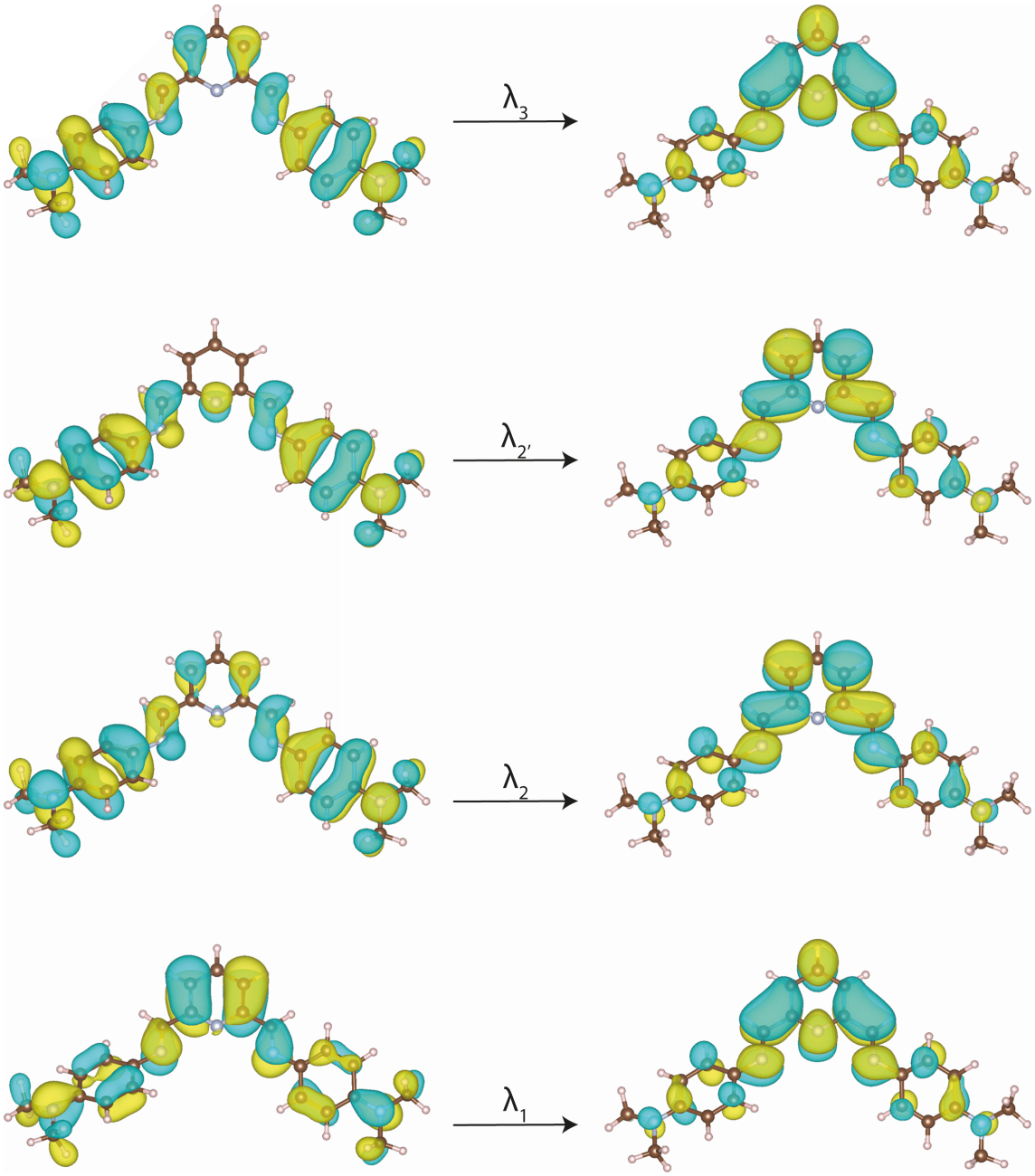

Figure III.**S9** Natural transition orbitals (NTOs) involved in the more significant electronic transitions for the optimized geometry of the 4-NMe_2PDI derivative in the LS state. Isosurfaces are shown setting cut-off at 0.02 e $bohr^{-3}$. Colour code: light blue, nitrogen; brown, carbon; pink, hydrogen.

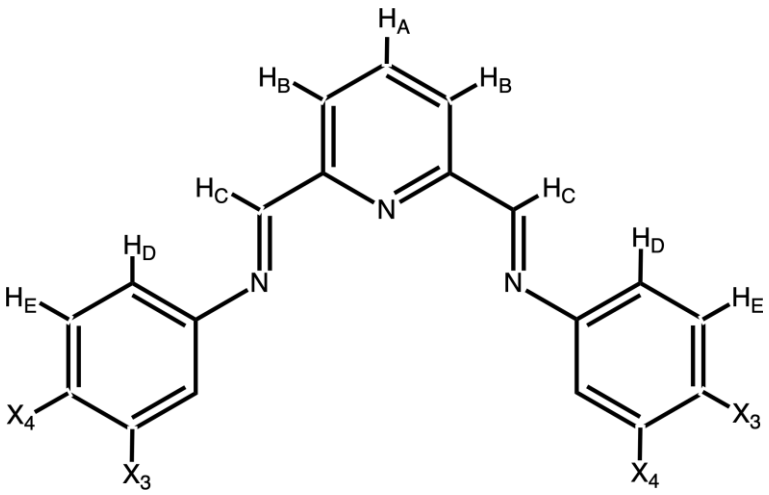

Scheme III.S1 A PDI ligand showing labelled hydrogen nucleus.

Table III.S1 Calculated ^{1}H NMR chemical shifts (δ, in ppm) for hydrogen nucleus, labelled according to Scheme III.S1, in the optimised geometries of 4-MePDI, 4-Me_2NPDI, 2,4-Me_2PDI ligands, and 4-MePDI built by removing 2-Me groups from the 2,4-Me_2PDI in its optimised geometries (4-MePDI*).

H site	δ (4-MePDI)	δ (4-Me_2NPDI)	δ (2,4-Me_2PDI)	δ (4-MePDI*)
H_A	8.23	8.07	8.23	8.23
H_B	7.78	7.56	7.79	7.79
H_C	8.71	8.87	8.60	8.60
H_D	7.32	7.70	7.09	7.08
H_E	7.46	6.75	7.28	7.42

Electrochemical measurements

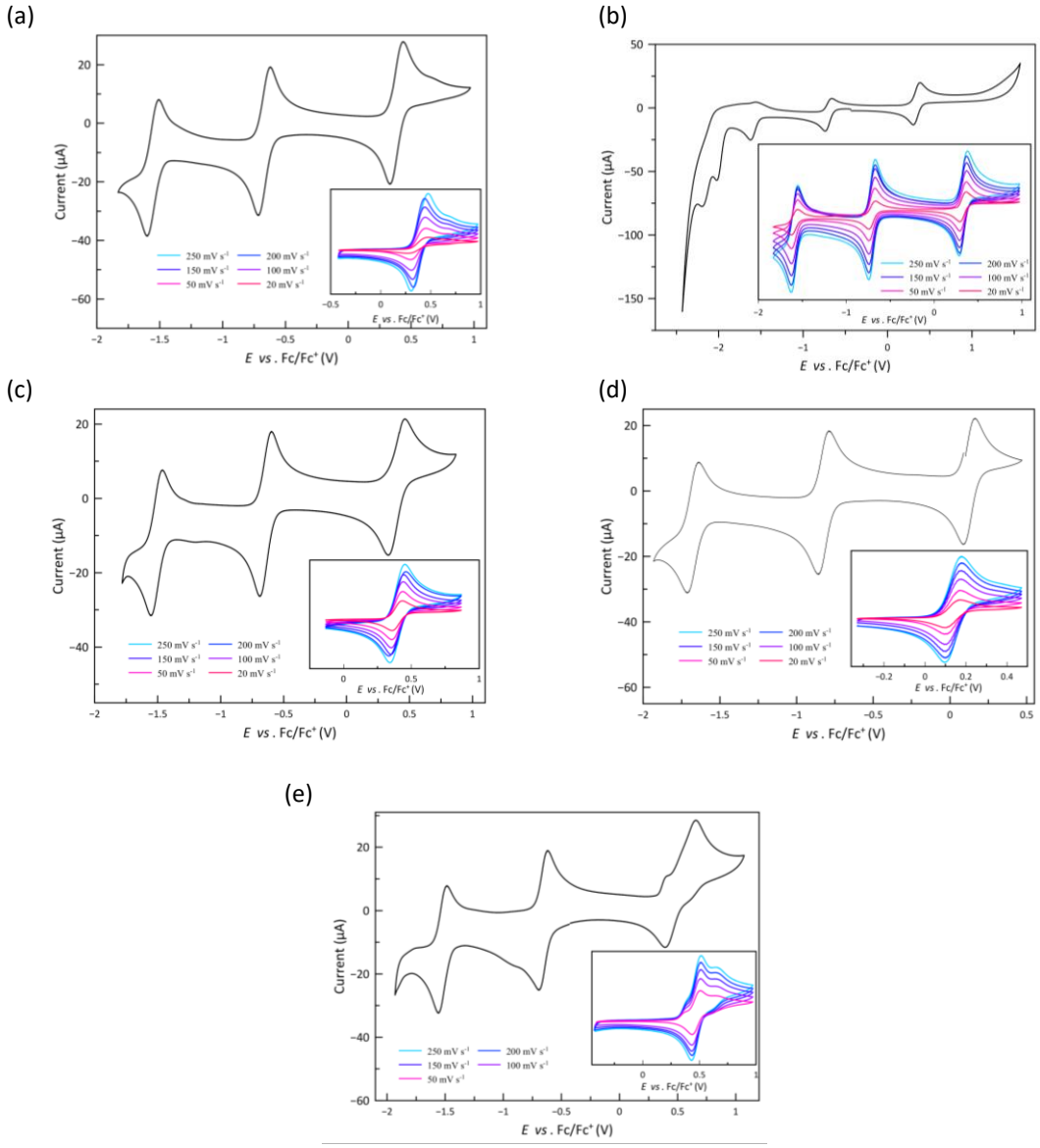

Figure III.S10 Cyclic voltammograms of **1**–**5** (a–e) in acetonitrile (0.1 M nBu$_4$NPF$_6$) at 25 ˚C and 200 mV s^{-1}. The insets show the cyclic voltammograms of the oxidation wave in the scan rate range of 20–250 mV s^{-1}.

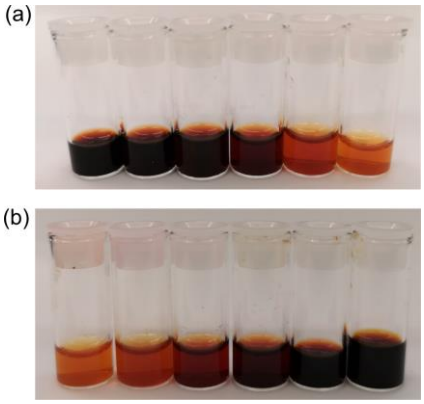

Figure III.S11 Pictures of aliquot solution samples taken at regular time intervals (from left to right) during the successive electrochemical oxidation (a) and reduction (b) of $[Co^{II}(4\text{-MeOPhPDI})_2]^{2+}$ in acetonitrile at 0 °C (E_{ox} = +1 V and E_{red} = 0 V, respectively).

Static and dynamic magnetic measurements

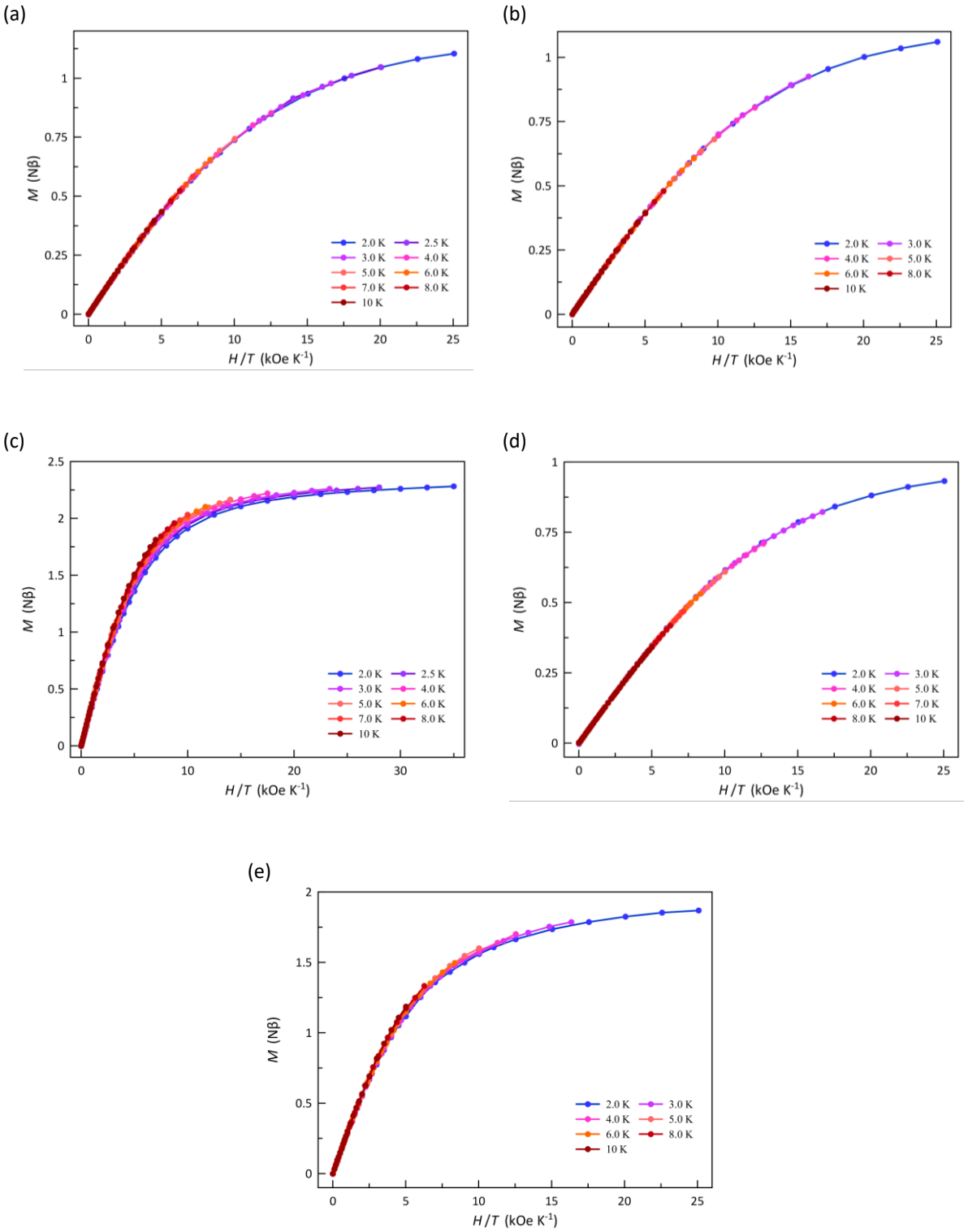

Figure III.S12 *M* vs *H*/*T* plots for **1** (a), **2** (b), **3** (c), **4** (d) and **5** (e) in the temperature range of 2.0–10 K. The solid lines are only eye-guides.

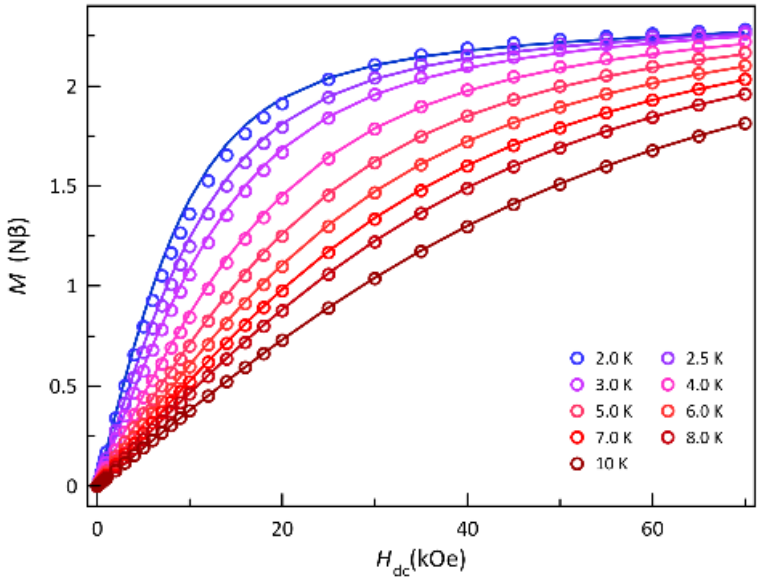

Figure III.S13 Field dependence of *M* curves for **3** in the range 2.0–10 K: experimental (**o**); best-fit curves (**–**) to the experimental data, see text.

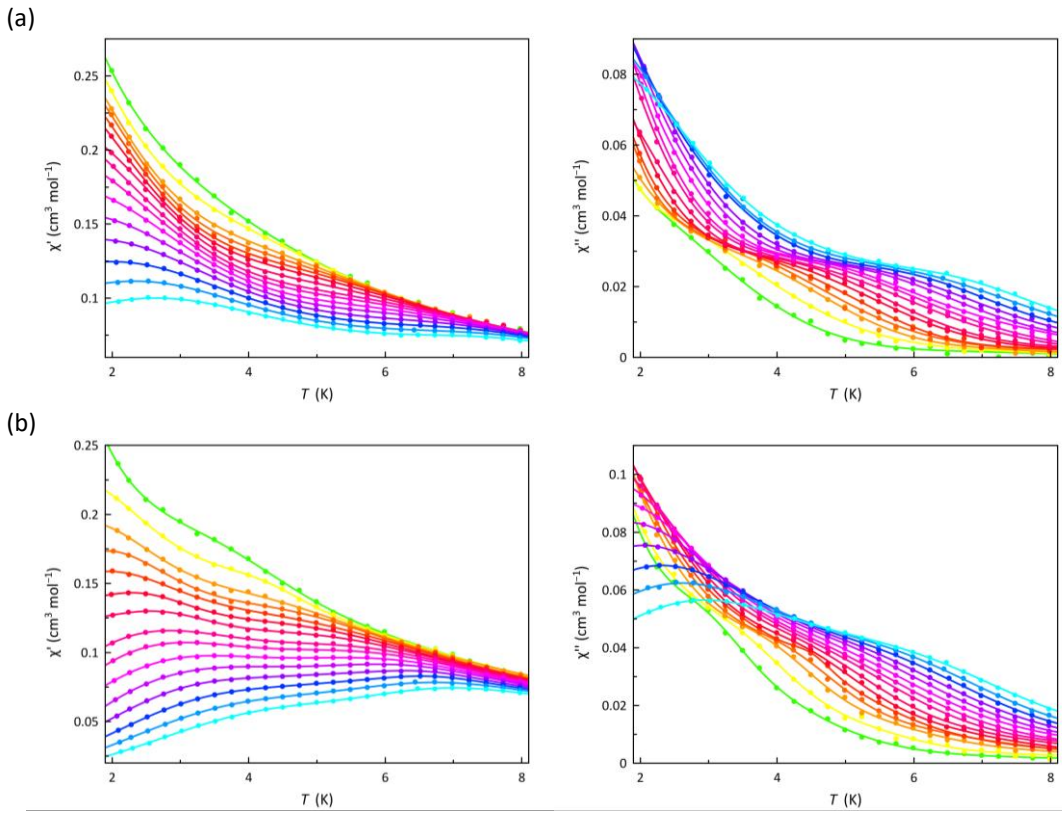

Figure III.S14 Temperature dependence of χ_M' (left) and χ_M'' (right) for **1** at a ±5.0 G oscillating field in the frequency range of 0.3–10.0 kHz (green to cyan) under applied static magnetic fields of 1.0 (a) and 2.5 kOe (b). The solid lines are only eye-guides.

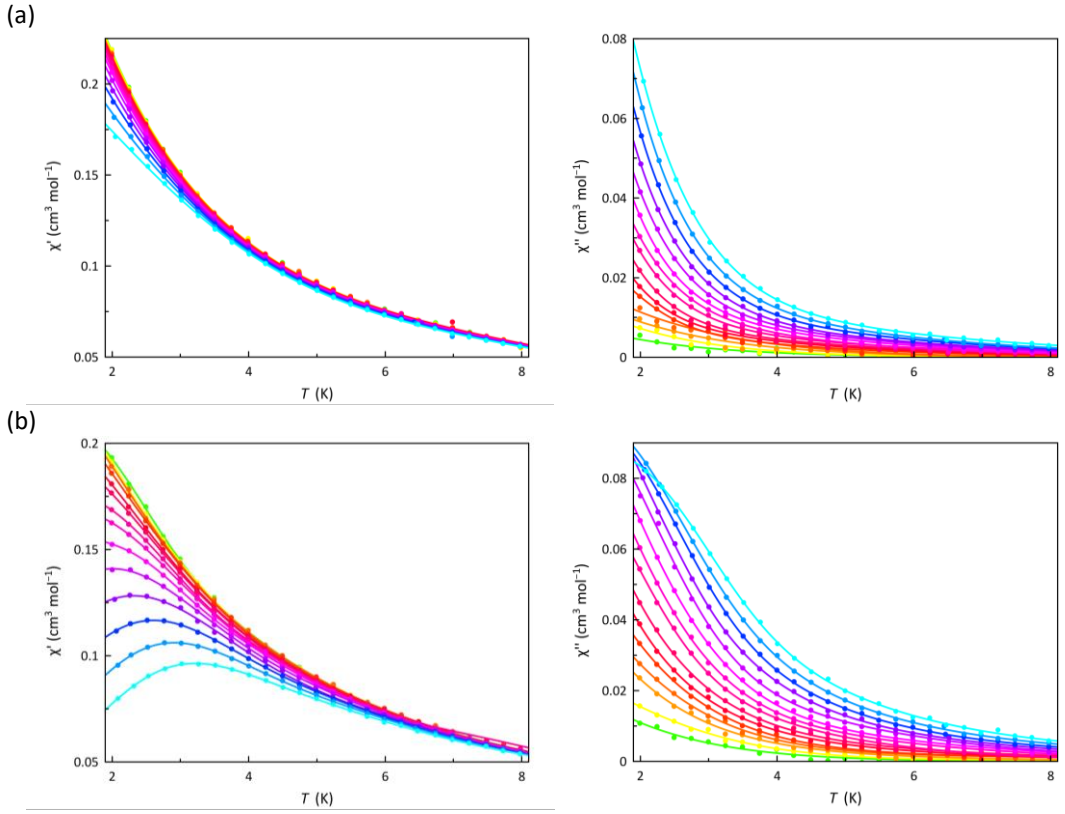

Figure III.S15 Temperature dependence of χ_M' (left) and χ_M'' (right) for **2** at a ±5.0 G oscillating field in the frequency range of 0.3–10.0 kHz (green to cyan) under applied static magnetic fields of 1.0 (a) and 2.5 kOe (b). The solid lines are only eye-guides.

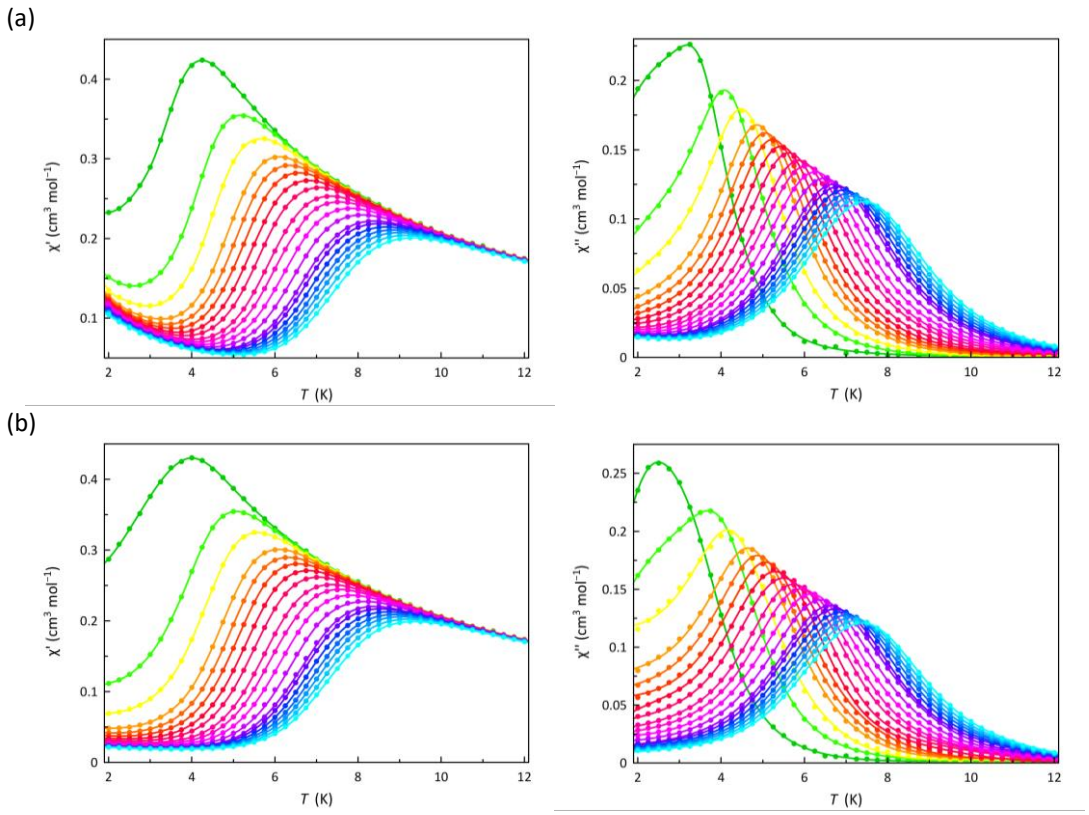

Figure III.S16 Temperature dependence of χ_M' (left) and χ_M'' (right) for **3** at a ±5.0 G oscillating field in the frequency range of 0.3–10.0 kHz (green to cyan) under applied static magnetic fields of 1.0 (a) and 2.5 kOe (b). The solid lines are only eye-guides.

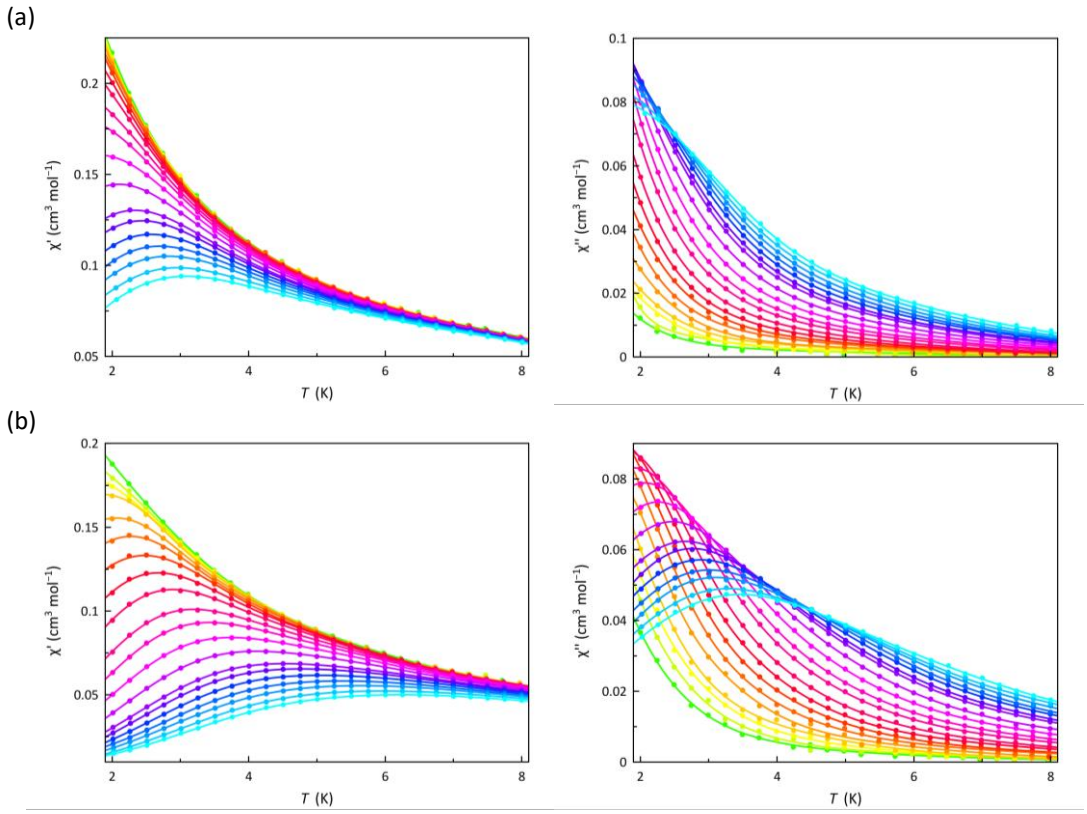

Figure III.S17 Temperature dependence of χ_M' (left) and χ_M'' (right) for **4** at a ±5.0 G oscillating field in the frequency range of 0.3–10.0 kHz (green to cyan) under applied static magnetic fields of 1.0 (a) and 2.5 kOe (b). The solid lines are only eye-guides.

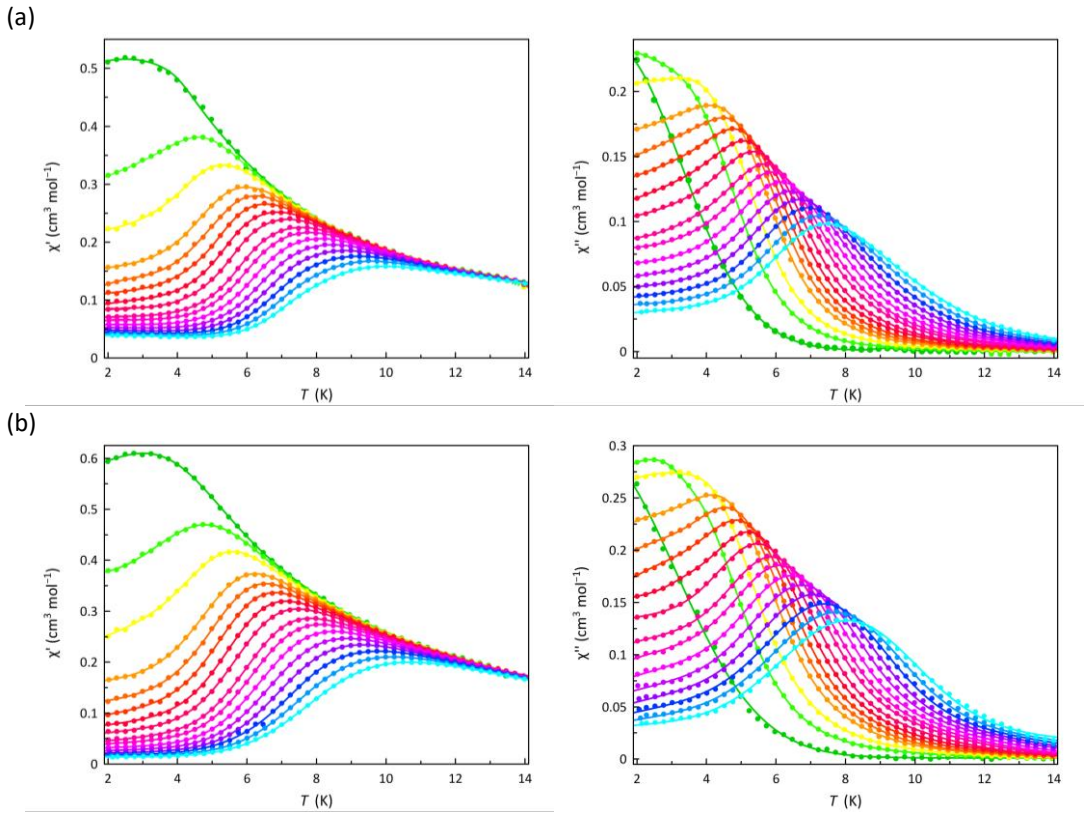

Figure III.S18 Temperature dependence of χ_M' (left) and χ_M'' (right) for **5** at a ±5.0 G oscillating field in the frequency range of 0.3–10.0 kHz (green to cyan) under applied static magnetic fields of 1.0 (a) and 2.5 kOe (b). The solid lines are only eye-guides.

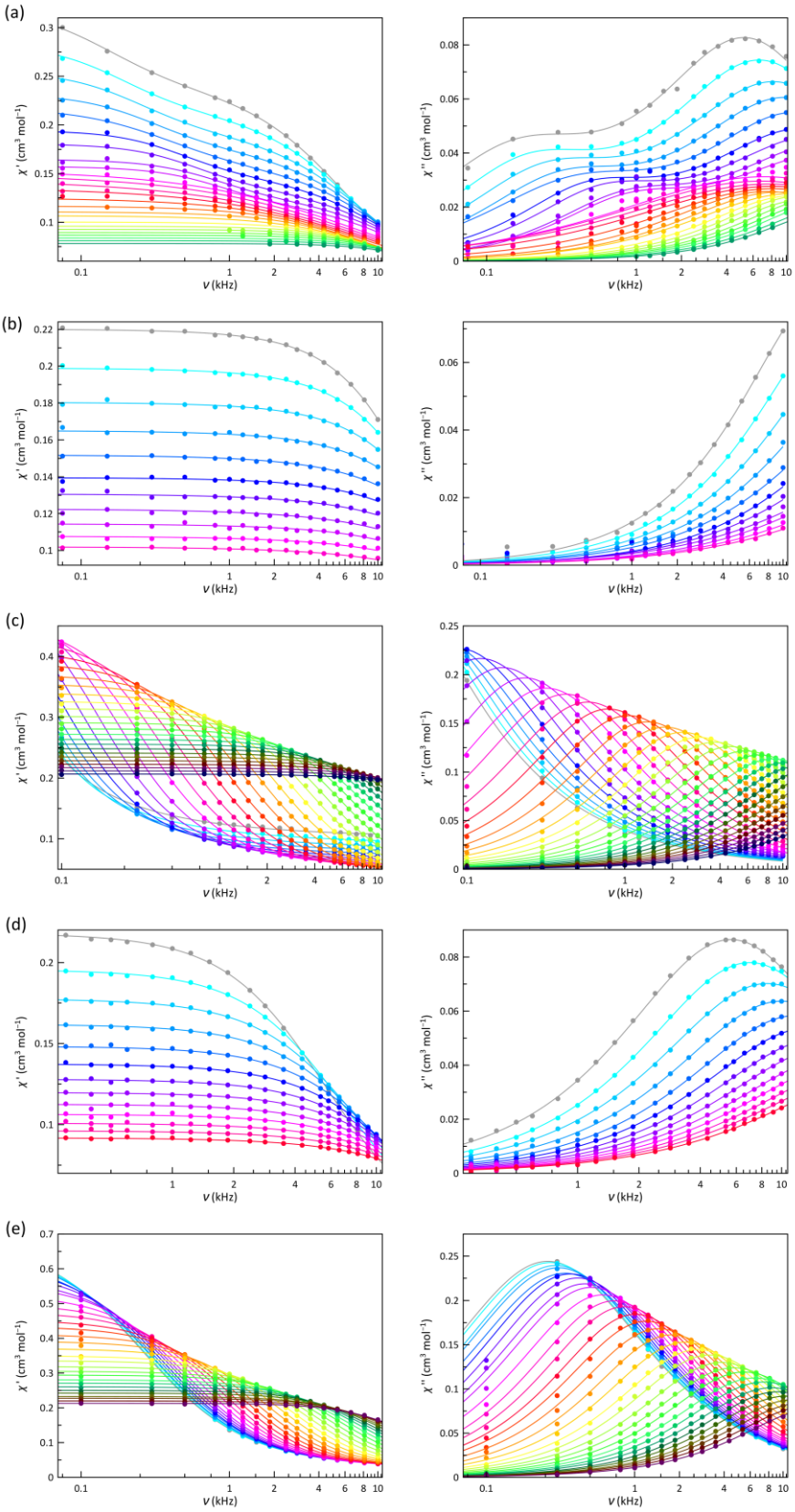

Figure III.S19 Frequency dependence of χ_M' (left) and χ_M'' (right) for **1** (a), **2** (b), **3** (c), **4** (d) and **5** (e) at a ±5.0 G oscillating field in the temperature range of 2.0–10 K under an applied static magnetic field of 1.0 kOe. The solid lines are the best fit curves simulated by using the generalized Debye model (see text).

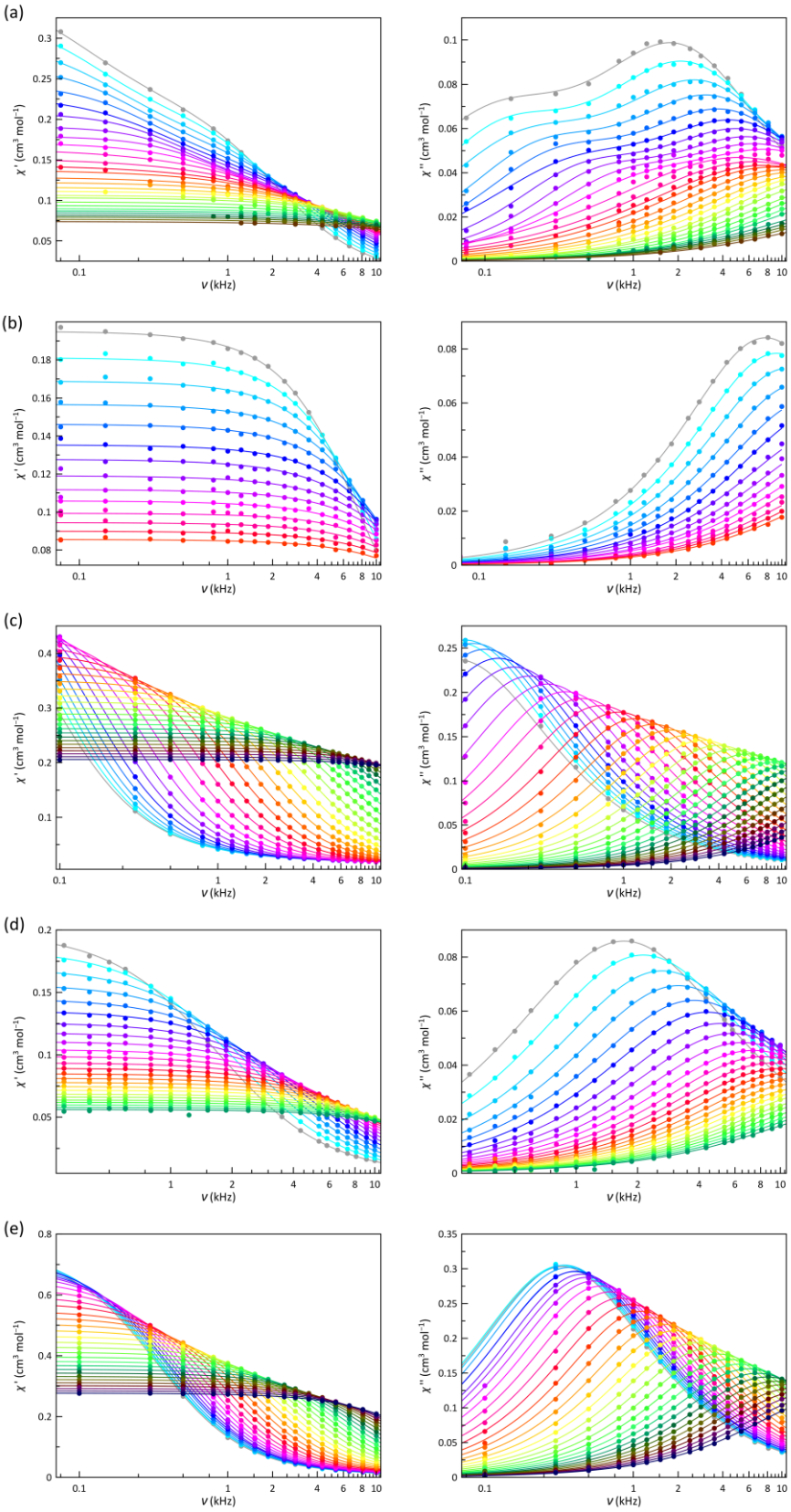

Figure III.S20 Frequency dependence of χ_M' (left) and χ_M'' (right) for **1** (a), **2** (b), **3** (c), **4** (d) and **5** (e) at a ±5.0 G oscillating field in the temperature range of 2.0–10 K under an applied static magnetic field of 2.5 kOe. The solid lines are the best fit curves simulated by using the generalized Debye model (see text).

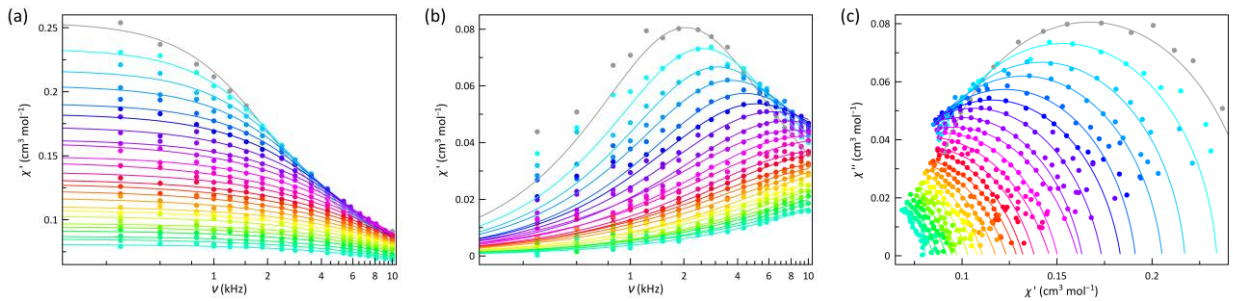

Figure III.S21 Frequency dependence of χ_M' (a) and χ_M'' (b) and Argand plots (c) for **2** in frozen acetonitrile at a ±5.0 G oscillating field in the temperature range of 2.0–8.0 K under an applied static magnetic field of 2.5 kOe. The solid lines are the best fit curves simulated by using the generalized Debye model (see text).

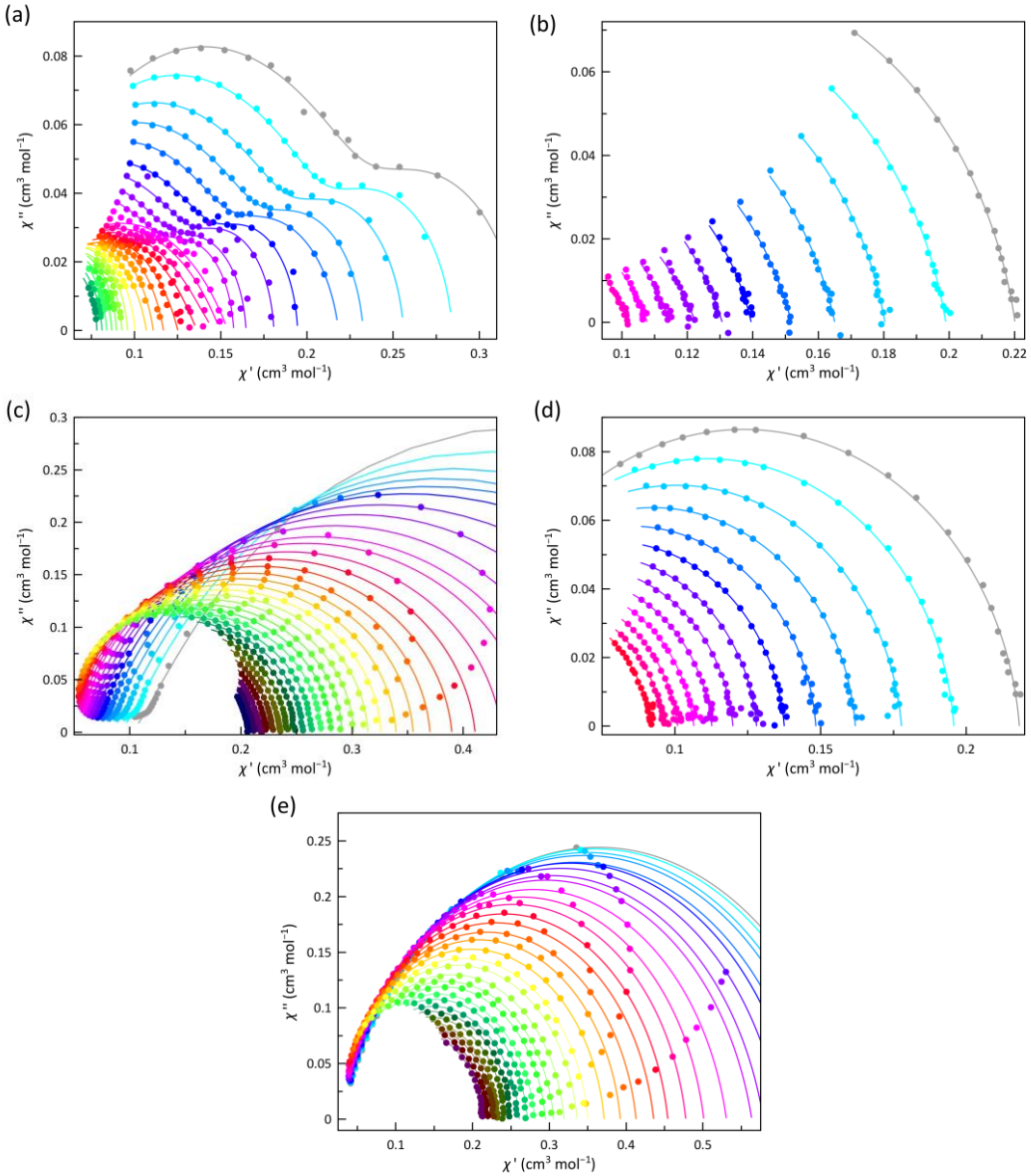

Figure III.S22 Argand plots for the calculated magnetic relaxation times (τ) of **1**–**5** (a–e) under an applied *dc* magnetic field of 1.0 kOe. The solid lines are the simulated curves by using the best-fit parameters obtained through the fitting of the χ_M' and χ_M'' *vs* ν plots by the generalized Debye model.

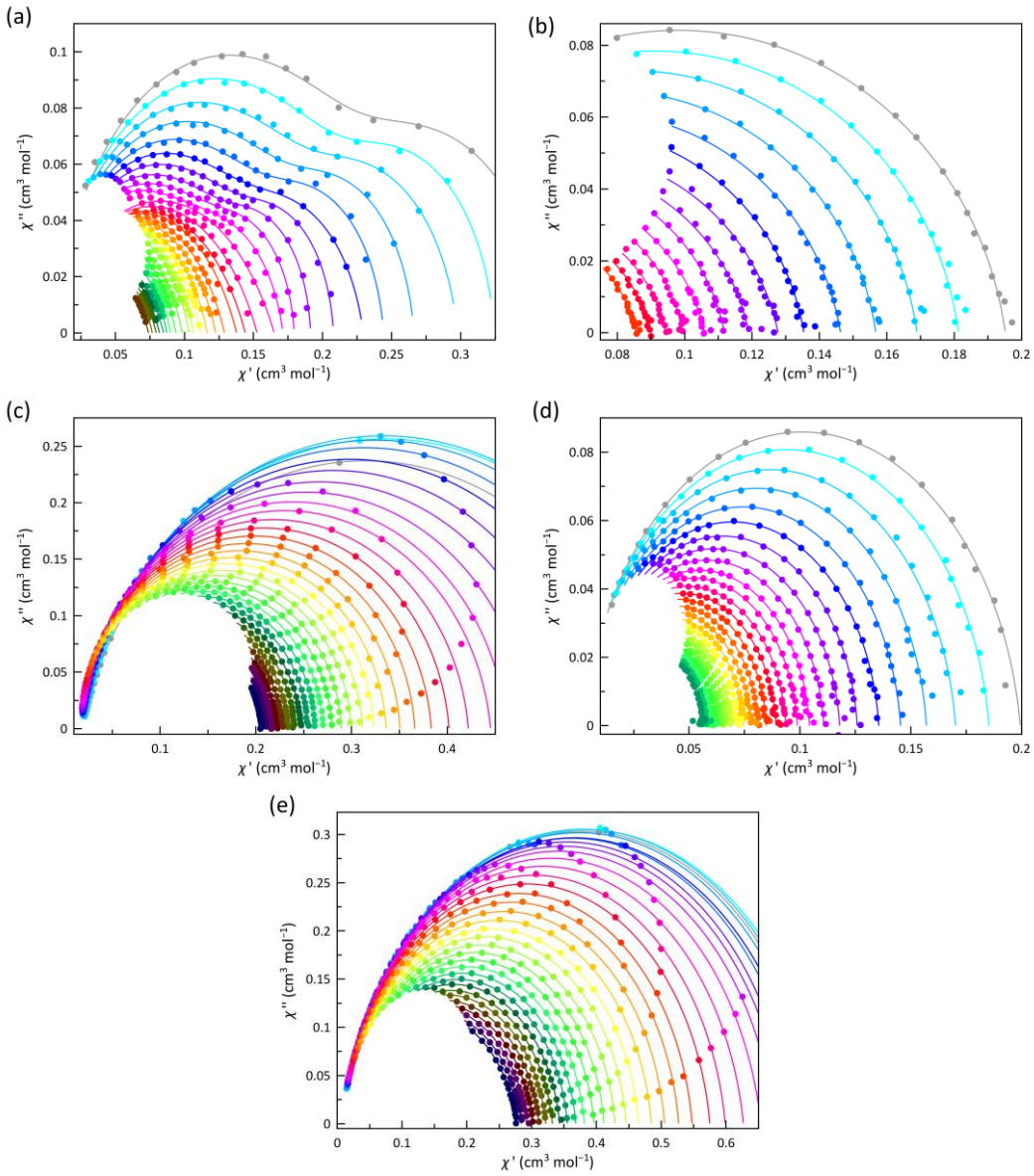

Figure III.S23 Argand plots for the calculated magnetic relaxation times (τ) of **1**–**5** (a–e) under an applied *dc* magnetic field of 2.5 kOe. The solid lines are the simulated curves by using the best-fit parameters obtained through the fitting of the χ_M' and χ_M'' *vs* ν plots by the generalized Debye model.

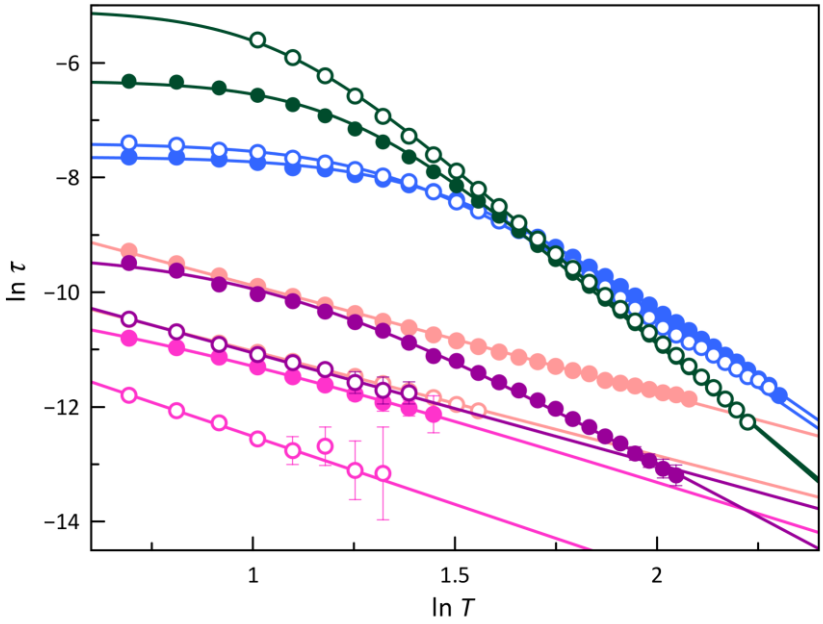

Figure III.S24 The lnτ *vs* ln*T* plots for the calculated magnetic relaxation times (τ) of **1** (purple), **2** (pink), **3** (green), **4** (pale pink) and **5** (blue) under applied *dc* magnetic fields of 1.0 (○) and 2.5 kOe (●). Dashed and solid lines are the best-fit curves (see text). Vertical error bars denote the standard deviation.

CHAPTER IV

LUMINESCENT SPIN CROSSOVER
MOLECULAR NANOMAGNETS

IV.1 – Background and Highlights

Molecular Opto-Spintronics (MOS) is a new emerging area of Molecular Spintronics (MS) that deals with optical manipulation and addressing molecular qubits, quantum gates and spintronic devices. Current efforts in this area are devoted to introducing additional photophysical[1–5] or photochemical[6–9] activities through ligand design to get optically addressable, multifunctional and multiresponsive magnetic molecules as new prototypes of spintronic nanodevices and quantum computers.[10–17] Compared with other chemical and electrochemical inputs, light offers a convenient, cleaner alternative to access and control a molecular spin system, which can be done remotely without difficulty and with high precision.[18]

Spin crossover (SCO) compounds constitute unique cases of photomagnetic molecules for MOS applications. The most illustrative synergetic interaction between SCO and light is the light-induced excited spin state trapping (LIESST) phenomenon observed in octahedral iron(II) complexes.[2,3] The SCO iron(II) centre has a diamagnetic $^1A_1$ LS state (S_{Fe} = 0) at low temperature, which is thermally induced to give a paramagnetic $^5T_2$ HS state (S_{Fe} = 2) at high temperature. By irradiating with green light (λ = 515 nm) in the temperature range of 4.0–50 K is possible to trap the metastable $^5T_2$ HS state (S_{Fe} = 2). The LIESST phenomenon has been widely studied in SCO iron(II) complexes and still represents a possibility to consider when designing SCO dynamic systems, but, unfortunately, a non-accessible option for cobalt-based SCO materials.

However, a barely explored synergetic effect between the SCO and light could take advantage of luminescent properties for reading spin state information. This proposal is based on the electronic absorption spectral change of the SCO complex upon the HS ↔ LS transition.[15] Thus, the spin state of SCO complexes will modulate the emission of the intrinsic luminophore ligands contained in them. The LS state is a better energy acceptor due to the strong absorption of the ligand-to-metal charge transfer (LMTC) transition, which is close in energy with the intraligand (IL) transition of the common luminophores (energy donors). This situation leads to an efficient overlap between the donor emission and acceptor absorption and, consequently, to the luminescence's quenching. That is not the case in the HS state, which generally features weak and less energetic absorptions, minimising or preventing the quenching of the luminophore's luminescence.

Along this line, luminescence was integrated into some SCO systems as an additional functional property.[19–21] The first report about the synergetic effect between SCO and luminescence was observed by Jiao on the mononuclear iron(II) compound $[Fe(bpp)_2](BF_4)_2$ [bpp = 2,6-bis-(pyrazol-1-yl)pyridine],[22] showing an abrupt enhancement of the luminescence in the solid state at the spin transition temperature. This result means that optical methods could perform the readout of the spin state, which is always an advantage for physical implementation.

Inside this context, spin crossover molecular nanomagnets (SCO/SMMs) would constitute a unique class of multistable photomagnetic molecules with potential applications in MOS and quantum computing nanotechnologies. The development of SCO/SMMs dynamic systems accessible by an optical method that can interact with the thermally induced spin transition and, eventually, on the slow magnetic relaxation may expand their applications to many interests like magneto-optical molecular switches and chemical sensors. But more importantly, this type of system could act as optically initialising qubits, which may integrate all-photonic logic circuits in the future.[23–25] In the search for new optically addressable SCO/SMM dynamic systems, we present in this chapter a set of cobalt(II)-PDI complexes with oligoacene (naphthalene and anthracene) luminophores as substituents (Scheme IV.1), which provide the extra luminescent response to the class of multifunctional and multiresponsive SCO/SMMs.

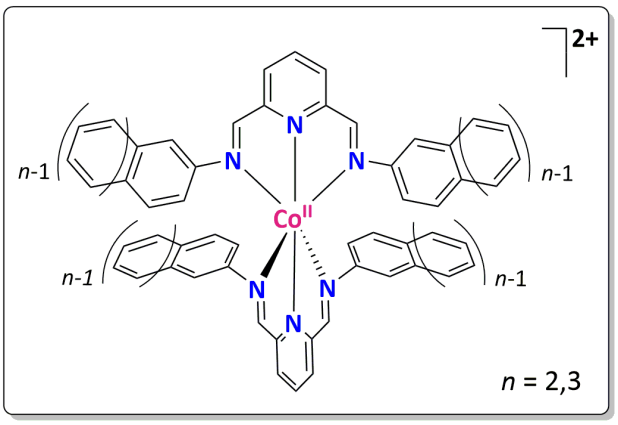

Scheme IV.1 General chemical structure of the oligoacene-substituted $[Co^{II}(PDI)_2]^{2+}$ complex cations in **1**–**3**.

Here we report on the syntheses, structural and spectroscopic characterisation, thermal stability and sorption properties, and static and dynamic magnetic properties of mononuclear cobalt(II) complexes with the novel luminescent 2-naphthyl-, and 2-anthryl-disubstituted PDI ligands of general formula $[Co^{II}L_2](ClO_4)_2{\cdot}xSolv$ [L = 2,6-bis(*N*-2-naphthylformimidoyl)pyridine (2-NaphPDI), Solv = H_2O with x = 1.5 (**1**) and 0 (**1'**) or S = MeCN with x = 2 (**2**), 1 (**2'**), and 0 (**2''**); L = 2,6-bis(*N*-2-anthrylformimidoyl)pyridine (2-AnthPDI), Solv = $MeCO_2Et$ with x = 1.5 (**3**)], as well as a preliminary study of their solvent-dependent photophysical properties in both solution and in the solid state. Hence, the two related series of cobalt(II)-2-NaphPDI complexes here studied constitute a unique solvatomorphic family of SCO/SMMs featuring a solvato-tuning of the thermal-assisted spin transition, the field-induced slow magnetic relaxation and luminescence in solid and solution, proposing then a proof-of-concept design of a luminescent spin solvato-switch.

IV.2 – Ligand Design and Synthetic Strategy

The synthetic experience gathered along Chapters II and III were used to design this fourth one. The novelty of this new set of compounds is the attachment of classic luminophore groups to the imine nitrogen atoms of the PDI ligands. The substituent groups selected for this study were classical luminophore naphthalene and anthracene, broadly used in photophysical studies (Scheme IV.1). At first glance, it is a simple idea from the synthetic point of view, but that can bring promising results to our SCO/SMM dynamic systems on the road toward multifunctional and multiresponsive photomagnetic molecules for MS and MOS.

Moreover, cooperative effects on the SCO behaviour are expected when the supramolecular interactions in the crystal packing are maximised. One efficient way to improve strong intermolecular contacts is through π-π stacking interactions. That being so, by introducing large extended polycyclic aromatic rings as substituents on the PDI ligands, such as oligoacenes, abrupt SCO behaviours may arise in their Co(II) complexes. Furthermore, oligoacenes possess a well-recognised and rich photochemical reactivity, including uni- and bimolecular reactions.[26–34] For instance, the thermally reversible intermolecular [4+4] photodimerisation of anthracene and its 1- and 2-substituted derivatives through the carbon atoms at the 9,10 and 9',10' (*meso*) positions of the central benzene rings is one of the oldest known photochemical reactions.[31] Although naphthalene is much less photoreactive than anthracene, some 1- and 2-substituted derivatives also undergo intermolecular [4+4] photodimerisation at the 1,4 and 1',4' (*a*) carbon atoms of the substituted benzene rings.[32,33] In that case, a photomagnetic switch is expected upon conversion to the [4+4] photocycloaddition oligo- or polymeric products, provided that the π-stacked oligoacene substituents of the mononuclear complexes are favourably oriented in the solid state.[34–39]

The 2-NaphPDI and 2-AnthPDI ligands were prepared from the straightforward condensation of pyridine-2,6-diformaldehyde and 2-naphthyl or 2-anthrylamine (1:2 molar ratio) in ethanol under catalytic acid conditions (see IV.10 – Experimental Section). **1** and **2** were synthesised from the stoichiometric reaction of 2-NaphPDI with cobalt(II) perchlorate hexahydrate (2:1 molar ratio) in acetonitrile. On the other hand, the rate of reaction of 2-AnthPDI with cobalt(II) perchlorate is very slow. So, **3** was alternatively prepared through the *in situ* template reaction of pyridine-2,6-diformaldehyde with cobalt(II) perchlorate hexahydrate and the 2-anthrylamine. **2** and **3** were isolated as X-ray quality single crystals in good yields (65–92%) by slow diffusion of ethyl acetate in an acetonitrile/chloroform 2:1 (v/v) solvent mixture in a glass tube. In contrast, single crystals of **1** were obtained by slow evaporation of an acetonitrile/chloroform/ethyl acetate solvent mixture. The ligands and their complexes were characterised by elemental (C, H, N) and thermogravimetric analyses (TGA), together with Fourier-transform infrared (FT-IR), electronic absorption (UV/Vis), and electron paramagnetic resonance (EPR) spectroscopies (see IV.10 – Experimental Section).

IV.3 – Thermal Stability

Crystals of **1** were air-stable at room temperature, but occasionally, they were obtained together with the anhydrous derivative **1'** as a side product, as shown by the PXRD patterns (Figure IV.S1a). Unlike **1**, crystals of **2** were not stable when separated from the mother liquor, and they rapidly loosed crystallisation acetonitrile molecules in air at room temperature to afford the partially desolvated derivative **2'**. In fact, the TGA profile of crushed crystals of **2** under a dry N_2 atmosphere showed a gradual small mass loss (*ca*. 1%) from room temperature to around 75 °C followed by an abrupt large mass loss around 140 °C (4%) that approximately correspond to the release of 0.25 and 1 MeCN molecules, respectively (solid green line in Figure IV.1b). In contrast, the TGA profile of a sample of **1** under a dry N_2 atmosphere showed a single abrupt mass loss (3%) at 135 °C corresponding to the release of 1.5 H_2O molecules (solid pink line in Figure IV.1a).

The partially or totally desolvated derivatives **1'**, **2'**, and **2''** were then prepared in pure form by thermal desolvation of the

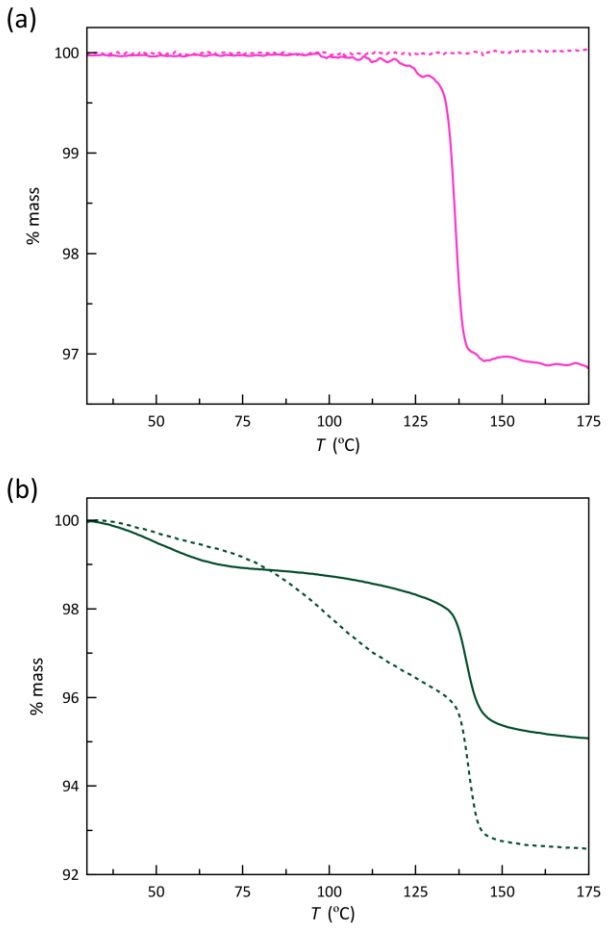

Figure IV.1 TGA profiles of **1** (a) and **2** (b) under N_2 atmosphere (solid red and green lines, respectively). The TGA profiles after one day of exposition of **1'** and **2''** under saturated solvent atmosphere are also shown for comparison (dotted red and green lines, respectively).

precursors **1** and **2** following a slow heating and cooling cycle (3 h + 3 h) between room temperature and 90 (**1'** and **2''**) and 50 °C (**2'**). Crystals of **1'** and **2'**, suitable for single-crystal X-ray diffraction (XRD), were obtained by embedding the crystals of **1** and **2** in paratone before the heating cycle. Unfortunately, when trying to obtain **2''** under the same conditions, crystals were fragmented and became opaque. Each solvatomorphic pair, **1/1'** and **2/2'**, shows similar powder diffractograms, suggesting a slight variation in the molecular and crystal structures upon the desolvation (Figures IV.S1a and b). However, the two distinct anhydrous derivatives **1'** and **2''** show a completely different pattern and, therefore, they are not isostructural (Figures IV.S1a and b). Single-crystal XRD confirmed the chemical identity of the two solvatomorphic pairs **1/1'** and **2/2'** (see IV.10 – Experimental Section).

IV.4 – Description of the Structures

The two members of each solvatomorphic pair, **1/1'** and **2/2'**, are isostructural and they crystallise in the triclinic *P*–1 and monoclinic $P2_1/n$ space groups, while **3** crystallises in the triclinic *P*–1 space group (Table IV.1). The desolvated derivatives **1'** and **2'** have smaller unit cell dimensions than their solvated precursors **1** and **2** (*a*, *b* and *c*; Table IV.1). This feature announces minor but non-negligible changes in the molecular and crystal structures for each pair of solvatomorphs upon total (**1/1'**) or partial (**2/2'**) loss of the crystallisation solvent molecules, as discussed below.

The crystal structures of **1/1'**, **2/2'** and **3** consist of mononuclear bis(chelating) cobalt(II) complex cations, $[Co^{II}L_2]^{2+}$ (Figures IV.2–4), and counterbalancing perchlorate anions, together with a variable amount of water (**1**), acetonitrile (**2/2'**) or ethyl acetate (**3**) molecules of crystallisation (Figures IV.5–7 and IV.S5–S7).

Molecular structures. The complexes in **1/1'**, **2/2'** and **3** are composed of two meridional tridentate *N*-oligoacene-substituted PDI ligands coordinated to the Co^{II} ion through the pyridine and imine nitrogen atoms to form a distorted CoN_6 octahedron core (Figures IV.2–4). They exhibit a distorted C_{2v} molecular symmetry, depending on the nature of the aromatic oligoacene ligand substituent and the crystallisation solvent molecule, with two almost perpendicularly oriented ligands.

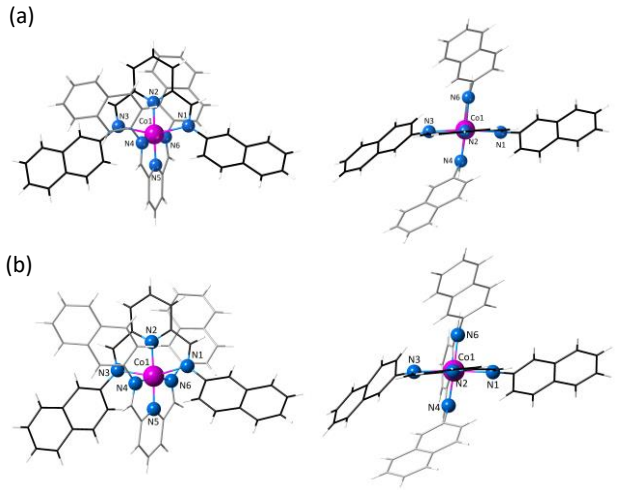

Figure IV.2 Front (left) and top (right) views of the cationic mononuclear cobalt(II) units of **1** (a) and **1'** (b) with the atom numbering scheme for the first coordination sphere of the metal atom. The ligand backbones are drawn in grey and black colours for clarity. The pink cobalt atoms correspond to the LS configuration.

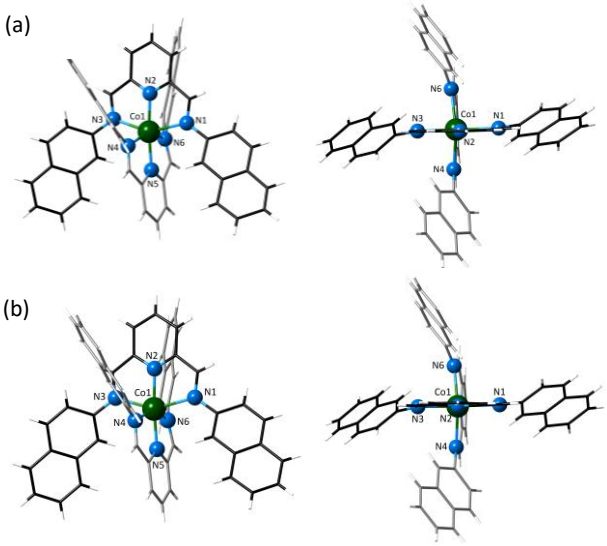

Figure IV.3 Front (left) and top (right) views of the cationic mononuclear cobalt(II) units of **2** (a) and **2'** (b) with the atom numbering scheme for the first coordination sphere of the metal atom. The ligand backbones are drawn in grey and black colours for clarity. The green cobalt atoms correspond to the HS configuration.

Table IV.1 Summary of Crystallographic Data for **1/1'**, **2/2'** and **3**

	1	**1'**	**2**	**2'**	**3**
Formula	$C_{54}H_{38}Cl_2CoN_6O_{9.5}$	$C_{54}H_{38}Cl_2CoN_6O_8$	$C_{58}H_{44}N_8O_8Cl_2Co$	$C_{56}H_{41}N_7O_8Cl_2Co$	$C_{76}H_{58}Cl_2CoN_6O_{11}$
M (g mol^{-1})	1055.78	1028.77	1110.87	1069.82	1361.17
Crystal system	Triclinic	Triclinic	Monoclinic	Monoclinic	Triclinic
Space group	*P*–1	*P*–1	$P2_1/n$	$P2_1/n$	*P*–1
a (Å)	10.1031(7)	10.0472(10)	14.2213(4)	14.2199(4)	10.5503(4)
b (Å)	15.8963(12)	14.7304(14)	26.1256(8)	25.8669(8)	18.1442(7)
c (Å)	17.8291(13)	18.0865(17)	14.4718(4)	14.3705(5)	20.0744(8)
α (°)	113.837(2)	113.171(3)	90	90	65.327(1)
β (°)	94.479 (2)	91.053(3)	103.349(1)	102.872(1)	83.343(1)
γ (°)	99.323(2)	104.024(3)	90	90	85.933(1)
V (Å^3)	2551.64	2368.03	5231.58	5152.99	3467.33
Z	2	2	4	4	2
T (K)	150	150	150	150	150
R_1[a] [$I > 2\sigma(I)$]	0.0696	0.0875	0.0827	0.0786	0.0791

[a] $R_1 = \sum(|F_o| - |F_c|)/\sum|F_o|$.

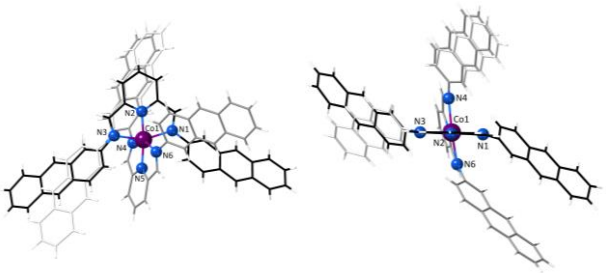

Figure IV.4 Front (left) and top (right) views of the cationic mononuclear cobalt(II) units of **3** with the atom numbering scheme for the first coordination sphere of the metal atom. The ligand backbones are drawn in grey and black colours for clarity, while the statistically disordered anthryl groups are shown in white colour. The purple cobalt atoms correspond to a mixed LS/HS configuration.

The two crystallographically independent ligands of each cobalt(II) unit are not planar, as reflected by the average values of the dihedral angle (Φ) between the 2,6-pyridinediimine fragment and the oligoacene aromatic substituents (Table IV.2; Figures IV.2–4, right). The loss of planarity could be associated with the steric hindrance between the imine hydrogen atoms and the 1- or 3-hydrogen atoms from the oligoacene groups. In fact, the 2-naphthyl substituents adopt a distinct *cis* (**1**/**1'**) or *trans* (**2**/**2'**) configuration with respect to the central pyridinediimine fragment by free rotation around the single C–N bond [φ = 34.7–50.9 (**1**)/37.0–53.7 (**1'**) and 144.7–147.2 (**2**)/144.3–145.8° (**2'**); Table IV.2], giving rise to either open (**1**/**1'**) or closed (**2**/**2'**) ligand forms for each pair of solvatomorphs (Figures IV.2 and 3, left). In contrast, two of the 2-anthryl substituents in **3** adopt a *cis* configuration [φ = 35.2 and 42.3°; Table IV.2], while the other two substituents exhibit a statistically disordered *trans/trans* or cis/*trans* conformations [φ = 151.3/152.9 and 151.9/139.5° (**2'**); Table IV.2] (Figure IV.4, left).

At this point, it should be possible to predict the spin state of each mononuclear cobalt(II) complex by analysing the mean axial (R_{ax}), equatorial (R_{eq}) and average (R) metal-ligand bond distances (Table IV.2). Hence, the solvatomorphic pair **1**/**1'** presents short Co–N bond lengths typical of a LS Co^{II} ion (Table IV.2), whereas long Co–N bond lengths are observed for the solvatomorphic pair **2**/**2'** (Table IV.2), suggesting the occurrence of the predominant HS configuration. On the other hand, a mixed proportion of LS and HS Co^{II} complexes resulting from an incomplete spin transition should be expected for **3**, which presents intermediate Co–N bond lengths (Table IV.2).

As occurs for the Co^{II}-PDI complexes presented in the past two chapters, the coordination environment at **1**/**1'**, **2**/**2'** and **3** is an axially compressed distorted octahedron composed of four imine nitrogen atoms (N_{im}) on the equatorial plane and two pyridine nitrogen atoms (N_{py}) occupying the axial positions. Again, the pyridinediimine fragment restrains shorter Co^{II}-N_{py} distances upon its complexation in a tridentate mode. Besides, the PDI ligands induce a severe ruffling distortion on the octahedron, deviating the N_{im} donor atoms from the equatorial mean plane. Such distortion correlates with the increasing proportion of HS Co^{II} ion, as reflected by the larger values of the mean out-of-plane N_{im} displacement (δ; Table IV.2).

Crystal structures. In the crystal lattice, the mononuclear units interact through intermolecular parallel-displaced ("face-to-face") π-stacking contacts between the neighbouring naphthyl or anthryl groups (Figures IV.S2–S4), leading to either π-bonded layer arrays of ladder-type double chains (**1**/**1'** and **3**) running along the crystallographic *a* axis or square grid-type layers (**2**/**2'**) growing within the *ac* plane (Figures IV.S5–S7). The intermolecular separation between the centroids of facing benzene rings and the dihedral angle between their mean planes are below the limiting values for face-to-face π-stacking interactions (h < 4.4 Å and θ < 30°).

A stacked array of adjacent cationic layers occurs along the crystallographic *b* axis, leading to small interlayer spaces occupied by half of the perchlorate anions (**1**/**1'** and **2**/**2'**) or the ethylacetate molecules of crystallisation (**3**) (Figures IV.S5–S7). The shortest intrachain (**1**/**1'** and **3**) and intralayer (**2**/**2'**) intermetallic distances are 10.103 (**1**)/10.047 (**1'**) and 10.550 (**3**), and 9.157 (**2**)/9.134 Å (**2'**), while the shortest interlayer intermetallic separation are 9.381 (**1**)/8.920 (**1'**), 11.481 (**2**)/11.443 (**2'**), and 12.267 Å (**3**). This situation evidences an overall both intra- and interlayer shrinkage effects for each pair of solvatomorphs **1**/**1'** and **2**/**2'** upon total or partial removal of

Table IV.2 Selected structural data for **1**/**1'**, **2**/**2'** and **3**

	1	**1'**	**2**	**2'**	**3**
R_1(Co–N_{im})[a] (Å)	2.248	2.227	2.247	2.243	2.242
R_2(Co–N'_{im})[a] (Å)	1.996	2.000	2.233	2.232	2.108
R_{ax}(Co–N_{py})[b] (Å)	1.894	1.896	2.032	2.032	1.973
R_{eq}[c] (Å)	2.122	2.114	2.240	2.238	2.175
R[d] (Å)	2.046	2.041	2.171	2.169	2.108
Δ_R[e]	0.111	0.107	0.096	0.095	0.096
δ_R[f]	0.119	0.107	0.006	0.006	0.062
N_{im}–Co–N'_{im}[g] (°)	86.2	85.0	93.6	93.6	84.6
	98.2	98.9	93.9	93.8	101.7
N_{py}–Co–N_{py}[h] (°)	177.8	175.5	173.7	174.5	173.2
δ[i] (Å)	±0.419	±0.393	±0.572	±0.567	±0.503
Φ[j] (°)	81.1	80.0	89.7	89.8	76.6
φ[k](°)	34.7	37.0	147.2	145.8	30.8
	50.9	53.7	144.7	144.3	44.65

[a]Average cobalt equatorial bond distances with the imine-nitrogen atoms from each ligand. [b]Average cobalt axial bond distances with the pyridine-nitrogen atoms from the two ligands. [c]Mean cobalt-nitrogen equatorial bond distances defined as $R_{eq} = (R_1 + R_2)/2$. [d]Mean cobalt-nitrogen bond distances defined as $R = (R_1 + R_2 + R_3)/3$. [e]Axial distortion parameter defined as $\Delta_R = (R_{eq} - R_3)/R$. [f]Rhombic distortion parameter defined as $\delta_R = (R_1 - R_2)/R_{eq}$. [g]Average cobalt equatorial bond angles with the two facing imine pyridine-nitrogen atoms from the two ligands. [h]Average cobalt axial bond angles with the pyridine-nitrogen atoms from the two ligands. [i]Average deviations of the imine-nitrogen atoms from the mean metal equatorial plane. [j]Dihedral angle between the mean planes of the pyridinediime ligand fragments from the two ligands. [k]Average torsion angle for the naphthylimine ligand fragments from the two ligands.

the crystallisation water and acetonitrile molecules, which accounts for the aforementioned reduction of the unit cell volume for the **1'** and **2'** derivatives.

The different supramolecular crystal packing features give rise to either small centrosymmetric (**1**/**1'** and **3**) or large non-centrosymmetric (**2**/**2'**), four-membered metallacyclic double pockets within each ladder-type double chain or square grid-type layer, which are filled by half (**1**/**1'** and **2**/**2'**) or all (**3**) of the perchlorate anions like in an "egg-box" and further stabilised by electrostatic interactions (Figures IV.S5–S7). The partially disordered water and remaining ethyl acetate molecules of crystallisation in **1** and **3**, respectively, are located out of these intraladder hydrophobic pockets (Figures IV.5a and IV.7), establishing weak to moderate hydrogen bonding interactions among each other and with the inner perchlorate anions [Ow–H···Ow = 2.623–2.685 Å and Ow–H···$OClO_3$ = 2.877 Å] or between the carbonyl acetate and the imine groups from the ligand counterparts [C–H···OCMeOEt = 2.498 Å]. The overall size and saucer-type shape of these four-membered metallacyclic double pockets are maintained upon total loss of the water molecules in **1'** (Figure IV.5b). Instead, the two distinct crystallisation acetonitrile molecules in **2** are alternately (up and down) placed within these intralayer hydrophobic pockets with their nitrile groups oriented toward the inner and outer sides, establishing very weak hydrogen bonding interactions with the naphthyl rings [C–H···N = 3.236–3.530 Å] (Figure IV.6a). This latter acetonitrile molecule is selectively lost upon partial desolvation without altering the pocket's overall size and calixarene-like shape in **2'** (Figure IV.6b).

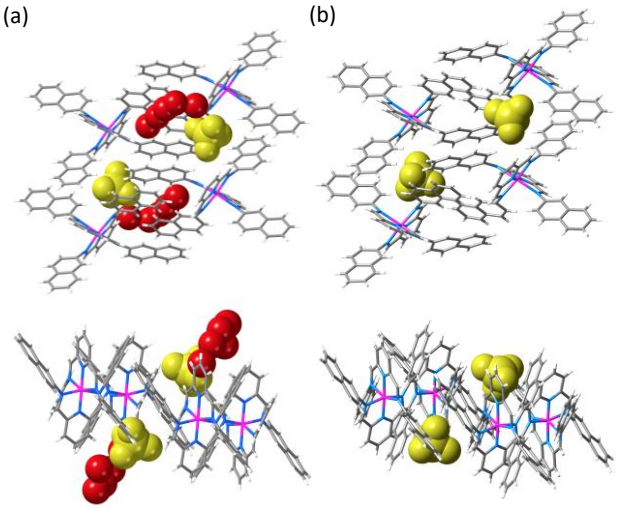

Figure IV.5 Front (top) and side (bottom) views of the four-membered metallacyclic double pocket within the π-bonded ladder-type double chains of **1** (a) and **1'** (b). The water crystallisation molecules and the perchlorate anions are shown in red and yellow colours, respectively, in the space-filling representation.

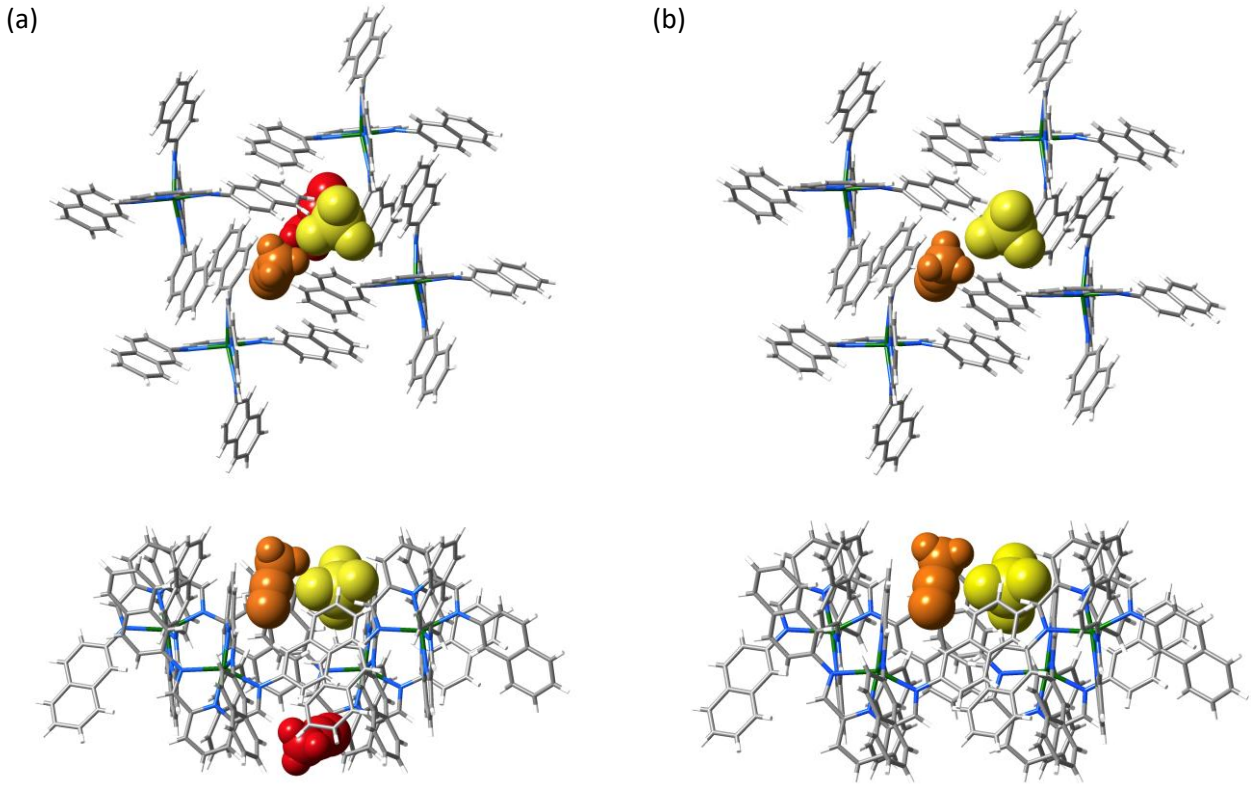

Figure IV.6 Front (top) and side (bottom) views of the four-membered metallacyclic double pocket within the π-bonded square grid-type layers of **2** (a) and **2'** (b). The two distinct acetonitrile crystallisation molecules and the perchlorate anions are shown in red, orange, and yellow colours, respectively, in the space-filling representation.

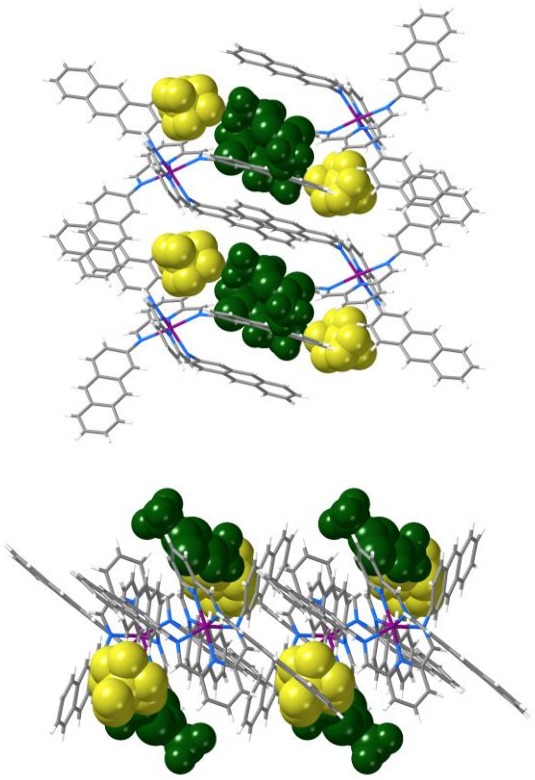

Figure IV.7 Front (top) and side (bottom) views of the four-membered metallacyclic double pocket within the π-bonded ladder-type double chains of **3**. The ethyl acetate crystallisation molecules and the perchlorate anions are shown in green and yellow colours, respectively, in the space-filling representation.

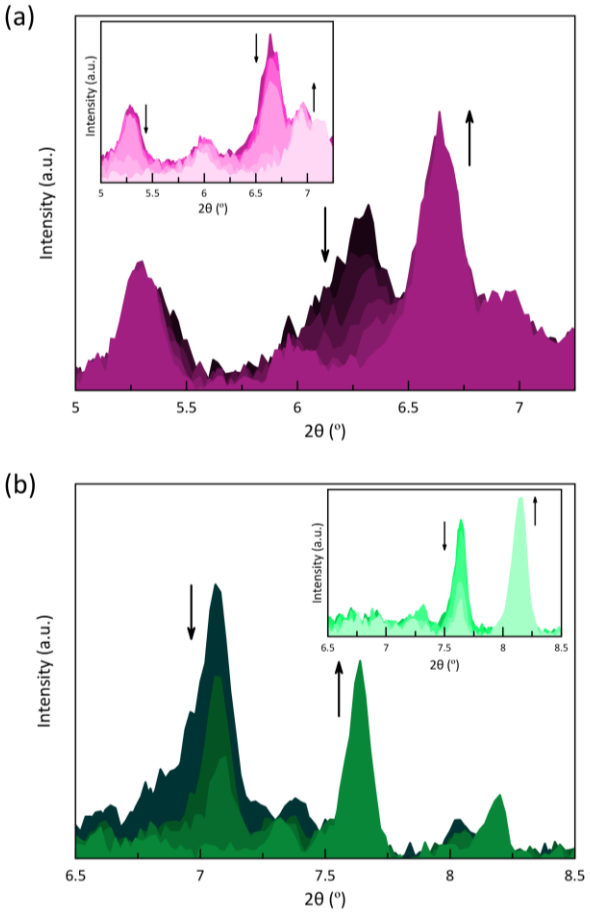

Figure IV.8 Experimental powder X-ray diffractograms obtained by gradual heating of **1** (a) and **2** (b) from 35 to 115 °C (from dark to light colours) and from 115 to 175 °C (insets).

IV.5 – Sorption Properties

The single-crystal-to-single-crystal (SC-SC) transformations through solvent removal and later uptake was investigated for the two solvatomorphic series (**1**/**1'** and **2**/**2'**/**2''**) to ascertain their reversibility (Figure IV.8).

The solvated precursors **1** and **2** exhibit a distinct desorption behaviour upon thermal desolvation. Hence, the powder diffractograms of **1** under gradual heating from room temperature to 115 °C (Figure IV.8a) show small progressive shifts of the main peaks, in perfect agreement with the calculated XRD patterns of **1**/**1'** (Figure IV.S1a). Further heating up to 175 °C gradually converts **1'** into an unknown desolvated crystalline phase, as indicated by the development of the peaks at 6.95 and 7.10° while those from **1'** begins to disappear (inset of Figure IV.8a). The subtlety of the dissimilarities in the XRD patterns of **2** and **2'** precludes distinguishing them by this technique. Instead, **2**/**2'** is entirely conversed in **2''** by warming up to 115 °C (with the main peak at 7.65°, Figure IV.8b), which, in turn, origins an unknown second desolvated phase by heating to 175 °C (main peak at 8.15°, inset of Figure IV.8b).

The resulting anhydrous derivatives **1'** and **2''** exhibit different adsorption behaviour in water or acetonitrile vapour saturated atmospheres, respectively (see Scheme IV.2). The powder diffractogram of the putative resolvated product of **1'** shows no peaks variation (data not shown), while that of **2''** recovers the diffraction pattern of **2** (dashed green line in Figure IV.S1b). The distinct irreversible (**1**/**1'**) or reversible (**2**/**2'**/**2''**) nature of these solvent-triggered SC-SC transformations is further supported by TGA (Figure IV.1). Hence, the TGA profile of **1'** after three days of exposition in a closed flask containing water at room temperature shows a broad plateau under heating from room temperature to 175 °C, with no mass loss (dotted pink line in Figure IV.1a). In contrast, the TGA profile of **2''** after one day of exposition in a closed flask containing acetonitrile exhibits two successive mass losses of 4% each from room temperature to around 175 °C that approximately correspond to the successive releases of two acetonitrile molecules in agreement with the formula of the original compound **2** (dashed green line in Figure IV.1b).

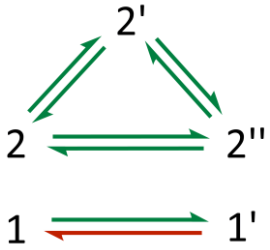

Scheme IV.2 Illustration of the interconversions through desolvation/resolvation in each solvatomorphic series of Naphtyl-substituted Co(II)-PDI complexes. The availability of the synthetic route is illustrated by green (possible) and red (not possible) arrows.

IV.6 – Magnetic Properties and EPR Spectra

Static magnetic behaviour. The dc magnetic properties of the original solvated precursors **1**–**3** are shown in Figures IV.9 and IV.10 in the form of the $\chi_M T$ *vs T* and *M vs H* plots (χ_M and *M* being the molar dc magnetic susceptibility and magnetisation per mononuclear unit). They are compared with those of the partially or totally desolvated derivatives **1'**, **2'** and **2''**.

The $\chi_M T$ versus *T* plots reveal a different magnetic behaviour depending on the aromatic oligoacene substituents and the crystallisation solvent molecules (Figure IV.9) that somehow agrees with the structural-based prediction (see section IV.4). At room temperature, $\chi_M T$ value for **2** (2.74 $cm^3\ mol^{-1}\ K$) is close to the expected for a HS Co^{II} ion with an unquenched orbital momentum contribution [$\chi_M T = (N\beta^2 g^2/3k_B)S(S+1) = 2.70\ cm^3\ mol^{-1}\ K$ with $S = 3/2$ and $g = 2.4$]. Upon cooling, $\chi_M T$ decreases smoothly to reach the value of 1.72 $cm^3\ mol^{-1}\ K$ at 2.0 K, revealing the occurrence of significant zero-field splitting (zfs) effects resulting from the first-order spin-orbit coupling (SOC). In **1** and **3**, the $\chi_M T$ values at room temperature are smaller than that of **2** [0.93 (**1**) and 2.20 $cm^3\ mol^{-1}\ K$ (**3**)]. Upon cooling, a gradual and complete spin transition takes place for **1**, as reflected by the slow decrease of $\chi_M T$ to reach a sort of plateau around 150 K. At 2.0 K, the $\chi_M T$ value of 0.48 $cm^3\ mol^{-1}$ K is as expected for an LS Co^{II} ion [$\chi_M T = (N\beta^2 g_{Co}^2/3k_B)S_{Co}(S_{Co}+1) = 0.45\ cm^3\ mol^{-1}\ K$ with $S_{Co} = 1/2$ and $g = 2.2$]. In contrast, **3** exhibits a gradual but incomplete spin transition upon cooling. The $\chi_M T$ value of 0.92 $cm^3\ mol^{-1}\ K$ at 2.0 K agrees with that estimated for a 1:2 HS/LS ratio [$\chi_M T = (1.85 + 2 \times 0.45)/3 = 0.92\ cm^3\ mol^{-1}\ K$], as was predicted by the single-crystal X-ray structure. Remarkable, **1** and **2** constitute a unique pair of solvatomorphs where the distinct crystallisation solvent molecules, water or acetonitrile, determine the overall spin state of the complex.

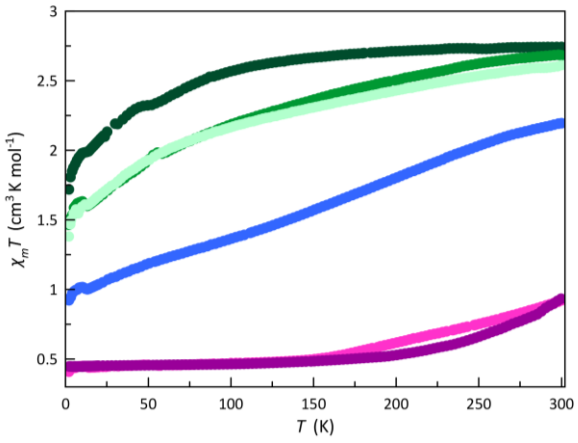

Figure IV.9 Temperature dependence of $\chi_M T$ for **1** (pink), **1'** (purple), **2** (dark green), **2'** (green), **2''** (pale green) and **3** (blue).

On the other hand, **1'** exhibits a gradual and complete spin transition behaviour similar to that observed for **1**, while **2'** and **2''** exhibit an almost identical gradual and incomplete SCO behaviour, differing from **2**. The $\chi_M T$ values of 1.46 and 1.38 $cm^3\ mol^{-1}\ K$ at 2.0 K for **2'** and **2''** roughly agree with that estimated average for two HS and one LS Co^{II} ions [$\chi_M T = (2 \times 1.85 + 0.45)/3 = 1.38\ cm^3\ mol^{-1}\ K$]. Even though the π-π interactions were increased by using extended oligoacene substituents for the PDI ligand, no cooperative effects were observed in the SCO behaviour of these compounds.

The similar (**1**/**1'**) or distinct (**2**/**2'**/**2''**) SCO behaviour upon partial or total desolvation along these solvatomorphic series are supported by the *M* versus *H* plots at 2.0 K (Figure IV.10). The values of *M* at *H* = 50 kOe for **1**/**1'** are 1.01/0.98 *Nβ*, being then close to the calculated one for the saturation magnetisation of a LS Co(II) complex ($M_s = gSN\beta = 1.10\ N\beta$ with $S = 1/2$ and $g = 2.2$). In contrast, *M* at 50 kOe for **2** is equal to 2.17 *Nβ*, a value which agrees with the calculated one for the saturation magnetisation for an HS cobalt(II) complex ($M_s = gSN\beta = 2.10\ N\beta$ with $S = S_{eff} = 1/2$ and $g = 4.2$). On the other hand, the *M* values at 50 KOe of 1.90, 1.91 and 1.38 *Nβ* for **2'**, **2''** and **3** are close to the estimated ones of the average saturation magnetisation considering two (**2'**/**2''**) or one (**3**) thirds as HS Co^{II} ions [$M_s = (2 \times 2.10 + 1.10)/3 = 1.77\ N\beta$ or $M_s = (2.10 + 2 \times 1.10)/3 = 1.43\ N\beta$, respectively].

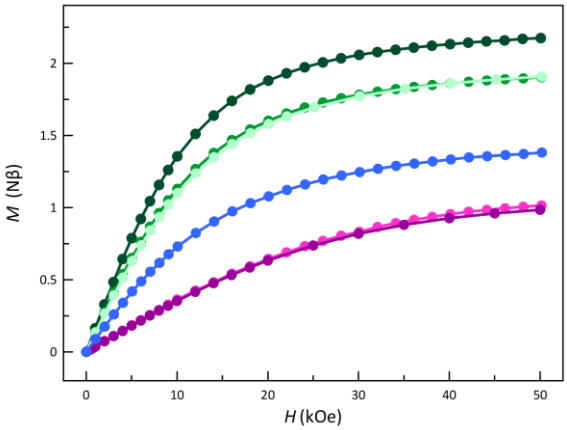

Figure IV.10 Magnetic field dependence of magnetisation at 2.0 K for **1** (pink), **1'** (purple), **2** (dark green), **2'** (green), **2''** (pale green) and **3** (blue). The solid lines are only eye-guides.

Moreover, the reduced magnetisation curves for **1**/**1'** superimpose below 10 K (Figure IV.S8a and b), as expected for magnetically isolated LS Co(II) complexes. In contrast, the little splitting of the analogous curves for **2**/**2'**/**2''** and **3** supports the presence of a large zfs resulting from the second-order spin-orbit coupling (SOC) of the HS Co(II) fractions in these compounds (Figure IV.S8c–f). Unfortunately, our attempts to fit the $\chi_M T$ *vs T* and *M vs H* data of **2** taking into account either a first-order SOC or a dominant axial zfs (*D*) were unsuccessful, a consequence of the presence of a residual LS phase, as evidenced by its EPR spectrum (see below).

EPR spectra. The distinct electronic structures for **1**/**1'**, **2**/**2'**/**2''** and **3** have been investigated through Q-band EPR spectroscopy in the solid state at 4.0 K (Figure IV.11). In general, all EPR spectra show a strong predominant signal around $g = 2.0$ (*ca*. 12000 G), typical for LS Co(II) complexes,[40] split in two because of the high axial and rhombic distorted geometry

imposed by the PDI ligands. Additionally, two low-field signals, whose patterns are characteristic of octahedral HS Co(II) complexes, are present in the spectra of **2**/**2'**/**2''** and **3**, being this coexistence of the LS and HS EPR signatures consistent with their incomplete spin transition deduced from the dc magnetic data (see Figures IV.9 and IV.10). Somehow the relative intensity between the HS and LS signals roughly reflects the HS fraction present in each compound at 4.0 K, although the relation of the intensities is not linear. Despite being a rough estimation, but agreeing with the conclusions drawn from magnetometry, as the fraction of the HS form increases, the ratio between the intensities of the HS and LS signals becomes larger.

The EPR spectra were simulated jointly for the LS and HS fractions, and considering a rhombically distorted octahedron ($g_1 \neq g_2 \neq g_3$). Two different LS sites were needed in the analysis to obtain good simulations for **1'**, which could be related to the presence of a small fraction of the aforementioned unknown dehydrate phase (see IV.5 – Sorption Properties). The parameters used for these simulations and the resulting curves are shown in Table IV.3 and Figure IV.11.

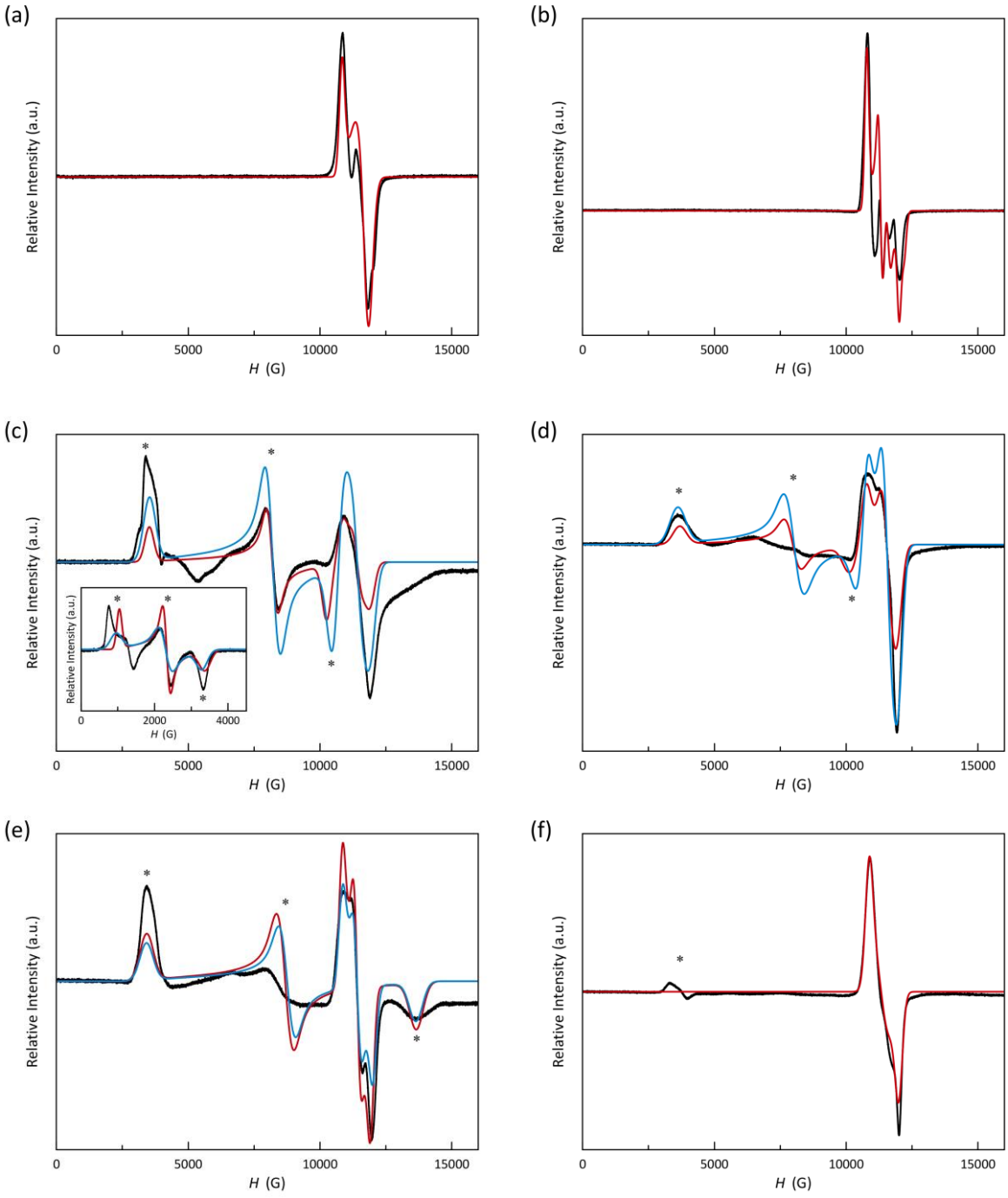

Figure IV.11 Experimental Q-band EPR spectra of **1** (a), **1'** (b), **2** (c), **2'** (d), **2''** (e) and **3** (f) in the solid state at 4.0 K (black solid lines). X-band spectrum of **2** appears as inset. Red and blue solid lines are the simulated curves for S_{eff} = 1/2 and anisotropic S = 3/2 approaches (see text).

Table IV.3 Best parameters for simulation of the Q-band EPR curves for the LS fraction present in **1/1'**, **2/2'/2''** and **3** from the experimental data in solid state at 4.0 K

	g_x	g_y	g_z	g^a
1	2.058	2.090	2.243	2.131
1'	2.023	2.151	2.254	2.145
	1.993	2.097	2.257	2.118
2	2.042	2.130	2.246	2.138
2'	2.040	2.106	2.262	2.138
2''	2.025	2.130	2.244	2.134
3	2.029	2.140	2.230	2.135

[a]Overall g value estimated by the equation $g^2 = (g_x^2 + g_y^2 + g_z^2)/3$ for the LS contribution.

Based on the magnetometry, **2** is the only compound presenting pure HS configuration at low temperatures for the cobalt(II) complex. So, the EPR signals marked with an asterisk in Figure II.11c (g_{eff} = [2.37, 2.97, 6.90]) correspond to the ground Kramers doublet of the HS form. These values are typical of a non-uniaxial zfs (D > 0) but not far from those of a uniaxial zfs (D < 0), proposed by *ab initio* CASSCF/NEVPT2 calculations for both **2** and **2'**, which is a feature of a large rhombicity, that is, a large E/D ratio. Thus, the calculations provide ratios above 0.28, close to its limit value (0.33), making difficult to establish the sign of D. The spectrum of **2** is well simulated after an analysis considering a zfs on the quartet ground state (g_x = 2.60, g_y = 2.74, g_z = 2.15, D >> 0, and E/D = 0.20). This same pattern of EPR signals with similar g values is repeated in the desolvated compounds **2'** and **2''**, allowing us to infer the predominance of a non-uniaxial zfs in the ground state in the HS fractions [g_x = 2.60 (**2'**)/2.55 (**2''**), g_y = 2.68 (**2'**)/2.65 (**2''**), g_z = 2.20 (**2'**)/2.30 (**2''**), D >> 0, and E/D = 0.20 (**2'**)/0.30 (**2''**)]. So, the subtle electronic and geometric variations derived from the weak interactions between the complexes and acetonitrile molecules occurring in the crystal packing do not seem to be important to significantly affect the HS electronic structures in this series of solvatomorphic compounds.

On the other hand, the split signal at H = 3750 G (g_{eff} = 6.60) in the spectrum of **3** is the only one undoubtedly ascribed to the HS fraction resulting from the incomplete spin transition, and its g_{eff} value is lower than the expected one for a uniaxial zfs. However, the EPR footprint of **3** is different from those of non-uniaxial **2/2'/2''** but very similar to those of the *p*-chloro- and *o*,*p*-dimethyl-substituted complexes of this doctoral dissertation (see Chapters II and III). In those cases, the simulations of both Q- and X-band spectra and the ab initio CASSCF/NEVPT2 calculations pointed out a negative sign for D. So, by comparing the EPR footprints, we can conclude the occurrence of a uniaxial anisotropy in **3**. Unfortunately, the lack of a crystal structure with pure HS complexes precludes theoretical calculations to support any decisive conclusions about the sign of D.

In summary, such distorted geometries likely lead to high rhombic anisotropies (expressed by E/D values close to 0.33), making it difficult to evaluate the sign of D properly through theoretical calculations. In this scenario, the EPR spectroscopy not only proved to be a sensible technique to determine the spin state and the presence of residual fractions upon the spin transition, but also it can provide information about the zfs.

Dynamic magnetic behaviour. The ac magnetic properties of **1/1'**, **2/2'/2''** and **3** under applied dc magnetic fields of 1.0 and 2.5 kOe are shown in Figures IV.S9–14 and Figures IV.S15–S20 in the form of χ_M' and χ_M'' *vs* T or ν plots (χ_M' and χ_M'' being the in-phase and out-of-phase ac molar magnetic susceptibilities).

Neither frequency dependence of χ_M' nor a χ_M'' signal were observed in the absence of a dc magnetic field (H_{dc}) for any of these compounds, more likely due to a fast quantum tunnelling of the magnetisation (QTM) or an intraKramer (IK) relaxation on the ground Kramers doublet of a LS or a non-uniaxial HS (D > 0) cobalt(II) complex, as mentioned in the previous chapters. However, frequency- and temperature-dependent maxima in χ_M' and χ_M'' arise by applying a H_{dc}. Distinct χ_M'' *vs* T and ν maxima characterise this field-induced slow magnetic relaxation, being they (T_{max} and ν_{max}) shifted by changing temperature, the frequency of the oscillating ac field (ν), or H_{dc} (Figures IV.S9–S14 and IV.S15–S20).

So, for instance, a significant increase in T_{max} is observed for **1'** relative to **1**, being more notable by increasing H_{dc} (Figures IV.S9b and IV.S10b). In contrast, T_{max} for both **2'** and **2''** shows a small but non-negligible decrease compared with **2**, regardless of H_{dc} (Figures IV.11b–13b). Overall, these changes in the field-induced SMM behaviour upon partial or total desolvation are, at first sight, surprising since they do not seem to be correlated with those observed in the SCO behaviour, which can be mainly related to the LS or HS electronic nature of the complexes. That is, in this family of compounds, the desolvation seems to favours the intermolecular interactions in the LS form, leading to the emergence of a fraction of this spin configuration in the solvated HS compounds, but a LS system cannot evolve. However, in other families, the cooperative effects in the SCO phenomenon, which depend on a framework of subtle intermolecular interactions, can revert this situation.

The magnetic relaxation time (τ) values were extracted by fitting the χ_M' and χ_M'' *vs* ν plots through the generalised Debye model (solid lines in Figures IV.S15–20). They are shown as Arrhenius plots in Figure IV.12. The magnetic relaxation of these complexes follows the same pattern that their parent *N*-phenyl disubstituted Co^{II}-PDI complexes presented in Chapters I and II, respectively.

On the one hand, although less significant than on the previous LS Co^{II}-PDI complexes, there is a switching between a faster-relaxing (FR) and slower-relaxing (SR) forms by increasing H_{dc} for **1/1'**, which does not occur in the HS compound (**2**) or is dimmed when an HS fraction is present. As discussed in the preceding chapters, this phenomenon results from the larger spin delocalisation on the HS configuration. On the other hand, regardless of H_{dc}, changes in the relaxation rate occur when the compounds are desolvated, but no trend is found either in the way nor in the magnitude (Figures IV.14). The spin configuration could be the cause of the distinct crystallisation solvent effect on the spin dynamics for these two series of solvatomorphs; but,

having in mind that, particularly for the LS compounds, the relaxation mainly occurs by a Raman mechanism prevailing at certain temperature regions, the contacts in the solvated and desolvated networks can play a crucial role. Anyway, the overall dependence of τ on the number and nature of crystallisation solvent molecules along this family of complexes makes them suitable candidates as spin quantum chemical sensors. Whereas **1/1'** show a single linear pattern in the ln τ *vs* ln T plot in the whole temperature range, this is split into two for the rest of the compounds, one at low and other at high temperature (Figure IV.S21). This fact indicates that one (**1/1'**) or two (**2/2'/2''** and **3**) Raman mechanisms ($\tau^{-1} = CT^n$), or similar, are competing to govern the spin reversal relaxation. As is the case for other LS cobalt(II) compounds, the n values found for **1** and **1'** roughly agree with a direct mechanism ($\tau^{-1} = AT$) for low H_{dc} and an optical phonon-assisted Raman ($n \approx 2$) at higher magnetic fields (Table IV.4). However, for those compounds with a partial or total fraction of the HS configuration, a double two-phonon Raman model ($\tau^{-1} = C_1T^{n1} + C_2T^{n2}$) was required. The n_i values thus obtained indicate that optical ($n \approx 2$) and acoustic ($n \approx 8$) phonons are involved in Raman spin-lattice relaxations, prevailing in the LT and HT regions, respectively. In any case, a typical temperature-independent Intra-Kramer (IK, $\tau^{-1} = \tau_{IK}$) mechanism of the LS configuration or an HS with easy-plane zfs ($D > 0$) does not contribute significantly above 2.0 K in this family of compounds.

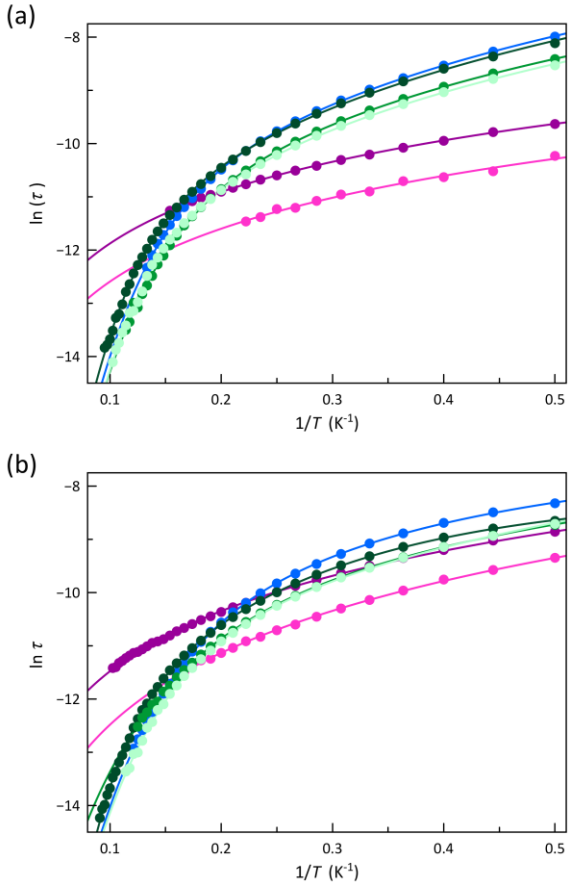

Figure IV.12 Arrhenius plots for **1** (pink), **1'** (purple), **2** (dark green), **2'** (green), **2''** (pale green) and **3** (blue) under applied *dc* magnetic fields of 1.0 (a) and 2.5 (b). The solid lines are the best-fit curves (see text).

Table IV.4 Selected parameters from the least-squares fit of the ac magnetic data of **1/1'**, **2/2'/2''** and **3**[a]

	H_{dc} (kOe)	C_1[b] ($s^{-1}K^{-n}$)	n_1[b]	C_2[b] ($s^{-1}K^{-n}$)	n_2[b]
1	1.0	11673 ± 800	1.37 ± 0.06	-	-
	2.5	2625 ± 90	2.04 ± 0.02	-	-
1'	1.0	5878 ± 40	1.380 ± 0.005	-	-
	2.5	2252 ± 30	1.632 ± 0.008	-	-
2	1.0	556 ± 20	2.50 ± 0.03	0.013 ± 0.005	7.7 ± 0.2
	2.5	1317 ± 80	1.97 ± 0.06	0.23 ± 0.09	6.5 ± 0.2
2'	1.0	939 ± 60	2.39 ± 0.06	0.06 ± 0.03	7.3 ± 0.2
	2.5	1208 ± 50	2.24 ± 0.03	0.33 ± 0.1	6.3 ± 0.2
2''	1.0	895 ± 80	2.31 ± 0.09	0.4 ± 0.2	6.6 ± 0.3
	2.5	1445 ± 100	2.02 ± 0.07	0.9 ± 0.3	6.2 ± 0.2
3	1.0	534 ± 20	2.44 ± 0.04	0.11 ± 0.05	7.0 ± 0.2
	2.5	1162 ± 50	1.74 ± 0.05	1.6 ± 0.3	5.84 ± 0.08

[a]The fits correspond to single (**1/1'**) or double (**2/2'/2''** and **3**). [b]Coefficient and polynomial factor for the single ($\tau^{-1} = CT^n$) or double ($\tau^{-1} = C_1T^{n1} + C_2T^{n2}$) Raman process.

IV.7 – Photophysical Properties

The influence of the extended π-conjugated aromatic character of the oligoacene substituents on the luminescence of the corresponding Co^{II}-PDI complexes with 2-naphthyl- and 2-anthryl substituents was investigated by photophysical methods. The electronic excitation and emission spectra of **2** and **3** were measured in acetonitrile solution for solubility reasons, and they were compared with those of their ligands counterparts (Figure IV.S22). Unfortunately, the insolubility of the 2-AnthPDI ligand precludes such studies in solution.

The electronic excitation spectra of **2** and **3** consist of an intense UV band at 288 and 330 nm, respectively, with two distinct shoulders at 360 and 380 nm in the latter case. They are attributed to π–π* intraligand transitions, also present in the spectrum of the 2-NaphPDI ligand. The large redshift of the main UV band of **3** compared with **2** is derived from the higher π-conjugated aromatic character of the anthracene chromophores relative to the naphthalene ones.

The emission spectra of **2** and **3** after excitation with UV light (λ_{exc} = 288 and 330 nm, respectively) are very different (Figure IV.13). The former presents a broad emission band centred at 398 nm, together with a distinct shoulder at 465 nm, while the latter has a more complex split structure with two emission maxima centred at 440 and 470 nm accompanied by two shoulders at 495 and 540 nm. The overall redshift of these emission bands of **3** compared to **2** is expected due to the higher π-conjugated aromatic character of the anthracene fluorophores relative to the naphthalene ones. Furthermore, the observed luminescence intensities of these emission bands for **3** are almost eight-fold greater than those for **2**, proving the outstanding ability of the anthracene group as luminophore. As expected, the luminescence from the ligand counterpart in these compounds is strongly quenched by the Co^{II} ion (Figure IV.S22a), most likely due to the occurrence of ligand-to-metal energy transfer processes.

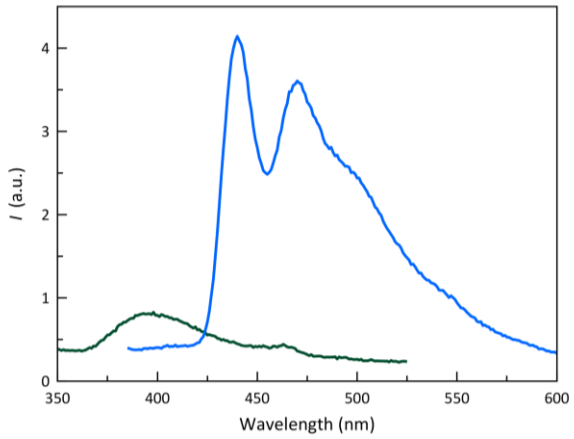

Figure IV.13 Electronic emission spectra of a 0.01 mM acetonitrile solution of **2** (green) and **3** (blue) at 25 °C.

One can be tempted to attribute the differences in emission intensities to the spin state, but this interpretation should be taken with care. Although the population of HS and LS states is different between **2** and **3** in the solid state, that definitely could not be the case in acetonitrile solution. Moreover, focusing on **2**, no shift in the emission frequency is observed compared with the 2-NaphPDI ligand, suggesting that the electronic nature of the ligand luminophore's emission is not affected by the complexation with Co^{II} ion in these conditions, being mainly assigned to the naphthalene group. So, the more accurate reasoning is that the Co^{II} ion quenches the luminescence equally for **2** and **3**, and the emission intensity depends mainly on the potential of the substituent groups as luminophores. Indeed, those facts agree with the majority of the studies in the literature that found no specific correlation between luminescence and spin state.[21] Thus, no conclusions about the difference in the ability of the HS and LS states to quench the ligand-based emission could be extracted from these studies in solution.

On the other hand, the emission spectra (λ_{exc} = 243 nm) recorded on crushed crystal samples of **1** and **2** show the same profile at room temperature and pressure (pink dashed and solid lines, Figure IV.14), confirming the common 2-NaphPDI ligand as the source of luminescence. Those spectra are constituted by a main emission at 387 nm with two shoulders at 347 and 335 nm. Besides the three-fold relationship of the emission intensity for **2** compared with **1**, the sample preparation method precludes a direct correlation with the spin state (see IV.10 – Experimental Section). When a reduced pressure (10^{-8} bar) is applied for one hour on the samples, the development of the two shoulders is observed, being then associated with the conversion to the partially desolvated phases **1'** and **2'** (blue dashed and solid lines). However, further cooling of the samples to 100 K results in a slight increase in the emission of **1** caused by suppression of thermal relaxation of the excited state. Meanwhile, a significant unusual decrease of the luminescence occurs for **2** (cyan dashed and solid lines, Figure IV.14). An explanation for this inverted tendency is the occurrence of the thermal-induced partial spin transition observed in **2'**, since the LS state is supposed to be more efficient in quenching the luminescence.[15,22] So, this result avails the possibility of reading out the spin state using light as the stimulus, which would be a big step toward the implementation of MOS technologies.

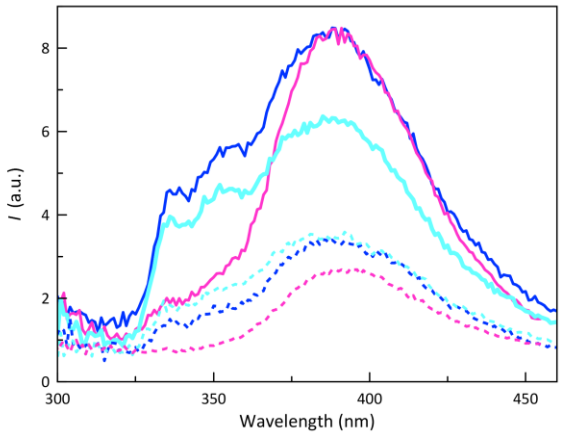

Figure IV.14 Solid state electronic emission spectra of **1** (dotted lines) and **2** (solid lines) at different conditions: (pink) room temperature and pressure; (blue) room temperature and reduced pressure; (cyan) 100 K and reduced pressure.

IV.8 – Proof-of-Concept of a Luminescent Spin Solvato-switch

Integrating luminescence as an additional functional property into a magnetic molecule through ligand design provides a convenient route to expand the applications of molecular spin quantum dynamic systems to many interests like magneto-optical switching and chemical sensing. In this respect, the studied solvatomorphic series possessing different magnetic properties (spin state and spin dynamics) in the solid state that depend on the nature and number of crystallisation solvent molecules prompted us to investigate the solvent influence on the inherent luminescence and magnetic properties to design a luminescent spin quantum solvato-switch. This section describes the proof-of-concept demonstration of a dual solvato-switching of the optical and magnetic properties in this unique example of luminescent spin crossover cobalt(II) molecular nanomagnet, as illustrated in Scheme IV.3.

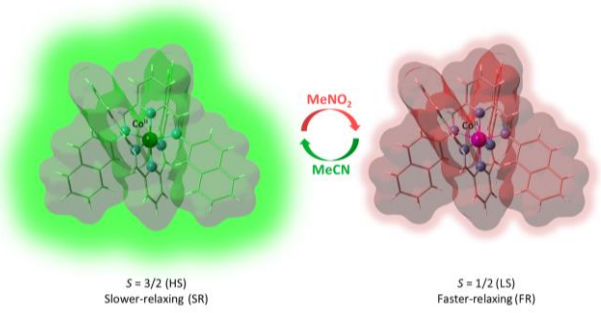

Scheme IV.3 Proposed proof-of-concept design for a spin solvato-switch based on a unique example of luminescent spin-crossover cobalt(II) molecular nanomagnet proceeding through the solvent-dependent HS/LS state of the slower-relaxing (SR)/faster-relaxing (FR) Co(II) complex.

For that, preliminary measurements of the luminescence activity of **2** were performed under the same experimental conditions in various organic solvent solutions of different

polarities (Figure IV.15). Due to a matter of solubility and stability of the complex, the selected solvents were dimethylformamide (DMF), acetonitrile (ACN), dichloromethane (DCM), acetone (ACT) and nitromethane (NTM). Curiously, in methanol solution, a massive enhancement of the emission produces a saturation of the detectors. This fact is attributed to stability issues of the Co(II)-PDI complexes in nucleophilic solvents (such as water or alcohols), where the hydrolysis of the ligand counterpart occurs. As expected, the effect of the solvent polarity on the luminescence of **2** substantially changes the position of the visible emission band from 384 (DCM) to 396 (ACN and ACT) and then 407 nm (DMF), while enhancing its relative emission intensity. This classical redshift with increasing the polarity of the solvent is a consequence of solvent relaxation.[41] However, a dramatic decrease in the emission intensity happens in nitromethane solution, accompanied by a significant redshift from 396 (ACN) to 455 nm (NTM). Such an abrupt quenching of the luminescence could be reasoned by a change in the spin state of the cobalt(II) complex since the LMTC absorption of the LS state overlaps more efficiently with the IL luminophore's emission than with that of the HS one.[15]

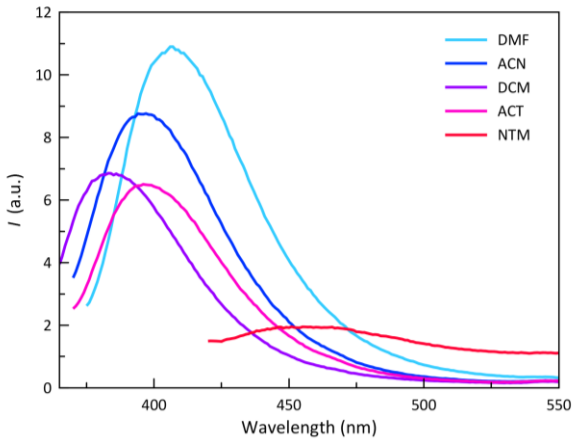

Figure IV.15 Electronic emission spectra of 0.01 mM dimethylformamide (cyan), acetonitrile (blue), dichloromethane (purple), acetone (magneta) and nitromethane (red) solutions of **2** at room temperature.

The hypothesis of the spin state change was checked through dc and ac magnetic measurements in acetonitrile and nitromethane solutions (see IV.10 – Experimental Section). The magnetisation curves at 2.0 K are shown in Figure IV.16. In acetonitrile solution, the magnetisation value of 2.19 $N\beta$ at 50 kOe is close to the saturation magnetisation one for a HS Co^{II} ion ($M_s = gSN\beta$ = 2.10 $N\beta$ with $S = S_{eff}$ = 1/2 and g = 4.2), being comparable to that found for **2** in the solid state (2.17 $N\beta$). In nitromethane, a lower value of 1.52 $N\beta$ is reached at 50 KOe, close to the saturation magnetisation for a 1:1 mixture of LS and HS configurations [M_s = (2.10 + 1.10)/2 = 1.60 $N\beta$]. Hence, the dc magnetometry results point out that the observed solvent-dependent quenching of the luminescence is a consequence of the synergetic relationship between luminescence and spin state, as earlier reported for the iron(II) complex of formula $[Fe(bpp)_2](BF_4)_2$ [bpp = 2,6-bis-(pyrazol-1-yl)pyridine] in solid state.[22] Furthermore, in both frozen acetonitrile and nitromethane solutions of **2**, χ_M'' signals arise in the presence of an H_{dc} (Figure IV.17), indicating that the SMM behaviour is retained in solution.

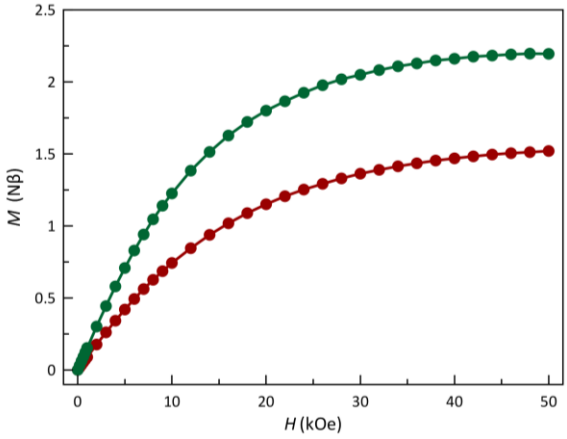

Figure IV.16 Field dependence of M for **2** in frozen acetonitrile (green) and nitromethane (red) solutions at T = 2.0 K. The solid lines are only eye-guides.

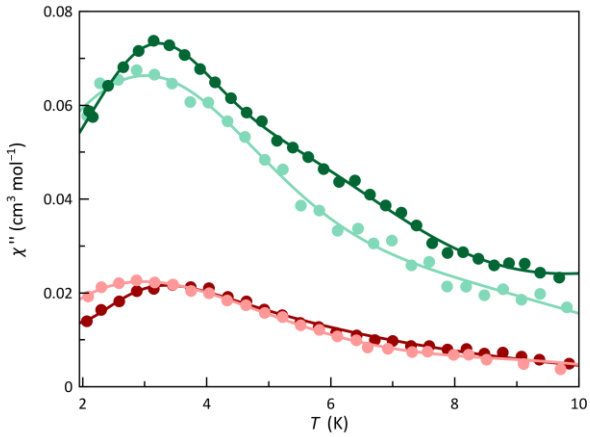

Figure IV.17 Temperature dependence of χ_M'' for **2** in frozen acetonitrile (green) and nitromethane (red) solutions at ν = 10 kHz of the ±5 Oe oscillating *ac* magnetic field and under applied dc magnetic fields of 2.5 and 5.0 kOe (light and dark colours). The solid lines are only eye-guides.

IV.9 – Concluding Remarks

In summary, a unique family of luminescent spin crossover cobalt(II) molecular nanomagnets shows the coexistence of different solid- and solution-state magnetic and luminescence properties, depending on the ligand, and the nature and number of crystallisation solvent. Gradual complete, partial HS ↔ LS transition or its absence were observed in this family with the occurrence of either faster-relaxing (FR) or slower-relaxing (SR) depending on the predominant LS or HS configuration of the cobalt(II) complexes at low temperature.

Moreover, there is a dual solvato-tuning of the field-induced SMM behaviour and the luminescence properties in some cases. In this respect, the irreversible character of the dehydration process precludes their use as humidity sensors. Otherwise, the reversible nature of the acetonitrile desorption/adsorption process opens the way for their use as chemical sensors of volatile organic compounds (VOCs) of biological or industrial interest.

The study of their photophysical activity in solution denotes the occurrence of a metal-promoted partial quenching of the ligand luminescence, which is accompanied by a significant change of the emission intensity and energy with solvent polarity making them promising candidates for spin switches in chemical sensing. The proof-of-concept of a luminescent spin solvato-switch provides thoughtful insights into how this new class of luminescent SCO/SMMs can be used to design opto-spintronic devices in the emerging field of MOS. Moreover, our results suggest the possibility of reading out the spin state of these SCO/SMMs in solid state through optical methods, representing an essential step in the challenging road to optically addressable qubits.

Current efforts are devoted to investigating the photochemical reactivity towards intermolecular cycloaddition reaction in this unique family of solvato-switchable luminescent SCO/SMMs. The goal is to get a photo-switching of the quantum coherence properties upon UV light irradiation for future applications as prototypes of optically addressable molecular spin quantum bits (qubits) in quantum information processing (QIP).

IV.10 – Experimental Section

Materials. Reagent grade pyridine-2,6-diformaldehyde, 2-aminonaphthalene, 2-aminoanthracene, acetic acid, and cobalt(II) perchlorate hexahydrate were purchased from commercial sources and used as received.

Physical techniques. Elemental (C, H, N) analyses were performed at the Servicio Central de Soporte a la Investigación (SCSIE) at the Universitat de València (Spain). FT–IR spectra were recorded on a Nicolet-5700 spectrophotometer as KBr pellets. Q-band EPR spectra (ν = 34.5 GHz) of frozen-matrix acetone solutions were recorded under non-saturating conditions on a Bruker ER 200 D spectrometer equipped with a helium cryostat. X-ray powder diffraction (XRPD) patterns of powdered crystalline samples were collected at room temperature on a D8 Avance A25 Bruker diffractometer using graphite-monochromated Cu-Kα radiation (λ = 1.54056 Å).

Thermal and sorption measurements. The thermogravimetric analysis (TGA) was performed on powdered samples under a dry N_2 atmosphere within the range of 25–175 °C with a Mettler Toledo TGA/STDA 851 thermobalance operating at a heating rate of 10 °C min^{-1}. Caution: perchlorate salts are potentially explosive. They should be treated with the utmost care and manipulated in small quantities.

Temperature-dependent XRPD patterns were collected on a LYNXEYE XE 1-dimensional detector for ultra-fast X-ray diffraction measurements using an Anton Paar chamber working under a controlled relative humidity of 12%. Measurements were carried out in a continuous way every 10 °C over the angular range of $5 \leq 2\theta \leq 7.25°$ (**1**) and $6.5 \leq 2\theta \leq 8.5°$ (**2**), where there exist significant differences in the peak positions of the solvated precursors and the partially or totally desolvated derivatives.

Photophysical measurements. Electronic absorption spectra were recorded on a Jasco UV/Vis/NIR V-670 spectrophotometer, whereas the emission spectra in solution were registered with a modular spectrofluorimeter. For the photoluminescence experiments in solid state, crushed crystals of **1** and **2** were dispersed on a 0.5 x 1.0 cm carbon surface, and their emission spectra were measured using a Horiba-Jobin Yvon spectrofluorometer, Model Fluorolog-3 (FL3−221), under excitation with a 450 W Xe arc lamp and Horiba PPD-850 ps photon detector in the UV−vis region. Low-temperature spectra were recorded using a closed-cycle cryostat model CS202AI-X15 (ARS Cryo), monitoring the temperature with a Lake Shore model 332 controller.

Static and dynamic magnetic properties. Variable-temperature (2–300 K) direct current (*dc*) magnetic susceptibility measurements under applied fields of 0.25 (T < 20 K) and 5.0 kOe (T > 20 K) and variable-field (0–50 kOe) magnetisation measurements at 2.0 K were carried out on crushed crystals with a Quantum Design SQUID magnetometer. The magnetic susceptibility data were corrected for the diamagnetism of the constituent atoms and the sample holder. The *ac* magnetic measurements in solution were carried out using a quartz tube (8 cm height × 5 mm outer diameter with 0.5 mm wall thickness) that contains the concentrated acetonitrile or nitromethane solutions samples (5 mm height). The magnetic susceptibility data were corrected for the diamagnetism of the constituent atoms and the sample holder.

Variable-temperature (2.0–12 K) alternating current (*ac*) magnetic susceptibility measurements under ±5.0 Oe oscillating field at frequencies in the range of 0.15–10 kHz were carried out on crushed crystals under different *dc* magnetic fields (H_{dc} = 1.0 and 2.5 kOe) with a Quantum Design Physical Property Measurement System (PPMS). The *ac* magnetic measurements in acetonitrile or nitromethane solutions were performed at the highest frequency of 10 kHz using different *dc* magnetic fields (H_{dc} = 2.5 and 5.0 kOe).

Crystal structure data collection and refinement. X-ray diffraction data on a single crystals of **1**/**1'**, **2**/**2'** and **3** were collected on an Agilent Supernova diffractometer equipped with an EosS2 detector with Mo-Kα radiation (λ = 0.71073 Å) at 150 K. Diffraction data were collected, scaled, and integrated using the CrysAlisPro software.[42,43] The structures were solved by intrinsic phasing methods incorporated into the SHELXTL software[44] with the Olex2 platform.[45] The obtained models were refined with the version 2018/3 of SHELXL against F^2 on all data by full-matrix least squares. All non-hydrogen atoms were refined anisotropically. Hydrogen atoms in water molecules were neither found nor fixed. The remaining ones were set on geometrical positions and refined with a riding model. The graphical manipulations and calculations were performed with the CRYSTALMAKER[46] and MERCURY[47] programs.

Preparation of the ligands and complexes.

2,6-bis(N-2-naphthylformimidoyl)pyridine (2-NaphPDI): Pyridine-2,6-diformaldehyde (0.135 g, 1.0 mmol) and 2-aminonaphthalene (0.286 g, 2.0 mmol) were dissolved in 5.0 mL of ethanol containing 100 µL of acetic acid. The reaction mixture was refluxed for 30 min and cooled in an ice bath. The yellow crystalline solid was collected by filtration, washed with a small amount of ethanol and dried in the open air. Yield: 96 %. Anal. Calc. for $C_{27}H_{19}N_3$ (*MW* = 385.47 g mol^{-1}): C, 84.13; H, 4.97; N, 10.90. Found: C, 84.39; H, 5.02; N, 10.73 %. IR (KBr, cm^{-1}): 1613(m) [ν(C=N) from pyridine], 1592(m) [ν(C=C) from aromatic rings].

2,6-bis(N-2-anthrylformimidoyl)pyridine (2-AnthPDI): Pyridine-2,6-diformaldehyde (0.135 g, 1.0 mmol) and 2-aminoanthracene (0.386 g, 2.0 mmol) were dissolved in 5.0 mL of ethanol containing 100 µL of acetic acid. The reaction mixture was refluxed for 30 min and cooled in an ice bath. The yellow crystalline solid was collected by filtration, washed with a small amount of ethanol and dried in the open air. Yield: 96 %. Anal. Calc. for $C_{35}H_{23}N_3$ (*MW* = 485.59 g mol^{-1}): C, 86.57; H, 4.77; N, 8.65. Found: C, 86.32; H, 4.55; N, 8.92 %. IR (KBr, cm^{-1}): 1606(m) [ν(C=N) from pyridine], 1580(m) [ν(C=C) from aromatic rings].

*$[Co^{II}(2\text{-}NaphPDI)_2](ClO_4)_2{\cdot}1.5H_2O$ (**1**)*: An acetonitrile solution (3.0 mL) of cobalt(II) perchlorate hexahydrate (0.037 g, 0.1 mmol) was added dropwise to a suspension of 2-NaphPDI (0.077 g, 0.2 mmol) in acetonitrile (2.0 mL). The reaction mixture was heated at 50 °C for 30 min. Then, 20 mL of ethyl acetate was added and the resulting brown solution was allowed to evaporate in a hood. X-ray quality crystals of **1** were founded in the very next day. Yield: 85 %. Anal. Calc. for $C_{54}H_{41}N_6O_{9.5}Cl_2Co$ (*MW* = 1055.78 g mol^{-1}): C, 65.46; H, 4.17; N, 8.48 %. Found: C, 65.92; H, 4.09; N, 8.30%. IR (KBr, cm^{-1}): 3441(m) [ν (O–H) from water], 1610(m) [ν (C=N) from the ligand], 1694(m) [ν (C=C) from ligand], 1098(vs) [ν (Cl–O) from perchlorate].

*$[Co^{II}(2\text{-}NaphPDI)_2](ClO_4)_2$ (**1'**)*: Crystals of the hydrated precursor **1** (0.053 g, 0.05 mmol) were placed on a ceramic sample pan, and then they were slowly heated and cooled (3 h + 3 h) between room temperature and 90 °C under air in an oven. The microcrystalline powder of **1'** was stored at room temperature under Ar. Yield: 0.051 g (100%). Anal. Calc. For $C_{54}H_{38}N_6O_8Cl_2Co$ (M_w = 1028.77 g mol^{-1}): C, 63.05; H, 3.72; N, 8.17 %. Found: C, 63.22; H, 3.68; N, 8.10%. IR (KBr, cm^{-1}): 1610(m) [ν (C=N) from the ligand], 1592 [ν (C=C) from ligand], 1096(vs) [ν (Cl–O) from perchlorate]. Crystals of **1'** suitable for single-crystal XRD were obtained by embedding the crystals of **1** in paratone before prolonged heating and cooling (36 h + 36 h) between room temperature and 90 °C under air in an oven.

*$[Co^{II}(2\text{-}NaphPDI)_2](ClO_4)_2{\cdot}2CH_3CN$ (**2**)*: An acetonitrile solution (1.0 mL) of cobalt(II) perchlorate hexahydrate (0.018 g, 0.05 mmol) was added dropwise to a suspension of 2-NaphPDI (0.038 g, 0.1 mmol) in acetonitrile (2.0 mL). The reaction mixture was heated at 50 °C until the volume was reduced by half of the original. A small quantity of chloroform was added to this mixture (0.5 mL). Finally, X-ray quality crystals of **2** were grown by slow diffusion of ethyl acetate through this saturated acetonitrile/chloroform solution in a glass test tube. Yield: 78 %. Anal. Calc. for $C_{58}H_{44}N_8O_8Cl_2Co$ (*MW* = 1110.87 g mol^{-1}): C, 62.71; H, 3.99; N, 10.09. Found: C, 62.94; H, 3.85; N, 10.22 %. IR (KBr, cm^{-1}): 2242(w) [ν (C≡N) from acetonitrile], 1592(w) [ν (C=N) from the ligand], 1581(w) [ν (C=C) from ligand], 1095(vs) [ν (Cl–O) from perchlorate].

*$[Co^{II}(2\text{-}NaphPDI)_2](ClO_4)_2{\cdot}CH_3CN$ (**2'**)*: Crystals of the solvated precursor **2** (0.055 g, 0.05 mmol) were placed on a ceramic sample pan, and then they were slowly heated and cooled (3 h + 3 h) between room temperature and 50 °C under air in an oven. The microcrystalline powder of **2'** was stored at room temperature under Ar. Yield: 0.053 g (100%). Anal. Calc. for $C_{56}H_{41}N_7O_8Cl_2Co$ (*MW* = 1069.82 g mol^{-1}): C, 62.87; H, 3.86; N, 9.16 %. Found: C, 62.69; H, 3.90; N, 9.23 %. IR (KBr, cm^{-1}): 1611(m) [ν (C=N) from the ligand], 1593(m) [ν (C=C) from ligand], 1097(vs) [ν (Cl–O) from perchlorate]. Crystals of **2'** suitable for single-crystal XRD were obtained by embedding the crystals of **2** in paratone before prolonged heating and cooling (36 h + 36 h) between room temperature and 50 °C under air in an oven.

*$[Co^{II}(2\text{-}NaphPDI)_2](ClO_4)_2$ (**2''**)*: Crystals of the solvated precursor **2** (0.055 g, 0.05 mmol) were placed on a ceramic sample pan, and then they were slowly heated and cooled (3 h + 3 h) between room temperature and 90 °C under air in an oven. The microcrystalline powder of **2''** was stored at room temperature under Ar. Yield: 0.051 g (100%). Anal. Calc. for $C_{54}H_{38}N_6O_8Cl_2Co$ (*MW* = 1028.77 g mol^{-1}): C, 63.05; H, 3.72; N, 8.17 %. Found: C, 63.14; H, 3.66; N, 8.25%. IR (KBr, cm^{-1}): 1593(m) [ν (C=N) from the ligand], 1575(m) [ν (C=C) from ligand], 1093(vs) [ν (Cl–O) from perchlorate].

*$[Co^{II}(2\text{-}AnthPDI)_2](ClO_4)_2{\cdot}2EtOAc$ (**3**)*: Cobalt(II) perchlorate hexahydrate (0.037 g, 0.1 mmol) was added to an acetonitrile solution (5.0 mL) of pyridine-2,6-diformaldehyde (0.027 g, 0.2 mmol). Then, 2-aminoanthracene (0.077 g, 0.4 mmol) was added to the reaction mixture, and it was heated at 50 °C for one hour while the volume was reduced to one-half of the original to result in a dark red solution. A small quantity of chloroform was added to this mixture (1.0 mL). X-ray quality crystals of **3** were grown by slow diffusion of ethyl acetate through this saturated acetonitrile/chloroform solution in a glass test tube. Yield: 65 %. Anal. Calc. for $C_{70}H_{46}N_6O_8Cl_2Co$ (*MW* = 1361.17 g mol^{-1}): C, 67.06; H, 4.30; N, 6.17. Found: C, 67.36; H, 4.59; N, 6.04 %. IR (KBr, cm^{-1}): 1726(w) [ν (COO) from ethyl acetate], 1623(m) [ν (C=N) from the ligand], 1603 [ν (C=C) from ligand], 1095(vs) [ν (Cl–O) from perchlorate].

References

1 Verma, P.; Weir, J.; Mirica, L.; Stack, T. D. Tale of a Twist: Magnetic and Optical Switching in Copper(II) Semiquinone Complexes. *Inorg. Chem.* **2011**, *50*, 9816–9825.

2 Feng, X.; Mathonière, C.; Jeon, I.-R.; Rouzières, M.; Ozarowski, A.; Aubrey, M. L.; Gonzalez, M. I.; Clérac, R.; Long, J. R. Tristability in a Light-Actuated Single-Molecule Magnet. *J. Am. Chem. Soc.* **2013**, *135*, 15880–15884.

3 Mathonière, C.; Lin, H.-J.; Siretanu, D.; Clérac, R.; Smith, J. M. Photoinduced Single-Molecule Magnet Properties in a Four-Coordinate Iron(II) Spin Crossover Complex. *J. Am. Chem. Soc.* **2013**, *135*, 19083–19086.

4 Urtizberea, A.; Roubeau, O. Switchable Slow Relaxation of Magnetization in the Native Low Temperature Phase of a Cooperative Spin-Crossover Compound. *Chem. Sci*. **2017**, *8*, 2290–2295.

5 Konstantinov, N.; Tauzin, A.; Noumbé, U. N.; Dragoe, D.; Kundys, B.; Majjad, H.; Brosseau, A.; Lenertz, M.; Singh, A.; Berciaud, S.; Boillot, M.-L.; Doudin, B.; Mallah, T.; Dayen, J.-F. Electrical Read-Out of Light-Induced Spin Transition in Thin Film Spin Crossover/Graphene Heterotructures. *J. Mat. Chem. C* **2021**, *9*, 2712–2720.

6 Paquette, M. M.; Plaul, D.; Kurimoto, A.; Patrick, B. O.; Frank, N. L. Opto-Spintronics: Photoisomerization-Induced Spin State Switching at 300 K in Photochrome Cobalt-Dioxolene Thin Films. *J. Am. Chem. Soc.* **2018**, *140*, 14990–15000.

7 Tissot, A.; Boillot, M.-L.; Pillet, S.; Codjovi, E.; Boukheddaden, K.; Daku, L. M. L. Unidirectional Photoisomerization of Styrylpyridine for Switching the Magnetic Behavior of an Iron(II) Complex: A MLCT Pathway in Crystalline Solids. *J. Phys. Chem. C* **2010**, *114*, 21715–21722.

8 Hasegawa, Y.; Takahashi, K.; Kume, S.; Nishihara, H. Complete Solid State Photoisomerization of Bis(dipyrazolylstyrylpyridine)iron(II) to Change Magnetic Properties. *Chem. Commun*. **2011**, *47*, 6846–6848.

9 Rösner, B.; Milek, M.; Witt, A.; Gobaut, B.; Torelli, P.; Fink, R. H.; Khusniyarov, M. M. Reversible Photoswitching of a Spin-Crossover Molecular Complex in the Solid State at Room Temperature. *Angew. Chem. Int. Ed.* **2015**, *54*, 12976–12980.

10 Real, J. A.; Gaspar, A. B.; Muñoz, M. C. Thermal, Pressure and Light Switchable Spin-Crossover Materials. *Dalton Trans.* **2005**, 2062–2079.

11 Evangelio, E.; Ruiz-Molina, D. Valence Tautomerism: New Challenges for Electroactive Ligands. *Eur. J. Inorg. Chem*. **2005**, 2957–2971.

12 Sato, O.; Tao, J.; Zhang, E.-J. Control of Magnetic Properties through External Stimuli. *Angew. Chem. Int. Ed*., **2007**, *46*, 2152–2187.

13 Khusniyarov, M. M. How to Switch Spin-Crossover Metal Complexes at Constant Room Temperature. *Chem. Eur. J.* **2016**, *22*, 15178–15191.

14 Ferrando-Soria, J.; Vallejo, J.; Castellano, M.; Martínez-Lillo, J.; Pardo, E.; Cano, J.; Castro, I.; Lloret, F.; Ruiz-García, R.; Julve, M. Molecular Magnetism, *Quo Vadis*? A Historical Perspective from a Coordination Chemistry Viewpoint. *Coord. Chem. Rev.* **2017**, *339*, 17–103.

15 Kumar, K. S.; Ruben, M. Emerging Trends in Spin Crossover (SCO) Based Functional Materials and Devices. *Coord. Chem. Rev*. **2017**, *347*, 176–205.

16 Doistau, B.; Benda, L.; Hasenknopf, B.; Marvaud, V.; Vives, G. Switching Magnetic Properties by a Mechanical Motion. *Magnetochemistry* **2018**, *4*, 5.

17 Meng, Y.-S.; Liu, T. Manipulating Spin Transition to Achieve Switchable Multifunctions. *Acc. Chem. Res.* **2019**, *52*, 1369–1379.

18 Silva, A. S.; Gunaratne, H. Q. N.; McCoy, C. P. A Molecular Photoionic ADN Gate Based on Fluorescent Signalling. *Nature* **1993**, *364*, 42–44.

19 Kumar, K. S.; Salitros, I.; Heinrich, B.; Fuhr, O.; Ruben, M.; A Charge Neutral Iron(ii) Complex with an Above Room Temperature Spin Crossover (SCO) and Hysteresis Loop. *J. Mater. Chem. C* **2015**, *3*, 11635–11644.

20 Hasegawa, M.; Renz, F.; Hara, T.; Kikuchi, Y.; Fukuda, Y.; Okubo, J.; Hoshi, T.; Linert, W. Fluorescence Spectra of Fe(II) Spin Crossover Complexes with 2,6-bis(benzimidazole-2-yl)pyridine. *Chem. Phys.* **2002**, *277*, 21–30.

21 Santoro, A.; Cook, L. J. K.; Kulmaczewski, R.; Barrett, S.A.; Cespedes, O.; Halcrow, M. A. Iron(II) Complexes of Tridentate Indazolylpyridine Ligands: Enhanced Spin-Crossover Hysteresis and Ligand-Based Fluorescence. *Inorg. Chem.* **2015**, *54*, 682–693.

22 Jiao, Y.; Zhu, J.; Guo, Y.; He, W.; Guo, Z. Synergetic Effect between Spin Crossover and Luminescence in the $[Fe(bpp)_2][BF_4]_2$ (bpp =2,6-bis(pyrazol-1-yl)pyridine) Complex. *J. Mater. Chem. C* **2017**, *5*, 5214–5222.

23 Wang, C.-F.; Li, R.-F.; Chen, X.-Y.; Wei, R.-J.; Zheng, L.-S.; Tao, J. Synergetic Spin Crossover and Fluorescence in One-Dimensional Hybrid Complexes. *Angew. Chem. Int. Ed*. **2015**, *54*, 1574–1577.

24 González-Pietro, R.; Fleury, B.; Scharamm, F.; Zopellaro, G.; Chandrasekar, R.; Fuhr, O.; Lebekin, S.; Kappes, M.; Ruben, M. Tuning the Spin-Transition Properties of Pyrene-Decorated 2,6-Bispyrazolylpyridine Based Fe(II) Complexes. *Danton Trans.* **2011**, *40*, 7564–7570.

25 Wang, J.-L.; Lui, Q.; Lv, X.-J.; Wang, R.-L-; Duan, C.-Y.; Liu, T. Magnetic Fluorescent Bifunctional Spin-Crossover Complexes. *Dalton Trans.* **2016**, *45*, 18552–18558.

26 McCullough, J. J. Photoadditions of Aromatic Compounds. *Chem. Rev*. **1987**, *87*, 811–860.

27 Becker, H. D. Unimolecular Photochemistry of Anthracenes. *Chem. Rev*. **1993**, *93*, 145–172.

28 Bouas-Laurent, H.; Castellan, A.; Desvergne, J.-P.; Lapouyade, R. Photodimerization of Anthracenes in Fluid Solution: Structural Aspects. *Chem. Soc. Rev*. **2000**, *29*, 43–55.

29 Mondal, R.; Tönshoff, C.; Khon, D.; Neckers, D.C.; Bettinger, H.F. Synthesis, Stability, and Photochemistry of Pentacene, Hexacene, and Heptacene: A Matrix Isolation Study. *J. Am. Chem. Soc.* **2009**, *131*, 14281–14289.

30 Zade, S.S.; Zamoshchik, N.; Reddy, A.R.; Fridman-Marueli, G.; Sheberla, D.; Bendikov, M. Products and Mechanism of Acene Dimerization. A Computational Study. *J. Am. Chem. Soc.* **2011**, *133*, 10803–10816.

31 Bowen, E.J. *Advances in Photochem*istry, John Wiley & Sons, Inc, New York-London, 1963, 23.

32 Bradshaw, J.S.; Hammond, G.S. Mechanisms of Photochemical Reactions in Solution. XIX. Photodimerization of Methyl β-Naphthyl Ether. *J. Am. Chem. Soc*. **1963**, *85*, 3953–3955.

33 Selinger, B.K.; Sterns, M. The Crystal Structure of 2-Methoxynaphthalene Photodimer. *J. Chem. Soc*., *Chem. Commun.* **1969**, 978–979.

34 Cao, D.-K.; Gu, Y.-W.; Feng, J.-Q.; Cai, Z.-S.; Ward, M. D. Mononuclear Lanthanide Complexes Incorporating an Anthracene Group: Structural Modification, Slow Magnetic Relaxation and Multicomponent Fluorescence Emissions in Dy Compounds. *Dalton Trans.* **2013**, *42*, 11436-11444.

35 Huang, X.-D.; Kurmoo, M.; Bao, S.-S.; Fan, K.; Xu, Y.; Hu, Z.-B.; Zheng, L.-M. Coupling Photo-, Mechano- and Thermochromism and Single-Ion-Magnetism of Two Mononuclear Dysprosium–Anthracene–Phosphonate Complexes. *Chem. Commun.* **2018**, *54*, 3278-3281.

36 Huang, X.-D. Xu, Y.; Fan, K.; Bao, S.-S.; Kurmoo, M.; Zheng, L.-M. Reversible SC-SC Transformation involving [4+4] Cycloaddition of Anthracene: A Single-Ion to Single-Molecule Magnet and Yellow-Green to Blue-White Emission. *Angew. Chem. Int. Ed.* **2018**, *57*, 8577-8581.

37 Huang, X.-D.; Jia, J.-G.; Kurmoo, M.; Bao, S.-S.; Zheng, L.-M. Interplay of Anthracene Luminescence and Dysprosium Magnetism by Steric Control of Photodimerization. *Dalton Trans.* **2019**, *48*, 13769-13779.

38 Liu, J.-C.; Huang, X.-D.; Zou, Q.; Bao, S.-S.; Wang, X.-Z.; Ma, J.-Y.; Zheng, L.-M. Synergetic Magnetic and Luminescence Switching via Solid State Phase Transitions of the Dysprosium–Dianthracene Complex *J. Mater. Chem. C* **2020**, *8*, 7369-7377.

39 Huang, X.-D.; Wen, G.-H.; Bao, S.-S.; Jia, J.-G.; Zheng, L.-M. Thermo- and Light-Triggered Reversible Interconversion of Dysprosium–Anthracene Complexes and their Responsive Optical, Magnetic and Dielectric Properties. *Chem. Sci.* **2021**, *12*, 929-937.

40 Krivokapic, I., Zerara, M., Daku, M. L., Vargas, A., Enachescu, C., Ambrus, C., Tregenna-Piggott, P., Amstutz, N., Krausz, E., Hauser, A. Spin-Crossover in Cobalt(II) Imine Complexes. *Coord. Chem. Rev.* **2007**, *251*, 364–378.

41 Lakowicz, J.R. Effects of Solvents on Fluorescence Emission Spectra. In: Principles of Fluorescence Spectroscopy, Springer, Boston, 1983.

42 Bruker. *SAINT*. Bruker AXS Inc., Madison, Wisconsin, USA, **2012**.

43 Agilent. *CrysAlis PRO*. Agilent Technologies Ltd, Yarnton, Oxfordshire, England, **2014**.

44 Sheldrick, G. M. SHELXT - Integrated Space-Group and Crystal-Structure Determination. *Acta Cryst.* **2015**, *A71*, 3–8.

45 Dolomanov, O.V., Bourhis, L.J., Gildea, R.J, Howard, J.A.K. & Puschmann, H. *J.* OLEX2: A Complete Structure Solution, Refinement and Analysis Program. *Appl. Cryst*. **2009**, *42*, 339-341.

46 *CrystalMaker*, CrystalMaker Software, Bicester, England, **2015**.

47 *Mercury*, The Cambridge Crystallographic Data Centre, Cambridge, UK.

Supporting Information

TABLE OF CONTENTS

General characterisation (Figure IV.S1)

X-ray crystallographic data collection and structure refinement (Figures IV.S2 – IV.S7)

Static and dynamic magnetic measurements (Figures IV.S8 – IV.S21)

Photophysical measurements (Figure IV.S22)

General characterisation

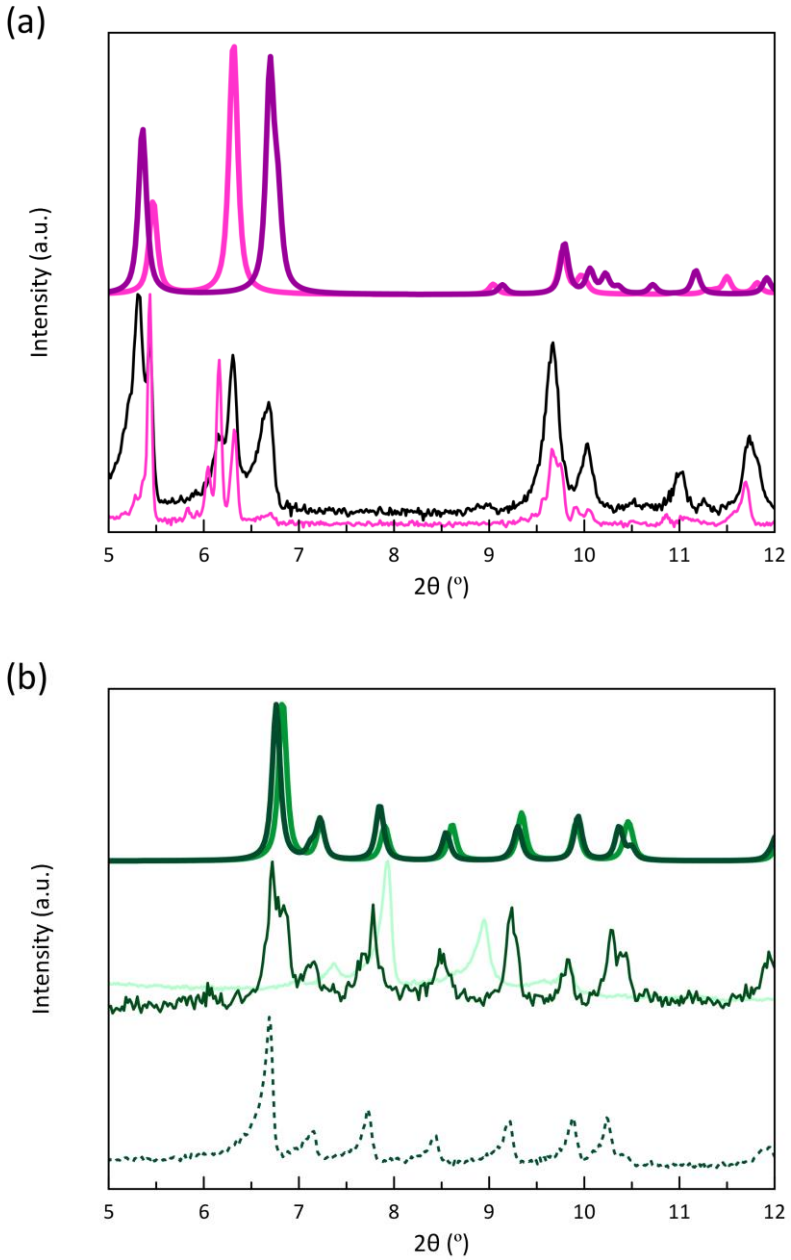

Figure IV.S1 (a) Top: Calculated PXRD patterns for **1** (pink) and **1'** (purple); Bottom: Experimental XPRS patterns of **1** (pink) and the partially dehydrated mixture (black). (b) Calculated (top) and experimental (middle) PRXD patterns of **2** (dark green) and **2'** (light green). Desolvated phase (**2"**, pale green) and resolvated compound after 1 day of exposition in acetonitrile vapour saturated atmosphere (dotted line) in middle and bottom, respectively.).

X-Ray crystallographic data and refinement

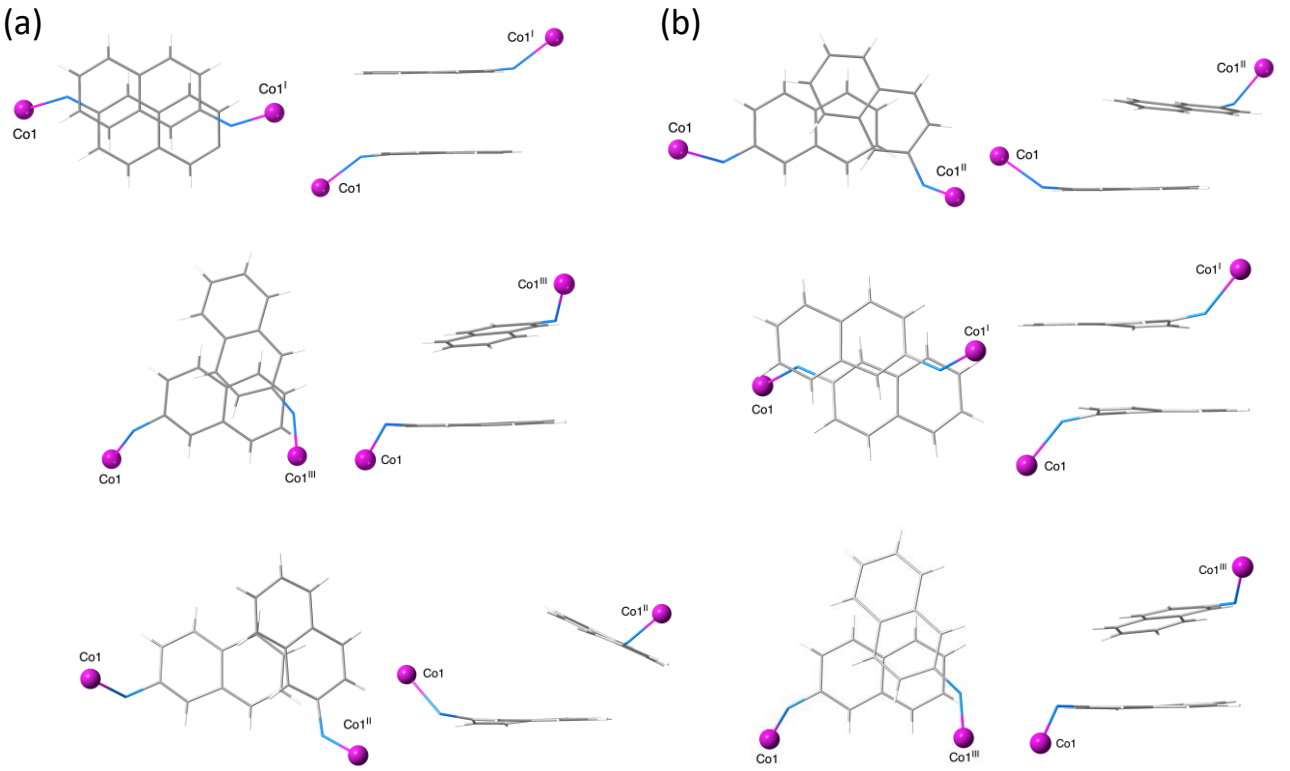

Figure IV.S2 Top (left) and front (right) views of the π-bonded naphthalene dimers within the ladder-type double chains of **1** (a) and **1'** (b) with the atom numbering scheme [symmetry code: (i) = 1 – *x*, 1 – *y*, 1 – *z*; (ii) = – *x*, 1 – *y*, 1 – *z*; (iii) = 1 + *x*, *y*, *z*]. The pink cobalt atoms correspond to the LS configuration.

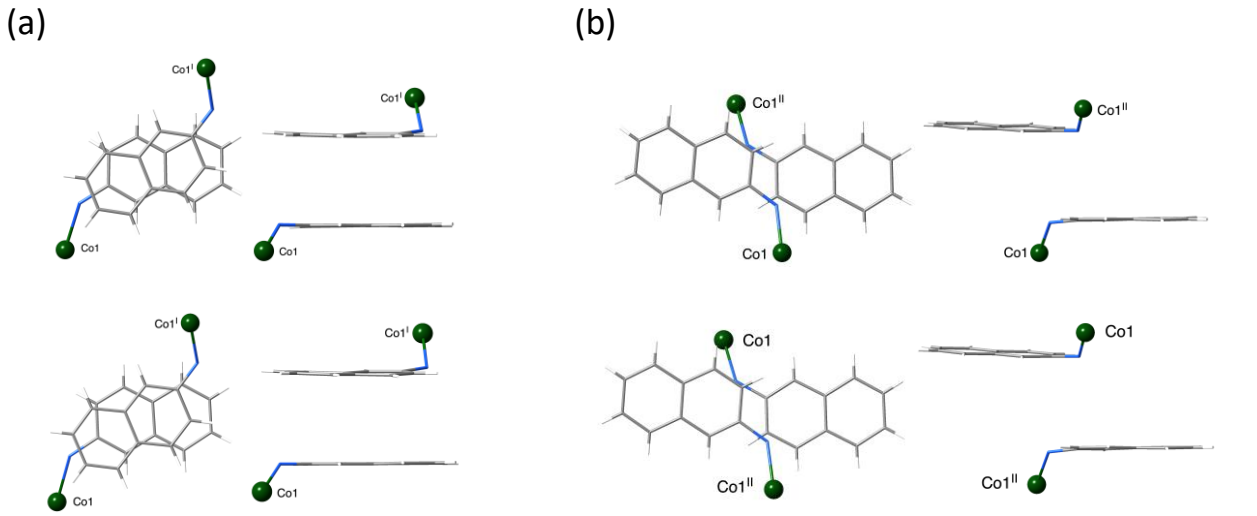

Figure IV.S3 Top (left) and front (right) views of the π-bonded naphthalene dimers within the square grid-type layers of **2** (a) and **2'** (b) with the atom numbering scheme [symmetry code: (i) = 1/2 + *x*, 1/2 – *y*, –1/2 + *z* (**2**)/ –1/2 + *x*, 1/2 – *y*, 1/2 + *z* (**2'**); (ii) = 1/2 + *x*, 1/2 – *y*, 1/2 + *z* (**2**)/ –1/2 + *x*, 1/2 – *y*, –1/2 + *z* (**2'**); (iii) = 1 + *x*, *y*, *z* (**2**)/ –1 + *x*, *y*, *z* (**2'**)]. The green cobalt atoms correspond to the HS configuration.

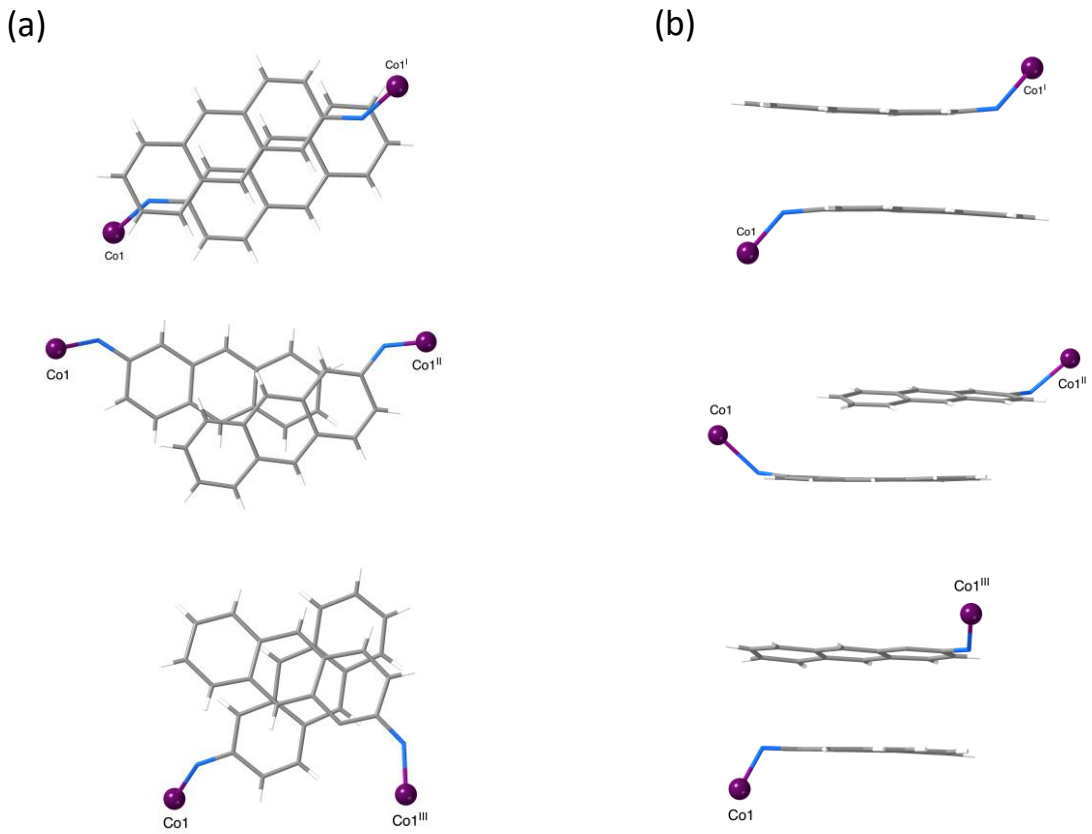

Figure IV.S4 Top (left) and front (right) views of the π-bonded anthracene dimers within the ladder-type double chains of **3** with the atom numbering scheme [symmetry code: (i) = 1 – *x*, 1 – *y*, 1 – *z*; (ii) = – *x*, 1 – *y*, 1 – *z*; (iii) = 1 + *x*, *y*, *z*]. The purple cobalt atoms correspond to a mixed LS/HS configuration.

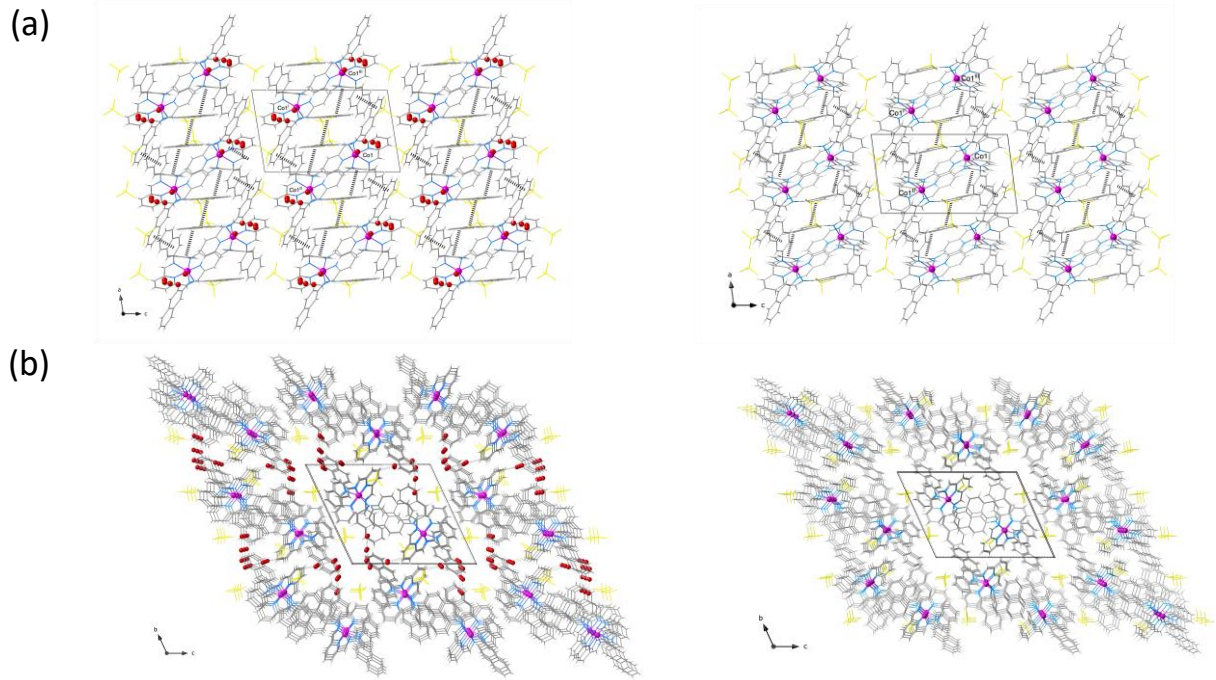

Figure IV.S5 (a) Projection view of the π-bonded layer array of double chains of **1** (left) and **1'** (right) along the crystallographic *b* axis. (b) Perspective view of the crystal packing of **1** (left) and **1'** (right) along the crystallographic *a* axis. The intermolecular π-stacking interactions are drawn as hashed lines, respectively. The pink cobalt atoms correspond to the LS configuration, while the crystallisation water molecules and the perchlorate anions are shown in red and yellow colours, respectively.

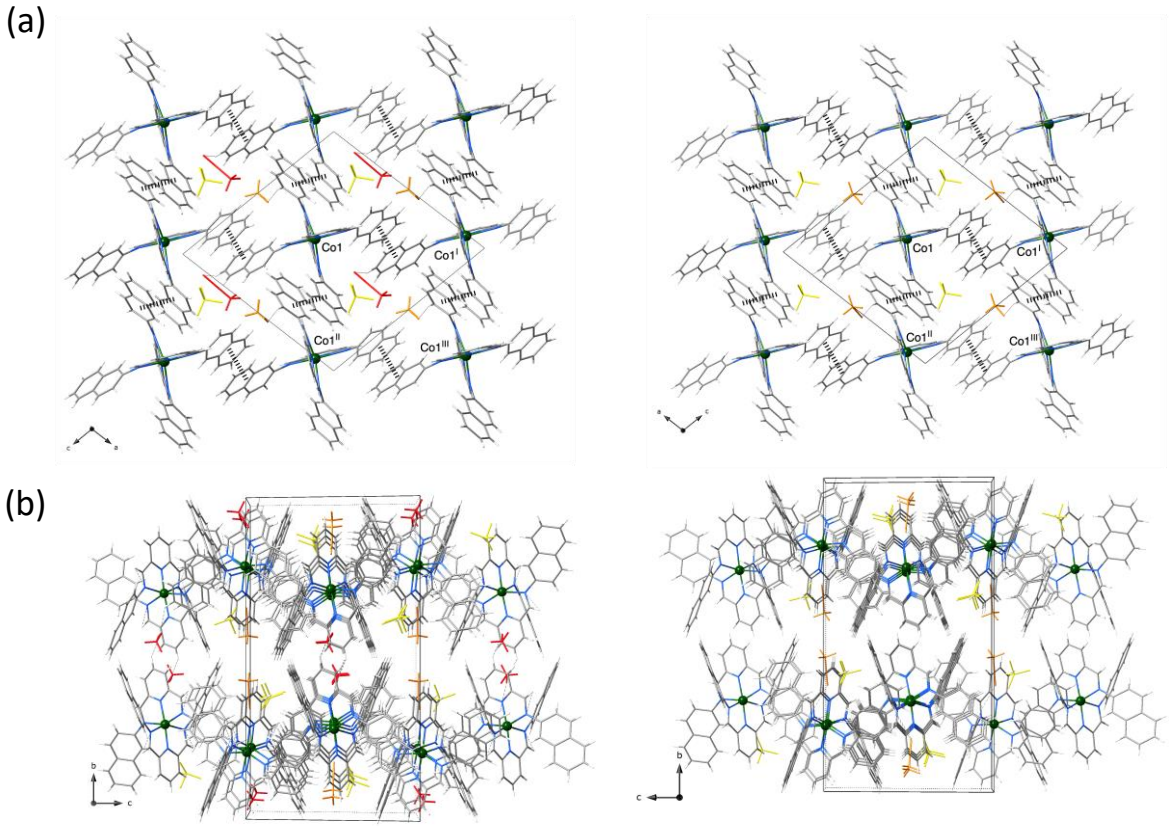

Figure IV.S6 (a) Projection view of the π-bonded square-grid layers of **2** (left) and **2'** (right) along the crystallographic *b* axis. (b) Perspective view of the crystal packing of **2** (left) and **2'** (right) along the crystallographic *a* axis. The intermolecular π-stacking interactions are drawn as hashed lines, respectively. The green cobalt atoms correspond to the HS configuration, while the two distinct crystallisation acetonitrile molecules and the perchlorate anions are shown in red, orange, and yellow colours, respectively.

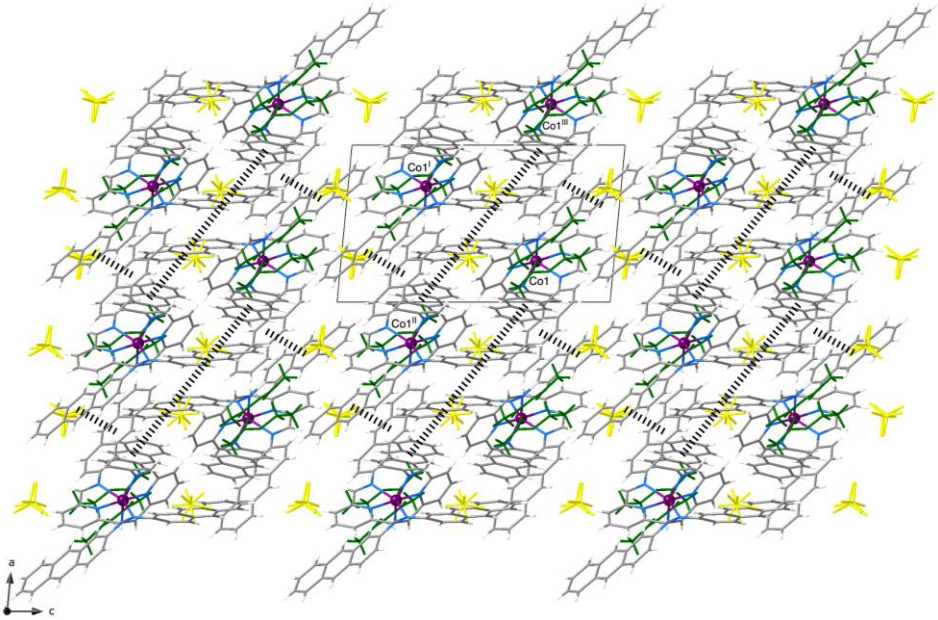

Figure IV.S7 Perspective view of the crystal packing of **3** along the crystallographic *b* axis. The intermolecular π-stacking contacts are drawn as hashed lines, respectively. The purple cobalt atoms correspond to the HS/LS configuration, while the ethylacetate water molecules and the perchlorate anions are shown in green and yellow colours, respectively.

Static and dynamic magnetic measurements

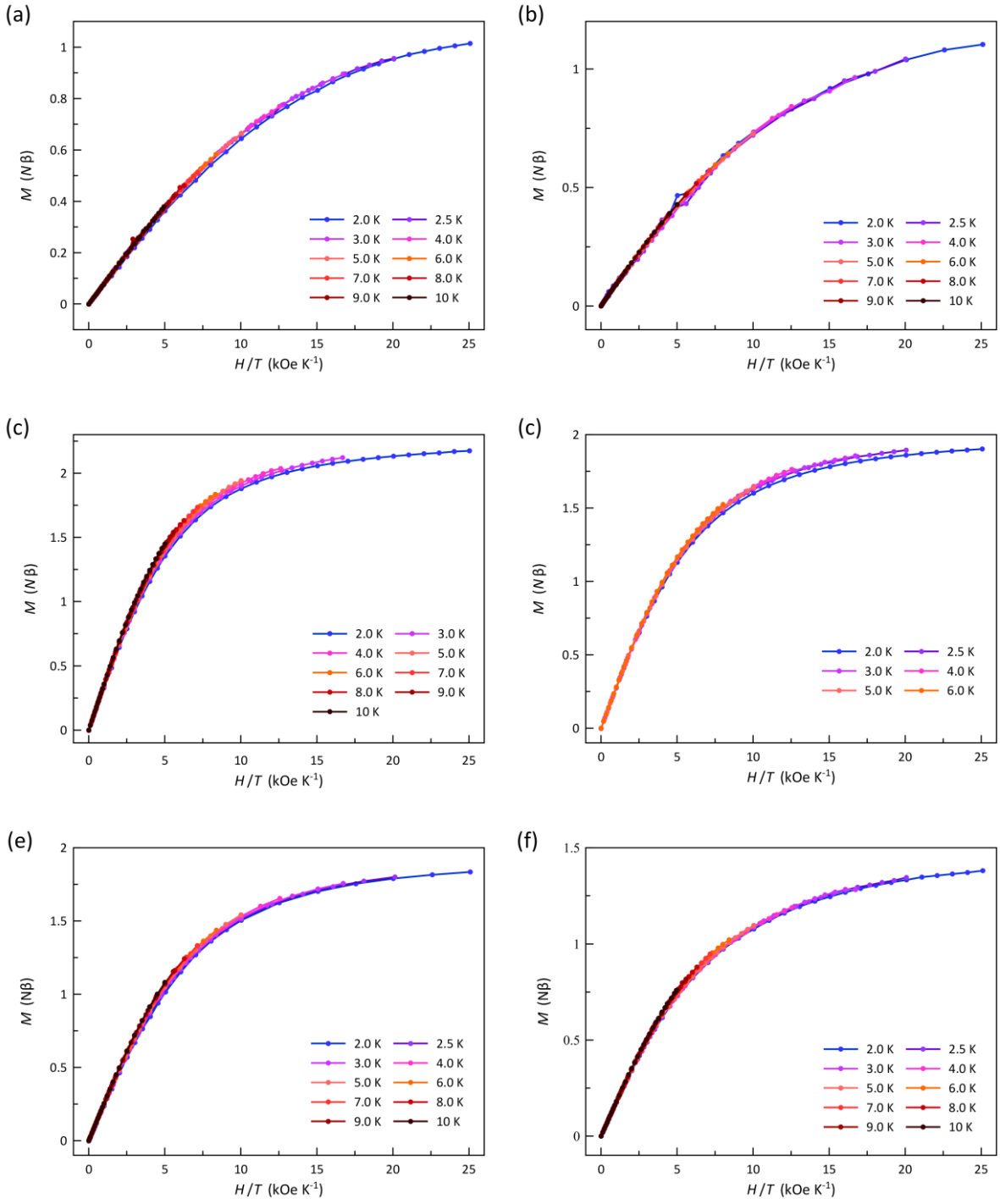

Figure IV.S8 *M vs H/T* plots for **1/1'**, **2/2'/2''** and **3** (a/b, c/d/e and f, respectively) in the temperature range of 2.0–10 K. The solid lines are only eye-guides.

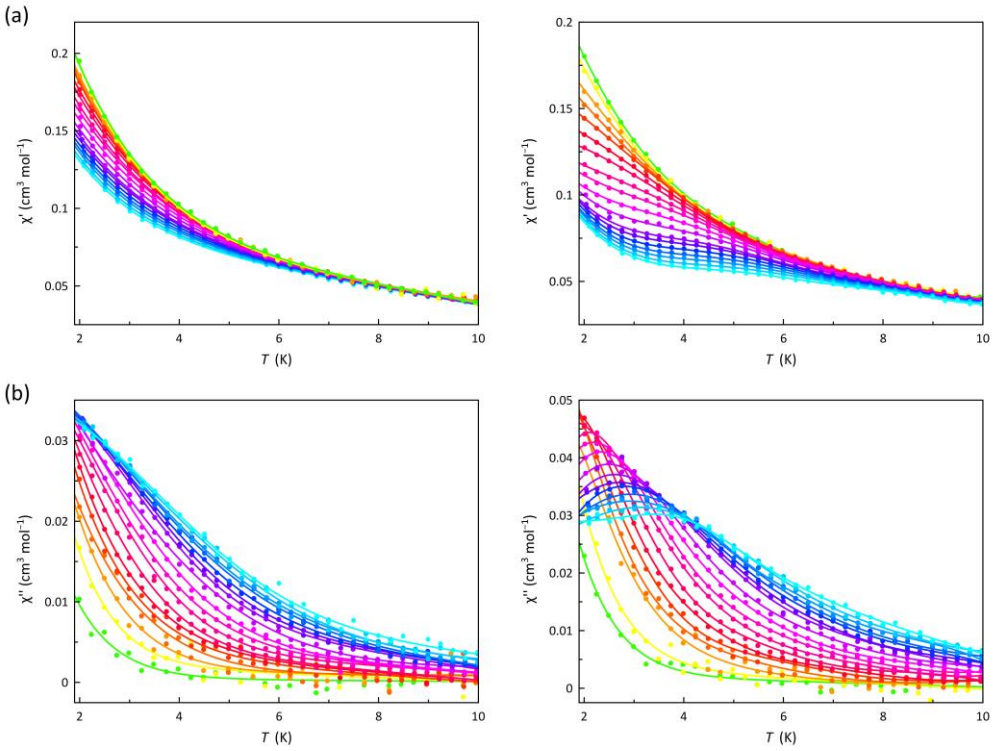

Figure IV.S9 Temperature dependence of χ_M' (a) and χ_M'' (b) of **1** under dc magnetic fields of 1.0 (left) and 2.5 kOe (right) at ±0.5 Oe oscillating field in the frequency range of 0.1–10 kHz (from cyan to green colours).

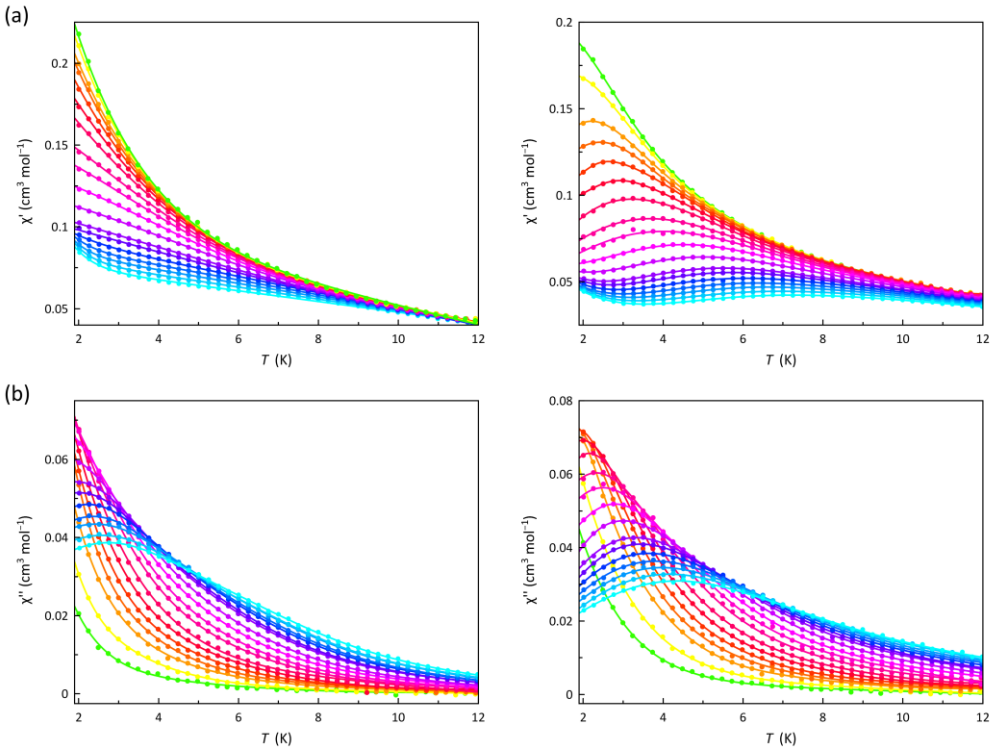

Figure IV.S10 Temperature dependence of χ_M' (a) and χ_M'' (b) of **1'** under dc magnetic fields of 1.0 (left) and 2.5 kOe (right) at ±0.5 Oe oscillating field in the frequency range of 0.1–10 kHz (from cyan to green colours).

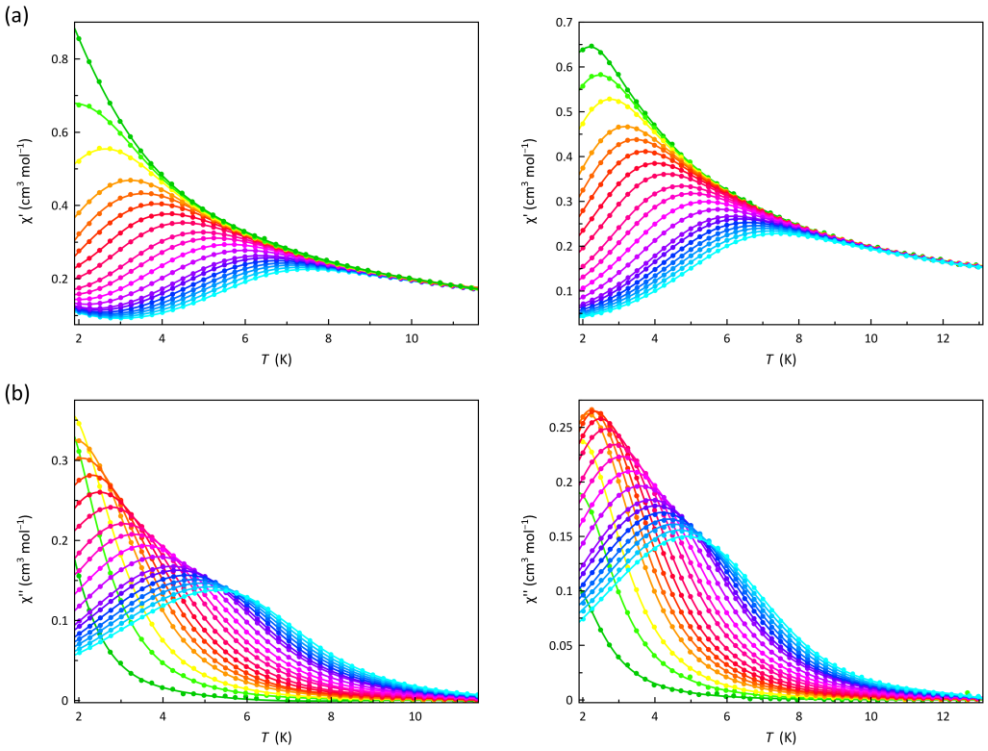

Figure IV.S11 Temperature dependence of χ_M' (a) and χ_M'' (b) of **2** under dc magnetic fields of 1.0 (left) and 2.5 kOe (right) at ±0.5 Oe oscillating field in the frequency range of 0.1–10 kHz (from cyan to green colours).

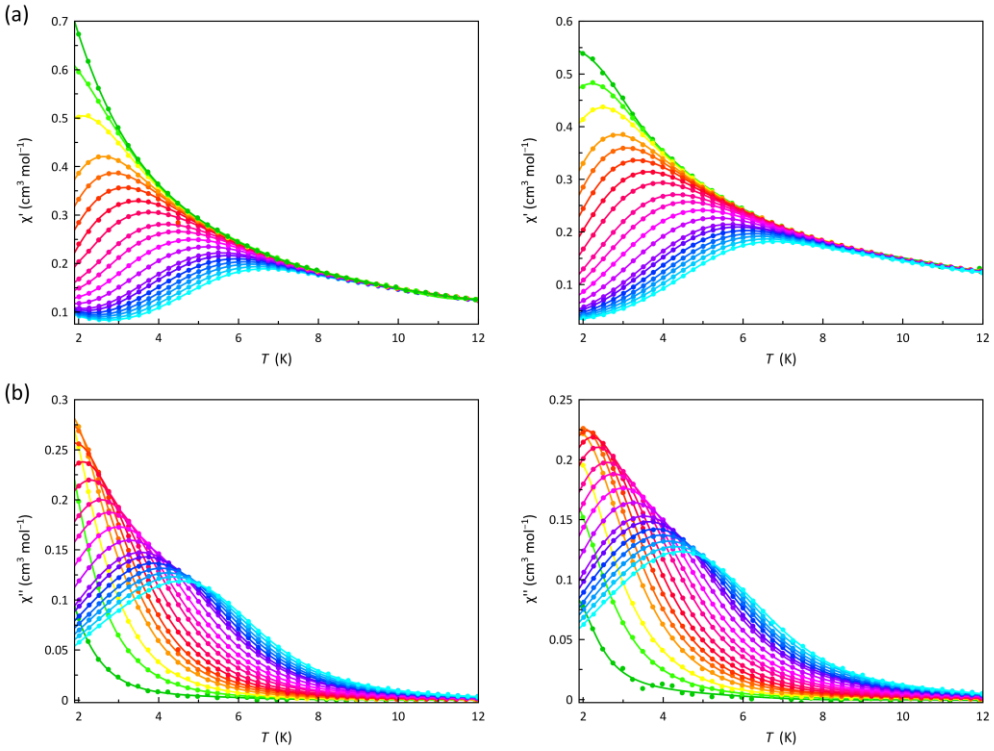

Figure IV.S12 Temperature dependence of χ_M' (a) and χ_M'' (b) of **2'** under dc magnetic fields of 1.0 (left) and 2.5 kOe (right) at ±0.5 Oe oscillating field in the frequency range of 0.1–10 kHz (from cyan to green colours).

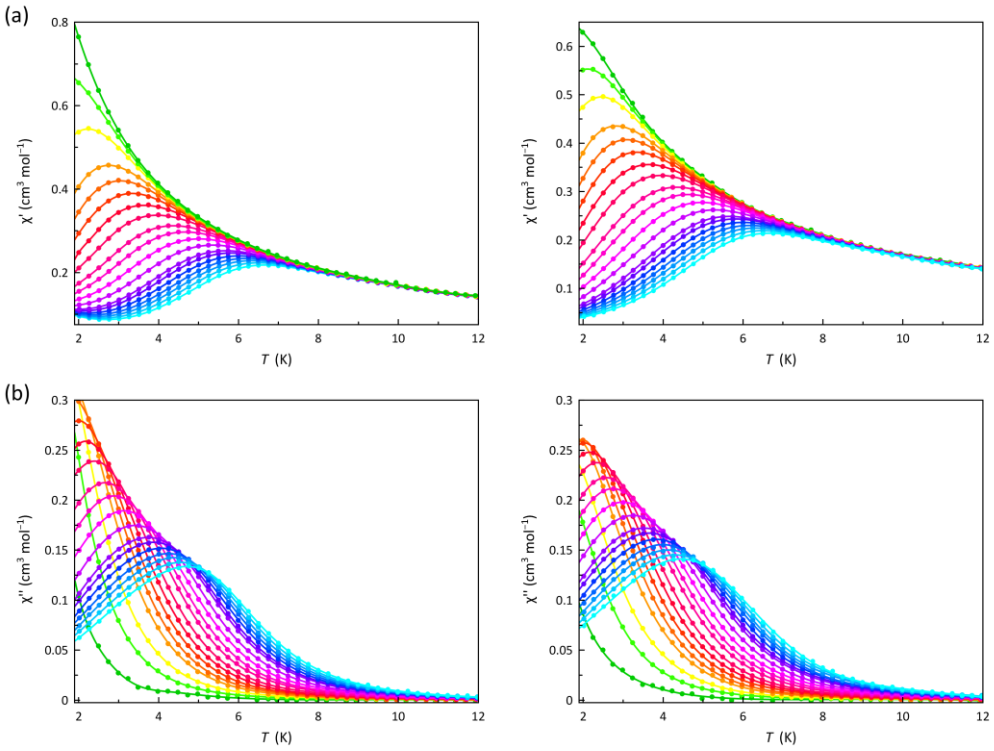

Figure IV.S13 Temperature dependence of χ_M' (a) and χ_M'' (b) of **2''** under dc magnetic fields of 1.0 (left) and 2.5 kOe (right) at ±0.5 Oe oscillating field in the frequency range of 0.1–10 kHz (from cyan to green colours).

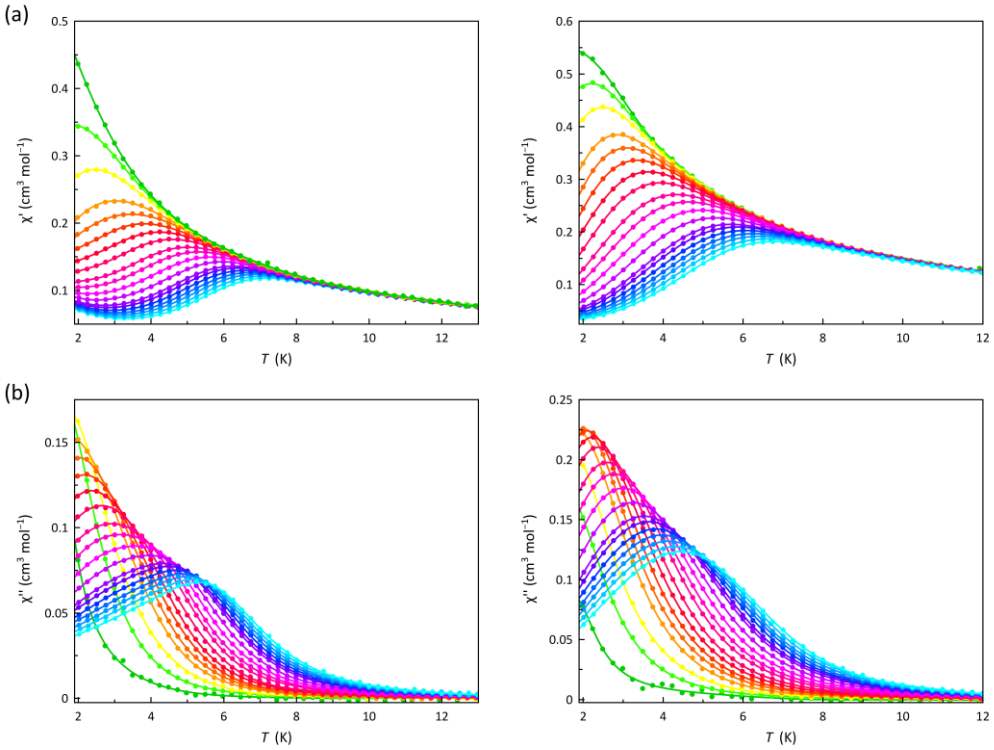

Figure IV.S14 Temperature dependence of χ_M' (a) and χ_M'' (b) of **3** under dc magnetic fields of 1.0 (left) and 2.5 kOe (right) at ±0.5 Oe oscillating field in the frequency range of 0.1–10 kHz cyan to green colours).

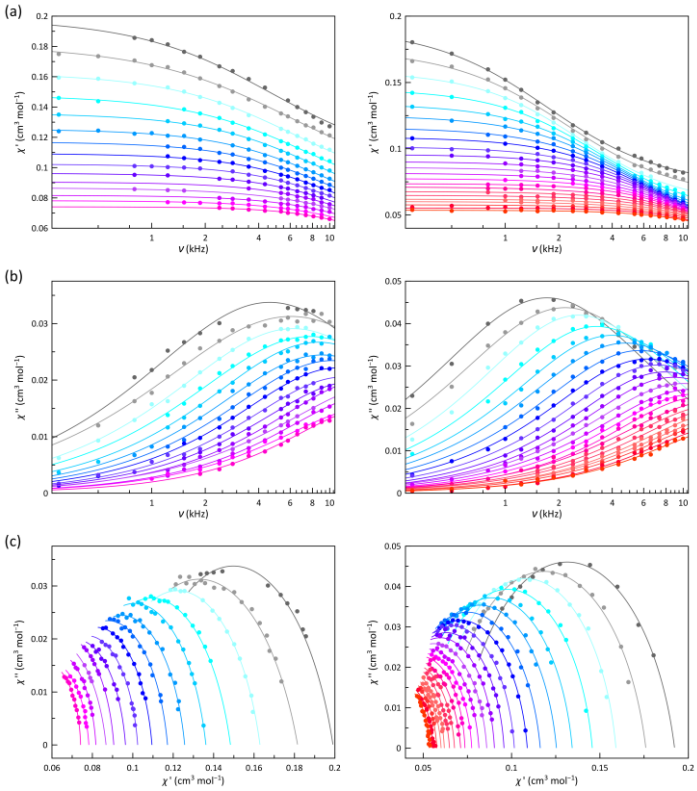

Figure IV.S15 Frequency dependence of χ_M' (a) and χ_M'' (b) and Argand plots (c) of **1** under dc magnetic fields of 1.0 (left) and 2.5 kOe (right) at ±0.5 Oe oscillating field in the temperature range of 2.0–7.5 K (from grey to warmer colours).

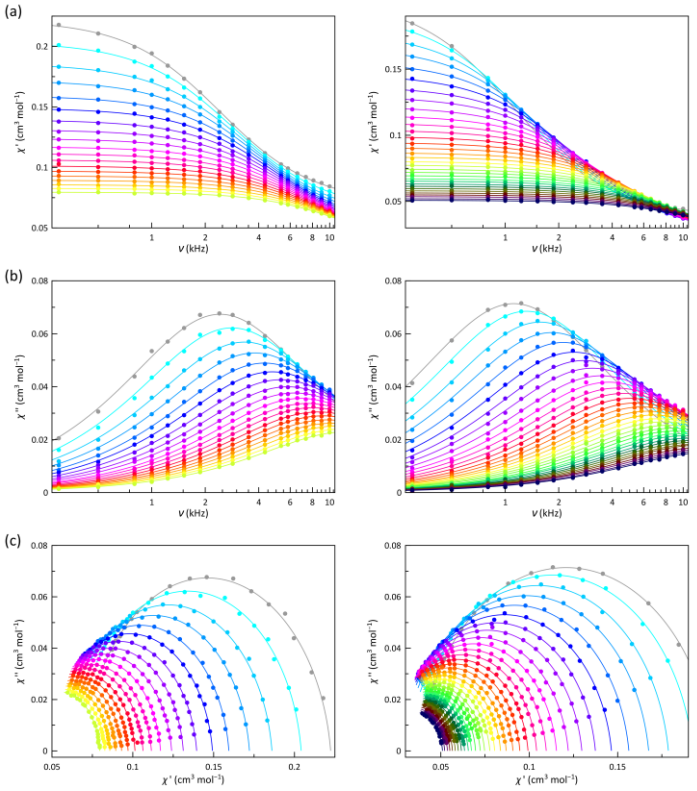

Figure IV.S16 Frequency dependence of χ_M' (a) and χ_M'' (b) and Argand plots (c) of **1'** under dc magnetic fields of 1.0 (left) and 2.5 kOe (right) at ±0.5 Oe oscillating field in the temperature range of 2.0–10 K (from grey to warmer colours).

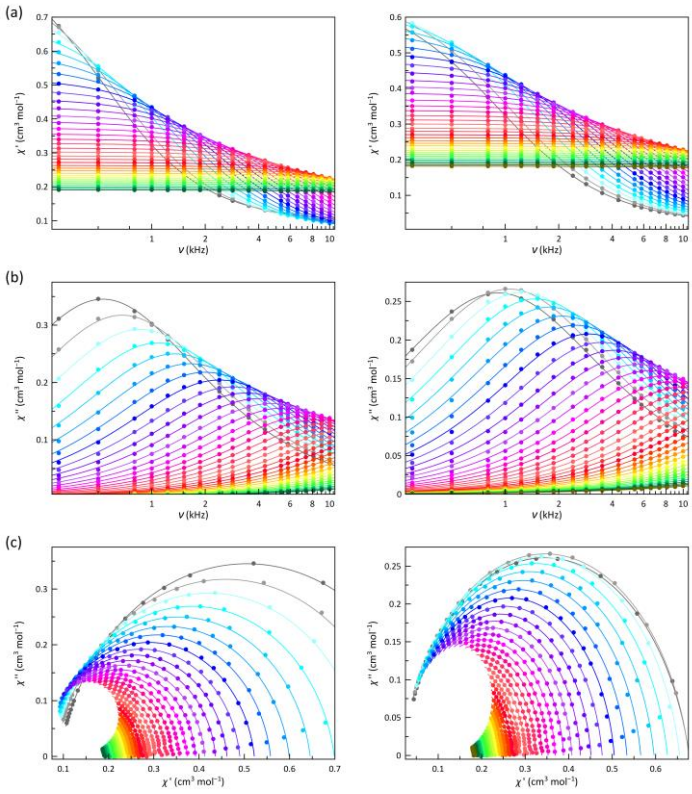

Figure IV.S17 Frequency dependence of χ_M' (a) and χ_M'' (b) and Argand plots (c) of **2** under dc magnetic fields of 1.0 (left) and 2.5 kOe (right) at ±0.5 Oe oscillating field in the temperature range of 2.0–9.5 K (from grey to warmer colours).

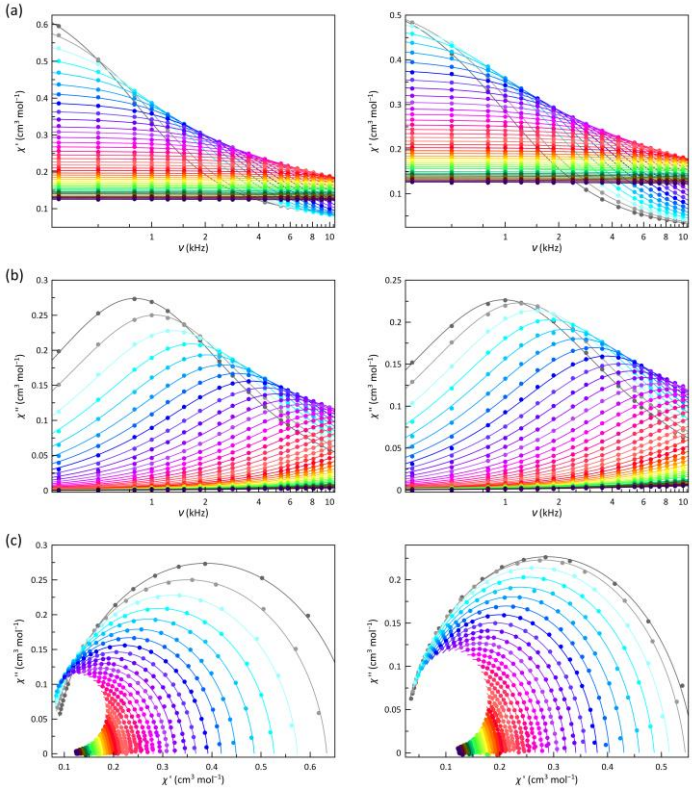

Figure IV.S18 Frequency dependence of χ_M' (a) and χ_M'' (b) and Argand plots (c) of **2'** under dc magnetic fields of 1.0 (left) and 2.5 kOe (right) at ±0.5 Oe oscillating field in the temperature range of 2.0–10 K (from grey to warmer colours).

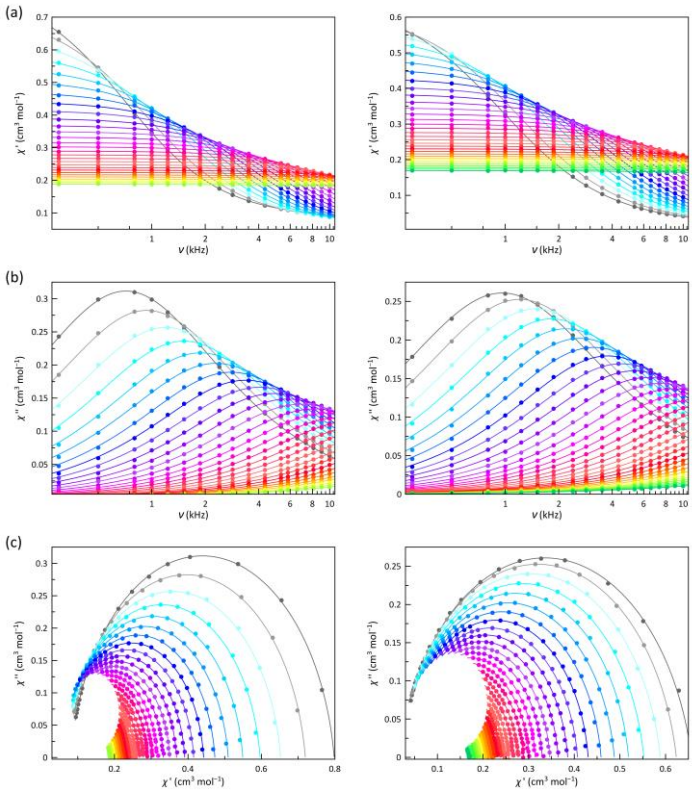

Figure IV.S19 Frequency dependence of χ_M' (a) and χ_M'' (b) and Argand plots (c) of **2''** under dc magnetic fields of 1.0 (left) and 2.5 kOe (right) at ±0.5 Oe oscillating field in the temperature range of 2.0–9.0 K (from grey to warmer colours).

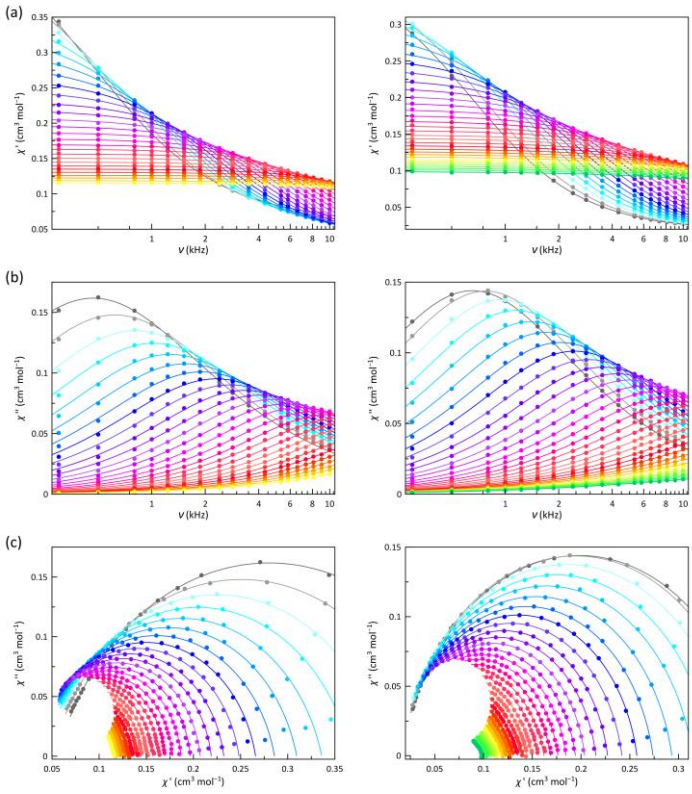

Figure IV.S20 Frequency dependence of χ_M' (a) and χ_M'' (b) and Argand plots (c) of **3** under dc magnetic fields of 1.0 (left) and 2.5 kOe (right) at ±0.5 Oe oscillating field in the temperature range of 2.0–9.0 K (from grey to warmer colours).

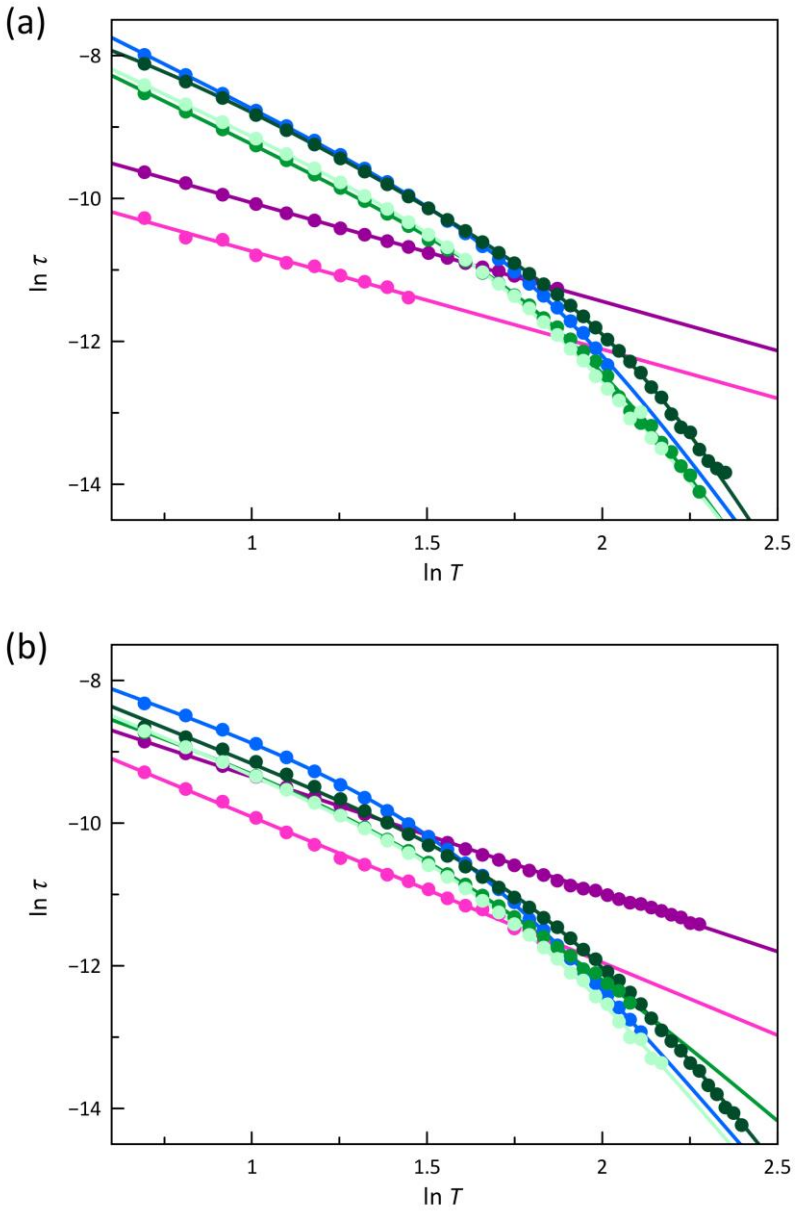

Figure IV.S21 ln τ *vs* ln *T* plots for **1** (pink), **1'** (purple), **2** (dark green), **2'** (green), **2''** (pale green) and **3** (blue) under applied *dc* magnetic fields of 1.0 (a) and 2.5 (b). The solid lines are the best-fit curves (see text).

Photophysical measurements

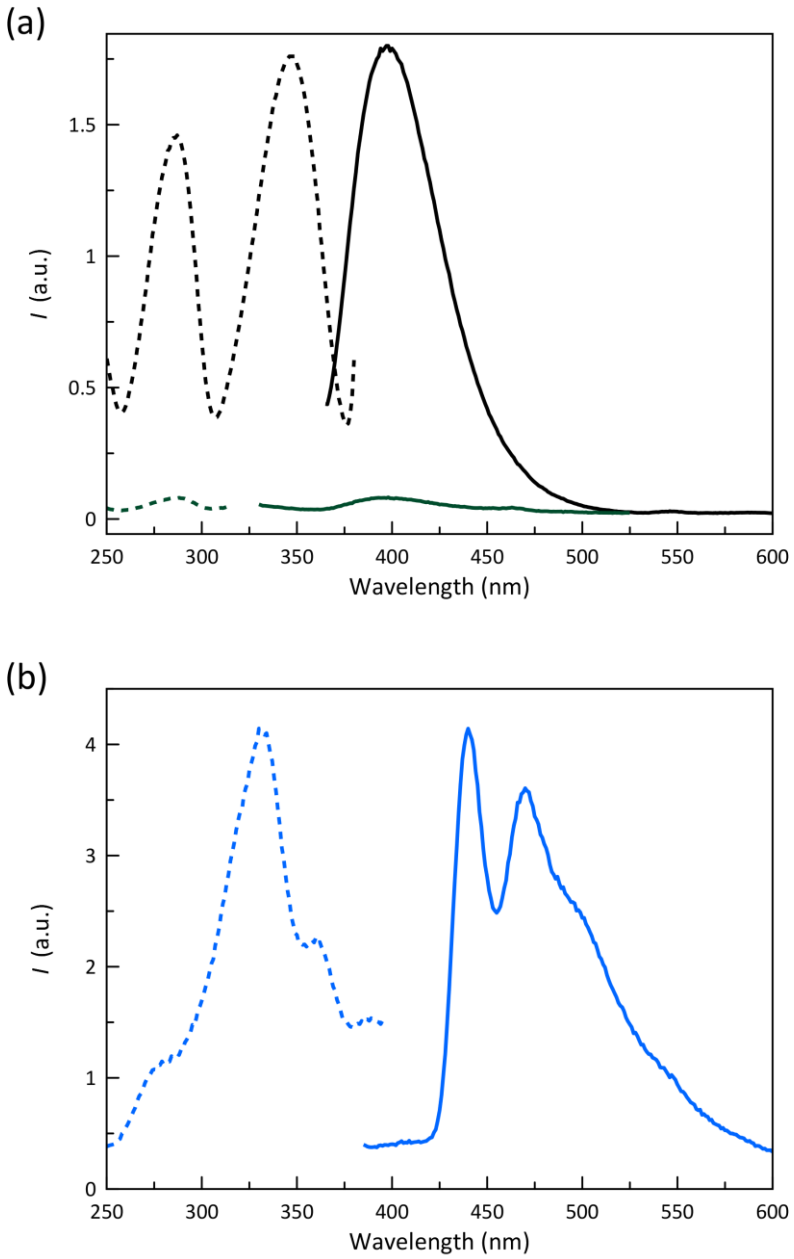

Figure VI.S22 Electronic excitation (dotted lines) and emission (solid lines) spectra of a 0.01 mM acetonitrile solution of (a) **2** (green) compared to those of a 0.01 mM acetonitrile solution of 2-NaphPDI ligand (black) and (b) **3** at room temperature. See text.

CHAPTER V

PHOTOCHEMICALLY-ACTIVE SPIN CROSSOVER MOLECULAR NANOMAGNETS

V.1 – Background and Highlights

A major goal in the emerging field of Molecular Opto-Spintronics (MOS) is the control of long-lived photomagnetic states through light-induced processes enabled by photochemically-active components that are part of the molecular material.[1–6] The current challenge is increasing the lifetime of the photomagnetic states to allow the implementation of the molecular systems as novel room temperature-operative spintronic and quantum computing nanodevices. In this sense, mononuclear spin crossover (SCO) and related valence tautomeric (VT) transition metal complexes with potential photochemically-active ligands are capital to MOS nanotechnologies.[7–19]

The attractiveness of SCO and VT systems results from the versatility of those systems and the possibility of generating long-lived photomagnetic states through ligand-driven, light-induced spin crossover (LD-LISC)[1,20–24] and valence tautomerism (LD-LIVT). [25–29] These related processes involve a spin state change of the SCO or VT active centre induced by a ligand-field variation associated with the ligand's photochemical reaction. Representative examples of LD-LISC and LD-LIVT are the mononuclear $[Fe^{II}(stpy)_4(NCS)_2]$ and $[Co^{II}(stpy)_2(DTBSQ)_2]$ complexes with the non-innocent photoactive 4-styrylpyridine (stpy) ligand (DTBSQ = 3,5-di-*t*-butylsemiquinone radical anion).[20,25] Both complexes undergo reversible cis(*Z*)-trans(*E*) photoisomerisation of the stpy ligand upon UV irradiation of different wavelengths. In the former case, the subtle variations on the ligand field derived from this light-induced process result in the ON-OFF switching below 100 K between the paramagnetic *Z*-stpy HS (ON) and diamagnetic *E*-stpy LS (OFF) states. In the cobalt(II) complex, the switch between the VT transition *Z*-stpy Co^{II}-$SQ^{\bullet}$/$SQ^{\bullet}$ HS and *E*-stpy Co^{III}-$SQ^{\bullet}$/CAT LS states ($SQ^{\bullet}$ = semiquinonate radical and CAT = chatecholate dianion) provides distinct thermally-induced gradual VT behaviours.

Following the same approach, the iron(II) complex with the terpyridine-like ligand 2,6-di(1*H*-pyrazol-1-yl)-4-styrylpyridine (dpzstpy) features one-way photoisomerisation of this ligand from *Z* to *E* forms by visible irradiation in both solution and solid state.[22] While the *Z* form of the complex behaves as a HS Fe^{II} ion at any temperature, its *E* form undergoes a gradual and incomplete SCO to give a non-diamagnetic phase below 100 K.

In this chapter, we present the synthesis, structural and spectroscopic characterisation, and the static and dynamic magnetic properties of two isostructural mononuclear cobalt(II) complexes with a TERPY derivative containing a photoactive trans(*E*)-styryl substituent of general formula $[Co^{II}(E\text{-StyTERPY})_2]X_2$ [X = ClO_4^- (**1**) and PF_6^- (**2**); *E*-4-StyTERPY = (*E*)-4′-styryl-2,2′/6′,2″-terpyridine]. **1** and **2** constitute a unique pair of spin-crossover molecular nanomagnets (SCO/SMMs) exhibiting a counteranion tuning of the single-molecule magnet (SMM) behaviour in the solid state. A study of their photochemical activity in solution supports the occurrence of a cis-trans (*Z*/*E*) geometric ligand photoisomerisation upon UV light irradiation, making them promising candidates for future applications as spin quantum photoswitches in MOS (Scheme V.1).

V.2 – Ligand Design and Synthetic Strategy

In the preceding chapters, we have reported a family of multifunctional and multiresponsive mononuclear cobalt(II) complexes with pyridine-2,6-diimine (PDI)-type ligands that undergo both thermal-assisted low-spin (LS)/high-spin (HS) and magnetic field-induced faster-relaxing (FR)/slower-relaxing (SR) transitions. They include some examples of molecular spin quantum dynamic systems (switches) controlled by a variety of internal electronic (metal oxidation and spin states) or steric factors (ligand substituents and conformation) and external chemical (solvent) or physical stimuli (temperature, magnetic field and light). In particular, we have demonstrated the reversible solvatoswitching of the magnetic (SCO and SMM) and

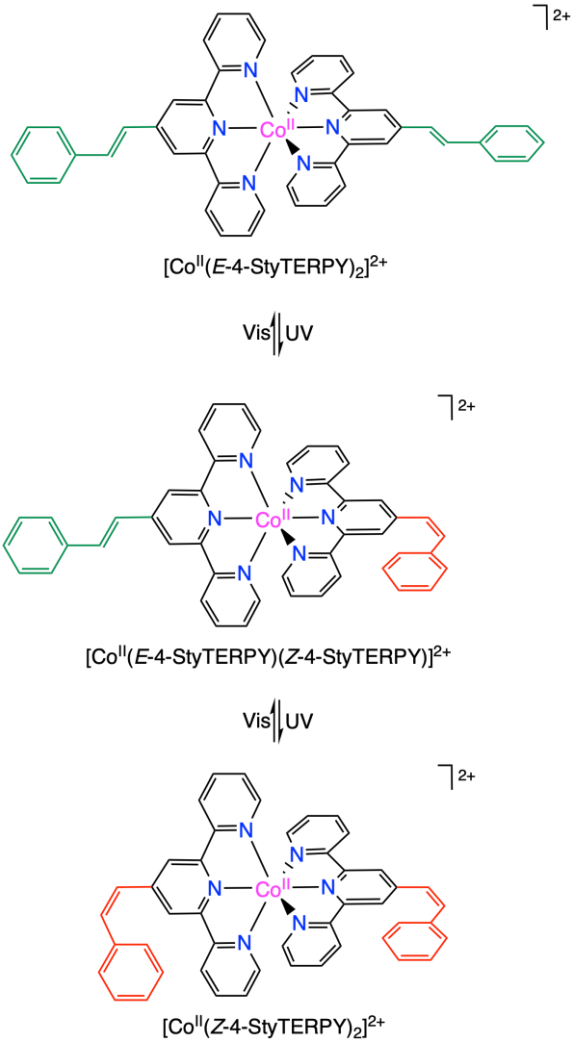

Scheme V.1 Illustration of the photochemical transfer series of mononuclear octahedral cobalt(II)-(*E*/*Z*)-4-StyTERPY complexes showing the corresponding *cis-trans* (*Z*/*E*) geometric ligand photoisomerisation equilibria.

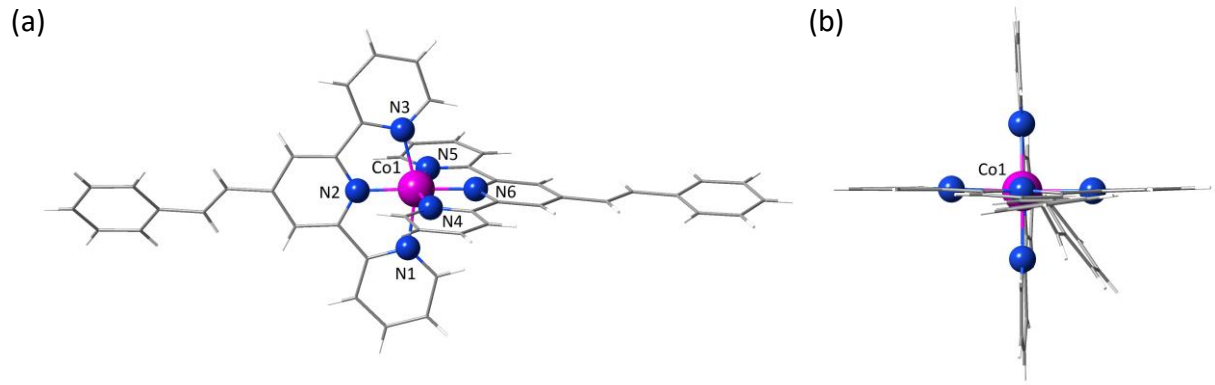

Figure V.1 Front (a) and side (b) views of the cationic mononuclear cobalt(II) unit of **1** with the atom numbering scheme for the first coordination sphere of the metal atom.

optical (luminescent) behaviours in the mononuclear octahedral cobalt(II) complex with a photoactive 2-naphthyl-disubstituted PDI ligand (see Chapter IV).

In this line, we would try to develop a novel family of multifunctional and multiresponsive SCO/SMMs based on mononuclear cobalt(II) complexes with 2,2′/6′,2″-terpyridine (TERPY) and derivatives as ligands. Hence, Shao and Hayami have independently reported on the reversible on-off solvatoswitching of the SCO and SMM in octahedral cobalt(II) complexes with the TERPY ligand itself or its 4-bromophenyl-substituted derivative after dehydration/rehydration.[30,31] In the search for new optically addressable SCO/SMM dynamic systems, we present herein a set of cobalt(II)-TERPY complexes with photoactive *trans* (*E*)-styryl substituents to provide the additional photochemical activity towards *cis*-*trans* (*Z*/*E*) geometric ligand isomerisation into the class of multifunctional and multiresponsive SCO/SMMs (Scheme V.1).

The stable trans isomer of the ligand *E*-4-StyTERPY was prepared as reported earlier[32] from the successive three-step condensation of (*E*)-cinnamaldehyde, 2-acetylpyridine, and pyridine (1:2:1 molar ratio) in methanol (Scheme V.2).

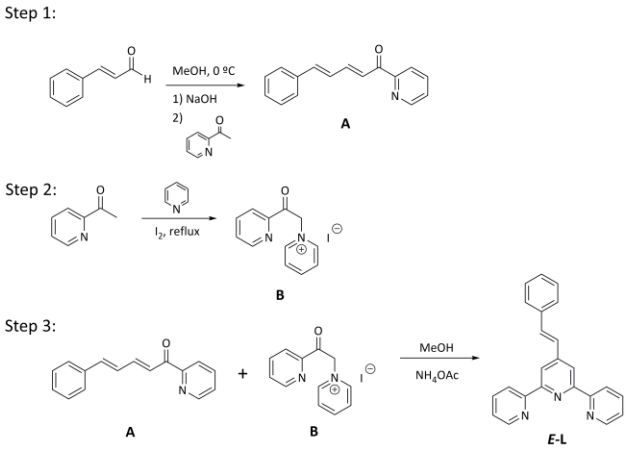

Scheme V.2 Synthetic route for the *trans* (*E*) isomer of the styryl-substituted terpyridine ligand.

1 and **2** were then synthesised from the stoichiometric reaction (2:1 molar ratio) of *E*-4-StyTERPY with either cobalt(II) perchlorate hexahydrate or cobalt(II) nitrate trihydrate and potassium hexafluorophosphate (see section V.7 - Experimental Section). Both compounds were isolated as X-ray quality single crystals in good yields (76–80%) by slow diffusion of methanol/chloroform solutions in a glass test tube at room temperature. They were characterised by elemental analyses (C, H, N), Fourier-transform infrared (FT-IR), electronic absorption (UV/Vis) and electron paramagnetic resonance (EPR) spectroscopies (see V.7 - Experimental Section).

Attempts to isolate the *Z* derivative of the mononuclear cobalt(II) complex by UV irradiation of 1.0 mM acetone solutions of **1** gave a poorly characterised solid. Current efforts are devoted to synthesising the *cis* complex from the *Z*-4-StyTERPY ligand, which should be previously isolated by straightforward synthesis from the *cis* (*E*)-cinnamaldehyde precursor or irradiating the *E*-4-StyTERPY ligand and further purification by column chromatography.

The experimental powder X-ray diffractograms of **1** and **2** show a similar pattern, suggesting that they are isostructural regardless of the counteranion [X = ClO_4^- (**1**) and PF_6^- (**2**)] (Figure V.S1).

V.3 – Description of the Structures

Both compounds crystallise in the same *C*2/c space group of the monoclinic system, but **2** has larger unit cell dimensions to accommodate the bulkier PF_6^- anion [*V* = 8270 (**1**) and 8627 Å^3 (**2**); Table V.1]. Their structures consist of mononuclear bis(chelating) cobalt(II) complex cations, $[Co^{II}(E\text{-StyTERPY})_2]^{2+}$ (Figure V.1 and Figure V.S2), and ordered or partially disordered perchlorate (**1**) or hexafluorophosphate (**2**) anions counterbalancing the charge (Figures V.2–4).

Molecular structures. Cobalt atoms in **1** and **2** exhibit an axially compressed octahedral geometry with a partial rhombic distortion. The two pairs of distal pyridine nitrogen atoms (N_d) from each *E*-4-StyTERPY ligand define the equatorial plane, while the pair of central pyridine nitrogen atoms (N_c) occupies the axial positions (Figures V.1 and V.S2, left). Selected structural data for **1** and **2** are summarised in Table V.2.

Table V.1 Summary of Crystallographic Data for **1** and **2**

	1	**2**
Formula	$C_{46}H_{34}N_6O_8Cl_2Co$	$C_{46}H_{34}N_6F_{12}P_2Co$
M (g mol^{-1})	928.65	1019.68
Crystal system	Monoclinic	Monoclinic
Space group	*C2/c*	*C2/c*
a (Å)	35.6309(13)	36.5770(14)
b (Å)	8.8864(2)	8.7494(2)
c (Å)	26.1368(7)	26.9611(8)
α (°)	90	90
β (°)	92.088(3)	90.947(4)
γ (°)	90	90
V (Å^3)	8270.21	8627.1
Z	8	8
T	150	150
$R_1{}^a$ [$I > 2\sigma(I)$]	0.0887	0.05407

^{a} $R_1 = \sum(|F_o| - |F_c|)/\sum|F_o|$.

Overall, the metal-nitrogen bond lengths are typical of LS Co^{II} ions, being slightly larger for **2** [R = 2.031 (**1**)/2.036 Å (**2**); Table V.2]. The average values of the axial Co–N_c bond lengths are notably shorter than those of the equatorial Co–N_d ones for both isomorphs [R_{ax} = 1.913 (**1**)/1.919 Å (**2**) and R_{eq} = 2.091 (**1**)/2.095 Å (**2**); Table V.2]. Yet, a greater fluctuation of the equatorial Co–N_d bond lengths is found for **1**, as expressed by the axial and rhombic structural distortion parameters [Δ_R = 0.088 (**1**)/0.086 (**2**) and δ_R = 0.044 (**1**)/0.001 (**2**); Table V.2]. Moreover, a severe non-planar ruffling distortion deviates the N_d atoms from the equatorial mean plane of the metal ion, as reflected by the average values of the mean out-of-plane N_d displacement [δ = ± 0.389 (**1**)/0.402 Å (**2**); Table V.2].

The $[Co^{II}(E\text{-4-StyTERPY})_2]^{2+}$ units possess a rod-like shape of approximate 1.0 nm diameter × 2.5 nm height dimensions (Figures V.1a and V.S2a). They have a pseudo C_{2v} molecular symmetry with two almost perpendicularly oriented ligands (Figures V.1b and V.S2b). There are larger deviations from this orthogonality and ligand planarity in **1**, as reflected by the values of the dihedral angle between the mean planes of the terpyridine fragments [Φ = 84.0 (**1**)/89.4° (**2**); Table V.2] and those between the terpyridine and the styryl fragments [φ = 7.9 (**1**)/12.3 (**2**) and 34.6 (**1**)/31.4° (**2**); Table V.2]. This slight flip-flop motion of one of the styryl groups is also evidenced by a modest increase in the carbon-carbon bond lengths within the middle vinyl group for the non-planar terpyridine fragment compared to the planar one [d(C=C) = 1.327 (**1**)/1.335 (**2**) and 1.318 (**1**)/1.325 Å (**2**), respectively; Table V.2], reflecting thus a partial loss of π-conjugation between the terpyridine and styryl fragments in **1**.

Table V.2 Selected Structural Data for **1** and **2**

	1	**2**
R_1(Co–N_d)^a (Å)	2.137	2.096
R_2(Co–N_d)^a (Å)	2.044	2.093
R_3(Co–N_c)^b (Å)	1.913	1.919
$R_{eq}{}^c$ (Å)	2.091	2.095
R^d (Å)	2.031	2.036
$\Delta_R{}^e$	0.088	0.086
$\delta_R{}^f$	0.044	0.001
N_d–Co–$N_d{}^g$ (°)	92.0	92.1
N_c–Co–$N_c{}^h$ (°)	176.7	178.4
δ^i (Å)	±0.389	±0.402
Φ^j (°)	84.0	89.4
φ^k (°)	7.9	12.3
	34.6	31.4
d(C=C)^l (Å)	1.318	1.325
	1.327	1.335

^{a}Average equatorial bond lengths from each ligand. ^{b}Average axial bond lengths. ^{c}Average equatorial bond lengths defined as $R_{eq} = (R_1 + R_2)/2$. ^{d}Average cobalt-nitrogen bond distances defined as $R = (R_1 + R_2 + R_3)/3$. ^{e}Axial distortion parameter defined as $\Delta_R = (R_{eq} - R_3)/R$. ^{f}Rhombic distortion parameter defined as $\delta_R = (R_1 - R_2)/R_{eq}$. ^{g}Average equatorial bond angles. ^{h}Average axial bond angles. ^{i}Average deviations of the distal pyridine-nitrogen donor atoms from the mean metal equatorial plane. ^{j}Dihedral angle between the mean planes of the terpyridine ligand fragments. ^{k}Dihedral angle between the mean planes of the terpyridine and the styryl groups from each ligand. ^{l}Carbon-carbon bond distances for the vinyl group from each ligand.

Crystal structures. In **1** and **2**, there are some intermolecular "edge-to-face" π-stacking interactions involving the phenyl and the distal pyridine rings from neighbouring $[Co^{II}(E\text{-4-StyTERPY})_2]^{2+}$ units [C–H···C = 2.7392–2.8992 Å (**1**) and 2.8640–3.1600 Å (**2**)]. These intermolecular π-π interactions are likely responsible for the aforementioned deviations from the molecular ligand planarity. Such interactions give rise to a π-bonded double layer of cationic mononuclear cobalt(II) units growing in the *ab* plane (Figure V.2 and Figure V.S3).

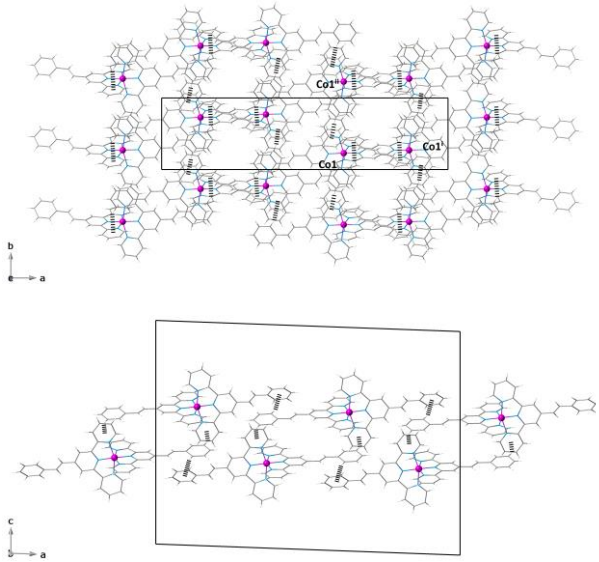

Figure V.2 Top and side projection views of a π-bonded double layer of cationic mononuclear cobalt units in **1** along the crystallographic *c* (top) and *b* (bottom) axes [symmetry code: (i) = 1/2 - *x*, 3/2 - *y*, 1 - *z*; (ii) = *x*, 1+*y*, *z*]. The "edge-to-face" π-stacking interactions are drawn as hashed lines.

A segregated array of adjacent double layers occurs along the *c* direction leading to a densely packed structure (Figures V.3 and V.4). The partially disordered perchlorate and hexafluorophosphate anions occupy the small voids within each layer, while the ordered perchlorate and hexafluorophosphate anions reside in the interlayer space (Figures V.3 and V.4, bottom). They establish moderate to weak intermolecular hydrogen-bonding interactions with the distal pyridine rings from the terpyridine fragments [C–H···$OClO_3$ = 2.4588–2.7073 Å (**1**) and C–H···FPF_5 = 2.4127–2.6179 Å (**2**)] (Figures V.3 and V.4, top). The distinct nature of the intermolecular hydrogen interactions involving the perchlorate (**1**) and hexafluorophosphate (**2**) anions would be responsible for the different rhombicity of the coordination sphere between these

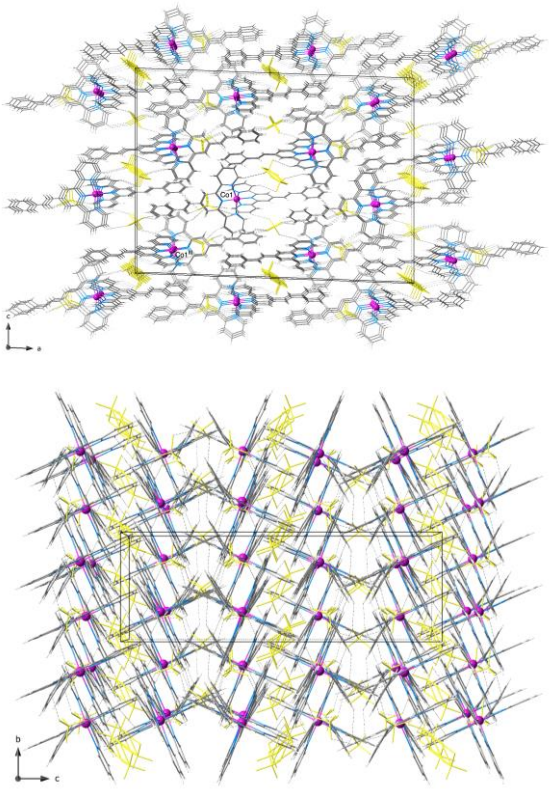

Figure V.3 Perspective views of the crystal packing of **1** along the crystallographic *b* (top) and *a* (bottom) axes [symmetry code: (iii) = 1/2 - *x*, 1/2 - *y*, 1/2 - *z*]. The intermolecular hydrogen bonding and π-π interactions are drawn as dashed and dotted lines, respectively.

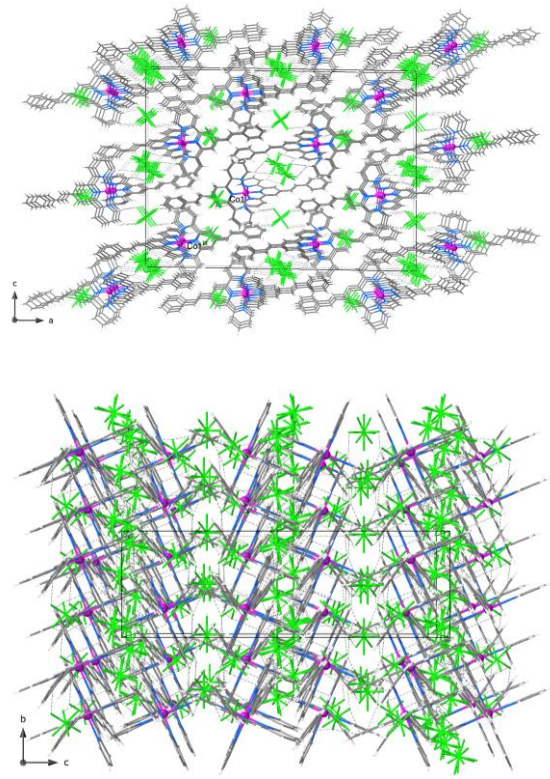

Figure V.4 Perspective views of the crystal packing of **2** along the crystallographic *b* (top) and *a* (bottom) axes [symmetry code: (iii) = 1/2 - *x*, 1/2 - *y*, 1/2 - *z*]. The intermolecular hydrogen bonding and π-π interactions are drawn as dashed and dotted lines, respectively.

two isomorphs. The intralayer intermetallic distances through the edge-to-face π-stacked motif are very large [Co1···Co1^{i} = 10.484(2) (**1**)/11.076(3) Å (**2**) and Co1···Co1^{ii} = 8.886(3) (**1**)/8.749(3) Å (**2**) Å; symmetry code: (i) = 1/2 – *x*, 3/2 – *y*, 1 – *z*; (ii) = *x*, 1 + *y*, *z*] and comparable with the shortest interlayer separation [Co1···Co1^{iii} = 11.298(2) (**1**)/11.830(3) Å (**2**); symmetry code: (iii) = 1/2 – *x*, 1/2 – *y*, 1/2 – *z*].

V.4 – Magnetic Properties and EPR Spectra

The magnetic properties of the isomorphs **1** and **2** were measured in both direct (*dc*) and alternating current (*ac*) regimes to investigate the influence of the counteranion in the SCO and SMR behaviour in the solid state (see section V.7 - Experimental Section).

Static magnetic behaviour. The $\chi_M T$ *versus* T plots (χ_M being the *dc* molar magnetic susceptibility per mononuclear unit) show a gradual, either complete (**1**) or incomplete (**2**), thermally-induced SCO (Figure V.5). Despite the presence of intermolecular π-stacking and hydrogen bonding interactions, no hysteresis was found, as reported earlier for the vast majority of cobalt(II) complexes with terpyridine-type ligands (with only a few exceptions).[33] The $\chi_M T$ values of 1.57 (**1**)/1.59 cm^3 mol^{-1} K (**2**) at room temperature are similar, being lower than the expected one for a HS Co^{II} ion with an unquenched orbital momentum contribution ($\chi_M T$ = 2.70 cm^3 mol^{-1} K with S = 3/2 and g = 2.4). Upon cooling, $\chi_M T$ decreases smoothly to reach a plateau around 100 K. The $\chi_M T$ value of 0.42 cm^3 mol^{-1} K for **1** at 2.0 K is as expected for a LS Co^{II} ion while that of 0.46 cm^3 mol^{-1} K for **2** is somewhat higher ($\chi_M T$ = 0.43 cm^3 mol^{-1} K with S = 1/2 and g = 2.15).

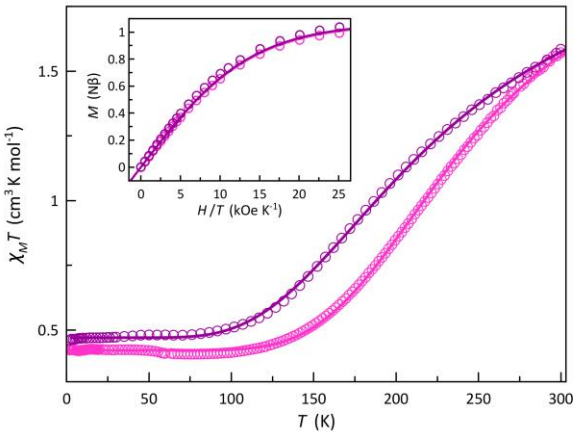

Figure V.5 Temperature dependence of $\chi_M T$ for **1** (pink) and **2** (purple). Solid lines. The solid lines are the theoretical curves through a simple thermodynamic spin transition model (see text). The inset shows the field dependence of M for **1** (pink) and **2** (purple) at T = 2.0 K. The solid line is the Brillouin curve for a doublet state (see text).

Isothermal magnetisation curves at 2.0 K as M *versus* H/T plots (M being the magnetisation per mononuclear unit, inset of Figure V.5), perfectly reproduced by the Brillouin function with S = 1/2 and g = 2.13 (**1**)/2.20 (**2**), confirms this conclusion. The experimental magnetic susceptibility data were well simulated through a simple thermodynamic model that takes into account

the enthalpy [ΔH = 752.7 (**1**)/ 450.7 kJ mol^{-1} (**2**)] and entropy changes [ΔS = 3.02 (**1**)/ 1.75 J mol^{-1} (**2**)] associated to the spin transition with a common Landé factor for both HS and LS Co^{II} ions [g = 2.12 (**1**)/ 2.24 (**2**)] (solid lines in Figure V.5).[34]

EPR spectra. The solid-state Q-band EPR spectra of the isomorphs **1** and **2** at 4.0 K show a strong high-field signal centred at g = 2.13 (**1**) and 2.14 (**2**) typical for LS Co^{II} ions in a rhombically distorted, axially compressed octahedral geometry [g_x = 2.02 (**1**)/2.02 (**2**), g_y = 2.12 (**1**)/2.13 (**2**), and g_z = 2.24 (**1**)/2.27 (**2**) with overall g = 2.128 (**1**)/2.142 (**2**)] (Figure V.6). These values agree with a larger rhombicity for **1** found from the molecular structures. In addition, two weak low-field signals around H = 4.0 and 8.0 G characteristic of HS Co^{II} ions are observed for **2**, suggesting that its higher $\chi_M T$ and M can be derived from the residual HS fraction (inset of Figure V.6).

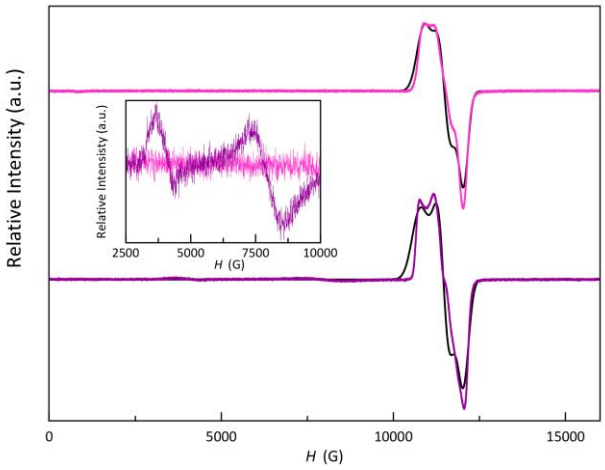

Figure V.6 Q-band EPR spectra of **1** (pink line) and **2** (purple line) at 4.0 K in the solid state. The inset shows an amplification of the low-field region. The black lines are the simulated spectra for S = 1/2 LS Co^{II} ion (see text).

Dynamic magnetic behaviour. The χ_M' and χ_M'' *versus* T plots for **1** and **2** (χ_M' and χ_M'' being the in-phase and out-of-phase *ac* molar magnetic susceptibilities) under applied *dc* magnetic fields in the range 1.0–5.0 kOe are typical of field-induced SMMs (Figures V.S4–S6). Only a χ_M' maximum and a χ_M'' signal in their thermal dependences at ν = 10 kHz appear when a H_{dc} is applied (Figure V.S7), being this maximum progressively shifted to higher temperatures when increasing H_{dc}. Besides, the incipient χ_M'' signal for **1** evolves to a distinct maximum characteristic of the magnetic blocking with increasing H_{dc} but remains incipient for **2**. However, the maximum observed for **1** disappears at the highest H_{dc} applied (5.0 kOe).

The magnetic relaxation times (τ) were calculated from the joint analysis of the χ_M' and χ_M'' *vs* ν plots through the generalised Debye equations (Figures V.S8–S10). The corresponding χ_M'' *vs* χ_M' (so-called Argand) plots give either incomplete or almost perfect semicircles for **1** and **2**, well-matched by the α, τ, χ_S, and χ_T values obtained from the fitting through the generalised Debye model (Figures V.S8c–V.S10c). The small α values, less than 0.06 in both cases, support a narrow distribution of magnetic relaxation processes (0 and 1 for single and infinite processes). More likely, the slight increase of α on cooling below 6.0 K responds to weak intermolecular interactions.

The τ values so obtained are displayed as lnτ vs 1/T, so-called Arrhenius plots (Figure V.7). In general, **2** relaxes faster than **1** at any H_{dc}; and, as for the LS mononuclear cobalt(II)-PDI complexes in the preceding chapters, τ increases markedly with H_{dc} in both compounds. However, this trend is reversed at temperatures above 5.0 K under a H_{dc} of 2.5 kOe for **2**. Although the difference between these two compounds only lies in the counteranion, it is not easy to understand how this can affect the different behaviour of **2** under H_{dc} = 2.5 kOe.

Remarkably, the LS (S_{Co} = 1/2) Co^{II} ion is a genuine two-level magnetic quantum system, represented by the pair of m_S = +1/2 and –1/2 states, which can play the role of a qubit for quantum computing applications.[35] The magnetic relaxation time for a doublet spin ground state is the spin-lattice time (T_1 = τ), which acts in turn as a limiting factor for the phase memory time ($T_m \leq T_1$). The relatively long T_1 values at T = 2.0 K found for **1** (from 29 to 86 μs) leave the door open to also great decoherence times, make it a suitable qubit candidate for testing its quantum coherence properties.

The Arrhenius and lnτ *vs* ln$T$ plots were satisfactorily simulated considering a double relaxation mechanism described by the equation: $\tau^{-1} = CT^n + IK$ (solid lines in Figures V.7 and V.S11). The first term is the well-known two-phonon Raman magnetic relaxation process operating in the high-temperature region, whereas the second is the intra-Kramer (IK) term that accounts for the spin-reversal relaxation between the Zeeman-split m_S = ±1/2 Kramers ground doublet in the low-temperature region. However, the inclusion of the IK term was not necessary for the Arrhenius simulation of **2** at the smallest H_{dc} fields.[29] The best-fit parameters are summarised in Table V.3.

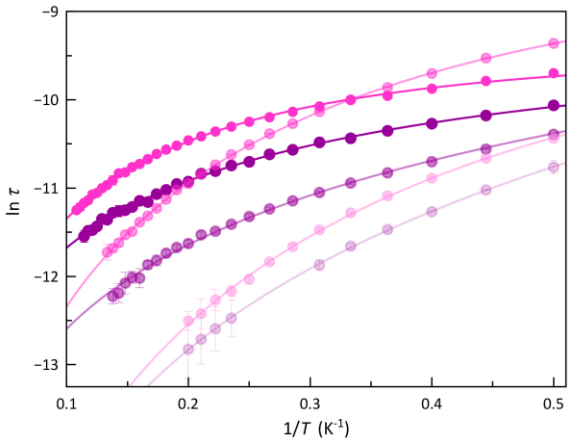

Figure V.7 Arrhenius plots of **1** (pink) and **2** (purple) under applied *dc* magnetic fields of 1.0, 2.5 and 5.0 kOe (light to dark colours). The solid lines are the best-fit curves for a double relaxation mechanism described by the equation $\tau^{-1} = CT^n + IK$ (see text). Vertical error bars denote the standard deviations.

The low values of the exponential factor n for **1** and **2** justify the needless inclusion of a first-order direct relaxation term ($\tau^{-1} = AT$) or suggest the presence of optical rather than acoustic phonons, as reported in the previous chapters for the related family of mononuclear cobalt(II)-PDI complexes with a LS

ground state. In both cases, an overall decrease of the *n* is found with increasing H_{dc}; however, they are slightly greater for **1** [*n* = 1.62–2.60 (**1**) and 1.29–2.26 (**2**); Table V.3], accounting thus for their distinct spin dynamics in the high-temperature region. Beside the anomaly at 5.0 KOe for **1**, a parallel increase of the τ_{IK} also occurs with increasing H_{dc}, which corresponds to a decrease in the spin-reversal rate, as expected when increasing the energy gap within the Zeeman-split Kramers ground doublet. In any case, the substantial dependency of the $\ln\tau$ *vs* $\ln T$ plots (Figure V.S11) with H_{dc} indicates that the mechanisms mainly governing magnetic relaxation in the study temperature region must be IK or one-phonon direct, as discussed in Chapter II.

Table V.3. Selected parameters from the least-squares fit of the ac magnetic data at different applied dc magnetic fields through two-phonon Raman plus temperature-independent Intra-Kramer processes for **1** and **2** (see text)

	$H_{dc}{}^a$ (kOe)	C^b (s^{-1} K^{-n})	n^b	$\tau_{IK}{}^c$ (x 10^{-3} s)
1	1.0	4150 ± 530	2.60 ± 0.08	0.11 ± 0.03
	2.5	1788 ± 70	2.10 ± 0.02	0.25 ± 0.02
	5.0	1750 ± 130	1.62 ± 0.03	0.087 ± 0.003
2	1.0	9800 ± 100	2.262 ± 0.010	-
	2.5	12150 ± 400	1.394 ± 0.019	-
	5.0	5630 ± 700	1.29 ± 0.05	0.097 ± 0.014

[a]Applied dc magnetic field. [b]The pre-exponential and exponential coefficients for the Raman mechanism [$\tau^{-1} = CT^n$]. [c]Coefficient for the temperature-independent intra-Kramer mechanism [$\tau^{-1} = IK$].

V.5 – Spectrophotochemical Solution Studies

A preliminary study in acetonitrile solution of the photochemical activity of the styryl-substituted terpyridine ligand and the corresponding cobalt(II) complex supports the occurrence of a *cis-trans* (*Z*/*E*) ligand isomerisation upon UV light irradiation (see Scheme V.1) monitored by UV/Vis, X-band EPR, and ^{1}H NMR spectroscopies (see V.7 – Experimental Section).

When a deuterated acetone solution of the *E*-isomer of the ligand is irradiated (λ_{max} = 355 nm) for 50 min at room temperature, the ^{1}H NMR peaks at 7.71 and 7.81 ppm from the *trans*-styryl protons progressively disappear as another corresponding to the *Z*-isomer arise at 6.85 and 6.95 ppm. After this time, the photostationary state is reached, showing 70 per cent of conversion, i.e. only 30 per cent of the *E*-isomer has not been converted (Figure V.8).

An equivalent behaviour is also observed in the electronic absorption spectra on both acetone solutions of *E*-4-StyTERPY and **1**, although two hours of irradiation are now required to reach the photostationary state (Figure V.9).

In both cases, there is a progressive fading of two intense π-π* transitions from the styryl derivatives centred around 280 and 340 nm, together with a large blueshift of this latter down to *ca.* 320 nm.[36] Once the photostationary state was reached for both *E*-4-StyTERPY and **1**, no further spectral changes were observed upon standing for several hours at room temperature (data not shown), suggesting thus a very slow thermal relaxation of the *Z*-derivatives in solution.

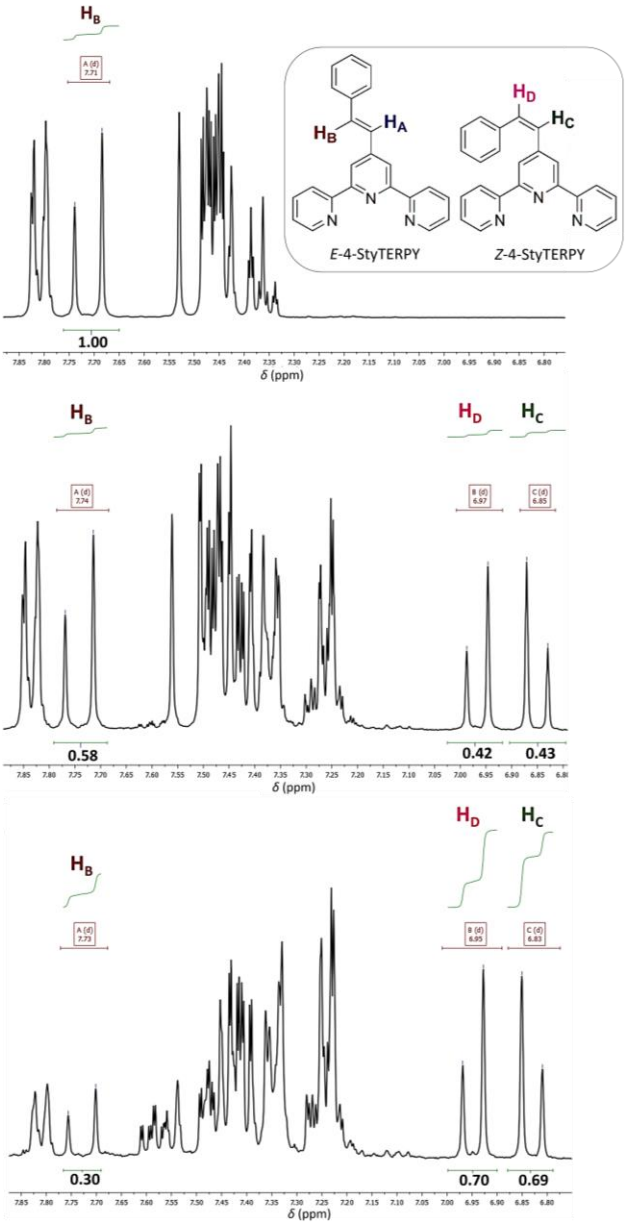

Figure V.8 ^{1}H NMR spectra of a 0.1 mM deuterated acetone solution of *E*-4-StyTERPY before (a) and after irradiation (λ_{max} = 355 nm) at room temperature for 20 (b) and 50 min (c).

Although the spectrophotochemical studies suggest that the *Z*/*E* ligand photoisomerisation also occurs for the corresponding complex, no significant differences were found in the frozen-matrix X-band EPR spectra of acetone solutions of **1** before and after UV-A light irradiation (data not shown), meaning no correlation between the electronic changes, spin state and photoisomerisation can be established by this experiment. This is not surprising since the coordination environment of the Co^{II} ion does not change substantially with the geometric modification. In solid state the photoisomerisation could result in important changes in the crystal packing interactions and they, in turn, could affect the spin state. However, these interactions are expected to be very similar for both geometric isomers in a frozen-acetone matrix. Unfortunately, the penetration of light is reduced in crystalline

solid samples and photoisomerisation may not be appreciated or even occur.

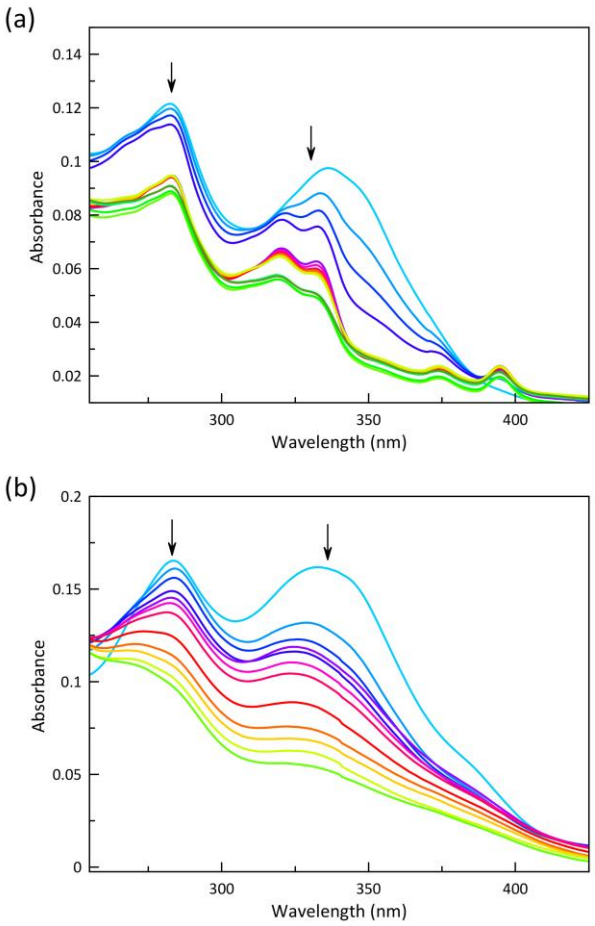

Figure V.9 Evolution of electronic absorption spectra at room temperature of 0.01 mM acetone and acetonitrile solutions of *E*-4-StyTERPY (a) and **1** (b), respectively, during two hours of irradiation (λ_{max} = 355 nm). The arrows indicate the course of the photochemical reaction.

V.6 – Concluding Remarks

A novel pair of isomorphic perchlorate and hexafluorophosphate salts of the mononuclear cobalt(II) complex with a mononuclear cobalt(II) complexes with a photoactive *trans (E)*-styrylterpyridine ligand has been obtained, exhibiting a counteranion tuning of the thermal-assisted spin transition and field-induced slow magnetic relaxation in the solid state. A preliminary study of their photochemical activity supports the occurrence of a *cis-trans* (*Z*/*E*) geometric ligand photoisomerisation upon UV light irradiation in solution. Current efforts are devoted to investigating the photoswitching of the spin dynamics and quantum coherence properties upon *cis-trans* (*Z*/*E*) geometric ligand photoisomerisation in this unique pair of SCO/SMMs, either in solution or in dispersed (solid solution) media, for their future applications as prototypes of molecular spin quantum photoswitches in molecular spintronics and quantum computing nanotechnologies.

V.7 – Experimental Section

Materials. Reagent grade 2-acetylpyridine, *trans*-cinnamaldehyde, iodine, anhydrous pyridine, sodium hydroxide, ammonium acetate, potassium hexafluorophosphate, cobalt(II) nitrate trihydrate, and cobalt(II) perchlorate hexahydrate were purchased from commercial sources and used as received. The ligand was prepared in three steps according to the literature procedure.[32]

Physical techniques. Elemental (C, H, N) analyses were performed at the Servicio Central de Soporte a la Investigación (SCSIE) at the Universitat de València (Spain). FT–IR spectra were recorded on a Nicolet-5700 spectrophotometer as KBr pellets. UV/Vis spectra were recorded in acetonitrile solutions at room temperature on a Jasco UV/Vis/NIR V-670 spectrophotometer. Q-band EPR spectra (ν = 34.463 GHz) measurements were carried out on crushed crystal samples of **1** and **2** at 4.0 K. X-band EPR spectra (ν = 9.463 GHz) of frozen-matrix acetone solutions were recorded under non-saturating conditions on a Bruker ER 200 D spectrometer equipped with a helium cryostat. ^{1}H NMR spectra were registered at room temperature on a Bruker AC 300 (300 MHz) spectrometer. Deuterated acetone was used as solvent and internal standard (δ = 2.05 ppm). X-ray powder diffraction (XRPD) patterns of powdered crystalline samples were collected at room temperature on a D8 Avance A25 Bruker diffractometer using graphite-monochromated Cu-Kα radiation (λ = 1.54056 Å).

Static and dynamic magnetic measurements. All studies were accomplished on crushed crystals of **1** and **2**. For variable-temperature (2–300 K) direct current (dc) magnetic susceptibility measurements under magnetic fields of 0.25 (T < 20 K) and 5.0 kOe (T > 20 K), and variable-field (0–50 kOe) magnetisation measurements at 2.0 K, a Quantum Design SQUID magnetometer was employed. The magnetic susceptibility data were corrected for the diamagnetism of the constituent atoms and the sample holder. Variable-temperature (2–12 K) alternating current (ac) magnetic susceptibility measurements under different dc magnetic fields (H_{dc} = 1.0 and 2.5 kOe) and a ± 5.0 Oe oscillating field at frequencies in the range of 0.15–10 kHz were conducted on a Quantum Design Physical Property Measurement System (PPMS).

Crystal structure data collection and refinement. X-ray diffraction data on a single crystal of **1** and **2** were collected on an Agilent Supernova diffractometer equipped with an EosS2 detector with Mo-Kα radiation (λ = 0.71073 Å) at 150 K. Diffraction data were collected, scaled, and integrated using the CrysAlisPro software.[37,38] The crystal structures were solved by intrinsic phasing methods integrated into the SHELXTL software[39] with the Olex2 platform.[40] The obtained models were refined with the version 2018/3 of SHELXL against F^2 on all data by full-matrix least squares. All non-hydrogen atoms were anisotropically refined. Hydrogen atoms, except those not found in water molecules and not fixed, were set on geometrical positions and refined with a riding model. The graphical manipulations and calculations were performed with the CRYSTALMAKER[41] and MERCURY[42] programmes.

Solution Spectrophotochemical Measurements. The irradiation experiments were undertaken at room temperature in a Luzchem photoreactor equipped with twelve UV-A lamps (λ_{max} = 355 nm). Diluted solutions of **1** and *E*-4-StyTERPY in acetone (0.01 mM) or concentrated solutions of *E*-4-StyTERPY in deuterated acetone (0.1 mM) were degassed with Ar in a sealed quartz cell designed for solution spectrophotochemical studies. The electronic absorption, EPR, and ^{1}H NMR spectra of the irradiated solutions were recorded at regular time intervals until reaching a photostationary state.

Preparation of the ligand and complexes.

*5-phenyl-1-(2-pyridinyl)-penta-2,4-diene-1-one (**A**): trans*-cinnamaldehyde (2.85 mL, 22.7 mmol) was added to a NaOH methanolic solution (0.952 g, 23.75 mmol in 15 mL) and the suspension was stirred for 15 minutes at 0 °C. Later, 2-Acetylpyridine (2.67 mL, 23.8 mmol) was added, and the resulting mixture was kept at 0 °C for two hours under vigorous stirring. The yellow precipitate of ***A*** (step 1 in Scheme V.2) was filtrated and washed with cold methanol. Yield 79%.

*[2-oxo-2-(2-pyridyl)ethyl]pyridinium iodide (**B**):* 2-Acetylpyridine (4.4 mL, 33.0 mmol) and iodine (9.6 g, 38 mmol) were refluxed in anhydrous pyridine (55 mL) for 12 hours under atmosphere of argon. The solution was cooled to room temperature, which allowed the precipitation of compound ***B*** (step 2 in Scheme V.2). The solid was filtered and decolourised by activated charcoal in a methanolic solution. Yellow crystals of **B** appeared by cooling the solution to -5 °C. They were filtered and air-dried. Yield 63%.

(E)-4'(4-styryl)-2,2'/6',2''-terpyridine (E-4-StyTERPY): A mixture of ***A*** (1.0 g, 4.25 mmol), ***B*** (1.5 g, 4.6 mmol), and ammonium acetate (1.0 g, excess) in methanol (25 mL) was refluxed for 24 hours to afford *E*-4-StyTERPY (step 3 in Scheme V.2). The solvent was evaporated under reduced pressure. Then, a dichloromethane solution (50 mL) of the obtained brown solid was washed with water (3 x 25 mL). The dichloromethane phase was dried using anhydrous sodium sulphate, and the solvent was then evaporated under pressure leading to a brown oil. The brown oil was purified through a silica gel column using dichloromethane as eluent, leading to a yellowish solid after evaporation of the recovered solution. Yield 72 %. Anal. Calc. for $C_{23}H_{17}N_3$ (MW = 355.41 g mol^{-1}): C, 82,36; H, 5.11; N, 12.53. Found: C, 82,13; H, 5.05; N, 12.64%. IR (KBr, cm^{-1}): 1689w and 1665w [ν(C=N) from pyridine rings], 1623w [ν(C=C) from styryl group], 1583s [ν(C=C) from aromatic rings], 1391m [ν(C=N) from pyridine rings], 794s and 737s [out-of-plane *δ*(C–H) from the aromatic rings].

*[Co(E-4-StyTERPY)$_2$](ClO$_4$)$_2$ (**1**)*: A solution of *E*-4-StyTERPY (13 mg, 0.04 mmol) in chloroform (0.5 mL) was placed in a glass test tube. Then, over it, a layer of the 4:1 (v/v) methanol/chloroform solvent mixture (8.0 mL) was carefully added. At last, a methanolic solution (0.5 mL) of cobalt(II) perchlorate hexahydrate (9.0 mg, 0.02 mmol) was added to the top of the tube. X-ray quality red crystals of **1** were obtained after one week by slow diffusion. Yield 80%. Anal. Calc. for $C_{46}H_{34}N_6O_8Cl_2Co$ (MW = 928.65 g mol^{-1}): C, 59.50; H, 3.69; N, 9.05. Found: C, 59.35; H, 3.64; N, 9.12%. IR (KBr, cm^{-1}): 1652s [ν(C=N) from pyridine rings of *E*-4-StyTERPY], 1089vs [ν(Cl–O) from perchlorate anion], 792m [out-of-plane *δ*(C–H) from the aromatic rings of *E*-4-StyTERPY].

*[Co(E-4-StyTERPY)$_2$](PF$_6$)$_2$ (**2**)*: A solution of *E*-4-StyTERPY (13 mg, 0.04 mmol) in chloroform (0.5 mL) was placed in a glass test tube. Then, over it, a layer of the 4:1 (v/v) methanol/chloroform solvent mixture (8.0 mL) was carefully added. At last, a mixture of cobalt(II) nitrate hexahydrate (7.0 mg, 0.02 mmol) and potassium hexafluorophosphate (15 mg, 0.08 mmol) in methanol (0.5 mL) was added on the top of the tube. X-ray quality red crystals of **2** were obtained after one week by slow diffusion. Yield 76%. Anal. Calc. for $C_{46}H_{34}N_6F_{12}P_2Co$ (MW = 1019.68 g mol^{-1}): C, 54.18; H, 3.36; N, 8.24. Found: C, 54.65; H, 3.24; N, 8.37%. IR (KBr, cm^{-1}): 1650s [ν(C=N) from pryridine rings of *E*-4-StyTERPY], 863vs [ν(P–F) from hexafluorophosphate anion], 789m [out-of-plane *δ*(C–H) from the aromatic rings of *E*-4-StyTERPY].

References

1 Thies, S.; Sell, H.; Schutt, C.; Bornholdt, C.; Nather, C.; Tuczek, F.; Herges, R. Light-Induced Spin Change by Photo-dissociable External Ligands: A New Principle for Magnetic Switching of Molecules. *J. Am. Chem. Soc.* **2011**, *133*, 16243−16250.

2 Paquette, M. M.; Plaul, D.; Kurimoto, A.; Patrick, B. O.; Frank, N. L. Opto-Spintronics: Photoisomerization-Induced Spin State Switching at 300 K in Photochrome Cobalt-Dioxolene Thin Films. *J. Am. Chem. Soc.* **2018**, *140*, 14990–15000.

3 Venkataramani, S.; Jana, U.; Dommaschk, M.; Sonnichsen, F. D.; Tuczek, F.; Herges, R. Magnetic Bistability of Molecules in Homogeneous Solution at Room Temperature. *Science* **2011**, *331*, 445−448.

4 Dommaschk, M.; Peters, M.; Gutzeit, F.; Schutt, C.; Nather, C.; Sonnichsen, F. D.; Tiwari, S.; Riedel, C.; Boretius, S.; Herges, R. Photoswitchable Magnetic Resonance Imaging Contrast by Improved Light-Driven Coordination-Induced Spin State Switch. *J. Am. Chem. Soc.* **2015**, *137*, 7552−7555.

5 Hirose, T.; Helmich, F.; Meijer, E. W. Photocontrol over Cooperative Porphyrin Self-Assembly with Phenylazopyridine Ligands. *Angew. Chem., Int. Ed.* **2013**, *52*, 304−309.

6 Sato, O.; Tao, J.; Zhang, E.-J. Control of Magnetic Properties through External Stimuli. *Angew. Chem. Int. Ed*. **2007**, *46*, 2152–2187.

7 Ferrando-Soria, J.; Vallejo, J.; Castellano, M.; Martínez-Lillo, J.; Pardo, E.; Cano, J.; Castro, I.; Lloret, F.; Ruiz-García, R.; Julve, M. Molecular Magnetism, *Quo Vadis*? A Historical Perspective from a Coordination Chemistry Viewpoint. *Coord. Chem. Rev.* **2017**, *339*, 17–103.

8 Real, J. A.; Gaspar, A. B.; Muñoz, M. C. Thermal, Pressure and Light Switchable Spin-Crossover Materials. *Dalton Trans.* **2005**, 2062–2079.

9 Kumar, K. S.; Ruben, M. Emerging Trends in Spin Crossover (SCO) Based Functional Materials and Devices. *Coord. Chem. Rev.* **2017**, *347*, 176–205.

10 Doistau, B.; Benda, L.; Hasenknopf, B.; Marvaud, V.; Vives, G. Switching Magnetic Properties by a Mechanical Motion. *Magnetochemistry* **2018**, *4*, 5.

11 Meng, Y.-S.; Liu, T. Manipulating Spin Transition to Achieve Switchable Multifunctions. *Acc. Chem. Res.* 2019, **52**, 1369–1379.

12 Matsumoto, T.; Newton, G. N.; Shiga, T.; Hayami, S.; Matsui, Y.; Okamoto, H.; Kumai, R.; Murakami, Y.; Oshio, H. Programmable Spin-State Switching in a Mixed-Valence Spin-Crossover Iron Grid. *Nat. Commun.* **2014**, *5*, 3865.

13 Meded, V.; Bagrets, A.; Fink, K.; Chandrasekar, R.; Ruben, M.; Evers, F.; Bernand-Mantel, A.; Seldenthuis, J. S.; Beukman, A.; van der Zant, H. S. J. Electrical Control over the Fe(II) Spin Crossover in a Single Molecule: Theory and Experiment. *Phys. Rev. B* **2011**, *83*, 245415.

14 Zhang, X.; Palamarciuc, T.; Létard, J.-F.; Rosa, P.; Lozada, E.; V.; Torres, F.; Rosa, J. G.; Doudin, B.; Dowben, P. A. The Spin State of a Molecular Adsorbate Driven by the Ferroelectric Substrate Polarization. *Chem. Commun.* **2014**, *50*, 2255–2257.

15 Jornet-Mollá, V.; Duan, Y.; Giménez-Saiz, C.; Tang, Y.-Y.; Li, P.-F.; Romero, F. M.; Xiong, R.-G. A Ferroelectric Iron(III) Spin Crossover Material. *Angew. Chem. Int. Ed.* **2017**, *56*, 14052–14056.

16 Otsuki, Y.; Kimura, S.; Awaji, S.; Nakano, M. Magnetocapacitance Effect and Magnetostriction by the Field-Induced Spin Crossover in [Mn^{III}(taa)]. *AIP Adv*. **2019**, *9*, 085219.

17 Chikara, S.; Gu, J.; Zhang, X. G.; Cheng, H.-P.; Smythe, N.; Singleton, J.; Scott, B.; Krenkel, E.; Eckert, J.; Zapf, V. S. Magnetoelectric Behavior Via a Spin State Transition. *Nat. Commun*. **2019**, *10*, 4043.

18 Akiyoshi, R.; Komatsumaru, Y.; Donoshita, M.; Dekura, S.; Yoshida, Y.; Kitagawa, H.; Kitagawa, Y.; Lindoy, L. F.; Hayami, S. Ferroelectric and Spin Crossover Behavior in a Cobalt(II) Compound Induced by Polar-Ligand-Substituent Motion. *Angew. Chem. Int. Ed.* **2021**, *60*, 12717–12722.

19 Jakobsen, V. B.; Chikara, S.; Yu, J.-X.; Dobbelaar, E.; Kelly, C. T.; Ding, X.; Weickert, F.; Trzop, E.; Collet, E.; Cheng, H.-P.; Morgan, G. G.; Zapf, V. S. Giant Magnetoelectric Coupling and Magnetic-Field-Induced Permanent Switching in a Spin Crossover Mn(III) Complex. *Inorg. Chem*. **2021**, *60*, 6167–6175.

20 Roux, C.; Zarembowitch, J.; Gallois, B.; Granier, T.; Claude, R. Toward Ligand-Driven Light-Induced Spin Changing. Influence of the Configuration of 4 Styrylpyridine (stpy) on the Magnetic Properties of $Fe^{II}(stpy)_4(NCS)_2$ Complexes. Crystal Structures of the Spin-Crossover Species Fe(trans-stpy)$_4$(NCS)$_2$ and of the High-Spin Species Fe(cis-stpy)$_4$(NCS)$_2$. *Inorg. Chem.* **1994**, *33*, 2273–2279.

21 Khusniyarov, M. M. How to Switch Spin-Crossover Metal Complexes at Constant Room Temperature. *Chem. Eur. J.* **2016**, *22*, 15178–15191.

22 Hasegawa, Y.; Takahashi, K.; Kume, S.; Nishihara, H. Complete Solid State Photoisomerization of Bis(dipyrazolylstyrylpyridine)iron(II) to Change Magnetic Properties. *Chem. Commun*. **2011**, *47*, 6846–6848.

23 Rösner, B.; Milek, M.; Witt, A.; Gobaut, B.; Torelli, P.; Fink, R. H.; Khusniyarov, M. M. Reversible Photoswitching of a Spin-Crossover Molecular Complex in the Solid State at Room Temperature. *Angew. Chem. Int. Ed.* **2015**, *54*, 12976–12980.

24 Samanta, S.; Demesko, S.; Dechert, S.; Meyer, F. A Two-in-one Pincer Ligand and its Diiron(II) Complex Showing Spin State Switching in Solution through Reversible Ligand Exchange. *Angew. Chem., Int. Ed.* **2015**, *54*, 583−587.

25 Milek, M.; Heinemann, F. W.; Khusniyarov, M. M. Spin Crossover Meets Diarylethenes: Efficient Photoswitching of Magnetic Properties in Solution at Room Temperature. *Inorg. Chem.* **2013**, *52*, 11585−11592.

26 Witt, A.; Heinemann, F. W.; Khusniyarov, M. M. Bidirectional Photoswitching of Magnetic Properties at Room Temperature: Ligand-Driven Light-Induced Valence Tautomerism. *Chem. Sci.* **2015**, *6*, 4599−4609.

27 Evangelio, E.; Ruiz-Molina, D. Valence Tautomerism: New Challenges for Electroactive Ligands. *Eur. J. Inorg. Chem*. **2005**, 2957–2971.

28 Tissot, A.; Boillot, M.-L.; Pillet, S.; Codjovi, E.; Boukheddaden, K.; Daku, L. M. L. Unidirectional Photoisomerization of Styrylpyridine for Switching the Magnetic Behavior of an Iron(II) Complex: A MLCT Pathway in Crystalline Solids. *J. Phys. Chem. C* **2010**, *114*, 21715–21722.

29 Verma, P.; Weir, J.; Mirica, L.; Stack, T. D. Tale of a Twist: Magnetic and Optical Switching in Copper(II) Semiquinone Complexes. *Inorg. Chem.* **2011**, *50*, 9816–9825.

30 Hayami, S.; Komatsu, Y.; Shimizu, T.; Kamihata, H.; Lee, Y. H. Spin-Crossover in Cobalt(II) Compounds Containing Terpyridine and its Derivatives. *Coord. Chem. Rev.* **2011**, *255*, 1981–1990.

31 Shao, D.; Shi, L.; Yin, L.; Wang, B.-L.; Wang, A.-X.; Zhang, Y.-Q.; Wang, X.-Y. Reversible On-Off Switching of both Spin Crossover and Single-Molecule Magnet Behaviours via a Crystal-To-Crystal Transformation. *Chem. Sci.* **2018**, *9*, 7986–7991.

32 Kadjane, P.; Charbonnière, L.; Camerel, F.; Lainé, P. P.; Ziessel, R. Improving Visible Light Sensitization of Luminescent Europium Complexes. *J. Fluoresc.* **2008**, *18*, 119–129.

33 Nakaya, M.; Ohtani, R.; Shin, J. W.; Nakamura, M.; Lindoy, L. F.; Hayami, S. Abrupt Spin Transition in a Modified-Terpyridine Cobalt(II) Complex with a Highly-Distorted [CoN_6] Core. *Dalton Trans.* **2018**, *47*, 13809–13814.

34 Slicher, C. P.; Drickamer, H. G. Pressure-Induced Electronic Changes in Compounds of Iron. *J. Chem. Phys.* **1972**, *56*, 2142–2160.

35 Xu, M.-X.; Liu, Z.; Dong, B.-W.; Cui, H.-H. Wang, Y.-X.; Su, J.; Wang, Z.; Song, Y.; Chen, X.-T.; Jiang, S.-D.; Gao, S. Single-Crystal Study of a Low Spin Co(II) Molecular Qubit: Observation of Anisotropic Rabi Cycles. *Inorg. Chem.* **2019**, *58*, 2330–2335.

36 Neckers, D. C.; Volman, D. H.; von Bünau, G. Advances in Photochemistry, John Wiley & Sons, *Vol. 19*, New York, **1995**.

37 Bruker. *SAINT*. Bruker AXS Inc., Madison, Wisconsin, USA, **2012**.

38 Agilent. *CrysAlis PRO*. Agilent Technologies Ltd, Yarnton, Oxfordshire, England, **2014**.

39 Sheldrick, G. M. SHELXT - Integrated Space-Group and Crystal-Structure Determination. *Acta Cryst.* **2015**, *A71*, 3–8.

40 Dolomanov, O.V., Bourhis, L.J., Gildea, R.J, Howard, J.A.K. & Puschmann, H. *J.* OLEX2: a Complete Structure Solution, Refinement and Analysis Program. *Appl. Cryst*. **2009**, *42*, 339-341.

41 *CrystalMaker*, CrystalMaker Software, Bicester, England, **2015**.

42 *Mercury*, The Cambridge Crystallographic Data Centre, Cambridge, UK.

Supporting Information

TABLE OF CONTENTS

General characterisation (Figure V.S1)

X-ray crystallographic data collection and structure refinement (Figures V.S2 and V.S3)

Static and dynamic magnetic measurements (Figures V.S4 – V.S11)

General characterisation

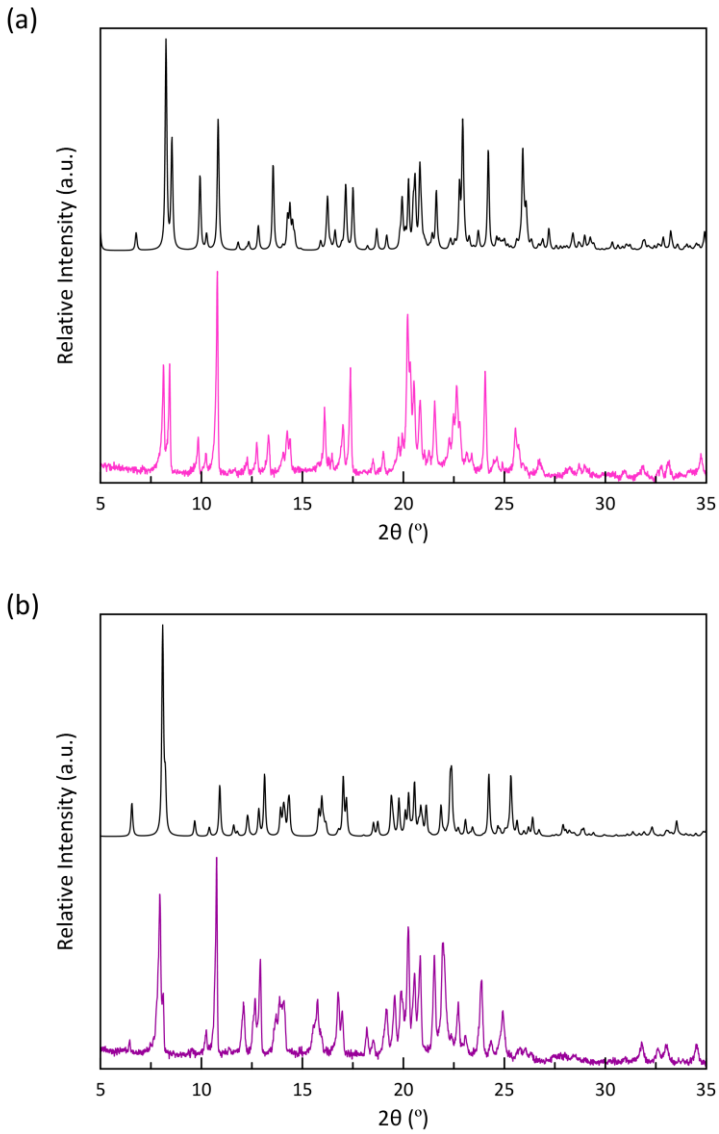

Figure V.S1 Experimental XRPD pattern (pink and purple lines) of **1** (a) and **2** (b) compared to the calculated ones (black lines).

X-ray crystallographic data collection and structure refinement

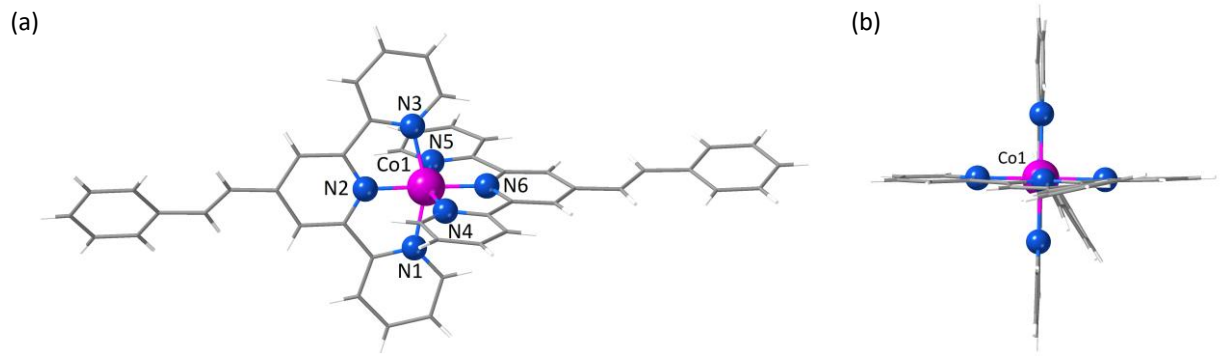

Figure V.S2 Front (a) and side (b) views of the cationic mononuclear cobalt(II) unit of **2** with the atom numbering scheme for the first coordination sphere of the metal atom.

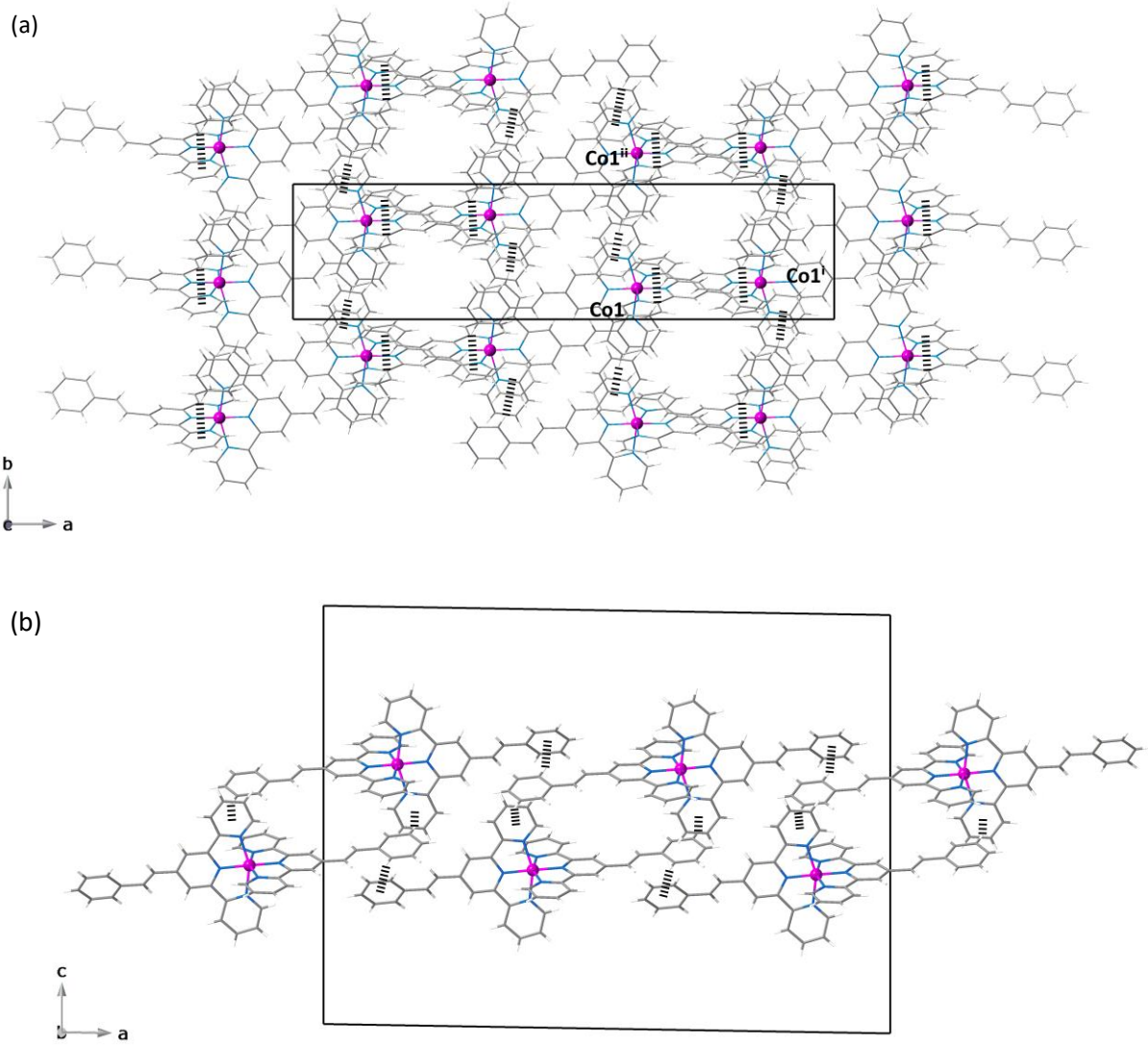

Figure V.S3 Top (a) and side (b) projection views of a π-bonded double layer of cationic mononuclear cobalt units in **2** along the crystallographic *c* and *b* axes [symmetry code: (i) = 1/2 - *x*, 3/2 - *y*, 1 - *z*; (ii) = *x*, 1+*y*, *z*]. The "edge-to-face" π-stacking interactions are drawn as hashed lines.

Static and dynamic magnetic measurements

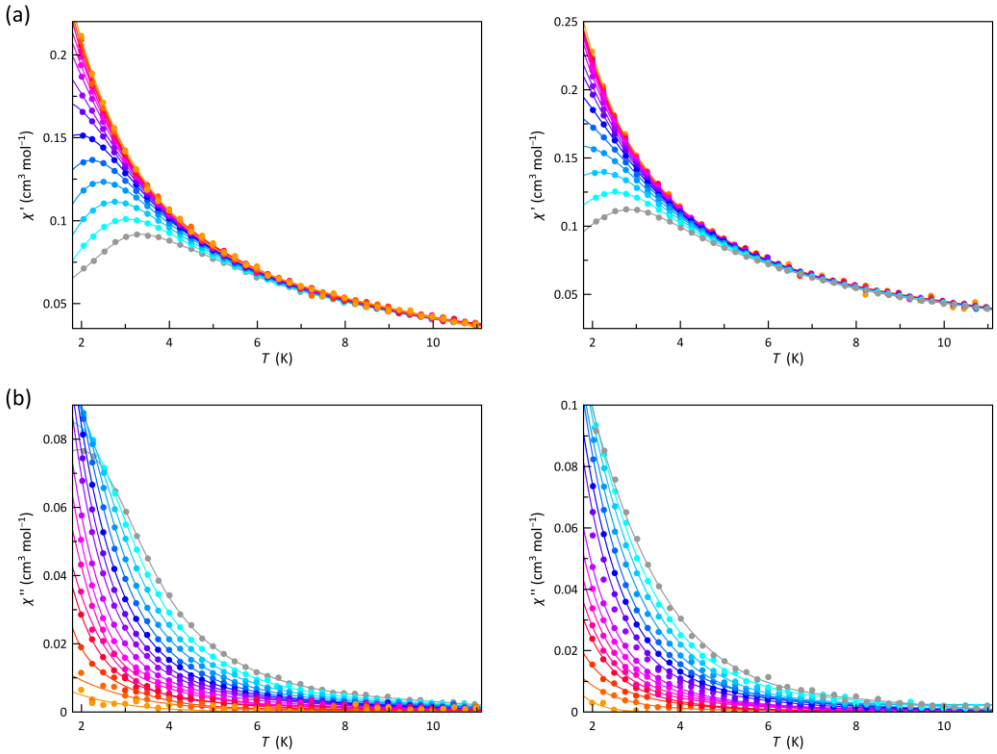

Figure V.S4 Temperature dependence of χ_M' (a) and χ_M'' (b) of **1** (left) and **2** (right) under a static magnetic field of 1.0 kOe at ±0.5 Oe oscillating field in the frequency range of 10–0.1 kHz (from grey to orange colours).

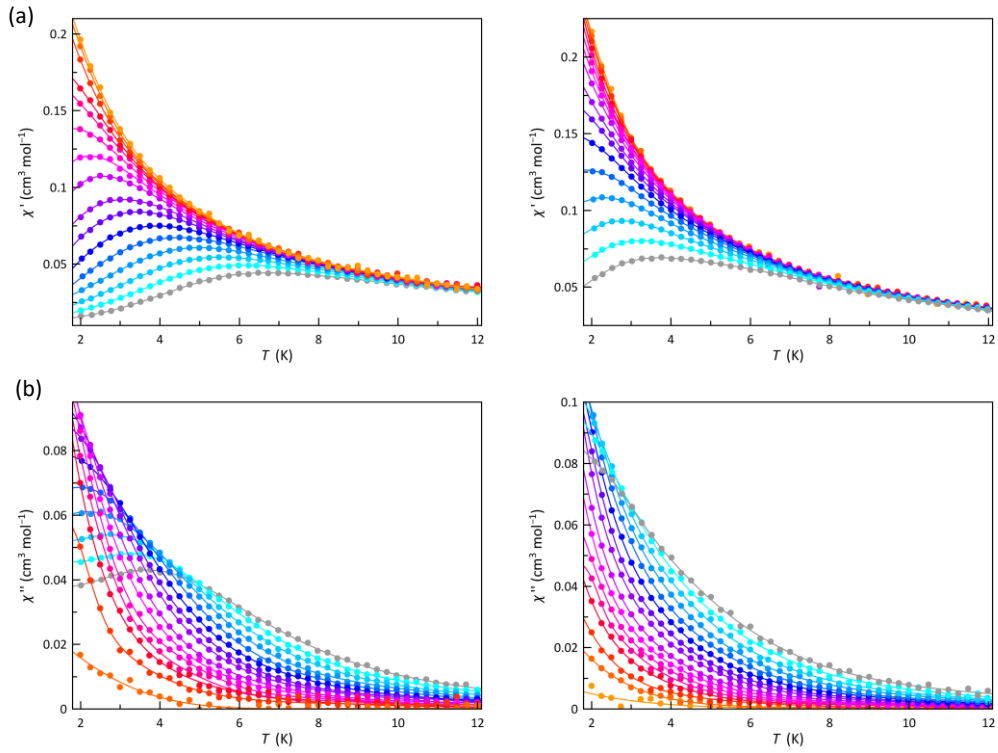

Figure V.S5 Temperature dependence of χ_M' (a) and χ_M'' (b) of **1** (left) and **2** (right) under a static magnetic field of 2.5 kOe at ±0.5 Oe oscillating field in the frequency range of 10–0.1 kHz (from grey to orange colours).

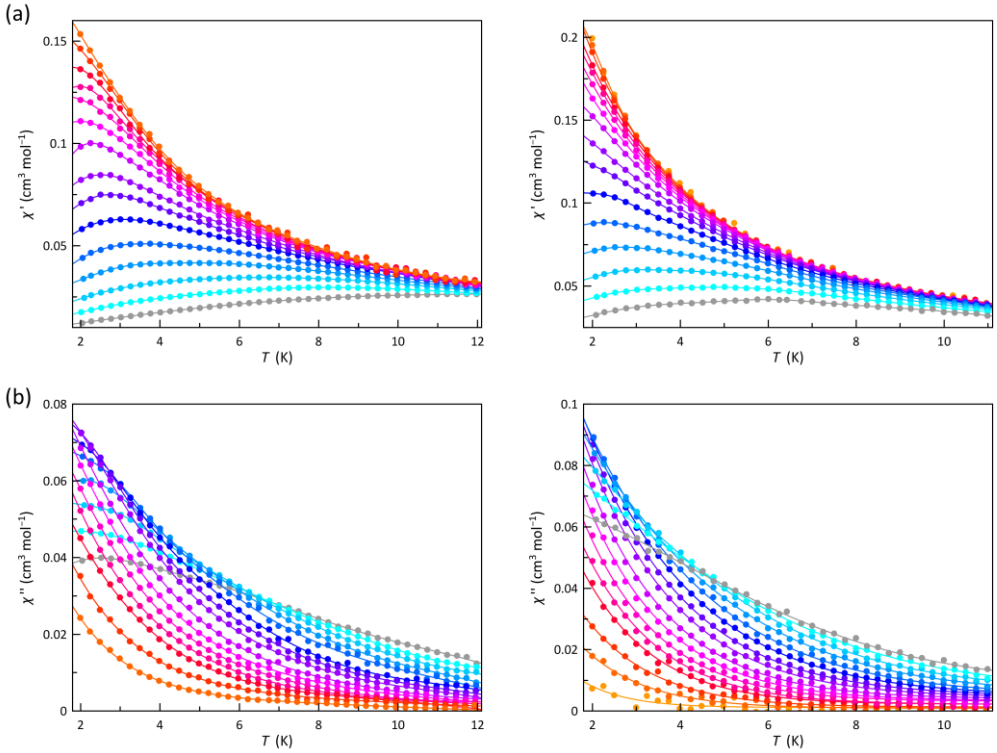

Figure V.S6 Temperature dependence of χ_M' (a) and χ_M'' (b) of **1** (left) and **2** (right) under a static magnetic field of 5.0 kOe at ±0.5 Oe oscillating field in the frequency range of 10–0.1 kHz (from grey to orange colours).

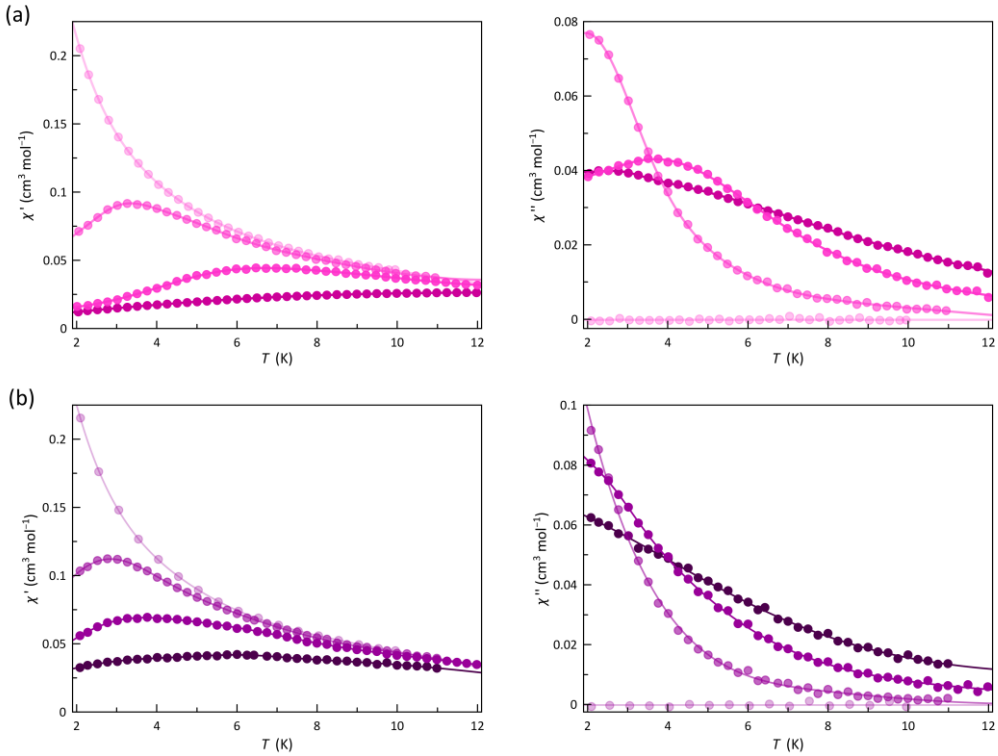

Figure V.S7 Temperature dependence of χ_M' (left) and χ_M'' (right) for **1** (a) and **2** (b) at ν = 10 kHz of the ±5 Oe oscillating *ac* magnetic field and under applied *dc* magnetic fields of 0, 1.0, 2.5 and 5.0 kOe (from light to dark colours). The solid lines are only eye-guides.

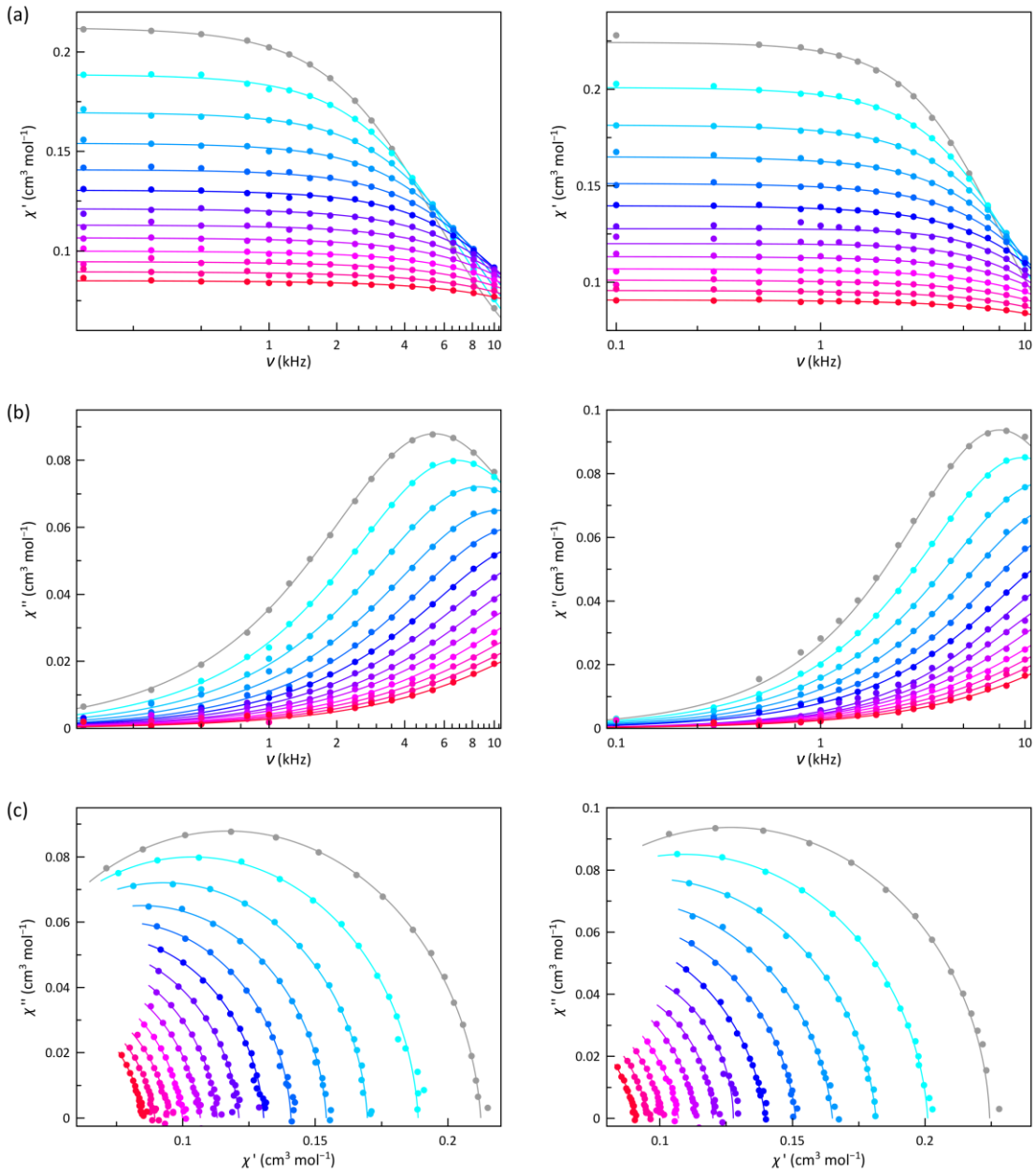

Figure V.S8 Frequency dependence of χ_M' (a), χ_M'' (b), and the Argand plot (c) of **1** (left) and **2** (right) under static magnetic field of 1.0 at ±0.5 Oe oscillating field in the temperature range of 2.0–5.0 K, in steps of 0.25 K (from grey to warmer colours). The solid lines are the best-fit curves simulated by using the values of χ_S, χ_T, τ and α.

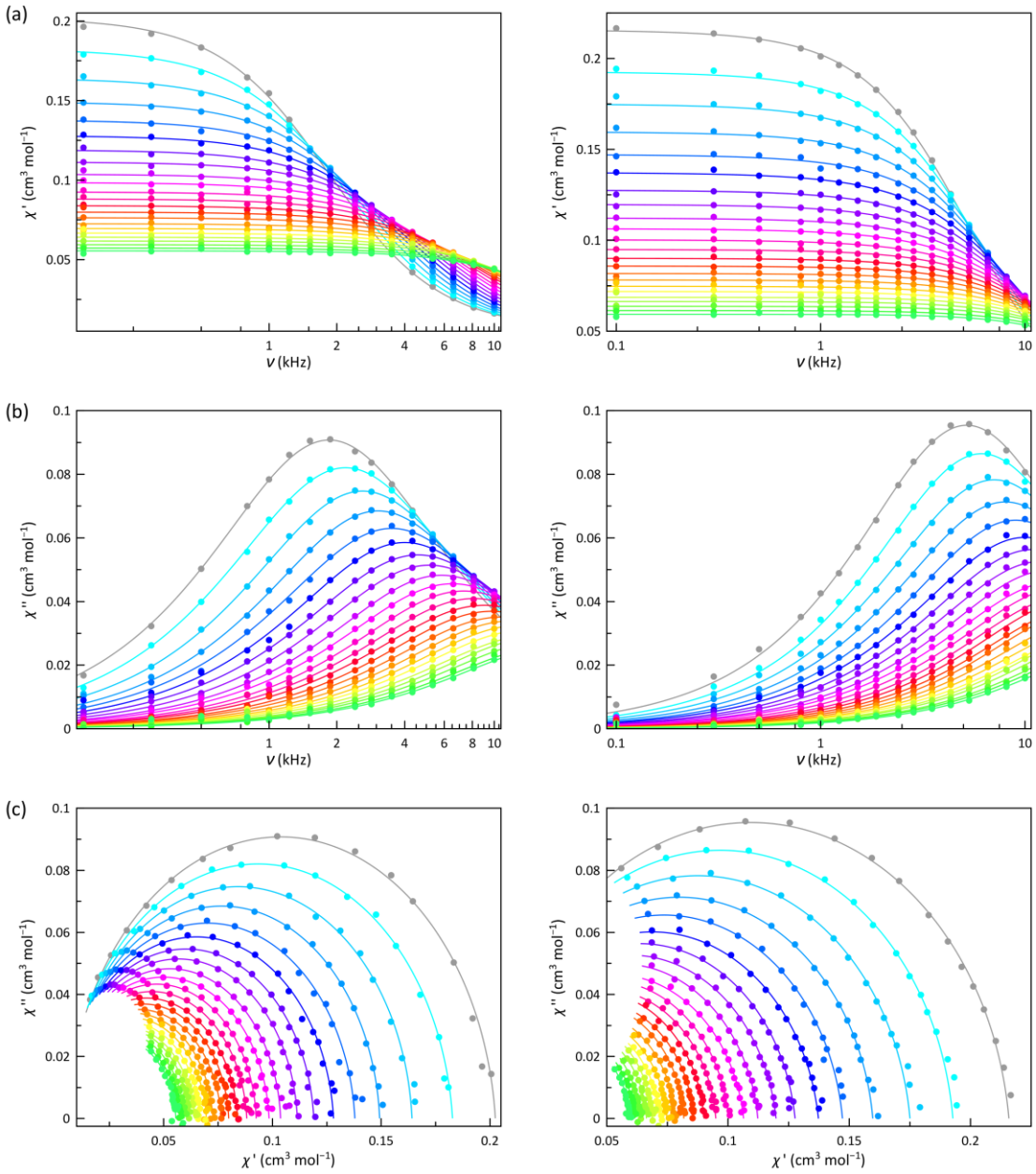

Figure V.S9 Frequency dependence of χ_M' (a), χ_M'' (b), and the Argand plot (c) of **1** (left) and **2** (right) under static magnetic field of 2.5 at ±0.5 Oe oscillating field in the temperature range of 2.0–7.5 K, in steps of 0.25 K (from grey to warmer colours). The solid lines are the best-fit curves simulated by using the values of χ_S, χ_T, τ and α.

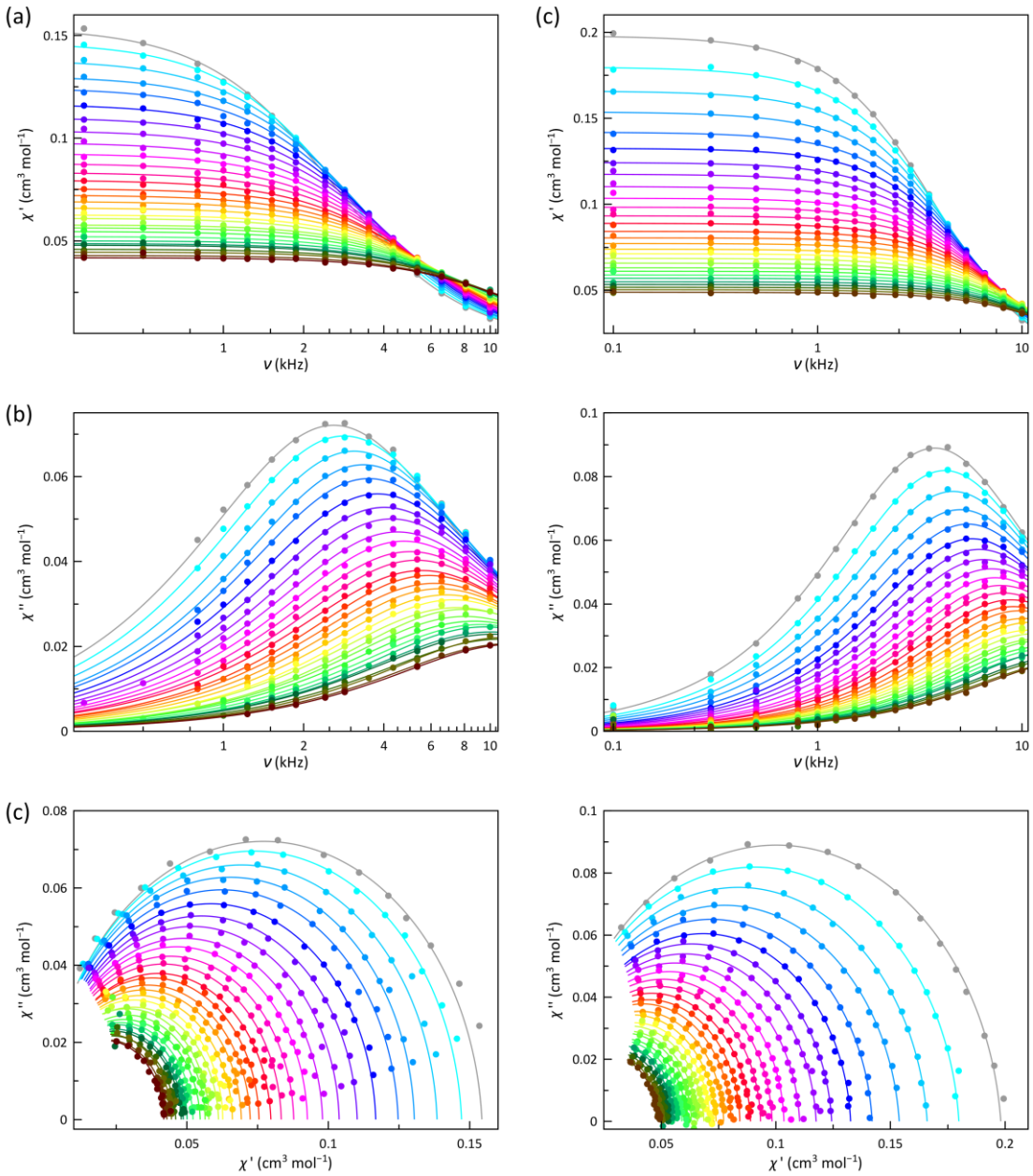

Figure V.S10 Frequency dependence of χ_M' (a), χ_M'' (b), and the Argand plot (c) of **1** (left) and **2** (right) under static magnetic field of 5.0 at ±0.5 Oe oscillating field in the temperature range of 2.0–9.0 K, in steps of 0.25 K (from grey to warmer colours). The solid lines are the best-fit curves simulated by using the values of χ_S, χ_T, τ and α.

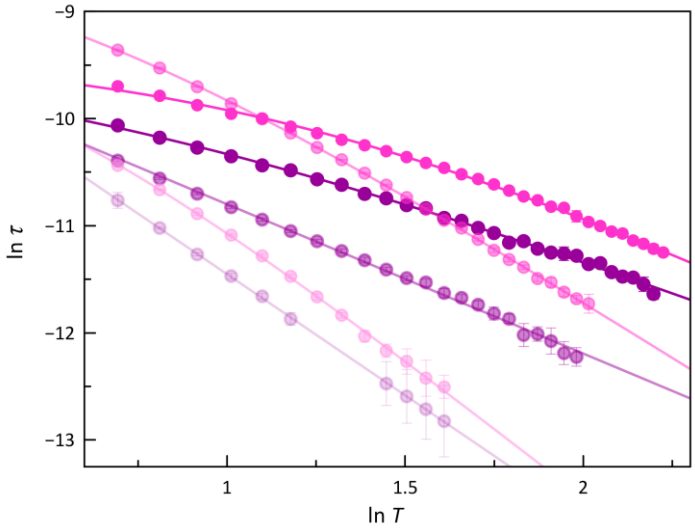

Figure V.S11 ln τ vs ln T plots of **1** (pink) and **2** (purple) under applied *dc* magnetic fields of 1.0, 2.5 and 5.0 kOe (light to dark colours). The solid lines are the best-fit curves for a double relaxation mechanism described by the equation $\tau^{-1} = CT^n + IK$ (see text). Vertical error bars denote the standard deviations.

CHAPTER VI

CHEMICALLY-ACTIVE SPIN CROSSOVER MOLECULAR NANOMAGNETS

Chemically-active Spin Crossover Molecular Nanomagnets

VI.1 – Background and Highlights

Coordination compounds of transition metal ions with non-innocent ligands have attracted much attention in diverse areas of nanoscience due to their unusual combination of chemical (Brønsted or Lewis acidity, redox, and catalytic) and physical (optical or luminescent, conducting, and magnetic) properties resulting from the metal and the ligand counterpart.[1–12] The ongoing crucial step towards new nanotechnologies is to successfully modulate their physicochemical properties through a variety of internal factors, either electronic (metal oxidation and spin states) or steric ones (ligand substituents and conformation),[5] and eventually to switch them under the presence of external stimuli, either of chemical (pH and chemical analytes) or physical nature (temperature, hydrostatic pressure, light, electric and magnetic fields).[4,11]

This goal has been successfully achieved using mononuclear first-row transition metal complexes as both synthetic and theoretical models of dynamic molecular systems (DMS).[13–48] Hence, this simple class of multifunctional and multiresponsive molecular materials has been found helpful as optical and magnetic sensors for chemical and biological sensing,[13,14] photoluminescent emitters for light-emitting electrochemical cells (LECs),[15–17] electro- and photocatalysts for bio-inspired molecular recognition and catalysis,[18–23] photo- and chemoresponsive contrast agents for magnetic resonance imaging (MRI),[24–26] electrochemical and electrochromic devices for redox flow batteries (RFB), and capacitors for molecular electronics.[27,28] In particular, mononuclear spin crossover (SCO) complexes with potentially electro- or photoactive (non-innocent) ligands are promising candidates for the realisation of spintronic devices or advanced qubits and quantum gates for molecular spintronics and quantum information processing (QIP).[29–48]

Along this line, we report in this chapter the synthesis, structural and spectroscopic characterisation, and the magnetic, luminescence and electrochemical properties of two novel mononuclear cobalt(II) complexes with a terpyridine-type ligand containing benzoic/benzoate substituents of formula $\{[Co^{II}(HL)_2][Co^{II}(HL)L]\}(ClO_4)_3{\cdot}9H_2O$ (**1**) and $[Co^{II}L_2]{\cdot}5H_2O$ (**2**) [L = 4'-(4-carboxylatephenyl)-2,2':6',2"-terpyridine = 4-CO_2PhTERPY] (Scheme VI.1). **1** and **2** are two rare examples of SCO molecular systems that undergo a thermal-assisted low-spin (LS)/high-spin (HS) transition and a field-induced blockage of the magnetisation.[49–55] Moreover, they constitute a unique proton transfer series of spin crossover molecular nanomagnets that combine optical (luminescent), redox, and magnetic tuning under pH control, being thus proposed as a prototype of pH-effect spin quantum transformers (PHE-SQTs) for molecular spintronics and quantum computing nanotechnologies.

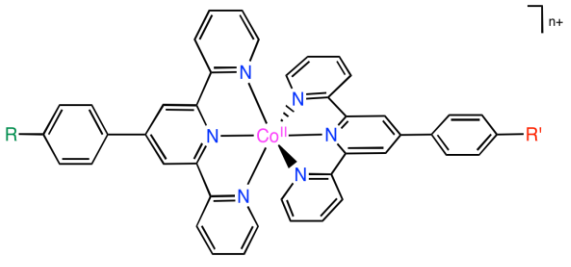

		R	R'
1	$[Co^{II}(4\text{-}HCO_2PhTERPY)_2]^{2+}$	CO_2H	CO_2H
	$[Co^{II}(4\text{-}HCO_2PhTERPY)(4\text{-}CO_2PhTERPY)]^{+}$	CO_2H	CO_2^-
2	$[Co^{II}(4\text{-}CO_2PhTERPY)_2]$	CO_2^-	CO_2^-

Scheme VI.1 General chemical formula of the mononuclear entities present in **1** and **2**.

VI.2 – Ligand Design and Synthetic Strategy

In the search for a novel pH-responsive dynamic molecular system based on mononuclear spin crossover cobalt(II) complexes, we have turned our attention to TERPY-type ligands such as those shown in the previous chapter. Hence, our choice was a non-innocent TERPY-type ligand containing benzoic acid substituents with a well-known Bronsted acidity that will be transferred to the corresponding mononuclear cobalt(II) complexes. Besides, due to the Lewis basicity of the deprotonated benzoate group substituents, they can sense the presence of metal ions of biological or environmental interest, such as alkaline and alkaline earth (Na^+, K^+ and Ca^+) or transition metal ones (Zn^{2+}, Cd^{2+} and Hg^{2+}).

The 4-benzoic acid-substituted TERPY ligand was then synthesised following a previously reported procedure.[56] The first step consists of the condensation of 2-acetylpyridine and methyl 4-formylbenzoate (1:1 molar ratio) in basic media to afford the methyl ester benzoic acid derivative (MeL) (Scheme VI.2). The deprotonated and protonated forms of the ligand were successively obtained after basic hydrolysis of the methyl ester acid derivative with NaOH, followed by acid treatment until pH = 3, being isolated as its tetrahydrate sodium salt (NaL) and monoprotic acid (HL). They were obtained as white crystalline solids in good to excellent yields [42 (MeL), 64 (HL), and 95% (NaL)], and characterised by elemental analysis (C, H, N), proton nuclear magnetic resonance (^{1}H NMR), Fourier-transform infrared (FT-IR), and electronic absorption (UV-Vis) spectroscopies.

The cobalt(II) complexes were synthesised by reaction of the stoichiometric amounts (2:1 ligand to metal molar ratio) of HL with cobalt(II) perchlorate hexahydrate in acetonitrile/methanol mixture for **1**, and NaL with cobalt(II) acetate tetrahydrate in dimethylsulfoxide/water mixture for **2** (see VI.7 – Experimental section). The procedure used by us differs from that reported earlier for **2**.[56] Compounds **1** and **2** are soluble in dimethylformamide and dimethylsulfoxide, but they are sparingly soluble in water or organic solvents like acetonitrile and methanol. X-ray quality crystals of **1** and **2** were obtained in moderate to good yields (62–83%) by slow evaporation in acetonitrile at room temperature (**1**) or under hydrothermal

conditions at 100 ºC (**2**). They were characterised by elemental (C, H, N) and thermogravimetric analyses (TGA), energy dispersive X-ray (EDX), Fourier-transform infrared (FT-IR), electronic absorption (UV-Vis), and electron paramagnetic resonance (EPR) spectroscopies (see VI.7 – Experimental section).

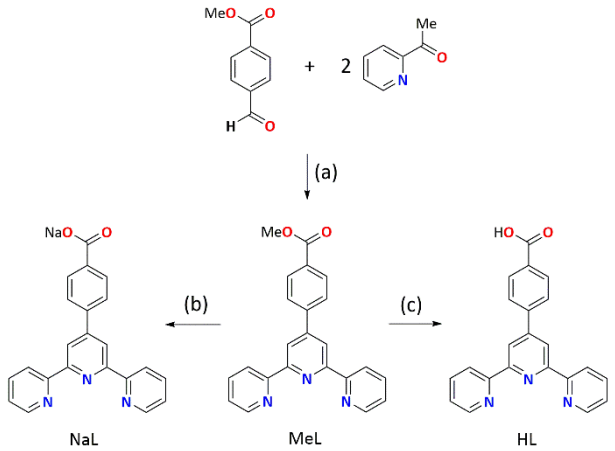

Scheme VI.2 General synthetic procedure for the preparation of the deprotonated form of the ligand as a sodium salt (NaL) and its protonated acid (HL) from the methyl ester precursor (MeL). Reaction conditions: (a) NaOH (PEG200, 0 °C) and NH_4OAc (100 °C); (b) NaOH (H_2O, 100 °C); (c) HCl (H_2O, 25 °C).

The EDX and TGA analyses for **1** and **2** agree with the proposed chemical formula regarding the ligand protonation degree and the water contents. Hence, the TGA profiles show 6.1 (**1**) and 10% (**2**) mass losses from 25 up to 225 °C that correspond to three and five water molecules per formula unit, respectively (Figure VI.S1). The EDX analysis for **2** shows no chorine peak as expected for a neutral deprotonated $[Co^{II}L_2]$ form. However, **1** reveals a 3:2 Cl to Co molar ratio, according to the coexistence of protonated dicationic and hemiprotonated monocationic forms, as a consequence of the weak acid character of the ligand (see discussion below). Unfortunately, our attempts to obtain single crystals of the pure protonated $[Co^{II}(HL)_2]^{2+}$ form in an acid medium were unsuccessful.

A comparison of the FT-IR spectra of **1** and **2** allows to firmly establish the distinct protonation degree of the ligands in their complexes (Figure VI.S2). Hence, **1** and **2** show strong bands corresponding to the characteristic asymmetric stretching vibrations of carboxylic acid and carboxylate groups [$\nu_{as}(CO_2H)$/ $\nu_s(CO_2H)$ = 1698/1263 (**1**) and $\nu_{as}(CO_2)$/ $\nu_s(CO_2)$ = 1554/1371 cm^{-1} (**2**)], which are found at similar location for the corresponding protonated and sodium salt forms of the ligand [$\nu_{as}(CO_2H)/\nu_s(CO_2H)$ = 1706/1261 (HL) and $\nu_{as}(CO_2)/\nu_s(CO_2)$ = 1562/1402 cm^{-1} (NaL)] (Figures VI.S2a and b). The observed larger shift between both stretching vibrations for **1** compared to **2** [$\Delta = \nu_{as} - \nu_s$ = 435 (**1**) and 183 cm^{-1} (**2**)] is as expected for the presence of protonated carboxylic acid and deprotonated carboxylate groups.[57]

The chemical identity of **1** and **2** was further supported by single-crystal X-ray diffraction. Indeed, the experimental powder X-ray diffraction (PXRD) patterns of the polycrystalline samples are identical to the calculated ones from the single-crystal XRD analysis (Figure VI.S3), confirming the purity of the bulk materials.

VI.3 – Description of the Structures

1 and **2** crystallise in the *P*–1 space group of the triclinic system (Table VI.1). The structure of **1** consists of statistically disordered protonated and hemiprotonated mononuclear cobalt(II) complex cations, $[Co^{II}(HL)_2]^{2+}$/$[Co^{II}(HL)L]^{+}$, together with partially disordered, charge counterbalancing perchlorate anions and water molecules of crystallisation (Figures VI.1, VI.S4 and VI.S5). Nevertheless, **2** contains only neutral deprotonated mononuclear cobalt(II) complexes, $[Co^{II}L_2]$, and free water molecules (Figures VI.2, VI.S6 and VI.S7), in agreement with the earlier reported structure of **2**.[56]

Table VI.1 Summary of Crystallographic Data for **1** and **2**

	1	**2**
Formula	$C_{88}H_{74}N_{12}O_{28.5}Cl_3Co_2$	$C_{44}H_{38}N_6O_9Co$
M (g mol^{-1})	1962.67	853.65
Crystal system	Triclinic	Triclinic
Space group	*P*–1	*P*–1
a (Å)	9.224(4)	8.7247(5)
b (Å)	12.380(5)	13.4869(7)
c (Å)	19.363(7)	16.4323(8)
α (°)	85.759(15)	93.298(2)
β (°)	77.184(15)	97.277(2)
γ (°)	89.430(15)	91.254(2)
V (Å^3)	2150.0(14)	1913.99(18)
Z	1	2
ρ_{calc} (g cm^{-3})	1.516	1.481
μ (mm^{-1})	0.570	0.517
T (K)	120	120
Reflect. collec.	46691	100316
Reflect. obs. [$I > 2\sigma(I)$]	7617 (6578)	23465 (9769)
Data/restraints/parameters	7617/468/635	23465/0/569
R_1[a] [$I > 2\sigma(I)$] / R_1 (all)	0.0730 / 0.0817	0.0987 / 0.2509
wR_2[b] [$I > 2\sigma(I)$] / wR_2 (all)	0.2146 / 0.2240	0.1599 / 0.2183
S[c]	1.046	1.013

[a] $R_1 = \sum(||F_o| - |F_c||)/\sum|F_o|$. [b] $wR_2 = [\sum w(F_o^2 - F_c^2)^2/\sum w(F_o^2)^2]^{1/2}$. [c] $S = [\sum w(|F_o| - |F_c|)^2/(N_o - N_p)]^{1/2}$.

Molecular structures. The mononuclear cobalt(II) units of **1** and **2** exhibit similar but not identical molecular dimensions and conformations (Table VI.2). They show a cylindrical shape of approximate dimensions 2.0 (length) and 1.0 nm (width) with a pseudo C_{2v} molecular symmetry possessing two almost perpendicularly oriented non-planar ligands, regardless of the ligand protonation degree (Figures VI.1b and VI.2b). The values of the dihedral angle between the mean planes of the terpyridine fragments are Φ = 83.57(3) (**1**) and 89.65(2)° (**2**) (Table VI.2), and those between the terpyridine and the benzoic/benzoate fragments from each ligand are ϕ = 7.08(8)/43.62(11) (**1**) and 14.30(5)/29.57(6)° (**2**) (Table VI.2). These minor but non-negligible deviations from orthogonality give rise to two distinct chiral (helical) isomers, both enantiomers (*M* and *P*) being present in the crystal lattice. In addition, there is an overall bending along the long axial molecular axis of the mononuclear cobalt(II) unit in **2** compared to **1** (Figures VI.1a and VI.2a), as shown in Figure VI.S8.

The protonation degree of each ligand in the protonated/hemiprotonated and deprotonated complexes can

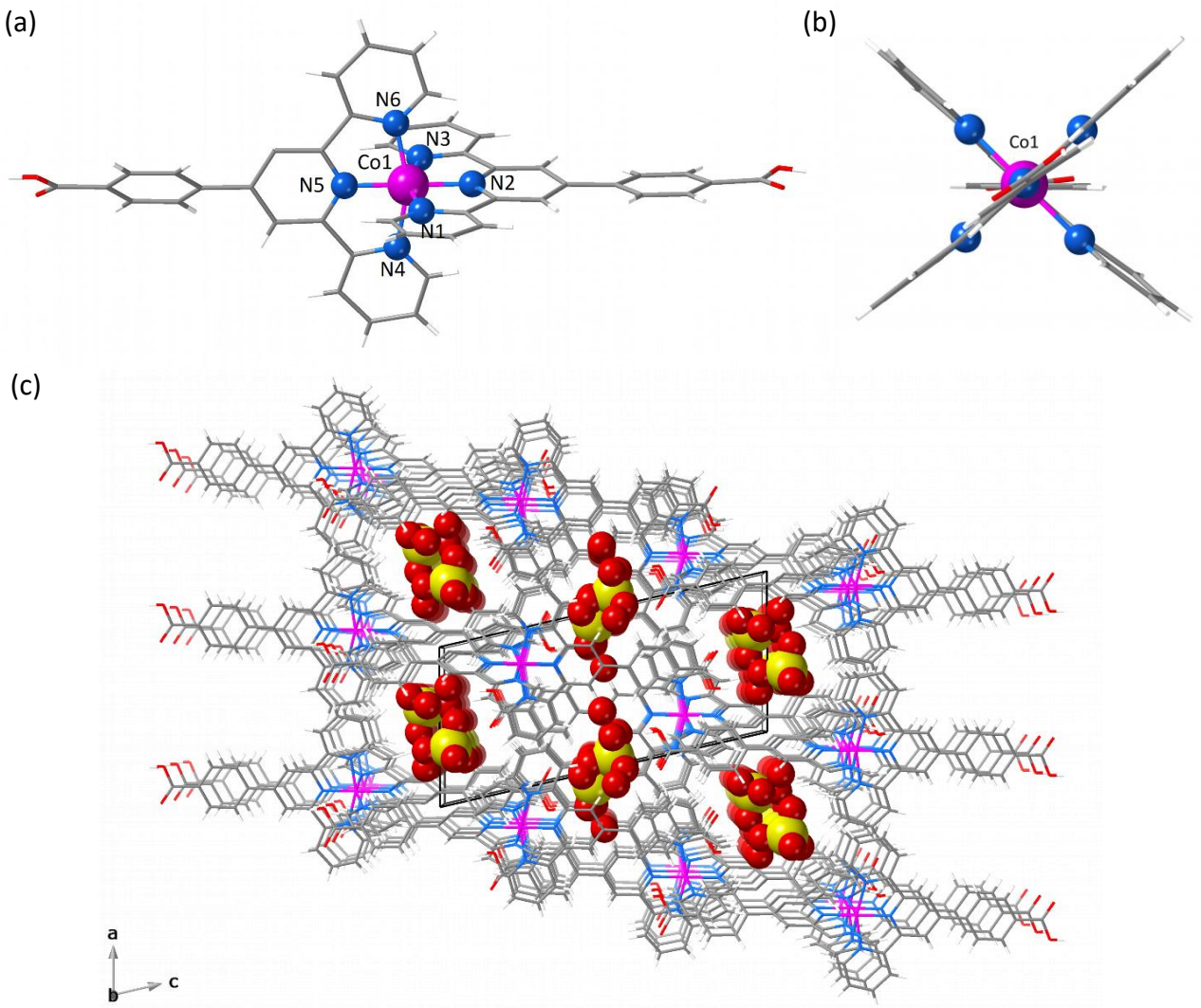

Figure VI.1 (a) Front and (b) side views of the cationic mononuclear cobalt(II) unit of **1** with the atom numbering scheme for the first coordination sphere of the metal atom. (c) Perspective view of the crystal packing of **1** along the crystallographic *b* axis showing the occupation with perchlorate anions and crystallisation water molecules of the small channels built by the parallel array of cationic mononuclear cobalt(II) units. The perchlorate anions and the crystallisation water molecules are depicted in a space-filling representation.

be evaluated from the bond lengths into the benzoic and benzoate fragments. Hence, the two distinct carbon-oxygen bond lengths from the carboxylic groups at each ligand in **1** are rather different and correspond to the expected for a double and simple bond lengths [d_1(C=O) = 1.205(6)/1.214(8) and d_2(C–O) = 1.308(6)/1.295(7) Å; Table VI.2]. Meanwhile, those in **2** are almost identical [d_1(C=O) = 1.263(3)/1.256(4) and d_2(C–O) = 1.260(4)/1.252(4) Å; Table VI.2], an evidence of the resonance occurring in the carboxylate form.

The coordination sphere in **1** and **2** exhibits an axially compressed octahedral geometry with partial rhombic distortions. The equatorial plane is defined by the two pairs of distal pyridine nitrogen atoms from each ligand (N_d and N'_d), whereas the central pyridine nitrogen atoms (N_c) occupy the axial positions (Figures VI.1a and VI.2a). Overall, the metal-to-nitrogen bond lengths in **1** and **2** are typical of LS Co^{II} ions, regardless of the ligand protonation degree. The average values of the axial Co–N_c lengths are notably shorter than those of the equatorial Co–N_d ones for both compounds [R_{ax} = 1.893(4) (**1**)/1.898(2) Å (**2**) and R_{eq} = 2.064(4) (**1**)/2.072(4) Å (**2**); Table VI.2]. The variation of the axial Co-N_c lengths are similar between **1** and **2** and greater compared to the equatorial ones, whereas a larger variation of the equatorial Co–N_d lengths is found in **2** [Δ_R = 0.085(6) (**1**)/ 0.086(6) (**2**) and δ_R = 0.017(6) (**1**)/0.042(4) (**2**); Table VI.2]. Besides, the bis(chelating) coordination mode of the two tridentate ligands featuring two five-membered fused rings imposes a severe non-planar ruffling distortion, as reflected by the average values of the mean out-of-plane N_d displacement [δ = ±0.403(4) (**1**) and ±0.429(2) Å (**2**); Table VI.2].[56]

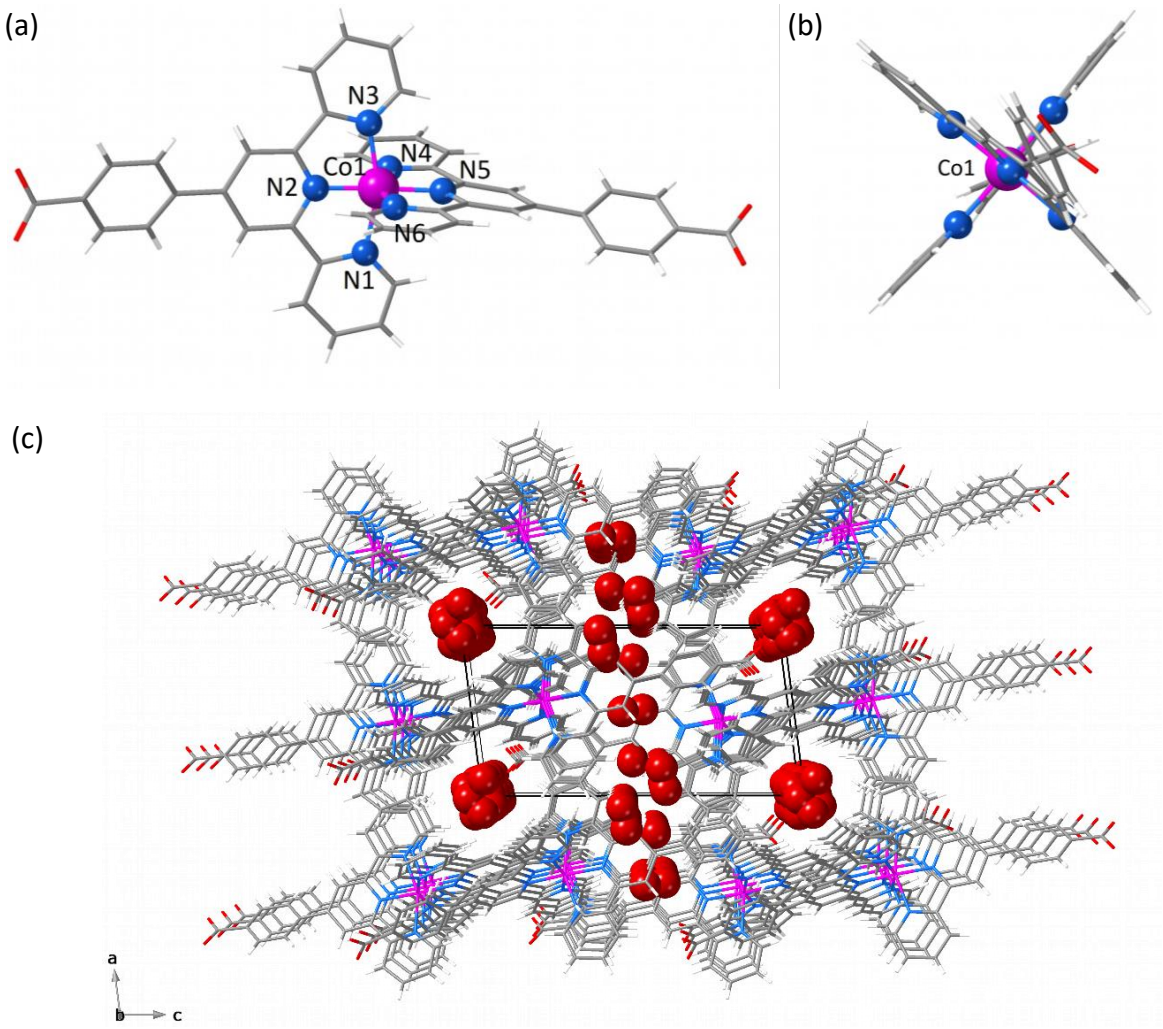

Figure VI.2 (a) Front and (b) side views of the neutral mononuclear cobalt(II) unit of **2** with the atom numbering scheme for the first coordination sphere of the metal atom. (c) Perspective view of the crystal packing of **2** along the crystallographic *b* axis showing the occupation with crystallisation water molecules of the small channels built by the parallel array of neutral mononuclear cobalt(II) units. The crystallisation water molecules are depicted in a space-filling representation.

Table VI.2 Selected Structural Data for **1** and **2**

	1	**2**
R_1(Co–N_p)[a] (Å)	2.080(4)	2.030(2)
R_2(Co–N'_p)[a] (Å)	2.046(4)	2.113(2)
R_3(Co–N_c)[b] (Å)	1.893(4)	1.897(2)
R_{eq}[c] (Å)	2.063(4)	2.071(2)
R[d] (Å)	2.006(4)	2.013(2)
Δ_R[e]	0.085(4)	0.086(2)
δ_R[f]	0.017(4)	0.040(2)
N_p–Co–N'_p[g] (º)	94.664(15)	92.25(8)
N'_p–Co–N_p[g] (º)	89.13(15)	91.35(8)
N_c–Co–N_c[h] (º)	179.74(16)	176.46(9)
Δ[i] (Å)	±0.403(4)	±0.429(2)
Φ[i] (º)	83.57(3)	89.65(2)
ϕ[k] (º)	7.08(8)/43.62(11)	14.30(5)/29.57(6)
d_1(C=O)[l] (Å)	1.205(6)/1.214(8)	1.258(4)
d_2(C–O)[l] (Å)	1.308(6)/1.295(7)	-
Δ_{CO}[m] (Å)	0.092(7)	-

[a]Average equatorial bond lengths from each ligand. [b]Average axial bond lengths. [c]Average equatorial bond lengths defined as $R_{eq} = (R_1 + R_2)/2$. [d]Average cobalt-nitrogen bond lengths defined as $R = (R_1 + R_2 + R_3)/3$. [e]Axial distortion parameter defined as $\Delta_R = (R_{eq} - R_3)/R$. [f]Rhombic distortion parameter defined as $\delta_R = (R_1 - R_2)/R_{eq}$. [g]Average equatorial bond angles. [h]Average axial bond angles. [i]Average deviations of the distal pyridine-nitrogen donor atoms from the mean metal equatorial plane. [j]Dihedral angle between the mean planes of the terpyridine ligand fragments. [k]Dihedral angle between the mean planes of the terpyridine and the benzoic/benzoate fragments. [l]Carbon-oxygen bond lengths of each ligand. [m]Difference between the carbon-oxygen bond lengths from the carboxylic/carboxylate groups of each ligand defined as $\Delta_{CO} = (d_2 - d_1)$.

Crystal structures. The mononuclear complexes in **1** and **2** are parallelly settled in the crystal packing with their long molecular axis oriented along the crystallographic *c* axis (Figure VI.S5 and VI.S7). The water molecules of crystallisation are involved in a variety of hydrogen bonding interactions among them and with the carboxylic and carboxylate groups [Ow–H···Ow = 2.41(1)–3.04(1) (**1**) and 2.385(9)–2.927(9) Å (**2**); Ow–H···O = 2.587(5)–2.90(2) (**1**) and 2.695(6)–2.841(4) Å (**2**)]. This situation gives rise to hydrogen-bonded single (**1**) or multiple layers (**2**) of mononuclear cobalt(II) units within the *ac* or *bc* planes (Figures VI.S4 and VI.S6). The values of the shortest intralayer Co1···Co1[i] distances across the hydrogen-bonded water molecules are similar in **1** and **2** [28.517(3) and 26.042(1)], being rather larger than those of the shortest interpair or interlayer Co1···Co1[ii] separations [11.274(1)/ 9.224(1) and 8.725(6) Å] [symmetry codes: (i) = 1–*x*, 1–*y*, 1–*z*; (ii) = 1–*x*, 1–*y*, –*z*].

There is a parallel displaced arrangement of hydrogen-bonded single layers of dicationic and monocationic mononuclear cobalt(II) units in **1** that grow in the *ac* plane (Figure VI.S4). In contrast, a triple interpenetration of parallelly

displaced hydrogen-bonded multi-layered nets of neutral mononuclear cobalt(II) units along the crystallographic *c* axis occurs for **2** (Figures VI.S6 and S7). In each case, however, the parallel array of supramolecular 2D layers in **1** or the triply interpenetrated 3D network in **2** lead to small channels along the mutually perpendicular [100] and [010] directions, which are occupied by the hydrogen-bonded water molecules of crystallisation together with the counterbalancing perchlorate anions in the former case (Figures VI.1c and VI.2c). Hence, the estimated empty volume excluding the water molecules (V_0) represents *ca.* 87 (**1**) and 85 % (**2**) of the potential void space per unit cell volume. Once again, the distinct protonation degree of each ligand in the protonated/hemiprotonated and deprotonated mononuclear cobalt(II) complexes of **1** and **2**, respectively, is ultimately responsible for the differences in the crystal packing and potential porosity (relative to the water contents) between both pH isomers.

VI.4 – Magnetic Properties and EPR Spectra

The magnetic properties of **1** and **2** have been measured in both direct (dc) and alternating current (ac) regimes in order to investigate the influence of the protonation degree in the spin crossover and spin dynamics in the solid state for this unique proton transfer pair of mononuclear cobalt(II) complexes (see VI.7 – Experimental Section).

Static magnetic behaviour. The $\chi_M T$ *vs* T plots (χ_M being the *dc* molar magnetic susceptibility per mononuclear unit) for **1** and **2** show a similar SCO magnetic behaviour (Figure VI.3). A gradual but complete, thermally-induced HS-LS transition is observed for both cases, regardless of the protonation degree of each ligand. As reported earlier for the parent cobalt(II) complexes with 2,2′:6′,2″-terpyridine and its derivatives,[58] no hysteresis occurs despite the presence of intermolecular π-π stacking and hydrogen bonding interactions among the mononuclear units through the water molecules of crystallisation in the solid state.

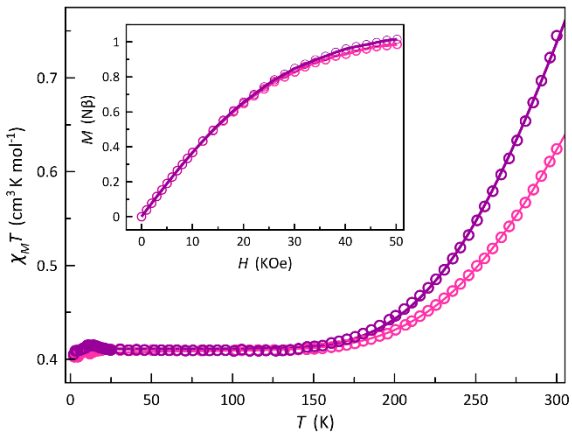

Figure VI.3 (a) Temperature dependence of $\chi_M T$ for **1** (pink) and **2** (purple). The solid lines are the theoretical curves through a simple thermodynamic spin transition model (see text). The inset shows the field dependence of M for **1** (pink) and **2** (purple) at T = 2.0 K. The solid lines are the simulated curves through the Brillouin equation for a doublet spin state (see text).

At room temperature, the $\chi_M T$ value of 0.75 cm^3 mol^{-1} K for **2** is slightly higher than that of 0.62 cm^3 mol^{-1} K for **1**, both of them being rather lower than the expected one for a HS Co^{II} ion with an unquenched orbital momentum contribution ($\chi_M T$ = 2.70 cm^3 mol^{-1} K with S = 3/2 and g = 2.4). Upon cooling, $\chi_M T$ decreases smoothly to reach a sort of plateau around 150 K with a $\chi_M T$ value of 0.41 cm^3 mol^{-1} K at 2.0 K, as expected for a LS Co^{II} complex ($\chi_M T$ = 0.45 cm^3 mol^{-1} K with S = 1/2 and g = 2.2). The $\chi_M T$ data for **1** and **2** are well simulated through a simple thermodynamic model that takes into account the enthalpy (ΔH) and entropy (ΔS) changes associated with the spin transition with an average g factor for both HS and LS Co^{II} ions.[59] The best-fit parameters are ΔH = 1.042 (**1**)/1.055 kJ mol^{-1} (**2**), ΔS = 2.143 (**1**)/2.546 J mol^{-1} (**2**) and g = 2.083 (**1**)/2.094 (**2**) (solid lines in Figure VI.3).

This situation is also supported by the M *vs* H plots (M being the magnetisation per mononuclear unit and H the applied *dc* magnetic field). In both cases, the isothermal magnetisation curves at 2.0 K can be perfectly reproduced by the Brillouin function with S = 1/2 and g = 2.110 (**1**) and 2.137 (**2**) (inset of Figure VI.3). In fact, the solid-state Q-band EPR spectra at 4.0 K exhibit a rhombic pattern [g_x = 2.02 (**1**)/2.03 (**2**), g_y = 2.08 (**1**)/2.12 (**2**), and g_z = 2.22 (**1**)/2.25 (**2**)] with average g values of 2.11 (**1**) and 2.14 (**2**), regardless of the protonation degree of each ligand in the corresponding pH isomers (Figure VI.4). This situation is in agreement with the aforementioned rhombic distortion observed in the LS Co^{II} ion for the molecular structures of the corresponding mononuclear $[Co(HL)_2]^{2+}$/$[Co(HL)L]^+$ (**1**) and $[CoL_2]$ (**2**) units.

Overall, the physical properties described until now are similar for both compounds, regardless of the ligand protonation degree.

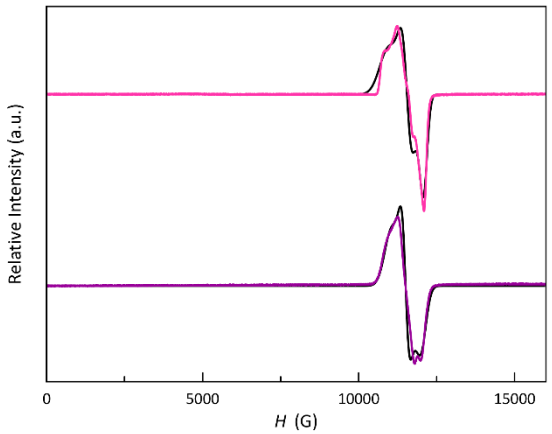

Figure VI.4 Q-band EPR spectra of **1** (pink line) and **2** (purple line) at 4.0 K in the solid state. The black lines are the simulated spectra for S = 1/2 LS Co^{II} ion (see text).

Dynamic magnetic behaviour. The χ_M' and χ_M'' *vs* ν plots of **1** and **2** (χ_M' and χ_M'' being the in-phase and out-of-phase *ac* molar magnetic susceptibilities) under applied *dc* magnetic fields in the range 1.0–5.0 kOe are characteristic of field-induced SMMs (Figures VI.5 and VI.S9–VI.S11).

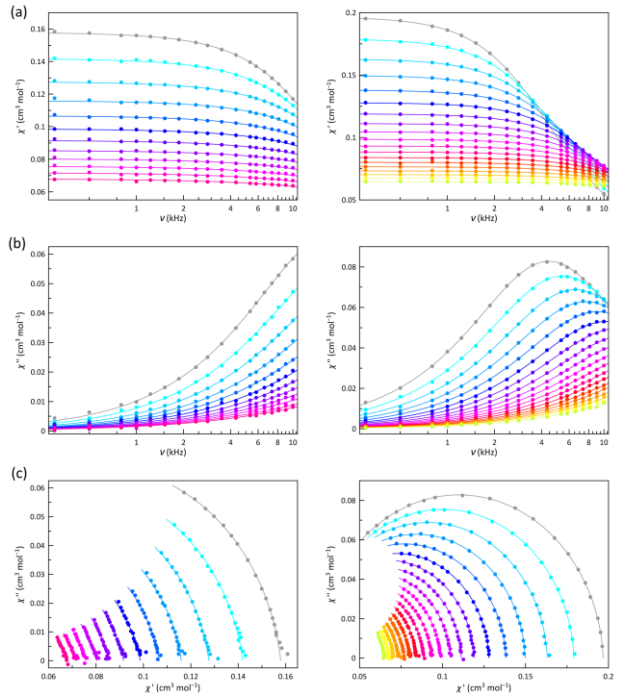

Figure VI.5 Frequency dependence of χ_M' (a) and χ_M'' (b) and the corresponding Argand plots (c) of **1** (left) and **2** (right) under a static magnetic field of 1.0 kOe with ±0.5 Oe oscillating field in the temperature ranges 2.0–4.75 K (**1**) and 2.0–6.5 K (**2**) with ΔT = 0.25 K (from grey to warmer colours). The solid lines are the best-fit curves (see text).

Neither frequency dependence of χ_M' nor a χ_M'' signal are observed in the lack of a *dc* magnetic field (data not shown). However, in the presence of the weakest *dc* magnetic field (H_{dc} = 1.0 kOe), **1** develops incipient χ_M'' signals and **2** exhibits a distinct maximum in the χ_M'' against ν plot that progressively shifts toward lower frequencies as the temperature decreases (Figure VI.5b). This maximum also arises in **1** and shifts toward lower frequencies when increasing H_{dc} (Figures VI.S9b–S11b).

The values of the magnetic relaxation time (τ) were calculated from the joint analysis of the frequency-dependence of χ_M' and χ_M'' through the generalised Debye equations, which consider the adiabatic (χ_S) and isothermal (χ_T) magnetic susceptibilities, and the exponential factor (α) that describes the broadness of the spectra, as additional fitting parameters (solid lines in Figures VI.5a and b, VI.S9a–S11a and VI.S9b–S11b). The corresponding χ_M' *vs* χ_M'' (so-called Argand) plots give either incomplete or almost perfect semicircles for **1** and **2**, which can be well simulated by the best-fit α, τ, χ_S and χ_T values (Figures VI.5c and VI.S9c–S11c). The small α values [0.032–0.24 (**1**) and 0.016–0.055 (**2**)] support a narrow distribution of magnetic relaxation processes (α = 0 and 1 for an ideal Debye model with a single and infinite magnetic relaxation processes). The slight increase of α when decreasing the temperature below 5.0 K more likely results from the presence of tiny non-negligible intermolecular dipolar interactions (Figure VI.S12a). At the same time, a monotonical increase of the χ_S and χ_T occurs upon cooling (Figures VI.S12b and S12c).

The calculated τ values are displayed in the form of the Arrhenius and lnτ vs ln$T$ plots in Figure VI.6 and VI.S13. The most remarkable feature is the systematic more significant τ for **2** (Figure VI.6). This situation conforms with a transistor-like magnetic switch exchanging from a field-induced "faster-relaxing" (FR) to "slower-relaxing" (SR) LS Co^{II} ions upon ligand deprotonation. In both cases, the increase of H_{dc} is followed by a monotonical increase of τ from 8.46 (**1**) and 35.8 μs (**2**) up to 23.6 (**1**) and 47.0 μs (**2**) at 2.0 K for H_{dc} = 1.0 and 5.0 kOe, respectively. This situation agrees with that found for related octahedral SCO cobalt(II)-4-StyTERPY complexes reported in Chapter V, which undergoes a field-induced slow magnetic relaxation of the LS Co^{II} ion.

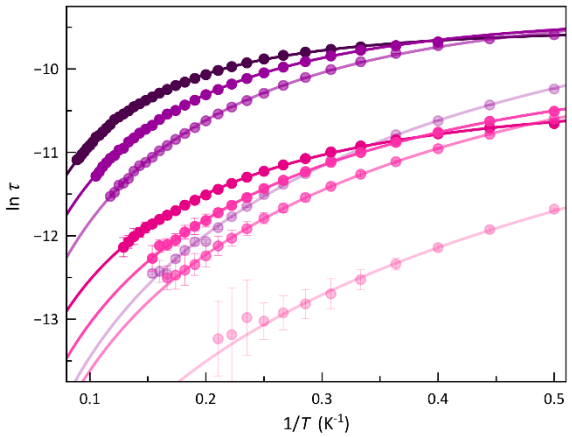

Figure VI.6 Arrhenius plots of **1** (pink) and **2** (purple) under applied *dc* magnetic fields of 1.0, 2.5, 3.5, and 5.0 kOe (light to deep pink and purple colours, respectively). The solid lines are the best-fit curves for a double Raman plus intra-Kramer (IK) relaxation mechanisms (see text). Vertical error bars denote the standard deviations.

The Arrhenius plots for **1** and **2** were satisfactorily simulated considering a double relaxation mechanism described by the equation: $\tau^{-1} = CT^n + \tau_{IK}^{-1}$ (solid lines in Figures VI.6 and S13). The first term is the well-known two-phonon Raman magnetic relaxation process; the second is a temperature-independent term that accounts for the spin-reversal relaxation between the Zeeman-split m_S = ±1/2 ground Kramers doublet. This intra-Kramer (IK) contribution should be seen as a zero-order term of a direct mechanism and not as a quantum tunnelling of the magnetisation (QTM) process, which is physically meaningless for an S = 1/2 spin ground state since it cannot establish an energy barrier.[55]

The calculated parameters corresponding to this double Raman plus IK relaxation mechanisms for **1** and **2** appear summarised in Table VI.3, while their variation with H_{dc} is illustrated in Figure VI.7. For the IK process operating in the range of lower temperatures, τ_{IK} decreases with increasing H_{dc} (Figure VI.7a). Nevertheless, the Raman process prevails at higher temperatures, being C almost one order of magnitude larger in **1**, which would account for their distinct spin dynamics. However, similar exponential H_{dc} dependence of C is found for both compounds (Figure VI.7b). Otherwise, n values, close to 2, suggest that the slow magnetic relaxation (SMR) is associated with resonant phonon trapping through a phonon-bottleneck process, a rather optical than acoustic phonon.

Table VI.3. Selected parameters from the least-squares fit of the *ac* magnetic data at different applied *dc* magnetic fields through two-phonon Raman plus temperature-independent Intra-Kramer processes for **1** and **2** (see text)

	H_{dc}[a] (kOe)	C[b] (s^{-1} K^{-n})	n[b]	IK[c] ($\times 10^{-3}$ s^{-1})
1	1.0	30873 ± 1000	1.96 ± 0.04	-
	2.5	6284 ± 300	2.13 ± 0.03	0.078 ± 0.005
	3.5	5253 ± 200	1.93 ± 0.02	0.062 ± 0.003
	5.0	3752 ± 200	1.82 ± 0.03	0.0354 ± 0.0009
2	1.0	4700 ± 800	2.16 ± 0.09	0.15 ± 0.06
	2.5	1213 ± 60	2.02 ± 0.02	0.109 ± 0.003
	3.5	841 ± 40	1.95 ± 0.02	0.095 ± 0.002
	5.0	400 ± 20	2.01 ± 0.02	0.0764 ± 0.0009

[a]Applied *dc* magnetic field. [b]The pre-exponential and exponential coefficients for the Raman mechanism [$\tau^{-1} = CT^n$]. [c]Coefficient for the temperature-independent intra-Kramer mechanism [$\tau^{-1} = IK$].

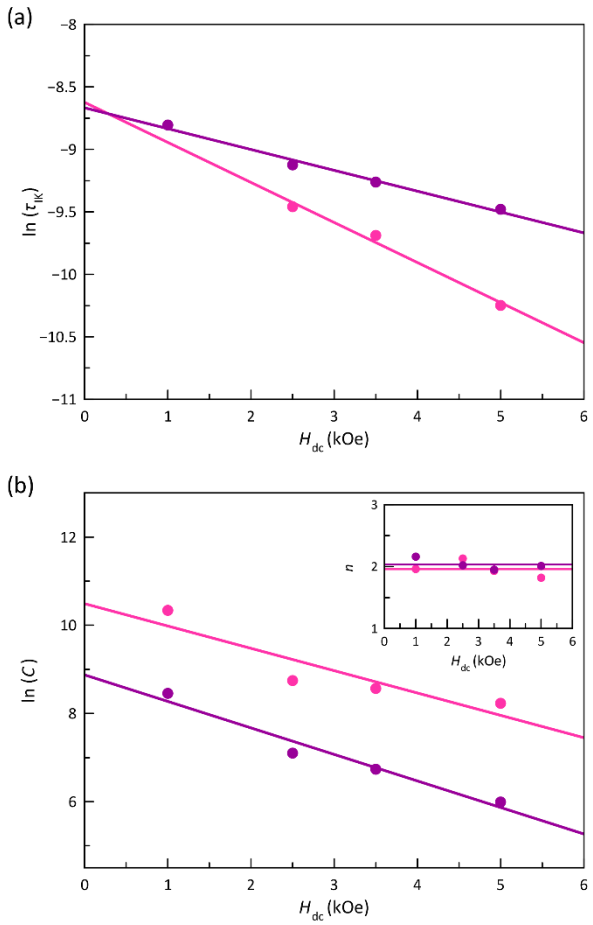

Figure VI.7 Field dependence of the calculated values of τ_{IK} (a) and C (b) for a double Raman plus intra-Kramer (IK) relaxation mechanisms in **1** (pink) and **2** (purple). The inset show the field dependence of the calculated n values. The solid lines are the best-fit curves (see text).

As observed throughout this dissertation, the relaxation of the magnetisation of the LS configuration in cobalt(II) complexes depends significantly on the magnetic field, at least for $H_{dc} \leq 2.5$ kOe. However, as it occurs in the compounds of chapter V, this dependence is dampened and even stabilises at higher or more intense H_{dc}. There are only two types of relaxation that depend on the magnetic field, and they are predominant at low temperatures: those governed by the IK [B_1 / (1 + B_2H^2)] and direct (A_1H^4T) mechanisms. Although an H_{dc}-independent Raman relaxation is usually assumed in the T^9 term (R_9T^9) for ground Kramers doublets, there is a usually negligible influence of H_{dc} on the T^7 term ($\alpha_7R_7T^7H^2$). In these terms, R_9 and R_7 are material specific parameters, and α_7 is a constant. When only an IK relaxation acts at lower temperatures, the spin-reversal gradually slows down with increasing H_{dc} (Figure VI.S14a); however, a direct relaxation should become faster. Thus, if both mechanisms coincide, a change in the trend followed by lnτ with H_{dc} should be reached (Figure VI.S14b) and there should be a H_{dc} range in which it does not significantly affect lnτ. The presence of a Raman mechanism assisted by optical phonons manifested at lower temperatures and competing with the IK one does not speed up the magnetic relaxation, but it does reduce its slowing down, at least in the operating temperature range (Figure VI.S14c). One of these two circumstances must occur in the LS complexes shown in this and preceding chapters. This particular region in which H_{dc} weakly influences magnetic relaxation should be reached in HS systems at lower magnetic field due to their larger spin momentum, and so should be the effect induced by H_{dc}, which agrees with that observed in chapters II–IV.

The magnetic relaxation time for a doublet spin ground state is identical to the spin-lattice time ($T_1 = \tau$), which acts in turn as a limiting factor for the phase memory time ($T_m \leq T_1$). So, rather longer T_1 values are available for **2** relative to **1,** but all in the nanoscale time. In fact, a related square pyramidal LS cobalt(II) complex has been positively tested as a qubit prototype by observing anisotropic Rabi cycles with long enough quantum phase memory times ($T_m \approx 1$ µs at $T = 5.0$ K).[52] These results suggest the possibility to switch the spin dynamics and quantum coherence (QC) of the LS Co^{II} ions in **1** and **2** under pH control, opening thus the way for the applications of this novel class of pH-responsive spin crossover cobalt(II) molecular nanomagnets as molecular magnetic devices in a future spin-based quantum computing machine. Hence, different QC properties can be presumed for the (total or partially) protonated FR (**1**) and deprotonated SR (**2**) forms upon reversible ligand deprotonation/protonation. Hence, the switching of the SMR and QC in this proton transfer series of octahedral SCO cobalt(II)-terpyridine complexes could be exploited to develop a new type of PHE-SQTs.

VI.5 – Proof-of-Concept of a Spin Chemo-switch

The reversible interconversion between the different pH isomers along this proton transfer series of cobalt(II) complexes (Scheme V.3) has been monitored through both electronic adsorption/emission spectra and cyclic voltammetry in order to evaluate the pH-based optical, luminescent and redox chemoswitching in solution (see VI.7 - Experimental section).

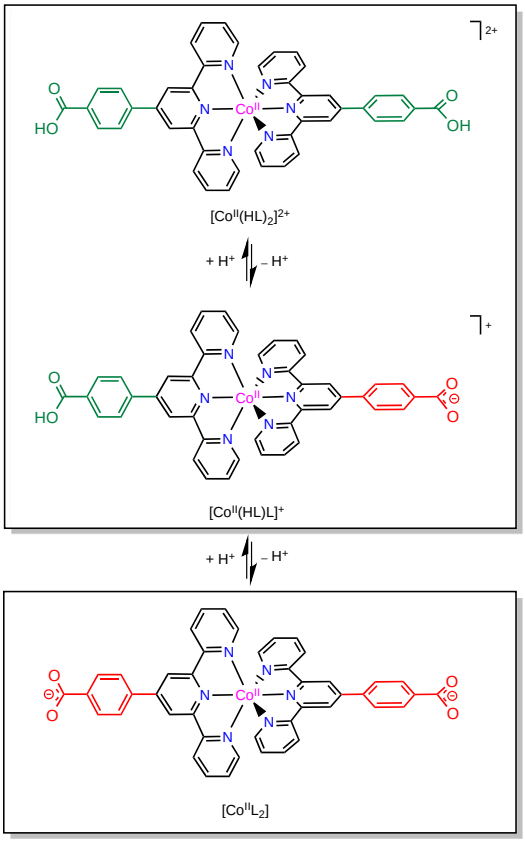

Scheme VI.3 Illustration of the proton transfer series of bis(benzoic acid-substituted terpyridine)cobalt(II) complexes showing the corresponding acid-base equilibria between the protonated, hemiprotonated, and deprotonated pH isomers. The boxed structures represent the solid-state isolated species in **1** (top) and **2** (bottom).

pH-switchable luminescent behaviour. The electronic absorption/emission spectra of aqueous solutions of $[Co^{II}(HL)_2]^{2+}$ (pH = 3) and $[Co^{II}L_2]$ (pH = 8) at room temperature are compared with those of their HL and NaL ligand counterparts in Figure VI.S15.

The electronic absorption spectra of $[Co^{II}(HL)_2]^{2+}$ and $[Co^{II}L_2]$ consist of an intense band located in the far UV region at 290 nm with a distinct shoulder at *ca.* 330 nm (solid dark green and dark red lines, respectively; Figures VI.S15a and VI.S15b). They are attributed to intraligand (IL) π–π* transitions, which are also present in somewhat perturbed yet identifiable form in the spectra of HL and NaL (dashed black lines in Figures VI.S.15a and VI.S15b). These absorptions show a slight but non-negligible bathochromic shift with respect to those of the corresponding protonated and deprotonated forms of the ligand [λ_{max} = 280/325(sh) (HL) and 280/320(sh) nm (NaL)], which is likely explained by the ligand electronic delocalisation on the Co^{II} ion. Additionally, a weak absorption band in the visible region is observed for both $[Co^{II}(HL)_2]^{2+}$ and $[Co^{II}L_2]$ (pH = 3.0 and 8.0, respectively) at 521 nm, which is assigned to a ligand-to-metal charge transfer (LMCT) transition.

The corresponding electronic emission spectra of $[Co^{II}(HL)_2]^{2+}$ and $[Co^{II}L_2]$ after excitation with UV light (λ_{exc} = 295 nm) show the typical Stokes shift of the π*–π ligand emission transitions located in the near UV region at 370 nm with a distinct shoulder that extends into the visible region at *ca.* 465 nm (solid pale green and pale red lines in Figure VI.S15a and VI.S15b). The same situation is found in the emission spectra of the corresponding protonated and deprotonated forms of the ligand [λ_{max} = 367/460 (sh) (HL) and 360/460(sh) nm (NaL)]. However, a net five to three-fold decrease of the emission intensity is observed for both $[Co^{II}(HL)_2]^{2+}$ and $[Co^{II}L_2]$ complexes when compared to their ligand counterparts, as expected due to the quenching effect of the coordinated Co^{II} ion.

The electronic emission spectra recorded upon acid-base titration of a 0.01 mM DMSO/H_2O (80:20 v/v) solution of **1** at 25 °C (see VI.7 – Experimental section) are depicted in Figure VI.8a. They show an overall and progressive development of the asymmetric UV band centred at 370 nm upon increasing the pH from 2.8 to 6.9 up to the attainment of the stationary state corresponding to the total formation of the deprotonated $[Co^{II}L_2]$ species. Upon further increasing the pH (pH >> 8), a dramatic enhancement of the luminescence is observed resulting from the well-known formation of hydroxo-bridged cobalt(II)-4-CO_2PhTERPY species with the release of free highly luminescent 4-CO_2PhTERPY ligands (data not shown).

The analysis of the pH variation of the normalised emission intensity (I/I_0) after acid-base titration was carried out through a simple model that takes into account the presence of two acid-base equilibria between the protonated, hemiprotonated and deprotonated forms of the mononuclear cobalt(II) complexes, $[Co^{II}(HL)_2]^{2+}$, $[Co^{II}(HL)L]^{+}$ and $[Co^{II}L_2]$, respectively (Scheme VI.3). However, only one global acidity constant could be determined with a value of $-\log\beta$ = 8.10(2), corresponding to the overall reaction (Eqn. 1). $[Co(HL)_2]^{2+} \rightleftharpoons [CoL_2] + 2H^+$. The determination of the two individual stepwise constants (Eqn. 2 and 3) was not possible since the fitting software was unable to discriminate between them, meaning that the two pK_a values are too close to each other to individually adjust them to fit the experimental data ($pK_{a,1} = pK_{a,2} = -\log\beta/2$). This is not surprising because the carboxylic groups at each ligand are sufficiently far from each other to exert any influence on their acidity equilibria. In this way, we can only conclude that each pK_a value is close to 4.05, leading thus to a high degree of overlap between the three coexisting species around pH = 4. As shown in the distribution diagram of Figure VI.8b, the dominant species at pH > 5 is the deprotonated complex, while almost only the protonated form is found at pH values less than 3 (> 90%). The hemiprotonated $[Co^{II}(HL)L]^{+}$ form is found only at pH 4, with a percentage of formation not greater than 30%.

$$[Co^{II}(HL)_2]^{2+} \rightleftharpoons [Co^{II}L_2] + 2H^+ \quad (1)$$

$$[Co^{II}(HL)_2]^{2+} \rightleftharpoons [Co^{II}(HL)L]^{+} + H^+ \quad (2)$$

$$[Co^{II}(HL)L)]^{+} \rightleftharpoons [Co^{II}L_2] + H^+ \quad (3)$$

The significant enhancement of the luminescence along this proton transfer series of cobalt(II) complexes after the successive deprotonation of the carboxylic groups from each of the two benzoic acid-substituted terpyridine ligands allows proposing this unique example of dynamic molecular system as a prototype of an optical (luminescent) acid sensor.[60,61] As a

matter of fact, the representation of the normalised emission intensities (I/I_0) after five acid-base titration cycles in the pH range 3–8 evidences a completely reversible behaviour without any fatigue damage (inset of Figure VI.8a). Indeed, this feature is mandatory when practical applications of mononuclear transition metal complexes as pH luminescent probes are envisaged.

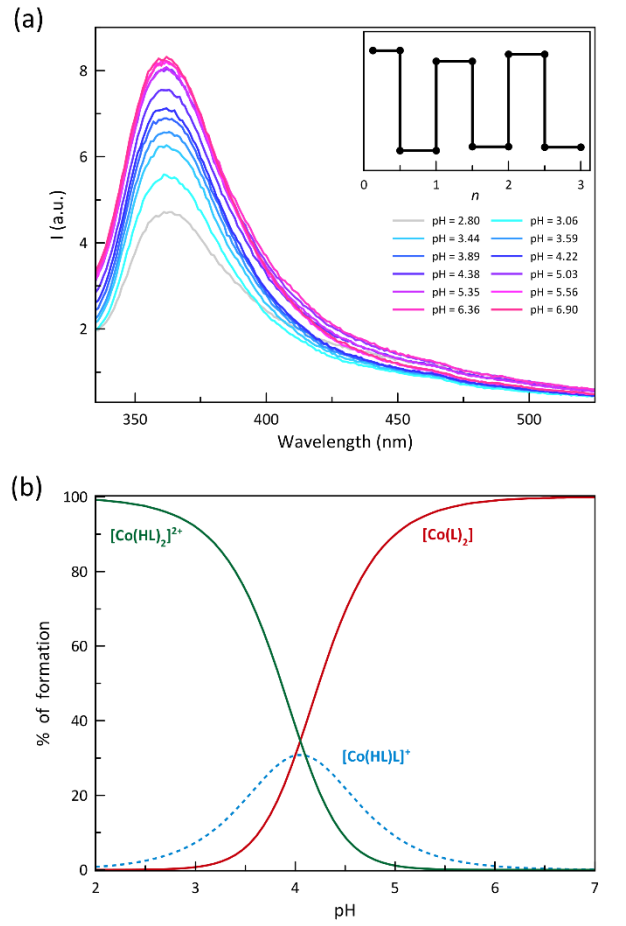

Figure VI.8 (a) Electronic emission spectra of an DMSO/H_2O (80:20 v/v) solution of **1** ($[\mathbf{1}]_0$ = 0.01 mM) after acid-base titration at 25 °C. The inset shows the normalised emission intensity (I/I_0) after several cycles (n) of acid-base titration. (b) Distribution diagram for the various pH isomers: $[Co^{II}(HL)_2]^{2+}$ (green solid line), $[Co^{II}(HL)L]^{+}$ (blue dashed line) and $[Co^{II}L_2]$ (red solid line).

pH-switchable redox behaviour. The redox behaviour of the bis(benzoic acid-substituted terpyridine)cobalt(II) complexes was investigated through cyclic voltammetry (see VI.7 – Experimental Section).

The cyclic voltammogram (CV) of **2** in dimethylformamide (DMF) shows four distinct redox processes (Figure VI.S16), one of them being a reversible oxidation (E_0 = –0.110 V *vs* Fc/Fc^+) and the other three non-reversible reductions (E_1 = –1.08, E_2 = –1.50 and E_3 = –1.98 V *vs* Fc^+/Fc). The reversible oxidation wave is assigned to one-electron metal oxidation leading to the corresponding cobalt(III) complex. The formal potential of this Co^{III}/Co^{II} pair is less negative than that reported for the parent cobalt(II)-2,2′:6′,2″-terpyridine complex $[Co^{II}(TERPY)_2]^{2+}$ (E = –0.136 V *vs* Fc/Fc^+ in DMF) as a consequence of the electron-withdrawing nature of the benzoate substituent.[62,63] The first and third reduction waves are attributed to the stepwise one-electron metal reduction Co^{II}/Co^{I} and Co^{I}/Co^{0} pairs, according to the literature, while the completely irreversible second one is most likely a result of a ligand-based reduction process. These metal reductions also are affected by the benzoate group, occurring at less negative formal potentials when compared to the parent $[Co^{II}(TERPY)_2]^{2+}$ complex (E = –1.19 V and –2.08 V *vs* Fc/Fc^+).[62]

The CVs corresponding to the reversible metal-based oxidation wave recorded upon acid-base titration of a 1.0 mM DMF solution of **2** at 25 °C (see VI.7 - Experimental Section) are depicted in Figure VI.9a. During this experiment, the acid-base equilibria have been simultaneously monitored by electronic absorption spectroscopy (Figure VI.S17).

The gradual and continuous decrease of pH by adding subsequent amounts of a 3.0 M HCl aqueous solution causes a loss in the reversibility of the Co^{III}/Co^{II} redox process, as evidenced by the asymmetric shape of the CV for $[Co^{II}(HL)_2]^{2+}$ at pH = 3 relative to the symmetric one for $[Co^{II}L_2]$ at pH = 8 (Figure VI.9a). This loss of reversibility is accompanied by a decline of the visible LMCT band centred at 521 nm (Figure VI.S17a), which is followed by a colour change from red to orange upon conversion from $[Co^{II}L_2]$ to $[Co^{II}(HL)_2]^{2+}$ (inset of Figure VI.9a). On the other hand, the signal of the cathodic peak current and the intensity of

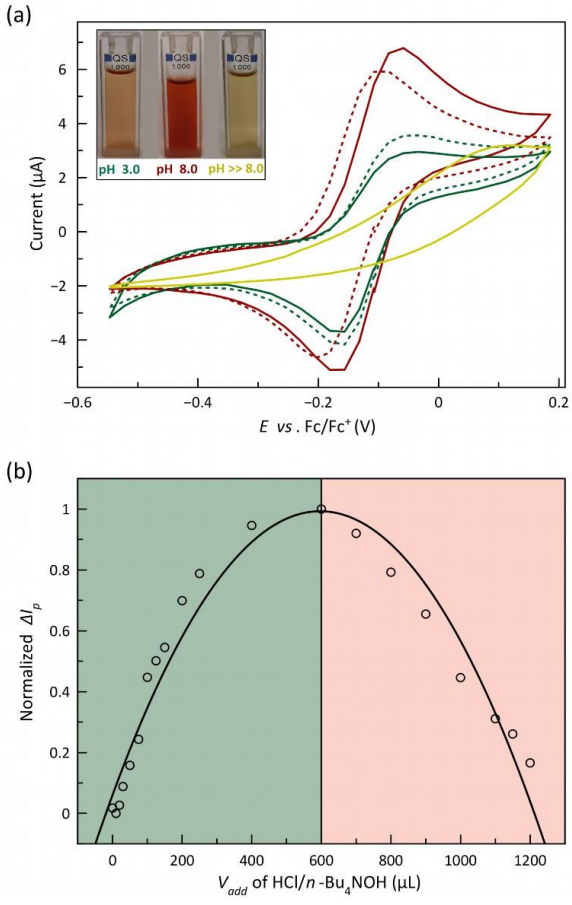

Figure VI.9 (a) Cyclic voltammograms of a solution of **2** in DMF [0.1 M n-Bu_4NPF_6] at 25 °C and 200 mV s^{-1} in both acidic (green lines) and basic (red lines) and strong basic media (yellow line). The restoration of the current signal after one cycle is represented as dashed lines (see text). The inset shows the corresponding voltammetry solutions at each pH condition. (b) Normalized ΔI_p against the added volume of HCl (green region) or (n-$Bu)_4NOH$ (red region). The solid black line is only an eye-guide (see text).

the visible band are restored upon increasing the pH by the addition of subsequent amounts of a 3.0 M NaOH aqueous solution, to match almost perfectly the initial CV and UV-Vis spectrum of $[Co^{II}L_2]$ (dashed red lines in Figures VI.9a and VI.S17a). The slight differences are attributed to the difficulty of controlling the exact pH value in DMF solution and to dilution effects. Curiously, the current signal and the visible band disappear entirely when an excess of base is added, which is accompanied by a colour change from red to yellow (yellow lines in Figures VI.9a and VI.S17a). These features could be attributed to the aforementioned formation of hydroxo-bridged cobalt(II)-terpyridyl species, which cannot stabilise the cobalt(III) oxidation state.

The reversible nature of the pH-triggered chemo-switching of the redox and optical behaviour is reflected in the representation of the normalised ΔI_p and $\Delta\varepsilon$ values [ΔI_p and $\Delta\varepsilon$ being defined as the difference between the absolute values of anodic (I_{ap}) and cathodic (I_{cp}) current peaks and those between the molar extinction coefficient, respectively] as a function of the added volume of acid/base (Figures VI.9b and VI.S17b). At the maximum acid addition, ΔI_p reaches the highest value, indicating that the Co^{III}/Co^{II} redox process is less reversible in acidic medium. Otherwise, $\Delta\varepsilon$ attains the lowest value at the maximum addition of acid, being fully restored with the addition of base, evidencing the reversible interconversion between the $[Co(L)_2]$ and $[Co(HL)_2]^{2+}$ species.

In Chapter III, we reported on the reversible electro-switching (ON/OFF) of the single-molecule magnet (SMM) behaviour in an octahedral SCO cobalt(II)-4-MeOPhPDI complex, featuring one-electron oxidation from the slow-relaxing paramagnetic LS Co^{II} (S_{Co} = ½, ON) to the diamagnetic LS Co^{III} (S_{Co} = 0, OFF) state in solution.[55] In that case, the metal oxidation occurs at +0.39 V *vs* Fc/Fc^+, a much higher former potential than that for the cobalt(II)-4-HO_2CPhTERPY. This fact suggests that a more favoured magnetic electroswitch can be achieved among the two distinct $[Co^{II}(HL)_2]^{2+}/[Co^{III}(HL)_2]^{3+}$ and $[Co^{II}L_2]/[Co^{III}L_2]^+$ redox pairs under pH control.

VI.6 – Concluding Remarks

In this chapter, we presented a novel pH-responsive dynamic molecular system based on a mononuclear SCO cobalt(II) complex in the form of pair of pH isomers. It constitutes a unique example of how the control of a single input (pH) can produce reversible changes in the optical (luminescence), redox, and magnetic (spin crossover and spin dynamics) properties, either in solution or in the solid state.

Thermal-assisted spin transition and field-induced slow magnetic relaxation coexist in the solid state with field-induced "faster-relaxing" (FR) or "slower-relaxing" (SR) octahedral Co^{II} ions in the LS state, depending on the ligand protonation. A progressive enhancement of the luminescence in the UV region occurs upon acid-base equilibria in solution among the protonated, hemiprotonated and deprotonated forms, which can be reversibly interconverted upon pH variation. They also show one-electron oxidation of the paramagnetic LS Co^{II} ion to the diamagnetic LS Co^{III} ion in solution, whose reversibility is partially lost with decreasing the pH but is restored with increasing it.

The reported optical, electronic, and magnetic multistability along this proton transfer series of mononuclear cobalt(II) complexes illustrates the potential of dynamic SCO/SMM molecules, offering fascinating possibilities as advanced multifunctional and multiresponsive magnetic devices for molecular spintronics and quantum computing such as PHE-SQTs and spin quantum chemoswitches for pH sensing.

VI.7 – Experimental Section

Materials. Reagent grade 2-acetylpyridine, methyl 4-formylbenzoate, sodium hydroxide, ammonium acetate, cobalt(II) acetate tetrahydrate, cobalt(II) perchlorate hexahydrate, and polyethyleneglycol-200 were purchased from commercial sources and used as received.

Physical techniques. Elemental (C, H, N) and energy dispersive X-ray (EDX) analyses were performed at the Servicio Central de Soporte a la Investigación (SCSIE) at the Universitat de València (Spain). The thermogravimetric analysis (TGA) was performed on powdered samples under a dry N_2 atmosphere within the range of 25–225 °C with a Mettler Toledo TGA/STDA 851 thermobalance operating at a heating rate of 10 °C min^{-1}. FT–IR spectra were recorded on a Nicolet-5700 spectrophotometer as KBr pellets. ^{1}H NMR spectra were registered at room temperature on a Bruker AC 300 (300 MHz) spectrometer. Deuterated dimethylsulfoxide (DMSO-d_6) was used as solvent and internal standard (δ = 2.5 ppm). Powder X-ray diffraction (PXRD) patterns of powdered crystalline samples were collected at room temperature on a D8 Avance A25 Bruker diffractometer using graphite-monochromated Cu-K_α radiation (λ = 1.54056 Å). Variable-temperature (2–300 K) direct current (d) magnetic susceptibility measurements under applied fields 0.25 (T < 20 K) and 5.0 kOe (T > 20 K) and variable-field (0–50 kOe) magnetisation measurements at T = 2.0 K were carried out on crushed crystals of **1** and **2** with a Quantum Design SQUID magnetometer. The magnetic susceptibility data were corrected for the diamagnetism of the constituent atoms and the sample holder. Variable-temperature (2–300 K) alternating current (ac) magnetic susceptibility measurements under ±5.0 Oe oscillating field at frequencies in the range 0.1–10 kHz were carried out under different dc magnetic fields (H_{dc} = 1.0, 2.5, 3.5 and 5.0 kOe) with a Quantum Design Physical Property Measurement System (PPMS).

Solution Studies. Electronic absorption spectra were recorded on a Jasco UV/Vis/NIR V-670 spectrophotometer, whereas the emission spectra were recorded with a modular spectrofluorimeter in the range λ_{em} = 335–550 nm with an excitation wavelength of λ_{exc} = 295 nm. The emission spectra of a 0.01 mM of **1** in DMSO/H_2O (80:20) solution were recorded at different pH values at 25 °C. Diluted aqueous solutions of HCl and NaOH were used to adjust the hydrogen ion concentration of the

medium and the pH value was measured with a pH meter, previously calibrated with standardized buffer solutions at two pH values (pH 4.01 and 7.00). The computer program HypSpec[64] was used to estimate the stability constants from spectroscopic data.

Cyclic voltammetry studies were performed using an AUTOLAB 204 scanning potentiostat operating at a scan rate of 200 mV s^{-1}. Cyclic voltammograms were recorded at room temperature using 0.1 M (n-Bu_4)NPF_6 as supporting electrolyte and 1.0 mM of **2** in DMF. The reference electrode was an AgCl/Ag, while a platinum disk (0.32 cm^2) and a glassy carbon rod (76 mm) were used as working and auxiliary electrodes. All experiments were performed in standard electrochemical cells. The investigated potential was in the range from –2.0 to +1.0 V *vs* AgCl/Ag. Ferrocene (Fc) was added at the end of the measurements as an internal standard. Formal potentials were defined as half-wave potentials, except for the irreversible reduction waves for which the anodic peak potentials were given instead. They were measured at a scan rate of 200 mV s^{-1} and referred to the Fc^+/Fc couple. The formal potential and the anodic to cathodic peaks separation of ferrocene under the same conditions were $E(Fc^+/Fc)$ = +0.42 V *vs* AgCl/Ag and $\Delta E_p(Fc^+/Fc)$ = 127 mV (DMF, 0.1 M (n-Bu_4)NPF_6, 25 °C). The pH variable measurements were carried out by adding progressive amounts of aqueous 3.0 M HCl or (n-Bu_4)NOH solutions. For each recorded cyclic voltammogram, the electronic spectrum was registered in a Jasco UV/Vis/NIR V-670 spectrophotometer between 400 and 700 nm on an aliquot, later returned to the electrochemical cell.

Crystal structure data collection and refinement. X-ray diffraction data on a single crystal of **1** and **2** were collected on a Bruker D8 Venture diffractometer with a PHOTON II detector by using monochromatic Mo-K_α radiation (λ = 0.71073 Å) at 120 K. Diffraction data of **1** and **2** were collected, scaled, and integrated using the Bruker SAINT software.[65] The structures were solved by intrinsic phasing methods integrated into the SHELXTL[66] software with the Olex2 platform.[67] The obtained models were refined with the version 2018/3 of SHELXL against F^2 on all data by full-matrix least squares. The diffraction of the single crystal of **2** was somewhat poor, with a low average $I/2\sigma(I)$ and a rather large R_{int} (0.1745). All non-hydrogen atoms were refined anisotropically, except those of one disordered perchlorate anion in the structure of **1** because the refinement, even constrained, was unstable. Hydrogen atoms in water molecules were neither found nor fixed. The remaining ones were set on geometrical positions and refined with a riding model. Hydrogen atoms of each one the carboxylic groups of **1** were set in the longest C–O bond [C22–O2: 1.309(6) Å vs C22–O1: 1.205(6) Å and C44–O4: 1.293(7) Å vs C44–O3: 1.214(7) Å], with an unrefined site occupancy factor of 0.75. The two perchlorate anions in **1** were disordered and constraints (EADP), and soft and rigid restraints (SADI or DFIX) were used to refine the disorder in a model accounting for two positions. The somewhat high residual electron density corresponds to disordered solvent around the water molecules O16 and O17. Further modelling of the disorder creates a messy refinement model. The low residual electron density was not squeezed with a mask to avoid the inclusion of artifices. In the crystal structure of **2**, some occupation factors for water molecules (O6, O7, O8 and O10) were refined and later fixed to the closest round value (s.o.f. set at 0.5). The water molecules O11 and O12 were refined with the s.o.f. values linked, leading to values also close to 0.5. The graphical manipulations and calculations were performed with the CRYSTALMAKER and MERCURY programs.[68,69]

Preparation ligands and complexes.

Methyl 4'-(4-carboxyphenyl)-2,2':6',2"-terpyridine (MeL): 2-Acetylpyridine (3.10 mL, 27.5 mmol) was added to PEG200 (40 mL) containing NaOH (1.10 g, 27.5 mmol), and the resulting suspension was stirred for 15 minutes at 0 °C. Methyl 4-formylbenzoate (2.25 g, 13.75 mmol) was added to the previous mixture, and the whole was kept at 0 °C for two hours under vigorous stirring. Then, an excess of ammonium acetate (6.70 g, 87.0 mmol) was added to the reaction mixture and further heated at 100 °C for two hours. The reaction mixture was cooled to room temperature, and 200 mL of water was added to cause the precipitation of the yellow crude methyl ester acid product (MeL). The yellow solid was collected by filtration and washed with water and cold ethanol. Yield *ca* 42%. Anal. Calc. for $C_{22}H_{15}N_3O_2$ (HL): C, 74.78; H, 4.28; N, 11.89. Found: C, 74.43; H, 4.25; N, 11.94%. IR (KBr, cm^{-1}): 3421m [ν(O–H) from the carboxylic acid substituent of MeL], 2950w [$\nu(C_{sp3}$–H) from the methyl substituents of MeL], 1706s [$\nu(COO)_s$ from carboxylic acid substituent], 1579s [ν(C=N) from the pyridine rings of MeL], 1288s [$\nu(COO^-)_{ass}$ from the carboxylic acid substituent], 767s [out-of-plane $\delta(C_{sp2}$–H) from the pyridine ring of MeL]. ^{1}H NMR (DMSO; 300 MHz, ppm): δ = 9.16-8.84 (m, 3H), 8.42 (d, 1H, J = 6.3 Hz), 8.19 (q, 2H, J = 8.4 Hz), 7.93 (s, 1H).

4'-(4-carboxyphenyl)-2,2':6',2"-terpyridine (HL): The hydrolysis of the methyl ester acid derivative was carried out under basic medium by treating MeL (0.30 g, 0.80 mmol) with a 2.0 M NaOH aqueous solution (25 mL) overnight at 100 °C. After cooling at room temperature, the pH of the suspension was adjusted to 3.0 with 3.0 M HCl solution. The white powder which formed was filtered and washed several times with water. Yield 95%. Anal. Calc. for $C_{22}H_{15}N_3O_2$ (HL): C, 74.78; H, 4.28; N, 11.89. Found: C, 74.43; H, 4.25; N, 11.94%. IR (KBr, cm^{-1}): 3417m [ν(O–H) from the carboxylic acid substituent of HL], 1706s [$\nu(COO)_{ass}$ from carboxylic acid substituent of HL], 1595s [ν(C=N) from the pyridine rings of HL], 1261s [$\nu(COO^-)_s$ from the carboxylic acid substituent of HL], 771s [out-of-plane $\delta(C_{sp2}$–H) from the pyridine ring of HL]. ^{1}H NMR (DMSO; 300 MHz, ppm): δ = 9.16-8.84 (m, 3H), 8.42 (d, 1H, J = 6.3 Hz), 8.19 (q, 2H, J = 8.4 Hz), 7.93 (s, 1H).

Sodium 4'-(4-carboxylatephenyl)-2,2':6',2"-terpyridine tetrahydrate (NaL): The hydrolysis of the methyl ester acid derivative was carried out on basic medium by treating MeL (0.50 g, 0.80 mmol) with a 2.0 M NaOH aqueous solution (15 mL)

overnight at 100 °C. Yield 64%. Anal. Calc. for $C_{22}H_{22}N_3O_6Na$ (NaL): C, 59.06; H, 4.96; N, 9.39. Found: C, 60.33; H, 4.70; N, 9.14%. IR (KBr, cm^{-1}): 3421-2800 [ν(O–H) from the carboxylic acid substituent of NaL], 1562s [$\nu(COO)_{ass}$ from carboxylic acid substituent], 1602s [ν(C=N) from the pyridine rings of NaL], 1402s [$\nu(COO^-)_s$ from carboxylic acid substituent of NaL], 775s [out-of-plane $\delta(C_{sp2}–H)$ from the pyridine ring of NaL]. ^{1}H NMR ($CDCl_3$; 300 MHz, ppm): δ = 8.70 (s, 2H, H_{im}), 8.24 (d, 2H, *m*-H_{py}, J = 7.8 Hz), 7.90 (t, 1H, *p*-H_{py}, J = 7.8 Hz), 7.36 (d, 4H, *o*-H_{ph}, J = 8.9 Hz), 6.96 (d, 4H, *m*-H_{ph}, J = 8.9 Hz), 3.85 (s, 6H, *p*-H_{OMe}).

*{[$Co^{II}(HL)_2$][$Co^{II}(HL)L$]}$(ClO_4)_3 \cdot 9H_2O$ (**1**)*: A methanolic solution (3.0 mL) of cobalt(II) perchlorate hexahydrate (0.018 g, 0.05 mmol) was added dropwise to a suspension of HL (0.0354 g, 0.10 mmol) in acetonitrile (15.0 mL) under stirring. The mixture was stirred for one hour under gentle warming at 50 °C. The resulting red solution was allowed to evaporate in a hood slowly, and X-ray quality dark red crystals of **1** were obtained after one week. The crystals were collected on filter paper and gently washed with acetonitrile. Yield 72 %. Anal. Calc. for $C_{41}H_{35}N_6O_{12}Cl_2Co$ (**1**): C, 53.18; H, 4.04; N, 8.86. Found: C, 53.98; H, 4.17; N, 8.90%. IR (KBr, cm^{-1}): 3439s [ν(O–H) from the carboxylic acid substituent of HL and crystallisation water molecules], 1689s [$\nu(COO)_{as}$ from the carboxylic acid and carboxylate substituents of HL and L], 1263s [$\nu(COO)_s$ from the carboxylic acid and carboxylate substituents of HL and L], 1614 [ν(C=N) from the pyridine rings of HL and L], 1110vs [ν(Cl–O) from perchlorate anions], 775s [out-of-plane $\delta(C_{sp2}–H)$ from the pyridine rings of HL and L].

*[$Co^{II}L_2$]$\cdot 5H_2O$ (**2**)*: An aqueous solution (15 mL) of cobalt(II) acetate tetrahydrate (0.025 g, 0.10 mmol) was added dropwise to a suspension of NaL (0.075 g, 0.20 mmol) in dimethylsulfoxide (5.0 mL) under stirring. The mixture was stirred for one hour at room temperature. The polycrystalline powder was filtered and washed with a small quantity of water. X-ray quality dark red crystals of **2** were obtained by treating the polycrystalline powder under hydrothermal conditions at 100 °C for four days. Yield 91 %. Anal. Calc. for $C_{44}H_{38}N_6O_9Co$ (**2**): C, 61.90; H, 4.49; N, 9.84. Found: C, 61.75; H, 4.32; N, 9.90%. IR (KBr, cm^{-1}): 3407s [ν(O–H) from crystallisation water molecules], 1554s [$\nu(COO)_{as}$ from carboxylate substituent of L], 1553s [ν(C=N) from the pyridine rings of L], 1371s [$\nu(COO^-)_s$ from carboxylate substituent of L], 785s [out-of-plane $\delta(C_{sp2}–H)$ from the pyridine ring of HL].

References

1 Dei, A.; Gatteschi, D.; Sangregorio, C.; Sorace, L. Quinonoid Metal Complexes: Toward Molecular Switches *Acc. Chem. Res.* 2004, **37**, 827–835.

2 Real, J. A.; Gaspar, A. B.; Muñoz, M. C. Thermal, Pressure and Light Switchable Spin-Crossover Materials. *Dalton Trans.* **2005**, 2062–2079.

3 Evangelio, E.; Ruiz-Molina, D. Valence Tautomerism: New Challenges for Electroactive Ligands. *Eur. J. Inorg. Chem.* **2005**, 2957–2971.

4 Sato, O.; Tao, J.; Zhang, E.-J. Control of Magnetic Properties Through External Stimuli. *Angew. Chem. Int. Ed*. **2007**, *46*, 2152–2187.

5 Castellano, M.; Ruiz-García, R.; Cano, J.; Ferrando-Soria, J.; Pardo, E.; Fortéa-Pérez, F. R.; Eddine-Stiriba, S.; Julve, M.; Lloret, F. Dicopper(II) Metallacyclophanes as Multifunctional Magnetic Devices: A Joint Experimental and Computational Study. *Acc. Chem. Res.* **2015**, *48*, 510–520.

6 Sarkar, B.; Schweinfurth, D.; Deibel, N.; Weisser, F. Functional Metal Complexes Based on Bridging "Imino"-Quinonoid Ligands. *Coord. Chem. Rev.* **2015**, *293*, 250–262.

7 Aguilà, D.; Prado, Y.; Koumousi, E. S.; Mathonière, C.; Clérac, R. Switchable Fe/Co Prussian Blue Networks and Molecular Analogues. *Chem. Soc. Rev*. **2016**, *45*, 203–224.

8 Khusniyarov, M. M. How to Switch Spin-Crossover Metal Complexes at Constant Room Temperature. *Chem. Eur. J.* **2016**, *22*, 15178–15191.

9 Ferrando-Soria, J.; Vallejo, J.; Castellano, M.; Martínez-Lillo, J.; Pardo, E.; Cano, J.; Castro, I.; Lloret, F.; Ruiz-García, R.; Julve, M. Molecular Magnetism, Quo Vadis? A Historical Perspective from a Coordination Chemist Viewpoint. *Coord. Chem. Rev.* **2017**, *339*, 17–103.

10 Doistau, B.; Benda, L.; Hasenknopf, B.; Marvaud, V.; Vives, G. Switching Magnetic Properties by a Mechanical Motion. *Magnetochemistry* **2018**, *4*, 1–15.

11 Meng, Y.-S.; Liu, T. Electrochemical Oxidative Cross-Coupling with Hydrogen Evolution Reactions. *Acc. Chem. Res.* **2019**, *52*, 3309–3324.

12 Römelt, C.; Weyhermüller, T.; Wieghardt, K. Structural Characteristics of Redox-Active Pyridine-1,6-Diimine Complexes: Electronic Structures and Ligand Oxidation Levels. *Coord. Chem. Rev.* **2019**, *380*, 287–317.

13 Nowak, R.; Prasetyanto, E. A.; De Cola, L.; Bojer, B.; Siegel, R.; Senker, J.; Rössler, E.; Weber, B. Proton-Driven Coordination-Induced Spin State Switch (PD-CISSS) of Iron(II) Complexes. *Chem. Commun.* **2017**, *53*, 971–974.

14 Vallejo, J.; Pardo, E.; Viciano-Chumillas, M.; Castro, I.; Amorós, P.; Déniz, M.; Ruiz-Pérez, C.; Yuste-Vivas, C.; Krzystek, J.; Julve, M.; Lloret, F.; Cano. J. Reversible Solvatomagnetic Switching in a Single-Ion Magnet from an Entatic State. *Chem. Sci.* **2017**, *8*, 3694–3702.

15 Elie, M.; Weber, M. D.; Di Meo, F.; Sguerra, F.; Lohier, J.-F.; Pansu, R. B.; Renaud, J.-L.; Hamel, M.; Linares, M.; Costa, R. D.; Gaillard, S. Role of the Bridging Group in Bis-Pyridyl Ligands: Enhancing Both the Photo- and Electroluminescent Features of Cationic (IPr)CuI Complexes. *Chem. Eur. J.* **2017**, *23*, 16328–16337.

16 Weber, M. D.; Fresta, E.; Elie, M.; Miehlich, M. E.; Renaud, J.-L.; Meyer, K.; Gaillard, S.; Costa, R. D. Rationalizing Fabrication and Design Toward Highly Efficient and Stable Blue Light-Emitting Electrochemical Cells Based on NHC Copper(I) Complexes. *Adv. Funct. Mater*. **2018**, *28*, 1707423.

17 Carbonell-Vilar, J. M.; Fresta, E.; Armentano, D.; Costa, R. D.; Viciano-Chumillas, M.; Cano, J. Photoluminescent Cu(I) vs. Ag(I) Complexes: Slowing Down Emission in Cu(I) Complexes by Pentacoordinate Low-Lying Excited States. *Dalton Trans.* **2019**, *48*, 9765–9775.

18 Fatur, S. M.; Shepard, S. G.; Higgins, R. F.; Shores, M. P.; Damrauer, N. H. A Synthetically Tunable System to Control MLCT Excited-State Lifetimes and Spin States in Iron(II) Polypyridines. *J. Am. Chem. Soc.* **2017**, *139*, 4493–4505.

19 Gotico, P.; Boitrel, B.; Guillot, R.; Sircoglou, M.; Quaranta, A.; Halime, Z.; Leibl, W.; Aukauloo, A. Second-Sphere Biomimetic Multipoint Hydrogen-Bonding Patterns to Boost CO_2 Reduction of Iron Porphyrins. *Angew. Chem. Int. Ed*. **2019**, *58*, 4504–4509.

20 Vo, N. T.; Mekmouche, Y.; Tron, T.; Guillot, R.; Banse, F.; Halime, Z.; Sircoglou, M.; Leibl W.; Aukauloo, A. A Reversible Electron Relay to Exclude Sacrificial Electron Donors in the Photocatalytic Oxygen Atom Transfer Reaction with O_2 in Water. *Angew. Chem. Int. Ed.* **2019**, *58*, 16023–16027.

21 Gotico, P.; Roupnel, L.; Guillot, R.; Sircoglou, M.; Leibl, W.; Halime, Z.; Aukauloo, A. Atropisomeric Hydrogen Bonding Control for CO2 Binding and Enhancement of Electrocatalytic Reduction at Iron Porphyrins. *Angew. Chem. Int. Ed.*, **2020**, *59*, 22451–22455.

22 Gotico, P.; Moonshiram, D.; Liu, C.; Zhang, X.; Guillot, R.; Quaranta, A.; Halime, Z.; Leibl, W.; Aukauloo, A. Spectroscopic Characterisation of a Bio-Inspired Ni-Based Proton Reduction Catalyst Bearing a Pentadentate N_2S_3 Ligand with Improved Photocatalytic Activity. *Chem. Eur. J.* **2020**, *26*, 2859–2868.

23 Ruan, G.; Engelberg, L.; Ghosh, P.; Maayan, G. A Unique Co(III)-Peptoid as a Fast Electrocatalyst for Homogeneous Water Oxidation with Low Overpotential. *Chem. Commun.* **2021**, *57*, 939–942.

24 Venkataramani, S.; Jana, U.; Dommaschk, M.; Sönnichsen, F. D.; Tuczek, F.; Herges, R. Magnetic Bistability of Molecules in Homogeneous Solution at Room Temperature. *Science* **2011**, *331*, 445–448.

25 Dommaschk, M.; Peters, M.; Gutzeit, F.; Schütt, C.; Näther, C.; Sönnichsen, F. D.; Tiwari, S.; Riedel, C.; Boretius, S.; Herges, R.; Photoswitchable Magnetic Resonance Imaging Contrast by Improved Light-Driven Coordination-Induced Spin State Switch. *J. Am. Chem. Soc.* **2015**, *137*, 7552–7555.

26 Botár, R.; Molnár, E.; Trencsényi, G.; Kiss, J.; Kálmán, F. K.; Tircsó, G. Stable and Inert Mn(II)-Based and pH-Responsive Contrast Agents. *J. Am. Chem. Soc.* **2020**, *142*, 1662–1666.

27 Wang, H.; Sayed, S. Y.; Zhou, Y.; Olsen, B. C.; Luber, E. J.; Buriak, J. M. Water-Soluble pH-Switchable Cobalt Complexes for Aqueous Symmetric Redox Flow Batteries. *Chem. Commun.* **2020**, *56*, 3605–3608.

28 Mansoor, I. F.; Wozniak, D. I.; Wu, Y.; Lipke, M. C. A Delocalized Cobaltoviologen with Seven Reversibly Accessible Redox States and Highly Tunable Electrochromic Behaviour. *Chem. Commun.* **2020**, *56*, 13864–13867.

29 Parks, J. J.; Champagne, A. R.; Costi, T. A.; Shum, W. W.; Pasupathy, A. N.; Neuscamman, E.; Flores-Torres, S.; Cornaglia, P. S.; Aligia, A. A.; Balseiro, C. A.; Chan, G.-K.-L; Abruña, H. D.; Ralph, D. C. Mechanical Control of Spin States in Spin-1 Molecules and the Underscreened Kondo Effect. *Science* **2010**, *328*, 1370–1373.

30 Mahfoud, T.; Molnár, G.; Cobo, S.; Salmon, L.; Thibault, C.; Vieu, C.; Demont, P.; Bouseksou, A. Electrical Properties and Non-Volatile Memory Effect of the $[Fe(HB(pz)_3)_2]$ Spin Crossover Complex Integrated in a Microelectrode Device. *App. Phys. Lett*. **2011**, *99*, 053307.

31 Cowan, M. G.; Olguín, J.; Narayanaswamy, S.; Tallon, J. L.; Brooker, S. Reversible Switching of a Cobalt Complex by Thermal, Pressure, and Electrochemical Stimuli: Abrupt, Complete, Hysteretic Spin Crossover. *J. Am. Chem. Soc*. **2012**, *134*, 2892–2894.

32 Aravena, D.; Ruiz, E. Coherent Transport through Spin-Crossover Single Molecules. *J. Am. Chem. Soc*. **2012**, *134*, 777–779.

33 Ruiz, E. Charge Transport Properties of Spin Crossover Systems. *Chem. Phys*. **2014**, *16*, 14–22;

34 Harzmann, G. D.; Frisenda, R.; van der Zant, H. S. J.; Mayor, M. Single-Molecule Spin Switch Based on Voltage-Triggered Distortion of the Coordination Sphere. *Angew. Chem. Int. Ed.* **2015**, *54*, 13425–13430.

35 Devid, E. J.; Martinho, P. N.; Kamalakar, M. V.; Salitros, I.; Prendergast, U.; Dayen, J.-F.; Meded, V.; Lemma, T.; González-Prieto, R.; Evers, F.; Keyes, T. E.; Ruben, M.; Doudin, B.; van der Molen, S. J. Spin Transition in Arrays of Gold Nanoparticles and Spin Crossover Molecules. *ACS Nano* **2015**, *9*, 4496–4507.

36 Aragonès, A. C.; Aravena, D.; Cerdá, J. I.; Acís-Castillo, Z.; Li, H.; Real, J. A.; Sanz, F.; Hihath, J.; Ruiz, E.; Díez-Pérez, I. Large Conductance Switching in a Single-Molecule Device through Room Temperature Spin-Dependent Transport. *Nano Lett.* **2016**, *16*, 218–226.

37 Wickramasinghe, L. D.; Mazumder, S.; Kpogo, K. K.; Staples, R. J.; Schlegel, H. B.; Verani, C. N. Electronic Modulation of the SOMO–HOMO Energy Gap in Iron(III) Complexes towards Unimolecular Current Rectification. *Chem. Eur. J.*, **2016**, *22*, 10786–10790.

38 Aragonès, A. C.; Aravena, D.; Valverde-Muñoz, F. J.; Real, J. A.; Sanz, F.; Hihath, J.; Díez-Pérez, I.; Ruiz, E. Metal-Controlled Magnetoresistance at Room Temperature in Single-Molecule Devices. *J. Am. Chem. Soc.* **2017**, *139*, 5768–5778.

39 Jasper-Toennies, T.; Gruber, M.; Karan, S.; Jacob, H.; Tuczek, F.; Berndt, R. Robust and Selective Switching of an Fe^{III} Spin-Crossover Compound on Cu2N/Cu(100) with Memristance Behavior. *Nano Lett*. **2017**, *17*, 6613–6619.

40 Su, Q.-Q.; Yuan, Q.; Wu, X.-F.; Chen, S.-H.; Xiang, J.; Jin, X.-X.; Wang, L.-X.; Wang, B.-W.; Gao, S.; Lau, T.-C. Slow Magnetic Relaxation in Structurally Similar Mononuclear 8-Coordinate Fe(II) and Fe(III) Compounds. *Chem. Commun.*, **2021**, *57*, 781–784.

41 Jornet-Mollá, V.; Giménez-Saiz, C.; Cañadillas-Delgado, L.; Yufit, D. S.; Howard, J. A. K.; Romero, F. M. Interplay between Spin Crossover and Proton Migration along Short Strong Hydrogen Bonds. *Chem. Sci.* **2021**, *12*, 1038–1053.

42 Tissot, A.; Boillot, M.-L.; Pillet, S.; Codjovi, E.; Boukheddaden, K.; Daku, L. M. L. Unidirectional Photoisomerization of Styrylpyridine for Switching the Magnetic Behavior of an Iron(II) Complex: A MLCT Pathway in Crystalline Solids. *J. Phys. Chem. C* **2010**, *114*, 21715–21722.

43 Hasegawa, Y.; Takahashi, K.; Kume, S.; Nishihara, H. Complete Solid State Photoisomerization of Bis(dipyrazolylstyrylpyridine)iron(II) to Change Magnetic Properties. *Chem. Commun.* **2011**, *47*, 6846–6848.

44 Meded, V.; Bagrets, A.; Fink, K.; Chandrasekar, R.; Ruben, M.; Evers, F.; Bernand-Mantel, A.; Seldenthuis, J. S.; Beukman, A.; van der Zant, H. S. J. Electrical Control over the Fe (II) Spin Crossover in a Single Molecule: Theory and Experiment. *Phys. Rev. B* **2011**, *83*, 245415.

45 Rösner, B.; Milek, M.; Witt, A.; Gobaut, B.; Torelli, P.; Fink, R. H.; Khusniyarov, M. M.; Reversible Photoswitching of a Spin-Crossover Molecular Complex in the Solid State at Room Temperature. *Angew. Chem. Int. Ed.*, **2015**, *54*,12976–12980.

46 Verma, P.; Weir, J.; Mirica, L.; Stack, T. D. Tale of a Twist: Magnetic and Optical Switching in Copper(II) Semiquinone Complexes. *Inorg. Chem.*, **2011**, *50*, 9816–9825.

47 Witt, A.; Heinemann, F. W.; Khusniyarov, M. M. Bidirectional Photoswitching of Magnetic Properties at Room Temperature: Ligand-Driven Light-Induced Valence Tautomerism. *Chem. Sci.* **2015**, *6*, 4599–4609.

48 Paquette, M. M.; Plaul, D.; Kurimoto, A.; Patrick, B. O.; Frank, N. L. Opto-Spintronics: Photoisomerization-Induced Spin State Switching at 300 K in Photochrome Cobalt–Dioxolene Thin Films. *J. Am. Chem. Soc.* **2018**, *140*, 14990–15000.

49 Urtizberea, A.; Roubeau, O. Switchable Slow Relaxation of Magnetization in the Native Low Temperature Phase of a Cooperative Spin-Crossover Compound. *Chem. Sci.* **2017**, *8*, 2290–2295.

50 Cui, H.-H.; Wang, J.; Chen, X.-T.; Xue, Z.-L. Slow Magnetic Relaxation in Five-Coordinate Spin-Crossover Cobalt(II) Complexes *Chem. Commun.* **2017**, *53*, 9304–9307.

51 Chen, L.; Song, J.; Zhao, W.; Yi, G.; Zhou, Z.; Yuan, A.; Song, Y.; Wang, Z.; Ouyang, Z.-W. A Mononuclear five-coordinate Co(II) Single Molecule Magnet with a Spin Crossover between the S = 1/2 and 3/2 States. *Dalton Trans.* **2018**, *47*, 16596–16602.

52 Xu, M.-X.; Liu, Z.; Dong, B.-W.; Cui, H.-H.; Wang, Y.-X.; Su, J.; Wang, Z.; Song, Y.; Chen, X.-T.; Jiang, S.-D.; Gao, S. Single-Crystal Study of a Low Spin Co(II) Molecular Qubit: Observation of Anisotropic Rabi Cycles. *Inorg. Chem.* **2019**, *58*, 2330–2335.

53 Shao, D.; Shi, L.; Yin, L.; Wang, B.-L.; Wang, A.-X.; Zhang, Y.-Q.; Wang, X.-Y. Reversible on–off Switching of both Spin Crossover and Single-Molecule Magnet Behaviours via a Crystal-to-Crystal Transformation. *Chem. Sci.* **2018**, *9*, 7986–7991.

54 Kobayashi, F.; Komatsumaru, Y.; Akiyoshi, R.; Nakamura, M.; Zhang, Y.; Lindoy, L. F.; Hayami, S. Water Molecule-Induced Reversible Magnetic Switching in a Bis-Terpyridine Cobalt(II) Complex Exhibiting Coexistence of Spin Crossover and Orbital Transition Behaviors. *Inorg. Chem.* **2020**, *59*, 16843–16852.

55 Rabelo, R.; Toma, L.; Moliner, N.; Julve, M.; Lloret, F.; Pasán, J.; Ruiz-Pérez, C.; Ruiz-García, R.; Cano, J. Electroswitching of the Single-Molecule Magnet Behaviour in an Octahedral Spin Crossover Cobalt(II) Complex with a Redox-Active Pyridinediimine Ligand. *Chem. Commun.* **2020**, *56*, 12242–12245.

56 Yang, J.; Hu, R.-X.; Zhang, M.-B. Construction of Monomers and Chains Assembled by 3d/4f Metals and 4′-(4-carboxyphenyl)-2,2′:6′,2″-terpyridine. *J. Solid State Chem.* **2012**, *196*, 398–403.

57 Nakamoto, K. *Infrared and Raman Spectra of Inorganic and Coordination Compounds*, Wiley, New York, 4th edn., 1986, p 232.

58 Hayami, S.; Komatsu, Y.; Shimizu, T.; Kamihata, H.; Lee, Y. H. Spin-Crossover in Cobalt (II) Compounds containing Terpyridine and its Derivatives. *Coord. Chem. Rev.*, **2011**, *255*, 1981–1990.

59 Slicher, C. P.; Drickamer, H. G. Pressure-Induced Electronic Changes in Compounds of Iron. *J. Chem. Phys.* **1972**, *56*, 2142–2160.

60 Steinegger, A.; Wolfbeis, O. S.; Borisov, S. M. Optical Sensing and Imaging of pH Values: Spectroscopies, Materials, and Applications. *Chem. Rev.* **2020**, *120*, 12357–12489.

61 Chen, W.; Ma, X.; Chen, H.; Liu, S. H.; Yin, J. Fluorescent Probes for pH and Alkali Metal Ions. *Coord. Chem. Rev.* **2021**, *427*, 213584.

62 Arana, C.; Yan, S.; Keshavarz, M.; Potts, K. T.; Abruna, H. D. Electrocatalytic Reduction of Carbon Dioxide with Iron, Cobalt, and Nickel Complexes of Terdentate Ligands. *Inorg. Chem.* **1992**, *31*, 3680–3682.

63 Ferreira, H.; Conradie, M. M.; Conradie, J.; Electrochemical and Electronic Properties of a Series of Substituted Polypyridine Ligands and their Co(II) Complexes. *Inorg. Chim. Acta* **2019**, *486*, 26–35.

64 Gans, P.; Sabatini, A.; Vacca, A. Investigation of equilibria in solution. Determination of equilibrium constants with the HYPERQUAD suite of programs. *Talanta* **1996**, *43*, 1739−1753.

65 Bruker. *SAINT*. Bruker AXS Inc., Madison, Wisconsin, USA, **2012**.

66 Sheldrick, G. M. SHELXT - Integrated Space-Group and Crystal-Structure Determination. *Acta Cryst.* **2015**, *A71*, 3–8.

67 Dolomanov, O.V., Bourhis, L.J., Gildea, R.J, Howard, J.A.K. & Puschmann, H. *J.* OLEX2: A Complete Structure Solution, Refinement and Analysis Program. *Appl. Cryst*. **2009**, *42*, 339–341.

68 *CrystalMaker*, CrystalMaker Software, Bicester, England, **2015**.

69 *Mercury*, The Cambridge Crystallographic Data Centre, Cambridge, UK.

Supporting Information

TABLE OF CONTENTS

General characterisation (Figures VI.S1 – VI.S3)

X-ray crystallographic data collection and structure refinement (Figures VI.S4 – VI.S8)

Static and dynamic magnetic measurements (Figures VI.S9 – VI.S14)

Spectrochemical measurements (Figure VI.S15)

Electrochemical measurements (Fig. VI.S16 and VI.S17)

General characterisation

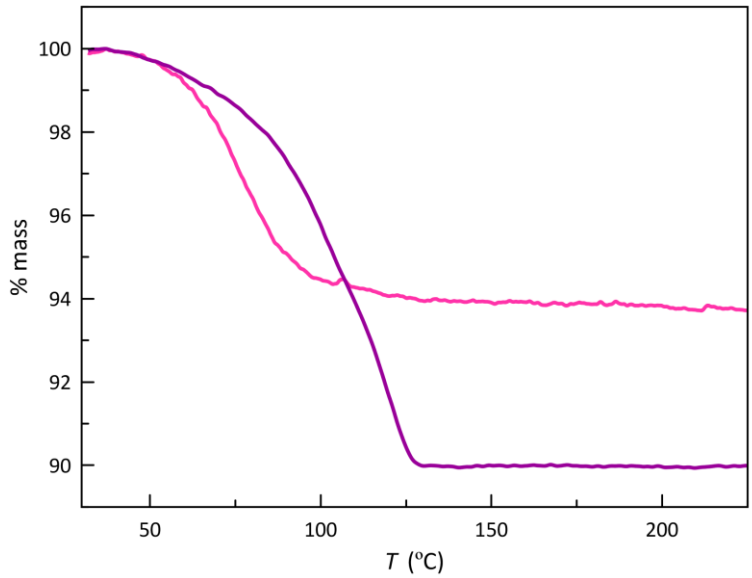

Figure VI.S1 TGA profiles for **1** (pink) and **2** (purple) under N_2 atmosphere.

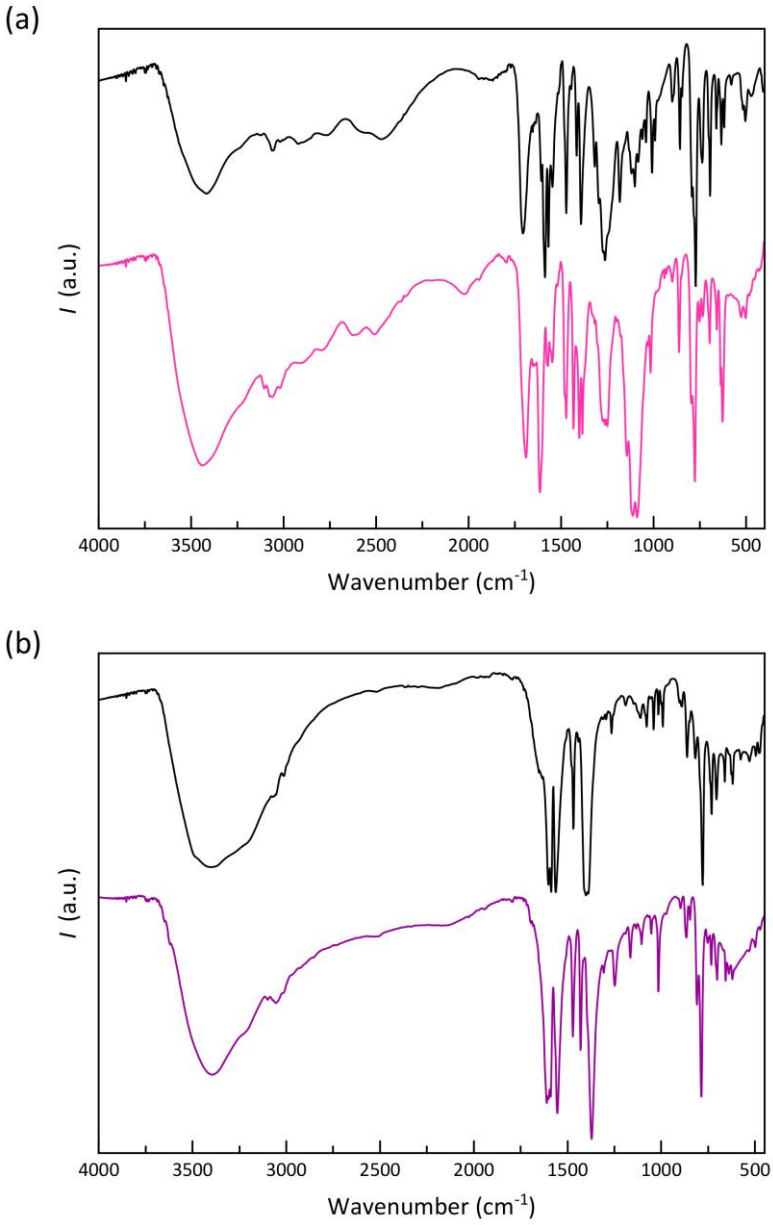

Figure VI.S2 FT-IR spectra of **1** in pink (a) and **2** in purple (b) compared to those of HL and NaL, respectively (black lines).

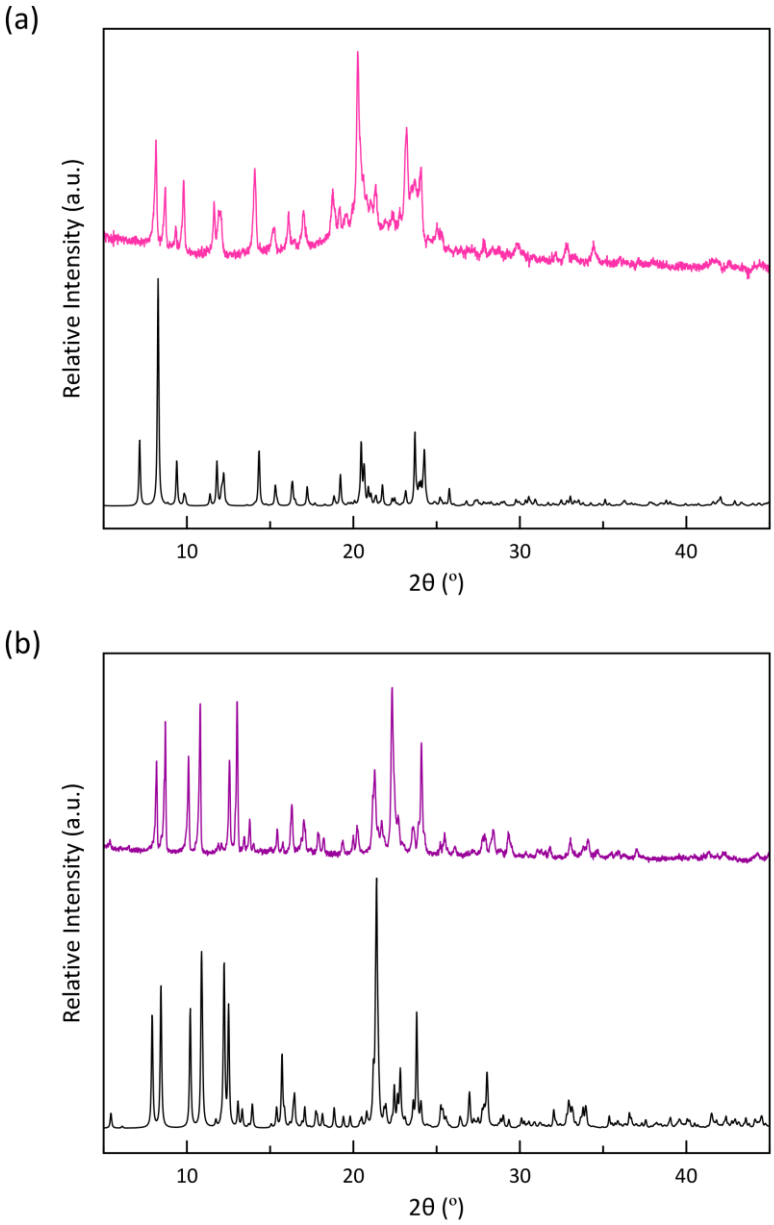

Figure VI.S3 Experimental PXRD pattern of **1** in pink (a) and **2** in purple (b) compared to the calculated ones (black lines).

X-ray crystallographic data collection and structure refinement

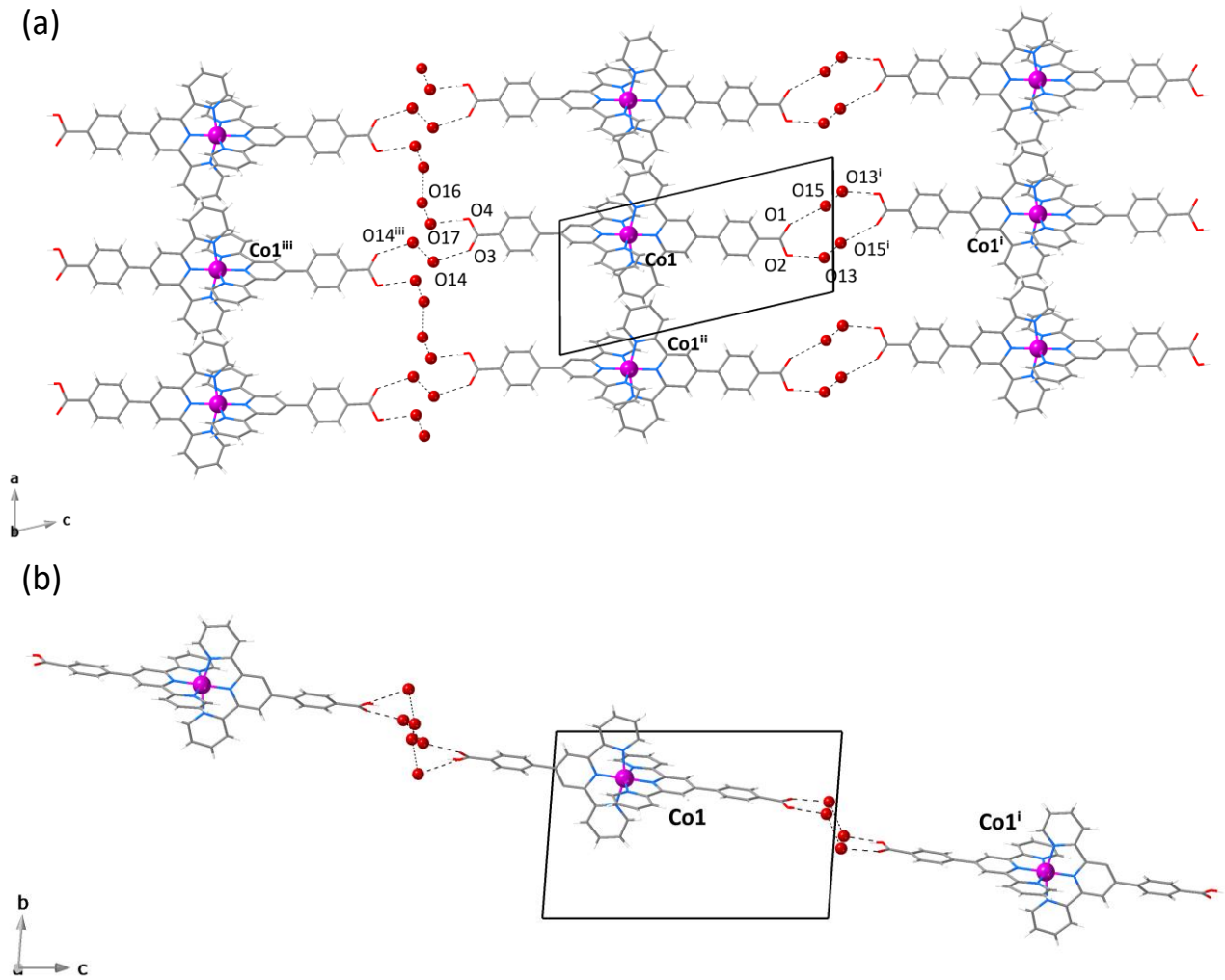

Figure VI.S4 (a) and (b) Views of a single layer of hydrogen-bonded cationic mononuclear cobalt(II) units of **1** along the crystallographic *a* and *c* axes respectively, with the atom numbering scheme for the hydrogen-bonded network of perchlorate anions and crystallisation water molecules [symmetry codes: (i) = –*x*, –*y*, –*z*; (ii) = –*x*, –*y*, –*z* – 1; (iii) = –*x*, –*y*, 3–*z*]. The hydrogen bonding interactions involving the perchlorate anions and the crystallisation water molecules are drawn as dotted lines.

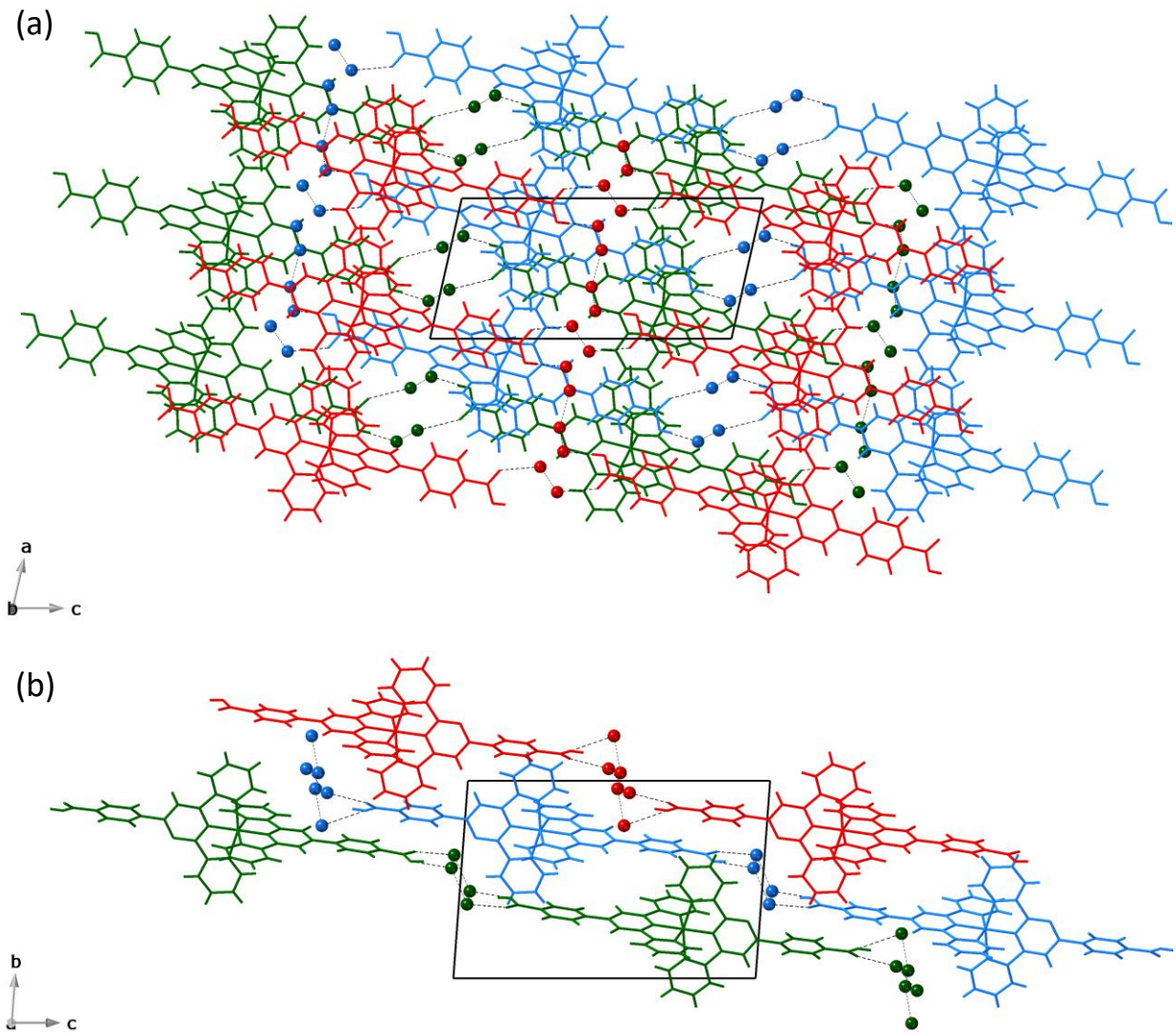

Figure VI.S5 Perspective views of the crystal packing of **1** along the *b* and *a* axes (a and b, respectively) showing the occupation with the crystallisation water molecules of the small channels built by the parallel array of cationic mononuclear cobalt(II) units.

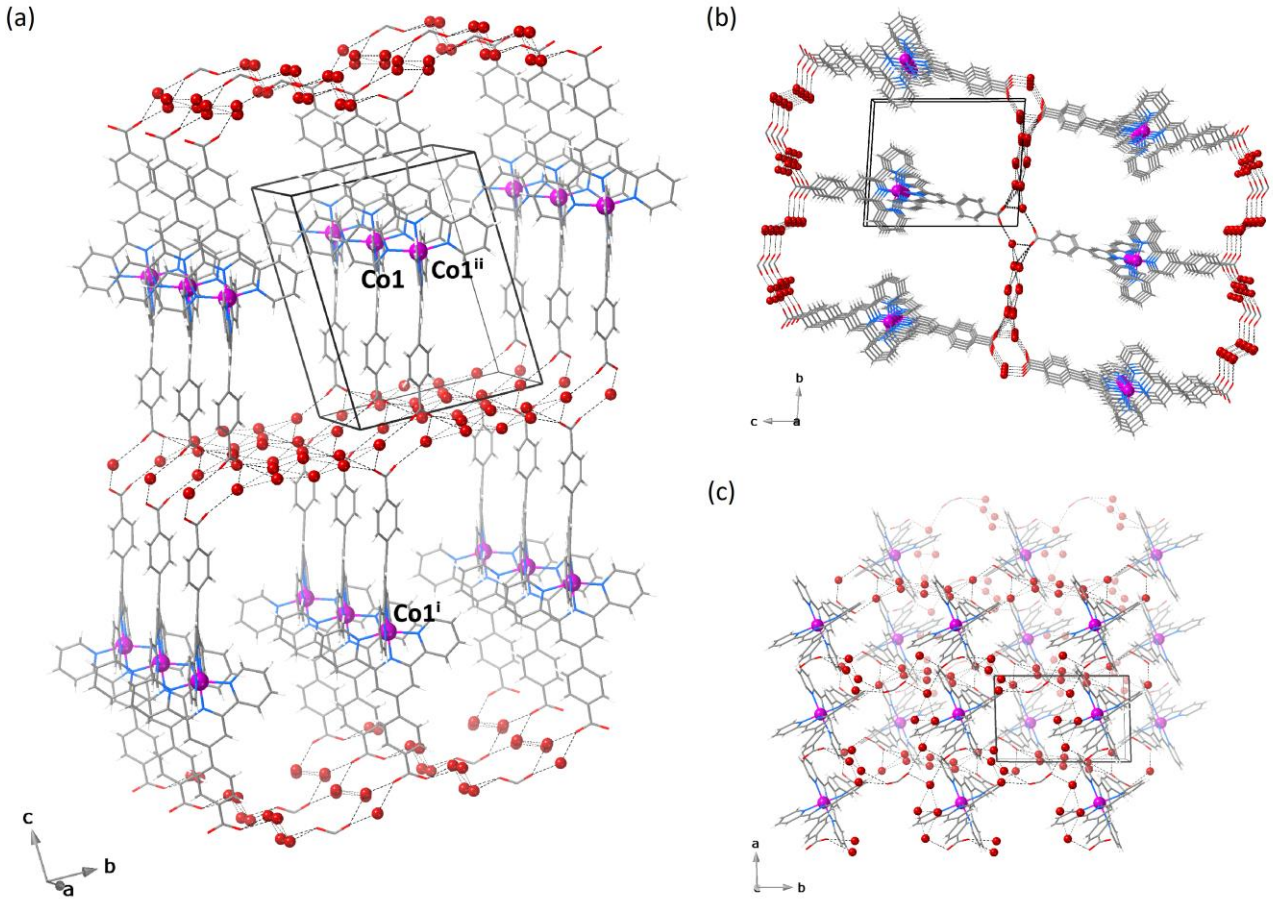

Figure VI.S6 (a) View of a single pillared layer 3D array of hydrogen-bonded neutral mononuclear cobalt(II) units of **2** with the atom numbering scheme for the hydrogen-bonded network of crystallisation water molecules [symmetry codes: (i) = *–x*, *–y*, *–z*; (ii) = *–x*, *–y*, *–z* – 1]. (b) and (c) Perspective views of a hydrogen-bonded pillared layer 3D array along the crystallographic *a* and *c* axes, respectively. The hydrogen bonding interactions involving the crystallisation water molecules are drawn as dotted lines.

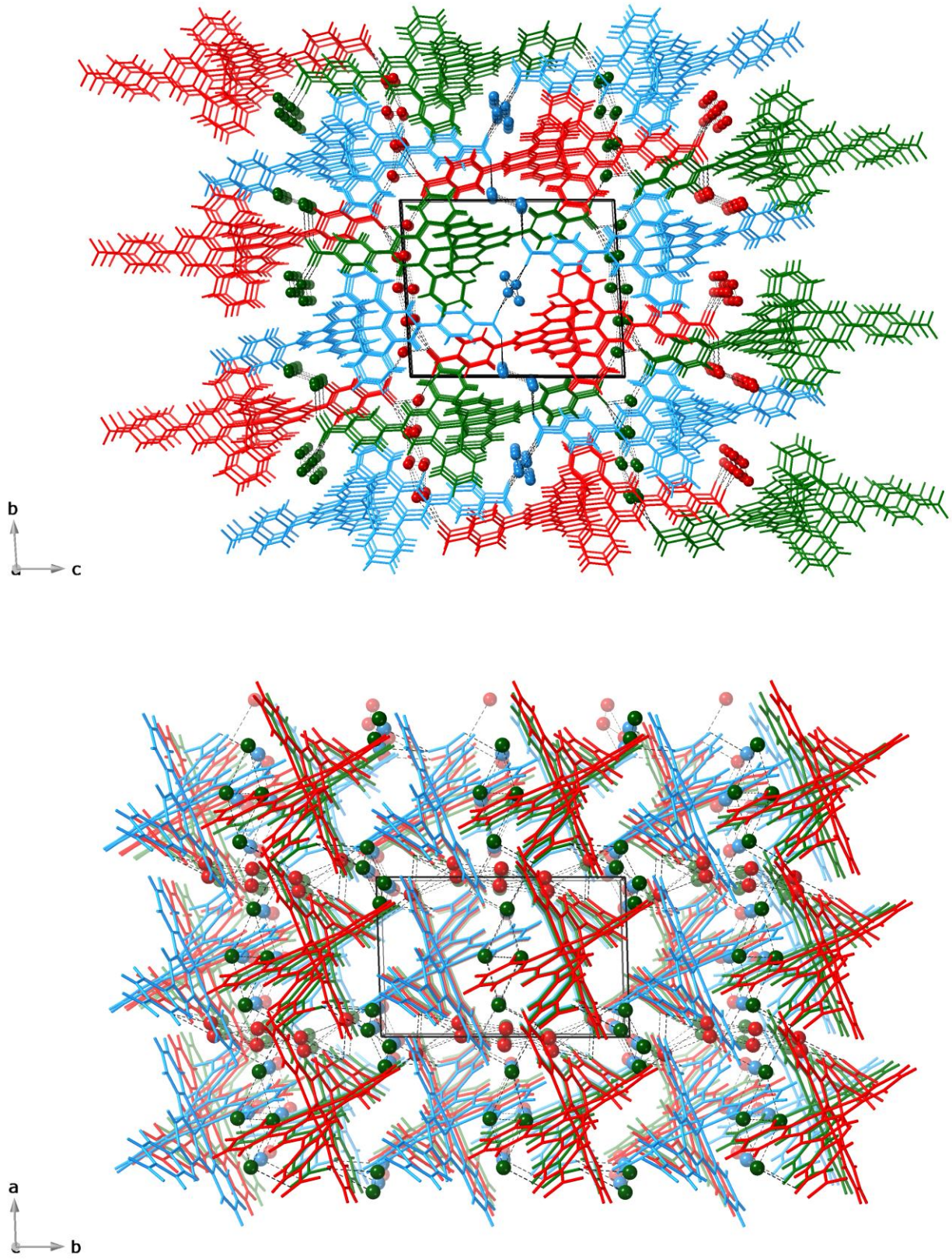

Figure VI.S7 Projection views of the triply interpenetrated 3D array of hydrogen-bonded neutral mononuclear cobalt(II) units of **2** along the crystallographic *a* and *c* axes (a and b, respectively). The hydrogen bonding interactions with the crystallisation water molecules are drawn as dotted lines.

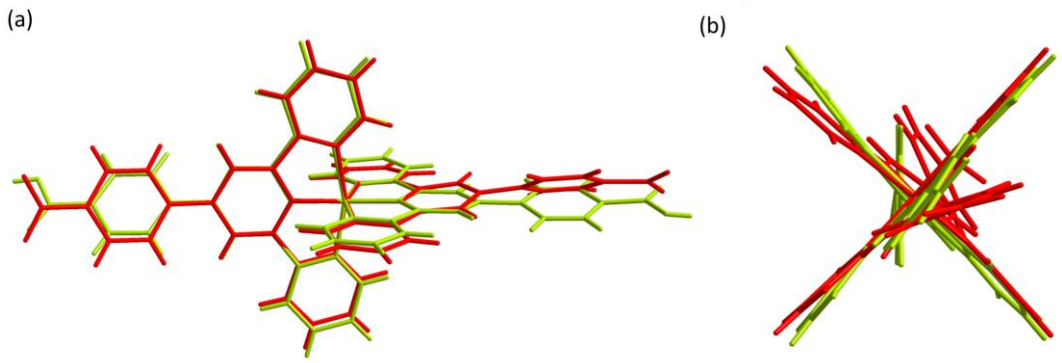

Figure VI.S8 (a) Front and (b) side superposition views of the cationic protonated and hemiprotonated (green) and neutral deprotonated (red) mononuclear cobalt(II) units of **1** and **2**. The ligand backbones are shown in green and red colours, respectively.

Static and dynamic magnetic properties

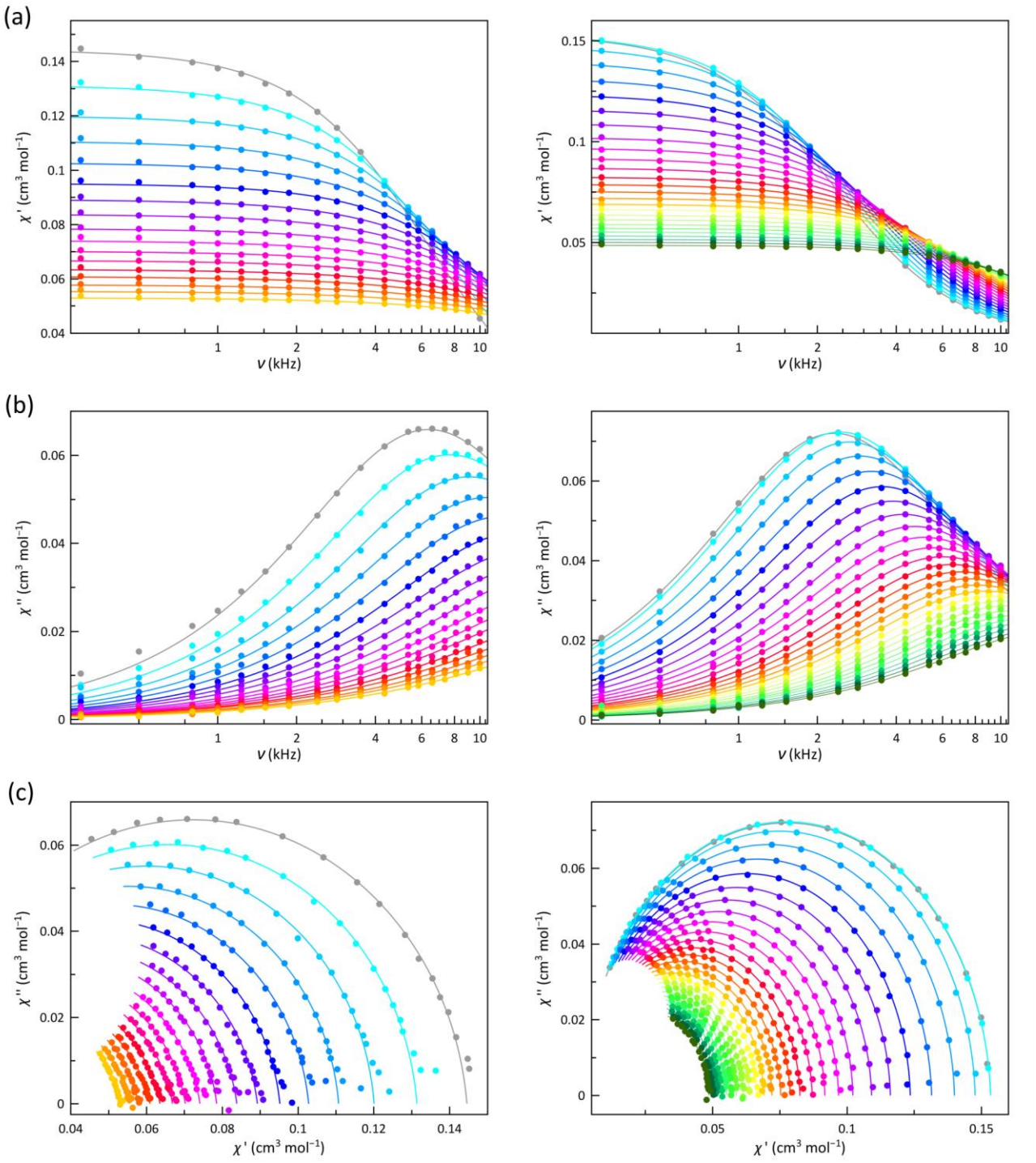

Figure VI.S9 Frequency dependence of χ_M' (a), χ_M'' (b), and the Argand plot (c) of **1** (left) and **2** (right) under static magnetic field of 2.5 KOe ±0.5 Oe oscillating field in the temperature range of 2.0–6.0 K and 2.0–8.5 K, respectively, in steps of 0.25 K (from grey to green). The solid lines are the best-fit curves simulated by using the values of χ_S, χ_T, τ and α shown in Figure S15.

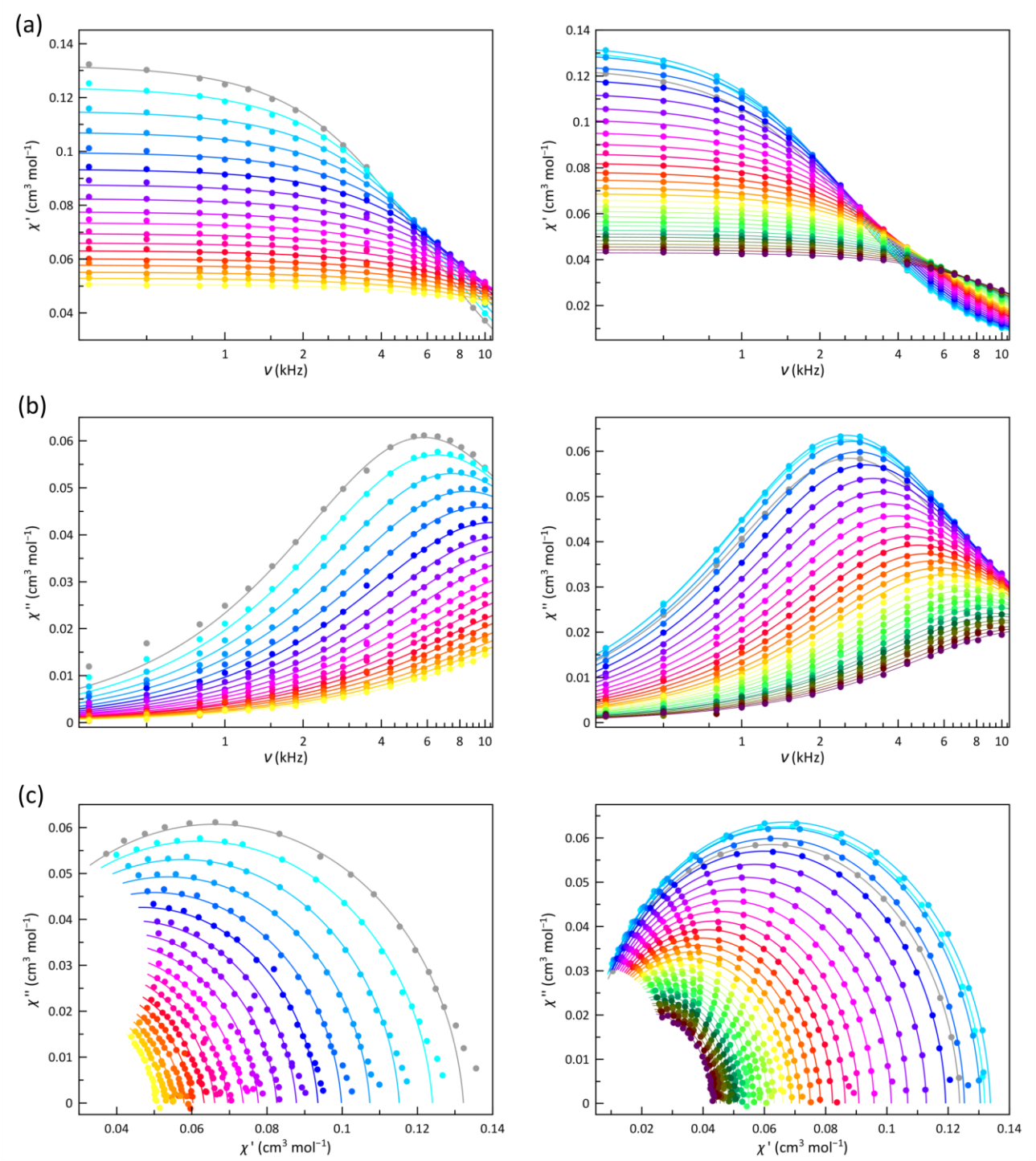

Figure VI.S10 Frequency dependence of χ_M' (a), χ_M'' (b), and the Argand plot (c) of **1** (left) and **2** (right) under static magnetic field of 3.5 KOe ±0.5 Oe oscillating field in the temperature range of 2.0–6.25 K and 2.0–9.5 K, respectively, in steps of 0.25 K (from grey to green). The solid lines are the best-fit curves simulated by using the values of χ_S, χ_T, τ and α shown in Figure S15.

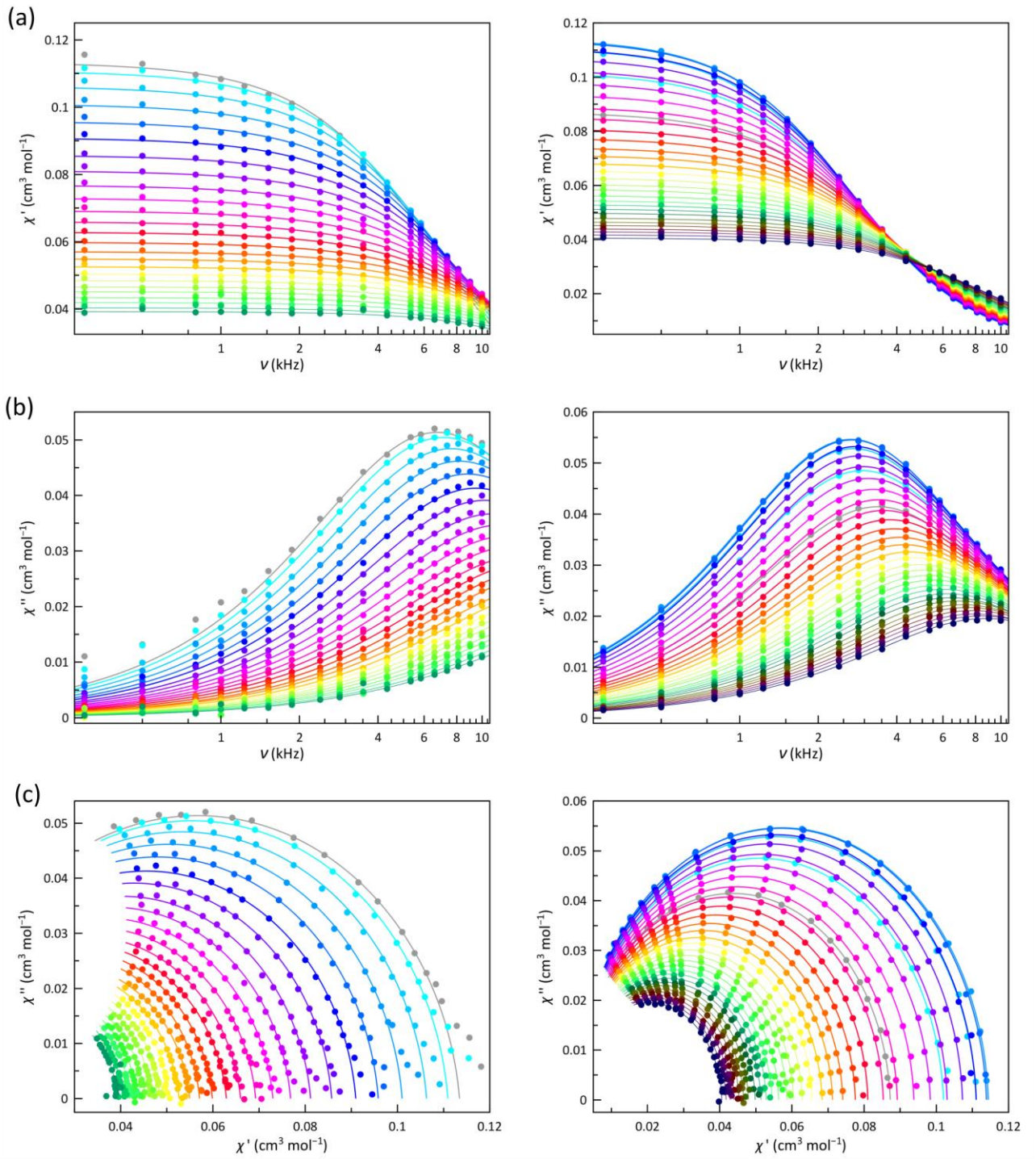

Figure VI.S11 Frequency dependence of χ_M' (a), χ_M'' (b), and the Argand plot (c) of **1** (left) and **2** (right) under static magnetic field of 5.0 KOe ±0.5 Oe oscillating field in the temperature range of 2.0–8.0 K and 2.0–10 K, respectively, in steps of 0.25 K (from grey to darker colours). The solid lines are the best-fit curves simulated by using the values of χ_S, χ_T, τ and α shown in Figure S15.

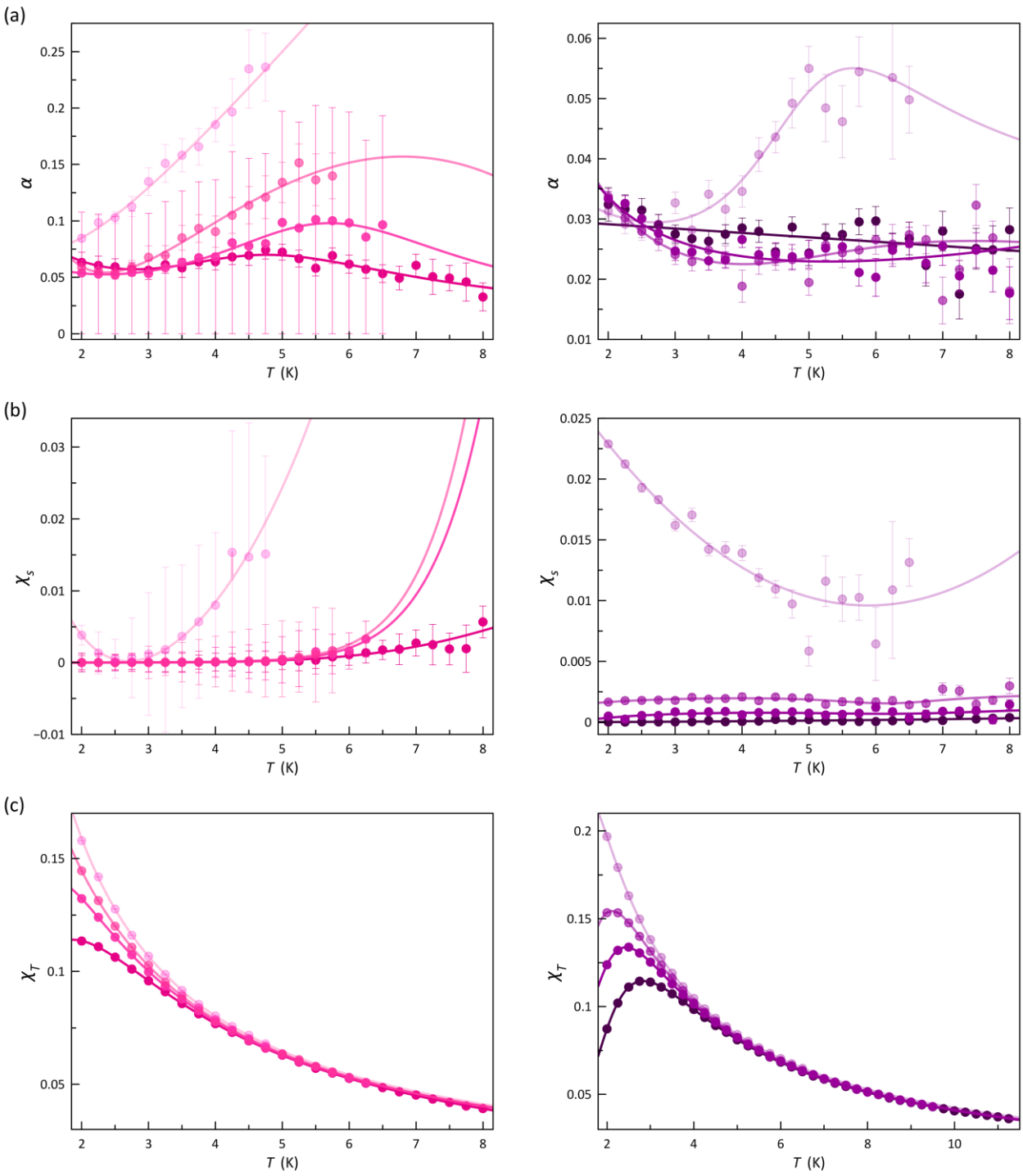

Figure VI.S12 Temperature dependence of α (a), χ_S (b), and χ_T (c) of **1** (left) and **2** (right) under applied *dc* magnetic fields of 1.0, 2.5, 3.5 and 5.0 kOe in solid state. The solid lines are only eye-guides. Standard deviations are given as vertical error bars.

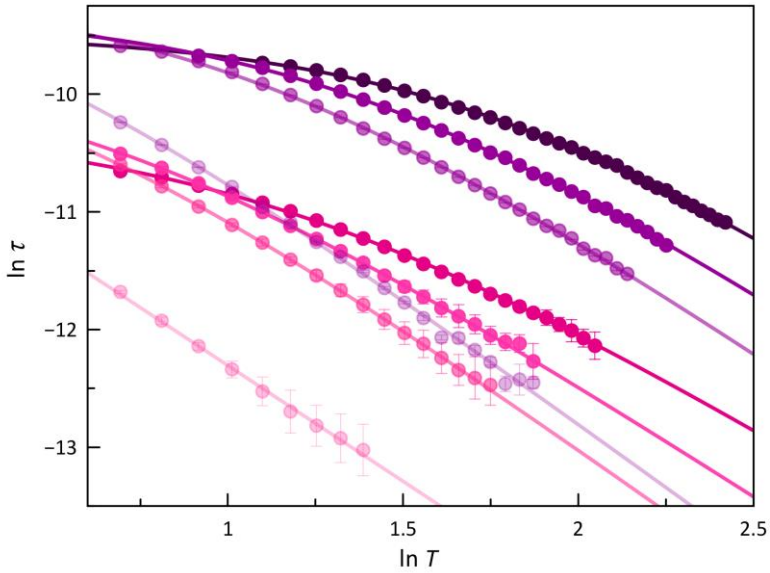

Figure VI.S13 ln τ *vs* ln T plots of **1** (pink) and **2** (purple) under applied *dc* magnetic fields of 1.0, 2.5, 3.5, and 5.0 kOe (light to deep green and red colours, respectively). The solid lines are the best-fit curves for a double Raman plus intra-Kramer (IK) relaxation mechanisms (see text). Vertical error bars denote the standard deviations.

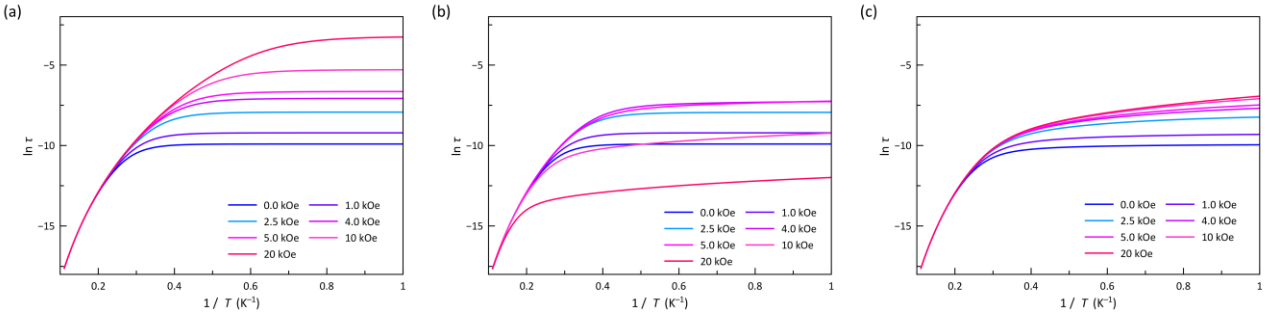

Figure V.S14. Magnetic field dependence of the Arrhenius plots generated from a model considering IK, direct, and Raman mechanisms, last one from optical and acoustic phonons [$\tau^{-1} = B_1/(1 + B_2H^2) + A_1H^4T + R_2T^2 + R_9T^9$]. In all simulations, B_1 = 20000 s^{-1}, B_2 = 1 kOe^{-2}, and R_9 = 1 $s^{-1}K^{-9}$.(a) IK plus acoustic Raman: A_1 = 0.0 $s^{-1}kOe^{-4}K^{-1}$ and R_2 = 0.0 $s^{-1}K^{-2}$; (b) IK plus acoustic Raman plus direct: A_1 = 1.0 $s^{-1}kOe^{-4}K^{-1}$ and R_2 = 0.0 $s^{-1}K^{-2}$; and (c) IK plus acoustic Raman plus optical Raman: A_1 = 0.0 $s^{-1}kOe^{-4}K^{-1}$ and R_2 = 1000.0 $s^{-1}K^{-2}$.

Spectrochemical measurements

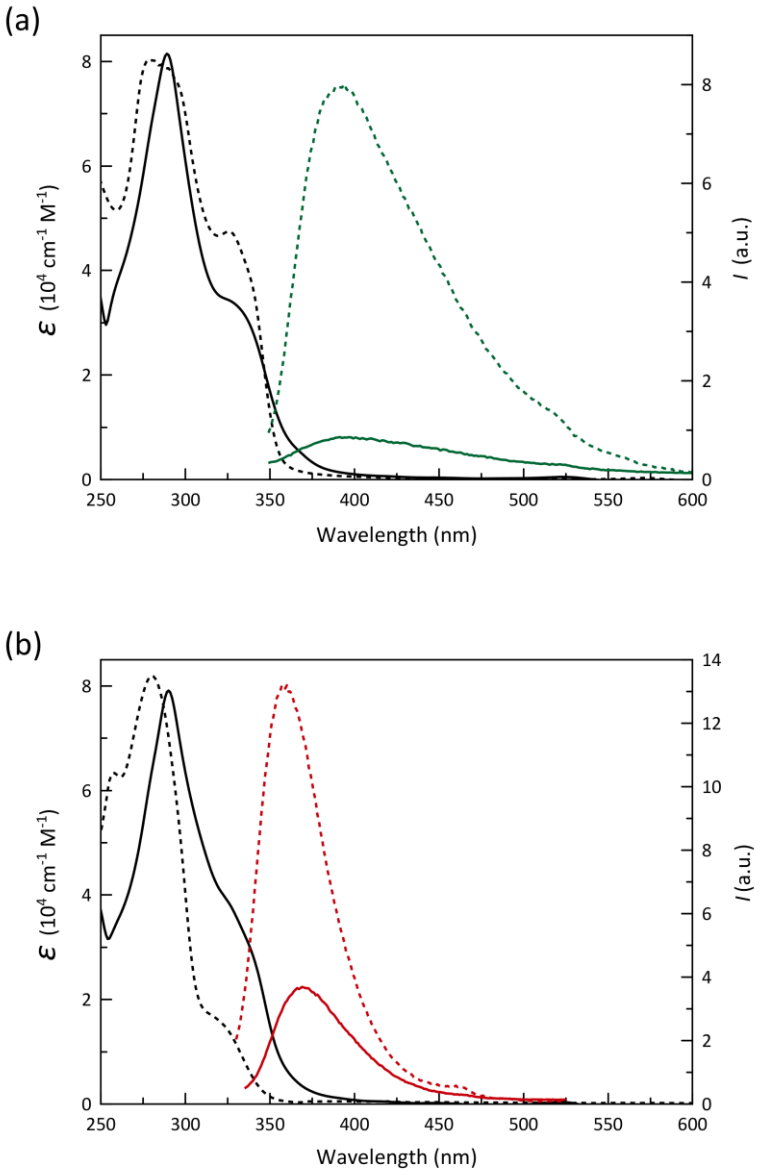

Figure VI.S15 (a) Electronic absorption (black) and emission (green/red) spectra (λ_{exc} = 295 nm) of 0.01 mM solution of **1** at pH ca. 3.0 (a) and 8.0 (b) at room temperature, compared to those of 0.01 mM solutions of the corresponding protonated and deprotonated forms of the ligand, respectively (dashed lines). See text.

Electrochemical measurements

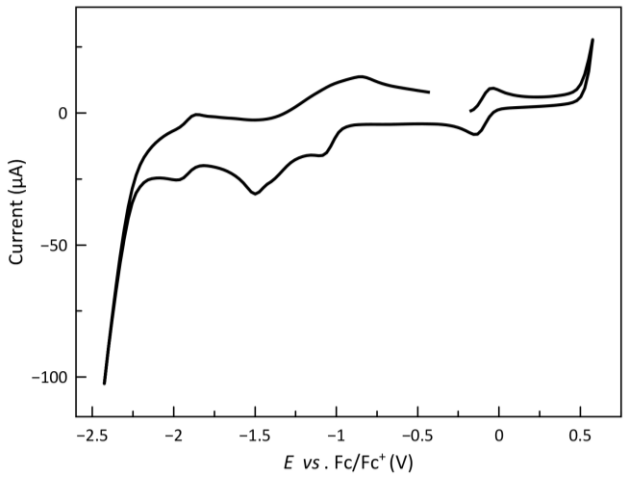

Figure VI.S16 Cyclic voltammograms of **2** in DMF [0.1 M (n-Bu$_4$)N PF$_6$] at 25 °C and 200 mV s^{-1}.

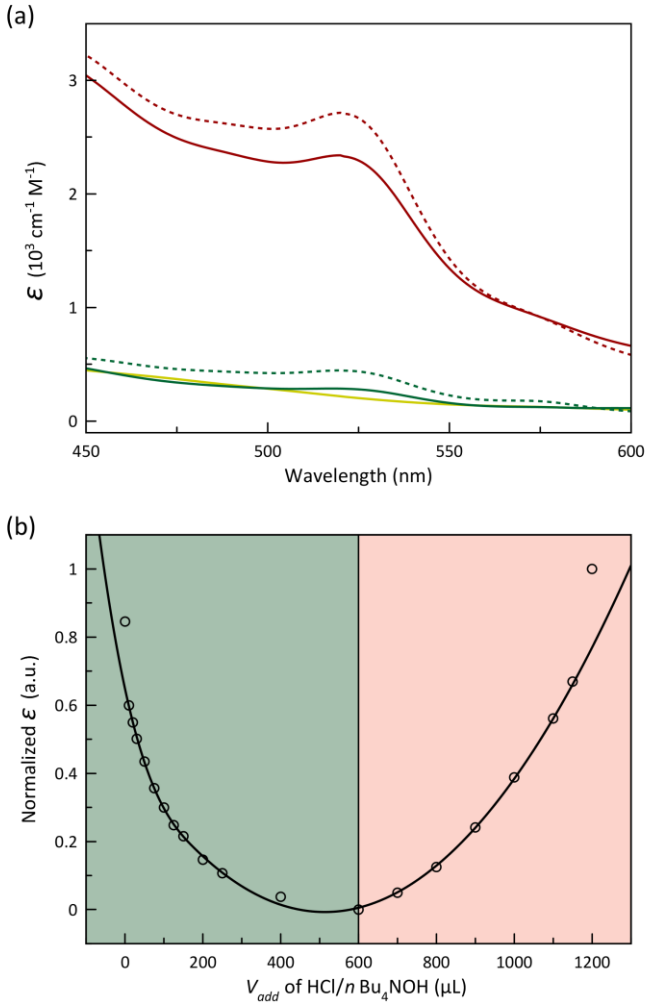

Figure VI.S17 (a) Electronic spectra of a solution of **1** in DMF [0.1 M n-Bu$_4$NPF$_6$] at 25 ºC and 200 mV s^{-1} in both acidic (green lines) and basic (red lines) and strong basic media (yellow line). The restoration of the molar absorptivity one cycle is represented in dashed lines (see text). (b) Normalized ΔI_p versus added volume of HCl (green region) or N(n-Bu)$_4$OH (red region). The solid black line is only an eye-guide (see text).

CHAPTER VII

CONCLUSIONS AND OUTLOOK

A Coordination Chemistry Approach from Molecular Magnetism and Molecular Spintronics towards Quantum Computing Nanotechnologies

"There is plenty of room at the bottom" – Respectfully, I would like to make my second free interpretation of Richard Feynman's most famous phrase, based on this selfish and unilateral sense of permission rights granted by and to me on the opportunity of this PhD Thesis. Obviously, the intention is not to undermine the original meaning of his priceless visionary thoughts that inspired and gave birth to so many fields of Molecular Sciences but to provide additional insights that this sentence triggers in me.

Undoubtedly, Molecular Sciences have travelled a long way, and their outstanding and remarkable advances brought us to the sense of awareness we experience nowadays. It is also a common agreement that Nanoscience and Nanotechnology have only explored the tip of the iceberg. These fields are so competitive and move on so quickly that there is a natural tendency to focus only on the major and recent results, the "top of the tip". While focusing on the top, many results remain neglected due to being reported "too early". Thus, the lack of knowledge and precise techniques at the reported date backfired as a whole batch of results lost in scientific oblivion, what I call "the bottom". They are still waiting for new enthusiastic scientists who will recognise their value and conceive a proper makeover for them in the light of the current comprehension and leading-edge machinery. It means that there is plenty of room at the bottom.

We thus realised that a new multifunctional system should not always arise from developing novel properties. Looking into "the bottom", new materials may instead be created from reasoned and innovative designs that allow putting together several well-known properties, establishing synergy between them. In this PhD Thesis, we followed the simple (but not effortless) idea of using two $Co^{II}N_6$ platforms with 2,2':6',2''-terpyridine (TERPY) and related pyridine-2,6-diimine (PDI) ligands known for decades to successfully create a new chemical library of Spin Crossover Molecular Nanomagnets. Their multifunctional and multiresponsive character, chemical modulation and switchable behaviour regarding both spin crossover (SCO) and single-molecule magnet (SMM) phenomena illustrate the full potential of this new class of dynamic molecular systems (DMS).

"Every adventure requires a first step". Trite but true, even and especially for science. The results presented in the past five chapters of this PhD Thesis also represent the first steps of our research group along the line of multifunctional and multiresponsive magnetic devices based on spin crossover molecular nanomagnets (SCO/SMMs) in the emerging fields of Molecular Spintronics (MS) and Quantum Information Processing (QIP).[1]

Spin Crossover Cobalt(II) Molecular Nanomagnets as DMS in MM and MS

For a long time, Molecular Magnetism (MM) has travelled on the route of the chemical approach of Coordination Chemistry to dig up and construct the current understanding of magnetic phenomena that occur in the molecular and quantum scales. From the pioneering studies on SCO and related valence tautomerism until the more recent ones on spin dynamics and quantum coherence of molecular nanomagnets, the old but evergreen field of Coordination Chemistry has offered the complete toolkit to take MM wherever it needs to go and beyond.[1]

Although MM's journey pursuing these topics has travelled far, the limitless capability of Coordination Chemistry makes them an ongoing relevant topic in the field. There are still unclarified exciting physical aspects of mononuclear SCO and SMMs, and that is why these systems are still a matter of debate. That being so, the magneto-structural data of the mononuclear cobalt(II) SCO/SMM compounds reported herein are of immense interest in the field. However, putting both behaviours together in new multistable DMSs in the way we did can be considered our entrance into the intercrossing area of MM and MS.

Our cobalt(II) complexes with TERPY and related PDI derivatives constitute a common class of **SCO systems exhibiting gradual HS ↔ LS transitions**. However, the observation of cooperative effects in the solid state is scarce and constitutes the main reason these compounds have been less investigated in searching for new multifunctional and multiresponsive materials. Our strategy focused on different facets of the SCO phenomenon by studying the influence of (i) ligand substituents (Chapters II, III and IV), (ii) crystallisation solvent molecules (Chapter IV), (iii) counteranions (Chapter V), (iv) ligand conformation (Chapter V) and (iv) ligand protonation degree (Chapter VI). This systematic and comprehensive investigation has provided deep insights into accomplishing multiple SCO behaviours even without abrupt spin state transitions in these two TERPY and PDI series of cobalt(II) complexes.

Following this approach, we conclude that Co^{II}-PDI complexes are excellent platforms for SCO modulation due to their easy handling and quite simple synthetic character. These features allowed us to prepare a vast chemical library varying the ligand substituent to obtain, in each family, examples of pure HS and LS phases as well as intermediate situations that undergo an incomplete gradual SCO, with either one-third HS and two-thirds LS fractions or vice versa at low temperature (Chapters II, III and IV). On the other hand, our Co^{II}-TERPY complexes gave mainly LS phases below 150 K, presenting HS fractions at room temperature (Chapters V and VI). Furthermore, our results suggest that the ligand design chemical approach can be a valuable tool to achieve desired properties through the modulation of the SCO. For sure, more efforts should be driven

in searching for cooperative effects to give rise to complete, abrupt, and hysteretic spin transitions taking place at different temperature regions by playing with the extended aromatic nature of the substituents.

Although the **SMM behaviour with a field-induced blockage of the magnetisation** is widespread in HS Co^{II} (S = 3/2) SMMs, the reports on LS Co^{II} (S = 1/2) SMMs are scarce. In this PhD Thesis, we not only provide new magneto-structural data about slow magnetic relaxation in HS Co^{II} SMMs with both positive (D > 0) and negative (D < 0) magnetic anisotropy, but we have also enriched the exiguous literature on LS Co^{II} SMMs.

The magnetic relaxation dynamics of the Co^{II} ion were different between LS and HS electronic configurations. The LS Co^{II} SMMs are characterised by a strongly field-dependent faster magnetic relaxation (FMR) and very low blocking temperatures, which cause the predominance of incipient signals in χ_M'' at low fields and distinct maxima only at high fields. In contrast, the HS Co^{II} SMMs account for a field-induced slower magnetic relaxation (SMR) occurring at higher blocking temperatures, although almost independent of the applied dc magnetic field. This distinct spin dynamics are explained by the larger spin delocalisation on the HS form, polarising spin densities into neighbouring atoms, and even into some internal orbitals of the own metal ion. So, the spin reversal becomes more difficult and its rate is slowed down.

In the present PhD Thesis, we spread an accurate method of analysis of the frequency and magnetic field dependence of the spin relaxation dynamics in mononuclear HS and LS Co(II) SMMs. Moreover, our conclusions about the relaxation mechanisms slightly diverge from those reported in the literature. Herein we proposed for the first time the involvement of a temperature-independent (zero-order) intra-Kramer (IK) process at low temperatures, contributing to a new subject for discussion. We argue that the IK process is the most agreeing mechanism for spin reversal in this type of Co(II) system rather than a temperature-independent quantum tunnelling of magnetisation (QTM), which is inconsistent with the absence of an energy barrier separating the m_S states. Finally, to our knowledge, this is the first time that the slow magnetic relaxation effects have been observed in solution for LS Co(II) complexes, offering thus an alternative to solid dilution experiments to study the spin relaxation dynamics of a well-isolated single molecule. The occurrence of SMM behaviour in mononuclear octahedral HS cobalt(II) complexes with a m_S = ±3/2 Kramers doublet ground state (D > 0) precludes the existence of an energy barrier and eventually, the operation of an Orbach process in the spin relaxation mechanism. This fact is most noticeable in LS cobalt(II) complexes, which do not have any other excited Kramer doublet apart from the S = 1/2 ground state (m_S = ±1/2). However, even in our examples with negative anisotropy (D < 0) we demonstrate that the energy barrier for the magnetic relaxation is not consistent with the one arising from the zfs. Alternatively, the magnetic relaxation occurs most likely via Raman mechanisms assisted by both optical and acoustic phonons acting predominantly at the low- and high-temperature regions, respectively.

Looking at the proposed ligand design of this new class of SCO/SMM compounds, so-called spin crossover molecular nanomagnets, our intuition dictates the primary goal of creating a system where SCO and SMM behaviours operate in the same temperature region, establishing the synergy between these two bistabilities. As already explained, that is not an easy task given the relatively low blocking temperatures currently found for both LS and HS Co(II) SMMs (T_b < 10 K) and the LS ↔ HS transition cannot occur at such low temperatures. One ingineous possibility to overcome this paradox is by achieving the LS-to-HS switch via light-induced excited spin-state trapping (LIESST and reverse LIESST). Unfortunately, our attempts to switch our SCO/SMM compounds upon light irradiation with available red and green light (808 and 515 nm), both in the solid state and in solution, were unsuccessful. This feature is most likely due to the lifetimes of the photo-generated metastable states were not sufficiently large.

Again, these were only the first steps. The systems reported herein broaden the still preliminary and meagre list of spin-crossover molecular nanomagnets. Indeed, more examples are needed to elucidate raised questions about the dynamics of the spin transition and slow magnetic relaxation. Also, more efforts should be devoted to increasing the blocking temperature of the magnetisation and achieving cooperative effects responsible for abrupt HS ↔ LS transitions with magnetic hysteresis in cobalt(II) SCO/SMM compounds. Moreover, innovative ligand designing will turn both magnetic bistabilities operative in the same temperature region, making the states reversibly accessible through chemical (pH or analyte) or physical (magnetic and electric field, electrical current or light irradiation) stimuli. This way, potent multifunctional and multiresponsive DMS materials may arise in the near future from the results provided by this PhD Thesis on cobalt(II) SCO/SMM compounds.

To keep going farther on the road from MM to MS, the travelled way led us to some new insightful outcomes that we would like to present in the following. These ideas can indeed supply crucial information to bulk up the consolidated field of MM and provide alternative routes in the emerging field of MS. Hence, the unusual combination of chemical (redox and Brønsted or Lewis acidity) and physical (magnetic and optical or luminescent) properties resulting from the metal and the ligand counterpart in Co^{II}-PDI and TERPY complexes allows designing advanced multifunctional and multiresponsive magnetic materials for MS nanotechnology. In particular, they appear as promising candidates for spintronic nanodevices like spin capacitors and switches, as illustrated in Figure VII.1.

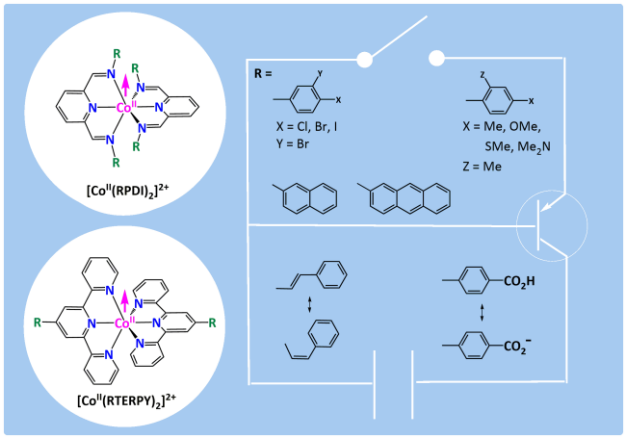

Figure VII.1 Illustrative representation of the potential of spin crossover cobalt(II) molecular nanomagnets for building active components in highly integrated spintronic circuits for MS.

Cobalt(II) SCO/SMMs as molecular spin capacitors or supercapacitors. Transition metal complexes containing non-innocent electroactive ligands have been extensively studied as single-molecule spintronic devices for charge storage applications.[2–4] The electrochemical access to multiple (up to four) ligand-based electron reductions and one metal-based oxidation makes electroactive Co^{II}-PDI complexes with electron acceptor halogen substituents (see Chapter II) promising candidates for molecular spin capacitors in charge storage and delivery in a spintronic circuit. Moreover, the high degree of reversibility ensures countless charging and discharging cycles without compromising efficiency.

Going one step further on this line, we will encounter the supercapacitor concept. It applies to molecules storing energy and executing rapid and stable faradaic processes (like charge/discharge cycles) to deliver high amounts of charge during a circuit operation.[5,6] Current efforts have been devoted to studying the anthraquinone-substituted Co^{II}-PDI complex as molecular spin supercapacitors (Figure VII.2). Anthraquinone derivatives are well-recognised for their π-acceptor character and redox chemistry, comprising the quinone, semiquinone radical and quinolate forms (Figure VII.2a).[7,8] Those anthraquinone moieties can then act as efficient multielectron reservoirs to develop a new class of charge storage spintronic devices: the molecular spin supercapacitors. When attached to the PDI ligand, they may provide an additional reduction capacity of two electrons per anthraquinone group, which means up to twelve ligand-based electron reductions at the Co^{II}-PDI complex (Figure VII.2b).

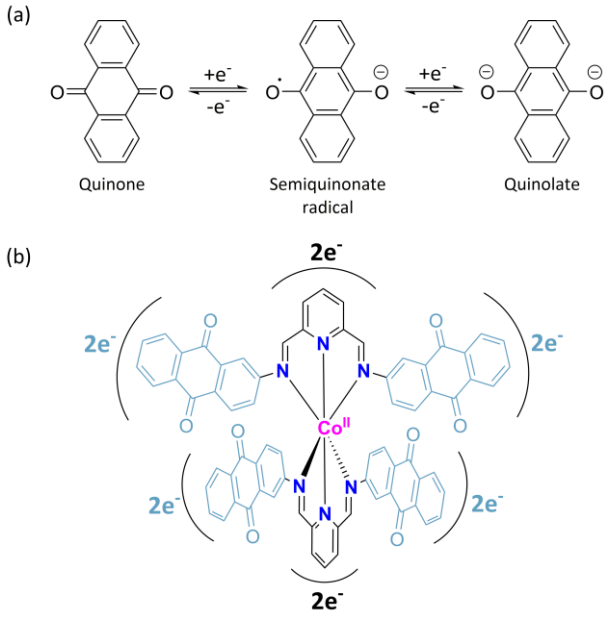

Figure VII.2 (a) Redox equilibria of anthraquinone derivatives in aprotic media. (b) Schematic illustration of the charge storage/delivery of the redox-active anthraquinone-substituted Co^{II}-PDI complex proposed as potential molecular spin supercapacitors.

Cobalt(II) SCO/SMMs as molecular spin electro-, chemo- or photo-switches. Molecular switches are essential components in any highly integrated molecular spintronic circuit, being responsible for allowing and interrupting electron transport through the molecule by altering the molecular electronic state. Aware of this need, in this PhD thesis we presented the design of molecular switches whose spin state (LS or HS) and spin dynamics (FMR or SMR) can be triggered through electrochemical, chemical or photonic events, referred to as molecular spin electro-, photo- or chemo-switches.

The ON-OFF electro-switching behaviour exemplified by the detailed study on the metal-based one-electron reversible oxidation of the electron donor methoxy-substituted Co^{II}-PDI complex (see Chapter III) demonstrates how these cobalt(II) SCO/SMMs can work as molecular spin electro-switches at room temperature. The passage from the paramagnetic LS Co^{II} ion (S = 1/2, ON) to the diamagnetic LS Co^{III} ion (S = 0, OFF) and vice versa can be accessed through either chemical or electrochemical redox inputs.[9]

The second design of a molecular spin switch is based on the chemo-switching found in the benzoic/benzoate-substituted Co^{II}-TERPY complexes (see Chapter VI). We demonstrated how a single input (proton) could switch a single molecule's redox, luminescent and spin dynamics without virtually altering the SCO properties. The dynamic equilibrium involving the protonated and deprotonated forms illustrates well the great potential of this advanced new class of multiresponsive pH-switches.

The photo control of the magnetic properties constitutes a capital challenge in MS. The inclusion of photoactive styryl substituents in the Co^{II}-TERPY complex allowed us to explore an innovative design of molecular switches centred on the well-known *cis-trans* (*Z-E*) photoisomerisation reaction of styrene derivatives and the duality of the magnetic relaxation dynamics of the Co^{II} ion depending on its electronic configuration (Figure VII.3). The LS OFF and the HS ON states are a consequence of the changes in the ligand field strength caused by the different aromaticity associated with planar *E* or non-planar *Z* conformations.[10] Unfortunately, the available experimental methods could not prove the efficiency of this switch and no variation between the LS and HS population was detected upon

UV and Vis light irradiation, neither in solution nor in the solid state (see Chapter V). Current efforts are devoted to further exploring this alternative ligand-driven, light-induced spin change (LD-LISC) route on the photoactive azobenzene-substituted Co^{II}-TERPY complex.

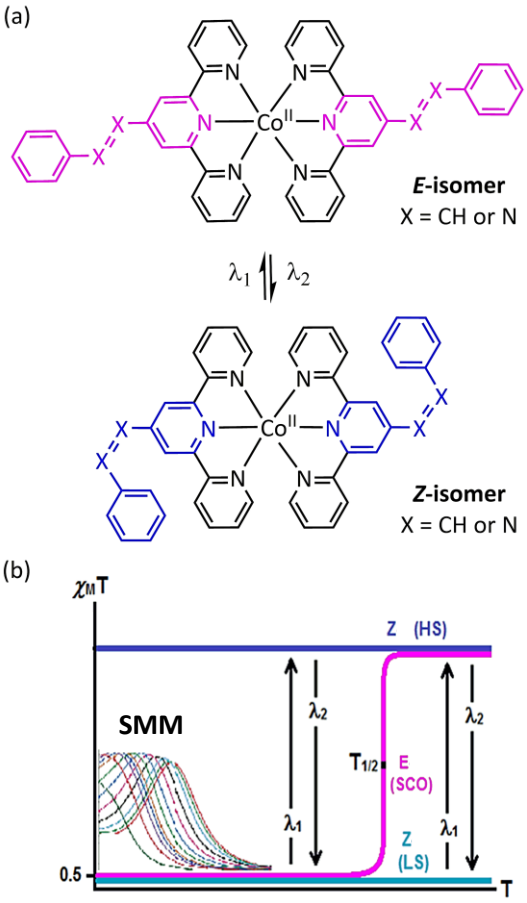

Figure VII.3 (a) Photoisomerisation *cis-trans* (*Z*-*E*) equilibria of styryl- and azobenzene-substituted Co^{II}-PDI complexes under UV and Vis light irradiation. (b) Schematic illustration of their potentiality as a new class of molecular spin photo-switches.

Cobalt(II) SCO/SMMs as electro-, chemo- or photo-switchable molecular spin machines. We could not help but notice the similarities between our Co^{II}-PDI complexes and the precursors of the classical [2]catenane molecular machines. Both count with perpendicular coordinating groups (PDI for us) with reactive spots allowing the double-cyclisation reaction.

The less risky strategy to synthesise [2]catenanes starts with the pre-synthesised macrocycle before the template reaction. Then, by mixing the macrocycle, the Co^{II} ion and the open-ligand fragment in a 1:1:1 ratio, the only possible complex formed is the desired intermediated one. The final step is to convert the open-chain fragment into another macrocycle to lead the two interlocked rings.[11,12] In other words, from a macrocycle (link), a metal complex is formed to then close the second link.

At this point, different approaches might be targeted depending on the functionality selected for the potentially switchable molecular spin machine (Figure VII.4). The vast chemical versatility of this kind of potential switchable molecular spin system allows selecting its functionality, but different approaches might be targeted:

(i) Metal-based electro-switch using mixed TERPY and PDI macrocycles to unite both platforms of SCO/SMM Co(II) complexes explored in this PhD Thesis. Hopefully, the interplay might be triggered by either chemical or electrochemical metal oxidation, causing a sliding motion to match the further stabilisation conferred to the Co^{III} ion in the TERPY coordination environment.

(ii) Ligand-based chemo-switch using a polyether-functionalised TERPY/PDI macrocycle which may interact with the alkali cations Na^{I} and K^{I}, causing a sliding motion of the catenane and the consequent release of the coordinated Co^{II} ion (Figure VII.4b). This feature can make this type of catenanes work as molecular playgrounds for Na^{+}/K^{+} and Co^{II}. In the presence of Co^{II}, both SCO/SMM are in the ON state, whereas high concentrations of the alkali metals switch the behaviours to the OFF state.

(iii) Ligand-based photo-switch using photoactive vinyl-functionalised TERPY/PDI macrocycles. The photocontrol of the catenane relies on the *cis-trans* photoisomerisation of the double bond in each ring. Even subtle structural and electronic changes are expected to cause substantial variations in the ligand field strength that would switch the SCO and SMM behaviours of the catenane-type cobalt(II) complex.

This innovative design may open up the path to a new class of mechanically-bonded, catenane-type Co^{II} SCO/SMM as unique examples of dynamic molecular systems with multiple switchable properties triggered by an internal molecular motion.

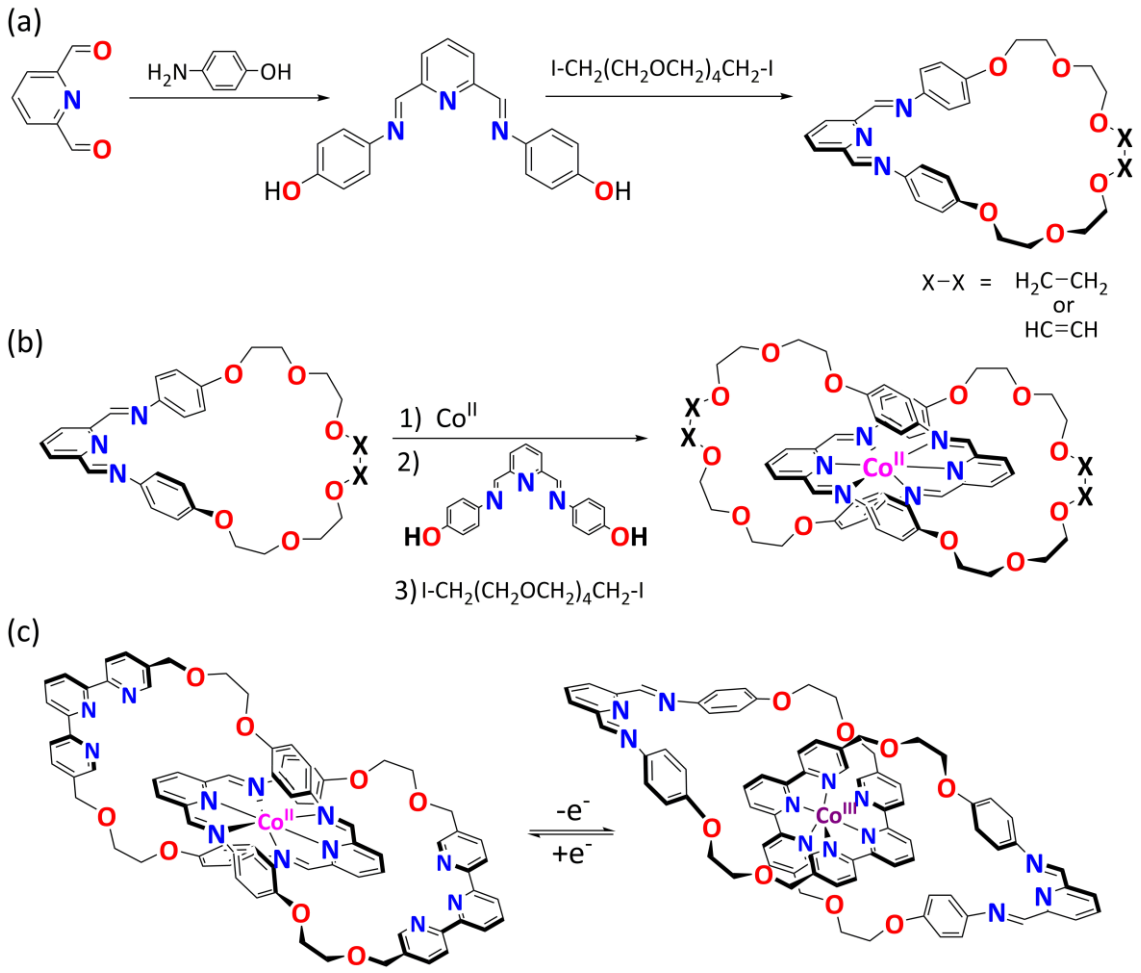

Figure VII.4 Proposed synthetic routes for (a) functionalised PDI macrocyclic and (b) catenane-type Co(II)-PDI SCO/SMM complexes through metal-directed template and double-cyclisation reactions leading to chemo- and photo-switchable molecular spin machines. (c) Electrochemically triggered sliding motion on mixed TERPY and PDI catenane-type Co(II) SCO/SMM.

Addressing of Spin Crossover Cobalt(II) Molecular Nanomagnets as Molecular Spin Nanodevices for MS

The expectation for using this novel class of SCO cobalt(II) molecular nanomagnets in information data storage and processing are associated with the possibility of building spintronic devices where these molecules are uniformly organised over different supports while preserving their singular magnetic behaviour.

The current challenge along this latter avenue of MS is the further addressing of these individual magnetic molecules to study their **spin-dependent electron transport properties** when integrated into real molecular junctions. There are basically three ways to address molecules for electron transport: (i) placing the molecules between two electrodes and measuring the conductance in the device, (ii) depositing the molecules on surfaces and using the tip of a scanning tunnelling microscope (STM) as a lead to measure the electron transport properties across the individual molecule, and (iii) integrating the molecules in quantum dots or anchoring them to carbon-based nanostructures like carbon nanotubes (CNT) or nanographenes (NG) through supramolecular interactions, using molecules for their spin, while electron transport occurs through the quantum dot or the carbon nanostructure. Promising prototypes of spintronic devices based on either SCO or SMM molecules have arisen following these three strategies (see Boxes A and B in Chapter I).

Because of their nanometer size and how easily they can be handled, the Co^{II} SCO/SMM compounds that constitute the leitmotif of this PhD Thesis appear as suitable candidates for the study of the spin dependence of the electron transport through single molecules, envisaging a magnetic control of the electron transport. Let us briefly anticipate some of the expected results as spin transistors, filters or valves on single-molecule electron transport.

Cobalt(II) SCO/SMMs in gold molecular junctions as molecular spin transistors. Like in most of the transition metal-based mononuclear SMMs, the presence of a fast quantum tunnelling of magnetisation (QTM) or Intra-Kramer relaxation (IK) in our cobalt(II) SCO/SMMs in the absence of a *dc* magnetic field provides an alternative and very efficient relaxation mechanism that severely limits their use in high-density information storage devices. Otherwise, the dramatic variation

of the magnetic relaxation rate with increasing the external magnetic field found in most LS cobalt(II) SMMs could be exploited to develop a new class of magnetic field-effect (MFE) molecular spin transistors for applications in MS. In contrast to conventional electronic devices that are controlled by an electric field (see Box A in Chapter I), the electrical current flow, in such a case, would be governed by a magnetic field.

So, for instance, the thiomethylphenyl-substituted Co^{II}-PDI complex of formula $[Co^{II}(MeSPhPDI)_2]^{2-}$ (see Chapter III) is a very appealing candidate for the experimental observation of the MFE transistor-like behaviour because of the high affinity for gold electrodes through the sulphur atoms of the thiomethyl substituents. Two opposite thiomethyl substituents from one ligand would be connected to the source and drain electrodes setting the electron flux (Figure VII.5).

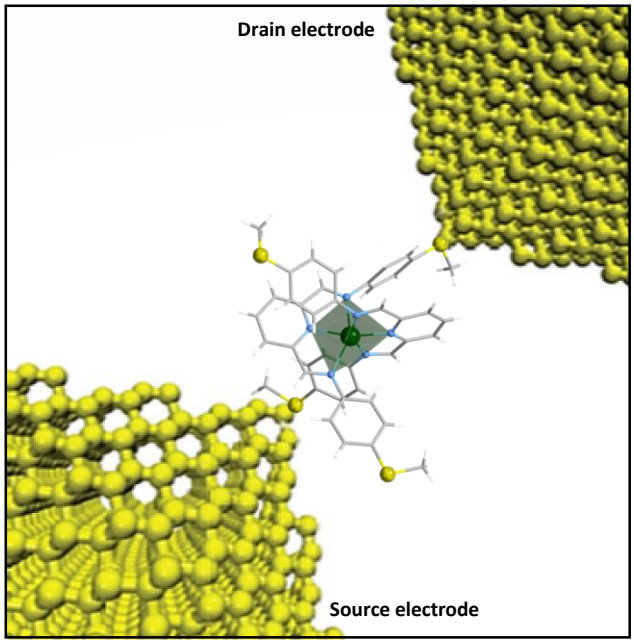

Figure VII.5 Illustration of the proposed molecular junction device constructed by the thiomethylphenyl-substituted cobalt(II) complex connecting two gold electrodes.

In fact, different electrical conductances can be presumed for the FMR and SMR LS Co^{II} ions, occurring in the absence or in the presence of an external magnetic field respectively, as reported earlier for the HS and LS Fe^{II} ions in the related mononuclear *trans*-bis(thiocyanate)iron(II) complexes of formula $[FeL_2(NCS)_2]$ [L = 3-(2-pyridyl)[1-3]triazolo[1,5-*a*]-pyridine (tzpy) and *N,N'*-bis(1-pyridin-2-ylethylidene)-2,2-dimethylpropane-1,3-diamine (bepydmp)].[13,14]

Cobalt(II) SCO/SMMs in quantum dots as spin filters. Remarkable results were achieved by addressing individual SCO molecules between a gold surface and the ferromagnetic nickel tip of the STM. In their seminal work, Aragonès *et al.* found out that, when subjected to a spin-polarised current, the device showed spin state dependence of the electron transport, in which the SCO centre acts as a spin filter, showing an increase of the single-molecule conductance upon changing the polarisation of the Ni electrode from spin-up (α) to spin-down (β).[14] Those results agreed with previous calculations of Aravena *et al.* that predicted higher conductance for the aforementioned paramagnetic HS Fe(II) complex with tzpy ligand if compared with the diamagnetic LS state when connected between two gold electrodes through the sulphur atoms of the thiocyanate ligands.[13] In contrast, the electrical conductance remains constant when the diamagnetic LS Fe(II) complex with the bepydmp ligand is the one connecting the electrodes through the sulphur atoms of the thiocyanate ligands.[14] These results demonstrate the crucial role of the addressing of single-molecules in searching for new functionalities that would give birth to future nanoscale spintronic devices.

Inside this context, we found the electroactive Co^{II}-PDI complexes with electron donor thiomethyl substituents a suitable opportunity to design a new class of spin filters due to (i) the sulphur affinity for a variety of metallic substrates, (ii) its HS ground state, which seems to be a natural booster of the conductance through the quantum dot and (iii) the possibility to tune the spin dynamics properties when applied an external magnetic field as occurs for the bulk material. Moreover, the electrochemical metal oxidation can play the role of an ON-OFF switch for the spin filter device. Thus, while the paramagnetic HS ON Co^{II} ion would filter the spin-up (α) electrons, the diamagnetic LS OFF Co^{III} ion would have no selectivity in distinguishing the spin-polarised electrons.

Cobalt(II) SCO/SMM in carbon-based nanostructures as spin valves. Hybrid materials may be the key to enhancing and thoroughly exploring the spin dynamic properties of SMMs. It was pursuing this idea that Ruben *et al.* proposed to anchor a lanthanide-based mononuclear SMM on a single-walled carbon nanotube (SWCNT). For this to happen, a rational design of the SMM was necessary to incorporate anchoring groups that will interact with the SWCNT via supramolecular π-π interactions. In their work, a heteroleptic derivative of the archetypical double-decker $[Tb(Pc)_2]$ bearing one modified pyrene and six hexyl groups were successfully self-assembled in the SWCNT.[15] Remarkably, the energy barrier and the relaxation time both increased upon anchoring, a result likely assigned to the suppression of the intermolecular interactions between the SMM units. Based on these results, a new molecular spintronic device has emerged: the supramolecular spin valve (see Box B in Chapter I).[16]

It is important to stress that our mononuclear Co^{II}-PDI complexes with oligoacene naphthalene and anthracene substituents presented in Chapter IV are suitable to prepare this type of hybrid metallocarbon nanotube and nanographene architectures. However, the proper choice might be new Co^{II}-PDI derivatives with better anchoring extended aromatic groups like pyrenes or its derivatives with flexible aliphatic linkers (Figure VII.6).

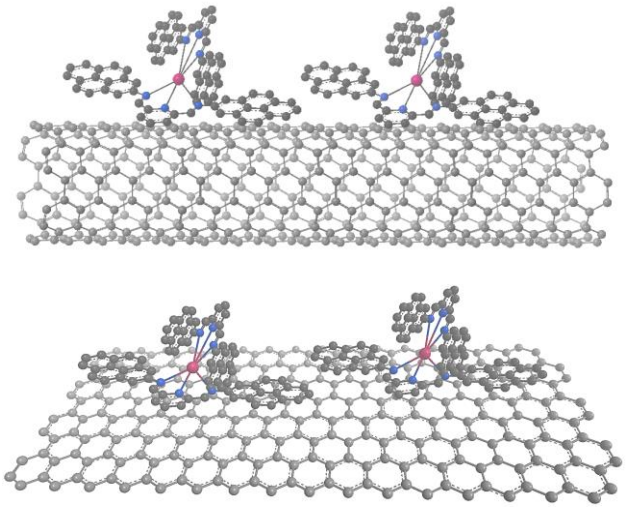

Figure VII.6 Illustration of the supramolecular carbon-based nanotubes (top) and nanographenes (bottom) for spin valves with pyrene-substituted Co^{II}-PDI molecules.

Scaling of Spin Crossover Cobalt(II) Molecular Nanomagnets as Molecular Spin Quantum Bits for QIP

The molecular approach to quantum computing nanotechnologies can be considered a three-step process that works analogously to the bottom-up strategy in supramolecular chemistry. Each step raises the complexity level of the previous one to build the new material. These three steps might be classified as (i) design of qubits, (ii) scaling for implementation of the quantum gate and (iii) conception of the quantum computing device to store and process the quantum information. It is worthy to remark that the last step, which is the final goal, is still barely explored. However, outstanding advances were achieved in the design and control of the qubit.

On the road to minimising quantum decoherence, some robust candidates for realising a molecular-based qubit have emerged that incorporate many first-row transition metal ions from vanadium to copper.[1] They include the vanadium(IV), iron(III) and chromium(III) complexes of formula $[V(C_8S_8)_3]^{2-}$, $[Fe(C_5O_5)_3]^{3-}$ and $[Cr(C_3S_5)_2]^{3-}$.[17–19] Note that the ligands in these complexes are composed of only nuclear spin-free elements with a very low abundance of nuclear spin-active isotopes (C, O and S). This feature grants them long coherence times (T_2 or T_m) since nuclear spins are the main source of the magnetic noise and thus the decoherence. By changing the chemical matrix to a spin-free solvent like CS_2 or SO_2, it was also possible to increase the values of T_2.[20] Other remarkable candidates for qubit are the copper(II)-maleonitrile $[Cu(nmt)_2]^{2-}$ and vanadyl(IV)-phthalocyanine [VO(Pc)] complexes, owing coherence times of 1 μs (T_2), despite possessing donor atoms or atoms near the metal centre with nuclear spin-active isotopes (N).[21,22]

As mentioned above, scalability is an essential requirement on the road to spin-based quantum computing. This term, somehow related to the entanglement, can be translated as the possibility of increasing the number of qubits in arrays that will preserve the ability to manipulate and read out the information without jeopardising the quantum coherence. This topic is a challenging step in the development of a spin-based quantum computer. Each array presents its advantages and disadvantages, so it is a solid point to have a versatile and easy-to-handle qubit platform that may be processed in various architectures like our Co^{II}-TERPY and Co^{II}-PDI complexes. To follow, we provide some attempts to exemplify the potentiality and versatility in the design, scaling and addressing of the spin crossover cobalt(II) molecular nanomagnets presented in this PhD Thesis as building components for quantum computing technologies (Figure VII.7). In this sense, the new construction could be achieved through diverse supramolecular Co^{II}-SCO/SMM architectures obtained through ligand design.

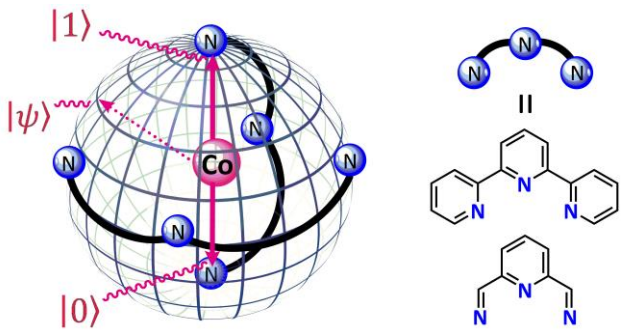

Figure VII.7 Selected TERPY and PDI platforms for the creation of a new chemical library of Co^{II}-SCO/SMM molecules as candidates to quantum bits.

Hopefully, our results will open a pathway toward the **design of operative molecular spin qubits or qubit arrays**, projecting the physical implementation of a new class of multifunctional electrical, optical, chemical and magnetic materials for QIP. Once identified the key design criteria to improve the SCO and SMM performance of the mononuclear cobalt(II)-PDI and TERPY complexes, two critical challenges should be addressed to achieve this goal: (i) identifying the major sources of quantum decoherence in spin crossover cobalt(II) molecular nanomagnets, (ii) building supramolecular arrays of spin crossover cobalt(II) molecular nanomagnets of increasing complexity with very weak (but non-negligible) and potentially switchable intermolecular interactions, and (iii) addressing suited spin crossover cobalt(II) molecular nanomagnets and their supramolecular arrays on surfaces and other solid supports.

Cobalt(II) SCO/SMMs as molecular spin quantum bits. In cobalt(II) SCO/SMMs, the LS Co^{II} ion is a genuine two-level magnetic quantum system represented by the m_S = +1/2 and –1/2 states, which can play the role of the superposed 0 and 1 states in a qubit for quantum computing applications. By comparison, the HS Co^{II} state, due to the large first-order spin-orbit coupling, possesses an effective doublet ground spin state (S_{eff} = 1/2) coming from the m_S = ±1/2 ground Kramers doublet (for $D > 0$), which could be an alternative as a "single" qubit with a thermally accessible m_S = ±3/2 excited Kramers doublet (or *vice versa*, for $D < 0$).

In general, the magnetic relaxation time for a doublet spin ground state is identical to the spin-lattice time ($T_1 = \tau$), which

acts in turn as a limiting factor for the phase memory time ($T_m \leq T_1$). So, rather long T_1 values are available for our styryl- or benzoic/benzoate-substituted LS Co^{II} TERPY complexes at T = 2.0 K, varying from 8.5 to 86 μs (see Chapters V and VI). Such values are smaller than the T_1 values of 11.1 and 1.3 ms found in the related square-planar or square-pyramidal LS cobalt(II)-phthalocyanine and 1,4,7,10-tetramethyl-1,4,7,10-tetraazacyclododecane complexes.[23,24] However, complete studies of the pulsed EPR technique should be performed on both LS and HS octahedral cobalt(II) complexes presented in this PhD Thesis to characterise and evaluate their fitting as new candidates for the realisation of a spin qubit.

In fact, our research group have recently devoted pulsed EPR studies on the $[Co(Me_2phen)_2(Sal)]^+$ octahedral HS cobalt(II) complex (Me_2phen = 2,9-dimethyl-1-10-phenantroline; Sal = salicylaldehyde) with positive D value,[25] estimating a T_m comparable with other qubit candidates (1 μs).[17-22] It is noteworthy that its dc and ac magnetic or cw EPR characteristics are similar to those found for HS configurations of our PDI complexes, which emerge thus as potential candidates for molecular spin quantum bits.

Cobalt(II) SCO/SMMs as optically, chemically or electrochemically, electrically and magnetically addressable molecular spin quantum bits. This unique class of multifunctional and multiresponsive spin-crossover cobalt(II) molecular nanomagnets appears as up-and-coming candidates for the multiple (optical, chemical or electrochemical, electrical or magnetic) addressing of qubits for future applications in QIP. The presented results constitute an essential step in the chase for advanced addressable qubits and the controlled resetting of the quantum gate.

All the compounds presented in this PhD Thesis may be considered attractive to develop advanced qubits with electrical readout. The electroswitch between paramagnetic LS/HS Co^{II} and diamagnetic LS Co^{III} states offers an excellent opportunity to erase and reinitiate the qubit at the end and beginning of the information processing. Moreover, when subjected to a suitable combination of two or more stimuli like (i) external magnetic field, (ii) gate voltage, (iii) light irradiation and (iv) proton concentration, the Co^{II} SCO/SMM compounds can act as a quantum logic gate reading out all the inputs in a single output.

In the hunting for the ideal qubits, it is a consensus that the all-optically addressable ones are the best shot due to a set of reasons: (i) light is an environmentally green stimulus, (ii) they can be remotely controlled with time and position precision, (iii) they enable a direct and precise single-spin readout and initialisation and (iv) they can be orthogonally coupled with other switchable entities in a single-spin in order to build logic multitaskers with a high level of complexity. This appealing need in the Quantum Computing field has moved us to invest efforts in creating and studying a family of optically active Co^{II} SCO/SMM by simply introducing oligoacene luminophore groups to our Co^{II}-PDI platform. A preliminary study of their photophysical activity in solution makes evident the occurrence of a significant metal-promoted quenching of the ligand luminescence upon UV light irradiation at room temperature, likely due to the ligand-to-metal energy transfer process leading to a short-lived excited state of the Co^{II} ion (analogous to the LIESST excited state that is not readily available in our Co^{II} SCO/SMMs).

Cobalt(II) SCO/SMMs in soft matter as exotic arrays of molecular spin quantum bits. Once the major sources of quantum decoherence in solution or solid-state (diluted solid solutions) are identified, related investigations on spin-crossover cobalt(II) molecular nanomagnets in soft media would be valuable for their potential applications in QIP.

Although some questions about the SCO and SMM behaviours in the crystalline solid state remain unclear, these topics are still largely studied. That is not the case when it comes to soft matter. Bulk assemblies like colloids, liquid crystals, polymers, vesicles and Langmuir-Blodgett (LB) films that incorporate SCO and SMM behaviours are still unexplored. However, the few works reported along this line provided promising results on how can improve SCO behaviour. Examples of this feature include the LB films based on an amphiphilic $Fe^{II}(L)_2(NCS)_2$complex [L = 4,4'-diheptadecyl-2,2'-bipyridine], which undergoes thermally assisted cycle-dependent SCO.[26,27] This atypical behaviour is attributed to the melting of the alkyl chain groups that helps recover the organisation favouring the SCO process. Sun *et al.* also prepared SCO vesicular nanospheres based on the series of neutral $[Fe^{II}(H_2Bpz_2)_2(R_2bpy)]$ complexes with 2,2'-bipyridine-4,4'-dicarboxamide ligands. The spin transition temperature of these nanospheres significantly changed, taking place at room temperature while in the bulk material was around 160 K.[28]

The $[Co^{II}(C_{16}\text{-TERPY})_2]^{2+}$ complex constitutes an exciting example because it shows a reverse spin transition unexpectedly triggered by a structural vitreous phase transition.[29] However, the possible SMM behaviour based on the reverse HS state was not studied. Facing this hideous path, mononuclear Co^{II}-PDI and TERPY complexes with long polyalkyl substituents offer a suitable Co^{II} SCO/SMM platform to study both phenomena and, eventually, test for the first time their qubit performance in soft matter (Figure VII.8).

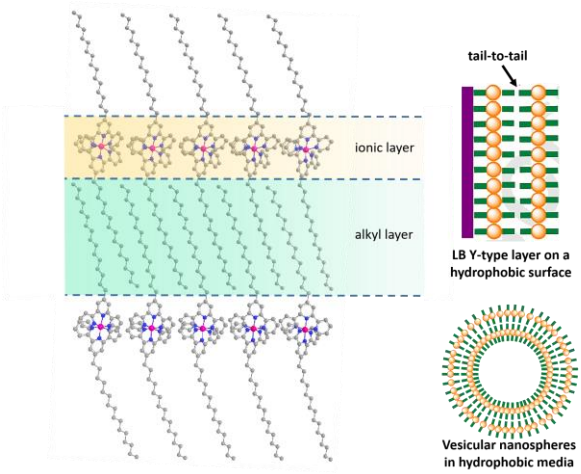

Figure VII.8 Examples of LB films and vesicular nanospheres from cobalt(II) SCO/SMM with long polyalkyl-substituted TERPY ligands as building blocks for arrays of entangled and potentially switchable qubits.

Cobalt(II) SCO/SMMs in porous MOF-based materials. Metal-Organic Frameworks (MOFs) have been extensively studied for their applications in gas storage and separation, drug delivery, molecular recognition, transport and catalysis, as well as for their use as a template for the growth of nanoparticles and the encapsulation of a wide variety of functional moieties.[30–34] An original approach to address individual spin crossover cobalt(II) molecular nanomagnets within matrixes would be to take advantage of the combined host-guest chemistry and geometrical features of Metal-Organic Frameworks (MOFs) to produce a new class of hybrid materials.

Owing to their porosity and their consequent rich host-guest chemistry, MOFs are excellent playgrounds for designing a new class of multifunctional and multiresponsive materials resulting from the hosting of spin crossover molecular nanomagnets within the MOF matrix. On the one hand, the quantum decoherence of the adsorbed Co^{II} SCO/SMMs can be investigated in a confined media, and the results compared with those obtained in typical solution and solid-state studies, or more exotic soft matter, in order to optimise their performance as qubits for future applications in QIP.

On the other hand, long-range magnetic ordering from the magnetic MOF host and slow magnetic relaxation of the incorporated Co^{II} SCO/SMM guests can be merged into a single solid, tentatively resulting in an interplay of both magnetic phenomena. Previously, our research group reported the partial incorporation of cationic LS iron(III)-Schiff's base and HS manganese(III)-porphyrin SMM complexes, independently, into the extensive channels of an anionic oxamato-based copper(II)-manganese(II) 3D MOF via cation-exchange single crystal-to-single crystal (SC-SC) processes. The resulting host-guest hybrid materials exhibit hysteretic SCO behaviour or internal field-induced partial quenching of the QTM for Fe(III) and Mn(III) guests.[35,36] These features constitute unique proofs of the synergy effects between the guests' spin dynamics and the host's long-range magnetic ordering, demonstrating thus that this class of porous magnets appear as very suitable platforms for the controlled addressing of SMMs.

Preliminary studies during the development of this PhD Thesis revealed that the parent cationic $[Co^{II}(PhPDI)_2]^{2+}$ SCO/SMM complex is hosted inside the large pores of the aforementioned anionic ferrimagnetic copper(II)-manganese(II) MOF (Figure VII.9).[37] The EDX analysis indicates that the new guest successfully replaced all exchangeable Na^{I} ions over one week. This promising result offers a new perspective of how SCO/SMM behaviour could be modulated by addressing the spin carriers as hybrid materials. Along this line, we plan to investigate the quantum decoherence through pulsed EPR experiments of partially exchanged diluted samples of the $[Co^{II}(PhPDI)_2]^{2+}$ complex adsorbed into the diamagnetic nickel(II)-magnesium(II) host derivative.

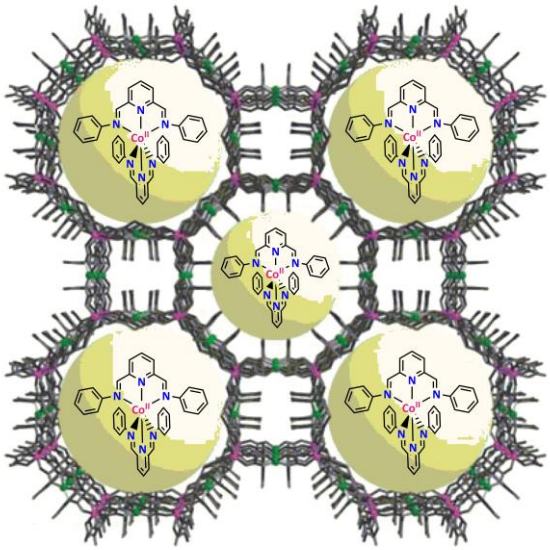

Figure VII.9 Illustrative representation of the chemisorption of the Co^{II}-PDI complexes into the giant pores of the anionic MOF of formula $\{Mn_4[Cu_2(Me_3mpba)_2]_3\}^{4-}$.

MOFs of cobalt(II) SCO/SMMs as entangled and potentially switchable ordered arrays of qubits. Designing and synthesising ordered arrays of very weak interacting (entangled) and potentially switchable qubits is mandatory for constructing a quantum computer. Hence, the first commercial quantum computer realised under Feynman's vision, the Sycamore processor, is based on microscopic superconducting circuits showing a square grid array of 54 qubits (53 operatives), each connected to its four nearest neighbours with appropriate couplers (Figure VII.10a and b).[38] This result prompted us to think that the unique challenge of a spin-based quantum computing machine could be met in the near future.

MOFs consisting of metal ions (or small metal clusters) linked through a wide diversity of organic spacers are especially suited for this task.[39] Our group has demonstrated that the bottom-up "complex as ligand" strategy is an effective way to create new MOFs. In that, metal complexes with additional coordinating groups act as ligands (metalloligands) towards

other metal ions (or small metal clusters), giving rise to high dimensional MOFs structures.

In this regard, the Co^{II}-TERPY and PDI complexes appear as promising metalloligand units since different peripheral substituents can be placed to match the Lewis acidity of a diversity of metal ions leading to nD (n = 2 and 3) SCO/SMM nets. Oxygen donor carboxylatephenyl groups (like in the TERPY derivative presented in Chapter VI) fit well with hard ions like lanthanides, while nitrogen donor groups from pyridines are a proper choice to interact with most first-row transition metals. Also, these platforms are directionally distinct, and this will favour different topologies of MOFs like diamond-type (for Co^{II}-PDI), 2D square-grid or 3D cubic Yaghi-type MOFs[40,41] (for Co^{II}-TERPY), in which the Co^{II}-TERPY and Co^{II}-PDI complexes will occupy the edges and the second metal ion (or secondary building unit) the nodes (Figure VII.10c). Note that our carboxylatephenyl-substituted TERPY cobalt(II) complex is much longer than the traditional dicarboxylates used in Yaghi-type MOFs, which would allow higher porosity to the new material.

The results and perspectives gathered in this last chapter of the PhD Thesis are only a *first step* in the ligand design approach to molecular spintronics and quantum computing nanotechnologies. However, they represent the main reason motivating us to pursue this research avenue. Indeed, most proposals concerning the scaling and addressing of spin-crossover cobalt(II) molecular nanomagnets as multifunctional and multiresponsive DMS prototypes for single-molecule spintronic devices are more like daydreams than real achievements. In the years to come, we would like to accomplish some of these *dream worlds* concerning the physical realisation of quantum information processing. In this respect, this PhD Thesis is also meant to be a *message in a bottle* for materials scientists with extensive expertise in the manipulation and measurement of single-molecule electron transport properties and the processing and addressing of molecules into different supports, as well as for those theoretical physicists who may be interested in our work for the conception and scaling of molecules as spin quantum bits in future quantum computers.

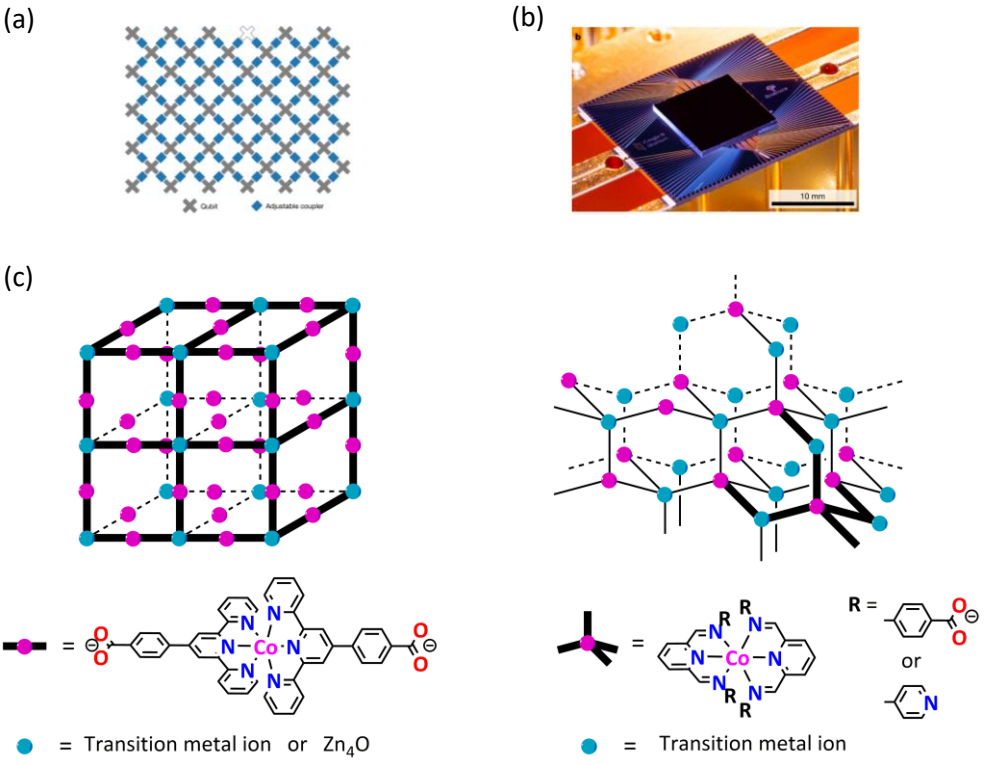

Figure VII.10 (a) Design of the array of the 54 qubits contained in (b) the Sycamore chip processor for QIP. (c) Examples of MOF topologies from cobalt(II) SCO/SMM with carboxylatephenyl- or pyridine-substituted TERPY and PDI ligands as building blocks for arrays of entangled and potentially switchable qubits. Adapted with permission from Ref [38].

References

1 Ferrando-Soria, J.; Vallejo, J.; Castellano, M.; Martínez-lillo, J.; Pardo, E.; Cano, J.; Castro, I.; Lloret, F.; Ruiz-García, R.; Julve, M. Molecular Magnetism, quo vadis? A Historical Perspective from a Coordination Chemist Viewpoint. *Coord. Chem. Rev.* **2017**, *339*, 17–103.

2 Ruben, M.; Rojo, J.; Romero-Salguero, F. J.; Uppadine, L. H.; Lehn, J.-M. Grid-Type Metal Ion Architectures: Functional Metallosupramolecular Arrays. *Angew. Chem. Int. Ed.* **2004**, *43*, 3644–3662.

3 Moriuchi, T.; Hirao, T. Design and Redox Function of Conjugated Complexes with Polyanilines or Quinonediimines. *Acc. Chem. Res.* **2012**, *45*, 347–360.

4 Mansoor, I. F.; Wozniak, D. I.; Wu, Y.; Lipke, M. C. A Delocalized Cobaltoviologen with Seven Reversibly Accessible Redox States and Highly Tunable Electrochromic Behaviour. *Chem. Comm.* **2020**, *56*, 13864–13867.

5 Liu, Q.; Liu, X.; Shi, C.; Zhang, Y.; Feng, X.; Cheng, M.-L.; Su, S.; Gu, J. A Copper-Based Layered Coordination Polymer: Synthesis, Magnetic Properties and Electrochemical Performance in Supercapacitors. *Dalton Trans* **2015**, *44*, 19175–19184.

6 Zhang, Q.; Uchaker, E.; Candelaria, S. L.; Cao, G. Nanomaterials for Energy Conversion and Storage. *Chem. Soc. Rev.* **2013**, *42*, 3127–3171.

7 Durfee, W. S.; Pierpont, C. G. Complexes of quinone-functionalised chelating ligands for multiple electron/proton transfer reduction reactions. *Inorg. Chem.* **1993**, *32*, 493–494.

8 Malwitz, J.; Alkire, N.; Durfee, W. Quinone-functionalized Transition Metal Complexes for Multi-Electron Transfer. The Electrochemistry of a Bis - Naphthoquinone-Functionalized Schiff Base Ni(II) complex. *J. Coord. Chem.* **2010**, *55*, 641–650.

9 Rabelo R.; Toma, L.; Moliner, N.; Julve, M.; Lloret, F.; Pasán, J.; Ruiz-Pérez, C.; Ruiz-García, R.; Cano, J. Electro-Switching of the Single-Molecule Magnet Behaviour in an Octahedral Spin Crossover Cobalt(II) Complex with a Redox-Active Pyridinediimine Ligand, *Chem. Commun.* **2020**, *56*, 12242–12245.

10 Roux, C.; Zarembowitch, J.; Gallois, B.; Granier, T.; Claude, Renee. Toward Ligand-Driven Light-Induced Spin Changing. Influence of the Configuration of 4-Styrylpyridine (stpy) on the Magnetic Properties of $Fe^{II}(stpy)_4(NCS)_2$ Complexes. Crystal Structures of the Spin-Crossover Species Fe(trans-stpy)$_4$(NCS)$_2$ and of the High-Spin Species Fe(cis-stpy)$_4$(NCS)$_2$. *Inorg. Chem.* **1994**, *33*, 2273–2279.

11 Dietrich-Buchecker, C. O.; Sauvage, J.-P.; Kintzinger, J.-P. Une nouvelle famille de molécules: les métallo-caténanes, *Tetrahedron Lett.* **1983**, *24*, 5095–5098.

12 Mohr, B.; Sauvage, J.-P.; Grubbs, R. H.; Weck, M. High-Yield Synthesis of [2] catenanes by intramolecular ring-closing metathesis. *Angew. Chem. Int. Ed.* **1997**, *36*, 1308–1310.

13 Aravena, D.; Ruiz, E. Coherent Transport through Spin-Crossover Single Molecules. *J. Am. Chem. Soc.* **2012**, *134*, 777–779.

14 Aragonès, A.C.; Aravena, D.; Cerdá, J.I.; Acís-Castillo, Z.; Li, H.; Real, J.A.; Sanz, F.; Hihath, J.; Ruiz, E.; Díez-Pérez, I. Large Conductance Switching in a Single-Molecule Device through Room Temperature Spin-Dependent Transport. *Nano Lett.* **2016**, *16*, 218.

15 Kyatskaya, S.; Galán-Mascarós, J.R.; Bogani, L.; Hennrich, F.; Kappes, M.; Wernsdorfer, W.; Ruben, M. Anchoring of Rare-Earth-Based Single-Molecule Magnets on Single-Walled Carbon Nanotubes. *J. Am. Chem. Soc.* **2009**, *131*, 15143–15151.

16 Urdampilleta, M.; Klyatskaya, S.; Cleuziou, J-P.; Ruben, M.; Wernsdorfer, W. Supramolecular spin valves. *Nature Materials* **2011**, *10*, 502–506.

17 Zadrozny, J. M.; Niklas, J.; Poluektov, O. G.; Freedman, D. E. Multiple Quantum Coherences form Hyperfine Transitions in a Vanadium(IV) Complex. *J. Am. Chem. Soc.* **2014**, *136*, 15841–15844.

18 Zadrozny, J. M.; Freedman, D. E. Qubit Control Limited by Spin-Lattice Relaxation in a Nuclear Spin-Free Iron(III) Complex. *Inorg. Chem.*, **2015**, *54*, 12027–12031.

19 Fataftah, M. S.; Zadrozny, J. M.; Coste, S. C.; Graham, M. J.; Rogers, D. M.; Freedman, D. E. Employing Forbidden Transitions as Qubits in a Nuclear Spin-Free Chromium Complex. *J. Am. Chem. Soc.* **2016**, *138*, 1344–1348.

20 Yu, C. J.; Graham, M. J.; Zadrozny, J. M.; Niklas, J.; Krzyaniak, M.; Wasielewski, M. R.; Poluektov, O. G.; Freedman, D. E. Long Coherence Times in Nuclear Spin-Free Vanadyl Qubits. *J. Am. Chem. Soc.* **2016**, *138*, 14678–14685.

21 Bader, K.; Dengler, D.; Lenz, S.; Endeward, B.; Jiang, S.-D.; Neugebauer, P.; van Slageren, J. Room Temperature Quantum Coherence in a Potential Molecular Qubit. *Nature Comm.* **2014**, *5*, 5304–5308.

22 Atzori, M.; Tesi, L.; Morra, E.; Chiesa, M.; Sorace, L.; Sessoli, R. Room-Temperature Quantum Coherence and Rabi Oscillations in Vanadyl Phthalocyanine: Toward Multifunctional Molecular Spin Qubits. *J. Am. Chem. Soc.* **2016**, *138*, 2154–2157.

23 Bader, K.; Winkler, M.; van Slageren, J. Tuning of Molecular Qubits: Very Long Coherence and Spin–Lattice Relaxation Times. *Chem. Comm.* **2016**, *52*, 3623–3626.

24 Xu, M.-X.; Liu, Z.; Dong, B.-W.; Cui, H.-H. Wang, Y.-X.; Su, J.; Wang, Z.; Song, Y.; Chen, X.-T.; Jiang, S.-D.; Gao, S. Single-Crystal Study of a Low Spin Co(II) Molecular Qubit: Observation of Anisotropic Rabi Cycles. *Inorg. Chem.* **2019**, *58*, 2330–2335.

25 José Miguel Carbonell Vilar. Estudio de Propiedades Magnéticas en Compuestos de Coordinación Multifuncinales. Chapter III: Assembling Cobalt(II) SIMs as Potential Qu-Gates. PhD Thesis, Univertita de València, 2021.

26 Soyer, H.; Mingotaud, C.; Boillot, M. L.; Delhaes, P. Spin Crossover of a Langmuir−Blodgett Film Based on an Amphiphilic Iron(II) Complex. *Langmuir* **1998**, *14*, 5890−5895.

27 Soyer, H.; Mingotaud, C.; Boillot, M. L.; Delhaes, P. Spin-Crossover Complex Stabilized on a Formamide/Water Subphase. *Thin Solid Films* **1998**, *329*, 435−438.

28 Luo, Y.-H.; Liu, Q.-L.; Yang, L.-J.; Sun, Y.; Wang, J.-W.; You, C.-Q.; Sun, B.-W. Magnetic observation of above room-temperature spin transition in vesicular nano-spheres. *J. Mater. Chem. C* **2016**, *4*, 8061–8069.

29 Hayami, S.; Shigeyoshi, Y.; Akita, M.; Inoue, K.; Kato, K.; Osaka, K.; Takata, M.; Kawajiri, R.; Mitani, T.; Maeda, Y. Reverse Spin Transition Triggered by a Structural Phase Transition. *Angew. Chem. Int. Ed.* **2005**, *44*, 4899–4903.

30 Kitagawa, S.; Kitaura, R.; Noro, S. I. Functional Porous Coordination Polymers. *Angew. Chem. Int. Ed.* **2004**, *43*, 2334–2375.

31 Kitagawa, S.; Matsuda, R. Chemistry of Coordination Space of Porous Coordination Polymers. *Coord. Chem. Rev.* **2007**, *251*, 2490–2509.

32 Férey, G.; Serre, C. Large breathing effects in three-dimensional porous hybrid matter: facts, analyses, rules and consequences. *Chem. Soc. Rev.* **2009**, *38*, 1380–1399.

33 Mon, M.; Bruno, R.; Ferrando-Soria, J.; Armentano, D.; Pardo, E. Metal–organic framework technologies for water remediation: towards a sustainable ecosystem. *J. Mat. Chem. A* **2018**, *6*, 4912–4947.

34 Viciano-Chumillas, M.; Mon, M.; Ferrando-Soria, J.; Corma, A.; Leyva-Pérez, A.; Armentano, D.; Pardo, E. Metal–Organic Frameworks as Chemical Nanoreactors: Synthesis and Stabilisation of Catalytically Active Metal Species in Confined Spaces. *Acc. Chem. Res.* **2020**, *53*, 520–531.

35 Abhervé, A.; Grancha, T.; Ferrando-Soria, J.; Clemente-León, M.; Coronado, E.; Waerenborgh, J. C.; Lloret, F.; Pardo, E. Spin-Crossover Complex Encapsulation within a Magnetic Metal–Organic Framework. *Chem. Comm.* **2016**, *52*, 7360–7363.

36 Mon, M.; Pascual-Álvarez, A.; Grancha, T.; Cano, J.; Ferrando-Soria, J.; Lloret, F.; Gascon, J.; Pasán, J.; Armentano, D.; Pardo, E. Solid-State Molecular Nanomagnet Inclusion into a Magnetic Metal–Organic Framework: Interplay of the Magnetic Properties. *Chem. Eur. J.* **2016**, *22*, 539–545.

37 Ferrando-Soria, J.; Ruiz-García, R.; Cano, J.; Stiriba, S.-E.; Vallejo, J.; Castro, I.; Julve, M.; Lloret, F.; Amorós, P.; Pasán, J.; Ruiz-Pérez, C.; Journaux, Y.; Pardo, E. Reversible Solvatomagnetic Switching in a Spongelike Manganese(II)–Copper(II) 3D Open Framework with a Pillared Square/Octagonal Layer Architecture. *Chem. Eur. J.* **2012**, *18*, 1608–1617.

38 Arute, F.; Arya, K.; Babbush, R. *et al*. Quantum Supremacy Using a Programmable Superconducting Processor. *Nature* **2019**, *574*, 505–510.

39 Graham, M. J.; Zadrozny, J. M.; Fataftah, M. S.; Freedman, D. E. Forging Solid-State Qubit Design Principles in a Molecular Furnace. *Chem. Mater.* **2017**, *29*, 1885–1897.

40 Yaghi, O. M; O'Keeffe, M.; Eddaoudi, M.; Chae, K.; Kim, J.; Ockwing, N. W. Reticular Synthesis and the Design of New Materials. *Nature* **2003**, *423*, 705–714.

41 Long, J. R.; Yaghi, O. M. The Pervasive Chemistry of Metal–Organic Frameworks. *Chem. Soc. Rev.* **2009**, *38*, 1213–1214.

RESUMEN

Nanoimánes de transición de espín como systemas moleculares dinámicos en Magnetismo Molecular y Espintrónica Molecular

Los complejos mononucleares de iones metálicos paramagnéticos de la primera serie de transición con ligandos "no-inocentes" hechos a medida han surgido recientemente como prototípicos de sistemas moleculares dinámicos (DMSs, del inglés “dynamic molecular systems”). El enorme impacto de los DMSs en varios dominios de la nanociencia y nanotecnología molecular se debe a su capacidad para ejecutar funciones específicas y selectivas bajo el control de un estímulo externo que modula adecuadamente sus propiedades estructurales y electrónicas (ópticas, redox y magnéticas). En esta Tesis Doctoral, a lo largo de siete capítulos describimos la química y las propiedades físicas de una clase única de nano-imanes moleculares basados en complejos mononucleares octaédricos de cobalto(II) de transición de espín con ligandos del tipo piridindiimina (PDI) y terpiridina (TERPY) potencialmente quimio-, electro- o fotoactivos. Debido a su inusual combinación de propiedades químicas (acidez de Brønsted o Lewis y rédox) y físicas (ópticas o luminiscentes y magnéticas) resultantes del metal y del ligando, pueden ser usados en el diseño de materiales magnéticos avanzados multifuncionales y de respuesta múltiple para tecnologías de espintrónica molecular y computación cuántica. Uno de los principales logros de esta Tesis Doctoral fue poder modular sus propiedades de transición de espín (SCO, del inglés “spin crossover”) y de molécula imán (SMM, del inglés “single-molecule magnet”) mediante el diseño de ligando a través de una variedad de factores internos, ya sean electrónicos (oxidación y estados de espín de metales) o estéricos (sustituyentes y conformación de ligandos), y eventualmente canjearlos bajo la presencia de un estímulo externo, ya sea químico (pH y analitos químicos) o físico (luz, campos eléctricos y magnéticos). Por lo tanto, los complejos mononucleares octaédricos de cobalto(II)-PDI y -TERPY que se comportan como nano-imanes moleculares de transición de espín proporcionan un excelente conjunto químico de modelos de DMS para estudios fundamentales sobre los fenómenos de la relajación lenta de la magnetización inducida por el campo magnético y quimio-, rédox- o foto-desencadenada. En particular, parecen ser candidatos prometedores para la espintrónica molecular y los dispositivos de computación cuántica como interruptores y capacitores o transistores de espín y qubits. Además, tal como se señala brevemente en el último capítulo, los nano-imanes moleculares de transición de espín presentados en esta Tesis Doctoral son particularmente adecuados para su procesamiento en diferentes soportes, incluidas las uniones moleculares metálicas y las redes metalorgánicas porosas (MOF, del inglés “metal-organic framework”), y para medir su transporte de electrones molecular y sus propiedades de coherencia cuántica, que son dos temas principales de la espintrónica molecular y la computación cuántica.

Así nos dimos cuenta de que un nuevo sistema multifuncional no siempre debería surgir del desarrollo de nuevas propiedades. Mirando hacia “el fondo”, en cambio, se pueden crear nuevos materiales a partir de diseños razonados e innovadores que permitan juntar varias propiedades conocidas, estableciendo sinergia entre ellas. En esta Tesis Doctoral, seguimos la idea simple (pero no fácil) de usar dos plataformas $Co^{II}N_6$ con ligandos *2,2':6',2''*-terpiridina (TERPY) y piridina-2,6-diimina (PDI) relacionados conocido durante décadas por crear con éxito una nueva biblioteca química de nanoimánes moleculares de transición de espín (Figura R.1). Su carácter multifuncional y de respuesta múltiple, la modulación química y el comportamiento conmutable con respecto a los fenómenos de transición de espín (SCO) e imán de molécula única (SMM) ilustran todo el potencial de esta nueva clase de sistemas moleculares dinámicos (DMS).

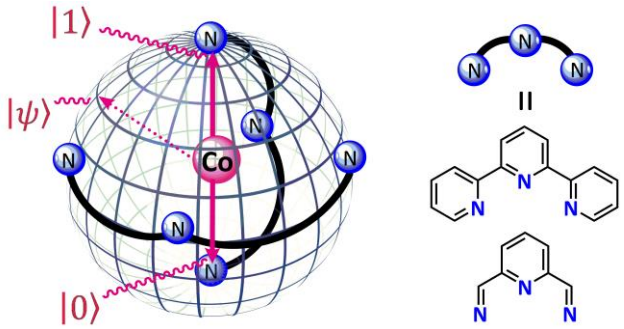

Figure R.1 Plataformas TERPY y PDI seleccionadas para la creación de una nueva biblioteca química de moléculas SCO/SMM de cobalto(II) como candidatas a bits cuánticos.

“Toda aventura requiere un primer paso”. Cliché, pero cierto, incluso y sobre todo para la ciencia. Los resultados presentados en los capítulos II a VI de esta Tesis Doctoral también representan los primeros pasos de nuestro grupo de investigación en la línea de dispositivos magnéticos multifuncionales y multisensibles basados en nanoimánes moleculares de traniscion de espín (SCO/SMM) en los campos emergentes de la espintrónica molecular (MS) y procesamiento de información cuántica (QIP).

La memoria de tesis se encuentra dividida en siete capítulos, siendo el primero de introducción, donde tópicos generales y específicos de la química de coordinación, magnetismo molecular, sistemas moleculares dinámicos y espintrónica molecular situarán al lector en el tema estudiado. Por otra parte, en este capítulo también se facilitan las herramientas necesarias para comprender y discutir los resultados obtenidos y conclusiones alcanzadas en el resto de capítulos. La memoria finaliza con un capítulo dedicado a conclusiones y perspectivas. En este capítulo se muestran los

aspectos más generales de los resultados obtenidos, ayudando a concebir unas conclusiones más genéricas y mostrando el trabajo como un todo y no como una secuencia de capítulos independientes o inconexos. Además, en este capítulo también se plasman propuestas para futuros estudios que aprovecharán los sistemas estudiados ahora, o variaciones de ellos, en la construcción de dispositivos espintrónicos.

Objetivos

En esta memoria se pretende combinar la biestabilidad magnética que acompaña al fenómeno SCO con la aparición de comportamientos de SMM. De este modo, se postula obtener sistemas dinámicos que podrían ser aprovechados en nanodispositivos (interruptores de espín) dentro del marco de la Espintrónica Molecular. A esta nueva clase de compuestos, le hemos llamado Nanoimánes Moleculares de Transición de Espín (SCO/SMM). Sin embargo, aunar fenómenos SCO y SMM en un mismo material constituye una de las mayores paradojas en el Magnetismo Molecular ya que un comportamiento SMM ocurre a bajas temperaturas y, en principio, requiere de un moderado o alto desdoblamiento a campo nulo o zero-field splitting (zfs), a veces equivocadamente conocido como anisotropía magnética. Sin embargo, este zfs adolece de un sentido físico cuando se aplica a estados singulete (S = 0) o doblete (S = ½), que son los correspondientes a un estado bajo-espín encontrado a baja temperatura de un complejo SCO. Por otra parte, un proceso SCO ocurrirá, si éste es posible, sólo a temperaturas relativamente altas (T > 100 K), lo que imposibilita que los fenómenos SCO y SMM operen en la misma región de temperatura. A lo largo de la memoria, se discutirá tanto el modo de poder interaccionar a la vez con los dos fenómenos como la aparición de posibles características físicas "inesperadas" que nos puedan ser útiles para alcanzar nuestra meta.

Metodología

La estrategia común seguida a lo largo de esta secuencia de estudios ha sido elegir una familia de complejos de cobalto(II). Como consecuencia de un acoplamiento espín-órbita (SOC) de primer orden, este ion metálico se caracteriza por presentar el mayor zfs entre los iones metálicos involucrados en el fenómeno SCO. Pero este fenómeno SCO no ocurre en cualquier complejo de cobalto(II), sino que es necesario unos ligandos que generen un campo de ligando adecuado para que ninguno de los dos estados de espín se vea netamente favorecido, como aquellos del tipo piridinadiimina (PDI) y terpiridina (terpy). Por otra parte, el diseño racional permite funcionalizar los ligandos con grupos redox-activos (Capítulos II y III), luminiscentes (Capítulo IV), foto-activos (Capítulo V) y químicamente-activos (Capítulo VI) para obtener sistemas moleculares dinámicos que permitirán modular las propiedades SCO y SMM a través de estímulos externos físicos o químicos y, eventualmente, intercambiarlos reversiblemente.

En los capítulos II y III, se presentan nueve complejos SCO/SMMs. En ellos, los ligandos son derivados con diferentes grupos electro-atractores o -dadores. Estos complejos muestran distintos comportamientos SCO, que varían desde su ausencia, exhibiendo únicamente la forma HS, hasta transiciones de espín graduales completas e incompletas. Esta familia constituye así una excelente base de estudio para evaluar y distinguir los mecanismos que gobiernan el comportamiento SMM en los estados alto- (HS, del inglés "high-spin") y bajo-espín (LS, del inglés "low-spin"). Se observa que, habitualmente, a temperaturas muy bajas (T < 4 K), la relajación de la magnetización de la forma HS es más lenta y está poco influenciada por el campo magnético (H). Mientras, esta relajación en la forma LS es claramente más rápida, pero se ralentiza notablemente al aumentar H. La mayor deslocalización de la densidad electrónica y, principalmente, de la densidad de espín en la configuración electrónica HS es la posible causa de este hecho, ya que la inversión por un campo oscilante de la densidad de espín requerirá el concierto de toda la distribución de estas densidades, no únicamente de la situada sobre el centro metálico.

La presencia de un centro metálico y grupos redox-activo en los ligandos confiere a esta familia de SCO/SMMs tres procesos redox reversibles: una oxidación metálica y dos reducciones del ligando. La prueba de concepto de un Espín Electro-Switch (Capítulo III, sección III.7), es decir, un cambio del comportamiento magnético por procesos redox fue testeada en uno de los compuestos. Así, la interconversión en disolución entre las formas paramagnética Co(II) de LS y diamagnética Co(III) de LS realizada química- y electroquímicamente concluye que este sistema dinámico se comporta como un genuino interruptor magnético molecular.

En el Capítulo IV, la propiedad de luminiscencia es incorporada a nuestros sistemas SCO/SMM con la adición de los grupos luminóforos naftaleno y antraceno a los ligandos PDI. Esta familia de compuestos incluye dos series de solvatomorfos que muestran una influencia de la pérdida de moléculas de disolvente en sus propiedades magnéticas SCO/SMM, permitiendo estudiar el efecto del estado de espín sobre la luminiscencia del complejo. El espectro de emisión del complejo derivado naftaleno en diferentes disolventes, juntamente con medidas magnéticas en disolución sugieren que los cambios observados están asociados a un cambio del estado de espín, donde el estado LS actúa inhibiendo más fuertemente la luminiscencia que el estado HS, lo que también fue confirmado en estado sólido. La posibilidad de obtener información sobre el estado de espín utilizando la luz como estímulo representa un gran paso hacia la implementación de nanotecnologías espintrónicas ópticas.

En el quinto capítulo, se modifica el conocido ligando terpiridina anclando una unidad fenilo por medio de un grupo estilbeno, fotoactivamente activo, permitiendo la conversión en los dos sentidos entre las geometrías cis y trans. Este cambio geométrico o de topología inducido por irradiación afecta directamente al estado sólido, es decir, cómo entidades discretas se organizan en él. Dado que el fenómeno SCO depende fuertemente de la cooperatividad en la red, estos cambios deben afectarle sustancialmente. En este sentido, se estudiaron las propiedades magnéticas de dos compuestos isoestructurales obtenidos variando el contraión. Un estudio por espectroscopías ^{1}H RMN (solo ligando) y UV-Vis de la fotoisomerización del ligando y el complejo confirman la isomerización geométrica tras un período de irradiación con luz

UV. Sin embargo, no se observaron cambios significativos en los espectros de EPR en disolución antes y después de ser irradiada la muestra, indicando que la fotoisomerización no ha conducido al deseado cambio de estado de espín. El mismo estudio en sólido no proporcionó ningún resultado relevante ya que la fotoisomerización no tuvo lugar probablemente debido a la baja penetración de la radiación electromagnética empleada.

En el siguiente capítulo, se intentan extender las ideas desarrolladas previamente, pero ahora se actúa o influye sobre las propiedades SCO/SMM mediante un estímulo químico. En consonancia con el anterior capítulo, se modifica el ligando terpiridina con un grupo benzoato o su forma protonada. Con ellos, se obtuvieron los correspondientes complejos de cobalto(II), los cuales pueden ser estimulados químicamente con iones Na^+ y K^+, de gran interés en sistemas biológicos, y principalmente H^+. La protonación reversible del grupo carboxilato provoca cambios, reversibles también, en sus propiedades magnéticas, ópticas y redox. El estudio concluyó que la forma desprotonada es mejor fluoróforo, su proceso de oxidación/reducción centrado en el metal es más reversible y su magnetización relaja más rápidamente que la forma protonada. En este capítulo se queda demostrado el potencial de los sistemas moleculares SCO/SMM dinámicos, en el que un simple estímulo (pH) es capaz de producir cambios reversibles en las propiedades magnéticas, ópticas y redox.

Conclusiones

Durante mucho tiempo, el Magnetismo Molecular (MM) ha recorrido la ruta del enfoque químico de la Química de Coordinación para desenterrar y construir la comprensión actual de los fenómenos magnéticos que ocurren en las escalas molecular y cuántica. Desde los estudios pioneros sobre SCO y el tautomerismo de valencia relacionado hasta los más recientes sobre la dinámica de espín y la coherencia cuántica de los nanoimánes moleculares, el antiguo pero siempre verde campo de la química de coordinación ha ofrecido el conjunto de herramientas completo para llevar la MM adonde sea necesario y más allá.

Aunque el viaje de MM en busca de estos temas ha recorrido mucho, la capacidad ilimitada de Coordination Chemistry los convierte en un tema relevante en curso en el campo. Todavía hay aspectos físicos emocionantes sin aclarar de SCO mononucleares y SMM, y es por eso que estos sistemas siguen siendo un tema de debate. Siendo así, los datos magnetoestructurales de los compuestos SCO/SMM de cobalto(II) mononuclear informados aquí son de gran interés en el campo. Sin embargo, poner ambos comportamientos juntos en nuevos DMS multiestables de la forma en que lo hicimos puede considerarse nuestra entrada en el área de transición de MM y MS.

Nuestros complejos de cobalto(II) con TERPY y derivados de PDI relacionados constituyen una clase común de sistemas SCO que exhiben transiciones graduales HS ↔ LS. Sin embargo, la observación de efectos cooperativos en estado sólido es escasa y constituye la razón principal por la que estos compuestos han sido menos investigados en la búsqueda de nuevos materiales multifuncionales y multiresponsivos. Nuestra estrategia se centró en diferentes facetas del fenómeno SCO mediante el estudio de la influencia de (i) sustituyentes de ligandos (Capítulos II, III y IV), (ii) moléculas de solventes de cristalización (Capítulo IV), (iii) contraaniones (Capítulo V), (iv) conformación del ligando (Capítulo V) y (v) grado de protonación del ligando (Capítulo VI). Esta investigación sistemática y exhaustiva ha proporcionado conocimientos profundos sobre cómo lograr múltiples comportamientos de SCO incluso sin transiciones abruptas de estado de espín en estas dos series TERPY y PDI de complejos de cobalto(II).

Siguiendo este enfoque, concluimos que los complejos Co^{II}-PDI son excelentes plataformas para la modulación de SCO debido a su fácil manejo y carácter sintético bastante simple. Estas características nos permitieron preparar una amplia biblioteca química variando el sustituyente del ligando para obtener, en cada familia, ejemplos de fases puras HS y LS, así como situaciones intermedias que experimentan un SCO gradual incompleto, con un tercio HS y dos tercios fracciones LS o viceversa a baja temperatura (Capítulos II, III y IV). Por otro lado, nuestros complejos Co^{II}-TERPY dieron principalmente fases LS por debajo de 150 K, presentando fracciones HS a temperatura ambiente (Capítulos V y VI). Además, nuestros resultados sugieren que el enfoque químico de diseño de ligandos puede ser una herramienta valiosa para lograr las propiedades deseadas a través de la modulación del SCO. Sin duda, se deben realizar más esfuerzos en la búsqueda de efectos cooperativos para dar lugar a transiciones de espín completas, abruptas e histeréticas que tienen lugar en diferentes regiones de temperatura jugando con la naturaleza aromática extendida de los sustituyentes.

Aunque el comportamiento de SMM con un bloqueo de la magnetización inducido por campo está muy extendido en SMM Co^{II} de HS (S = 3/2), los informes sobre SMM de Co^{II} de LS (S = 1/2) son escasos. En esta tesis doctoral, no solo proporcionamos nuevos datos magnetoestructurales sobre la relajación magnética lenta en SMM de Co^{II} de HS con anisotropía magnética tanto positiva (D > 0) como negativa (D < 0), sino que también hemos enriquecido la exigua literatura sobre LS Co^{II} SMM.

La dinámica de relajación magnética del ion Co^{II} fue diferente entre las configuraciones electrónicas LS y HS. Los SMM de Co(II) se caracterizan por una relajación magnética más rápida (FMR) fuertemente dependiente del campo y temperaturas de bloqueo muy bajas, lo que provoca el predominio de señales incipientes en χ_M'' en campos bajos y máximos distintos solo en campos altos. Por otro lado, los SMM de Co(II) de HS cuentan con una relajación magnética más lenta (SMR) inducida por el campo que se produce a temperaturas de bloqueo más altas, aunque es casi independiente del campo magnético aplicado. Esta dinámica distinta del espín se explica por la mayor deslocalización del espín en la forma HS, que polariza las densidades de espín en átomos vecinos e incluso en algunos orbitales internos del propio ion metálico. Por lo tanto,

la inversión de giro se vuelve más difícil y su velocidad se ralentiza.

En la presente tesis doctoral, difundimos un método preciso de análisis de la dependencia de la frecuencia y el campo magnético de la dinámica de relajación del espín en SMM mononucleares de Co(II) de HS y LS. Además, nuestras conclusiones sobre los mecanismos de relajación difieren ligeramente de las reportadas en la literatura. Aquí propusimos por primera vez la participación de un proceso intra-Kramer (IK) independiente de la temperatura (orden cero) a bajas temperaturas, lo que contribuye a un nuevo tema de discusión. Argumentamos que el proceso IK es el mecanismo más concordante para la inversión de espín en este tipo de sistema de Co(II) en lugar de un mecanismo independiente de la temperatura.

Para seguir avanzando en el camino de MM a MS, el camino transitado nos llevó a algunos nuevos resultados perspicaces que nos gustaría presentar a continuación. De hecho, estas ideas pueden proporcionar información crucial para aumentar el campo consolidado de MM y proporcionar rutas alternativas en el campo emergente de MS. Por lo tanto, la combinación inusual de propiedades químicas (redox y acidez de Brønsted o Lewis) y físicas (magnéticas y ópticas o luminiscentes) resultantes del metal y la contraparte del ligando en los complejos Co^{II}-PDI y TERPY permite diseñar materiales magnéticos avanzados multifuncionales y de respuesta múltiple para MS. nanotecnología En particular, aparecen como candidatos prometedores para nanodispositivos espintrónicos como capacitores de espín e interruptores, como se ilustra en la Figura R.2.

Se ha preparado una serie novedosa de nanoimánes moleculares de cobalto(II) con transición de espín mononuclear mediante el diseño de ligandos a partir de una serie de ligandos tridentados de *N*,*N*'-difenil-sustituidos con actividad redox multicanal (n-XPhPDI) que contienen sustituyentes de yodo, bromo o cloro aceptores de electrones en las posiciones *para* o *meta* de los anillos fenilo. Poseen actividad tanto de oxidación centrada en el metal como de reducción centrada en el ligando debido al carácter dual de donante σ y aceptor π de los ligandos n-XPhPDI no-inocentes. Se encuentra una correlación general del comportamiento redox con la naturaleza atractora de electrones de los sustituyentes del ligando, que son finalmente responsables de la diferente estabilidad termodinámica y cinética del cobalto(III) correspondiente y el radical π de tipo imida simple o doble. especies de anión cobalto(II) dependiendo del patrón de sustitución para o meta de los grupos fenilo terminales.

Esta serie de compuestos exhibe desde una transición de espín inducida térmicamente, completa y gradual, hasta su ausencia, incluidas las transiciones parciales. A lo largo de esta

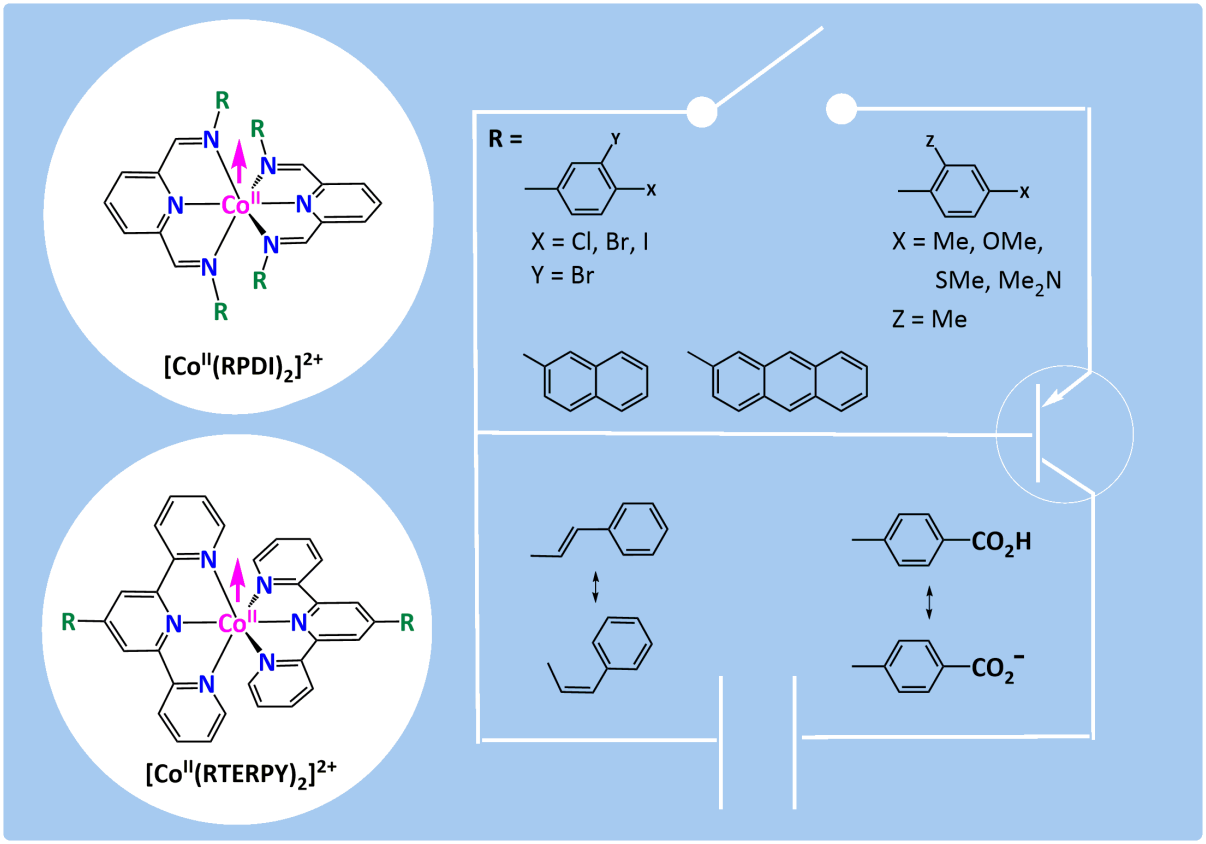

Figura R.2 Representación ilustrativa del potencial de los nanoimánes moleculares de espín de transición de cobalto(II) para construir componentes activos en circuitos espintrónicos altamente integrados para MS.

serie no se observa una correlación directa de la fenomenología del SCO con la naturaleza aceptora de electrones de los sustituyentes del ligando. Por lo demás, cabe destacar el papel que juega la red cristalina a través de su organización mediante enlaces covalentes o interacciones intermoleculares en el fenómeno SCO. Entonces, los efectos de los contactos intermoleculares de halógeno···halógeno parecen ser los responsables del comportamiento distintivo de SCO.

Estos complejos de cobalto(II)-n-XPhPDI muestran una dinámica de relajación de doble espín bajo un campo magnético con un carácter de relajación más lenta (SR, del inglés "slower-relaxing") y más rápida (FR, del inglés "faster-relaxing") según la magnitud del campo magnético aplicado o su naturaleza LS y HS. Este comportamiento SMM inducido por múltiples campos está dominado por IK o QTM más procesos Raman en regiones de baja y alta temperatura. Los mecanismos Raman observados son asistidos por fonones tanto ópticos como acústicos, que involucran estados virtuales que pueden atribuirse a modos vibratorios de baja energía. La presencia de procesos Raman de dos fonones a temperaturas más altas se confirmó por su débil o nula dependencia del campo magnético; sin embargo, al menos para la configuración LS, la fuerte influencia del campo magnético sugiere que IK, QTM o incluso mecanismos directos gobiernan la inversión de espín a temperaturas más bajas. Nuestros resultados y estudios teóricos respaldan que la mayor deslocalización del espín en la configuración HS ralentiza la relajación magnética.

Finalmente, nos gustaría señalar que el diseño y la implementación de múltiples propiedades SMM en esta familia única de compuestos octaédricos de cobalto(II) de SCO aparece como una ruta conveniente para obtener una nueva clase de materiales SCO/SMM multifuncionales y de respuesta múltiple. como candidatos de qubit de espín molecular multiestable en QIP. Por lo tanto, nuestros resultados sugieren la posibilidad de manipular las propiedades SMM de los iones de cobalto(II) de LS bajo el control de un campo magnético externo, abriendo así el camino para sus aplicaciones como dispositivos magnéticos moleculares en una futura máquina de computación cuántica basada en espín. El cambio de la dinámica de relajación del espín entre el campo magnético bajo FR y las formas SR de campo magnético alto podría, en principio, explotarse para desarrollar una nueva clase de transistores de espín molecular con efecto de campo magnético (MFE-MST). Se pueden suponer diferentes propiedades de coherencia cuántica para los complejos de cobalto(II) FR y SR al variar el campo magnético. A diferencia de los transistores electrónicos convencionales de las computadoras clásicas controlados por un voltaje eléctrico, el funcionamiento de los MFE-MST en las computadoras cuánticas estaría gobernado por un campo magnético. Los esfuerzos actuales se dedican a investigar el efecto del campo magnético en las propiedades de coherencia cuántica de esta nueva clase de nanoimánes moleculares de cobalto(II) con trasición de espín.

Esta serie única de complejos de cobalto(II)-PDI con actividad redox posee actividad electroquímica centrada tanto en el metal como en el ligando debido a la fuerte capacidad donadora de σ de los sustituyentes del ligando donador de electrones en los grupos fenilo y el carácter de aceptor π de el fragmento de ligando de piridindiimina central. A lo largo de esta serie se observa una correlación global entre el comportamiento redox y la naturaleza donante de electrones del *para*-sustituyente del ligando. Por otro lado, el comportamiento redox distinto del derivado *orto*, *para*-dimetil probablemente se deba a los efectos estéricos del grupo *orto*-metilo, por lo que las desviaciones más grandes de la planaridad del ligando causan una reducción significativa de los efectos del donante inductivo de tipo π del grupo *para*-metilo.

Esta investigación magnética y electroquímica combinada, junto con la información obtenida en el capítulo anterior, nos permitió obtener correlaciones magnetoestructurales y redox apropiadas, que ayudarían al diseño y la síntesis de materiales magnéticos SCO/SMM multifuncionales y de respuesta múltiple como candidatos para cargas multiestables. Dispositivos espintrónicos de almacenamiento como condensadores e interruptores de espín molecular. Esta nueva clase de nanoimán molecular triplemente térmico, magneto y electro-conmutable posee múltiples estados redox y de espín basados en metales o ligandos, que se interconvierten reversiblemente bajo diferentes estímulos externos (temperatura, campo magnético y potencial redox). La multiestabilidad magnética y electrónica informada aquí ilustra el potencial de las moléculas SCO/SMM multifuncionales y de respuesta múltiple en los campos emergentes de la espintrónica molecular y la computación cuántica.

Una familia única de nanoimánes moleculares de cobalto(II) de transición de espín luminiscente muestra la coexistencia de diferentes propiedades magnéticas y de luminiscencia en estado sólido y en solución, según el ligando, y la naturaleza y el número de disolvente de cristalización. En esta familia se observó una transición gradual completa, parcial HS ↔ LS o su ausencia con la aparición de relajación más rápida (FR) o relajación más lenta (SR) dependiendo de la configuración predominante LS o HS de los complejos de cobalto(II) en baja temperatura.

Además, hay un ajuste de solvato dual del comportamiento SMM inducido por campo y las propiedades de luminiscencia en algunos casos. En este sentido, el carácter irreversible del proceso de deshidratación impide su uso como sensores de humedad. De lo contrario, la naturaleza reversible del proceso de desorción/adsorción de acetonitrilo abre el camino para su uso como sensores químicos de compuestos orgánicos volátiles (COV) de interés biológico o industrial.

El estudio de su actividad fotofísica en solución denota la ocurrencia de una extinción parcial de la luminiscencia del ligando promovida por el metal, que se acompaña de un cambio significativo de la intensidad de emisión y la energía con la polaridad del solvente, lo que los convierte en candidatos prometedores para interruptores de espín en la detección química. La prueba de concepto de un interruptor de solvato de espín luminiscente proporciona información detallada sobre cómo se puede utilizar esta nueva clase de SCO/SMM

luminiscentes para diseñar dispositivos opto-espintrónicos en el campo emergente de MOS. Además, nuestros resultados sugieren la posibilidad de leer el estado de espín de estos SCO/SMM en estado sólido a través de métodos ópticos, lo que representa un paso esencial en el desafiante camino hacia los qubits ópticamente direccionables.

Los esfuerzos actuales se dedican a investigar la reactividad fotoquímica hacia la reacción de cicloadición intermolecular en esta familia única de SCO/SMM luminiscentes conmutables por solvato. El objetivo es obtener una fotoconmutación de las propiedades de coherencia cuántica tras la irradiación de luz ultravioleta para aplicaciones futuras como prototipos de bits cuánticos de espín molecular (qubits) direccionables ópticamente en el procesamiento de información cuántica (QIP).

Se ha obtenido también un nuevo par de sales isomórficas de perclorato y hexafluorofosfato del complejo mononuclear de cobalto(II) con un complejo mononuclear de cobalto(II) con un ligando fotoactivo trans (*E*)-estirilterpiridina, que exhibe un ajuste de contraanión de la transición de espín asistida térmicamente y relajación magnética lenta inducida por campo en estado sólido. Un estudio preliminar de su actividad fotoquímica respalda la aparición de una fotoisomerización del ligando geométrico cis-trans (*Z*/*E*) tras la irradiación con luz UV en solución. Los esfuerzos actuales están dedicados a investigar la fotoconmutación de la dinámica de espín y las propiedades de coherencia cuántica en la fotoisomerización del ligando geométrico cis-trans (*Z*/*E*) en este par único de SCO/SMM, ya sea en solución o en medios dispersos (solución sólida), para sus futuras aplicaciones como prototipos de fotointerruptores cuánticos de espín molecular en espintrónica molecular y nanotecnologías de computación cuántica.

Finalmente, en el último capítulo, presentamos un nuevo sistema molecular dinámico sensible al pH basado en un complejo de cobalto(II) SCO mononuclear en forma de un par de isómeros de pH. Constituye un ejemplo único de cómo el control de una sola entrada (pH) puede producir cambios reversibles en las propiedades ópticas (luminiscencia), redox y magnéticas (transición de espín y dinámica de espín), ya sea en solución o en estado sólido.

La transición de espín asistida térmicamente y la relajación magnética lenta inducida por campo coexisten en estado sólido con iones Co^{II} octaédricos de "relajación más rápida" (FR) o "relajación más lenta" (SR) inducidos por campo en el estado LS, dependiendo del ligando protonación. Se produce un aumento progresivo de la luminiscencia en la región UV con los equilibrios ácido-base en solución entre las formas protonadas, hemiprotonadas y desprotonadas, que pueden interconvertirse reversiblemente con la variación del pH. También muestran la oxidación de un electrón del complejo paramagnético Co^{II} de LS al complejo diamagnético de Co^{III} de LS en solución, cuya reversibilidad se pierde parcialmente al disminuir el pH, pero se restaura al aumentarlo.

La multiestabilidad óptica, electrónica y magnética reportada a lo largo de esta serie de transferencia de protones de complejos mononucleares de cobalto(II) ilustra el potencial de las moléculas dinámicas SCO/SMM, ofreciendo fascinantes posibilidades como dispositivos magnéticos avanzados multifuncionales y de respuesta múltiple para espintrónica molecular y computación cuántica como quimiointerruptores cuánticos de espín para detección de pH.

Con suerte, nuestros resultados abrirán un camino hacia el diseño de qubits de espín molecular operativos o matrices de qubits, proyectando la implementación física de una nueva clase de materiales multifuncionales eléctricos, ópticos, químicos y magnéticos para QIP. Una vez identificados los criterios de diseño clave para mejorar el rendimiento de SCO y SMM de los complejos mononucleares de cobalto(II)-PDI y TERPY, se deben abordar dos desafíos críticos para lograr este objetivo: (i) identificar las principales fuentes de decoherencia cuántica en SCO/SMMs de cobalto(II), (ii) construir matrices supramoleculares de SCO/SMMs de complejidad creciente con interacciones intermoleculares muy débiles (pero no despreciables) y potencialmente conmutables, y (iii) depositar los SCO/SMMs moleculares y sus arranjos supramoleculares sobre superficies y otros soportes sólidos.